Université Paris 7 Diderot
UFR de Physique

THÈSE D'HABILITATION
À DIRIGER DES RECHERCHES

Présentée par

Stéphane CORBEL

Universalité des jets relativistes dans les trous noirs accrétants

---

Soutenue le 3 décembre 2007 devant le jury composé de :

Prof. Jonathan E. Grindlay	Rapporteur
Prof. Etienne Parizot	Rapporteur
Prof. Guy Pelletier	Rapporteur
Prof. Philip Kaaret	Examinateur
Dr. Robert Mochkovitch	Examinateur
Prof. Peter von Ballmoos	Examinateur

Service d'Astrophysique, DSM/DAPNIA/SAp, CEA/Saclay
Orme des Merisiers, bât. 709
91191 Gif sur Yvette cedex
France

On regarde en l'air et l'on ne voit pas ce que l'on a à ses pieds.
— Lucien

À

Claire,
Juliette, Yoen et Pablo

Table des matières

Table des figures

Liste des acronymes

ADAF : Advection Dominated Accretion Flow
AGN : Active Galactic Nuclei, équivalent de noyau actif de galaxie
ASM : All Sky Monitor. Instrument à bord de RXTE
ATCA : Australia Telescope Compact Array
AXP : Anomalous X-ray Pulsar
BATSE : Burst And Transient Source Experiment (à bord de CGRO)
BL Lac : (ou BL Lacertae) sous type de blazar
CDAF : Convection Dominated Accretion Flow
CGRO : Compton Gamma-Ray Observatory
FRI/II : Fanaroff–Riley Type I ou II
Γ : Facteur de Lorentz
GBI : Green Bank Interferometer
GRB : Gamma-Ray Burst ou sursaut gamma
GRIP-2 : Gamma-Ray Imaging Payload 2
HID : Hardness Intensity Diagramm (Diagramme Intensité – Dureté X)
HST : Hubble Space Telescope
ISCO : Inner Stable Circular Orbit. Dernière orbite stable du dique d'accrétion
JDAF : Jet Dominated Accretion Flow
LINER : Galaxie de type Low-Ionisation Nuclear Emission Region
LLAGN : Low Luminosity Active Galactic Nuclei
L_{Edd} : Luminosité d'Eddington.
MCD : Multi-Color Disc : Modèle de disque d'accrétion
MHD : Magneto HydroDynamique
MOST : Molonglo Observatory Synthesis Telescope
NAG : Noyau Actif de Galaxie
NLSey : Galaxie de type Narrow Line Seyfert
PCA : Proportional Counter Array. Instrument à bord de RXTE
QPO : Quasi-Periodic Oscillation
RXTE : Rossi X-ray Timing Explorer
SED : Spectral Energy Distribution
SNR : SuperNova Remnant
SGR : Soft Gamma Ray Repeater
SSC : Synchrotron Self Compton
ULX : Ultra Luminous X-ray Sources

VLA : Very Large Array
VLBA : Very Long Baseline Array
VLBI : Very Long Baseline Interferometry
VLT : Very Large Telescope
XRB : X-Ray Binary ou système binaire X

Première partie

Informations liminaires

Chapitre 1
Contexte général

D'un oeil, observer le monde extérieur, —
de l'autre regarder au fond de soi-même.
— Amedeo Modigliani

1.1 Introduction historique

L'astronomie observationnelle est resté longtemps cantonnée à l'étude des astres par les télescopes optiques au sol. Une nouvelle vision de l'Univers s'offrit à nous, lorsque les progrès techniques permirent d'accéder à de nouveaux domaines de longueur d'onde, en plaçant des détecteurs au dessus de l'atmosphère terrestre. L'accès au ciel X et γ révéla la présence d'une population de sources de haute énergie (Giacconi et al. 1962), dont on sait aujourd'hui qu'elles représentent les derniers stades de l'évolution stellaire. La source d'énergie de ces systèmes étant l'accrétion, il apparut essentiel de mieux les comprendre, car il s'agissait d'un laboratoire unique pour tester la physique sous des conditions extrêmes – pression, température, densité, ... Trois décades exploratoires ont suivi cette découverte initiale, pendant lesquelles les différents observatoires mis en place ont révélé tout un bestiaire d'astres exotiques : trous noirs, pulsars, magnétars, sources Atoll et Z ...

Néanmoins, à cette époque pionnière, les observations au sol n'ont évidemment pas cessé pour autant. On montrait alors que ces sources X pouvaient être très variables. Leur étude fut rarement conduite dans différents domaines de longueur d'onde. Les émissions correspondantes devaient être d'origine physique différente, puisque des corrélations ou anti-corrélations entre les intensités de ces rayonnements étaient mises à jour. On peut voir un des premiers exemples d'observations simultanées en X et radio de Cyg X−1 en 1971 (Figure 1.1). Par la suite, nous verrons que ces premières observations comportaient déjà partiellement l'essence de ce que nous allons discuter dans ce mémoire. Néanmoins, ces aspects ne furent pas jugés essentiels à cette époque pionnière du début de l'astronomie des hautes énergies, où il fallait arpenter l'espace ouvert par l'ouverture de cette nouvelle frontière.

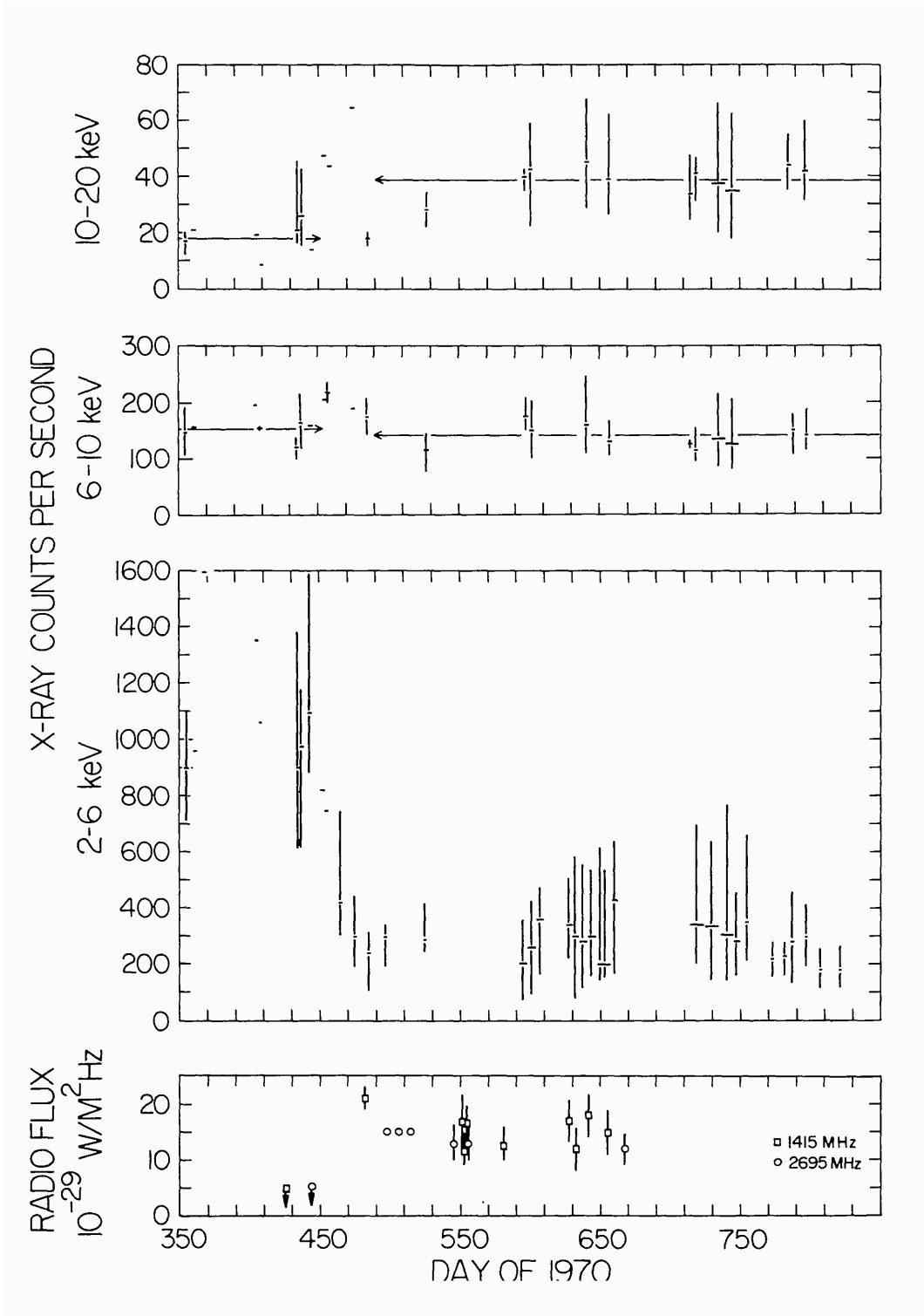

FIG. 1.1 – Observations historiques de Cyg X−1 en 1971. (Haut) : Taux de comptage *Uhuru* de Cyg X−1 dans trois bandes du domaine X. (Bas) : Courbe de lumière de Cyg X−1 aux fréquences radio de 1415 et 2695 MHz. Figure extraite de Tananbaum et al. (1972).

1.2 Trous noirs, accrétion et éjection

Bien qu'étant les objets les plus exotiques de l'Univers, les trous noirs sont aussi les plus simples. En effet, comparé à la multitude de paramètres nécessaires pour caractériser entièrement une planète par exemple, un trou noir isolé est entièrement décrit par sa masse, son taux de rotation et éventuellement sa charge électrique. Étant isolés, ces trous noirs n'ont quasiment aucune chance d'être détectés. Compte tenu de la fréquence – plus de la moitié – des étoiles en couple, une quantité de trous noirs se trouve aujourd'hui dans des systèmes binaires – dits systèmes binaires X ou XRB – après l'évolution terminale de l'étoile la plus massive. En plus de ces trous noirs stellaires dans les binaires, Salpeter (1964) suggéra que le rayonnement extrême des noyaux actifs de galaxie pouvait être expliqué par la présence de trous noirs super-massifs en leur centre. Les trous noirs sont trahis par leurs effets sur le rayonnement issu des processus d'accrétion et sur leur environnement.

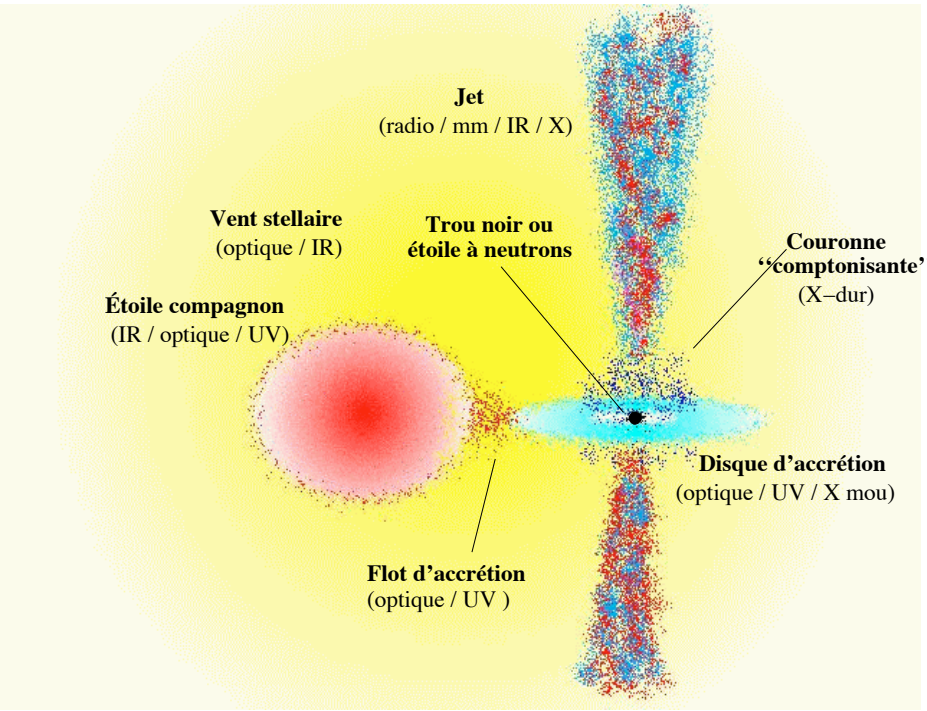

FIG. 1.2 – Contribution des composantes d'un système binaire à l'émission dans les différents domaines de longueur d'onde.

En effet, pour les trous noirs stellaires dans des systèmes binaires X de masse $\sim 10\ M_\odot$, la matière accrétée – par vent stellaire ou débordement du lobe de Roche – transite vers la sphère d'influence du trou noir par l'intermédiaire d'un disque d'accrétion, suite au transfert du moment angulaire vers l'extérieur du disque. Tout en s'approchant du trou noir, cette matière perd de l'énergie potentielle qui se retrouve ultérieurement rayonnée dans les X sous forme d'une émission de type corps noir pour les systèmes binaires ou dans l'optique-ultraviolet pour les trous noirs super-massifs – de 10^6 à $10^9\ M_\odot$. De plus, les spectres X et γ indiquent la présence d'une composante additionnelle d'émission, la couronne dans le modèle standard, où les photons du disque seraient diffusés par effet Compton inverse sur un plasma chaud – kT $\sim$ 100 keV. Ces sources sont très variables et évoluent entre des périodes de repos (aussi nommée

quiescence) – l'essentiel de leur vie – et des phases d'activité, où les caractéristiques spectrales et temporelles changent de la radio aux domaines X et γ (McClintock & Remillard 2006).

Au delà du domaine traditionnel d'étude des systèmes binaires – X et γ –, les années 90 ont vu le développement des observations multi-longueurs d'onde. Les mesures optiques et infrarouges étaient déjà largement utilisées pour l'étude du compagnon stellaire et/ou des propriétés du disque d'accrétion. En revanche, les observations radio permettant l'identification de la contrepartie radio et sa localisation précise pouvaient parfois révéler un sursaut intense dans ce domaine de fréquence. Il était associé à la réactivation du système à la sortie de la phase de repos. Lors de ces phases éruptives, l'émission radio synchrotron fut attribuée à un évènement transitoire d'éjection de plasma relativiste (e.g. Han & Hjellming 1992). Les systèmes binaires X et les noyaux actifs de galaxie présentaient donc des ingrédients similaires : un trou noir, un disque disque d'accrétion et la présence de jets relativistes.

La formation des trous noirs super-massifs n'est pas aussi bien comprise que celle des trous noirs stellaires qui résultent de l'effondrement gravitationnel d'étoiles massives. La forte luminosité de certains noyaux actifs de galaxie (NAG ou AGN) indique que de la matière transite vers l'objet compact grâce à un disque d'accrétion. Il pourrait donc s'agir de leur principal mode de croissance. Néanmoins, il est aussi possible que des interactions dynamiques puissent contribuer à la croissance de ceux-ci (Begelman et al. 1984). L'existence d'une corrélation entre la masse des trous noirs super-massifs et la dispersion en vitesse des étoiles de la galaxie hôte (Ferrarese & Merritt 2000; Tremaine et al. 2002) semble suggérer une connexion très forte entre la formation des galaxies et la croissance des trous noirs. Comme nous le verrons ultérieurement, il est possible qu'il existe une population de trous noirs de masse intermédiaire – 10^2 à 10^4 $M_\odot$– éventuellement lié aux amas stellaires denses (e.g. Portegies Zwart et al. 1999).

Ces deux ou trois populations de trous noirs – aux environnements variés – peuvent donc offrir un cadre de travail permettant de tester les propriétés de l'accrétion et de l'éjection en présence de champ gravitationnel intense. Sachant que l'échelle de temps d'évolution des phénomènes étudiés est inversement proportionnelle à la masse du trou noir, les systèmes binaires présentent donc l'avantage de pouvoir évoluer très rapidement, en tout cas largement compatible avec la durée de vie d'un chercheur. L'idée est ensuite d'essayer d'unifier les propriétés physiques de ces populations de trous noirs.

1.3 Questions fondamentales

Compte tenu de la similarité des "ingrédients" dans les systèmes binaires X et les noyaux actifs de galaxie, un certain nombre de questions se présentent à nous. Certaines de ces interrogations sont très générales, tandis que d'autres demandent d'aller dans le détail. Elles peuvent se diviser en trois grandes catégories :

- **Propriétés fondamentales du flot d'accrétion :** Comment est transférée la matière à travers le disque d'accrétion ? Quel(s) est(sont) le(s) paramètre(s) déclencheur(s) d'une phase d'activité ? Comment évolue le taux d'accrétion dans le disque ? Comment se forme la couronne de plasma chaud supposée englober l'objet compact ? Comment évolue la géométrie du système en fonction de l'évolution du taux d'accrétion ? Comment rayonne un disque d'accrétion ? L'accrétion permet-elle au disque d'atteindre la dernière orbite stable autour d'un trou noir ? Si oui, est-il possible de tester la relativité générale dans la limite du champ gravitationnel intense ? L'étude des disques d'accrétion permettra-t'elle de mesurer le taux de rotation des trous noirs ?

- **Propriétés fondamentales des phénomènes d'éjection :** Comment, pourquoi et sous quelles conditions les jets relativistes se forment ? Est-ce que la puissance des jets est issue du flot d'accrétion ou existe-t-il un moyen d'extraire l'énergie de rotation du trou noir pour la conduire aux jets ? Comment sont accélérés et collimatés les jets ? Existe-t-il plusieurs formes de jets ? Quelle est l'origine de ces différents jets ? Quelle est la composition des jets : matière ou rayonnement électromagnétique ? S'il s'agit de matière, est-elle baryonique ou leptonique ? Ces jets sont-ils une source de production de messagers non-photoniques : neutrinos ou particules de très haute énergie ?

- **Liens entre populations d'objets compacts :** Quelles sont les différences entre les flots d'accrétion autour d'un trou noir et autour d'une étoile à neutrons ? La physique de l'accrétion et de l'éjection est-elle similaire – par simple loi d'échelle – entre les trous noirs stellaires et les trous noirs super-massifs, en passant par les trous noirs de masse intermédiaire s'ils existent ? Quel est l'impact des jets relativistes sur le milieu interstellaire ou intergalactique ? Les jets ont-ils un rôle sur l'évolution des galaxies ?

D'une certaine façon, les réponses à ces questions ont été relativement limitées à cause de l'organisation historique de l'astronomie autour de domaines de longueur d'onde bien distincts. Chacune des composantes d'émission (jet/disque/couronne) de ces objets est associée à un rayonnement dans un ou plusieurs domaines. Après la découverte et le recensement des sources X ; l'effort fut porté, pendant des décennies, sur la compréhension des composantes individuelles à partir des propriétés d'émission dans UN domaine unique. À partir de la fin des années 90, l'approche multi-longueurs d'onde a considérablement modifié notre perception des couplages accrétion–éjection. C'est dans cette logique que mes travaux de recherche s'inscrivent, sachant que mon éventail observationnel s'étend de la radio aux γ. Je signalerai aussi que pour déterminer correctement les mécanismes physiques sous-tendant les propriétés d'émission observées, il est nécessaire d'avoir un modèle physique capable de reproduire les données spectrales – évolution en fonction de l'énergie – ET les données temporelles.

1.4 Organisation du manuscrit

Ce manuscrit est supposé retranscrire l'ensemble de mes activités – recherche, enseignement, encadrement et administration – depuis la fin de ma thèse. Durant cette période de huit ans, j'ai abordé différents thèmes de recherche qu'il me faut essayer de présenter de manière cohérente. L'essentiel de mes travaux concerne des phénomènes transitoires et dont l'évolution au cours du temps peut être très rapide. Il est donc essentiel de les anticiper en ayant mis en place des programmes de cible d'opportunité (ToO pour Target of Opportunity) que l'on peut activer lorsque nos critères de déclenchement sont réunis. J'ai eu pour cela l'occasion d'utiliser de nombreux observatoires au sol (ATCA, VLA, SEST, IRAM, VLT) ou spatiaux (XMM-Newton, Chandra, Hubble, RXTE, Integral, CGRO), avec une difficulté supplémentaire qui consiste à obtenir la simultanéité des observations !!! L'originalité de mes travaux réside dans l'utilisation systématique de tous les moyens observationnels accessibles, afin de comprendre la dynamique des couplages accrétion – éjection au sein des systèmes accrétants.

Le mode d'emploi de ce mémoire est le suivant. Après cette introduction générale, j'entre dans l'exposition des faits saillants liés à mes activités de recherche. Sachant que les publications associées sont généralement incluses dans le manuscrit, je n'ai pas souhaité extraire toutes les informations s'y trouvant. Je me suis en général limité à saisir une information pertinente avec l'intention de produire un scénario général et cohérent.

C'est pour cela que je présenterai en premier lieu (chapitre 2) la mise en évidence des jets

compacts associés à un état spectral de faible accrétion. En étudiant la distribution spectrale énergétique de ces trous noirs, je m'intéresserai aux mécanismes d'émission des binaires à haute énergie. Dans le chapitre 3, je présenterai les propriétés des jets le long des différents états spectraux et terminerai par un schéma d'unification. Ensuite, nous nous éloignerons du trou noir pour observer le résultat de l'interaction des jets avec le milieu environnant (chapitre 4).

Nous effectuerons ensuite une excursion hors de notre Galaxie pour étudier les trous noirs de masse supérieure aux trous noirs stellaires. Nous ferons alors une étape auprès des sources X ultra-lumineuses – ULX dans le chapitre 5 – et terminerons notre voyage au pays des trous noirs par une visite aux noyaux actifs de galaxie (chapitre 6). Je présenterais ensuite une discussion sur la distance d'un magnétar pour illustrer le cheminement – et la perspicacité nécessaire – pour imposer un résultat scientifique. La fin de ce mémoire présentera diverses contributions scientifiques qui ont jalonné mon parcours, ainsi qu'une description administrative de l'ensemble de mes activités au sein de la communauté nationale et internationale depuis mon recrutement à l'Université Paris 7.

Deuxième partie

Exposé synthétique des recherches

Chapitre 2
Ubiquité des jets compacts dans l'état dur

—Le soleil ne se lève que pour celui
qui va à sa rencontre.
—Henri Le Saux

2.1 Introduction : les états spectraux

Depuis la découverte des sources X accrétantes dans les années 60, il est rapidement apparu que ces objets étaient variables et que leurs propriétés évoluaient en fonction du temps. Il est alors devenu adéquat de les décrire en terme d'états spectraux. La première transition d'état, observée par *Uhuru* sur Cyg X−1, correspondait à une décroissance d'un facteur quatre du flux 2–6 keV, accompagnée d'une augmentation d'un facteur deux de l'émission dans la bande 10–20 keV (Figure 1.1). Ce changement d'état fut décrit comme une transition d'un état mou – "soft" – vers un état dur – "low" – (Tananbaum et al. 1972), avec un changement significatif de la forme du spectre X (Figure 2.1). Comme nous l'avions vu en introduction (Figure 1.1), Hjellming et al. (1975) découvrirent, à cette occasion, une source radio associée à Cyg X−1 avec un rayonnement radio corrélé avec les X durs et anti-corrélé avec les X mous lors de la transition (Tananbaum et al. 1972; Hjellming et al. 1975).

Par la suite, l'amélioration des techniques a permis la découverte de nouvelles sources, ainsi qu'une meilleure description de leurs propriétés X. Compte tenu des propriétés spectrales X et γ, il est apparu que deux composantes principales dominaient le spectre à haute énergie : une composante thermique vers les X mous – définis de 0.1 à 10 keV – et une loi de puissance coupée jusqu'à quelques centaines de keV. Une troisième composante en loi de puissance très pentue pouvant aller jusqu'à quelques MeV est parfois détectée. La composante thermique correspond au rayonnement optiquement épais de corps noir du disque d'accrétion en accord avec le modèle de Shakura & Sunyaev (1973) avec une température au bord interne

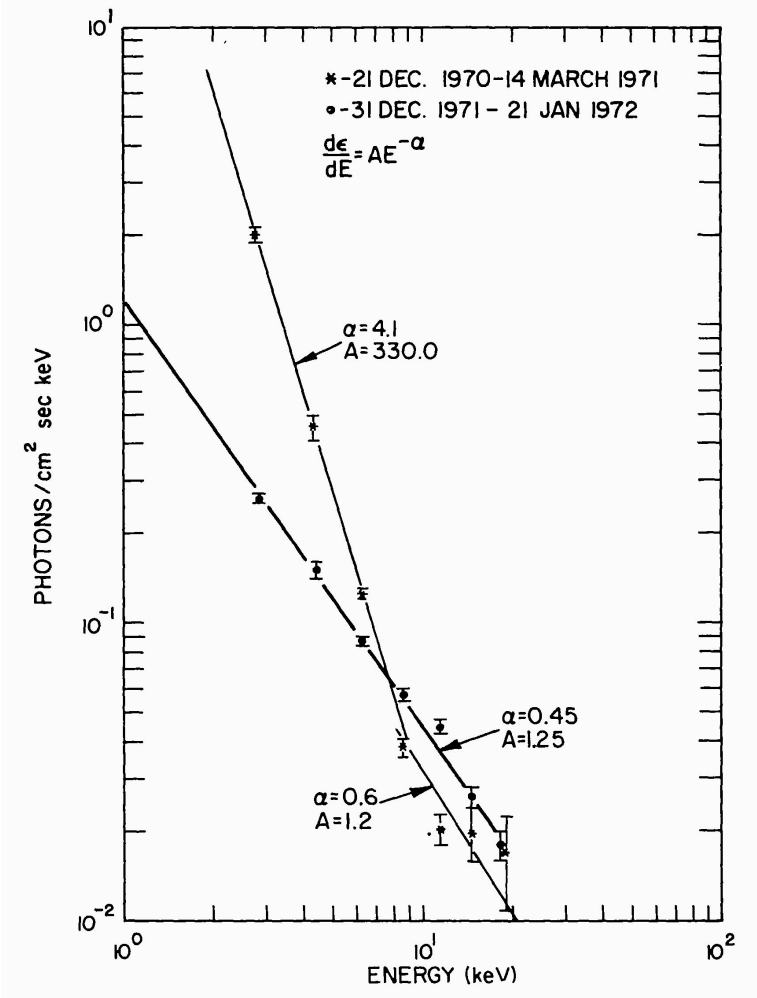

FIG. 2.1 – Spectres X moyens de Cyg X−1 avant et après la transition état mou ⇒ état dur. Figure extraite de Tananbaum et al. (1972).

du disque de l'ordre de 0.5 à 2 keV. Historiquement, la loi de puissance coupée est expliquée par l'émission Compton inverse d'une distribution thermique d'électrons et de positons (la "couronne") de température de $\sim$ 100 keV avec les photons du disque d'accrétion (Shapiro et al. 1976; Sunyaev & Titarchuk 1980). La géométrie de ce milieu optiquement mince que constitue la couronne n'est pas vraiment déterminée à ce jour et est parfois schématiquement représentée par un milieu sphérique englobant l'objet compact et parfois recouvrant partiellement le disque d'accrétion (Nowak 2003). En fonction de la domination de l'une ou l'autre de ces composantes, deux états spectraux principaux sont mis en évidence : l'état intense et mou – "high/soft state" – et l'état bas et dur – "low/hard state". À très forte luminosité X – proche de la limite d'Eddington pour un trou noir –, l'état très intense – "very high state" – fut mis en évidence dans les années 1990 (Miyamoto et al. 1991). Avec l'avènement de *RXTE* et ses observations très fréquentes, ajoutées à la prise en compte des propriétés temporelles – forme du spectre de puissance, oscillations quasi-périodiques, ...–, il est devenu possible de mieux définir ces états spectraux.

Deux approches ont été proposées : l'une basée sur la méthode historique de la forme des spectres X et sur la luminosité de la source (pour plus de détails, voir McClintock & Remillard

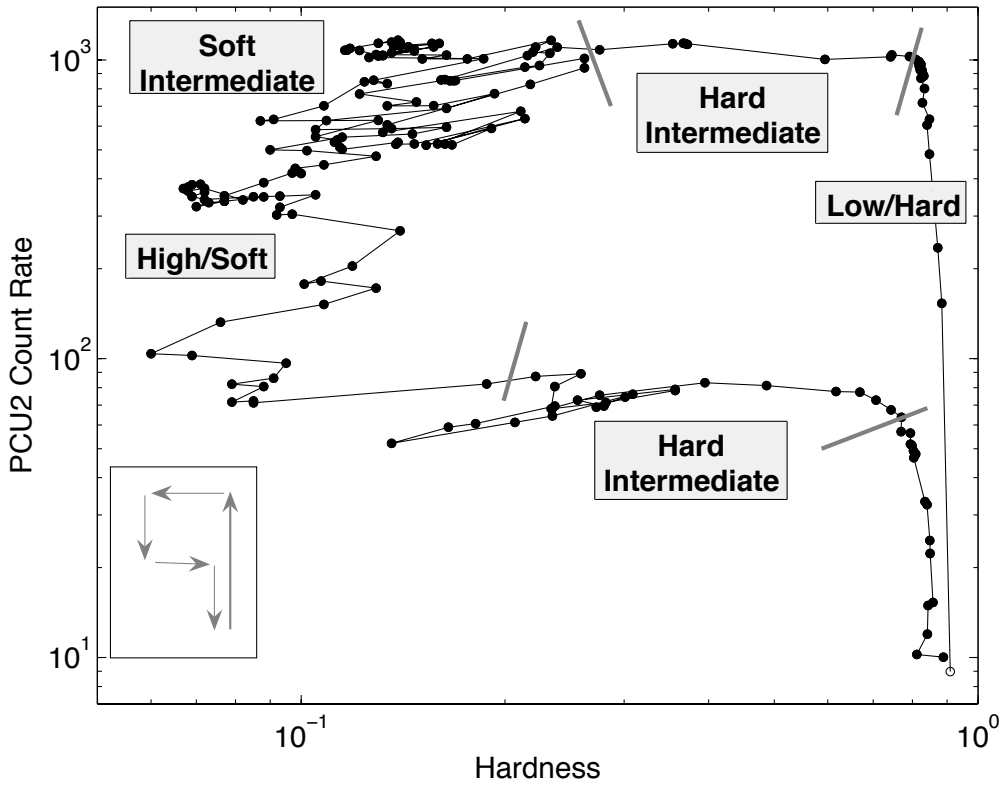

FIG. 2.2 – Diagramme intensité – dureté de GX 339−4 lors de son sursaut d'activité en 2002/03 (Belloni et al. 2005). L'insert à gauche indique l'ordre d'évolution dans ce diagramme. Figure adaptée de Belloni et al. (2005).

2006; Remillard & McClintock 2006) et une autre en cours de définition essentiellement liée aux transitions entres états (Homan & Belloni 2005; Belloni 2005). Pour cela, Homan & Belloni (2005) et Belloni (2005) utilisent une représentation du taux de comptage X en fonction de la dureté du spectre – les diagrammes intensité–dureté ou HID, voir figure 2.2. Dans ce cas, les branches de ce diagramme définissent les états spectraux (Figure 2.2). Ces deux groupes sont en accord sur la définition des états spectraux historiques, "high/soft et low/hard states", que nous appellerons par la suite l'état thermique – "thermal dominant state" – et l'état dur – "hard state" – respectivement, pour reprendre la terminologie de McClintock & Remillard (2006). Pour les autres, nous adapterons la terminologie de Homan & Belloni (2005) et Belloni (2005) en choisissant de nommer les branches horizontales du HID (voir figure 2.2) comme l'état intermédiaire dur et l'état intermédiaire mou – quasi équivalent à l'état très intense ou le "Steep Power Law state" de McClintock & Remillard (2006).

Ces dernières années, des progrès considérables ont été réalisés au niveau de la compréhension de la géométrie des disques d'accrétion des objets compacts – trous noirs essentiellement. On sait maintenant que la plupart des systèmes binaires X – XRB – sont transitoires et se trouvent habituellement en phase de repos, dite de "quiescence" en anglais. Les binaires entrent périodiquement – intervalle de quelques années à quelques décades – dans des phases d'activité où la luminosité X peut augmenter de plus de six ordres de grandeur en l'espace de quelques jours, phases durant lesquelles elles entrent successivement dans les différents états spectraux décrits ci-dessus. Les observations X réalisées à haut niveau de flux – $L_X \sim 10^{37-39}$ erg s^{-1}–

ont révélé des raies du Fer Kα gravitationnellement élargies (Miller et al. 2002; Reynolds & Nowak 2003) indiquant que le disque d'accrétion atteignait la dernière orbite stable – ISCO – autour du trou noir. De plus, des oscillations quasi-périodiques – QPO – à haute fréquence (100 – 500 Hz) sont détectées pour certains de ces systèmes (Remillard et al. 2002; McClintock & Remillard 2006). Actuellement, on pense que ces QPO proviendraient d'une zone proche du bord interne du disque d'accrétion standard de type Shakura & Sunyaev (1973), et donc constitueraient un argument de plus pour dire que le disque d'accrétion atteint l'ISCO lors des phases très brillantes. La nature de la composante dominant le spectre X/γ dans l'état dur est le sujet d'un débat très actif au sein de la communauté. Il est en partie dû aux nombreuses découvertes que nous allons présenter dans ce chapitre.

2.2 Mise en évidence des jets compacts dans l'état dur

Suite aux variations récurrentes du taux d'accrétion sur l'objet compact, les systèmes binaires sont connus pour transiter entre différents états spectraux (voir section 2.1) parmi lesquels l'état dur est l'un des plus fréquents. Il est observé en début et fin de sursaut (c.f. la branche verticale droite du HID, Figure 2.2). Dans cette partie, nous allons nous intéresser aux particularités de cet état avec la mise en évidence des jets compacts. La présence des jets compacts dans l'état dur a considérablement modifié notre vision des systèmes binaires ces dernières années. En effet, la prise en compte de ces jets pourrait imposer de sérieuses modifications du modèle standard "disque + couronne".

Ce n'est que vers le milieu des années 90, que nous avons procédé à l'étude de ces systèmes en dehors de la phase brillante de sursaut. Pour cela, nous nous sommes beaucoup intéressés à l'un des deux seuls candidats trous noirs quasi-persistents – connu à l'époque – de notre Galaxie : GX 339−4 qui se trouvait la plupart du temps dans l'état dur. Cette source a maintenant un comportement similaire aux novae X avec une succession de périodes de repos et d'activité. Nous avons par la suite élargi notre étude à l'ensemble des sources X en phase éruptive – essentiellement détecté par le moniteur de rayons X ASM à bord de RXTE.

Les fréquentes observations radio de GX 339−4 ont mis en évidence deux propriétés particulières de l'état dur (e.g. Corbel et al. 2000). Tout d'abord, cet état se caractérise par la présence systématique d'une source radio ayant une densité de flux plutôt faible – de l'ordre de quelques mJy. De plus, le spectre radio est légèrement inversé ou plat ($\alpha \geq 0$), avec la densité de flux $S_\nu \propto \nu^\alpha$, c'est à dire que le spectre radio est légèrement montant quand la fréquence augmente (voir Figure 2.3). Suite aux pertes d'énergie par expansion adiabatique, la présence d'une émission radio quasi-persistante implique la nécessité d'avoir une régénération quasi-continue du plasma relativiste. La source radio variant typiquement sur des échelles de temps de la journée implique une température de brillance de plus de 10^7 K et donc, fort probablement, un mécanisme d'émission non thermique comme le rayonnement synchrotron.

Dans l'état dur, l'observation des spectres radio plats ou inversés peut s'expliquer de façon relativement simple. Pour cela, il suffit de considérer que l'on observe un rayonnement provenant de différentes régions non résolues spatialement. On peut imaginer un jet de forme conique, la densité de plasma étant plus forte à la base de ce jet, ce milieu deviendra progressivement optiquement mince aux fréquences les plus basses au fur et à mesure que les particules accélérées s'éloignent de cette base. Ainsi, même avec une distribution d'électrons de la forme $N(E)\,dE \propto E^{-2}\,dE$, il est possible de produire des spectres plats. De tels modèles existent depuis fort longtemps pour expliquer l'émission radio du coeur compact des noyaux actifs de galaxie (e.g. Blandford & Konigl 1979). Hjellming & Johnston (1988) et Falcke & Biermann (1996) discutent de l'application de ce genre de géométrie aux systèmes binaires.

Les observations interférométriques à très longues bases (avec le VLBA) de Cyg X−1

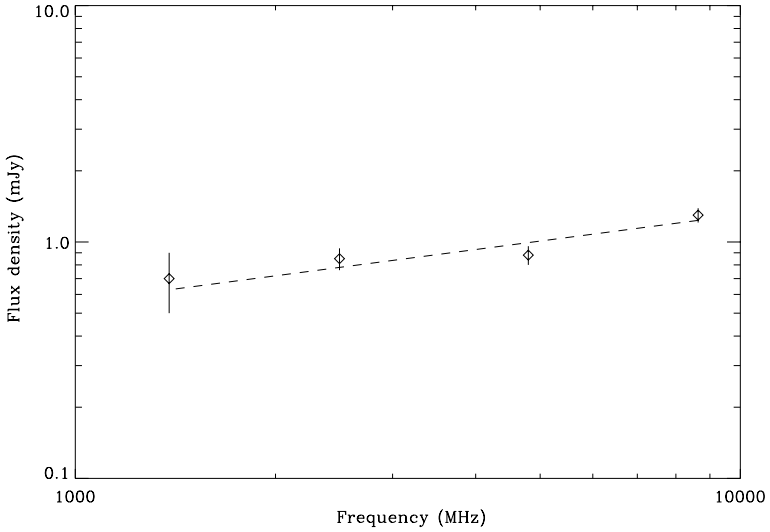

FIG. 2.3 – Spectre radio du jet compact de XTE J1550−564 mesuré avec ATCA le 1^{er} juin 2000. La ligne en pointillé correspond à l'ajustement des données avec une loi de puissance d'indice +0.37. Figure extraite de Corbel et al. (2001b).

(Stirling et al. 2001) ou de GRS 1915+105 (Dhawan et al. 2000; Fuchs et al. 2003) dans l'état plateau ont résolu spatialement la source radio associée au trou noir dans l'état dur sous la forme d'une structure collimatée de quelques millisecondes d'arc que l'on peut qualifier de jet compact. En prenant en compte la distance de ces sources, nous obtenons une taille caractéristique de ces jets de l'ordre de quelques dizaines d'unités astronomiques pour les régions à l'origine du rayonnement radio.

On peut aussi inférer la présence d'un jet compact à partir de l'action à long terme du jet sur le milieu interstellaire comme pour la nébuleuse radio de Cyg X−1 (Gallo et al. 2005a) ou les jets larges – quelques minutes d'arc ou parcsec – de 1E 1740.7−2942 (Mirabel et al. 1992) et de GRS 1758−258 (Martí et al. 2002) – quoique dans ces deux derniers cas, cela pourrait résulter de l'action répétée d'éjections impulsives.

On peut aussi ajouter que pour le trou noir GX 339−4 nous avons pu mesurer un taux de polarisation linéaire de l'ordre de 2 % (Corbel et al. 2000). Ce qui est conforme aux attentes théoriques d'un milieu optiquement épais si l'on tient compte d'un certain niveau de dépolarisation Faraday (maximum théorique de 12%). L'orientation du vecteur électrique dans les cartes de polarisation semble constante sur une période de deux ans (Corbel et al. 2000) et se trouve dans la même direction que le jet large – et optiquement mince – que nous avons détecté après le sursaut de 2002 de GX 339−4 (Gallo et al. 2004, voir chapitre 4), ce qui indique clairement qu'il existe une direction privilégiée dans ce système. De même, en réévaluant les observations de GS 2023+338 par Han & Hjellming (1992), il apparait là aussi un niveau de polarisation linéaire de l'ordre de quelques pour-cents avec un angle de position constant pendant deux mois. Il existe donc une orientation privilégiée dans ce système – celle du jet compact.

Finalement, les caractéristiques observationnelles de l'émission radio des trous noirs dans l'état dur – densité de flux faible, spectre inversé ou plat, faible niveau de polarisation avec une direction privilégiée, faible dimension – s'expliquent relativement bien si l'on considère que nous avons affaire au rayonnement synchrotron d'un milieu auto-absorbé d'une structure en jet

conique que nous avons nommé jet compact. Les jets compacts des systèmes binaires ont été mis en évidence pour GX 339−4, une source en permanence dans l'état dur dans les années 90. Mais avec son entrée en repos en 1999 (Corbel et al. 2000) et des sursauts en 2002, 2004, 2006 et 2007, GX 339−4 se comporte maintenant comme une nova X régulière. À chaque réactivation, nous avons assisté à la réapparition du jet compact (e.g. Gallo et al. 2004).

Les observations fréquentes (voir par exemple la section 3.3 et les publications associées) d'autres trous noirs dans l'état dur – aussi bien la phase initiale que finale du sursaut – indiquent que les jets compacts constituent une structure ubiquiste de l'état dur (e.g. Corbel et al. 2001b; Fender 2001; Corbel et al. 2004) et qu'il est nécessaire d'intégrer cette composante lorsqu'on veut modéliser les spectres d'émission de ces trous noirs. Nous reviendrons dans la partie 2.4 sur le bilan énergétique de ces jets compacts.

Il est à noter que les jets compacts ne sont pas uniquement l'apanage des trous noirs dans notre Galaxie et qu'il est fort probable que les étoiles à neutrons à faible champ magnétique – sources Atoll et Z – produisent elles aussi des jets compacts lorsqu'elles sont dans un état équivalent à l'état dur – de faible accrétion – des trous noirs stellaires (Migliari & Fender 2006).

2.3 Contribution des jets compacts en infra-rouge

Il est vite apparu que le rayonnement des jets compacts allait bien au delà du domaine classique du rayonnement synchrotron (c'est à dire le domaine radio). En effet, avec un spectre grimpant avec la fréquence, on pouvait s'attendre à une détection des jets compacts vers le millimétrique ou même l'infrarouge (proche ou lointain). Pour les coeurs compacts des NAG,

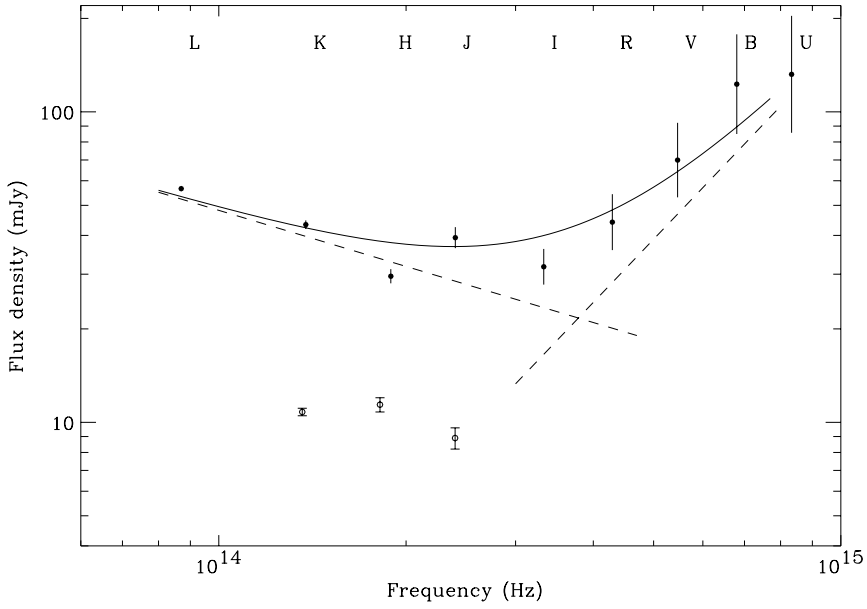

FIG. 2.4 – Densité de flux infrarouge et optique de GX 339−4 dérougis avec une extinction optique de $A_V = 3.7 \pm 0.3$ mag. Les cercles remplis correspondent aux observations de l'état dur de 1981 tandis que les cercles vides correspondent à un état dur en 1997. Pour les données 1981, les points sont ajustés par la somme de deux lois de puissance d'indice spectral –0.6 en infrarouge et + 2.1 en optique. Figure extraite de Corbel & Fender (2002).

on observe typiquement un changement de pente du spectre synchrotron du jet compact dès que l'on s'approche du domaine millimétrique (Bloom et al. 1994). La fréquence de coupure dépend de la dimension physique du jet à sa base et donc de la masse du trou noir (Falcke et al. 2004). Par simple loi d'échelle, elle serait donc attendue vers l'infrarouge moyen pour les trous noirs stellaires.

Pour Cyg X−1 ou XTE J1118+480, il fut démontré que le spectre plat du jet compact allait au moins de la radio au domaine millimétrique (Fender et al. 2000, 2001). De même, les variations corrélées de flux radio et infrarouge dans GS 2023+338 suggéraient la possibilité que le rayonnement des jets compacts se poursuivent jusqu'à l'infrarouge (Fender 2001). En réanalysant des données d'archives du sursaut historique de GX 339−4 en 1981, nous avons observé pour la première fois (Corbel & Fender 2002) la transition entre les régimes optiquement épais et optiquement mince du jet compact vers l'infrarouge proche (cf. Figure 2.4) en accord avec Falcke et al. (2004). Cela fut confirmé avec des données plus récentes de GX 339−4 (Corbel & Fender 2002; Homan et al. 2005) ou d'autres sources : XTE J1550−564 (Corbel et al. 2001b,a; Jain et al. 2001) ou 4U 1543−47 (Buxton & Bailyn 2004) par exemple. On peut noter que les variations optiques rapides de XTE J1118+480 ont elles aussi été interprétées comme étant une contribution synchrotron, probablement due au jet compact (e.g. Hynes et al. 2003).

Les étoiles à neutrons à faible champ magnétique montre de nouveau une similarité très forte avec GX 339−4. En effet, il faut signaler que Migliari et al. (2006) ont détecté avec *Spitzer* une composante non-thermique (Figure 2.5) probablement due au jet compact de 4U 0614+091. Ce résultat quasi-identique à nos observations de GX 339−4 (Figure 2.4) traduit aussi l'importance des jets compacts pour les étoiles à neutrons à faible champ magnétique. La fréquence de coupure du jet compact de 4U 0614+091 serait un facteur dix fois plus faible que celle de GX 339−4, peut-être lié à la différence de masse (ou de taux d'accrétion) entre ces deux objets (Migliari et al. 2006).

La détection de la fréquence de coupure vers l'infrarouge proche est importante, car elle permet de déterminer, dans le cadre des modèles radiatifs de jet (e.g. Markoff et al. 2005), la zone (ou la distance au trou noir) à partir de laquelle les particules commencent à être accélérées. Le problème de l'émission des jets compacts à haute énergie sera abordé dans la section 2.6.

2.4 Puissance des jets compacts

Une fois établi le fait que le rayonnement synchrotron du jet compact se poursuit au moins jusqu'à l'infrarouge proche, il est intéressant de calculer la puissance de ces jets compacts. Il s'agira d'un minimum car il demeure possible qu'ils contribuent aussi à plus haute énergie. Sachant que l'on ne peut pas appliquer les arguments standards du minimum d'énergie – on ne connaît pas la taille du jet –, on estime la luminosité synchrotron rayonnée par le jet compact en mesurant ses propriétés de la radio à l'infrarouge.

Ensuite il est nécessaire d'introduire une efficacité radiative η qui traduit le rapport de la puissance rayonnée à la puissance totale du jet. En effet, les pertes énergétiques sont liées à l'expansion adiabatique du plasma relativiste, plutôt qu'au rayonnement des particules. On tiendra éventuellement compte aussi des facteurs de correction liés au mouvement relativiste d'ensemble et des effets d'inclinaison. À partir de l'étude énergétique des éjections répétées de GRS 1915+105, Fender & Pooley (2000) établissent une valeur maximale de $\eta = 15\%$ pour cette efficacité radiative en accord avec la valeur maximale déduite par Blandford & Konigl (1979) pour les jets coniques. Par la suite nous prendrons une valeur conservatrice $\eta = 5\%$ (voir aussi Fender et al. 2001).

En prenant l'exemple de XTE J1550−564 le 1^{er} juin 2000 (Corbel et al. 2001b), la luminosité radio dans la bande 1 à 10 GHz est de 7×10^{28} erg s^{-1} pour une distance minimale de 2.5 kpc. Avec l'émission du jet compact qui s'étend jusqu'à l'infrarouge proche ($\sim 10^{14}$ Hz), on obtient une luminosité synchrotron radiative de l'ordre de 2×10^{34} erg s^{-1}, c'est à dire plusieurs pour-cents de la luminosité X de 5×10^{35} erg s^{-1} (bande 2–20 keV) mesurée le même jour.

Pour le cas de GX 339−4 où nous avons mesuré la coupure synchrotron en infrarouge (Corbel & Fender 2002) et où l'extinction optique est mieux contrainte, nous obtenons une luminosité synchrotron radiative aux environs de 10^{35} erg s^{-1} pour une distance de 4 kpc. Avec une efficacité radiative, η, de l'ordre de 5%, on obtient une puissance totale du jet compact de l'ordre de 2×10^{36} erg s^{-1}. Cette valeur pourrait augmenter sachant qu'il est possible que le jet possède aussi une composante d'énergie cinétique non négligeable, nous pouvons affirmer qu'il s'agit d'une valeur minimale extrême. Les observations X simultanées d'*Ariel 6* impliquent une luminosité X (1–200 keV) de 4×10^{37} erg s^{-1}, et donc que la puissance du jet compact représente au moins 5% de la luminosité bolométrique de GX 339−4 (Corbel & Fender 2002).

Fender (2001) obtient un résultat similaire pour Cyg X−1 en supposant que le rayonnement du jet compact se poursuit jusqu'à l'optique – impossible à mesurer à cause de l'émission thermique de l'étoile géante compagnon. Il est maintenant acquis que le rayonnement synchrotron du jet compact est continu de la radio jusqu'à l'infrarouge proche. Le résultat essentiel est que la puissance du jet est d'au moins 10% de la luminosité X pour tout trou noir dans l'état dur.

Pour le système à étoile à neutrons 4U 0614+091 mentionné précédemment, Migliari et al. (2006) en déduisent que la puissance du jet compact est comprise entre 0.05% et 5% de la luminosité bolométrique X. Il semblerait donc que le rapport puissance du jet sur luminosité

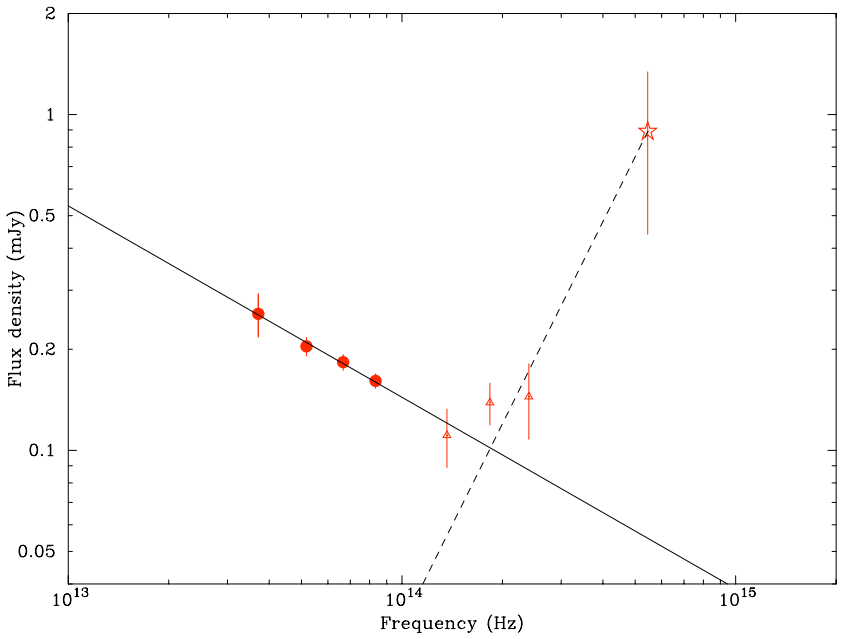

FIG. 2.5 – Observations infrarouges *Spitzer/IRAC* (cercles), UKIRT JHK (triangles) et niveau optique moyen (étoile) du système à étoile à neutrons 4U 0614+091. La ligne continue correspond à une approximation des données *Spitzer* en loi de puissance d'indice -0.57 ± 0.04 –typique du synchrotron optiquement mince –, tandis que la ligne discontinue (de pente +2) représente la loi de Rayleigh-Jeans de l'émission thermique du disque d'accrétion. Figure extraite de Migliari et al. (2006).

bolométrique X soit différent entre les trous noirs et les étoiles à neutrons. Il est donc peu probable que ces jets contribuent à haute énergie dans les sources Atoll. Nous reviendrons sur cet aspect dans la partie 3.1.

L'estimation de la puissance totale associée au jet compact peut être estimée en mesurant le résultat de leur interaction avec le milieu interstellaire (MIS) et la formation éventuelle de lobes radio (similaire aux AGN). Ces aspects des jets larges seront discutés dans le chapitre 4, mais nous évoquerons ici la détection par Gallo et al. (2005a) d'une nébuleuse radio semi annulaire perpendiculairement à l'axe du jet compact de Cyg X−1. L'étude des propriétés radiatives de ce lobe permet une estimation de l'énergie déposée dans le MIS. Il s'ensuit que la puissance totale associée au jet compact pourrait être une fraction significative (de 3 à 50%, voire le double en tenant compte du contre-jet) de la luminosité bolométrique (0.1–200 keV) de Cyg X−1. Il serait donc possible que dans l'état dur, l'essentiel de l'énergie issue de l'accrétion sur le trou noir se retrouve dans les jets compacts au lieu d'être dissipée localement dans le flot d'accrétion.

2.5 Mise en évidence de la corrélation radio/X

GX 339−4 a été observé de façon intensive de 1997 à 1999 – et encore plus depuis . L'accumulation de données simultanées dans les domaines X et radio a permis de mettre en évidence qu'il existait un très fort couplage entre les émissions X et radio (Corbel et al. 2000, 2003). Cela était partiellement apparent à partir de l'étude de Hannikainen et al. (1998), mais qui se basait uniquement sur des données MOST, RXTE/ASM et CGRO/BATSE accumulées sur quelques jours. L'utilisation d'ATCA et de RXTE/PCA nous a permis d'établir avec précision la corrélation des flux radio et X de GX 339−4 (voir figure 2.6) lorsqu'elle se trouve dans l'état dur.

Cette corrélation persiste jusqu'à la phase de repos (et donc sur plus de trois décades de flux X) et est maintenue sur une période de quatre ans, bien que la source ait effectué un sursaut intense en 1998 (Corbel et al. 2000, 2003). D'une certaine façon, il devenait possible de prévoir le flux radio en fonction du flux X (et vice versa). Cette corrélation prend la forme d'une fonction non linéaire avec $\mathrm{F_{Rad}} \propto F_{\mathrm{X}}^{0.71}$ ou $F_{\mathrm{X}} \propto \mathrm{F}_{\mathrm{Rad}}^{1.41}$, où $\mathrm{F_{Rad}}$ est la densité de flux radio à 8.6 GHz et F_{X} est le flux dans la bande 3 – 9 keV (ou 9 – 20 keV ; voir Corbel et al. (2003) pour plus de détails).

L'explication de cette corrélation est venue naturellement si l'on prenait en compte le modèle de jet compact (Markoff et al. 2003), décrit en partie 2.6. Dans ce modèle, l'émission radio est due au au rayonnement synchrotron auto-absorbé du jet compact, tandis que l'émission X correspondrait – dans la version initiale du modèle – au rayonnement synchrotron optiquement mince de la base du jet. L'idée est donc d'expliquer la relation $\mathrm{F_X} \propto F_{\mathrm{Rad}}^{m}$, avec $m = 1.41$, en utilisant les prédictions analytiques de ce modèle. Dans ces modèles de jets compacts type Blandford & Konigl (1979), les variations du rayonnement radio sont dues aux variations de la puissance du jet, Q_{j} (Falcke & Biermann 1995). Dans Markoff et al. (2003), nous obtenons une expression m telle que :

$$m = \frac{\frac{17}{12} - \frac{2}{3}\alpha_{\mathrm{X}}}{\frac{17}{12} - \frac{2}{3}\alpha_{\mathrm{RIR}}}, \tag{2.1}$$

où α_{X} et α_{RIR} sont respectivement les indices spectraux en X et radio-infrarouge. En prenant des valeurs typiques dans l'état dur de $\alpha_{\mathrm{X}} = 0.60$ et $\alpha_{\mathrm{RIR}} = 0.15$, on obtient que m = 1.38. Considérant le caractère relativement simpliste de ce modèle, ce résultat est particulièrement encourageant, sachant que la valeur observée est m = 1.41, en excellent accord avec les prédictions théoriques.

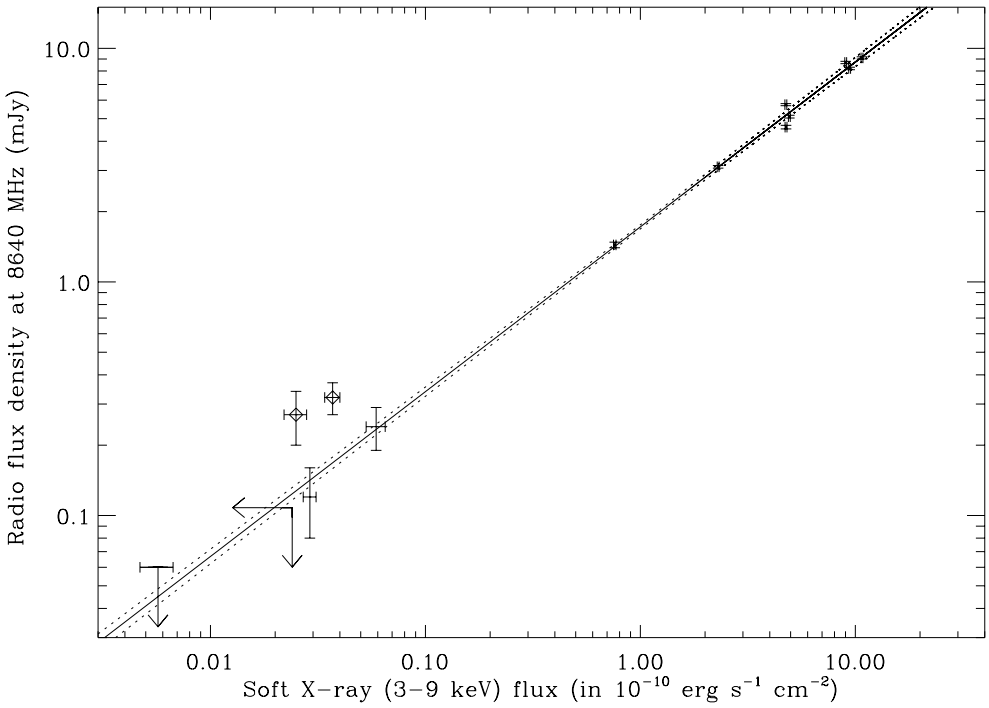

FIG. 2.6 – Corrélation des luminosités radio et X du trou noir GX 339−4 entre 1997 et 2000. Figure extraite de Corbel et al. (2003).

Une fois établie la corrélation des luminosités radio et X pour GX 339−4, Gallo et al. (2003b) se sont attachés à l'étude de cette même corrélation pour GS 2023+338 (V404 Cyg) à partir des données d'archives. À cette source s'ajoutent de nombreuses observations de Cyg X−1, ainsi que quelques autres sources X transitoires. Lorsque GS 2023+338 se trouve dans l'état dur, il existe une corrélation non linéaire entre les rayonnements X et radio, identique à celle de GX 339−4. Les autres sources sont elles aussi compatibles avec la relation que nous avons établie pour GX 339−4 ($F_{\rm Rad} \propto {\rm F_X^{0.7}}$; Corbel et al. 2003) jusqu'à des niveaux de 10^{-5} $L_{\rm Edd}$. Cette corrélation entre les rayonnements radio et X semblerait donc universelle pour tous les trous noirs accrétants dans l'état dur. Elle impliquerait une connexion entre le processus physique gouvernant le rayonnement radio (le jet compact) et celui régissant l'émission X des binaires. L'étude de la dispersion des mesures radio/X autour de la corrélation impliquerait de plus que le facteur d'ensemble de Lorentz du jet compact ne soit pas très élevé ($\Gamma < 2$ ou $\beta \sim 0.8$) et à priori plus faible que lors des éjections impulsives de plasma relativiste. Cette argumentation a été remise en cause par Heinz (2004), mais nous aurons l'occasion de discuter de la nature de leur échantillon et de la validité de leurs conclusions dans le chapitre 6. Néanmoins, un facteur de Lorentz faible pour les jets compacts est conforme aux attentes théoriques (section 2.6).

La présence de ce couplage radio/X est une contrainte très forte que les modèles théoriques se doivent d'expliquer. Comme signalé auparavant, les jets compacts expliquent naturellement cette corrélation (Corbel et al. 2003; Markoff et al. 2003). Zdziarski et al. (2003) l'expliquent par une correspondance entre le niveau d'émission X et un taux d'éjection de bulles de plasma à l'origine du jet compact.

Rapidement après la publication de cette corrélation universelle pour les trous noirs à faible accrétion, Heinz (2004) a montré que les modèles de type ADAF pouvait aussi expliquer cette

corrélation. Néanmoins, il reste à démontrer que des structures de type ADAF puissent servir de base aux jets compacts.

2.6 Une contribution des jets compacts à haute énergie ?

Au fur et à mesure que les données multi-longueurs d'onde s'accumulaient, il devenait naturel de vouloir comprendre les processus physiques impliqués en modélisant la distribution spectrale énergétique de ces systèmes. Le rayonnement du jet compact étant continu de la radio jusqu'à la fréquence de coupure vers l'infrarouge (section 2.3), nous constatons de plus que les spectres X sont compatibles (Figure 2.7) avec une extrapolation du régime optiquement mince de l'infrarouge aux X (Corbel & Fender 2002). D'où l'idée que les jets compacts pourraient contribuer eux aussi en complément ou à la place de la couronne standard. C'est le sujet d'un vif débat actuel dont nous allons maintenant discuter.

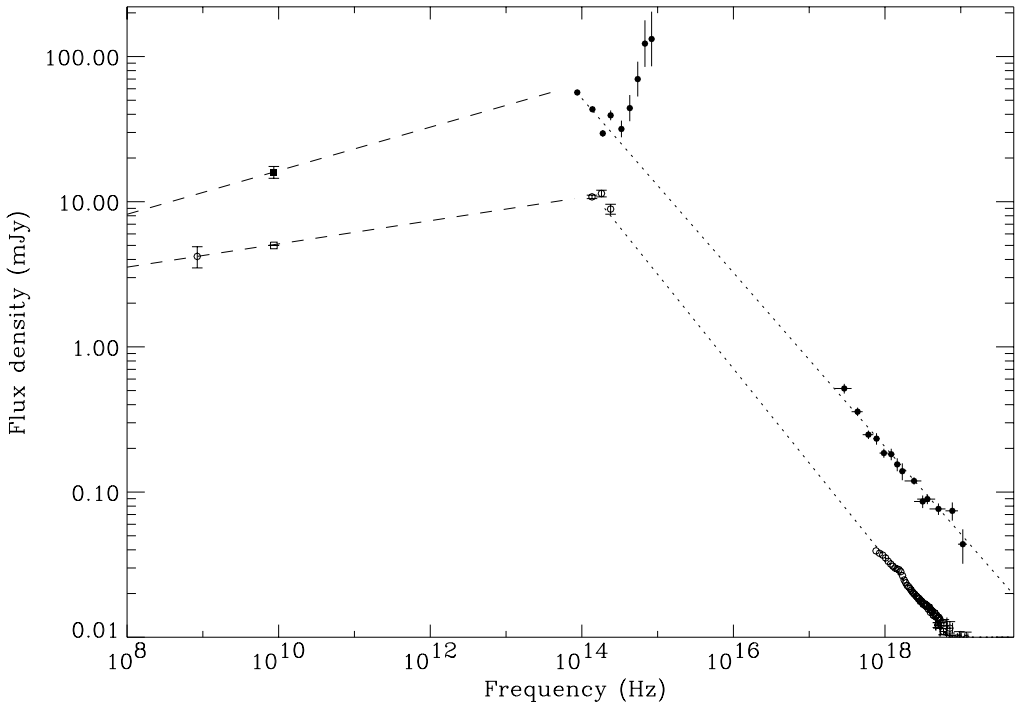

FIG. 2.7 – Spectres large bande de GX 339−4 lors d'un état dur en 1981 (symboles remplis) et en 1997 (symboles vides). Les spectres X sont compatibles avec l'extrapolation d'une loi de puissance d'indice spectrale $\sim$ –0.6 en provenance de l'infrarouge. Figure extraite de Corbel & Fender (2002).

En effet, il existe actuellement trois classes de modèle pour expliquer la structure et les mécanismes d'émission de l'état dur (Tomsick et al. 2004). Une idée consiste à dire que le disque standard (de type Shakura & Sunyaev 1973) se retire dans l'état dur – son rayon interne, $R_{\rm int}$, augmente – et qu'au centre se développe un flot d'accrétion de type ADAF ou une couronne sphérique, où l'essentiel de l'émission X est produit par effet Compton inverse (Esin et al. 1997; Dove et al. 1997). Dans le deuxième cas, le disque d'accrétion ne s'écarte pas forcément – $R_{\rm int}$ quasi-constant – du trou noir et des "bouffées" magnétiques produisent les électrons à l'origine de la comptonisation (Galeev et al. 1979; Merloni & Fabian 2002). La troisième possibilité correspondrait au modèle de jet mentionné précédemment (Markoff et al.

2005). Des modèles hybrides se mettent en place pour expliquer l'importance observationnelle que les jets compacts ont pris ces dernières années (Yuan et al. 2005; Malzac et al. 2004).

Nous allons décrire brièvement les grandes lignes actuelles de ce modèle (voir les publications suivantes pour plus de détails : Markoff et al. 2001, 2003, 2005; Markoff & Nowak 2004). Un jet compact (voir Figure 2.8) de forme conique se développe, de part et d'autre, orthogonalement au disque d'accrétion. Pour traduire notre ignorance actuelle des mécanismes de collimation, la base du jet est reliée au disque par une région cylindrique – dite le "nozzle"[1] – de rayon r_0 (dont la limite inférieure est la dernière orbite stable autour du trou noir).

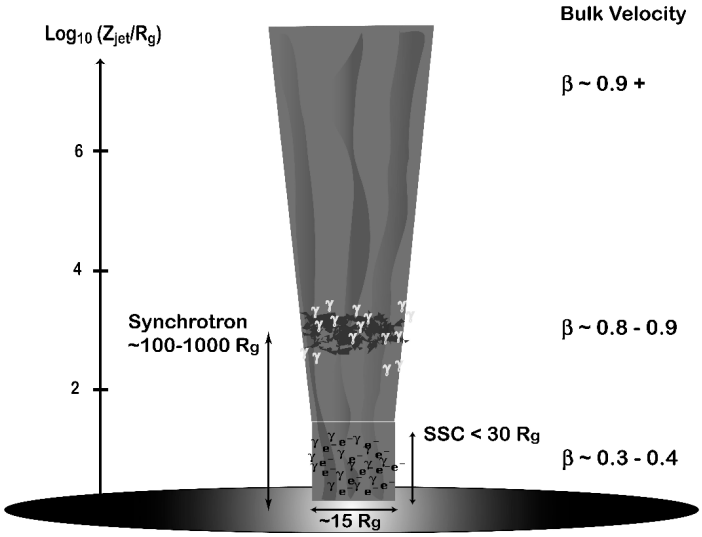

FIG. 2.8 – Schéma du modèle de jet compact de Markoff et al. Figure extraite de Markoff & Nowak (2004).

Les incertitudes au sujet de la physique de la formation des jets sont absorbées par la paramétrisation initiale de ce "nozzle". A la sortie de ce "nozzle" – au delà de $\sim$ 10 rayons gravitationnels, r_g – , le jet a une expansion latérale à la vitesse du son pour un plasma proton/électron – i.e. $\sim$ 0.4c – et est ensuite légèrement accéléré, de part la présence d'un gradient de pression longitudinal. L'équation d'Euler permet de calculer une solution exacte du profil de vitesse (Falcke 1996). Après une période d'accélération rapide immédiatement après le "nozzle", le gradient de vitesse diminue et la vitesse sature à des facteurs de Lorentz $\geq$ 2–3. Au bout d'une distance de 10 à 100 r_g les particules du jet qui avaient initialement une distribution quasi-thermique sont accélérées par des chocs et produisent une distribution énergétique non thermique sous forme de loi de puissance.

Les hypothèses de base de ce modèle sont les suivantes :

- la puissance totale du jet est proportionnelle à la luminosité d'accrétion, $\dot{M}c^2$, au bord interne du disque d'accrétion,
- le jet contient une population froide – non relativiste – de protons portant l'essentiel de l'énergie cinétique tandis que les leptons constituent les particules rayonnantes,
- les particules sont éventuellement accélérées – après le "nozzle" – en une distribution en forme de loi de puissance,
- cette distribution de particules accélérées est maintenue au sein du jet – après la première zone d'accélération.

[1] On pourrait traduire ce terme par "tuyère" en français, mais par soucis de cohérence avec les articles, je conserve cet anglicisme.

Au premier ordre, le spectre d'émission résultant de ces jets compacts consiste en la superposition (voir Figure 2.9) de :

1. un rayonnement synchrotron optiquement épais – spectre plat de la radio à l'infrarouge – provenant des régions externes du jet au delà de la première région de chocs,
2. un rayonnement synchrotron optiquement mince – spectre avec indice spectral négatif – provenant des régions proches de la zone des premiers chocs, émettant aux fréquences au delà desquelles le jet est transparent,
3. un rayonnement synchrotron – optiquement épais et mince – issu de la distribution thermique de particules dans le "nozzle" et
4. de la diffusion Compton externe des photons issus du disque d'accrétion – représenté pour un disque multi-couleur – et des photons – synchrotron self-Compton, SSC – provenant de la base du jet.

Les effets de refroidissement des particules de hautes énergies sont inclus dans le modèle. Les particules rayonnantes sont proches de l'équipartition avec le champ magnétique, mais il est possible d'étudier les situations hors équipartition. Ce modèle inclut aussi la composante de réflexion (Markoff & Nowak 2004). On trouvera l'ensemble de nombreux détails supplémentaires dans Markoff et al. (2005).

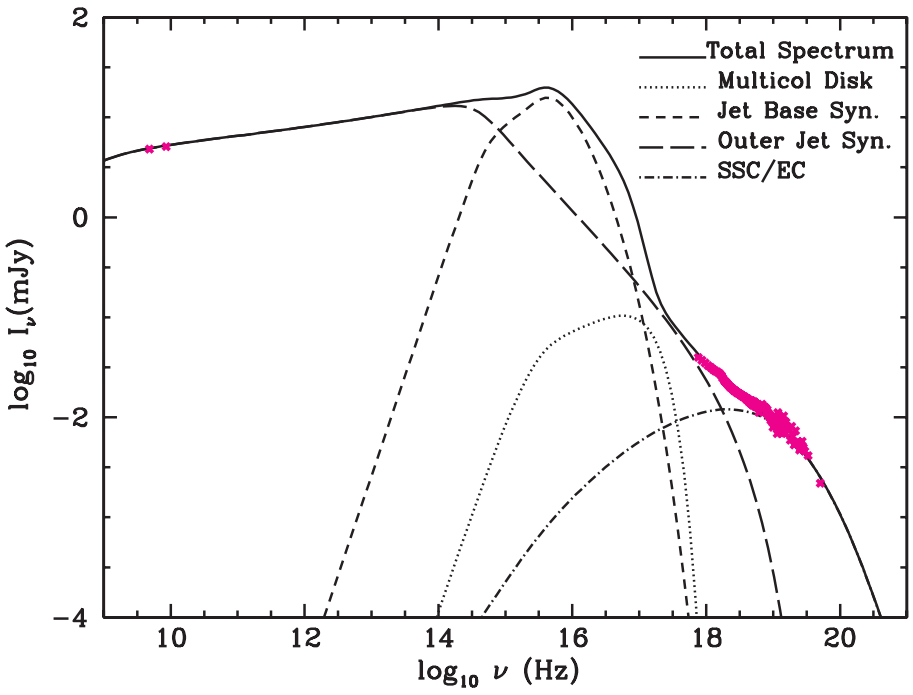

FIG. 2.9 – Composantes d'émission du modèle de jet compact de Markoff et al. Figure extraite de Markoff et al. (2005).

Ce modèle a originellement été appliqué à XTE J1118+480 qui était resté dans l'état dur pendant l'intégralité de son sursaut en 2000. La localisation de XTE J1118+480 à très haute latitude galactique (Chaty et al. 2003) impliquait une très faible absorption interstellaire et donc des observations d'excellente qualité de l'optique aux X en passant par l'ultraviolet. La version du modèle de jet appliquée à XTE J1118+480 était très simplifiée – pas de SSC – par rapport à son statut actuel – c.f. ci-dessus. Néanmoins, il permettait de reproduire l'intégralité des observations de la radio aux X durs (Markoff et al. 2001) et cela pour la première fois dans

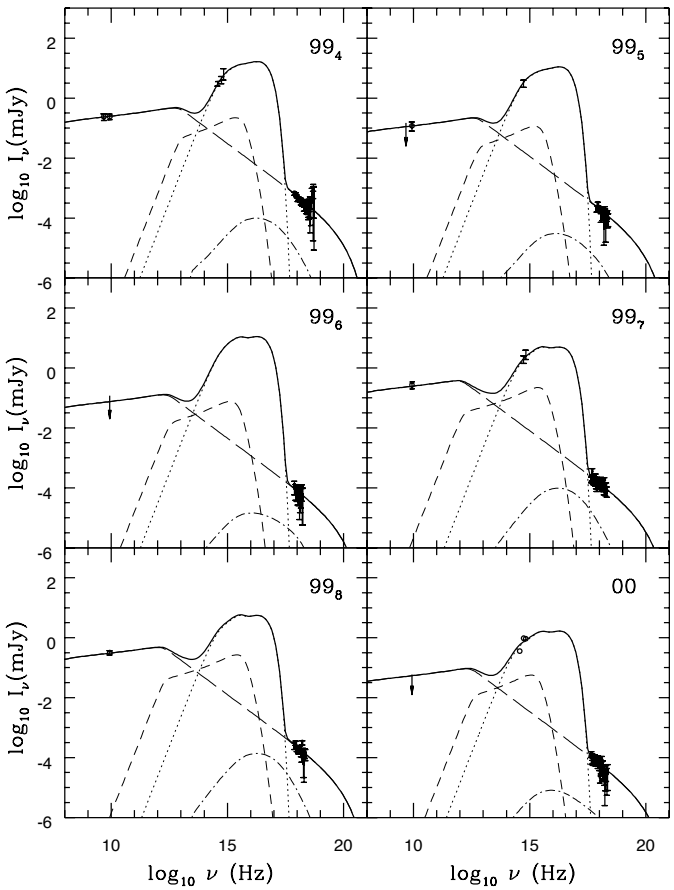

FIG. 2.10 – Modèle de jet compact appliqué à GX 339−4 pour différentes dates de 1997 à 2000. Figure extraite de Markoff et al. (2003).

le cas d'une binaire galactique. Dans le cas de XTE J1118+480, l'émission X correspondait au rayonnement synchrotron optiquement mince du jet compact.

Nous avons déjà vu (section 2.5) que ce modèle de jet compact prédisait correctement de façon analytique la corrélation des rayonnements radio et X observée sur GX 339−4 (Corbel et al. 2003) ou GS 2023+338 (Gallo et al. 2003b). Sachant que nous avions accumulé un grand nombre de distributions spectrales énergétiques (SED) de GX 339−4 de 1997 à 2000 – et encore plus depuis –, et en rajoutant les données du sursaut intense de 1981, nous disposions de données variées pour tester plus en détail ce modèle de jet (exemple sur le figure 2.10). Cela est effectué dans Markoff et al. (2003) où nous avons pu ajuster avec succès l'ensemble des SED avec ce modèle de jet en ne faisant varier que deux paramètres : la puissance du jet et la localisation de la zone où ont lieu les premières accélérations (Figure 2.11) – bien que ce dernier paramètre puisse être considéré comme quasiment constant –. Le rayonnement synchrotron pourrait donc être une voie possible qui permettrait d'expliquer l'ensemble des caractéristiques spectrales de GX 339−4 dans l'état dur (Markoff et al. 2003).

Le modèle dans sa version actuelle, et tel que décrit au début de cette partie, a évolué par rapport aux travaux présentés dans Markoff et al. (2001, 2003). Déjà, il est maintenant possible de réaliser des ajustements statistiques aux données – avec calculs d'erreurs – dans des logiciels

standards d'astronomie X. Les résultats obtenus montrent que d'un point de vue statistique – χ^2 réduit proche de 1 –, ce modèle est aussi satisfaisant que les modèles standards des hautes énergies – la couronne – et il reproduit sans souci (Markoff & Nowak 2004; Markoff et al. 2005; Homan et al. 2005) la coupure parfois observée vers $\sim$ 100 keV – qui était l'argument fort en faveur du modèle de couronne standard. En effet, il s'agissait d'une des critiques récurrentes (Poutanen & Zdziarski 2003; Zdziarski et al. 2003) sur ce modèle : impossible d'ajuster la coupure à haute énergie ou alors il fallait, selon les auteurs, un paramétrage fin – "fine tuning" – pour y arriver. Dans le modèle de jet, cette coupure résulte naturellement d'un équilibre entre le taux d'accélération des particules par choc diffusif – proportionnel au champ magnétique – et le taux de refroidissement de ces mêmes particules (voir l'appendice de Markoff et al. 2005, pour plus de détails).

Pour conclure sur cette partie, nous dirons que nous nous sommes focalisés sur ce modèle de jet car il explique parfaitement bien l'émission synchrotron observée – et parfois résolue – de la radio à l'infrarouge. Et de façon cohérente, il s'intéresse à la modélisation à haute énergie en tenant compte des contraintes issues des observations multi-longueurs d'onde. Il s'agit du seul modèle procédant de la sorte d'un point de vue statistique. Par exemple, l'indice spectral entre la radio et l'infrarouge va directement dépendre de l'inclinaison du jet. De plus, la fréquence de coupure observée en infrarouge proche (Corbel & Fender 2002) va déterminer la distance à laquelle l'accélération des particules commence – la fin du "nozzle" – et donc la contribution éventuelle du jet dans les X. Pour les hautes énergies, ce modèle est plus satisfaisant – en tout cas dans le trop peu d'exemples étudiés à ce jour – que les modèles standards de couronne. À ce jour, deux composantes se chevauchent vers les X/γ : la composante synchrotron optiquement mince dans les X et la composante de comptonisation – essentiellement SSC – au delà des X durs (voir Figure 2.8). Sachant que les modèles standards de comptonisation reproduisent parfaitement les spectres X depuis des décennies, nous trouvons que ce modèle de jet constitue une voie prometteuse, au vu de l'ubiquité des jets compacts dans l'état dur. Un scénario qui pourrait émerger dans les années futures serait que la couronne standard correspondrait à la base du jet compact.

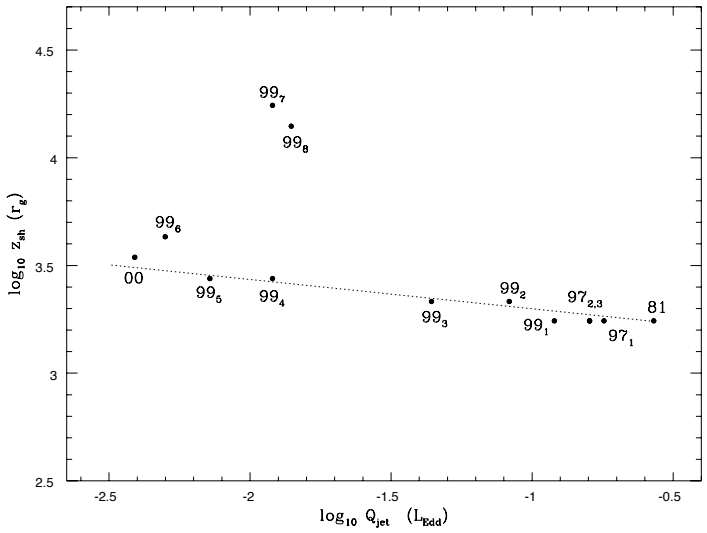

FIG. 2.11 – Corrélation entre la puissance du jet compact et la localisation de la première zone d'accélération des particules. Figure extraite de Markoff et al. (2003).

2.7 Articles de recherche

2.7.1

X-Ray States and Radio Emission in the Black Hole Candidate XTE J1550-564.

Article publié dans :

Astrophys. J., 2001, 554, 43-48

Corbel, S., Kaaret, P., Jain, R. K., Bailyn, C. D., Fender, R. P., Tomsick, J. A., Kalemci, E., McIntyre, V., Campbell-Wilson, D., Miller, J. M., McCollough, M. L.

THE ASTROPHYSICAL JOURNAL, 554:43–48, 2001 June 10

X-RAY STATES AND RADIO EMISSION IN THE BLACK HOLE CANDIDATE XTE J1550−564

S. CORBEL[1] AND P. KAARET
Harvard-Smithsonian Center for Astrophysics, 60 Garden Street, Cambridge, MA 02138; corbel@head-cfa.harvard.edu
R. K. JAIN AND C. D. BAILYN
Department of Astronomy, Yale University, P.O. Box 208101, New Haven, CT 06520-8101
R. P. FENDER
Astronomical Institute "Anton Pannekoek," University of Amsterdam; and Center for High Energy Astrophysics, Kruislaan 403, NL-1098 SJ Amsterdam, Netherlands
J. A. TOMSICK AND E. KALEMCI
Center for Astrophysics and Space Sciences, Mail Stop 0424, University of California at San Diego, La Jolla, CA 92093
V. MCINTYRE
Australia Telescope National Facility, P.O. Box 76, Epping, NSW 1710, Australia
D. CAMPBELL-WILSON
School of Physics, University of Sydney, Sydney, NSW 2006, Australia
J. M. MILLER
Center for Space Research, Massachusetts Institute of Technology, 70 Vassar Street, Cambridge, MA 02139
AND
M. L. MCCOLLOUGH
Universities Space Research Association, Huntsville, AL 35812
Received 2000 November 13; accepted 2001 February 2

ABSTRACT

We report on radio and X-ray observations of the black hole candidate (BHC) XTE J1550−564 performed during its 2000 X-ray outburst. Observations were conducted with the Australia Telescope Compact Array and allowed us to sample the radio behavior of XTE J1550−564 in the X-ray low hard and intermediate/very high states. We observed optically thin radio emission from XTE J1550−564 5 days after a transition to an intermediate/very high state, but we observed no radio emission 6 days later, while XTE J1550−564 was still in the intermediate/very high state. In the low hard state, XTE J1550−564 is detected with an inverted radio spectrum. The radio emission in the low hard state most likely originates from a compact jet; optical observations suggest that the synchrotron emission from this jet may extend up to the optical range. The total power of the compact jet might therefore be a significant fraction of the total luminosity of the system. We suggest that the optically thin radio emission detected 5 days after the transition to the intermediate/very high state is due to a discrete ejection of relativistic plasma during the state transition. Subsequent to the decay of the optically thin radio emission associated with the state transition, it seems that in the intermediate/very high state the radio emission is quenched by a factor greater than 50, implying a suppression of the outflow. We discuss the properties of radio emission in the X-ray states of BHCs.

Subject headings: accretion, accretion disks — black hole physics — radio continuum: stars — stars: individual (XTE J1550−564) — X-rays: stars

1. INTRODUCTION

The soft X-ray transient (SXT) XTE J1550−564 was first detected by the all-sky monitor (ASM) on board the *Rossi X-Ray Timing Explorer* (*RXTE*) on 1998 September 7 (Smith 1998). The outburst was characterized by a "double peaked" profile and a strong (6.8 crab) and brief (1 day) flare. XTE J1550−564 went through all canonical black hole states (Sobczak et al. 1999, 2000b; Homan et al. 2001) before its return to quiescence in 1999 May.

Low-frequency (0.08–18 Hz) X-ray quasi-periodic oscillations (QPOs) as well as a high-frequency variable (100–285 Hz) QPO were detected during some of the *RXTE* Proportional Counter Array (PCA) observations. This is the fourth black hole candidate (BHC) to display such a high-frequency QPO. Based on its strong aperiodic variability, QPOs, and X-ray spectrum, XTE J1550−564 is believed to harbor a black hole, but a mass function has still to be measured (Cui et al. 1999; Remillard et al. 1999; Wijnands, Homan, & van der Klis 1999; Sobczak et al. 2000a; Homan et al. 2001).

Soon after its discovery in X-rays, an optical counterpart was reported by Orosz, Bailyn, & Jain (1998). A brightening of 4 mag in the V band over the quiescence level was noted by Jain et al. (1999). Based on the interstellar absorption lines, a distance of 2.5 kpc and an optical extinction of 2.2 ± 0.3 mag have been deduced by Sánchez-Fernández et al. (1999). A radio counterpart to XTE J1550−564 has been detected at 843 MHz with a flux density of ~ 10 mJy by the Molonglo Observatory Synthesis Telescope (MOST; Campbell-Wilson et al. 1998). Subsequent radio observations indicated that the strong X-ray flare was accompanied by a large radio flare with ejection of relativistic plasma, possibly at superluminal velocities (Hannikainen et al. 2001).

[1] Université Paris VII and Service d'Astrophysique, CEA Saclay, F-91191 Gif sur Yvette, France.

XTE J1550−564 became active in soft X-rays again on 2000 April 2 (MJD 51,636; Smith et al. 2000). The Burst and Transient Source Experiment (BATSE) on board the *Compton Gamma Ray Observatory* (*CGRO*) detected XTE J1550−564 up to 300 keV (McCollough, Wilson, & Sun 2000). Simultaneously, a new optical outburst from XTE J1550−564 was reported (Masetti & Soria 2000; Jain & Bailyn 2000).

In this paper we report Australia Telescope Compact Array (ATCA) observations of the radio counterpart of XTE J1550−564, together with daily X-ray observations performed during the 2000 outburst with *RXTE* ASM and *CGRO* BATSE. These observations have been performed in different X-ray states, and we discuss the relation of radio emission within these states.

2. OBSERVATIONS AND RESULTS

2.1. *Soft and Hard X-Ray Observations*

The ASM, on board *RXTE* (Levine et al. 1996), monitors the activity in soft X-rays of any source in the sky in three energy bands (1.5–3, 3–5, and 5–12 keV). The ASM light curve in the energy band 1.5–12 keV is presented in the top panel of Figure 1, and in the lower panel, we plot the hardness ratio (5–12 keV/3–5 keV) using 1 day averages. The 20–100 keV light curve, obtained with BATSE on board *CGRO* using an Earth-occultation technique (Harmon et al. 1992), is presented in the middle panel of Figure 1. A power-law model with a variable spectral index has been folded through the BATSE response matrix for daily flux calculation. Due to precession of the *CGRO* orbit, XTE J1550−564 stopped being occulted on MJD 51,682, a few days before the end of the *CGRO* mission.

Figure 1 illustrates the soft and hard X-ray behavior of XTE J1550−564 during the 2000 X-ray outburst. During the initial rise, the soft X-ray flux increased slowly, whereas the hard X-ray flux was already strong when the orbital configuration of *CGRO* allowed its detection by BATSE. On April 26 (MJD 51,660), we note a rapid increase in soft X-rays as well as a decrease in hard X-rays, which then settled down in a plateau until the termination of *CGRO*. The decay of this outburst was a gradual decline in soft X-rays.

Analysis of the *RXTE* ASM hardness ratio curve and *RXTE* PCA data (Miller et al. 2001) allowed us to divide the outburst into three different parts. The outburst started and finished with a hard spectrum, whereas the central part was soft, but with detectable hard X-ray emission. This can be understood as an initial low hard state followed by a transition to the intermediate state (or very high state, as this state is now recognized as a higher count-rate version of the intermediate state; see Homan et al. 2001) on April 26, and then a return to the low hard state after May 13 (MJD 51,677). Preliminary analysis of *RXTE*/PCA observations confirm a change in power-law photon index from 2.30 to 1.74 between May 16 and May 24 (Tomsick, Corbel, & Kaaret 2001). We note that SXTs are rarely observed in the low hard state in the rising phase of their outbursts.

It is interesting to note that this new X-ray outburst occurred less than a year after the discovery outburst, which took place from 1998 September to 1999 May. Before that, XTE J1550−564 was believed to be in quiescence. This

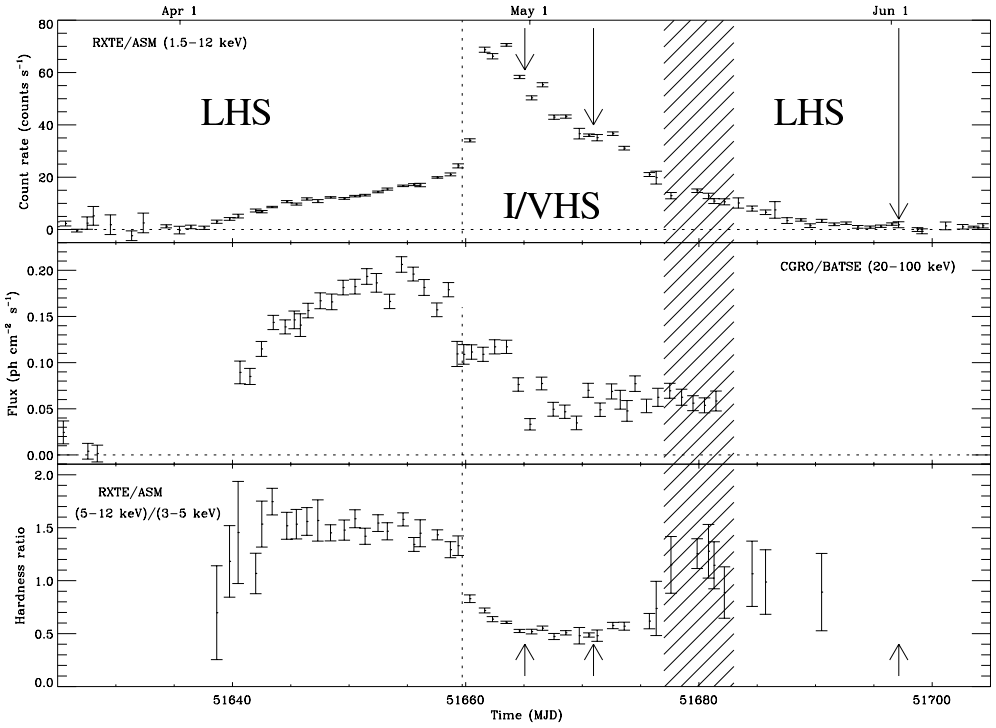

FIG. 1.—Light curve of XTE J1550−564 using 1 day averages. *Top*, *RXTE*/ASM (1.5–12 keV); *middle*, *CGRO*/BATSE 20–100 keV; *bottom*, hardness ratio (5–12/3–5 keV). Arrows indicate the dates of our ATCA radio observations, and the dotted line the likely period of the transition from the initial low hard state (LHS) to the intermediate/very high State (I/VHS). The hatched region shows the approximate date of the return to the final low hard state.

TABLE 1

ATCA OBSERVATIONS OF XTE J1550−564

DATE	MJD[b] (days)	DURATION (hr)	FLUX DENSITY[a] (mJy) 1384 MHz	2496 MHz	4800 MHz	8640 MHz	SPECTRAL INDEX
2000 Apr 30.....	51,665.07	8.0	[c]	[c]	7.45 ± 0.12	5.68 ± 0.06	−0.46 ± 0.05
2000 May 6	51,670.96	2.5	...	...	<0.10	<0.05	NA
2000 Jun 1	51,697.14	5.0	0.7 ± 0.2	0.85 ± 0.09	0.88 ± 0.08	1.30 ± 0.09	+0.37 ± 0.10

[a] Upper limits are given at the 1 σ level.
[b] Date refers to the beginning of the observation.
[c] No precise flux estimate possible due to the presence of a bright supernova remnant in the sidelobes.

renewed activity is unusual for SXTs with long recurrence times (XTE J1550−564 probably belongs to this class, as it has never been detected in past years, despite sensitive surveys of the Galactic plane). A parallel can be drawn with GRO J1655−40, which also had a new outburst a few months after the end of a series of outbursts and a period of quiescence (e.g., Hameury et al. 1997 and references therein). We should also note that both systems have relatively long orbital periods: 2.6 days for GRO J1655−40 (Bailyn et al. 1995) and 1.5 days for XTE J1550−564 (Jain et al. 2001). The spectral type (F3–F6) of its stellar companion (Orosz & Bailyn 1997) and its peculiar position in the Hertzsprung gap (Kolb et al. 1997) may be responsible for the recurrent outbursts of GRO J1655−40 (but see Regős, Tout, & Wickramasinghe 1998 for alternative explanations). The spectral type of the secondary in XTE J1550−564 has not been identified yet, but photometric data are consistent with a low-mass K0–K5 star (Sánchez-Fernández et al. 1999). Its precise determination would be of great interest to understand these SXTs with repeated outbursts. If XTE J1550−564 does have a K-type optical companion, it must be evolved in order to be large enough to fill its Roche lobe. An evolved companion could conceivably be the similarity that is responsible for the repeated outbursts from these systems.

2.2. *Radio Observations*

The radio continuum observations of XTE J1550−564 were carried out using ATCA, located in Narrabri, NSW, Australia. ATCA is a synthesis telescope consisting of six antennae, each with a 22 m diameter, aligned on a 6 km east-west array. The ATCA radio observations were conducted on three different dates in 2000: April 30, May 6, and June 1. The first two observations were performed in the 0.750D compact configuration, while the last observation was carried out in the high spatial resolution 6B array. The first and third observations were made at the central frequencies of 1384, 2496, 4800, and 8640 MHz, with a total bandwidth of 128 MHz; observations were made at only 4800 and 8640 MHz during the second observation.

The amplitude and bandpass calibrator was PKS B1934−638, and the antennae gain and phase calibration were derived from regular observations (every 20 minutes) of the point source calibrators B1554−64 (at 4800 and 8640 MHz) and B1549−790 (at 1384 and 2496 MHz). The editing, calibration, Fourier transformation, deconvolution, and image analysis were performed using the MIRIAD package (Sault, Teuben, & Wright 1995). Because of the proximity of a very strong (∼145 Jy at 1 GHz) supernova remnant (G326.3−1.8) close to the field of view, the shortest baselines have not been used in the analysis of the data at 1384 and 2496 MHz. The ATCA flux densities of XTE J1550−564 are tabulated in Table 1.

The first ATCA observation (on MJD 51,665) allows a detection of the radio counterpart at a weak level of 7.45 ± 0.12 mJy and 5.68 ± 0.06 mJy at 4800 and 8640 MHz, respectively. For a flux density $S_\nu \propto \nu^\alpha$, a spectral index of $\alpha = -0.46 \pm 0.05$ is derived. Before this first

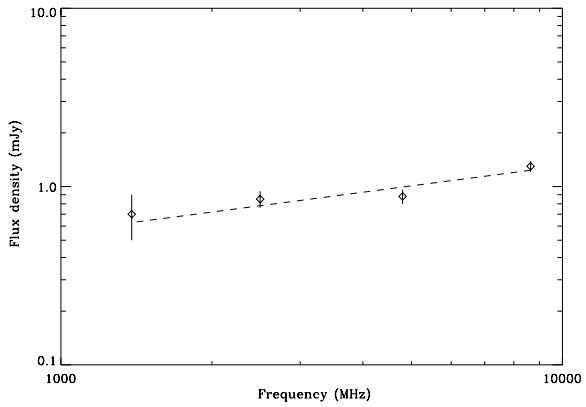

FIG. 2*a*

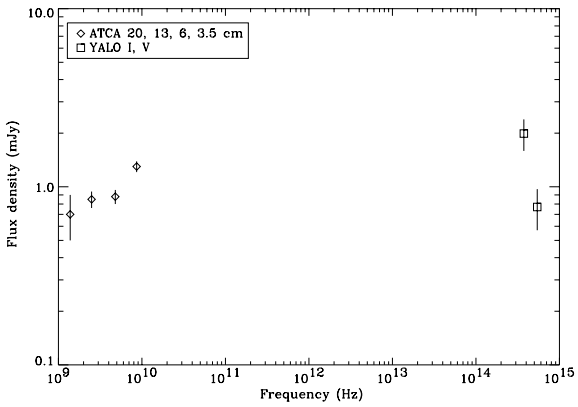

FIG. 2*b*

FIG. 2.—(*a*) Radio spectrum on 2000 June 1. The dotted line is the best-fit function $S_\nu \propto \nu^\alpha$ with $\alpha = +0.37$. (*b*) Radio and optical (V, I) measurements of XTE J1550−564 on June 1. The optical data originate from the Yale 1 m telescope (dereddened using an optical extinction of 2.2 ± 0.3 mag).

ATCA observation, the MOST performed several observations while XTE J1550−564 was in its initial low hard state, and detected the radio counterpart at a level of 8–15 mJy at 843 MHz. The second ATCA observations performed during the intermediate/very high state (on MJD 51,670) did not reveal significant radio emission from XTE J1550−564 with a strong 3 σ upper limit of 0.15 mJy at 8640 MHz.

After a transition back to the low hard state, we performed our third ATCA observation (on MJD 51,697) at nearly the end of the X-ray outburst. Radio emission is again detected at a level of $\sim$1 mJy at all four frequencies. The spectrum is slightly inverted with a spectral index of 0.37 ± 0.10 (Fig. 2*a*). The best position of the radio counterpart is $\alpha(\mathrm{J2000}) = 15^{\mathrm{h}}50^{\mathrm{m}}58^{\mathrm{s}}.7$ and $\delta(\mathrm{J2000}) = -56^{\circ}28'35''.2$, with a total uncertainty of $0''.3$; it is consistent with the position of the optical counterpart (Jain et al. 1999).

3. DISCUSSION

3.1. *A Compact Jet in the Low Hard State*

The detection (on June 1st) of a radio source with an inverted spectrum (spectral index of 0.37 ± 0.10) while XTE J1550−564 was in the low hard state is reminiscent of the behavior of the few other BHCs (transient or persistent) that have been observed at radio frequencies in the low hard state. Indeed, the persistent BHCs from our galaxy Cyg X-1 (Brocksopp et al. 1999), GX 339−4 (Corbel et al. 2000) and GRS 1758−258 (Lin et al. 2000), are found most of the time in the low hard state and are detected in radio with a flat (spectral index $\sim$0.0) or inverted spectrum (and also probably 1E 1740.7−2942). Among the SXTs, we should note that GS 2023+338 (Han & Hjellming 1992), GRO J0422+32 (Shrader et al. 1994), GS 1354−64 (Brocksopp et al. 2001), and XTE J1118+480 (Hynes et al. 2000; Fender et al. 2001) have been detected with similar properties (see discussion in Fender 2001). XTE J1550−564 should now be added to this list.

A flat or inverted radio spectrum can be interpreted as an optically thick synchrotron emission from a compact and conical jet, following the model of Hjellming & Johnston (1988). In this model, the higher frequencies come from the base of the compact jet, where the optical depth is the highest. Low-frequency radio emission arises from the region further from the base. Summing all contributions over the spatial extent of the jet results in a flat or inverted spectrum. Recent Very Long Baseline Array (VLBA) imaging of a compact jet in the radio core of Cyg X-1 (Stirling et al. 2001) confirms this interpretation. The stronger orbital modulation of the higher frequencies also favors this scenario (Pooley, Fender, & Brocksopp 1999). The physical size of these compact jets is believed to be of the order of $\sim$10 AU at 8.6 GHz (corresponding to the mas angular scale). More VLBA observations of BHC in the low hard state should increase the number of compact jet detections.

It is expected that the flat spectrum must cut off at high frequency. The spectrum of Cyg X-1 is flat up to 220 GHz (Fender et al. 2000). But in the case of GX 339−4 and XTE J1118+480 (Hynes et al. 2000; Fender et al. 2001), the inverted radio spectrum probably extends up to the near-infrared range. In Figure 2*b*, we show the simultaneous radio and optical observations of XTE J1550−564 taken on 2000 June 1 (see Jain et al. 1999, 2001 for a discussion of the YALO data). XTE J1550−564 is detected at $V = 18.9 \pm 0.1$ mag and $I = 16.7 \pm 0.1$ mag. An optical extinction of $A_V = 2.2 \pm 0.3$ mag (Sánchez-Fernández et al. 1999) has been used to deredden these data. Considering the uncertainties in the optical extinction, the spectral index between the two optical bands (-2.6 ± 1.0) appears to be nonthermal and is not compatible with the thermal spectrum of an optically thick accretion disk (spectral index greater than +0.3 in the optical range). It is therefore possible that a significant fraction of the optical, near-IR emission in XTE J1550−564 during the low hard state is (optically thin) synchrotron emission from the compact jet. If this interpretation is correct, the cutoff frequency lies in the near-infrared range (as in GX 339−4 and XTE J1118+480).

Using the June 1 observations, the radio luminosity (1–10 GHz band) of the compact jet is $\sim 7 \times 10^{28}$ ergs s^{-1} for a distance of 2.5 kpc. The luminosity of the compact jet in the radio band during the first part of the outburst may be an order of magnitude higher, as XTE J1550−564 was detected at a level of 8–15 mJy at 843 MHz with MOST. Assuming that the inverted spectrum extends to the near infrared ($\sim 10^{14}$ Hz), as discussed above, we find that the total radiative luminosity of the compact jet would be of order $\sim 2 \times 10^{34}$ ergs s^{-1} for the June 1 observation, several percent of the 2–20 keV band X-ray luminosity of 5×10^{35} ergs s^{-1} measured on the same day (Tomsick et al. 2001). Furthermore, taking into account the internal energy of particles within the jet and relativistic bulk motion is likely to increase the total power required to energize the jet (a precise estimate would require knowledge of the inclination angle of the jet). Thus, the compact jet is probably very powerful, with a total power close to the bolometric luminosity of the system (accretion disk and corona).

3.2. *Discrete Ejection Events at a State Transition*

The first ATCA observation was performed 5 days after the transition from the low hard state to the intermediate/very high state. XTE J1550−564 is detected around $\sim$6 mJy, but contrary to the low hard state, the radio spectrum has a spectral index of -0.46 ± 0.05, indicative of optically thin synchrotron emission. It is likely that this optically thin emission is due to a discrete ejection of relativistic plasma at the time of the state transition when the accretion disk is unstable. We would then be detecting the decaying radio emission from this event, and the emission from XTE J1550−564 would be low, consistent with our nondetection of radio emission later in the intermediate/very high state. During the second part of the 1998–1999 X-ray outburst, Homan et al. (2001) also reported an optically thin synchrotron event after a state transition. Similar discrete ejection events have been inferred during state transitions in GX 339−4 (Corbel et al. 2000). It is possible that almost all X-ray binaries (including neutron star systems) produce similar weak radio events during state transitions (see also Hjellming & Han 1995 and recent work by Fender & Kuulkers 2001).

We note that it was hypothesized that the transition to the very high state was accompanied by massive superluminal ejections (Fender 2000) and bright, flaring radio events. These new ATCA observations rule out such an interpretation, as no bright ejection event was observed. The formation of these superluminal ejection events might possibly require a transition from a quiescent state to a very

high state, i.e., a large and rapid increase of the mass accretion rate, and not a transition from a state where significant accretion is already occurring (such as the low hard state). Indeed, the discovery outburst of XTE J1550−564 was a transition from quiescence to a very high state. A bright radio event was detected after the transition and possibly resolved in two components moving at apparently superluminal velocities (Hannikainen et al. 2001).

3.3. *Quenched Radio Emission in the Intermediate/Very High State*

The second ATCA observation was performed when XTE J1550−564 was in the intermediate/very high state. At that time, XTE J1550−564 was not detected with ATCA at 4800 and 8640 MHz with a 3 σ upper limit of 0.15 mJy at 8640 MHz, i.e., a reduction of radio emission by a factor greater than 50 if we take into account the MOST detection in the initial low hard state. This is the first time radio observations of a BHC have been performed during an intermediate (or very high) state. Radio observations in this state are particularly important because usually, the radio emission is dominated by the decaying, optically thin synchrotron emission associated with the quiescent/active state transition (and therefore decoupled from the black hole/disk system); here, we view the intrinsic radio properties of the system in this state.

This nondetection is similar to the quenching of the compact jet of GX 339−4 during the 1998 high soft state (Fender et al. 1999). Following the discussion in Fender et al. (1999), it indicates that the compact jet is probably physically suppressed in the intermediate state. These new constraints lead us to conclude that, from a radio point of view, the intermediate (or very high) and high soft states are identical. We should note that Belloni et al. (1999) classified the 1996 outburst of Cyg X-1 as an intermediate state. At that time, radio observations (only performed at the end of the intermediate state, when Cyg X-1 was returning to its standard low hard state) revealed an increase of radio emission (Zhang et al. 1997), probably indicating that the radio emission was indeed lower in the intermediate state, as observed here in XTE J1550−564.

In the low hard state, there is a strong coupling between the compact jet and the luminosity of the corona (see Brocksopp et al. 1999 for Cyg X-1; Corbel et al. 2000 for GX 339−4). Despite the fact that the intermediate state has significant hard X-ray emission, it is not a sufficient condition to sustain the emission from the compact jet (the power-law index is different between the low hard state and the intermediate/very high state, but the hard X-ray emission is currently believed to originate from the corona in both states). Therefore, the low hard state does produce radio emission via a compact jet, whereas the states with a stronger soft component (high soft and intermediate/very high) lead to the quenching of these compact jets for a reason that is not understood. Evaporation processes in the standard geometrically thin disk, below a certain accretion rate, may possibly lead to coronal outflows (e.g., Meyer, Liu, & Meyer-Hofmeister 2000). It is also possible that high magnetic energy dissipation might be responsible for the formation of outflows (and therefore a compact jet above the corona) in the low hard state, whereas the soft states would be dominated by viscous energy dissipation in the accretion disk (e.g., Beloborodov 1999; Poutanen 1999; Di Matteo, Celotti, & Fabian 1999).

4. CONCLUSIONS

Radio emission was detected from XTE J1550−564 on two occasions during its 2000 outburst. Like other BHCs, observed (too rarely) in the low hard state, the radio spectrum of XTE J1550−564 is inverted. This likely implies that the radio emission is synchrotron emission from a compact jet. The total power in the compact jet may be a significant fraction of the total accretion luminosity. The intermediate/very high state (like the high soft state of GX 339−4) is characterized by a quenching of this compact jet. It appears that low hard states in BHCs produce compact outflows, whereas the states with a strong soft component from the accretion disk lead to suppression of a radio-emitting outflow. State transitions are accompanied by discrete ejection of relativistic plasma. More multiwavelength observations of BHCs in the low hard state are needed in order to understand the physics of these compact jets.

We thank Ron Ekers, Dave McConnell, and the ATCA TAC for allocating us target-of-opportunity observing time, Steven Tingay for conducting one of the ATCA observations, and George Nicolson for performing HartRAO radio observations of XTE J1550−564 (which resulted in only upper limits due to the proximity of the SNR). S. C. would like to thank Jean-Marie Hameury and Richard Hunstead for useful discussions and information. The Australia Telescope is funded by the Commonwealth of Australia for operation as a National Facility managed by the CSIRO. *RXTE* ASM results are kindly provided by the ASM/*RXTE* teams at MIT and at the *RXTE* SOF and GOF at NASA's GSFC. S. C. and P. K. acknowledge support from NASA grant NAG5-7405.

REFERENCES

Bailyn, C. D., Orosz, J. A., McClintock, J. E., & Remillard, R. A. 1995, Nature, 378, 157
Belloni, T., Méndez, M., van der Klis, M., Lewin, W. H. G., & Dieters, S. 1999, ApJ, 519, L159
Beloborodov, A. M. 1999, ApJ, 510, L123
Brocksopp, C., Fender, R. P., Larionov, V., Lyuty, V. M., Tarasov, A. E., Pooley, G. G., Paciesas, W. S., & Roche, P. 1999, MNRAS, 309, 1063
Brocksopp, C., Jonker, P. G., Fender, R. P., Groot, P. J., van der Klis, M., & Tingay, S. J. 2001, MNRAS, 323, 517
Campbell-Wilson, D., McIntyre, V., Hunstead, R., & Green, A. 1998, IAU Circ. 7010
Corbel, S., Fender, R. P., Tzioumis, A. K., Nowak, M., McIntyre, V., Durouchoux, P., & Sood, R. 2000, A&A, 359, 251
Cui, W., Zhang, S. N., Chen, W., & Morgan, E. H. 1999, ApJ, 512, L43
Di Matteo, T., Celotti, A., & Fabian, A. C. 1999, MNRAS, 304, 809
Fender, R. P. 2000, in The Neutron Star-Black Hole Connection, preprint (astro-ph/9911032)
Fender, R. P. 2001, MNRAS, 322, 31
Fender, R. P., et al. 1999, ApJ, 519, L165
Fender, R. P., Hjellming, R. M., Tilamus, R. P. J., Pooley, G. G., Deane, J. R., Ogley, R. N., & Spencer, R. E. 2001, MNRAS, 322, 23L
Fender, R. P., & Kuulkers, E. 2001, MNRAS, in press
Fender, R. P., Pooley, G. G., Durouchoux, P., Tilamus, R. P. J., & Brocksopp, C. 2000, MNRAS, 312, 853
Hameury, J. M., Lasota, J. P., McClintock, J. E., & Narayan, R. 1997, ApJ, 489, 234
Han, X., & Hjellming, R. M. 1992, ApJ, 400, 304
Hannikainen, D., Campbell-Wilson, D., Hunstead, R., McIntyre, V., Lovell, J., Reynolds, J., Tzioumis, T., & Wu, K. 2001, Ap&SS, in press
Harmon, B. A., et al. 1992, in Proc. Compton Observatory Science Workshop, ed. C. Shrader, N. Gehrels & B. Dennis (NASA CP-3137), 69
Hjellming, R. M., & Han, X. 1995, in X-Ray Binaries, ed. W. H. G. Lewin, J. van Paradijs, & E. P. J. van den Heuvel (Cambridge: Cambridge Univ. Press), 308

Hjellming, R. M., & Johnston, K. J. 1988, ApJ, 328, 600
Homan, J., Wijnands, R., van der Klis, M., Belloni, T., van Paradijs, J., Klein-Wolt, M., Fender, R. P., & Méndez, M. 2001, ApJS, 132, 377
Hynes, R. I., Mauche, C. W., Haswell, C. A., Shrader, C. R., Cui, W., & Chaty, S. 2000, ApJ, 539, L37
Jain, R. K., & Bailyn, C. D. 2000, IAU Circ. 7400
Jain, R. K., Bailyn, C. D., Orosz, J. A., McClintock, J. E., Sobczak, G. J., & Remillard, R. A. 2001, ApJ, 546, 1086
Jain, R. K., Bailyn, C. D., Orosz, J. A., Remillard, R. A., & McClintock, J. E. 1999, ApJ, 517, L131
Kolb, U., King, A. R., Ritter, H., & Frank, J. 1997, ApJ, 485, L33
Levine, A. M., et al. 1996, ApJ, 469, L33
Lin, D., et al. 2000, ApJ, 532, 548
Masetti, N., & Soria, R. 2000, IAU Circ. 7399
McCollough, M. L., Wilson, C. A., & Sun, X. 2000, IAU Circ. 7400
Meyer, F., Liu, B. F., & Meyer-Hofmeister, E. 2000, A&A, 354, L67
Miller, J. M. et al. 2001, ApJ, submitted
Orosz, J. A., & Bailyn, C. D. 1997, ApJ, 477, 876
Orosz, J. A., Bailyn, C. D., & Jain, R. K. 1998, IAU Circ. 7009
Pooley, G. G., Fender, R. P., & Brocksopp, C. 1999, MNRAS, 302, L1
Poutanen, J. 1999, in Theory of Black Hole Accretion Discs, ed. M. A. Abramowicz, G. Björnsson & J. E. Pringle (Cambridge: Cambridge Univ. Press), 100
Regös, E., Tout, C. A., & Wickramasinghe, D. 1998, ApJ, 509, 362
Remillard, R. A., McClintock, J. E., Sobczak, G. J., Bailyn, C. D., Orosz, J. A., Morgan, E. H., & Levine, A. M. 1999, ApJ, 517, L127
Sánchez-Fernández, C., et al. 1999, A&A, 348, L9
Sault, R. J., Teuben, P. J., & Wright, M. C. H. 1995, in ASP Conf. Ser. 77, Astronomical Data Analysis Software and Systems IV, ed. R. Shaw, H. E. Payne & J. J. E. Hayes, 433
Shrader, C. R., Wagner, R. M., Hjellming, R. M., Han, X. H., & Starrfield, S. G. 1994, ApJ, 434, 698
Smith, D. A. 1998, IAU Circ. 7008
Smith, D. A., Levine, A. M., Remillard, R., Fox, D., & Schaefer, R. 2000, IAU Circ. 7399
Sobczak, G. J., McClintock, J. E., Remillard, R. A., Cui, W., Levine, A. M., Morgan, E. H., Orosz, J. A., & Bailyn, C. D. 2000a, ApJ, 531, 537
———. 2000b, ApJ, 544, 993
Sobczak, G. J., McClintock, J. E., Remillard, R. A., Levine, A. M., Morgan, E. H., Bailyn, C. D., & Orosz, J. A. 1999, ApJ, 517, L121
Stirling, A. M., Spencer, R. E., de la Force, C. J., Garrett, M. A., Fender, R. P., & Ogley, R. N. 2001, MNRAS, submitted
Tomsick, J. A., Corbel, S., & Kaaret, P. 2001, ApJ, submitted
Wijnands, R., Homan, J., & van der Klis, M. 1999, ApJ, 526, L33
Zhang, S. N., Mirabel, I. F., Harmon, B. A., Kroeger, R. A., Rodríguez, L. F., Hjellming, R. M., & Rupen, M. P. 1997, in AIP Conf. Proc. 410, Proc. 4th Compton Symposium, ed. C. D. Dermer, M. S. Strickman & J. D. Kurfess (New York: AIP), 141

2.7.2

Near-Infrared Synchrotron Emission from the Compact Jet of GX 339-4.

Article publié dans :

Astrophys. J., 2002, 573, L35-L39

Corbel, S., Fender, R. P.

THE ASTROPHYSICAL JOURNAL, 573:L000–L000, 2002 July 1

NEAR-INFRARED SYNCHROTRON EMISSION FROM THE COMPACT JET OF GX 339−4

S. CORBEL
Université Paris VII and Service d'Astrophysique, Centre d'Etudes de Saclay, Orme des Merisiers, Batiment 709, F-91191 Gif-sur-Yvette, France; corbel@discovery.saclay.cea.fr
AND
R. P. FENDER
Astronomical Institute "Anton Pannekoek," University of Amsterdam, and Center for High Energy Astrophysics, Kruislaan 403, 1098 SJ Amsterdam, Netherlands; rpf@astro.uva.nl
Received 2002 January 22; accepted 2002 May 15; published 2002 June 6

ABSTRACT

We have compiled contemporaneous broadband observations of the black hole candidate X-ray binary GX 339−4 when in the low/hard X-ray state in 1981 and 1997. The data clearly reveal the presence of two spectral components, with thermal and nonthermal spectra, overlapping in the optical–near-infrared bands. The nonthermal component lies on an extrapolation of the radio spectrum of the source, and we interpret it as optically thin synchrotron emission from the powerful, compact jet in the system. Detection of this break from self-absorbed to optically thin synchrotron emission from the jet allows us to place a firm lower limit on the ratio of jet (synchrotron) to X-ray luminosities of ≥5%. We further note that extrapolation of the optically thin synchrotron component from the near-infrared to higher frequencies coincides with the observed X-ray spectrum, supporting models in which the X-rays could originate via optically thin synchrotron emission from the jet (possibly instead of Comptonization).

Subject headings: black hole physics — ISM: jets and outflows — radiation mechanisms: nonthermal — radio continuum: stars — stars: individual (GX 339−4)

1. COMPACT JET FROM BLACK HOLE CANDIDATES IN THE LOW/HARD X-RAY STATE

Radio emission from black hole X-ray binaries has long been associated with bright radio flares (>100 mJy) starting around the onset of an X-ray outburst. This is usually interpreted as synchrotron emission from relativistic electrons ejected from the system with large bulk velocities; in a few cases, such jets have been directly imaged. In the rising phase of the flares, the radio spectrum is usually flat or inverted, a characteristic of optically thick synchrotron emission (spectral index $\alpha \geq 0$ for a flux density $S_\nu \propto \nu^\alpha$), and then quickly evolves to a decay phase characterized by optically thin emission with negative spectral index. For recent reviews, see Hjellming & Han (1995), Mirabel & Rodríguez (1999), and Fender & Kuulkers (2001).

By observing the persistent black hole candidates (BHCs) in our Galaxy (in particular, GX 339−4 and Cyg X-1), it has been possible to show that they were usually associated with weak (a few millijanskys) radio counterparts with different properties than the bright radio flaring transient BHCs. Indeed, GX 339−4 and Cyg X-1 are most of the time characterized by a persistent radio source with a flat or slightly inverted ($\alpha \geq 0$) radio spectrum (Martí et al. 1996; Corbel et al. 2000). Such radio properties have been interpreted as arising from a conical, self-absorbed compact jet (on milliarcsecond scales), similar to those considered for flat-spectrum active galactic nuclei (AGNs; Blandford & Königl 1979; Hjellming & Johnston 1988; Falcke & Biermann 1996). This interpretation has been successfully confirmed with the direct imaging of a compact jet in Cyg X-1 (Stirling et al. 2001). Radio emission has also been shown to be correlated with soft and hard X-ray emission (Hannikainen et al. 1998; Brocksopp et al. 1999; Corbel et al. 2000). Observations of GX 339−4 have shown that the compact jet was quenched in the high/soft state (Fender et al. 1999; Corbel et al. 2000). Recent observations of X-ray novae have shown that the compact jet was a ubiquitous property of BHCs in the low/hard state (Fender 2001a; Corbel et al. 2001a and references therein). The compact jet seems to be quenched in the intermediate/very high states, i.e., in any state where a strong soft X-ray component exists (Corbel et al. 2001a).

Compact jet models predict a cutoff or break to the flat or inverted spectral component above a frequency at which the jet is no longer self-absorbed, even at the base. This break is observed in the millimeter range for the compact cores of most flat-spectrum AGNs (e.g., Bloom et al. 1994). To date, there has been no clear detection of such a high-frequency break in the self-absorbed synchrotron spectrum from an X-ray binary system. Detection of such a high-frequency cutoff is important, as a firm lower limit to the radiative luminosity of the self-absorbed part of the compact jet can be established by measuring this high-frequency cutoff. The secondary star in GX 339−4 is very likely an evolved low-mass star (e.g., Shahbaz, Fender, & Charles 2001; Chaty et al. 2002) without significant thermal contribution in the near-infrared range. GX 339−4 is therefore maybe the best candidate to look for a high-frequency cutoff to the compact jet spectral component. We, therefore, looked at all published (to our knowledge) optical and near-infrared observations of GX 339−4 while in the low/hard state. We present evidence that the cutoff frequency of the compact jet is in the near-infrared range, based on observations performed in a bright low/hard state in 1981. This is confirmed by later observations in 1997. We then discuss the implication of this cutoff on the energetic content of the compact jet related to the bolometric X-ray luminosity of the system.

2. OBSERVATIONS

2.1. *A Bright Low/Hard State of GX 339−4 in 1981*

Observations in 1981 revealed that GX 339−4 had been very active with transitions to various X-ray states. Indeed, in

1981 March, optical observations showed that the optical counterpart was very faint ($B \approx 20.34 \pm 0.15$ mag, $V \geq 19.5$ mag) and therefore indicated that GX 339−4 was in the off state (Ilovaisky & Chevalier 1981, 1987). X-ray observations performed by the *Hakucho* satellite on April 7 failed to detect GX 339−4 with an upper limit of 15 mCrab (Maejima et al. 1984). On May 7, GX 339−4 was already in a brighter optical state, with $V \sim 16.3$ mag (Grindlay 1981). Subsequent optical and X-ray observations (see below) revealed that GX 339−4 was in the standard low/hard state up to June 27, where the X-ray monitoring observations performed by *Hakucho* showed that GX 339−4 made a transition to a high/soft state (Maejima et al. 1984). According to Motch et al. (1983), the peak of the low/hard state was around May 28.

2.1.1. *Optical, Near-Infrared, and X-Ray Observations*

When GX 339−4 was found to be in a bright low/hard state in 1981 May, several observations were performed in the optical and near-infrared bands. Here we decided to concentrate on the period from May 24 to June 4, as the flux from GX 339−4 was observed to be similar in *V* and *B* filters on May 28 and June 4. Near-infrared observations in *J*, *H*, *K*, and *L* bands were performed with the ESO 3.6 m telescope in La Silla, Chile, on May 24 by Motch, Ilovaisky, & Chevalier (1981). Using the 1.5 m Danish telescope at La Silla, Motch et al. (1981) also performed optical observations in the *B*, *V*, *R*, and *I* bands on May 28. Pedersen (1981) conducted *U*-, *B*-, and *V*-band optical observations on June 4. A conservative error of 0.1 mag is applied in this study to the various optical and near-infrared measurements. An optical extinction of $A_V = 3.7 \pm 0.3$ mag, coupled with the extinction law of Cardelli, Clayton, & Mathis (1989), has been used to deredden these data (Zdziarski et al. 1998). The uncertainty on the dereddened flux estimates is dominated by the uncertainties on the optical extinction. The optical and near-infrared data have been discussed in various papers but in a different framework than the one presented here (Motch et al. 1983, 1985; an optical extinction of $A_V = 2$ mag was used in Motch et al. 1985). The data used in this Letter are summarized in Table 1.

An X-ray spectrum in the 1–50 keV range was obtained by the *Ariel 6* satellite on 1981 May 30–31. The data were best fitted with a power law of photon index ~1.5 (Ricketts 1983), typical for the low/hard X-ray state. As these X-ray data are simultaneous with the optical and near-infrared observations mentioned above, they have been used in this Letter to estimate the luminosity in soft and hard X-rays and are plotted in Figure 2.

2.1.2. *The Level of Radio Emission*

Hannikainen et al. (1998) first pointed out that the radio and X-ray emission in GX 339−4 were strongly correlated during the low/hard state, a correlation that has been studied in more detail by Corbel et al. (2000) using a longer, extensive set of data. Using simultaneous *Rossi X-Ray Timing Explorer* (*RXTE*; Proportional Counter Array and High-Energy X-Ray Timing Experiment) and radio observations, we have been able to improve significantly the quality of this study (previous works only used BATSE and *RXTE*/all-sky monitor [ASM] data). We observed a very strong power-law correlation between radio and soft and hard X-ray emissions in the low/hard state over 3 orders of magnitude in X-ray flux. The correlation corresponds to the relation $F_{\rm rad} = 1.72 F_{\rm X}^{0.71}$, where $F_{\rm rad}$ is the radio flux density (in millijanskys) at 8640 MHz and $F_{\rm X}$ the 3–9 keV flux (in units of 10^{-10} ergs s^{-1} cm^{-2}; S. Corbel et al. 2002, in preparation). As no radio observations were performed in 1981 (the radio counterpart was discovered in 1994 by Sood & Campbell-Wilson 1994), we can estimate the level of radio emission around the time of the optical–near-infrared observations, using the X-ray spectrum obtained simultaneously by *Ariel 6*. A flux of 22.3×10^{-10} ergs s^{-1} cm^{-2} in the 3–9 keV band is measured; the above mentioned fitting function therefore allows us to estimate the radio flux density of GX 339−4 to 16 mJy at 8640 MHz (with a conservative error of 1 mJy). As the correlation observed in GX 339−4 is maintained over several years (S. Corbel et al. 2002, in preparation), it is safe to assume that it represents the true level of radio emission of GX 339−4 that would have been detected on 1981 May 30. The typical spectral index of the inverted spectral component in the radio regime has been found to be around +0.15 during the most sensitive radio observations performed in the low/hard state (Corbel et al. 2000).

TABLE 1
LOG OF OPTICAL AND NEAR-INFRARED OBSERVATIONS

Band	Date	Telescope	Flux (mag)	Flux[a] (mJy)	Reference
U	1981 Jun 4	Danish 1.5 m	16.2	132.1 ± 59.1	1
B	1981 Jun 4	Danish 1.5 m	16.3	122.8 ± 46.4	1
V	1981 Jun 4	Danish 1.5 m	15.5	69.9 ± 19.6	1
R	1981 May 28	Danish 1.5 m	14.8	44.1 ± 9.2	2
I	1981 May 28	Danish 1.5 m	13.9	31.7 ± 4.2	2
J	1981 May 24	ESO 3.6 m	12.6	39.3 ± 3.1	2
H	1981 May 24	ESO 3.6 m	12.1	29.6 ± 1.6	2
K	1981 May 24	ESO 3.6 m	10.9	43.3 ± 1.4	2
L	1981 May 24	ESO 3.6 m	9.4	56.6 ± 0.9	2
J	1997 Jul 19	ESO 2.2 m	14.2	8.9 ± 0.7	3
H	1997 Jul 19	ESO 2.2 m	13.1	11.4 ± 0.6	3
K	1997 Jul 19	ESO 2.2 m	12.4	10.8 ± 0.3	3

[a] Dereddened fluxes using an optical extinction of $A_V = 3.7 \pm 0.3$ mag; a conservative error of 0.1 mag is assumed.

REFERENCES.—(1) Pedersen 1981; (2) Motch et al. 1981; (3) Chaty et al. 2002.

2.2. *Additional Observations Performed during a Low/Hard State*

In addition to the data from 1981, we found only one other case of near-infrared observation during a low/hard state, which appears not to be dominated by the thermal emission from the disk. It is data from the ESO 2.2 m telescope taken on 1997 July 19 (Chaty et al. 2002); they are presented in Table 1. Almost simultaneously, GX 339−4 was observed by the Molonglo Observatory Synthesis Telescope (MOST) at 843 MHz at a level of 4.2 ± 0.7 mJy on 1997 July 22. We also found that one X-ray observation (discussed in Wilms et al. 1999) was made by *RXTE* on 1997 July 7. We found that the *Compton Gamma Ray Observatory*/BATSE 20–100 keV and *RXTE*/ASM 2–12 keV fluxes were on average a factor of 1.75 fainter on July 7 compared to July 19. We therefore used this factor to scale the X-ray observation at the time of the near-infrared observations, as the shape of the X-ray energy spectrum stays almost constant in the low/hard state. Based on this *RXTE* spectrum and on the radio–X-ray correlation (S. Corbel et al. 2002, in preparation), the level of radio emission at 8640 MHz is estimated to be 5.0 ± 0.1 mJy, giving a spectral index of 0.08 ± 0.08 if we take into account the MOST detection.

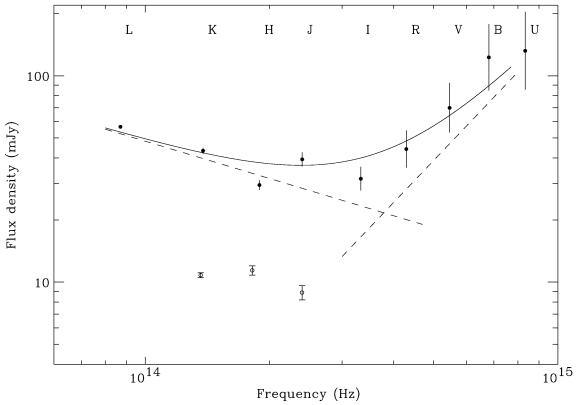

FIG. 1.—Optical and near-infrared magnitudes dereddened with an optical extinction of $A_V = 3.7 \pm 0.3$ mag. Filled circles are observations for the 1981 low/hard state, and open circles are for the 1997 low/hard state. For 1981, the data have been fitted with the sum (*solid line*) of two power-law components (*dotted lines*) with a spectral index of −0.6 for the near-infrared range and +2.1 for the optical range.

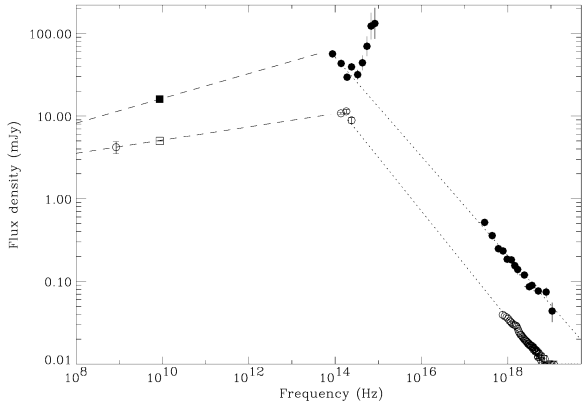

FIG. 2.—Broadband radio-infrared-optical and X-ray spectra of GX 339−4 during a low/hard state in 1981 (*filled symbols*) and 1997 (*open symbols*). Filled and open circles represent the various measurements obtained from quasi-simultaneous observations. The square symbol is the level of radio emission at 8640 MHz estimated from the measured X-ray fluxes based on the existing correlation between radio and X-ray emission (S. Corbel et al. 2002, in preparation). The long-dashed and short-dashed lines correspond to self-absorbed and optically thin regimes in the jet, respectively (spectral indexes of +0.15 and −0.6 for 1981; +0.08 and −0.65 for 1997). These two lines are for illustrative purposes only, as a smooth transition is expected between the two regimes (e.g., Markoff et al. 2001).

3. RESULTS AND DISCUSSION

3.1. *Spectral Energy Distribution in the Low/Hard State: Evidence of Near-Infrared Synchrotron Emission*

The optical and near-infrared flux, corrected for interstellar extinction, have been plotted in Figure 1 for the 1981 low/hard state data. At first inspection, it is obvious that the near-infrared data points clearly deviate from an extension of the optical slope. For illustration purposes, these observations have been fitted with a function consisting of a sum of two power laws, resulting in a spectral index of −0.6 for the near-infrared range and +2.1 for the optical data. The optical data are broadly consistent with thermal emission, presumably from an accretion disk. On the contrary, emission in the *J*, *H*, *K*, and *L* bands clearly points to an infrared excess of nonthermal origin.

In order to understand the nature of this infrared excess, we have plotted in Figure 2 the spectral energy distribution from radio to hard X-rays during the 1981 low/hard state of GX 339−4. Using an extrapolation of the radio spectrum (with typical spectral index) up to the infrared range, we find that the *L*-band data point is compatible with a simple extension of the power law originating from the radio domain. This seems to indicate that radio and near-infrared emission may have a common physical origin. Considering the fact that the radio emission of GX 339−4 or other BHCs in the low/hard state has been interpreted as the optically thick synchrotron emission from a compact jet (Corbel et al. 2000; Fender 2001a), it is likely that we are observing the near-infrared synchrotron emission from the compact jet of GX 339−4. The negative spectral index of the near-infrared data indicates that they lie above the optically thin break, which probably lies at a wavelength of a few microns.

In Figures 1 and 2, we also plot the broadband data from 1997 July. Again, the near-infrared level is compatible with an extension of the flat component originating in the radio domain. Connecting the *K*-band observation to the MOST detection with a power law results in a spectral index of 0.08, in agreement with the estimated spectral index in radio range. It is interesting to note that the radio, near-infrared, and X-ray emission all varied by about the same factor (~4 times fainter) between 1981 and 1997, which favors a direct link, if not a common physical origin, for all three spectral components. Inspection of Figure 1 may also indicate that the cutoff frequency was at slightly higher energy in 1997, but this would require verification by more observations.

In addition to GX 339−4, there has been some indication that near-infrared and/or optical synchrotron emission from a compact outflow also took place in a few other sources. Indeed, it has been shown that the inverted (or flat) radio spectra from GRO J0422+32, XTE J1118+480, GS 1354−64, XTE J1550−564, GRS 1915+105, and GS 2023+338 (see references in Fender 2001a and Corbel et al. 2001a) probably extend up to the near-infrared–optical range, but no high-frequency break to this component has yet been directly observed. Such a break has been inferred at a wavelength of a few microns for the low/hard state transient XTE J1118+480 (Markoff, Falcke, & Fender 2001); in this source, it seems clear that, whatever the model, there is excess flux in the near-infrared that cannot be explained by an accretion disk alone (Hynes et al. 2000; see also Hynes et al. 2002 for XTE J1859+226). In XTE J1550−564, there was fairly good evidence that the break frequency lies in the near-infrared (Corbel et al. 2001a, 2001b). Recently, Jain et al. (2001) confirmed our interpretation, based on their near-infrared and optical monitoring of XTE J1550−564 during the 2000 X-ray outburst. Indeed, a secondary flare (prominent in near-infrared but also visible in optical) was associated with the transition to the low/hard state and the reappearance of the compact jet.

With these observations of GX 339−4, taken during the bright low/hard state in 1981, we clearly detect two emission components in the near-infrared–optical domain. The optical data points typically represent the thermal emission from the outer part of the accretion disk, whereas the near-infrared points correspond to the optically thin regime of the synchrotron emission from the electron distribution. The high-frequency cutoff to the flat (or inverted) spectra from the compact jet therefore probably falls in the near-infrared range. This is the first time

that such a high-frequency break is unambiguously detected in the flat (or inverted) synchrotron spectrum from a compact jet. The observations taken during the 1997 low/hard state also show similar cutoff (Fig. 1) and therefore favor this scenario.

3.2. *A Powerful Compact Jet*

The detection of a high-frequency cutoff to the optically thick spectral component is vitally important in order to estimate the total radiative luminosity of the compact jet. In the rest of this Letter, we consider only the optically thick spectral component of the jet—while optically thin synchrotron emission may extend through the optical, UV, and X-ray bands (e.g., Markoff et al. 2001), in that energy regime disentangling its contribution from that of thermal, Comptonized, or other high-energy components is not straightforward. With the observed level of near-infrared emission, a spectral index of +0.15, and the high-frequency synchrotron break at a few microns (~10^{14} Hz), the total radiative luminosity of the compact jet of GX 339−4 (during the 1981 low/hard state) is about $L_J = 10^{35}$ ergs s^{-1} (10^{28} W) for a distance of 4 kpc. The total jet power, P_J, can be estimated as $P_J = L_J \eta^{-1} F(\beta, i)$, where η represents the radiative efficiency for the jet and $F(\beta, i)$ is a correction factor for bulk relativistic motion (dependent on the bulk motion velocity β in units of c and the angle i to the line of sight; see discussion in Fender 2001a, 2001b). A value of $\eta = 0.05$ seems a conservative estimate of the radiative efficiency of the jet, based on the minimum power requirement of the repeated ejections from GRS 1915+105 (Fender & Pooley 2000; Fender 2001b), which also have a flat spectrum from radio to near-infrared. The effect of bulk relativistic motion cannot be precisely determined, but this results in overestimating the jet power only for low values of the inclination angle (see Fig. 6 in Fender 2001a). As the jet is both radiatively inefficient and likely to have a large, possibly dominant, kinetic energy component, this represents a firm lower limit on the jet power. With these limitations in mind, a likely lower limit to the total power of the compact jet in GX 339−4 (during the 1981 low/hard state) is estimated to be around $P_J = 2 \times 10^{36}$ ergs s^{-1} (2×10^{29} W).

Based on the simultaneous *Ariel 6* observations (Fig. 2), the integrated X-ray luminosity of GX 339−4 in the 1–50 keV band is 2×10^{37} ergs s^{-1} (2×10^{30} W). As the X-ray luminosity of BHCs in the low/hard state is known to peak around ~100 keV, extrapolating the *Ariel 6* X-ray spectrum up to 200 keV results in a 1–200 keV X-ray luminosity of $L_X = 4 \times 10^{37}$ ergs s^{-1} (4×10^{30} W). Therefore, it is fairly safe to say that the jet power of GX 339−4 is at least 5% of the bolometric X-ray luminosity (which is presumed to reflect the accretion rate). (For the observations in 1997, we obtained a total jet power of $P_J = 5 \times 10^{35}$ ergs s^{-1} and a 1–200 keV X-ray luminosity $L_X = 5 \times 10^{36}$ ergs s^{-1}, resulting in a fraction of 8%.) In XTE J1550−564, Corbel et al. (2001a) derived a similar value for the ratio of jet to accretion luminosities. Based on similar arguments, Fender (2001a) obtained a similar value for the compact jet of Cyg X-1 using an extrapolation of the radio-millimeter spectrum up to the near-infrared range. A higher ratio (~20%) has been found for the recently discovered X-ray transient XTE J1118+480 (Fender et al. 2001). The general trend that is starting to emerge from these repeated multiwavelength observations of compact jet sources is that the power in the jet may be a significant fraction (similar in all sources?) of the total accretion luminosity.

The base of the jet is probably located very close to, or coexistent with, the corona (Fender et al. 1999), which would explain why there is a very strong coupling between the hard X-ray emission from the corona and the radio emission from the compact jet (Hannikainen et al. 1998; Corbel et al. 2000). This may arise via Comptonization of electrons in the base of the jet or, more radically, it may be that the X-ray emission observed in the low/hard spectral state is also optically thin synchrotron emission directly from the jet (Markoff et al. 2001). In Figure 2, as well as the radio-infrared-optical data, we also plot the contemporaneous X-ray data. Extrapolation of the optically thin synchrotron component in the near-infrared agrees remarkably well with the measured X-ray spectra. Despite the limited data sets, we consider this to be a support to the model of Markoff et al. (2001), but this interpretation will need to be confirmed by further broadband observations and will be discussed in another paper (S. Markoff et al. 2002, in preparation).

4. CONCLUSIONS

The compilation of data presented here for the black hole candidate X-ray binary GX 339−4 clearly reveals the presence of an additional, apparently nonthermal, spectral component in the optical/near-infrared spectral bands, above the thermal emission expected from the accretion flow/disk. We interpret this nonthermal spectral component as optically thin synchrotron emission from just above the frequency at which the self-absorbed spectrum observed in the radio band breaks to optically thin (i.e., it is no longer self-absorbed in any part of the jet). This is the strongest evidence to date that this break lies in the spectral region of the near-infrared to optical bands. We further note that extrapolation of this nonthermal component is coincident with the X-ray spectrum, supporting models in which the X-rays could arise via optically thin synchrotron emission from the jet (instead of Comptonization).

However, the interpretation of the X-ray spectra is necessarily complex, and the relative contributions of disk, Comptonized, synchrotron, and other components is not straightforward to separate. Our approximate measurement of the high-frequency extent of the self-absorbed synchrotron component does, however, give us a very firm and conservative lower limit to the power associated with the jet. Comparing this with the measured X-ray emission, we find that the jet requires *at least* 5% of the total accretion power. This is further evidence for the ubiquity of powerful jets in the low/hard spectral state of accreting black holes.

The authors acknowledge useful discussions with Sera Markoff.

REFERENCES

Blandford, R. D., & Königl, A. 1979, ApJ, 232, 34
Bloom, S. D., Marscher, A. P., Gear, W. K., Terasranta, H., Valtaoja, E., Aller, H. D., & Aller, M. F. 1994, AJ, 108, 398
Brocksopp, C., Fender, R. P., Larionov, V., Lyuty, V. M., Tarasov, A. E., Pooley, G. G., Paciesas, W. S., & Roche P. 1999, MNRAS, 309, 1063
Cardelli, J. A., Clayton, G. C., & Mathis, J. S. 1989, ApJ, 345, 245
Chaty, S., Mirabel, I. F., Geldoni, P., Mereghetti, S., Duc, P.-A., Martí, J., & Mignani, R. P. 2002, MNRAS, 331, 1065
Corbel, S., Fender, R. P., Tzioumis, A. K., Nowak, M., McIntyre, V., Durouchoux, P., & Sood, R. 2000, A&A, 359, 251

Corbel, S., et al. 2001a, ApJ, 554, 43
———. 2001b, in AIP Conf. Proc. 587, Gamma 2001: Gamma-Ray Astrophysics 2001, ed. S. Ritz, N. Gehrels, & C. R. Shrader (New York: AIP), 126
Falcke, H., & Biermann, P. L. 1996, A&A, 308, 321
Fender, R. P. 2001a, MNRAS, 322, 31
Fender, R. P. 2001b, Ap&SS Suppl., 276, 69
Fender, R. P., Hjellming, R. M., Tilanus, R. P. J., Pooley, G. G., Deane, J. R., Ogley, R. N., & Spencer, R. E. 2001, MNRAS, 322, L23
Fender, R. P., & Kuulkers, E. 2001, MNRAS, 324, 923
Fender, R. P., & Pooley, G. G. 2000, MNRAS, 318, L1
Fender, R. P., et al. 1999, ApJ, 519, L165
Grindlay, J. 1981, IAU Circ. 3613
Hannikainen, D. C., Hunstead, R. W., Campbell-Wilson, D., & Sood, R. K. 1998, A&A, 337, 460
Hjellming, R. M., & Han, X. 1995, in X-Ray Binaries, ed. W. H. G. Lewin, J. van Paradijs, & E. P. J. van den Heuvel (Cambridge: Cambridge Univ. Press), 308
Hjellming, R. M., & Johnston, K. J. 1988, ApJ, 328, 600
Hynes, R. I., Haswell, C. A., Chaty, S., Shrader, C. R., & Cui, W. 2002, MNRAS, 331, 169
Hynes, R. I., Mauche, C. W., Haswell, C. A., Shrader, C. R., Cui, W., & Chaty, S. 2000, ApJ, 539, L37
Ilovaisky, S. A., & Chevalier, C. 1981, IAU Circ. 3586
Ilovaisky, S. A., & Chevalier, C. 1987, IAU Circ. 4394
Jain, R. K., Bailyn, C. D., Orosz, J. A., McClintock, J. E., & Remillard, R. A. 2001, ApJ, 554, L181
Maejima, Y., Makishima, K., Matsuoka, M., Ogawara, Y., Oda, M., Tawara, Y., & Doi, K. 1984, ApJ, 285, 712
Markoff, S., Falcke, H., & Fender, R. 2001, A&A, 372, L25
Martí, J., Rodríguez, L. F., Mirabel, I. F., & Paredes, J. M. 1996, A&A, 306, 449
Mirabel, I. F., & Rodríguez, L. F. 1999, ARA&A, 37, 409
Motch, C., Ilovaisky, S. A., & Chevalier, C. 1981, IAU Circ. 3609
Motch, C., Ilovaisky, S. A., Chevalier, C., & Angebault, P. 1985, Space Sci. Rev., 40, 219
Motch, C., Ricketts, M. J., Page, C. G., Ilovaisky, S. A., & Chevalier, C. 1983, A&A, 119, 171
Pedersen, H. 1981, IAU Circ. 3613
Ricketts, M. J. 1983, A&A, 118, L3
Shahbaz, T., Fender, R., & Charles, P. A. 2001, A&A, 376, L17
Sood, R. K., & Campbell-Wilson, D. 1994, IAU Circ. 6006
Stirling, A. M., Spencer, R. E., de la Force, C. J., Garrett, M. A., Fender, R. P., & Ogley, R. N. 2001, MNRAS, 327, 1273
Wilms, J., Nowak, M. A., Dove, J. B., Fender, R. P., & Di Matteo, T. 1999, ApJ, 522, 460
Zdziarski, A. A., Poutanen, J., Mikolajewska, J., Gierliński, M., Ebisawa, K., & Johnson, W. N. 1998, MNRAS, 301, 435

2.7.3

Radio/X-ray correlation in the low/hard state of GX 339-4.

Article publié dans :

Astron. & Astrophys., 2003, 400, 1007-1012

Corbel, S., Nowak, M. A., Fender, R. P., Tzioumis, A. K., Markoff, S.

A&A 400, 1007–1012 (2003)
DOI: 10.1051/0004-6361:20030090

Astronomy & Astrophysics

Radio/X-ray correlation in the low/hard state of GX 339–4

S. Corbel[1], M. A. Nowak[2], R. P. Fender[3], A. K. Tzioumis[4], and S. Markoff[5]

[1] Université Paris VII and Service d'Astrophysique (Fédération APC), CEA Saclay, 91191 Gif-sur-Yvette, France
[2] Chandra X-ray Science Center, Massachusetts Institute of Technology, NE80-6077, 77 Massachusetts Ave., Cambridge MA 02139, USA
[3] Astronomical Institute "Anton Pannekoek", University of Amsterdam and Center for High Energy Astrophysics, Kruislaan 403, 1098 SJ Amsterdam, The Netherlands
[4] Australia Telescope National Facility, CSIRO, PO Box 76, Epping NSW 1710, Australia
[5] Massachusetts Institute of Technology, Center for Space Research, NE80-6035, 77 Massachusetts Ave., Cambridge MA 02139, USA

Received 6 November 2002 / Accepted 6 January 2003

Abstract. We present the results of a long-term study of the black hole candidate GX 339−4 using simultaneous radio (from the Australia Telescope Compact Array) and X-ray (from the Rossi X-ray Timing Explorer and BeppoSAX) observations performed between 1997 and 2000. We find strong evidence for a correlation between these two emission regimes that extends over more than three decades in X-ray flux, down to the quiescence level of GX 339−4. This is the strongest evidence to date for such strong coupling between radio and X-ray emission. We discuss these results in light of a jet model that can explain the radio/X-ray correlation. This could indicate that a significant fraction of the X-ray flux that is observed in the low-hard state of black hole candidates may be due to optically thin synchrotron emission from the compact jet.

Key words. black hole physics – radiation mechanisms: non-thermal – ISM: jets and outflows – radio continuum: stars – X-rays: stars – stars: individual: GX 339−4

1. Introduction

Since its discovery in 1973 by the X-ray satellite *OSO-7* (Markert et al. 1973), the black hole candidate (BHC) GX 339−4 has been the subject of many extensive studies from the radio bands to the hard X-rays. Nevertheless, the physical processes involved in its broadband energy spectra have not been fully identified and understood. As the source has displayed a wide range of accretion rates – it is one of the rare sources that has been observed in all canonical black hole X-ray states – it is a prime target for studying the accretion-ejection processes of accreting black hole systems (persistent or transient). Among the canonical states, it is perhaps the low/hard state (LHS) that has attracted the most attention in recent years. Observations of various components in the LHS spectral energy distribution (SED) have highlighted analogies with the flat spectra of low-luminosity active galactic nuclei (AGN) (Falcke & Biermann 1996).

Radio emission from GX 339−4 during the LHS is characteristic of a self-absorbed compact jet (Corbel et al. 2000), similar to that considered for flat spectrum AGNs (Blandford & Königl 1979). Regular radio observations have shown that the compact jet of GX 339−4 was quenched in the high/soft state (Fender et al. 1999; Corbel et al. 2000). Similar properties have now been observed in a growing number of persistent and transient BHCs (the jet has even been resolved in Cyg X−1, Stirling et al. 2001), thus suggesting that compact jets are ubiquitous in BHCs during the LHS (Fender 2001). In addition to being responsible for most of the emission in the radio regime, the compact jets may have a significant contribution in the infrared/optical bands (Corbel & Fender 2002) and could also be part of the processes involved in producing the X-ray emission (Markoff et al. 2001). In that case, it would imply that compact jets are very powerful and could dominate the entire SED of BHC during their low/hard states.

The other main components of the SED are a possible thermal contribution from the accretion disk, which extends from the near-infrared/optical to the soft X-rays, and the possible Comptonisation of accretion disk photons with a hot electron corona, which likely contribute mostly in soft and hard X-rays (Nowak et al. 2002; Done 2002). Despite not being observed, the companion star in the GX 339−4 system is likely an evolved low-mass star (Shahbaz et al. 2001; Chaty et al. 2002; Cowley et al. 2002).

A good way to assess the contribution of jets at high energy is to perform a broadband study of these systems

Send offprint requests to: S. Corbel,
e-mail: corbel@discovery.saclay.cea.fr

simultaneously at radio and X-ray frequencies, and in particular to study the correlation that could exist between these two emission domains. In fact, such a correlation has already been found for BHC in the LHS, e.g., GX 339−4 (Hannikainen et al. 1998; Corbel et al. 2000) and Cyg X−1 (Brocksopp et al. 1999) for BHC in the LHS. These radio/X-ray observations, however, only sampled a very limited range of X-ray and radio fluxes (or accretion rates). Most of these previous studies also suffered from the lack of sensitivity of the X-ray observations. A similar correlation also has been observed in the hard state of Cyg X−3 (McCollough et al. 1999; Choudhury et al. 2002). A more complex relation, but still indicating a relation between radio emitting electrons and the hard X-ray power law dominated state (like that in the LHS of BHC), is found in GRS 1915+105 (Klein-Wolt et al. 2002).

An interpretation for such a tight correlation is that it is the result of high energy synchrotron emission from the compact jet, as already has been proposed for XTE J1118+480 (Markoff et al. 2001). Alternatively, it possibly could be due to Compton scattering of photons from the companion star or the accretion flow off of the jet's leptons (Georganopoulos et al. 2002). In this paper, we report the results of a long-term study of GX 339−4 performed simultaneously in radio and X-ray during the years 1997–2000, in order to investigate the radio/X-ray correlation over many orders of magnitude with sensitive observations. Evidence for evolution of this correlation with energy is also presented. We discuss these results in light of the jet model of Markoff et al. (2003).

2. Observations

2.1. Radio observations

All radio observations were performed with the Australia Telescope Compact Array (ATCA). The ATCA synthesis telescope is an east-west array consisting of six 22 m antennas. The 8.6 GHz data that we used is from Corbel et al. (2000); however, we re-analaysed all (five) observations for which the radio flux densities were weaker than 1 mJy. Further details concerning the ATCA and its data reduction can be found in Corbel et al. (2000). We also added the result of a series of three new ATCA observations, for a total duration of nearly 20 hours, performed on 2000 September 12, 15 and 18, during the recent off state. These observations provided a strong (99% confidence level) upper limit of 60 μJy at 8.6 GHz, which is the best constraint we have for the level of radio emission originating from GX 339−4 during its off state.

2.2. X-ray observations

2.2.1. RXTE

We used the *Rossi X-ray Timing Explorer* (*RXTE*) to perform a number of observations of GX 339−4 from 1997–1999, most of which represent the LHS. Analysis of the brightest of these observations was previously presented (Nowak et al. 2002); here we also consider analyses of faint, "off state" observations from late 1999. All data extractions were performed in an identical manner as that described by Nowak et al. (2002). The flux in various energy bands was determined by fitting a model comprised of neutral hydrogen absorption ($N_{\rm H}$ was fixed to 6×10^{21} cm^{-2}), a multi-temperature disk blackbody (e.g., Mitsuda et al. 1984) with peak temperature fixed at 0.25 keV, an exponentially cut-off broken power law with break energy at ≈10 keV, and a (potentially) broad Gaussian line with peak energy fixed at 6.4 keV. The faintest observations were fit with a simpler absorbed, single power law, plus (fixed peak energy) line feature. Feng et al. (2001) found that the iron line is shifted to higher energies when GX 339−4 was observed at low X-ray fluxes. However, this shift is not intrinsic to GX 339−4, but is rather due to the Galactic diffuse emission (Wardzinski et al. 2003). Note that due to differences between the two sets of instruments that comprise *RXTE*, the *Proportional Counter Array* (*PCA*, ≈3−20 keV) and the *High Energy X-ray Timing Experiment* (*HEXTE*, ≈20–200 keV), a normalization constant between the *PCA* and *HEXTE* detectors was used, and all flux values are normalized to the *PCA* flux levels (for further descriptions of this process, see Wilms et al. 1999). The flux error bars were chosen to be the larger of the statistical error, or 1%, which is a reasonable estimate of the RXTE internal systematic error (e.g., Wilms et al. 1999). Short timescale (≤few seconds) X-ray variability is usually observed in the low-hard state of GX 339−4 (Smith & Liang 1999; Nowak et al. 2002). However, on a longer timescale (e.g. 10 min) the radio emission is steady (see Fig. 3 in Corbel et al. 2000) and so also is the X-ray spectrum of GX 339−4 integrated on those timescales (i.e., there is almost no very low frequency power in the power spectral densities, Nowak et al. 2002 and references therein). Therefore the error bars used in Table 1 are likely not affected by the variability of the source (which is quite steady on timescales greater than 10 min). Note that in Table 1 we quote the *absorbed* flux level; however, as we only consider energies ≥3 keV, this is at most a few percent different to the unabsorbed flux level.

RXTE has a broad ≈1° radius field of view, and therefore is potentially subject to contamination from faint background sources (or, in the case of GX 339−4, diffuse emission from the galactic ridge, Wardzinski et al. 2003). Four of the *RXTE* observations, however, were performed simultaneously with the much narrower field of view (≈4 arcmin radius) *Advanced Satellite for Cosmology and Astrophysics* (*ASCA*). Utilizing the same models described above, the 3–9 keV flux of the brightest two simultaneous observations determined by *ASCA* was 75–81% of that determined by the *PCA* – consistent with a well-known calibration offset between *PCA* and *ASCA* (see the discussion in Nowak et al. 2002). For the faintest two observations, the relative normalizations of the *ASCA* spectra substantially decreased with decreasing flux. This was taken as evidence for a faint background source or sources that lie within the field of view of the *PCA*, but not within the field of view of *ASCA*. The *RXTE* observation of 1999 July 29 is assumed to be heavily dominated by this contaminating source, and this spectrum, multiplied by 0.78, is subtracted as a "background correction" before model fitting and flux determination, from all *RXTE* observations occurring later than the observation of May 14 1999. With this additional background subtracted,

Table 1. Observing log of the simultaneous X-ray (PCA, unless otherwise noted) and radio (8.6 GHz) observations of GX 339−4 performed during a low/hard state. X-ray absorbed fluxes are all normalized to PCA. Upper limits are given at the one sigma level.

	X-ray flux				Radio flux density
Date	3–9 keV	9–20 keV	20–100 keV	100–200 keV	8.6 GHz
(y.m.d.)	(10^{-10} erg s^{-1} cm^{-2})				(mJy)
1997.02.03	10.74 ± 0.11	10.28 ± 0.10	29.05 ± 0.29	11.57 ± 0.12	9.10 ± 0.10
1997.02.10	9.41 ± 0.09	9.10 ± 0.09	26.81 ± 0.27	10.74 ± 0.11	8.20 ± 0.10
1997.02.17	9.02 ± 0.09	8.73 ± 0.09	25.50 ± 0.26	10.49 ± 0.11	8.70 ± 0.10
1999.02.12	4.76 ± 0.05	4.21 ± 0.04	11.80 ± 0.12	4.16 ± 0.40	4.60 ± 0.08
1999.03.03	4.75 ± 0.05	4.62 ± 0.05	14.91 ± 0.15	6.66 ± 0.32	5.74 ± 0.06
1999.04.02	4.93 ± 0.05	4.90 ± 0.05	15.87 ± 0.16	8.75 ± 0.45	5.10 ± 0.07
1999.04.22	2.30 ± 0.02	2.34 ± 0.02	7.37 ± 0.10	4.04 ± 0.36	3.11 ± 0.04
1999.05.14	0.76 ± 0.01	0.74 ± 0.01	2.23 ± 0.17	1.39 ± 0.29	1.44 ± 0.04
1999.06.25	0.059 ± 0.006	0.052 ± 0.005	<0.17	<0.29	0.24 ± 0.05
1999.07.07	0.029 ± 0.002	<0.01	<0.17	<0.33	0.12 ± 0.04
1999.07.29	<0.008	<0.012	<0.16	<0.29	<0.036
1999.08.17[a]	0.025 ± 0.003	0.019 ± 0.014	0.110 ± 0.046	<0.05	0.27 ± 0.07
1999.09.01[b]	0.037 ± 0.003	<0.01	<0.17	<0.29	0.32 ± 0.05
2000.09.10[c,d]	0.0057 ± 0.001	<0.0034	<0.005	<0.07	<0.02

[a] Flux (or upper limits) above 9 keV are deduced from the BeppoSAX observations performed on 1999.08.13.
[b] Average X-ray flux, based on the PCA observations on 1999.08.28 and 1999.09.04.
[c] Radio observations on 2000.09.12, 2000.09.15 and 2000.09.18.
[d] X-ray observations performed by BeppoSAX.

the *ASCA* determined fluxes of the faintest two simultaneous observations become 73% and 83% of the corrected *PCA* 3–9 keV flux levels. Good agreement also is obtained between the *ASCA* and the corrected *PCA* spectra.

2.2.2. BeppoSAX

During the recent off state of GX 339−4 we conducted an ~50 ks X-ray observation with *BeppoSAX* on September 10 2000. GX 339−4 is detected in the 1–10 keV energy range with both LECS and MECS, and the spectrum can be fitted with a power-law with a photon index 2.22 ± 0.24 (90% confidence level) with interstellar absorption fixed to 5.1×10^{21} cm^{-2} ($\chi^2_0 = 0.74$ for 35 degrees of freedom). The absorbed flux in the 3–9 keV energy range is 5.7×10^{-13} erg cm^{-2} s^{-1} (relative to the MECS normalization). To within a few percent, the fluxes normalized to MECS are consistent with the ones normalized to PCA (e.g. Della Ceca et al. 2001). We also re-analysed the BeppoSAX observation performed on August 13 1999 by Kong et al. (2000), as it was close to the date of one of our radio observations. All measurements (radio and X-ray) are tabulated in Table 1.

3. An extremely strong correlation between radio and X-ray emissions during the low/hard state

In Figs. 1 to 4, we utilize the results from Table 1 and display the radio flux density at 8.6 GHz versus the X-ray flux in different energy bands. It is apparent from these plots that a strong correlation exists between these two emission regimes in GX 339−4. As all these measurements have been taken during the low/hard state or during the transition to the off state (which appears to be a weak luminosity version of the low/hard state), we can further deduce that this correlation is a property of the low/hard state. We note that this strong correlation extends over more than three orders of magnitude in X-ray flux (e.g. the 3–9 keV band for which we have the best coverage). The correlation appears to hold for the entire four year period covered by the observations. Specifically, the 1997 measurements lie on the same line as the measurements performed during the transition to the off state in 1999 (Figs. 1 to 4), even though there was a transition to the soft state between these sets of observations (Belloni et al. 1999; Nowak et al. 2002).

In order to quantify the level of the correlation, we have calculated for each of the X-ray bands the Spearman rank correlation coefficient (Barlow 1989) between the radio and X-ray fluxes (Table 2). For this calculation, all detections have been taken into account (i.e. including even the points which are not strictly simultaneous or affected by a small reflare in hard X-rays: 1999.08.17 and 1999.09.01). It is clear from this analysis that the relationship between the radio and the soft and hard X-ray fluxes is extremely strong (a Student's t-test (Barlow 1989) shows the significance of the correlation is greater than 99.9% for each of the energy bands). This points to a persistent coupling between the mechanism(s) of the origin of the

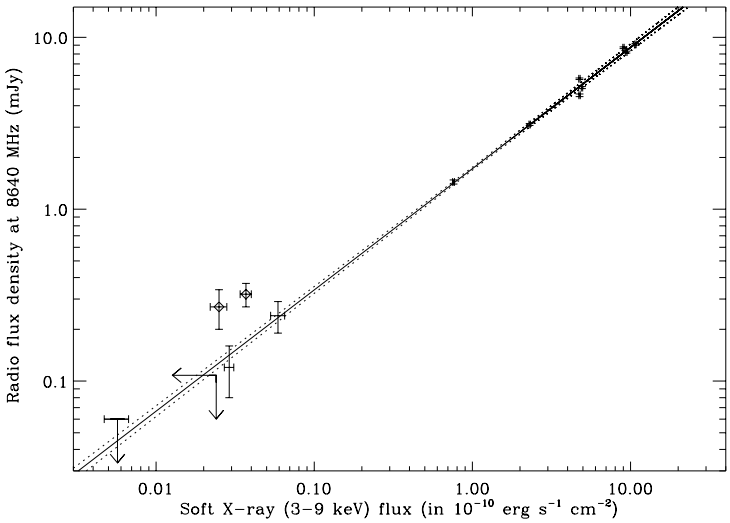

Fig. 1. The radio flux density at 8.6 GHz is plotted versus the X-ray flux in the 3–9 keV energy band. The continuous line denotes the fit to the data with the function described in the body of the paper and with the parameters estimated in Table 3, the dotted line represents the one-sigma deviation to those parameters. Upper limits are plotted at the three sigma level. The diamond points are those points that are not strictly simultaneous (1999.08.17) or maybe affected by a small reflare observed in hard X-rays (1999.09.01, see Fig. 15 in Corbel et al. 2000).

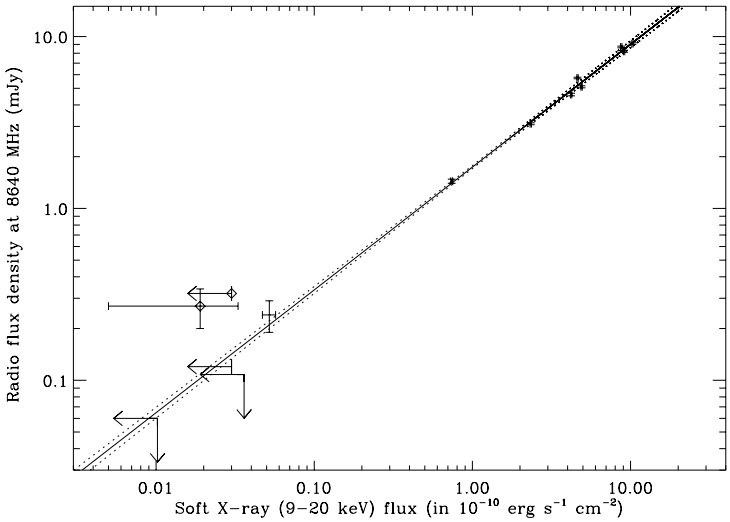

Fig. 2. Same as Fig. 1, but for the X-ray flux in the 9–20 keV energy band.

radio and X-ray emissions while GX 339−4 is in the low/hard state. This is the strongest evidence to date for such a persistent relation.

It is possible to estimate a functional relationship between the flux densities in radio (e.g. 8.6 GHz) and in the various X-ray bands. A linear fit (on a log-log scale) is satisfactory for the four X-ray bands. If we denote $F_{\rm Rad}$ as the radio flux density (in mJy) at 8.64 GHz and $F_{\rm X}$ as the X-ray flux (in units of 10^{-10} erg s^{-1} cm^{-2}) in a given energy band, the relation between these two fluxes can be expressed as $F_{\rm Rad} = a \times F_{\rm X}^{b}$, where a and b are the two constant coefficients given in Table 3. These relations are valid while GX 339−4 is in the standard low/hard state, as we recall that radio emission from GX 339−4 is quenched in the high/soft state (Fender et al. 1999; Corbel et al. 2000).

As the same correlation appears to be maintained over this four year period, it could be realistic to estimate the level of radio emission from GX 339−4 by only measuring its X-ray flux. We note that little scatter is observed around the fitting function for our measurements. This also indicates that there is probably little time delay between the radio and X-ray emission. We also note the index b apparently changes with X-ray energy band. This is consistent with previous X-ray observations that indicate that, with the hard state, the spectrum of GX 339−4

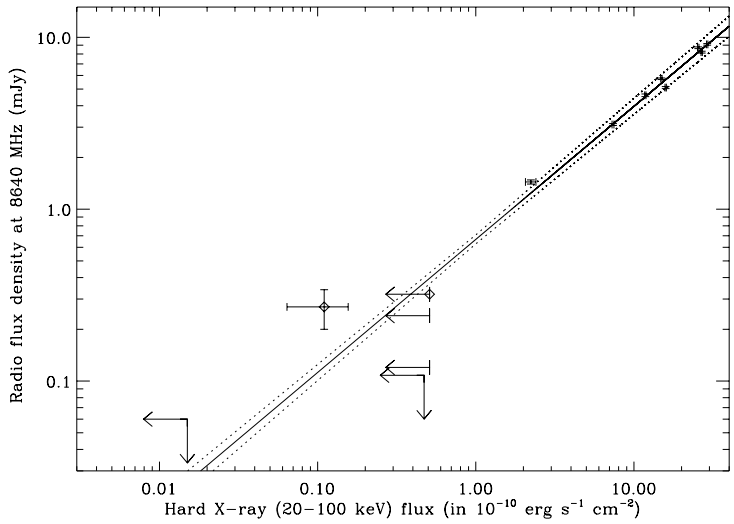

Fig. 3. Same as Fig. 11, but for the X-ray flux in the 20–100 keV energy band.

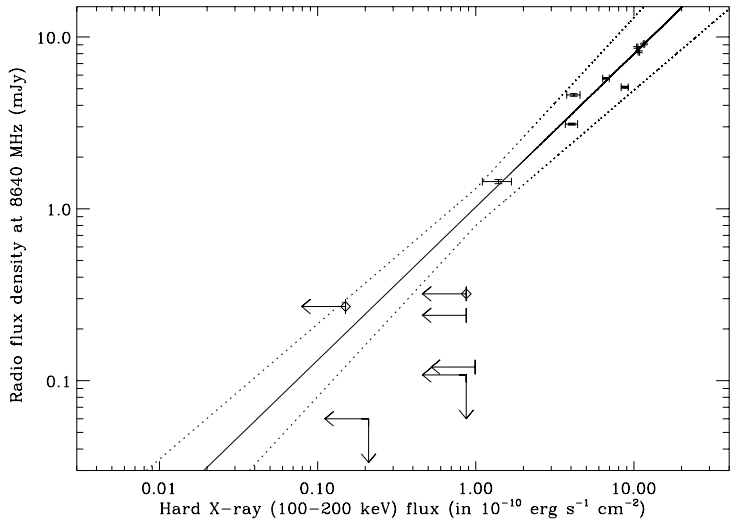

Fig. 4. Same as Fig. 1, but for the X-ray flux in the 100–200 keV energy band.

Table 2. Spearman rank correlation coefficient, r_s, and the two sided significance of its deviation from zero, p, between the radio flux density measured at 8.6 GHz and the X-ray flux measured in various energy bands. The number of data-points, N, used in the calculations is also indicated in the last column.

X-ray band	r_s	p	N
3–9 keV	0.94	7.0×10^{-7}	12
9–20 keV	0.96	7.3×10^{-6}	10
20–100 keV	0.97	2.2×10^{-5}	9
100–200 keV	0.95	2.6×10^{-4}	8

becomes spectrally harder as the source becomes fainter (e.g., Nowak et al. 2002).

4. Discussions

With this study, we showed that the previously observed correlation between X-ray and radio fluxes during the low-hard state of GX 339–4 (Hannikainen et al. 1998; Corbel et al. 2000) extends over more than three decades in X-ray luminosity. The observations, spread over almost four years, indicated that the same fitting functions probably hold during these years, despite an intervening state transition. The radio emission in GX 339–4 is likely associated with the optically thick synchrotron emission from the compact jet (Corbel et al. 2000). The very strong correlation of radio emission with X-ray flux indicates that synchrotron processes may also play a role at high energies.

Table 3. Parameters of the function used to fit the radio flux density (in mJy) at 8.6 GHz, $F_{\rm Rad}$, versus the flux, $F_{\rm X}$, measured in a given energy band ((in unit of 10^{-10} erg s^{-1} cm^{-2}). The relation is expressed as $F_{\rm rad} = a \times F_{\rm X}^{b}$.

X-ray band	a	b
3–9 keV	1.721 ± 0.035	0.706 ± 0.011
9–20 keV	1.739 ± 0.035	0.715 ± 0.011
20–100 keV	0.667 ± 0.041	0.774 ± 0.021
100–200 keV	1.024 ± 0.287	0.891 ± 0.104

It has already been pointed out for GX 339–4 that the near infrared/optical bands show a spectral break that may indicate that the X-ray spectrum is an extension of the optically thin synchrotron emission from the compact jet (Corbel & Fender 2002). Specifically, the infrared points are consistent with an extrapolation of the slope from the radio, while the infrared/optical break extrapolates to the observed X-rays. The jet model, originally developed for AGN and previously applied to XTE J1118+480 (Markoff et al. 2001), has been further improved and also applied to these datasets (with additional optical data), and is discussed in a companion paper (Markoff et al. 2003). Markoff et al. (2003) showed that the jet model can account for the broadband spectra of GX 339–4 radio through optical through X-ray, primarily by only changing two parameters: the jet power and the location of the acceleration zone. The fact that the correlation holds at very low X-ray luminosity indicates that a compact jet is also produced when the source is close to quiescence. Therefore, the broadband emission of the jets has to be taken into account when studying the bolometric luminosity of black hole in quiescence, e.g. Campana & Stella (2000) and Garcia et al. (2001).

It is interesting to note that the radio flux at 8.6 GHz is proportional to the X-ray flux as $F_{\rm rad} \propto F_{\rm X}^{+0.71}$ (in the 3–9 and 9–20 keV bands) and that the same behaviour with the same index b has recently been found to hold for the black hole transient V404 Cyg (Gallo et al. 2002). The jet model of Markoff et al. (2003) successfully explains this dependency analytically using the formalism developed in Falcke & Biermann (1996). Indeed, if the only varying parameter of the model is the power in the jet, then the X-ray flux is expected to vary as $F_{\rm X} \propto F_{\rm rad}^{+1.41}$, i.e. $F_{\rm rad} \propto F_{\rm X}^{+0.71}$, completely consistent with the behaviour of GX 339–4 and V404 Cyg. The current versions of the jet model, however, do not account for the evolution of the exponent, b, in $F_{\rm rad} \propto F_{\rm X}^{b}$, for the higher energy X-ray bands, as is found for GX 339–4 (Table 3). If a jet is the underlying cause of the overall radio/X-ray correlation, the model may need to be further developed in order to explain this detailed behavior. However, it is important to point out that these higher energies include the canonical "100 keV cutoff" region in the data, where one expects the X-rays to decrease in comparison to the radio emission. However, the simplified accretion disk model used by Markoff et al. (2003) currently does not include all spectral components, e.g., the contribution from reflection which are often observed in the hard state X-ray spectra of BHC (e.g., Done 2002). Studies like these clearly show, however, that including jet emission processes in any models of BHC spectra in their low/hard state is crucially important to fully understand the physical processes in these sources.

Acknowledgements. The Australia Telescope is funded by the Commonweath of Australia for operation as a National Facility managed by CSIRO. We would like to thank Ben Chan and Richard Dodson for conducting the September 2000 ATCA observations.

References

Barlow, R. J. 1989, in Statistics: A Guide to the Use of Statistical Methods in the Physical Sciences (John Wiley & Sons)
Blandford, R. D., & Königl, A. 1979, ApJ, 232, 34
Brocksopp, C., Fender, R. P., Larionov, V., et al. 1999, MNRAS, 309, 1063
Belloni, T., Méndez, M., van der Klis, M., Lewin, W. H. G., & Dieters, S. 1999, ApJ, 519, L159
Campana, S., & Stella, L. 2000, ApJ, 541, 849
Chaty, S., Mirabel, I. F., Goldoni, P., et al. 2002, MNRAS, 331, 1065
Choudhury, M., Rao, A. R., Vadawale, S. V., Ishwara-Chandra, C. H., & Jain, A. K. 2002, A&A, 383, L35
Corbel, S., Fender, R. P., Tzioumis, A. K., et al. 2000, A&A, 359, 251
Corbel, S., & Fender, R. P. 2002, ApJ, 573, L35
Cowley, A. P., Schmidtke, P. C., Hutchings, J. B., & Crampton, D. 2002, AJ, 123, 1741
Della Ceca, R., Pellegrini, S., Bassani, L., et al. 2001, A&A, 375, 781
Done, C. 2002, Philosophical Transactions of the Royal Society (Series A: Mathematical, Physical, and Engineering Sciences), submitted [astro-ph/0203246]
Falcke, H., & Biermann, P. L. 1996, A&A, 308, 321
Fender, R. P., Corbel, S., Tzioumis, A. K., et al. 1999, ApJ, 519, L165
Fender, R. P. 2001, MNRAS, 322, 31
Feng, Y. X., Zhang, S. N., Sun, X., et al. 2001, ApJ, 553, 394
Gallo, E., Fender, R. P., & Pooley, G. 2002, Proc. of the 4th Microquasar Workshop, ed. Ph. Durouchoux, Y. Fuchs, & J. Rodriguez [astro-ph/0207551]
Garcia, M. R., McClintock, J. E., Narayan, R., et al. 2001, ApJ, 553, L47
Georganopoulos, M., Aharonian, F. A., & Kirk, J. G. 2002, A&A, 388, L25
Hannikainen, D. C., Hunstead, R. W., Campbell-Wilson, D., & Sood, R. K. 1998, A&A, 337, 460
Klein-Wolt, M., Fender, R. P., Pooley, G. G., et al. 2002, MNRAS, 331, 745
Kong, A. K. H., Kuulkers, E., Charles, P. A., & Homer, L. 2000, MNRAS, 312, L49
Markert, T. H., Canizares, C. R., Clark, G. W., et al. 1973, ApJ, 184, L67
Markoff, S., Falcke, H., & Fender, R. 2001, A&A, 372, L25
Markoff, S., Nowak, M., Corbel, S., Fender, R., & Falcke, H. 2003, A&A, 397, 645
McCollough, M. L., Robinson, C. R., Zhang, S. N., et al. 1999, ApJ, 517, 951
Mitsuda, K., Inoue, H., Koyama, K., et al. 1984, PASJ, 36, 741
Nowak, M. A., Wilms, J., & Dove, J. B. 2002, MNRAS, 332, 856
Shahbaz, T., Fender, R., & Charles, P. A. 2001, A&A, 376, L17
Smith, I. A., & Liang, E. P. 1999, ApJ, 519, 771
Stirling, A. M., Spencer, R. E., de la Force, C. J., et al. 2001, MNRAS, 327, 1273
Wardzniski, G., Zdziarski, A. A., Gierlinski, M., et al. 2003, MNRAS, in press [astro-ph/0207598]
Wilms, J., Nowak, M. A., Dove, J. B., Fender, R. P., & di Matteo, T. 1999, ApJ, 522, 460

2.7.4

Is the "IR Coincidence" Just That ?

Article publié dans :

Astrophys. J., 2005, 626, 1006-1014

Nowak, M. A., Wilms, J., Heinz, S., Pooley, G., Pottschmidt, K., Corbel, S.

The Astrophysical Journal, 626:1006–1014, 2005 June 20

IS THE "IR COINCIDENCE" JUST THAT?

Michael A. Nowak,[1] Jörn Wilms,[2] Sebastian Heinz,[1,3] Guy Pooley,[4]
Katja Pottschmidt,[5,6] and Stephane Corbel[6,7]
Received 2004 September 22; accepted 2005 March 9

ABSTRACT

Previous work by Motch et al. suggested that in the low/hard state of GX 339−4 the soft X-ray power law extrapolated backward in energy agrees with the IR flux level. Corbel & Fender later showed that the typical hard-state radio power law extrapolated forward in energy meets the backward-extrapolated X-ray power law at an IR spectral break, which was explicitly observed twice in GX 339−4. This IR coincidence has been cited as further evidence that synchrotron radiation from a jet might make a significant contribution to the observed X-rays in hard-state black hole systems. We quantitatively explore this hypothesis with a series of simultaneous radio/X-ray observations of GX 339−4, taken during its 1997, 1999, and 2002 hard states. We fit these spectra, in detector space, with a simple, but remarkably successful, doubly broken power-law model that indeed requires an IR spectral break. For these observations, the break position and the integrated radio/IR flux have stronger dependences upon the X-ray flux than the simplest jet model predictions. If one allows for a softening of the X-ray power law with increasing flux, then the jet model can agree with the observed correlation. We also find evidence that the radio flux–X-ray flux correlation previously observed in the 1997 and 1999 GX 339−4 hard states shows a parallel track for the 2002 hard state. The slope of the 2002 correlation is consistent with observations taken in prior hard states; however, the radio amplitude is reduced. We then examine the radio flux–X-ray flux correlation in Cyg X-1 through the use of 15 GHz radio data obtained with the Ryle radio telescope and *Rossi X-Ray Timing Explorer* data from the All-Sky Monitor and pointed observations. We again find evidence of parallel tracks, and here they are associated with "failed transitions," or the beginning of a transition, to the soft state. We also find that for Cyg X-1 the radio flux is more fundamentally correlated with the hard, rather than the soft, X-ray flux.

Subject headings: accretion, accretion disks — black hole physics — radiation mechanisms: nonthermal — X-rays: binaries

1. INTRODUCTION

Both Cyg X-1 and GX 339−4 in their spectrally hard, radio-loud states have served as canonical examples of the so-called low state (or hard state) of Galactic black hole candidates (see Pottschmidt et al. 2003b; Nowak et al. 2002 and references therein). As we discuss below, in this state the X-ray spectrum is reasonably well approximated by a power law with photon spectral index (i.e., photon flux per unity energy $\propto E^{-\Gamma}$) of $\Gamma \approx 1.7$, with the power law exponentially cut off at high energies ($\approx$100 keV). It long has been suggested that such spectra are due to Comptonization of soft photons from an accretion disk by a hot corona in the central regions of the compact object system (e.g., Sunyaev & Trümper 1979). Comptonization models have been very successful in describing the broadband X-ray–soft gamma-ray spectra of both Cyg X-1 (Pottschmidt et al. 2003a) and GX 339−4 (Nowak et al. 2002).

It has recently been hypothesized, however, that the X-ray spectra of hard-state sources might instead be due to synchrotron and synchrotron self-Compton (SSC) radiation from a mildly relativistic jet (Markoff et al. 1991, 2003). Jet models have been prompted in part by multiwavelength (radio, optical, and X-ray) observations of hard-state systems. Although radio emission from Cyg X-1 was first observed quite some time ago (Braes & Miley 1971), it is more recently that a radio jet has been imaged (Stirling et al. 2001) and that the low/hard state X-ray flux has been shown to be positively correlated with the radio flux (Pooley et al. 1999).

Radio emission has also been discovered in GX 339−4 (Sood & Campell-Wilson 1994). The radio emission is correlated with X-ray flux in spectrally hard states (Hannikainen et al. 1998) but is quenched during spectrally soft states (Fender et al. 1999). Furthermore, in hard states of GX 339−4, the 3–9 keV X-ray flux (in units of 10^{-10} ergs cm^{-2} s^{-1}) is related to the 8.6 GHz radio flux (in mJy) by $F_{\rm X} \approx 0.46 \mathcal{F}_r^{1.42}$ (Corbel et al. 2003; note that throughout this paper we use calligraphic script to denote flux densities, i.e., flux per unit energy and roman script to denote flux integrated over an energy band). This correlation was seen to hold over several decades in X-ray flux and also to hold for two hard-state epochs that were separated by a prolonged intervening soft-state outburst. Similar correlations were found between energy bands in the 9–200 keV range and the radio flux (Corbel et al. 2003). It has been further suggested that the $F_{\rm X} \propto \mathcal{F}_r^{1.4}$ correlation is a universal property of the low/hard state of black hole binaries (Gallo et al. 2003).

This specific power-law dependence of the radio flux on the X-ray flux naturally arises in synchrotron jet models (Falcke &

[1] Massachusetts Institute of Technology, Center for Space Research, 70 Vassar Street, Cambridge, MA 02139; mnowak@space.mit.edu, heinzs@space.mit.edu.
[2] Department of Physics, University of Warwick, Coventry, CV4 7AL, UK; wilms@astro.uni-tuebingen.de.
[3] Chandra Fellow.
[4] Astrophysics Group, Cavendish Laboratory, University of Cambridge, Madingley Road, Cambridge CB3 OHE, UK; guy@mrao.cam.ac.uk.
[5] Max-Planck-Institut für extraterrestrische Physik, Giessenbachstrasse, 85748 Garching, Germany.
[6] INTEGRAL Science Data Center, Chemin d'Écogia 16, 1290 Versoix, Switzerland; Katja.Pottschmidt@obs.unige.ch.
[7] Université Paris VII and Service d'Astrophysique, CEA-Saclay, 91191 Gif-sur-Yvette Cedex, France; corbel@discovery.saclay.cea.fr.

TABLE 1
GX 339−4 Observed Fluxes (1 σ Confidence)

		Flux (mJy)					Flux (10^{-9} ergs cm^{-2} s^{-1})			
ObsID	Date	0.84 GHz	1.38 GHz	2.40 GHz	4.80 GHz	8.64 GHz	3–9 keV	9–20 keV	20–100 keV	100–200 keV
20181-01-01.....	1997 Feb 3	$7.0^{+0.6}_{-0.6}$	...	...	...	$9.1^{+0.1}_{-0.1}$	0.90	0.92	2.98	1.27
20181-01-02.....	1997 Feb 10	$5.5^{+0.7}_{-0.7}$	...	...	...	$8.2^{+0.2}_{-0.2}$	0.80	0.82	2.67	1.11
20181-01-03.....	1997 Feb 17	$5.6^{+0.7}_{-0.7}$	$5.4^{+0.2}_{-0.2}$	$6.0^{+0.2}_{-0.2}$	...	$8.7^{+0.2}_{-0.2}$	0.77	0.78	2.63	1.06
40108-01-03 (A).....	1999 Feb 12	...	...	...	$6.34^{+0.08}_{-0.08}$	$4.60^{+0.08}_{-0.08}$	0.41	0.39	1.18	0.48
40108-01-04 (B).....	1999 Mar 3	...	...	...	$6.07^{+0.06}_{-0.06}$	$5.74^{+0.06}_{-0.06}$	0.42	0.42	1.51	0.66
40108-02-01.....	1999 Apr 2	...	...	...	$4.75^{+0.06}_{-0.06}$	$5.10^{+0.06}_{-0.06}$	0.42	0.44	1.60	0.97
40108-02-02.....	1999 Apr 22	...	...	...	$2.92^{+0.06}_{-0.06}$	$3.20^{+0.06}_{-0.06}$	0.19	0.21	0.74	0.43
40108-02-03.....	1999 May 14	...	...	...	$1.25^{+0.06}_{-0.06}$	$1.44^{+0.06}_{-0.06}$	0.07	0.07	0.21	0.14
70109-01-02 (C).....	2002 Apr 3	...	$4.83^{+0.20}_{-0.20}$	$5.13^{+0.11}_{-0.11}$	...	...	1.30	1.47	5.34	2.09
40031-03-01 (D).....	2002 Apr 18	...	...	...	$13.04^{+0.06}_{-0.06}$	$14.16^{+0.07}_{-0.07}$	5.10	4.97	12.3	2.42

Note.—X-ray flux errors are taken to be 3.5%, the average of the fitted normalization difference between PCA and HEXTE, since this exceeds the statistical uncertainties.

Biermann 1995; Corbel et al. 2003; Markoff et al. 2003; Heinz & Sunyaev 2003). Both the location of the break from an optically thick[8] to an optically thin radio spectrum (presumed to continue all the way through the X-ray) and the amplitude of the optically thick portion of the radio spectrum vary with input power to the jet to produce the $F_X \propto \mathcal{F}_r^{1.4}$ scaling. Assuming, however, that the X-ray power of a disk or corona is proportional to $\dot{M}^2$, where $\dot{M}$ is the accretion rate, while the jet power is proportional to $\dot{M}$, also reproduces the scaling relationship (Markoff et al. 2003; Heinz & Sunyaev 2003; Fender et al. 2003; Merloni et al. 2003; Falcke et al. 2004).

Interestingly, nearly 20 years ago Motch et al. (1985) noted that for a set of simultaneous IR, optical, and X-ray observations of the GX 339−4 hard state, the extrapolation of the X-ray power law to low energy agreed with the overall flux level of the optical/IR data. Corbel & Fender (2002) reanalyzed these observations, which did not include simultaneous radio data, as well as a set of (not strictly simultaneous) radio/IR/X-ray observations from the 1997 GX 339−4 hard state. They showed that the low-energy extrapolation of the X-ray power laws and the high-energy extrapolation of the radio power law coincided with a spectral break in the IR. The spectral shapes below and above the IR break were roughly consistent with the radio and X-ray power laws, respectively. This IR coincidence has been cited as further evidence that not only does the jet account for the flat spectrum from radio through infrared, but also optically thin emission from the jet, occurring at energies above the IR break, provides a significant contribution to the observed X-rays (Corbel & Fender 2002; Corbel et al. 2003; Markoff et al. 2003).

In this paper, we quantitatively examine the IR coincidence with a series of simultaneous radio/X-ray spectra of GX 339−4. We use broken power-law fits to the combined radio and X-ray spectra to determine the extrapolated position of the break as a function of observed X-ray flux. We then reassess the correlation between radio and X-ray flux for GX 339−4 by including more recent hard-state observations that occurred at fairly high X-ray fluxes. Based on our results for GX 339−4, we also reassess this correlation for the case of Cyg X-1. We then summarize our results.

[8] By optically thick, we mean radio energy flux density $S_\nu \propto \nu^{\alpha_r}$, with $\alpha_r > 0$. Throughout this work, for both radio and X-ray spectra, we follow the convention $\alpha = 1 - \Gamma$.

2. THE IR COINCIDENCE IN GX 339−4

2.1. *Data Analysis*

We consider a set of 10 simultaneous radio/X-ray observations of GX 339−4, eight of which were discussed previously by us (Wilms et al. 1999; Nowak et al. 2002; Corbel et al. 2003) and come from the 1997 or 1999 hard state and two of which were discussed by Homan et al. (2005) and come from the 2002 hard state (approximately 1 month before a soft-state transition). All X-ray observations were performed with the *Rossi X-Ray Timing Explorer* (*RXTE*). Their observation IDs and associated radio flux densities and integrated X-ray fluxes are presented in Table 1. Note that four of these observations are further labeled A–D, as we single these out for special discussion below. Observations A and B (40108-01-03 and 40108-01-04) occurred immediately after the 1999 soft-to-hard state transition (Nowak et al. 2002) and have optically thin radio spectra ($\alpha_r < 0$). Observations C and D (70109-01-02 and 40031-02-01) have the brightest X-ray fluxes in our sample and are among the brightest hard X-ray states observed in GX 339−4 to date.

To analyze the X-ray spectra of these observations, *RXTE* response matrices were created using the software tools[9] available in HEASOFT 5.3. The Proportional Counter Array (PCA) data were rebinned to have a minimum of 30 counts per bin, uniform systematic uncertainties of 0.5% were applied, and only data between 3 and 22 keV were considered. The High-Energy X-Ray Timing Experiment (HEXTE) data were co-added from the two individual clusters and then were rebinned to have a minimum signal-to-noise ratio (after background subtraction) of 10 in each bin. We considered HEXTE data only in the 18–200 keV range. In the fits discussed below, a multiplicative constant was allowed between the PCA and HEXTE normalization,

[9] The use of HEASOFT 5.3 is very important here, as we find extremely good agreement between PCA and HEXTE when fitting power-law models to the Crab pulsar plus nebula system. This is true for both the power-law normalization and slope, both of which must be determined very accurately when extrapolating over a large range of energies between the radio and X-ray spectra. This spectral and flux agreement is in marked contrast to earlier versions of HEASOFT (see, e.g., the discussion of Wilms et al. 1999).

TABLE 2
GX 339−4 Spectral Fits (90% Confidence Level Errors)

ObsID	$E_{\rm cut}$ (keV)	$E_{\rm fold}$ (keV)	α_r	E_{b-r} (eV)	$\Gamma_{\rm soft}$	$E_{b-{\rm X}}$ (keV)	$\Gamma_{\rm hard}$	$A_{\rm line}$ (10^{-3})	$\sigma_{\rm line}$ (keV)	Constant	χ^2/dof
20181-01-01	37^{+7}_{-6}	155^{+22}_{-19}	$0.11^{+0.08}_{-0.07}$	$0.80^{+1.22}_{-0.48}$	$1.69^{+0.01}_{-0.01}$	$11.3^{+0.6}_{-0.5}$	$1.49^{+0.03}_{-0.02}$	$2.1^{+0.2}_{-0.3}$	$0.6^{+0.1}_{-0.1}$	$0.97^{+0.01}_{-0.02}$	110/108
20181-01-02	42^{+5}_{-5}	140^{+16}_{-14}	$0.17^{+0.10}_{-0.09}$	$0.37^{+0.66}_{-0.23}$	$1.68^{+0.01}_{-0.00}$	$11.0^{+0.6}_{-0.5}$	$1.48^{+0.02}_{-0.02}$	$1.8^{+0.3}_{-0.2}$	$0.7^{+0.1}_{-0.2}$	$0.95^{+0.01}_{-0.01}$	162/114
20181-01-03	53^{+14}_{-8}	133^{+33}_{-31}	$0.26^{+0.04}_{-0.04}$	$1.39^{+0.61}_{-0.40}$	$1.68^{+0.01}_{-0.00}$	$10.7^{+0.6}_{-0.7}$	$1.51^{+0.02}_{-0.02}$	$1.7^{+0.2}_{-0.2}$	$0.6^{+0.1}_{-0.1}$	$0.98^{+0.02}_{-0.02}$	90/90
40108-01-03 (A)	44^{+9}_{-11}	165^{+58}_{-41}	...	...	$1.80^{+0.01}_{-0.01}$	$10.2^{+1.0}_{-0.5}$	$1.59^{+0.02}_{-0.03}$	$1.2^{+0.1}_{-0.2}$	$0.7^{+0.1}_{-0.1}$	$1.03^{+0.01}_{-0.01}$	64/77
40108-01-04 (B)	69^{+14}_{-13}	138^{+59}_{-48}	$-0.09^{+0.04}_{-0.05}$	$13.5^{+37.0}_{-8.0}$	$1.69^{+0.01}_{-0.01}$	$10.6^{+0.6}_{-0.7}$	$1.53^{+0.01}_{-0.02}$	$0.9^{+0.1}_{-0.1}$	$0.6^{+0.1}_{-0.2}$	$1.03^{+0.02}_{-0.02}$	106/103
40108-02-01	32^{+21}_{-8}	345^{+133}_{-79}	$0.12^{+0.06}_{-0.05}$	$0.44^{+0.43}_{-0.20}$	$1.67^{+0.01}_{-0.01}$	$10.5^{+0.6}_{-0.6}$	$1.45^{+0.03}_{-0.02}$	$0.7^{+0.2}_{-0.1}$	$0.5^{+0.2}_{-0.2}$	$0.97^{+0.02}_{-0.02}$	115/93
40108-02-02	44^{+33}_{-18}	304^{+322}_{-142}	$0.16^{+0.07}_{-0.08}$	$0.12^{+0.18}_{-0.06}$	$1.63^{+0.01}_{-0.01}$	$10.7^{+1.2}_{-1.4}$	$1.47^{+0.03}_{-0.05}$	$0.4^{+0.1}_{-0.1}$	$0.5^{+0.1}_{-0.2}$	$0.95^{+0.03}_{-0.03}$	83/67
40108-02-03	...	...	$0.24^{+0.12}_{-0.12}$	$0.07^{+0.16}_{-0.04}$	$1.68^{+0.01}_{-0.02}$	$9.0^{+3.}_{-0.0}$	$1.62^{+0.03}_{-0.05}$	$0.1^{+0.1}_{-0.0}$	$0.6^{+0.2}_{-0.3}$	$0.95^{+0.07}_{-0.08}$	26/44
70109-01-02 (C)	34^{+2}_{-2}	112^{+6}_{-5}	$0.11^{+0.14}_{-0.11}$	$0.95^{+14.3}_{-0.81}$	$1.61^{+0.01}_{-0.01}$	$10.3^{+0.4}_{-0.4}$	$1.37^{+0.01}_{-0.02}$	$2.2^{+0.3}_{-0.4}$	$0.4^{+0.1}_{-0.1}$	$0.99^{+0.01}_{-0.01}$	180/148
40031-03-01 (D)	26^{+1}_{-2}	69^{+2}_{-3}	$0.14^{+0.02}_{-0.01}$	$3.88^{+0.69}_{-0.41}$	$1.73^{+0.01}_{-0.01}$	$11.1^{+0.5}_{-0.5}$	$1.53^{+0.02}_{-0.03}$	$17.7^{+2.0}_{-1.8}$	$0.8^{+0.1}_{-0.1}$	$0.99^{+0.02}_{-0.01}$	143/130

Notes.—The 20181 data are from the 1997 hard state (Wilms et al. 1999; Nowak et al. 2002), the 40108 data are from the 1999 hard state (post-1998 soft state; Nowak et al. 2002), and the 70109 and 40031 data are from the 2002 very luminous hard state (following a 3 yr duration quiescent state; Homan et al. 2005). Note that the radio spectral index, α_r, is defined to be positive for optically thick spectra and is related to the usual X-ray astronomy definition of the photon index by $\alpha_r = 1 - \Gamma_r$. (dof) degrees of freedom.

with the PCA constant fixed to unity. The normalizations of the two instruments were always found to be the same to within a few percent (see Table 2).

The radio data for observation D (40031-03-01) were obtained with the Australia Telescope Compact Array (ATCA) at 4.8 and 8.6 GHz. The radio data for observation C (70109-01-02) were also obtained with ATCA, but at 1.4 and 2.4 GHz. These radio data, as well as the data for observation B (40108-01-04), the 1999 April 22 observation (40108-02-02), and the 1999 May 14 observation (40108-02-03), have been reanalyzed by us. All other radio data come from Wilms et al. (1999), Nowak et al. (2002), and Corbel et al. (2000). In cases of small discrepancies between these latter references, we have adopted the radio flux values of Corbel et al. (2000), since, aside from the radio observations reanalyzed by us, that work represents the most up-to-date analysis of the radio data presented here.

Note that we have considered only data wherein we have nearly simultaneous radio and X-ray spectra. The radio/X-ray observations discussed by Nowak et al. (2002) all have a large degree of overlap between the radio and X-ray observing times, and they show very little long-timescale (>1000 s) variability (Corbel et al. 2000). Radio observations C and D occur approximately a half-day after their corresponding *RXTE* observations, but, again, neither the radio data nor the *RXTE* data show any evidence for long-term variability within the observations themselves. Still, the lack of strict simultaneity might be a relevant factor in some of the results discussed below.

We further require that the source be bright enough to fit the X-ray spectrum in both the PCA and the HEXTE data. As discussed by Corbel et al. (2003) and Wardziński et al. (2002), at low flux levels there is background contamination that affects the *RXTE* spectra of GX 339−4. The spectra can be corrected adequately to yield reasonably accurate integrated soft X-ray fluxes (Corbel et al. 2003); however, the contamination is much more problematic for the spectral extrapolations discussed here.

The observations were analyzed with the Interactive Spectral Interpretation System (ISIS; Houck & Denicola 2000). For our purposes, there are three major reasons for our use of ISIS. First, ISIS uses `s-lang` as a scripting language and hence has most of the programmability of Interactive Data Language or MATLAB, while retaining all the models of XSPEC (Arnaud 1996). Second, data input without a response matrix (i.e., the radio data) is automatically presumed to have an associated diagonal response with 1 cm^2 effective area and 1 s integration time. Thus, we used a fairly straightforward `s-lang` script to convert the radio data from mJy to photon rate in narrow bands around the observation frequencies. This then was used as input for the simultaneous radio/X-ray fits. (So long as they are narrow, the widths of the radio bands do not affect the fits.) We then set the fractional error bars of these "count rate" data equal to the fractional error from the radio measurements.

The third reason for using ISIS is that it treats "unfolded spectra" (shown in Fig. 1) in a model-independent manner. The unfolded spectrum in an energy bin denoted by h, as used to create Figure 1, is defined by

$$F_{\rm unfold}(h) = \frac{[C(h) - B(h)]/\Delta t}{\int R(h, E) A(E)\, dE}, \quad (1)$$

where $C(h)$ is the number of total detected counts, $B(h)$ is the number of background counts, Δt is the integrated observation time, $R(h, E)$ is the unit normalized response matrix describing the probability that a photon of energy E is detected in bin h, and $A(E)$ is the effective detector area at energy E. Contrary to indications of unfolded spectra produced by XSPEC (which are given by the model, rebinned to the output energy bins of the response matrix, and multiplied by the data counts divided by the forward-folded model counts, i.e., the ratio residuals), this definition produces a spectrum that is independent of the fitted model. In Figure 1, we overplot the fitted model (using the internal resolution of the ancillary response function [arf] used in the fitting process). The plotted residuals, however, are those obtained from a proper forward-folded fit.

Although previously we successfully fitted the X-ray spectra with sophisticated Comptonization models (Nowak et al. 2002), we obtain surprisingly good fits for 9 of the 10 radio/X-ray spectra using the following simple model (using the ISIS XSPEC model definitions): absorption (the `phabs` model with $N_{\rm H}$ fixed to 6×10^{21} cm^2) and a high-energy exponential cutoff (the `highecut` model) multiplying a doubly broken power law (the `bkn2pow` model with the first break in the far-IR–to–optical regime and the second break constrained to the 9–12 keV regime) plus a Gaussian line (with energy fixed at 6.4 keV). Results are presented in Table 2. When considering just the X-ray spectra, a singly broken power law fits all 10 spectra, with better results than any of the Comptonization models that we have tried. The 12–200 keV power law is typically seen to be harder than the 3–12 keV power law by $\Delta\Gamma \approx -0.2$. (Correlations of this

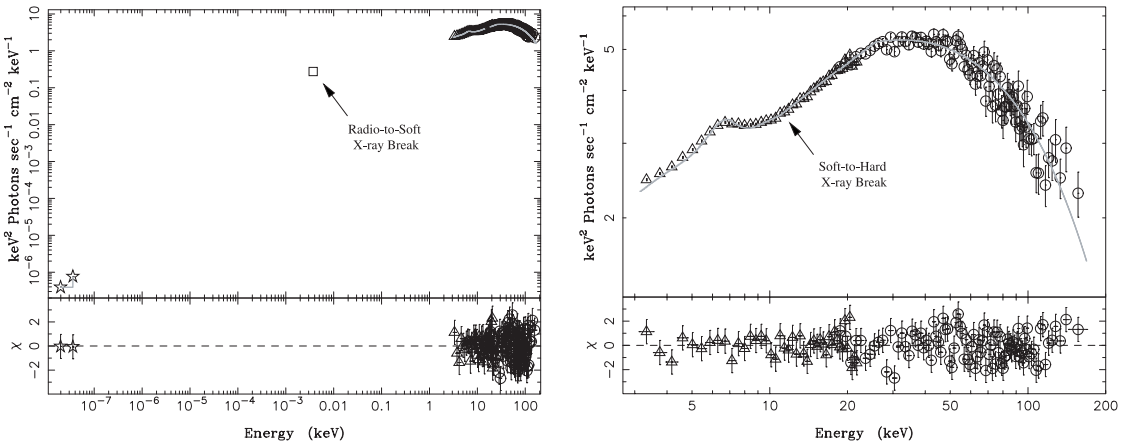

FIG. 1.—*Left*: Unfolded spectra of a simultaneous radio and X-ray spectrum of GX 339−4 (D, ObsID 40031-03-01, in Tables 1 and 2), fitted with an absorbed, exponentially cutoff, doubly broken power law and a Gaussian line. Residuals are from the proper forward-folded model fit. *Right*: Same unfolded spectrum as on the left, showing just the *RXTE* data.

spectral break with overall hardness will be presented for over 200 hard-state spectra of Cyg X-1 in a future work; J. Wilms et al. 2005, in preparation.)

The phenomenological power-law model was of course chosen because we are attempting to answer a phenomenological question: Do the extrapolated radio and X-ray spectra predict the amplitude of the IR flux and the location of any IR break? The power law provides the simplest model to extrapolate. The additional power-law break in the 9–12 keV band is required by the data. The energy band restriction in the fitting process was introduced to avoid spurious local minima caused by the break interfering with the Gaussian line at low energy or with the `highecut` model at high energy. All but one observation has break-energy values, including 90% confidence level error bars, that fall well within this 9–12 keV range.

Phenomenologically speaking, the X-ray break is consistent with the expectations from reflection models (Magdziarz & Zdziarski 1995). However, as shown in Figure 2, the identical broken power-law model described above provides a very good phenomenological description even for Cyg X-1 hard-state data with an extreme break. Although not mutually exclusive with the presence of reflection, such data require at least two broadband continuum components in the X-ray. For example, Figure 2 could be consistent with synchrotron and SSC radiation from jet models (Markoff & Nowak 2004; S. Markoff et al. 2005, in preparation) or a strong disk plus a Comptonization component from corona models. These issues will be explored in greater detail in a forthcoming work (J. Wilms et al. 2005, in preparation).

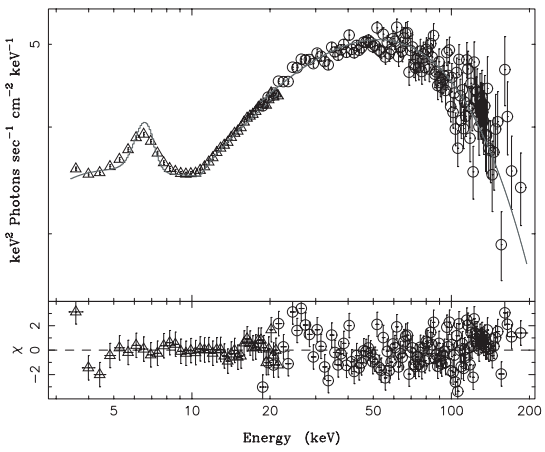

FIG. 2.—Unfolded *RXTE* spectra of Cyg X-1 (J. Wilms et al. 2005, in preparation), fitted with an absorbed, exponentially cutoff, broken power law and a Gaussian line. Residuals are from the proper forward-folded model fit.

2.2. *Predicted Radio–X-Ray Correlations*

Given only two radio points and an X-ray spectrum that is well fitted by a singly broken power law, it is not surprising that the doubly broken power-law models work as well. But how do the fitted locations of the radio–to–soft X-ray break compare to the IR coincidence breaks, and how do the fitted break locations scale with observed flux? In Figure 3 we show the fitted radio–to–X-ray break location as a function of 3–9 keV integrated flux. We also show in this figure the approximate integrated 3–9 keV flux and the IR break location for the 1997 observation discussed by Corbel & Fender (2002). For our GX 339−4 observations of comparable 3–9 keV flux, the doubly broken power-law models do indeed produce a break in the IR. Looking over the whole span of observed integrated X-ray fluxes, however, we see that the model fits presented here have predicted radio–to–X-ray breaks ranging all the way from the far–IR to the blue end of the optical (and into the X-ray, if one also considers observation B [40108-01-04], which has an optically thin radio spectrum).

To assess the correlation of radio–to–X-ray break energy with integrated X-ray flux, we exclude observation B (40108-01-04), which has an optically thin radio spectrum, and perform a regression analysis on the remaining eight data points. We weight the data uniformly, which is equivalent to assuming that intrinsic variations in any correlation dominate over statistical errors. (In the results discussed below, the derived regression slopes and errors encompass the values obtained if one weights the data by their error bars.) We find that the radio–to–X-ray break energy, in eV, scales with the 3–9 keV integrated flux as

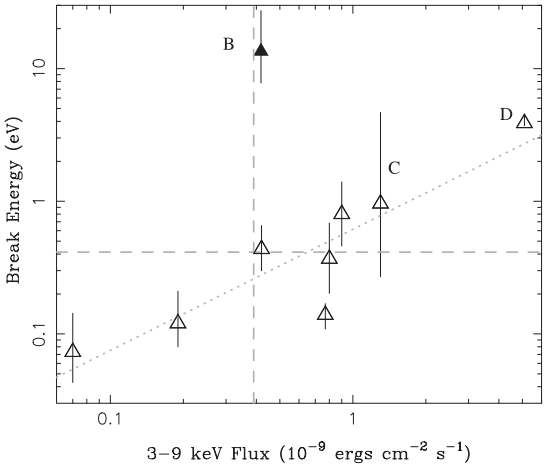

FIG. 3.—Results of broken power-law fits to GX 339−4, showing the location of the break between the radio and soft X-ray power law. Labels refer to Table 1 and are further described in the text. Here and throughout the remaining figures, solid points refer to observations A (not shown in the figure) and B, which have optically thin radio spectra. Dashed lines show the approximate integrated X-ray flux and IR spectral break energy previously observed in GX 339−4 (Corbel & Fender 2002). The dotted line shows $\propto F_{\rm X}^{0.91}$.

$0.61F_{\rm X}^{0.91\pm0.18}$. Does this agree with models wherein the observed soft X-ray spectrum is the optically thin synchrotron emission from a jet?

Using a scale invariance ansatz to describe the jet physics (Heinz & Sunyaev 2003; Heinz 2004; see also Falcke & Biermann 1995; Markoff et al. 2003), we can predict the scaling between the integrated X-ray synchrotron flux and the radio–to–X-ray break frequency in which the jet becomes optically thin to synchrotron self-absorption. For simplicity, we make the assumption that, at the base of the jet, the ratio of particle pressure to magnetic pressure is independent of that of accretion rate to jet power.

Given the above assumptions, the optically thick radio flux follows (Heinz & Sunyaev 2003)

$$\mathcal{F}_r \propto B^{[2p-(p+6)\alpha_r+13]/(p+4)}, \quad (2)$$

where α_r is the radio spectral index, p is the power-law index of the electron spectrum (at energies below any synchrotron cooling regime), and B is the magnetic field at the base of the jet. From Heinz (2004), using the same assumptions, the X-ray synchrotron flux integrated over a fixed energy band follows

$$F_{\rm X} \propto B^{1+2p+3\alpha_{\rm X}}, \quad (3)$$

where $\alpha_{\rm X}$ is the X-ray spectral index. (We again are using the convention that $\alpha \equiv 1-\Gamma$.) Combining these expressions, we find

$$\mathcal{F}_r \propto F_{\rm X}^{[2p-(p+6)\alpha_r+13]/[(p+4)(1+2p+3\alpha_{\rm X})]}. \quad (4)$$

If the X-ray band is unaffected by synchrotron cooling, the relation follows $\mathcal{F}_r \propto F_{\rm X}^{0.69\rightarrow0.81}$, for values of $2.6 < p < 2$, $-0.8 < \alpha_x = (1-p)/2 < -0.5$, and $0 < \alpha_r < 0.2$. This scaling is consistent with previous observations and is also consistent with prior descriptions of the jet model predictions (i.e., Corbel et al. 2003; Markoff et al. 2003).

The lower break frequency, ν_b, from an optically thick to optically thin spectrum is proportional to (Heinz & Sunyaev 2003)

$$\nu_b \propto B^{(6+p)/(4+p)}. \quad (5)$$

We thus can write the dependence of ν_b on $F_{\rm X}$ as

$$\nu_b \propto F_{\rm X}^{(6+p)/[(1+2p+3\alpha_{\rm X})(4+p)]} \propto F_{\rm X}^{[2(p+6)]/[(p+4)(p+5)]}, \quad (6)$$

where for the latter relation we have used $\alpha_{\rm X} = (1-p)/2$ from standard synchrotron theory. Again taking $-0.8 < \alpha_{\rm X} < -0.5$, we obtain $\nu_b \propto F_{\rm X}^{0.34}$ to $F_{\rm X}^{0.38}$. This prediction is flatter than the observed dependence of extrapolated break frequency on X-ray flux.

Equation (6) represents the scaling of the *actual location* of the break from an optically thick to optically thin spectrum (as appropriate for the IR coincidence yielding the appropriate location of an observed break). Our observations instead yield the scaling of the *inferred location* of the break, which has an additional dependence on the scalings of the spectral slopes, α_r and $\alpha_{\rm X}$. Specifically, if one assumes that there is an underlying radio/X-ray correlation given by $\mathcal{F}_r \propto F_{\rm X}^{\beta}$, yet allows evolution of the radio and X-ray spectral slopes, one can show that for the inferred break, ν_b,

$$\log\left(\frac{\nu_b}{\nu_0}\right) = \left[(1-\beta)\log\left(\frac{F_{\rm X}}{F_0}\right) + \log\left(\frac{\nu_r}{\nu_0}\right)\Delta\alpha_r - \log\left(\frac{\nu_{\rm X}}{\nu_0}\right)\Delta\alpha_{\rm X}\right] \times\left[(\alpha_r-\alpha_{\rm X}) + \Delta\alpha_r - \Delta\alpha_{\rm X}\right]^{-1}, \quad (7)$$

where ν_0 is the break energy measured at an X-ray flux of F_0, ν_r and $\nu_{\rm X}$ are the frequencies at which the radio and X-ray fluxes, respectively, are measured, and $\Delta\alpha_r$ and $\Delta\alpha_{\rm X}$ are the changes in radio and X-ray spectral indices as the X-ray flux changes to $F_{\rm X}$. (Note that small correction factors for the dependence of integrated X-ray flux on $\alpha_{\rm X}$, as opposed to solely power-law normalization, have been omitted.)

In the absence of evolution of the spectral indices, one expects the break frequency to scale with X-ray flux with a power of $(1-\beta)/(\alpha_r-\alpha_{\rm X}) \approx 0.35$, as described above. However, as noted elsewhere (Wilms et al. 1999; Nowak et al. 2002), many of the observations of GX 339−4 show a softening (hardening) with increasing (decreasing) X-ray flux. (For sources with optically thick radio spectra, notable exceptions to this trend are ObsIDs 40108-02-03 and 70109-01-02. A detailed discussion of flux and hardness trends can be found in Nowak et al. 2002.) Comparing ObsID 40108-02-02 to 20181-01-01, $\Delta\alpha_{\rm X} \approx 0.06$ for $\log(F_{\rm X}/F_0) \approx 0.7$. Combining this with $\alpha_r + \alpha_{\rm X} \approx 0.8$ and $\log(\nu_{\rm X}/\nu_0) \approx 4.9$ means that the break energy should scale with X-ray flux with a power of $(1-\beta+0.5)/0.8 \approx 1$. This is in much closer agreement with the observed trends.

Unlike $\alpha_{\rm X}$, there are no obvious trends for a dependence of α_r on X-ray flux. (This will be explored in a future work, with a larger set of observations from 2002 and 2004 outbursts of GX 339−4; S. Corbel et al. 2005, in preparation.) The mean value for all the optically thick radio data is $\langle\alpha_r\rangle = 0.16$, with a scatter of ±0.05. Combining this with $\log(\nu_r/\nu_0) \approx -3.5$ and that the difference from the faintest to brightest observation is a factor of $10^{1.9}$, we expect the variations in radio slope to account for correlation slope variations of up to 0.1.

We thus find that the observed correlation of inferred break energy is inconsistent with the expectations from the very simplest X-ray synchrotron jet model (i.e., the jet spectra scale with

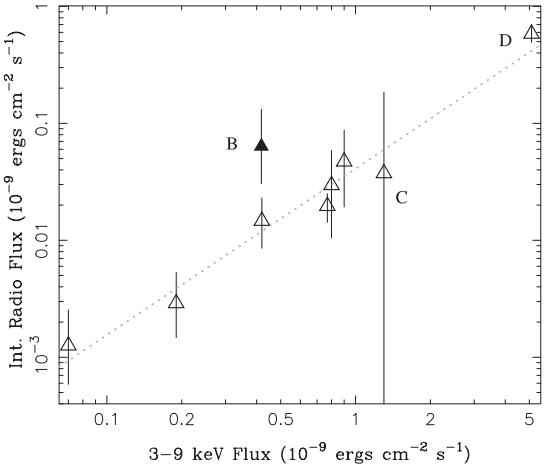

FIG. 4.—Flux of the radio power law, integrated from zero energy to the spectral break between the radio and soft X-ray, vs. the 3–9 keV (PCA) flux. Labels refer to Table 1 (observation A not shown) and are further described in the text. The dotted line shows $\propto F_{\rm X}^{1.4}$.

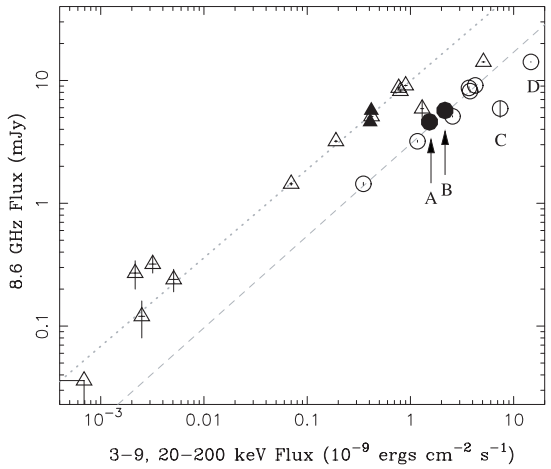

FIG. 5.—X-ray flux (units of 10^{-9} ergs cm s^{-1}) at 3–9 keV (*triangles*) and 20–200 keV (*circles*) from pointed *RXTE* observations of GX 339−4 vs. 8.6 GHz radio flux (in mJy). Labels refer to Table 1 and are further described in the text. Lines show power laws of the form $F_{\rm X}^{b}$, with $b = 0.72$ (*dotted line*) and $b = 0.75$ (*dashed line*).

input power, and there is no evolution of the radio or X-ray slopes). The observed trends can be recovered, however, if the differences from the simplest expectations are primarily driven by evolution of the X-ray spectral slope, $\alpha_{\rm X}$, with X-ray flux, with possible lesser contributions from variations of the radio spectral slope, α_r. We discuss this point further in § 5.

A further interesting correlation is seen when one looks at the dependence of radio flux, integrated between zero energy and the break frequency, on the integrated X-ray flux, as we show in Figure 4. Considering both in units of 10^{-9} ergs cm^{-2} s^{-1} and again weighting the data uniformly, we find $F_r = 0.04F_{\rm X}^{1.42\pm0.10}$. This implies that, even ignoring the energy of the particles and fields in the jet, the "jet radiation" up to the inferred break is 3%–10% of the integrated 3–9 keV X-ray flux and is 0.5%–5% of the 3–200 keV flux.

Again, we can compare this result to expectations from the simplest jet models. Utilizing our previous estimates, we find for the product of $\mathcal{F}_r\nu_b$

$$\mathcal{F}_r\nu_b \propto F_{\rm X}^{[19+3p-\alpha_r(p+6)]/[(p+4)(1+2p+3\alpha_{\rm X})]}. \quad (8)$$

Again using the ranges $-0.8 < \alpha_{\rm X} < -0.5$ and $0 < \alpha_r < -0.2$, this product should follow $\mathcal{F}_r\nu_b \propto F_{\rm X}^{1}$–$F_{\rm X}^{1.19}$. As before, for the *inferred value* we might expect to increase the scaling exponent by 0.5 ± 0.1, if we allow for an evolution of α_r and $\alpha_{\rm X}$ with X-ray flux.

3. RADIO–X-RAY CORRELATIONS IN GX 339−4

One of the interesting aspects of the radio–X-ray flux correlation in GX 339−4 identified by Corbel et al. (2003) is that it appeared to be consistent[10] in both slope and amplitude between the 1997 and 1999 low and hard states, despite the intervening radio-quiet, soft-state outburst (see Fig. 5). The high-luminosity observations C and D [70109-01-02 and 40031-03-01], however, were not part of the original correlation presented by Corbel et al. (2003). These two observations occurred in 2002, 14 days apart, in a bright, hard state as GX 339−4 was rising into an even brighter soft state.

In Figure 5 we plot the 8.6 GHz radio flux density[11] versus the 3–9 and 20–200 keV X-ray fluxes. As in Corbel et al. (2003), we have performed a regression fit for all the 1997 and 1999 observations for which we could determine *both* a 3–9 keV (PCA) and 20–200 keV (HEXTE) flux. (However, we also plot the 1999 low-flux observations from Corbel et al. 2003 that have only PCA data.) For the soft X-rays we find $\mathcal{F}_r = 9.9F_{\rm X}^{0.73\pm0.02}$, and for the hard X-rays we find $\mathcal{F}_r = 3.0F_{\rm X}^{0.75\pm0.02}$. The slight differences between these correlation slopes and those presented by Corbel et al. (2003) are due to our use of better calibrated *RXTE* response matrices (especially for the PCA). As discussed by Corbel et al. (2003), the correlations apply equally well to the 1997 and the 1999 data, including the low-flux 1999 data that were not formally part of the regression fit. The slopes between the soft and hard X-rays are also reasonably consistent with one another (Corbel et al. 2003).

The 2002 data, although only consisting of two points, deviate from these previously viewed trends. For these data, the radio flux versus the 3–9 keV flux correlation appears to have the expected slope but more than a factor of 2 times lower amplitude. The radio–hard X-ray correlation, however, appears to be less reduced in amplitude but has a steeper slope, with $\mathcal{F}_r \propto F_{\rm X}^{1.3}$. There is one major uncertainty in these results: the radio data associated with observations C and D were not strictly simultaneous with the X-ray data. We note, however, that the radio data, which fall below the previously observed trends, were taken after the X-ray data, while the source was rising in flux on timescales of several days.

[10] There are two radio points, however, from the 1999 decline into quiescence that deviate from the correlation (Fig. 5). Given the large degree of variability on week-long timescales in the quiescent state (Kong et al. 2000) and the fact that the magnitude of any time delay between the radio and X-ray flux variations is unknown, it was not clear how significant these deviations should be considered.

[11] Note that for observation C (70109-01-02), we have extrapolated the 2.4 GHz radio flux to 8.64 GHz using the fitted power law.

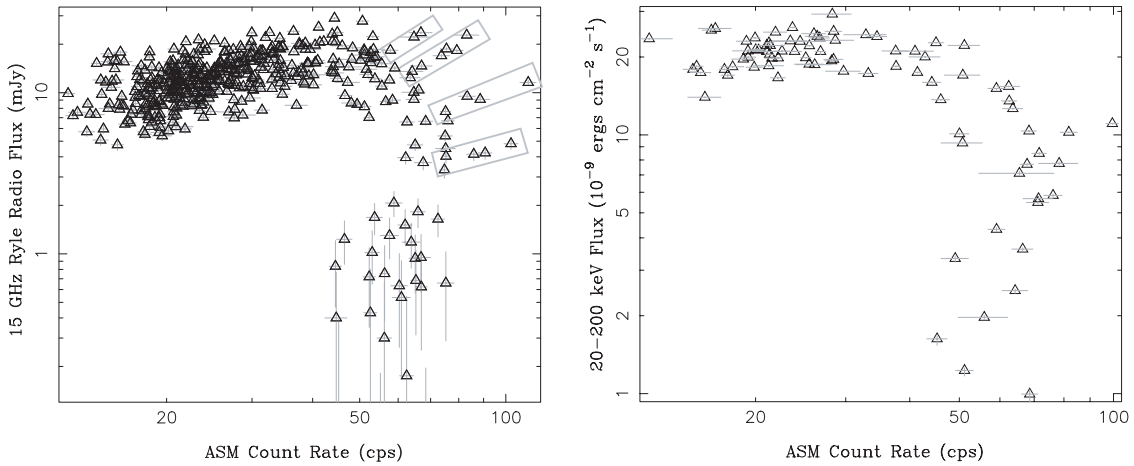

FIG. 6.—*Left*: Ryle radio flux (in mJy) at 15 GHz vs. the Cyg X-1 daily mean ASM count rate (see text). Gray boxes highlight data associated with failed state transitions, and the beginning of a transition to a prolonged soft state. *Right*: Flux (units of 10^{-9} ergs cm^{-2} s^{-1}) at 20–200 keV from pointed *RXTE* observations vs. Cyg X-1 daily mean ASM count rate (see text).

It is also possible that observations C and D, rather than being on a lower radio-amplitude parallel track, instead indicate a turnover in the correlation occurring at high X-ray flux. Such a turnover has been observed for the correlation seen in Cyg X-1 (Gallo et al. 2003; Fig. 6). If this latter hypothesis is correct, then given the observed 14.2 mJy flux for the highest flux observation, D, the deficit is a factor of 2.3 for the 3–9 keV correlation (which predicts 32.4 mJy) but only a factor of 1.6 for the 20–200 keV flux correlation (which predicts 22.7 mJy). Extrapolating the observed 2.4 GHz radio flux for observation C to 8.64 GHz yields 5.9 ± 0.9 mJy. This is a factor of $2^{+0.4}_{-0.2}$ below the value predicted by the radio–3–9 keV flux correlation and a factor of $2.2^{+0.4}_{-0.3}$ below the value predicted by the radio–20–200 keV flux correlation.

A further interesting fact to note also comes from the radio–hard X-ray correlation. Observations A and B (40108-01-03 and 40108-01-04) were the first observations taken after the 1999 return to the radio-loud hard state, and both have optically thin (i.e., $\alpha_r < 0$) radio spectra. Although they have nearly identical 3–9 keV integrated fluxes, they have different radio fluxes, and they straddle the radio–soft X-ray flux correlation shown in Figure 5. However, these points actually lie along the radio–hard X-ray flux correlation, as they have significantly different 20–200 keV fluxes. This might argue that the radio–hard X-ray flux correlation is the more fundamental relationship.

4. RADIO–X-RAY CORRELATIONS IN CYG X-1

The radio–X-ray correlations in GX 339−4 present us with two, not necessarily mutually exclusive, possibilities. The radio–X-ray correlation is more fundamentally tied to the hard X-rays, and/or different instances of the hard state can present the correlation with different amplitudes. To further explore these possibilities, we turn to radio/X-ray observations of Cyg X-1 (Pottschmidt et al. 2003b; Gallo et al. 2003). As described in Pottschmidt et al. (2003b), the radio data are 15 GHz observations performed at the Ryle Telescope, Cambridge (UK). These are single-channel observations, so a radio spectral slope cannot be determined. Most of these observations have occurred simultaneously with pointed *RXTE* observations (Pottschmidt et al. 2003b), and nearly all have very good contemporaneous coverage by the *RXTE* All-Sky Monitor (ASM). The ASM provides coverage in the 1.5–12 keV energy band (Remillard & Levine 1997) and therefore allows us to assess the radio–soft X-ray correlation in Cyg X-1.

In Figure 6 (*left*) we plot the daily average ASM count rate versus the daily average 15 GHz flux. Here we only include days for which there are at least 25 ASM data points (representing 70 s dwells) with a reduced $\chi^2 < 1.5$ for the ASM solution (see Remillard & Levine 1997). Ranging from approximately 10 to 50 counts s^{-1} in the ASM there is a clear loglinear correlation between the radio flux and the ASM count rate. As for GX 339−4, the radio flux rises more slowly than the ASM count rate ($\mathcal{F}_r$ scales approximately as the 0.8 power of the ASM count rate). Cyg X-1, however, shows much more scatter in the amplitude of the correlation than does GX 339−4. This scatter is *not* dominated by variations related to the orbital phase of the binary system (cf. Brocksopp et al. 1999).

As noted by Gallo et al. (2003), there is a sharp rollover for higher ASM count rates. However, one can clearly discern on the shoulder of this rollover (i.e., Fig. 6, *left, top right corner*) four "spokes," consisting of two to five data points each. In these spokes, the radio–X-ray correlation appears to hold to high count rates. We have confirmed[12] that each of these times is associated with "failed transitions" to the soft state, as described by Pottschmidt et al. (2003b), except for the lowest amplitude of these spokes, which occurs immediately preceding a prolonged soft-state outburst. In many ways these failed state transitions and the early stage of a soft-state outburst for Cyg X-1 are reminiscent of the data presented here for the 2002 GX 339−4 hard state. As for those latter GX 339−4 data, the Cyg X-1 spectra remain hard, although not as hard as low-luminosity hard states, to very high flux levels.

In Figure 6 (*right*) we plot the daily average ASM count rate versus the 20–200 keV flux from our pointed *RXTE* observations taken during the same 24 hr period (Pottschmidt et al.

[12] We have used the `vwhere` program (Noble 2005), which allows one to interactively filter one set of data, e.g., a color-color or color-intensity diagram, and then apply those filters to the same observations visualized in a different way, e.g., a time-intensity diagram. (The program is available at http://space.mit.edu/cxc/software/slang/modules.)

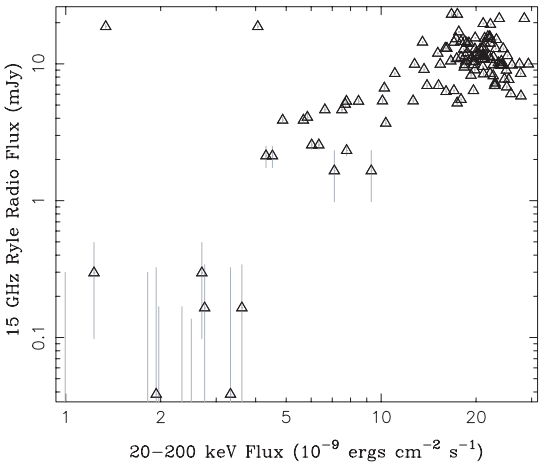

FIG. 7.—Flux (units of 10^{-9} ergs cm^{-2} s^{-1}) at 20–200 keV vs. the daily average 15 GHz Ryle radio flux (in mJy) for pointed observations of Cyg X-1.

2003b). Here, however, we only require three ASM data points per average, for a resulting 85 observations. We see that the hard X-ray–ASM data correlation traces a pattern similar to the radio-ASM data correlation. Indeed, when we plot the hard X-ray flux versus the daily average radio flux (representing 129 separate hard X-ray–pointed observations), we obtain a loglinear relationship, as shown in Figure 7 (see also Gleissner et al. 2004). (Two high–radio flux, but low X-ray–flux, data points are seen in Fig. 7, *top left*; these represent intraday hard X-ray variations.) Returning to the question that we posed in § 3 of whether we were seeing evidence for parallel tracks in the radio–X-ray correlation, or whether we were seeing a correlation more fundamental to the hard X-ray band, in Cyg X-1 the answer seems to be that both effects are discernible but that fundamentally the radio flux density does appear to be tied to the hard X-ray emission.

5. SUMMARY

In this work we have considered 10 simultaneous or nearly simultaneous *RXTE* radio observations of GX 339−4 and over 100 *RXTE* radio observations of Cyg X-1. We have fitted the former spectra with a very simple but remarkably successful phenomenological model consisting of a doubly broken power law with an exponential rollover plus a Gaussian line. For GX 339−4, the break between the radio and soft X-ray power laws occurs in the IR-to-optical range, in agreement with the prior work of Motch et al. (1985) and Corbel & Fender (2002) (i.e., the IR coincidence). In contrast to these prior works, we have fitted the X-ray data in detector space and provided a quantitative assessment of the extrapolated break location.

Is the IR coincidence just a coincidence? The spectral fits to the GX 339−4 data suggest that the answer is "possibly not." All the data with optically thick radio spectra are extremely well fitted by doubly broken power laws, with the break in the IR regime. Although the scaling of this break frequency with X-ray flux does not agree with the predictions of the simplest X-ray synchrotron jet models, if one allows for softening of the X-ray spectrum with increasing X-ray flux, then the jet model predictions agree with the observed correlations. There are several possible reasons why such a softening could occur. In terms of the jet model, for example, there could be cooling of the electron spectrum, leading to a steepening in the X-rays. A second possibility is that the soft X-rays are contaminated by excess emission from a disk component that becomes more prominent with increasing flux. What is clear is that for jet models to explain both the scaling of $\mathcal{F}_r \propto F_r^{0.72}$ and $\nu_b \propto F_r^{0.92}$, they must be more sophisticated than the very simplest considerations. Fits to some of these data sets with such models, which include disk emission, SSC emission, etc., are currently being considered in detail and will be discussed in a future work (S. Markoff et al. 2005, in preparation). The results presented here, however, are consistent with the notion that at least some fraction of the observed soft X-rays may be attributable to emission from the jet, as opposed to the disk or corona.

On the other hand, other facts suggest that the answer to the question of the IR coincidence is "maybe." We have tentative evidence in GX 339−4 and firmer evidence in the Cyg X-1 failed state transitions and soft-state transition that the correlation between radio flux and integrated X-ray flux can take on different amplitudes during different hard-state episodes. There is also evidence in Cyg X-1 that the radio–X-ray correlation is more fundamental to the hard X-ray band. In jet models, this band, which essentially encompasses the third, highest energy, power-law component in our model fits (and also encompasses the exponential cutoff), is possibly attributable to the SSC emission from the base of the jet (see, e.g., Markoff et al. 2003; Markoff & Nowak 2004). It is therefore quite reasonable to expect a strong coupling between the radio and hard X-ray flux; however, these models are more complex than simple pure synchrotron models and are only now beginning to be explored quantitatively (Markoff et al. 2003; Markoff & Nowak 2004). It is also worth noting that such radio–X-ray couplings can be expected in Compton corona models (e.g., Meier 2001; Merloni & Fabian 2002).

More problematic for pure jet models are GX 339−4 observations A and B (40108-01-03, 40108-01-04), both of which occurred very shortly after the 1999 return to the hard state. They have "typical" hard-state properties in terms of spectra and variability (Nowak et al. 2002), but they have optically thin radio spectra that do not neatly extrapolate into the observed soft X-ray spectra. They satisfy the radio flux density–integrated X-ray flux correlation; however, they agree better with the radio–hard X-ray flux correlation, for which these two observations are cleanly differentiated from one another (Fig. 5). It is possible that they represent an early, transient phase of the jet as it forms. It then remains for the jet model the theoretical question of whether it can describe a scenario in which the basic radio–X-ray flux correlation and "typical" steady state X-ray spectra hold, while the radio has not yet settled into a steady optically thick state.

The results presented here suggest, at the very least, some obvious observational strategies to arrive at a more definitive answer to the question that we have posed. Given the break-energy correlations, it would be extremely useful to have not only a radio amplitude for each X-ray observation, but also a radio slope. Furthermore, the inferred break for the brightest observation, D (40031-03-01), occurs in the blue end of the optical. Thus, ideally multiwavelength observations would consist of radio, broadband X-ray, and IR-through-optical coverage (see, e.g., Hynes et al. 2003; Malzac et al. 2004, which suggest the possibility of jet synchrotron radiation extending into the optical regime for the hard state of XTE J1118+48). This is an admittedly difficult task, but black hole candidates are demonstrating via spectral correlations that all these energy regimes are fundamentally related to activity near the central engine, i.e., the black hole, of the system.

Finally, it is important to obtain multiwavelength observations of multiple episodes of each of the spectral states. For example, if there are indeed parallel tracks in the radio–X-ray correlations, it would be interesting to determine whether the amplitude of the radio–X-ray correlation is related to the flux at which the outbursting source transits from the low/hard to high/soft state. We note that the low-amplitude radio–X-ray correlation of the 2002 GX 339−4 outburst was associated with a very high flux level for the hard-to-soft state transition. The low-amplitude spokes in the Cyg X-1 radio–X-ray correlation might be similar in that they are associated with failed state transitions. If such observations can be made with more quantitative detail, we will have vital clues to determining the relative contributions of coronae and jets and the coupling between these two components for black hole binary systems.

It is a pleasure to acknowledge useful conversations with Sera Markoff and Jeroen Homan and for their pointing us toward the 2002 data used in this work. A debt of gratitude is also owed to Mike Noble and John Houck for invaluable software assistance. This work has been supported by NASA grant SV3-73016 and NSF grant INT-0233441. S. H. received support from the National Aeronautics and Space Administration through Chandra Postdoctoral Fellowship Award PF3-40026.

REFERENCES

Arnaud, K. A. 1996, in ASP Conf. Ser. 101, Astronomical Data Analysis Software and Systems V, ed. J. H. Jacoby & J. Barnes (San Francisco: ASP), 17
Braes, L. L. E., & Miley, G. K. 1971, Nature, 232, 246
Brocksopp, C., Fender, R. P., Larionov, V., Lyuty, V. M., Tarasov, A. E., Pooley, G. G., Paciesas, W. S., & Roche, P. 1999, MNRAS, 309, 1063
Corbel, S., & Fender, R. P. 2002, ApJ, 573, L35
Corbel, S., Fender, R. P., Tzioumis, A. K., Nowak, M., McIntyre, V., Durouchoux, P., & Sood, R. 2000, A&A, 359, 251
Corbel, S., Nowak, M. A., Fender, R. P., Tzioumis, A. K., & Markoff, S. 2003, A&A, 400, 1007
Falcke, H., & Biermann, P. L. 1995, A&A, 293, 665
Falcke, H., Körding, E., & Markoff, S. 2004, A&A, 414, 895
Fender, R. P., Gallo, E., & Jonker, P. G. 2003, MNRAS, 343, L99
Fender, R., et al. 1999, ApJ, 519, L165
Gallo, E., Fender, R. P., & Pooley, G. G. 2003, MNRAS, 344, 60
Gleissner, T., et al. 2004, A&A, 425, 1061
Hannikainen, D. C., Hunstead, R. W., Campbell-Wilson, D., & Sood, R. K. 1998, A&A, 337, 460
Heinz, S. 2004, MNRAS, 355, 835
Heinz, S., & Sunyaev, R. A. 2003, MNRAS, 343, L59
Homan, J., Buxton, M., Markoff, S., Bailyn, C. D., Nespoli, E., & Belloni, T. 2005, ApJ, 624, 295
Houck, J. C., & Denicola, L. A. 2000, in ASP Conf. Ser. 216, Astronomical Data Analysis Software and Systems IX, ed. N. Manset, C. Veillet, & D. Crabtree (San Francisco: ASP), 591
Hynes, R. I., et al. 2003, MNRAS, 345, 292
Kong, A. K. H., Kuulkers, E., Charles, P. A., & Homer, L. 2000, MNRAS, 312, L49
Magdziarz, P., & Zdziarski, A. A. 1995, MNRAS, 273, 837
Malzac, J., Merloni, A., & Fabian, A. C. 2004, MNRAS, 351, 253
Markoff, S., Falcke, H., & Fender, R. 1991, ApJ, 372, L25
Markoff, S., & Nowak, M. 2004, ApJ, 609, 972
Markoff, S., Nowak, M., Corbel, S., Fender, R., & Falcke, H. 2003, A&A, 397, 645
Meier, D. L. 2001, ApJ, 548, L9
Merloni, A., & Fabian, A. C. 2002, MNRAS, 332, 165
Merloni, A., Heinz, S., & di Matteo, T. 2003, MNRAS, 345, 1057
Motch, C., Ilovaisky, S. A., Chevalier, C., & Angebault, P. 1985, Space Sci. Rev., 40, 219
Noble, M. 2005, in ASP Conf. Ser., Astronomical Data Analysis Software and Systems XIV (San Francisco: ASP), in press (astro-ph/0412003)
Nowak, M. A., Wilms, J., & Dove, J. B. 2002, MNRAS, 332, 856
Pooley, G. G., Fender, R. P., & Brocksopp, C. 1999, MNRAS, 302, L1
Pottschmidt, K., et al. 2003a, A&A, 411, L383
———. 2003b, A&A, 407, 1039
Remillard, R. A., & Levine, A. M. 1997, in All-Sky X-Ray Observations in the Next Decade, ed. N. Matsuoka & N. Kawai (Tokyo: Riken), 29
Sood, R., & Campell-Wilson, D. 1994, IAU Circ. 6006, 1
Stirling, A. M., Spencer, R. E., de la Force, C. J., Garrett, M. A., Fender, R. P., & Ogley, R. N. 2001, MNRAS, 327, 1273
Sunyaev, R. A., & Trümper, J. 1979, Nature, 279, 506
Wardziński, G., Zdziarski, A. A., Gierliński, M., Grove, J. E., Jahoda, K., & Johnson, W. N. 2002, MNRAS, 337, 829
Wilms, J., Nowak, M. A., Dove, J. B., Fender, R. P., & di Matteo, T. 1999, ApJ, 522, 460

2.7.5

Exploring the role of jets in the radio/X-ray correlations of GX 339-4.

Article publié dans :

Astron. & Astrophys., 2003, 397, 645-658

Markoff, S., Nowak, M., Corbel, S., Fender, R., Falcke, H.

A&A 397, 645–658 (2003)
DOI: 10.1051/0004-6361:20021497

Astronomy & Astrophysics

Exploring the role of jets in the radio/X-ray correlations of GX 339–4

S. Markoff[1,⋆], M. Nowak[2], S. Corbel[3], R. Fender[4], and H. Falcke[1]

[1] Max-Planck-Institut für Radioastronomie, Auf dem Hügel 69, 53121 Bonn, Germany
[2] Massachusetts Institute of Technology, Center for Space Research Rm. NE80-6077, 77 Massachusetts Ave., Cambridge, MA 02139, USA
[3] Université Paris VII and Service d'Astrophysique, CEA, CE-Saclay, 91191 Gif sur Yvette, France
[4] Astronomical Institute "Anton Pannekoek" and Center for High Energy Astrophysics, University of Amsterdam, Kruislaan 403, 1098 SJ Amsterdam, The Netherlands

Received 17 July 2002 / Accepted 14 October 2002

Abstract. The Galactic black hole candidate X-ray binary GX 339–4 spends most of its time in the low/hard state, making it an ideal candidate for modeling the assumedly low accretion phase. The radio emission correlates very tightly with the X-rays over more than two orders of magnitude in X-ray flux density, suggesting that the jet plasma also plays a role at the higher frequencies. We compare the predictions of our jet model, with and without acceleration, to thirteen broadband simultaneous or quasi-simultaneous spectra over this changing flux history. In addition, we consider a simple standard thin disk which transitions to an optically thin accretion flow, in order to account for the assumedly thermal optical data seen in some observations. A solution without acceleration cannot describe the data without unrealistic energy requirements, nor explain the non-thermal radio spectrum seen during recent radio outbursts. But because of the low disk luminosity, and possibly the assumed disk geometry, acceleration in the jet is limited only by synchrotron cooling and can extend easily into the X-rays. We present a model which can account for all the broadband spectra included here, by changing only two parameters in the jet model: the input power and the location of the first acceleration zone. However, the model is most sensitive to changes in the jet power, the varying of which can also account for the slope of the observed radio/X-ray correlation analytically. At the highest low/hard state luminosities, the synchrotron self-Compton emission from the jet could be detectable with missions such as *GLAST*, providing a way to test the extent of the synchrotron contribution. We conclude that jet synchrotron is a possible way to explain the broadband features and this correlation, and discuss ways of incorporating this component into the "standard" corona picture.

Key words. X-rays: binaries – X-rays: individual: GX 339–4 – radiation mechanisms: non-thermal – stars: winds, outflows – black hole physics – accretion, accretion disks

1. Introduction

The Galactic black hole candidate (BHC) X-ray binary (XRB) GX 339–4 displays a wide variety of spectral states, and has recently resurfaced at a high flux level after being in an extended "off" state since 1999 (see, e.g., Kong et al. 2000). It has been extensively, and often simultaneously, observed across broad energy bands: from the radio (Hannikainen et al. 1998; Fender et al. 1999; Corbel et al. 2000 – hereafter C00; Corbel et al. 2002, to be submitted – hereafter C02), infrared (IR) and optical (Soria et al. 1999; Shahbaz et al. 2001; Corbel & Fender 2002 – hereafter CF02), to the X-rays (Wilms et al. 1999 – hereafter W99; Nowak et al. 2002 – hereafter NWD). These data sets are relatively untainted by contamination from the companion star. This, and the fact that GX 339–4 often transitions between the canonical XRB states, makes it an ideal source for comparing the emission processes involved in these various states.

GX 339–4 spends the great majority of its time in the low/hard state (LHS) (for a review of BHC states, see Nowak 1995), at flux levels varying over roughly three orders of magnitude in the X-ray waveband (NWD; C02). Its LHS spectra are fairly "typical" in that they show a flat-to-inverted radio component, a weak thermal contribution, and a hard power-law in the soft to hard X-rays (Zdziarski et al. 1998; Fender 2001; Revnivtsev et al. 2001; NWD). Although no jets have yet been resolved, the radio emission shows 2% linear polarization, and the brightness temperature (defined as $S_\nu = \Omega B_\nu(T_B)$ where Ω is the solid angle of the emitting region) requires a spatial extension greater than the binary separation (W99; C00). At the time of writing, GX 339–4 briefly entered the very high state (VHS) and made a transient-like radio outburst which was five times brighter than the brightest radio emission ever observed in the LHS. The optically thin spectrum had

Send offprint requests to: S. Markoff,
e-mail: sera@space.mit.edu

⋆ Humboldt Research Fellow. Current address: Massachusetts Institute of Technology, Center for Space Research, Rm. NE80-6035, Cambridge, MA 02139, USA.

a spectral index $\alpha \sim -0.6$ ($F_\nu \propto \nu^\alpha$) (R. Fender, S. Corbel, private comm.), which is characteristic of a transient bright jet. This makes GX 339–4 the first source to show its radio properties clearly in the LHS, the high/soft state (HSS) and transient/VHS. Combined with the fact that jets have already been imaged in the other three persistent Galactic BHC which share similar LHS spectra (e.g., 1E1740.7-2942, Mirabel et al. 1992; GRS 1758-258, Rodríguez et al. 1992; and Cygnus X-1, Stirling et al. 2001), the case for a jet in this source is now very strong.

A special feature of GX 339–4 is that its radio emission has been observed to correlate tightly with the X-ray emission over the entire range of LHS luminosities, and also down to a very weak level of emission in the "off" state (Hannikainen et al. 1998; C00; C02). Similarly, during changeover to the HSS, the seemingly linked radio and hard (20-100 keV) X-ray emission show an anti-correlation with the assumed thermal disk emission in the softer (2–12 keV) X-ray band (Fender et al. 1999; C00). This suggests not only that the plasma leading to the synchrotron radiation plays some role at higher energy, but also that the jet is either quenched (Fender et al. 1999) or otherwise unable to form when the thermal disk component dominates (Meier 2001; Merloni & Fabian 2002).

On the other hand, the LHS X-ray spectra from GX 339–4 show additional features which have been interpreted as signs of reflection off colder disk material, and can be fit by one of several disk-corona models as discussed in detail in NWD. In this paper, the authors find correlations between the reflection covering fraction and both the soft X-ray flux (see also Zdziarski et al. 1999; Revnivtsev et al. 2001), and the time lags between the soft and hard X-ray variability. Similar to what Pottschmidt et al. (2000) report for Cyg X-1 – which also shows radio/X-ray correlations (Brocksopp et al. 1999) – NWD find that these time lags anti-correlate with the coronal compactness, and peak shortly after the transition from the HSS to the LHS, when the assumed jet emission begins to rise. They suggest an interpretation that the time lags may be associated with the extended synchrotron-emitting plasma.

While the model fits presented in NWD can well explain the X-ray features, and suggest a link between the corona and jet, they do not explore the nature of this link or how this emission is related to that of the radio. One model which can explain the tight radio/X-ray correlations proposes that the jets directly contribute to the LHS X-ray spectrum via synchrotron emission (Markoff et al. 2001 – hereafter MFF), as occurs in several AGN (e.g., 3C 66B, Hardcastle et al. 2001 and M87, Marshall et al. 2002; Wilson & Yang 2002). However, this model has only been applied until now to one source, XTE J1118+480, which may be unusual in that it has extremely weak or absent reflection features (Miller et al. 2002).

In this paper, we discuss the application of a jet model to the collected simultaneous or quasi-simultaneous data sets for GX 339–4 in order to investigate whether it succeeds in explaining the observed radio/X-ray correlations. We discuss how the model fares against the broadband data and compare the model parameters for the various data sets to each other, as well as to XTE J1118+480.

2. Data

The 1981 data set was compiled by CF02, where it is explained in further detail. The X-rays come from the Ariel 6 instrument (Ricketts 1983), with simultaneous optical/IR from Pedersen (1981) and Motch et al. (1981).

All radio observations were performed with the Australia Telescope Compact Array (ATCA) and, with the exception of the 2000 September 15 observation (to appear in C02), have been presented previously by C00. All observations from C00 in which the radio flux density was weak (i.e., $\lesssim$1 mJy) were reanalyzed for this paper.

The X-ray data presented here have been discussed previously by NWD and C02. All data were obtained by the Rossi X-ray Timing Explorer (RXTE), with the exception of the 2000 September 15 data, which were obtained by BeppoSAX.

In this work we are attempting to describe the *broadband features* of the jet model, and to simultaneously explain radio, IR, optical, and X-ray data (taken with a wide variety of instruments). Furthermore, we are not yet attempting to explain detailed features within the X-ray, e.g., Fe lines or reflection features. Therefore, rather than forward fold the jet models through the detector response matrices, we instead compare the models to "unfolded" count flux rates. This is not strictly fitting, as we cannot obtain chi-squared estimates from unfolded data in this way, but for simplicity we will use the word "fit" to describe the comparison to the data throughout the paper.

To unfold the X-ray data, the RXTE data extraction, data binning, response matrix generation, and background subtraction were carried out in an identical manner as presented by NWD. We then fit models comprised of: a multi-temperature disk blackbody (e.g., Mitsuda et al. 1984; Makishima et al. 1986) with peak temperature fixed at 0.25 keV, an exponentially cutoff broken power-law with break energy at $\approx$10 keV, and a (potentially) broad gaussian line with energy fixed to 6.4 keV. (This model is essentially identical to that discussed by W99.) These model fits were then unfolded through the detector response matrix and multiplied by the ratio of the count rate data to the fitted model folded through the detector response. For the RXTE observations, data was considered only for the 3–200 keV range or less for the faintest data sets. Furthermore, HEXTE data was normalized to the PCA data (e.g., see W99).

As discussed by C02, simultaneous RXTE/ASCA observations indicate a probable faint background source that contaminates the RXTE spectrum – but not the narrow field of view ASCA spectrum – at *extremely* low flux levels. The RXTE observation of 1999 July 29 is assumed to be heavily dominated by this contaminating source, and this spectrum, multiplied by 0.78, is subtracted, before model fitting and data unfolding, from all RXTE observations occurring later than the observation of 1999 May 14. This normalization was determined by comparison of spectra obtained simultaneously by RXTE and ASCA on two separate occasions (the required normalization constants for these two observations were 0.73 and 0.83; see C02). Note that the 2000 September 15 BeppoSAX observation is most likely *not* contaminated by this background source, which could easily be half a degree away and still affect the RXTE observations, as BeppoSAX has a narrower field

Table 1. Explanation of labels in figures.

Label	Data Set[a]	Date (y.m.d)
97_1	20181-01-01-00	1997.02.03
97_2	20181-01-02-00	1997.02.10
97_3	20181-01-03-00	1997.02.17
99_1	40108-02-01-00	1999.04.02
99_2	40108-02-02-00	1999.04.22
99_3	40108-02-03-00	1999.05.14
99_4	40105-02-02	1999.06.25
99_5	40108-03-01-00	1999.07.07
99_6	40108-03-02-00	1999.07.29
99_7	40108-03-03-00	1999.08.17
99_8	40104-01-08	1999.08.28[b]
00	21136001	2000.09.15[c]

[a]Data from W99, C00, C02 and NWD. All but 00 (which is BeppoSAX) are labeled according to RXTE conventions.
[b]Date for X-ray observation. Radio taken on 1999.09.01.
[c]Optical data shown in Fig. 4b were taken 3 months prior.

of view than RXTE. A more detailed discussion of this background source appears in C02.

The dates of the observations are listed in Table 1. Data sets labeled 20181 were first discussed by W99. Data sets 40108-02 were first discussed by NWD. Data sets 40108-03, first appearing in C02, were part of the same series of observations originally discussed by NWD; however, these latter observations were too faint for simultaneous spectral and X-ray variability analyses. Observations 40105-02-02, 40104-01-08 and 21136001 were part of a series of observations to study GX 339–4 in quiescence, and are discussed by C02.

3. Model

The details of the jet model can be found in MFF, and references therein, and we give a brief summary here. We consider that an accretion disk may contribute to the near infrared (NIR), optical and possibly soft X-ray emission, but that the radio through at least far infrared (FIR) are due to synchrotron emission from the jets, which could possibly extend through the NIR to the X-rays. The inverse Compton (IC) upscattering by the hot jet electrons of both the thermal disk photons, as well as the synchrotron photons, is also included.

Our disk model is relatively simplistic, since we are currently exploring its limits in terms of contribution and there are already many detailed disk models in existence (see Poutanen 1998; NWD for reviews). We here consider one commonly invoked model in which a standard thin, optically thick disk (SD) (Shakura & Sunyaev 1973) exists down to some transition radius $r_{\rm tr}$, at which point the flow becomes hotter, optically thin and relatively non-radiative (e.g., Esin et al. 1997). This type of non-radiative inner disk has also been invoked for low-luminosity AGN such as NGC 4258 (Yuan et al. 2002). The thermal bump – seen in several of the GX 339–4 data sets in the optical band – is assumed to originate in the disk, which also provides seed photons for jet IC as mentioned above. We assume for now that the jet is oriented 90° from the plane of the disk, but in the future we will consider other orientations (see, e.g., Maccarone 2002).

In their study of the BHC XTE J1118+480, MFF interpreted the extreme-ultraviolet (EUV) upper limits (Hynes et al. 2000) as the hottest, and thus innermost, emission from this outer disk. Therefore, they could place limits on its maximum temperature and luminosity. They derived a location for the transition radius of $r_{\rm tr} \sim 10^2$–$10^3\, r_{\rm g}$ which is consistent with other models (e.g., Liu et al. 1999; Esin et al. 2001). However, no EUV data exist for GX 339–4, and so we constrain $r_{\rm tr}$ with the low-frequency X-ray data. We have also made the outer disk slightly more realistic than the simple one-temperature component we used before by considering a multi-temperature blackbody spectrum as its representation (e.g., Shakura & Sunyaev 1973; Mitsuda et al. 1984; Makishima et al. 1986). We then explore its possible geometry using the data sets where its signature seems the most prevalent.

A significant problem for modeling GX 339–4 is that most of its system parameters are not well constrained. The only report of an orbital period based on optical photometry is from Callanan et al. (1992), who found 14.8 hours. This value remains unconfirmed (though Cowley et al. 2002 reconsidered the problem and found a similarly tentative period of 16.8 hours). However, it has been adopted over the years to limit the mass function, which is also problematic since the companion star is still unclassified. Finally, because the system has not yet been resolved, the inclination angle is also unknown but limited to $\lesssim 60°$ because of the lack of eclipsing. Based on reasonable assumptions, a distance of 4 kpc has been adopted (see Zdziarski et al. 1998; W99; but also Shahbaz et al. 2001, who argue for $\geq$5.6 kpc) and a mass for the black hole ranging from ~3–6 $M_\odot$, where we here use 5 $M_\odot$.

We fix the inner temperature of the SD, $T_{\rm in}$, based on the 1981 data set. We then estimate the outer radius, $r_{\rm out}$, of the SD based on the physical parameters above, the best fit inclination angle, $\theta_{\rm i}$, and assuming a companion of ~0.4 $M_\odot$, consistent with the 16.8 hour period. The exact luminosity contributed by the SD, $L_{\rm d}$, is not uniquely determined by the data, and so we can only roughly estimate the accretion rate, $\dot{M}_{\rm d}$. Because of the simplicity of our disk model, this is not a main focus of this work, but we want to be sure we are consistent in terms of the energy budget. We express $L_{\rm d}$ in units of $L_{\rm Edd} = 1.25 \times 10^{38} \left(\frac{M_{\rm BH}}{M_\odot}\right)$ erg s^{-1}.

For accreting black holes it has been argued that the jet power is of order $Q_{\rm j} \sim q_{\rm j} \dot{M}_{\rm d} c^2$ with an efficiency inferred to be of order $q_{\rm j} = 10^{-3} - 10^{-1}$ (Falcke & Biermann 1999, 2001). We consider $Q_{\rm j}$ a free parameter in our model, also expressed in units of $L_{\rm Edd}$ erg s^{-1}, and which we check for consistency with our limits on $\dot{M}_{\rm d}$. While the jet formation itself is still a looming question in the field, the physics of calculating most of the jet emission is relatively straightforward because the flat-to-inverted spectrum stems from the part of the jet where it is basically undergoing free expansion. We briefly summarize the jet component as follows (and see also Falcke & Markoff 2000, MFF).

At the inner edge of the optically thin accretion flow, hot plasma is ejected out from symmetric nozzles, where it

becomes supersonic. We assume free jets which accelerate along their axes only due to their longitudinal pressure gradients. This is the simplest scenario and provides a lower limit to the final velocity distribution. The velocity field along the jet is thus uniquely determined from the Euler equation (see, e.g., Falcke 1996), and at large distances z from the base has a dependence $\gamma_j(z)\beta_j(z) \propto \sqrt{\ln(z)}$. Thus, the maximum value of the bulk Lorentz factor γ_j is roughly determined by the distance at which the lowest frequency radio emission is emitted and is dependent on other parameters in this model but is itself not a fitted parameter. For both GX 339–4 and XTE J1118+480, we find $\gamma_{j,max} \sim 3$, which is consistent with the low beaming factors suggested by the recent work of (Gallo et al. 2002).

We further assume the jets expand sideways with their initial proper sound speed, $\gamma_s\beta_s c \simeq 0.4c$ for a hot electron/cold proton plasma. Beyond the nozzle region, the radius $r(z)$ is related to the distance z by the Mach number along the jet, $\gamma_j\beta_j/\gamma_s\beta_s$.

We choose the simplifying assumption that the internal energy, dominated by the magnetic field, is equal to the bulk kinetic energy of the particles, consistent with a magnetic launching mechanism. The plasma is assumed to originate in the hot accretion flow and therefore contains equal numbers of protons and electrons, with the exact temperature of the electrons at the base of the jet, T_e, remaining a fitted parameter. A process such as pair-loading via interactions with the disk photon field will not be efficient enough in the LHS to be significant (see, e.g., Sikora & Madejski 2000). Under these assumptions, the magnetic energy density and particle density in each jet can thus be defined as $B^2(z)/8\pi \simeq 0.25Q_j/(c\gamma_j\beta_j\pi r(z)^2)$ and $n(z) \simeq 0.25Q_j/(c\gamma_j\beta_j m_p c^2 \pi r(z)^2)$. Taking into account the non-constant velocity field, the dependencies of the magnetic field, B, and density, n, on distance are then similar to, but slightly stronger than, the canonical z^{-1} and z^{-2} dependencies for conical jets, respectively (Blandford & Königl 1979; Hjellming & Johnston 1988; Falcke & Biermann 1995). In this way, the basic physical properties governing the emission at each point in the jet are fixed after specifying the jet power Q_j and nozzle scale r_0, which determine B_0 and n_0.

The thermal particles travel along the jet until they encounter an acceleration region which begins at z_{sh}. An acceleration process is inferred because of the observed optically thin synchrotron power-law seen in the recent transient radio events, indicating the presence of non-thermal particles. This is a standard process invoked to explain many features of AGN jet emission (Marscher & Gear 1985). We consider the process to be diffusive shock acceleration, but it could really be one of a few possible scenarios (e.g., stochastic acceleration) which lead to a non-thermal power-law with spectral index p ($\frac{dN}{dE} \propto E^{-p}$). For standard shock acceleration theory, $p \sim 2.0$–2.5 (e.g., Jones & Ellison 1991). In order to maintain the non-thermal particles out along the jet to account for the entire radio spectrum, we assume distributed acceleration after z_{sh}. This is because the cooling timescales after acceleration are very fast compared to the dynamical timescales, a problem which has also required the assumption of distributed acceleration in the two best studied AGN jets, M87 and 3C 273 (Meisenheimer et al. 1996; Jester et al. 2001, but see also Perlman et al. 2001).

We assume that the accelerated distribution extends from the peak of the thermal distribution, with Lorentz factor $\gamma_e \sim 4 \cdot T_{e,10}$. As discussed in MFF, the maximum γ_e occurs when the acceleration rate (assuming Bohm diffusion) is matched by the cooling rate giving

$$\gamma_{e,max} \sim 10^8 \, (\xi B)^{-0.5} \left(\frac{u_{sh}}{c}\right), \quad (1)$$

where u_{sh} is the shock speed in the plasma frame and B is the magnetic field in Gauss. The parameter ξ is the ratio between the diffusive scattering mean free path and the gyroradius of the particle. It measures how many times the particle gyrates per shock crossing, where the most efficient acceleration possible is when it crosses the shock once per gyroradius, thus giving a lower limit of $\xi = 1$. For quasi-perpendicular shocks $\xi \leq c\gamma_e\beta_e/u_{sh}$, although in the case of a jet the field is likely quite tangled in which case an upper bound on ξ is not known. While we do not know the exact value of u_{sh}, it must be larger than the speed of sound at the shock, c_s, and no higher than the local bulk velocity. For very relativistic particles ξ can be quite large, but conservative values lie in the ~10–100 range (e.g., Jokipii 1987). If we define as a reference value $\xi = \xi_2 100$, the maximum synchrotron frequency is

$$\nu_{max} = 0.29\nu_c \simeq 1.2 \times 10^{20} \xi_2^{-1} \left(\frac{u_{sh}}{c}\right)^2 \quad \text{Hz} \quad (2)$$

where $\nu_c \simeq \frac{3}{4\pi}\gamma_{e,max}^2 (eB)/(m_e c)$ is the critical synchrotron frequency. This maximum corresponds approximately to the rollover of the power-law cutoff and in order to explain the "canonical" 100 keV cutoff for $\xi \approx 100$, we need $u_{sh} \gtrsim c_s$, consistent with our physical expectations. This cutoff is not dependent on the magnetic field, the jet power, or the shock location as long as we are in the synchrotron cooling dominated regime. Because we would expect XRBs to have similar shock structures, we should get roughly similar cutoffs for different sources and accretion rates. In this sense ξ and u_{sh} provide a reasonable physical explanation for the location of the cutoff in much the same way the coronal energy fraction and temperature determine it in coronal IC models (e.g., Sunyaev & Trümper 1979).

The location of the initial acceleration region is determined by the frequency where the flat, highly self-absorbed synchrotron spectrum turns over into the optically thin power-law produced at the shock. In MFF, we showed that from back-extrapolating the X-ray power-law, this maximum self-absorption frequency should occur somewhere in the IR/optical regime at $\sim 10^{14}$–10^{15} Hz for XTE J1118+480. It is interesting to note that this now holds true for several other BHC sources in the LHS including GX 339–4 and V404 Cyg (CF02; Brocksopp et al. 2002, in prep.; Gallo et al. 2002; Gallo et al. 2002, MNRAS, in prep.).

There are thus seven free parameters relating to the jet component, Q_j, T_e, z_{sh}, r_0, p and θ_i. These are not, however, entirely independent of each other. Furthermore, in our philosophy of comparing broadband spectral features to the jet model, we can

choose reasonable constraints for a number of these parameters. For instance, if the X-rays are due to synchrotron emission, the spectral index of the accelerated particles is uniquely determined ($\alpha_X = \frac{(p-1)}{2}$). Starting with reasonable assumptions of the underlying disk/jet geometry in order to constrain T_e and r_0, Q_j and θ_i can then be determined from the radio spectrum because they fix its normalization and spectral index, respectively. The beginning of the acceleration region, z_{sh}, is then uniquely determined by where the turnover must occur to link the X-ray to the radio spectrum. For the purposes of the spectral models that we describe here, the critical fitted parameters are Q_j and θ_i, as they most directly determine the radio spectrum. For θ_i, the only observational constraint is that it is $\lesssim 60°$.

As described above, there are also additional parameters describing the cutoff in the X-rays as well as the disk component, and we will also argue below for an additional irradiation component. However, these are not an integral part of our model, in that they do not constrain the conditions of the radiating plasma in the jet. We include them for completeness, and to open the way for more complex, combined disk/jet models.

Some fraction of the emitted X-rays from the jet base will either directly interact with, or be scattered by hot electrons into, the cold disk, resulting in reflection. This calculation is not attempted here, however, since again this is very dependent on the disk geometry and we are focusing on the role of the jet. This, as well as other issues, will be the focus of an upcoming paper.

4. Results

4.1. 1981 data set: Constraining the GX 339–4 model parameters

Of all the data sets for GX 339–4 considered here, the most interesting is that of May 1981 (see Fig. 1), which is at the highest flux so far for which simultaneous broadband data have been published in the LHS. The IR/optical wavebands seem to indicate the clear presence of both jet and disk components, which has not been seen explicitly in any other XRB. The IR band shows a first component with a negative slope suggesting that we are seeing the expected turnover from the optically thick to optically thin regimes. The shape of this spectrum at higher frequencies is hidden under a component which is likely due to thermal emission from the SD, as indicated by the sharp rise in the optical points. However, if the simultaneously measured X-rays are traced back to the IR, they line up with the turnover remarkably well, supporting their interpretation as synchrotron emission.

While no simultaneous radio observation exists, an estimate of the 8.6 GHz radio flux can be found by extrapolating the radio/X-ray correlation curve to higher fluxes (C00; C02 and see Fig. 6), and is shown as a point in Figs. 1 and 2). As mentioned above, several other LHS sources show this interesting "turnover coincidence". In the compact cores of most flat-spectrum AGN, the same kind of turnover is observed in the mm range (e.g., Bloom et al. 1994), but the more compact scales in XRBs push this to higher frequencies (e.g., Falcke et al. 2001).

The clear presence of the optically thick-to-thin turnover makes the 1981 data set a strong test of any theoretical model. Furthermore the radio/X-ray correlation, illustrated by the full set of simultaneous data shown here, suggest that any model for the X-rays from this source must address the lower-frequency data as well. This means that if – as is usually assumed – the X-rays are due entirely to IC upscattering off hot electrons in the base of the jet/coronal plasma, one has to show that these same electrons can reproduce the flat-to-inverted radio spectrum via their synchrotron emission, or that some other very strong coupling exists between "corona" and "jet". As Blandford & Königl (1979) explain, to fit the flat-to-inverted radio spectrum particularly in the cm-band, one needs a conical geometry with outflowing plasma, otherwise the emitted synchrotron spectrum will be too inverted. We therefore think that a corona which has no relation to the jet cannot explain the data for GX 339–4. However, the corona may provide the launching point for the jet (Merloni & Fabian 2002) or even comprise the base of the jet itself (Fender et al. 1999). Interestingly, Beloborodov (1999) found that magnetized plasma moving away from the disk with a velocity of $\sim 0.3c$ can explain the weak reflection features in Cyg X-1, which would be consistent with this picture.

In order to understand the IR/optical data, we must first consider how the disk may be contributing in this region. Unfortunately, addressing the thermal disk component is not a uniquely defined problem for GX 339–4. If we assume the SD component extends up to the first X-ray data points and then drops off, we find $T_{in} = 10^6$ K, which is the same value which W99 used for their fits to this source. We keep T_{in} fixed to this value for all models discussed in this paper. However, a naive fit to the rising optical data with a multi-temperature blackbody would then require almost the entire L_{Edd} being channeled into the SD emission. For the LHS, which is defined by its assumedly low accretion rate, this seems unrealistically high. One way around this is to assume a lower SD luminosity, and that the optical points are due to the irradiation of the outer disk material by intercepted X-rays. For the mass and inclination angle we use here, the outer disk radius would be on the order of $r_{out} \approx 10^5$ cm. We use this as the nominal scale for the X-ray irradiated shell, noting that there could easily be a factor of a few leeway due to the large uncertainties in the system's binary parameters. To fit the optical data, the temperature of this single blackbody needs to be $T_{BB} \sim 5 \times 10^4$ K. This high temperature is not in conflict with possible disk instability models (e.g., Cannizzo et al. 1988) because we are observing already in outburst, after the effects of the instability would be felt.

For the models presented in Fig. 1, we fix the SD luminosity to a characteristic value of $L_d \sim 0.1 L_{Edd}$, and then make up any deficit in the optical region via the irradiation component. The ensuing fraction of the jet power contained in the irradiated component then can be determined due to the fact that an IR/optical break is observed. For the other data sets included in this paper, however, this break is not observationally resolved. For those models we therefore assume that the luminosity of the irradiated emission can be linked to the power in the jet, and we set $L_{BB} = 0.1 Q_j$ as a canonical value.

It turns out that the 1981 data set is in fact so luminous that it creates a problem for our assumed black hole mass of 5 $M_\odot$. Even assuming $L_{\rm d} \sim 0.1\ L_{\rm Edd}$ in fact requires $\dot{m} \sim 0.5$ (in Eddington units) for the fixed $T_{\rm in} = 10^6$ K, which is much larger than one would expect for the LHS according to some models (e.g., Esin et al. 1997). We could solve this problem by choosing a lower $L_{\rm d}$ and $T_{\rm in}$, thus having the SD contribution truncate before the X-ray data. However, then this only increases the need for more intercepted jet power in the irradiated component, which we already require to be at the upper bound of physical limits. We discuss the parameters in detail for the models below, but feel this problem is too unconstrained at this time to make any conclusions about the exact nature of the disk contribution.

4.2. 1981 data set, no acceleration

Assuming that jets are responsible for the radio emission, the first issue to explore is how the solution would look if the jet plasma never encounters an acceleration region. This would be the simplest case model, where a portion of the thermal disk or coronal plasma is simply advected into the outflow, retaining its thermal or quasi-thermal distribution. In this case, the synchrotron spectrum from each segment of the jet will have a "hump" shape peaked around a particular self-absorption frequency determined from the physical parameters for the segment. The combination of all these humps, each located at a different frequency, gives a flat-to-inverted radio to at least IR spectrum which can be seen in Fig. 1. The slope of the spectrum depends on the amount of expansion and the velocity profile along the jet, as well as on $\theta_{\rm i}$.

As explained in the previous section, the electron temperature at the base of the jet is a free parameter, and so we explore two extremes for this scenario. The first, shown in Fig. 1a, is at the lowest end of the relativistic scale with electrons entering the jet base with initial $T_{\rm e} \sim 2 \times 10^9$ K, and in Fig. 1b we show a more relativistic solution, with $T_{\rm e} = 2 \times 10^{10}$ K, the maximum temperature we could accommodate in our modeling of XTE J1118+480 (MFF). In order to bring the highest frequency "hump" from the part of the jet closest to the accretion disk to low enough frequencies to come near the turnover in the IR data, we must vary the nozzle radius r_0 and the input power $Q_{\rm j}$, thus controlling the magnetic field B_0 and density n_0 at the base of the jet while the temperature remains fixed. Similarly we must adjust $\theta_{\rm i}$ to fit both the radio and the IR together with synchrotron, which changes the power requirements because of the beaming.

With the requirement that the non-accelerated models adequately describe the IR data as well as the maximum self-absorption turnover, the jet parameters for the fit shown in Fig. 1a are then $r_0 = 5 \times 10^3\ r_{\rm g}$, $Q_{\rm j} = 3.7 L_{\rm Edd}$ and $\theta_{\rm i} = 8°$, the former two being obviously unlikely values. The extremely high value of the the nozzle radius is necessary to decrease the self-absorption frequency to a value low enough to fit the IR data, which because of the resulting larger self-absorption also leads to a very peaked contribution from the denser nozzle. This does not seem feasible under the assumption that the jet originates at the inner edges of the accretion flow, or in the corona above it, and the match to the IR data itself is not particularly good. The "nozzle bump" is due to our assumption of this element of the geometry, as required for jet models of Sgr A* and LLAGN (e.g., Falcke & Markoff 2000; Yuan et al. 2002). Without a nozzle region, one could find a solution with a somewhat larger $\theta_{\rm i}$, but then this would require an even higher $Q_{\rm j}$ because the emission would be beamed away from the observer. The value of $Q_{\rm j}$ here is already several times higher than $L_{\rm Edd}$ for a 5 $M_\odot$ central object. The irradiation component can provide the required rise in the optical data if the outer disk intercepts a small fraction of the jet power in X-rays, $L_{\rm BB} \sim 0.03 Q_{\rm j}$. Overall, however, this model is not so satisfactory.

The observations are slightly better described, at least at low-frequency, for the more relativistic case shown in Fig. 1b. The higher temperature electrons lead to less self absorption, giving a broader nozzle bump and requiring a somewhat smaller nozzle radius of $r_0 = 1.2 \times 10^3\ r_{\rm g}$ with a more reasonable $Q_{\rm j} = 1.4 \times 10^{-2} L_{\rm Edd}$ for $\theta_{\rm i} = 15°$. This nozzle width is still rather untenable, however, in the context of jet/corona models. For this scenario we also run into more trouble with the disk modeling, because we would require the outer disk to intercept roughly $6 Q_{\rm j}$ in X-ray luminosity to account for the optical data.

For both cases shown in Fig. 1, the IC emission in the X-rays is dominated by the upscattered thermal disk emission but, because of the low densities, lies under the data and also has the wrong shape. In this and all other figures in this paper, we do not include IC of photons from far out in the jet, since they are orders of magnitude under the data and will not affect the fit. Changing the disk geometry so that the thin disk underlies the base of the jet/corona may provide more IC emission, but would still not address the fundamental problem of explaining the radio thru IR data with reasonable parameters.

In summary, the energy budget in the non-accelerated case is not large enough to create enough synchrotron to fit the radio for a non-relativistic plasma, since the required $Q_{\rm j}$ for the already weakly relativistic temperature of Fig. 1a is super-Eddington. Considering that the radio through IR bands are likely due to jet synchrotron in the LHS, we conclude, based on all the above difficulties, that a model which does not include particle acceleration in the jet is unlikely. The extent to which the energy budget falls short is in part due to assumptions of the equipartition of energy, as described earlier. However, corona or other accretion flow models which attempt to explain the low-frequency data without a standard jet solution do not seem very feasible.

4.3. 1981 data set, with acceleration

Therefore we want to focus on solutions where the particles in the jet are accelerated into a power-law distribution, as is typical in AGN. This solves the energy budget problem for the jet power, although we still need a very luminous thermal contribution.

We show four representative fits in Fig. 2, all with a nozzle radius of $3 r_{\rm g}$, which is more appropriate for the assumption that

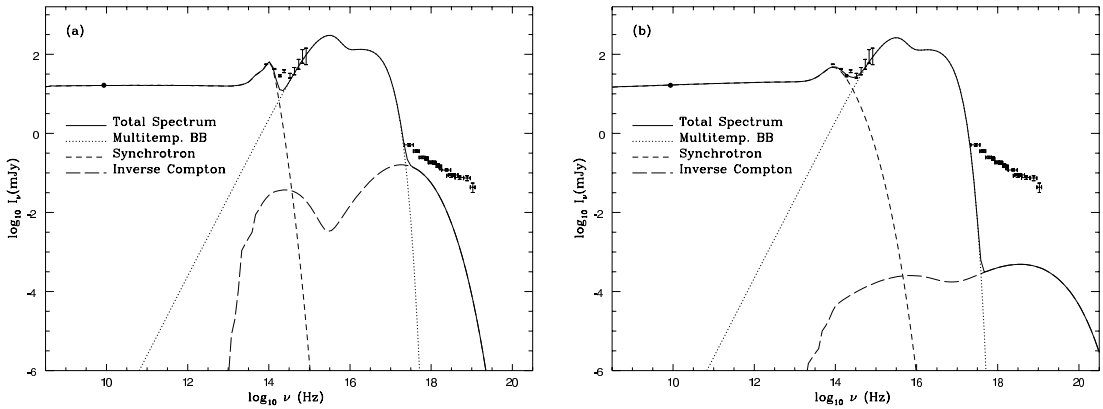

Fig. 1. Two fits to the GX 339–4 1981 data sets for the case of no particle acceleration in the jet, data references contained in CF02. The solid thick line is the total spectrum, the dotted line is the multi-temperature blackbody SD disk plus irradiation blackbody contribution , the short-dashed line is the synchrotron emission and the long-dashed line is the inverse Compton (IC) upscattered disk and jet photons. In both panels, the IC components do not include the outer part of the jet as its contribution is orders of magnitude under the data. **a)** The fit for the nearly non-relativistic initial electron temperature of 2×10^9 K and $r_0 = 5\times10^3\ r_g$, **b)** The fit for a temperature similar to the maximum derived for another XRB source, XTE J1118+480 (see MFF), of 2×10^{10} K, with $r_0 = 2\times10^3\ r_g$.

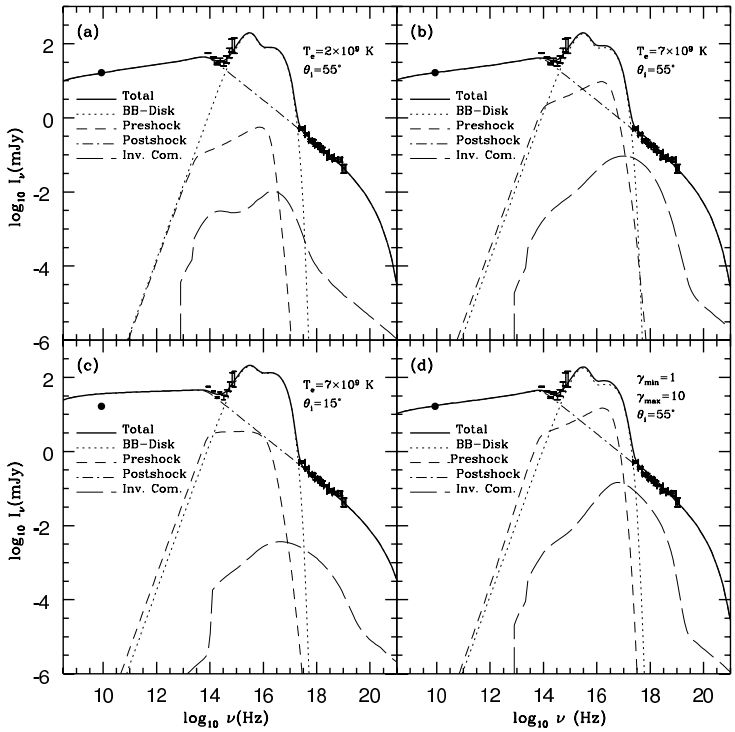

Fig. 2. Four fits for the 1981 data set shown in Fig. 1, with the radio point extrapolated from the correlation curves of C00 and C02. The solid thick line is the total spectrum, the dotted line is the multi-temperature blackbody outer disk plus single blackbody irradiation contribution, the short-dashed is the synchrotron emission from the jet before the shock acceleration region, the dot-dashed line is the synchrotron emission after acceleration, and the long-dashed line is the inverse Compton upscattered disk and jet photons. **a)** The fit for the mildly relativistic case of $T_e = 2\times10^9$ K, which requires an unrealistically large jet power of $Q_j \sim 0.6L_{Edd}$. **b)** A fit with the highest temperature electrons allowed which can give a good fit to the broadband spectrum, $T_e = 7\times10^9$. This solution also gives a more realistic jet power of $Q_j \sim 0.3L_{Edd}$. **c)** The case for the same temperature but with a much smaller inclination angle, requiring only $Q_j \sim 3\times10^{-2}L_{Edd}$, but which cannot fit the extrapolated radio point. **d)** The resulting fit from a power-law of particles at the base of the jet, rather than a thermal distribution, as may be expected near an accretion shock. This solution also requires a large jet power, $Q_j \sim 0.5L_{Edd}$, however.

the jet originates at the edge of an accretion flow. As discussed above, we fix $L_{\rm d} = 0.1L_{\rm Edd}$ with $T_{\rm in} = 10^6$ and $r_{\rm out} = 10^5 r_{\rm g}$ and then fit the optical data with the irradiated component, leaving the intercepted fraction of $Q_{\rm j}$, $L_{\rm BB}$, as a free parameter in the fit.

In panel (a) of Fig. 2, we show the resulting spectrum from a jet with mildly relativistic electrons, similar to the model shown in Fig 1a. The short-dashed line shows their contribution before encountering the acceleration region. Compared to Fig. 1 the nozzle "hump" lies at a higher frequency due to the more compact nozzle scale, and the slope is more inverted primarily to the greatly increased angle to the line-of-sight necessitated by the radio/IR fit, $\theta_{\rm i} = 55°$. The slope is flatter in the post-accelerated component (shown with the dot-dashed line), because of the effects of reacceleration and particle losses. Synchrotron from the accelerated particles dominates the entire spectrum with the exception of the optical, with the IR and X-rays stemming from the region near the start of the acceleration $z_{\rm sh}$, while the radio comes from much further out along the jet. For a fixed $T_{\rm e}$, $Q_{\rm j}$ and $\theta_{\rm i}$ are found by fitting the radio-IR spectrum, which then uniquely determines $z_{\rm sh}$ by fitting the IR turnover and extension to the X-rays. This also determines the slope of the accelerated particles, p. The jet parameter values for this mildly relativistic case are: $T_{\rm e} = 2{\times}10^9$ K, $Q_{\rm j} = 0.62L_{\rm Edd}$, $\theta_{\rm i} = 55°$, $z_{\rm sh} = 2.15{\times}10^3 r_{\rm g}$ and $p = 2.15$. The IC emission is dominated by upscattered thermal disk photons and is well under the synchrotron contribution.

The problem with this model is that – as in the model from Fig. 1a – the required power in the jet $Q_{\rm j}$ is unrealistically large, in order to compensate for the low electron temperature. This imbalance also leads to the magnetic field energy density in the jet being a few orders of magnitude super-equipartition with the hot, radiating electrons. While many jet formation models assume the magnetic energy density is in equipartition with the kinetic energy near the base of the jet (e.g., Blandford & Payne 1982; Li et al. 1992), which for a maximal jet would lead to magnetic domination, this may be rather extreme.

In Fig. 2b, we consider the highest temperature electrons allowed by this model, above which the X-ray predictions (from either synchrotron or IC from the jet) are too high, $T_{\rm e} = 7{\times}10^9$ K. The jet free parameters are now: $Q_{\rm j} = 0.27L_{\rm Edd}$, $\theta_{\rm i} = 55°$, $z_{\rm sh} = 1.75 \times 10^3 r_{\rm g}$ and $p = 2.15$. Raising the temperature thus serves mainly to reduce the power requirements and changes the location of the shock region slightly. With the same SD parameters as in (a), the irradiation component now comprises $0.4Q_{\rm j}$, still rather large but again given the uncertainties in the mass and outer radius, more viable. The hotter electrons now also contribute to a greater degree via IC upscattering, contributing some of the soft X-ray emission.

While there is no measurement of the inclination angle, some papers favor a lower value than what we find for our best fit above (e.g., Cowley et al. 2002). In Fig. 2c, we show what our model predicts for $\theta_{\rm i} = 15°$ and the same temperature as in panel (b). The decreased angle greatly reduces the power requirements in the jet, but at the same time flattens the predicted radio-IR slope significantly, making a good radio/IR fit impossible. The parameters are $Q_{\rm j} = 3.2{\times}10^{-2}L_{\rm Edd}$, $z_{\rm sh} = 2.15{\times}10^3 r_{\rm g}$ and $p = 2.15$. Although this radio point is only from an extrapolation of the radio/X-ray correlation relation (C00; C02), the slope is remarkably well-defined at these higher luminosities. On the other hand, $\theta_{\rm i} = 55°$ does give good fits to most of the other data sets discussed below. Because the beaming reduces the power requirements for the jet, a low inclination angle also means that more power must irradiate the outer disk than is available, making this model problematic.

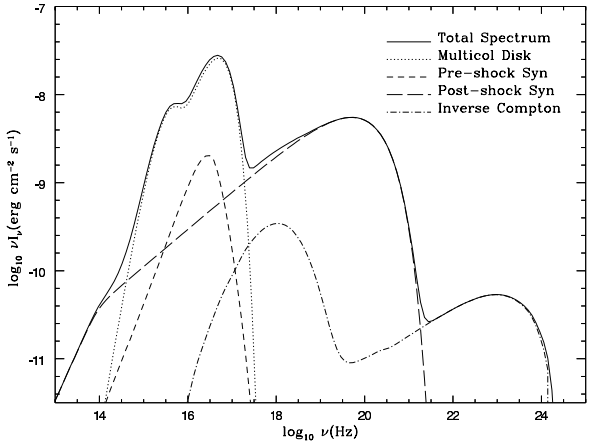

Fig. 3. The same model for the 1981 data set presented in Fig. 2b, in units of νI_ν to show the distribution of power across the frequency bands. Above 10^{18} Hz one can see an analogy to the "camel back" feature known from blazar spectra.

Finally in Fig. 2d we consider the case of a power-law of particles entering the base of the jet from the accretion flow instead of thermal particles, as may occur if acceleration also takes place at an accretion shock. Instead of defining a temperature, we take the minimum electron Lorentz factor $\gamma_{\rm e,min} = 1$, leaving $\gamma_{\rm e,max}$ a free parameter. In order to prevent the nozzle emission from violating the constraints of the soft X-ray data, we find $\gamma_{\rm e,max} \sim 10$, which would require extreme radiative cooling to truncate the accelerated power-law for this scenario to be realistic. This type of scenario may be necessary for certain low-luminosity AGN (see, e.g., Yuan et al. 2002). The other jet parameters are $Q_{\rm j} = 0.55L_{\rm Edd}$, $z_{\rm sh} = 2.15 \times 10^3 r_{\rm g}$, $\theta_{\rm i} = 55°$ and $p = 2.15$. The high required jet power means that the irradiated component needs only $0.02Q_{\rm j}$ to account for the optical data.

In this last model, the IC emission still lies under the synchrotron component, but not by much, and has the correct slope. In a different geometry where the SD underlies the corona/jet base, this may provide the best alternative for a solution where the IC dominates the synchrotron emission in the X-rays.

In all four model runs shown here, we needed a rather large fraction of the jet power to be intercepted by the outer disk and reradiated. If we allowed the SD to radiate $0.2L_{\rm Edd}$ away, we could lower the necessary $L_{\rm BB}$, but then again we would be basically at the Eddington accretion rate, as discussed for the non-acceleration case. This problem is clearly not very constrained for this source, and a central mass of ~15 instead of

5 $M_\odot$ (as in, e.g., GRS 1915+105; Greiner et al. 2001), would easily resolve these issues.

In Fig. 3 we show the same model as in Fig. 2b with the flux multiplied by the frequency to show the distribution of power across the wavebands. One can see that most power seems to fall in the disk component, with the synchrotron then creating the second peak around the cutoff. The IC component is in fact dominated by the upscattered disk photons, but this is hidden beneath the synchrotron emission. The self-Comptonized synchrotron component peaks at 10^{23} Hz, or ~400 MeV, corresponding to the synchrotron peak upscattered by the hot electrons near the shock. At high frequencies, the shape is similar to the "camel back" spectra seen in blazars (e.g., Fossati et al. 1998), and in fact at this highest observed flux level is above the sensitivity of GLAST for a one year all-sky survey at 100 MeV. The less powerful epochs of this source presented in the next section may not be so observable, however, as they are orders of magnitude lower.

In conclusion, we have shown that in order to explain the low-frequency data from the 1981 observation of GX 339–4, a jet solution must include some form of particle acceleration. And further, once that condition is fulfilled, X-rays from jet synchrotron (in addition to IC) are unavoidable as long as IC emission is not the main cooling channel. But under the assumption of a disk geometry where a SD transforms to an optically thin, hot accretion flow at some inner radius, synchrotron cooling will dominate in a maximal jet. It is possible, however, that in the alternative geometry of a corona/jet base lying directly on top of the SD could lead to so much IC cooling that the synchrotron cutoff would occur below $\sim 10^{17}$ Hz, thus accommodating a dominant IC contribution in the X-rays. This would not, however, explain the interesting coincidence of IR turnover/X-ray spectrum seen here and now also in several sources in addition to XTE J1118+480. It may also be difficult to explain the radio/X-ray correlation with an IC model (see Sect. 5). We will, however, soon explore combined jet/corona solutions using lower temperature cyclo-synchrotron and IC scattering in different geometries.

We have explored the relativistic electron parameter range for the 1981 data set and find that the most reasonable parameters are obtained for the case of a fully relativistic initial thermal electron distribution. Besides requiring too much power, a mildly relativistic initial electron distribution would also result in the magnetic energy density being much higher (and further out of equipartition with) the accelerated particles at the shock, more so than would likely be expected for magnetic confinement. For these reasons, in this paper we consider only the higher temperature solutions for all fits, corresponding to the type of fit shown in Fig. 2b.

4.4. Other data sets

For the 12 data sets compiled during the other LHS episodes of GX 339–4, we can either optimize each fit individually leaving all parameters free, or fix as many parameters as possible to see if essentially the same model can account for all observed spectra. We here choose to take this latter approach, in order to explore the fundamental physics of the model. We will fix some of the parameters to those best constrained by the 1981 set and then study the affect of changing only two jet parameters. Our emphasis is on understanding the radio/X-ray correlations, and thus the jet component. However, we address the SD contribution as well, and attempt to test the jet/disk connection by finding a scaling solution. We set $L_{\rm BB} = 0.1 Q_{\rm j}$ for all fits, and then fit $L_{\rm d}$ to the optical data, when present.

While it seems clear that there are small variations in the soft X-ray spectra of these data sets (this is discussed in NWD, who fit a broken power law – we are fitting the lower energy segment), we choose to fix the accelerated spectral index to $p = 2.15$ as in 1981. Similarly, while there are obvious changes in the SD contribution, they seem consistent with the likely underlying accretion changes that also affect the jet since both components decrease in luminosity with increasing time. We keep $T_{\rm in}$ fixed at 10^6 K and $T_{\rm e}$ fixed at 7×10^9 K based on the 1981 set, as a starting point. We will assume that the orientation of the jet remains fixed at 55° (statistically 57° is the most likely angle) and that the base of the jet is fixed at $r_0 = 3r_{\rm g}$. Thus the only jet parameters allowed to vary are $Q_{\rm j}$ and $z_{\rm sh}$, and the disk parameter $L_{\rm d}$ is then adjusted to fit the thermal data, when present.

Figures 4a and 4b show the broadband spectral fits to the data, with the corresponding fit parameters given in Table 2. For the data sets without optical data constraining the disk, $L_{\rm d}$ is rather arbitrary, and we scaled the luminosity to the jet power.

Although the fits are surprisingly good given the limited fitting parameters, there are obvious features in the X-ray waveband such as a flattening at higher frequencies and peaks which our model cannot account for. These features are likely due to the impacting X-rays on the cooler material of the SD, but we have not yet incorporated this into our model. The softest X-rays should not be affected by these additional components, however, so we focus our fitting at the lower X-ray frequencies. For the lowest flux level data sets of 1999, which we label 99_4–99_8, as well as 2000, the error bars are large enough to make the fitting more difficult.

The most important feature to note is that the radio/X-ray correlations detected in this source (C00; C02) can be explained by the variation of only one main parameter in the jet model: the input power. If we plot $z_{\rm sh}$ against the jet power $Q_{\rm j}$ (Fig. 5), we see that there is a slight dependence ($z_{\rm sh} \propto Q_{\rm j}^{-0.135}$), but this likely results from our rather artificially freezing of the other parameters. This small dependence is rather amazing when one thinks that $Q_{\rm j}$ is changing by about three orders of magnitude over the same range, if 1981 is included.

5. Understanding the radio/X-ray correlations

It seems likely that the real source of the variations is the power fed into the jet. In Fig. 6 we plot the prediction of our model against the data for the correlation between the 8.6 GHz radio flux and the integrated 3–9 keV X-rays (C02). We fix $z_{\rm sh} \sim 1.8 \times 10^3 r_{\rm g}$, to match the highest flux data point of 1981, which is not shown on this figure because the radio was not simultaneously measured. Then we adjust only $Q_{\rm j}$ while holding *every* other parameter constant, in order to fit the radio flux, and

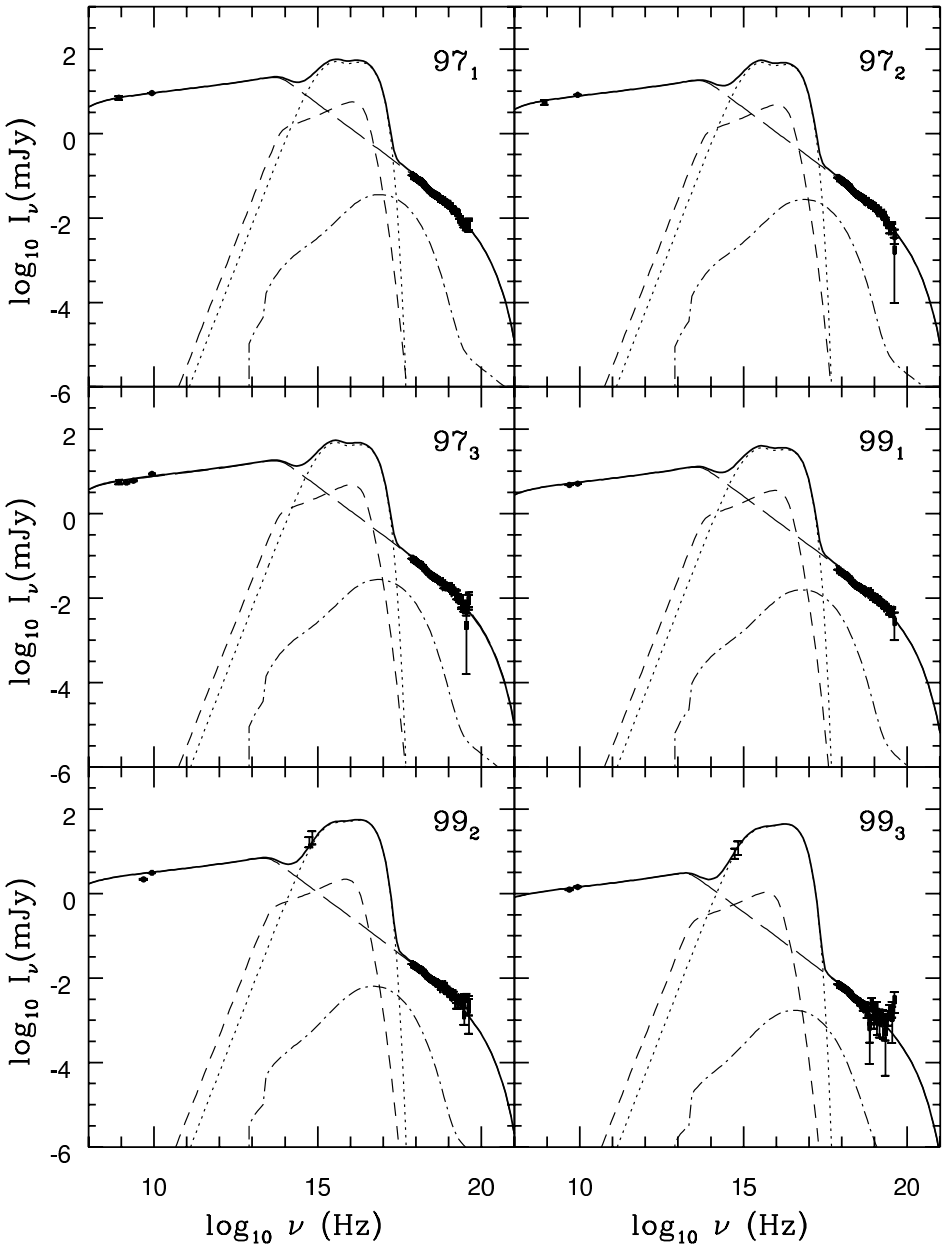

Fig. 4. a) Composite figure with 6 data sets with labels corresponding to the data sets of Table 1, taken from W99, C00, C02 and NWD. The solid thicker line is the total spectrum, the dotted line is the multi-temperature blackbody representing the outer thermal disk plus a single blackbody for irradiation, the short dashed line is the synchrotron emission from the jet before encountering the shock acceleration region, and the long-dashed line is that from after, and the dot-dashed line is the IC jet and disk emission upscattered by the jet plasma. Fit parameters are shown in Table 2.

plot the resulting integrated 3–9 keV X-ray flux. In removing the $z_{sh} \propto Q_j^{-0.135}$ dependence mentioned above, we are likely compromising the quality of the fit to some degree, but this could be compensated for if we allowed particularly the spectral index to vary.

By just changing the jet power we obtain a very good fit to the correlation data, with the exception of the two data sets 99_7 and 99_8. In fact, the radio data in 99_8 was taken a few days after the X-rays, and coincided with a small reflare in the hard X-rays (see Fig. 15 in C00). This is the likely explanation of the excess radio flux. Similarly, the reflare may also have an affect on 99_7, if there is, e.g., a lag between the changing fluxes.

The results shown in Fig. 6 provide strong support for a jet synchrotron model, since it correctly predicts the

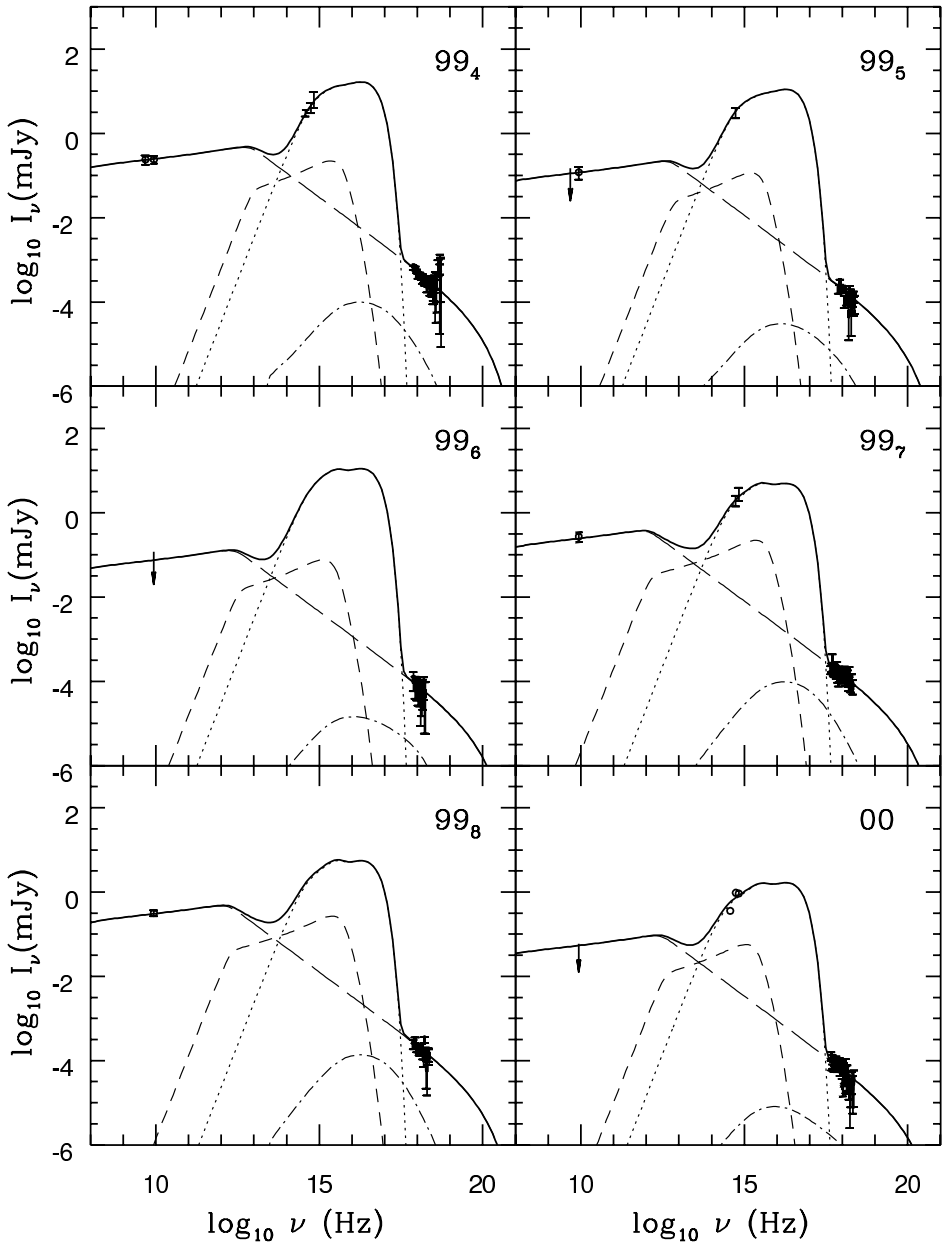

Fig. 4. b) Composite figure with 6 data sets with labels corresponding to the data sets of Table 1, taken from W99, C00, C02 and NWD. The arrows represent 3 – σ detection upper limits. The lines are the same as in Fig. 4a. For the "off" state in 2000, the optical data are from three months prior to the X-ray and radio observations, and should be seen as upper limits.

radio/X-ray correlation over orders of magnitude in flux levels, almost exactly matching the data. The fit is better at the higher flux end, where the error bars are smaller. The exact dependence (excluding 99_7 and 99_8) goes as $F_X \propto F_R^m$, where $m = 1.41$, F_R is the 8.6 GHz radio flux and F_X is the integrated 3–9 keV X-ray flux.

The value for m in fact follows directly from analytic predictions of the jet model. Equation (52) in Falcke & Biermann (1995) shows[1] that if all parameters except the power are fixed, as we have done to produce Fig. 6, the frequency where the optically thick flat-to-inverted spectrum turns over to the optically thin regime depends on the power as

$$\nu_{SSA} \propto Q_j^{2/3}. \quad (3)$$

[1] In Falcke & Biermann (1995), the quantities which we label ν_{SSA}, Q_j and F_{SSA} correspond to $\nu_{s,obs}$, $q_{j/1}L_{46}$ and $L_{\nu_s,obs}$, respectively.

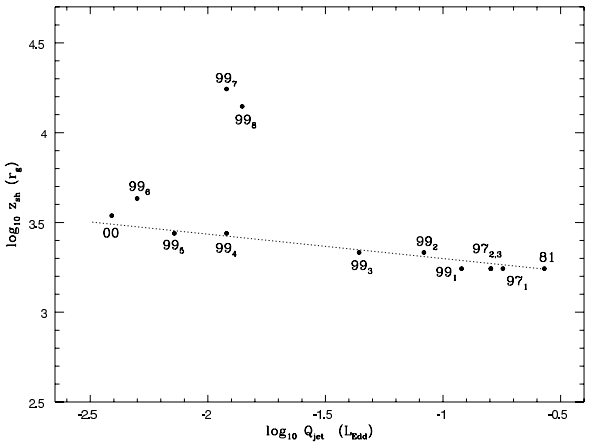

Fig. 5. Correlation between the input jet power Q_j and the location of the first acceleration zone z_{sh} for the fits in Figs. 2 and 4. The dashed line is to guide the eye for the upward trend in the data sets. The 1981 point represents the fit shown in Fig. 2b. The 99_8 data set is not strictly simultaneous, and the radio data are simultaneous with a small reflare in the hard X-rays, which may explain its excess. 99_7 may also be affected by this flare.

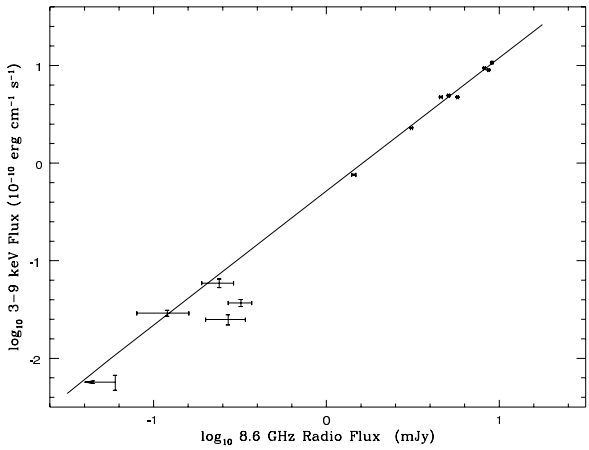

Fig. 6. The model-predicted radio (8.6 GHz)/X-ray (integrated 3–9 keV emission) correlation (solid line). The data are from C00 & C02. For this figure, z_{sh} is fixed at $\sim 1.8 \times 10^3\, r_g$ to match the 1981 highest flux result, and then the only changing parameter is the power input into the jet Q_j. The arrow represents $3-\sigma$ upper limits.

Table 2. Fit parameters for Figs. 3a and 3b.

Data Set	Q_j (L_{Edd})	z_{sh} (r_g)	L_d (L_{Edd})
97_1*	0.18	1.8×10^3	8.8×10^{-2}
97_2*	0.16	1.8×10^3	7.8×10^{-2}
97_3*	0.16	1.8×10^3	7.8×10^{-2}
99_1*	0.12	1.8×10^3	6.0×10^{-2}
99_2	8.3×10^{-2}	2.2×10^3	1.0×10^{-1}
99_3	4.4×10^{-2}	2.2×10^3	8.0×10^{-2}
99_4	1.2×10^{-2}	2.8×10^3	3.0×10^{-2}
99_5	7.2×10^{-3}	2.8×10^3	2.0×10^{-2}
99_6*	5.0×10^{-3}	4.3×10^3	2.0×10^{-2}
99_7	1.2×10^{-2}	1.8×10^4	9.0×10^{-3}
99_8*	1.4×10^{-2}	1.4×10^4	1.0×10^{-2}
00[a]	3.9×10^{-3}	3.5×10^3	3.0×10^{-3}

*Data sets where there is no direct constraint on the thermal disk component.
[a]The optical data constraining the SD are not simultaneous.

Similarly Eq. (56) (ibid.) shows that under the same freezing of other parameters, the flux at the turnover depends on the power as

$$F_{SSA} \propto Q_j^{17/12}. \quad (4)$$

These relations can then be normalized using the 1981 data set, where the flux and turnover frequency are visible.

Knowing these relations, and the spectral indices of the optically thick and thin components from the data, one can roughly calculate the expected correlation slope. Because the spectral indices for the radio-IR, α_{RIR}, and X-ray, α_X, do vary slightly over GX 339–4's observation history, taking constant values will make this less exact. We now want to calculate the slope between two points along the correlation curve, analogous to the model plotted in Fig. 6. Each point represents a different value of Q_{jet}, corresponding to different values of ν_{SSA} and F_{SSA}. The 8.6 GHz radio flux is then

$$F_{8.6} = F_{SSA}\left(\frac{\nu_{SSA}}{8.6\,\mathrm{GHz}}\right)^{\alpha_{RIR}}, \quad (5)$$

and then using Eqs. 3 and 4:

$$\log_{10} F_{8.6} = \log_{10} C_1 + \frac{17}{12}\log_{10} Q_j - \frac{2}{3}\alpha_{RIR}\log_{10} Q_j, \quad (6)$$

where C_1 absorbs the exact dependences of the flux and frequency at the turnover on Q_j, and other constants.

Similarly, the X-ray flux at any frequency (as long as it falls on the power-law) is

$$F_X = F_{SSA}\left(\frac{\nu_{SSA}}{\nu_X}\right)^{\alpha_X}, \quad (7)$$

which after using the forms from Eqs. (3) and (4) and integrating from 3–9 keV becomes

$$\log_{10}\int F_X d\nu = \log_{10} C_2 + \frac{17}{12}\log_{10} Q_j - \frac{2}{3}\alpha_X \log_{10} Q_j, \quad (8)$$

where again C_2 includes the constants of integration and the dependencies on Q_j.

For any two values of the jet power, Q_A and Q_B, the correlation slope is then

$$m = \frac{\log_{10}\int F_{X,B} - \log_{10}\int F_{X,A}}{\log_{10} F_{8.6,B} - \log_{10} F_{8.6,A}} \quad (9)$$

$$= \frac{\frac{17}{12} - \frac{2}{3}\alpha_X}{\frac{17}{12} - \frac{2}{3}\alpha_{RIR}}, \quad (10)$$

after algebraic cancellations. Taking the values from the power-law fits to the 1981 data set from CF02, $\alpha_{RIR} \sim 0.15$ and $\alpha_X \sim -0.6$, we find $\alpha_{cor} = 1.38$, which considering the simplifications in the model and our ignoring of the spectral variations,

is surprisingly close to the value of 1.4 found for GX 339–4. In addition, this type of radio/X-ray correlation has also been seen in V404 Cygni, with exactly the same slope (Gallo et al. 2002; Gallo et al. 2002, MNRAS, in prep.). Our preliminary models of this source also show a turnover in the IR band and have similar jet parameters (Markoff et al. 2002, in prep.).

The fact that the well-determined slope m extrapolates to the lower flux data also gives us greater confidence in the subtraction of the putative "background source" discussed in Sect. 2. Note also that the lowest flux point is from BeppoSAX, and therefore does *not* rely on the subtraction of a background source.

It is possible that an IC corona model could also explain the correlation slope, if the radio flux scales with the power (assumed to be linearly related to $\dot{M}$) as expected from the jet and the X-ray flux scales with $\dot{M}^2$. This may be the case in some optically thin accretion solutions. However, it has yet to be shown that a self consistent solution can be found which also well fits all the broadband data available for this source. Similarly this would not explain why the X-rays trace back to the turnover in the IR as 1981 data, or why most if not all LHS sources show this turnover coincidence.

6. Conclusions

We show that a model comprising a dominantly synchrotron jet component, in combination with an optically thin accretion flow transitioning to a standard thin disk, is able to explain the broadband spectral data from 13 observations of GX 339–4. At the same time, the model can easily explain the $m \sim 1.4$ slope of the radio/X-ray correlations by changing only the power input into the jet. This input power, Q_j, is assumed to be proportional to the accretion rate, and varies from $L_{Edd} \sim 0.003$–0.3 for a 5 $M_\odot$ black hole. Above the highest luminosity, the source would likely transition to the HSS.

This model assumes an underlying disk geometry in which the standard thin disk exists beyond ~100–1000 r_g, and has a relatively low accretion rate. In a situation where the SD extends all the way down to the last stable orbit, the photon field at the base of the jet may be high enough to affect our conclusions, which are dependent on synchrotron losses dominating the cooling. If the available photon field for inverse Compton upscattering becomes large enough, it may truncate the accelerated particle distribution and lessen the extent of the synchrotron emission.

With the exception of this model, the non-thermal X-ray spectral component in all XRB states has been modeled in terms of inverse Compton processes in a hot corona, located either above or within the standard thin disk. These classes of models have significant success explaining both the spectral features and timing characteristics in the X-ray waveband, but fail to address the radio/IR spectra which in at least GX 339–4, V404 Cyg and Cyg X-1 seem intimately linked to the higher frequencies.

However, the existence of a hot, magnetized plasma at the base of the jet leads to obvious considerations of a unification scheme between it and this concept of a corona, which until now has not been explicitly observed. Both scenarios (jet and corona) address important features from the observations, but either cannot or have not yet attempted to account for everything. We feel that a concatenation of these two components would be fruitful as the next stage of our investigation. It is, however, important to note that under reasonable physical assumptions, the jet can easily produce X-ray emission via synchrotron radiation, and has significant success explaining the data when it does. This possibility must therefore be considered in spectral modeling; whether it really dominates the entire spectrum is a question of the environment and local acceleration conditions. It may be that it indeed dominates only in those sources which show only weak reflection features (e.g., XTE J1118+480; Miller et al. 2002), but it likely has a wider impact in all sources than has so far been appreciated.

Interestingly, the parameters we derive for the power and location of the shock are roughly consistent with earlier results modeling XTE J1118+480, which because of the higher temperature ($T_e = 2 \times 10^{10}$ K) resulted in a lower necessary power input into the jet. In this source we found $z_{sh} \sim 10^2 r_g$ as compared to the $\sim 10^3 r_g$ found here, however considering that the jet can extend beyond $10^{10} r_g$, this range is quite small. In our recent modeling of other LHS BHC sources, we are in fact finding that all sources with simultaneous radio/X-ray data seem to require acceleration to begin in this same range, and we will discuss the physical implications of this elsewhere. For these sources we also find, as in GX 339–4 and XTE J1118+480, that if the X-rays are traced back to lower frequencies, the optically thick-to-thin turnover always occurs in the IR range. If this turnover coincidence is real, it offers us the chance to explore the physical conditions at the acceleration zone of XRB jets.

This work illustrates how critical simultaneous multiwavelength observations are to increasing our understanding of the physics in these sources. With the advent of higher energy missions such as *GLAST*, *INTEGRAL* and *ASTRO E-2*, soon we can hopefully begin to probe the contribution of these smaller jets to the hard X-ray and γ-ray bands.

Acknowledgements. This work is partially supported by AUGER Theory Grant O5CU1ERA/3 from the BMBF (S.M.). S.M. would like to thank Tom Maccarone and David Meier for very helpful discussions.

References

Beloborodov, A. M. 1999, ApJ, 510, L123
Blandford, R. D., & Königl, A. 1979, ApJ, 232, 34
Blandford, R. D., & Payne, D. G. 1982, MNRAS, 199, 883
Bloom, S. D., Marscher, A. P., Gear, W. K., et al. 1994, AJ, 108, 398
Brocksopp, C., Fender, R. P., Larionov, V., et al. 1999, MNRAS, 309, 1063
Callanan, P. J., Charles, P. A., Honey, W. B., & Thorstensen, J. R. 1992, MNRAS, 259, 395
Cannizzo, J. K., Shafter, A. W., & Wheeler, J. C. 1988, ApJ, 333, 227
Corbel, S., & Fender, R. 2002, ApJ, 573, L35 (CF02)
Corbel, S., Fender, R. P., Tzioumis, A. K., et al. 2000, A&A, 359, 251 (C00)
Cowley, A. P., Schmidtke, P. C., Hutchings, J. B., & Crampton, D. 2002, AJ, 123, 1741
Esin, A. A., McClintock, J. E., Drake, J. J., et al. 2001, ApJ, 555, 483

Esin, A. A., McClintock, J. E., & Narayan, R. 1997, ApJ, 489, 865
Falcke, H. 1996, ApJ, 464, L67
Falcke, H., Beckert, T., Markoff, S., et al. 2001, in Lighthouses of the Universe, Springer Verlag, ESO Astrophysics Symposia, ed. R. Sunyaev, M. Gilfanov, & E. Churazov, in press
Falcke, H., & Biermann, P. L. 1995, A&A, 293, 665
Falcke, H., & Biermann, P. L. 1999, A&A, 342, 49
Falcke, H., & Markoff, S. 2000, A&A, 362, 113
Fender, R., Corbel, S., Tzioumis, T., et al. 1999, ApJ, 519, L165
Fender, R. P. 2001, MNRAS, 322, 31
Fossati, G., Maraschi, L., Celotti, A., Comastri, A., & Ghisellini, G. 1998, MNRAS, 299, 433
Gallo, E., Fender, R., & Pooley, G. 2002, in Proc. of the 4th Microquasar Workshop, Center for Space Physics: Kolkata, ed. Durouchoux, Fuchs & Rodriguez [astro-ph/0207551]
Greiner, J., Cuby, J. G., & McCaughrean, M. J. 2001, Nature, 414, 522
Hannikainen, D. C., Hunstead, R. W., Campbell-Wilson, D., & Sood, R. K. 1998, A&A, 337, 460
Hardcastle, M. J., Birkinshaw, M., & Worrall, D. M. 2001, MNRAS, 326, 1499
Hjellming, R. M., & Johnston, K. J. 1988, ApJ, 328, 600
Hynes, R. I., Mauche, C. W., Haswell, C. A., et al. 2000, ApJ, 539, L37
Jester, S., Röser, H.-J., Meisenheimer, K., Perley, R., & Conway, R. 2001, A&A, 373, 447
Jokipii, J. R. 1987, ApJ, 313, 842
Jones, F. C., & Ellison, D. C. 1991, Space Science Reviews, 58, 259
Kong, A. K. H., Kuulkers, E., Charles, P. A., & Homer, L. 2000, MNRAS, 312, L49
Li, Z., Chiueh, T., & Begelman, M. C. 1992, ApJ, 394, 459
Liu, B. F., Yuan, W., Meyer, F., Meyer-Hofmeister, E., & Xie, G. Z. 1999, ApJ, 527, L17
Maccarone, T. J. 2002, MNRAS, submitted
Makishima, K., Maejima, Y., Mitsuda, K., et al. 1986, ApJ, 308, 635
Markoff, S., Falcke, H., & Fender, R. 2001, A&A, 372, L25 (MFF)
Marscher, A. P., & Gear, W. K. 1985, ApJ, 298, 114
Marshall, H. L., Miller, B. P., Davis, D. S., et al. 2002, ApJ, 564, 683
Meier, D. L. 2001, ApJ, 548, L9
Meisenheimer, K., Röser, H.-J., & Schlötelburg, M. 1996, A&A, 307, 61
Merloni, A., & Fabian, A. C. 2002, MNRAS, submitted [astro-ph/0112451]
Miller, J. M., Ballantyne, D. R., Fabian, A. C., & Lewin, W. H. G. 2002, MNRAS, 335, 865
Mirabel, I. F., Rodríguez, L. F., Cordier, B., Paul, J., & Lebrun, F. 1992, Nature, 358, 215
Mitsuda, K., Inoue, H., Koyama, K., et al. 1984, PASJ, 36, 741
Motch, C., Ilovaisky, S. A., & Chevalier, C. 1981, IAU Circ., 3609, 2
Nowak, M. A. 1995, PASP, 107, 1207
Nowak, M. A., Wilms, J., & Dove, J. B. 2002, MNRAS, in press [astro-ph/0201383] (NWD)
Pedersen, H. 1981, IAU Circ., 3613
Perlman, E. S., Biretta, J. A., Sparks, W. B., Macchetto, F. D., & Leahy, J. P. 2001, ApJ, 551, 206
Pottschmidt, K., Wilms, J., Nowak, M. A., et al. 2000, A&A, 357, L17
Poutanen, J. 1998, in Theory of Black Hole Accretion Disks (Cambridge University Press), 100
Revnivtsev, M., Gilfanov, M., & Churazov, E. 2001, A&A, 380, 520
Ricketts, M. J. 1983, A&A, 118, L3
Rodríguez, L. F., Mirabel, I. F., & Martí, J. 1992, ApJ, 401, L15
Shahbaz, T., Fender, R., & Charles, P. A. 2001, A&A, 376, L17
Shakura, N. I., & Sunyaev, R. A. 1973, A&A, 24, 337
Sikora, M., & Madejski, G. 2000, ApJ, 534, 109
Soria, R., Wu, K., & Johnston, H. M. 1999, MNRAS, 310, 71
Stirling, A. M., Spencer, R. E., de la Force, C. J., et al. 2001, MNRAS, 327, 1273
Sunyaev, R. A., & Trümper, J. 1979, Nature, 279, 506
Wilms, J., Nowak, M. A., Dove, J. B., Fender, R. P., & di Matteo, T. 1999, ApJ, 522, 460 (W99)
Wilson, A. S., & Yang, Y. 2002, ApJ, 568, 133
Yuan, F., Markoff, S., Falcke, H., & Biermann, P. L. 2002, A&A, 391, 139
Zdziarski, A. A., Lubiński, P., & Smith, D. A. 1999, MNRAS, 303, L11
Zdziarski, A. A., Poutanen, J., Mikolajewska, J., et al. 1998, MNRAS, 301, 435

Chapitre 3
Trous noirs et éjections relativistes : schéma d'unification

— Juliette aurait-elle aimé Roméo si Roméo avait eu quatre incisives manquantes, un grand trou noir au milieu ?.
— Albert Cohen

Note liminaire

Dans ce chapitre, nous nous intéresserons aux propriétés des différents états spectraux traduisant l'évolution du couplage accrétion – éjection au sein des systèmes binaires. Pour cela, l'apport des observations multi-longueurs d'onde a été crucial et constitue l'originalité de nos travaux. Cela a permis de mettre en évidence les nouvelles propriétés dont nous allons discuter dans ce chapitre.

3.1 État de "quiescence" ou de repos

3.1.1 De nouveaux trous noirs au repos

L'étude à haute énergie des jets larges (chapitre 4) nous a donné l'occasion d'étudier certains trous noirs dans leur phase de repos, ou dite de quiescence. Les observations X *Chandra* étaient habituellement réalisées bien en dehors des phases de sursaut. Ces observations nous ont permis de détecter pour la première fois V4641 Sgr (Figure 3.1) et XTE J1859+226 au repos (Tomsick et al. 2003a). Les luminosités dans la bande 0.3–8 keV sont de $(4.0^{+3.3}_{-2.2}) \times 10^{31}$ (d/7 kpc)^2 erg s^{-1} pour V4641 Sgr et $(4.2^{+4.8}_{-2.2}) \times 10^{31}$ (d/11 kpc)^2 erg s^{-1} pour XTE J1859+226, c'est-à-dire dans le même ordre de grandeur que les autres trous noirs détectés précédemment au repos.

Le spectre X de V4641 Sgr semblerait être beaucoup plus dur – indice de photons de 0.2 $\pm$ 0.9 – que les autres sources, mais cette conclusion est limitée par le faible nombre – 9 –

de photons détectés. Avec *BeppoSAX* (Corbel et al. 2000) et *Chandra* (Gallo et al. 2003a), nous détectons GX 339−4 au repos avec une luminosité X minimale de 1.7×10^{33} (d/6 kpc)^2 erg s^{-1} et un spectre X compatible avec une loi de puissance d'indice de photons -2.2. De manière similaire, des observations *XMM–Newton* nous permettent d'obtenir une limite supérieure du flux de 4U 1755−33 au repos de l'ordre de 6×10^{-16} erg s^{-1} cm^{-2} dans la bande 0.3–8 keV, équivalent à une limite supérieure de la luminosité de (1 à 6) $\times 10^{30}$ erg s^{-1} pour une distance de 4 à 9 kpc (Kaaret et al. 2006). Elle est compatible avec un trou noir de faible période orbitale, similaire à XTE J1118+480 ou A 0620−00.

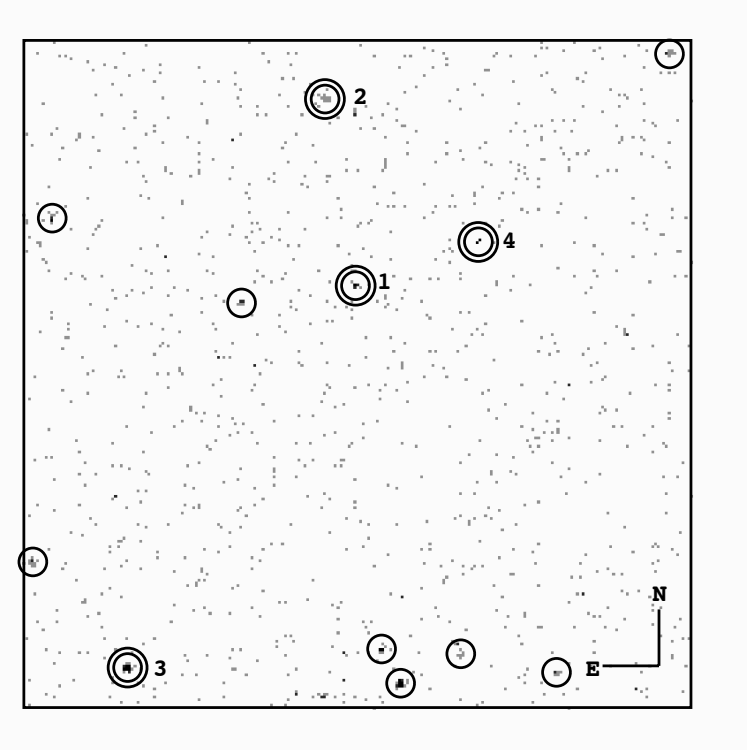

FIG. 3.1 – Image *Chandra* – de $1.4' \times 1.4'$– dans la bande 0.3 – 8 keV de V4641 Sgr au repos – source 1. Douze sources sont détectées en X, dont 4 avec une identification 2MASS – double cercle–. Figure extraite de Tomsick et al. (2003a).

Pour ajouter, nous avons obtenu beaucoup d'observations avec *Chandra*, lors de l'étude des jets en X, de XTE J1550−564 (7 observations, Corbel et al. 2002b) et de H 1743−322 (3 observations, Corbel et al. 2005). Ces deux sources sont détectées à leur plus bas niveau de flux. La luminosité non-absorbée dans la bande 0.5–10 keV est de 2×10^{32} (d/5 kpc)^2 erg s^{-1} pour XTE J1550−564 et 9×10^{31} (d/8 kpc)^2 erg s^{-1} pour H 1743−322. Ces luminosités – tout comme pour GX 339−4 – se trouvent dans la partie haute des niveaux observés pour les autres trous noirs au repos – mais inférieures à GS 2023+338 néanmoins –. Cela est sans doute lié à un taux d'accrétion plus élevé, suite à leur période orbitale plus grande (Corbel et al. 2006).

3.1.2 Nature du spectre X dans la phase de repos

Pour XTE J1550−564, les observations *Chandra* nous permettent de contraindre précisément la forme du spectre X comme une loi de puissance corrigée de l'absorption interstellaire d'indice

de photons de 2.25 ± 0.08. Ce résultat est indépendant de la densité de colonne d'hydrogène (Figure 3.2). Il s'agit de la plus forte contrainte sur la forme d'un spectre X d'un trou noir au repos (Corbel et al. 2006).

Nous mettons donc en évidence un changement de forme du spectre X entre l'état dur – indice de photons de l'ordre de ∼ 1.6 – et l'état de repos : le spectre devient plus mou – "softening". En compilant l'ensemble des rares spectres publiés (voir détails dans Corbel et al. 2006), nous constatons que d'autres sources sont compatibles avec ce comportement : XTE J1118+480 ou A 0620−00 (McClintock et al. 2003).

En allant même plus loin, on constate que les trous noirs ayant une période orbitale supérieure à ∼ 60 heures – GS 2023+338, GRO J1655−40 et V4641 Sgr – semblent montrer – statistiquement – un comportement inverse. Le spectre devient plus dur au repos (Corbel et al. 2006).

Néanmoins, ce résultat est dominé statistiquement par le spectre de GS 2023+338 publié par Kong et al. (2002) Nous avons, cependant, trouvé de nouvelles données publiques de *Chandra* ou d'*XMM–Newton* infirmant ce résultat : le spectre de GS 2023+338 est lui aussi compatible avec une loi de puissance d'indice de photons de 2.22 ± 0.10 (Corbel et al. in prep.), contrairement aux précédents travaux de Kong et al. 2002).

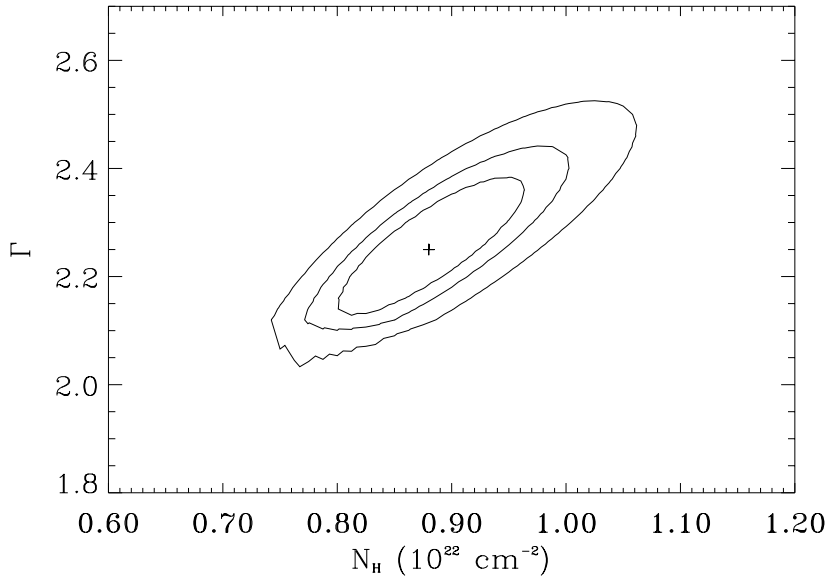

FIG. 3.2 – Densité de colonne d'hydrogène (N_H) et indice de la loi de puissance (Γ) du spectre X de XTE J1550−564 au repos (niveaux de confiance à 1, 2 et 3 σ) . Figure extraite de Corbel et al. (2006).

3.1.3 Origine de l'émission X des trous noirs au repos

La phase de repos des trous noirs stellaires serait donc bien différente de l'état dur. Dans Corbel et al. (2006), nous discutons de la nature de ce "ramollissement" du spectre X lors des phases de repos. Habituellement l'émission des trous noirs au repos est considérée comme une extension des propriétés de l'état dur (Corbel et al. 2000, 2003; Kong et al. 2000; Tomsick et al. 2004).

Les spectres X sont expliqués en invoquant la présence d'un flot d'accrétion dominé par l'advection de type ADAF. Celui-ci serait situé au centre d'un disque standard localisé à large distance du trou noir. Pour expliquer le spectre de XTE J1118+480, McClintock et al. (2003) échoue malgré tout avec un spectre purement ADAF. Ils ont besoin d'une réduction du taux d'accrétion à proximité de l'objet compact. Ils ne précisent pas ce que devient cette "masse manquante", qui pourrait prendre la forme d'un vent (Quataert & Narayan 1999). On retrouve alors des similarités avec le modèle ADIOS (Blandford & Begelman 1999).

De la même façon, Yuan et al. (2005) utilisent aussi un jet lié à un ADAF pour modéliser l'état de repos de XTE J1118+480 et Yuan & Cui (2005) prédisent un indice de photons de l'ordre de 2 comme nous l'avons observé pour plusieurs trous noirs (Corbel et al. 2006). Mais sachant que les ADAF sont convectivement instables à faible luminosité (on parlera alors de CDAF, Igumenshchev & Abramowicz 1999; Quataert & Gruzinov 2000), la structure du flot d'accrétion serait bien différente d'un ADAF. La convection réduisant considérablement le taux d'accrétion, là aussi des spectres X plus mous sont attendus au repos (Ball et al. 2001).

Pour les modèles standard "sphère+disque", un ramollissement des spectres X est aussi attendu à faible luminosité suite à la diminution de l'épaisseur optique de la couronne lorsque le taux d'accrétion diminue (e.g. Tomsick et al. 2004). Dans le cadre du modèle des "bouffées" magnétiques, un comportement similaire est attendu, car, à faible luminosité, la puissance provenant de l'accrétion est transférée dans les jets plutôt que de servir à chauffer les électrons.

Qu'en est-il du modèle de jet compact qui semble reproduire les caractéristiques observationnelles de l'état dur (Markoff et al. 2005) ? Habituellement, dans l'état dur, la distribution énergétique des électrons responsables de l'émission a une forme en loi de puissance d'indice 2.2–2.4. Si les électrons responsables de l'émission X au repos se trouvaient au dessus de l'énergie de coupure (ϵ_{cool} dans la figure 6.3), alors l'indice énergétique de la distribution d'électrons au dessus de ϵ_{cool} serait de 3.2–3.4, ce qui aurait pour conséquence de donner un indice de photons de –2.1 à –2.2 comme nous l'observons. Le refroidissement des particules pourrait être lié au fait qu'elles ne sont plus suffisamment ré-accélérées à faible luminosité. Alternativement, on peut aussi imaginer que le jet compact disparaisse lors du repos, pour laisser place à l'émission du "nozzle" (Corbel et al. 2006).

Pour conclure, tous ces modèles reproduisent le changement des spectres X lors des phases de repos, néanmoins on constate qu'ils semblent tous impliquer la présence de vent ou de jet pour expliquer les propriétés spectrales X.

Les observations multi-longueurs d'onde – essentiellement radio – pourraient-elle apporter un nouvel éclairage ? En effet, Corbel et al. (2003) et Gallo et al. (2003b) montrent que la corrélation observée entre les rayonnements radio et X dans l'état dur est maintenue jusqu'à l'état de repos pour GX 339−4 et GS 2023+338. De plus, le spectre radio de GS 2023+338 est plat (Gallo et al. 2005b) indiquant qu'un jet compact est toujours produit à 10^{-6} $L_{\rm Edd}$. De façon similaire, A 0620−00 est détecté au repos et ses propriétés sont en accords avec l'extension de la corrélation radio/X jusqu'à un niveau de luminosité de $10^{-8.5}$ $L_{\rm Edd}$ (Gallo et al. 2006). Cela confirme donc l'existence d'un couplage non linéaire entre les rayonnements X et radio de l'état dur jusqu'à la phase de repos. De plus, ces travaux de Gallo et al. (2006) sembleraient indiquer que la puissance cinétique du jet de A 0620−00 au repos représente une fraction non négligeable – $> 50\%$ – de la puissance d'accrétion du système. Les jets – ou vents – pourraient même constituer la voie préférée d'évacuation de l'énergie potentielle d'accrétion du système et ainsi cela favoriserait les modèles de jets ou ADIOS – au détriment des flots de type ADAF –. Ce scénario est aussi compatible avec le modèle proposé par Ferreira et al. (2006), où un disque externe standard englobe un disque interne faiblement radiatif à la base d'un jet MHD.

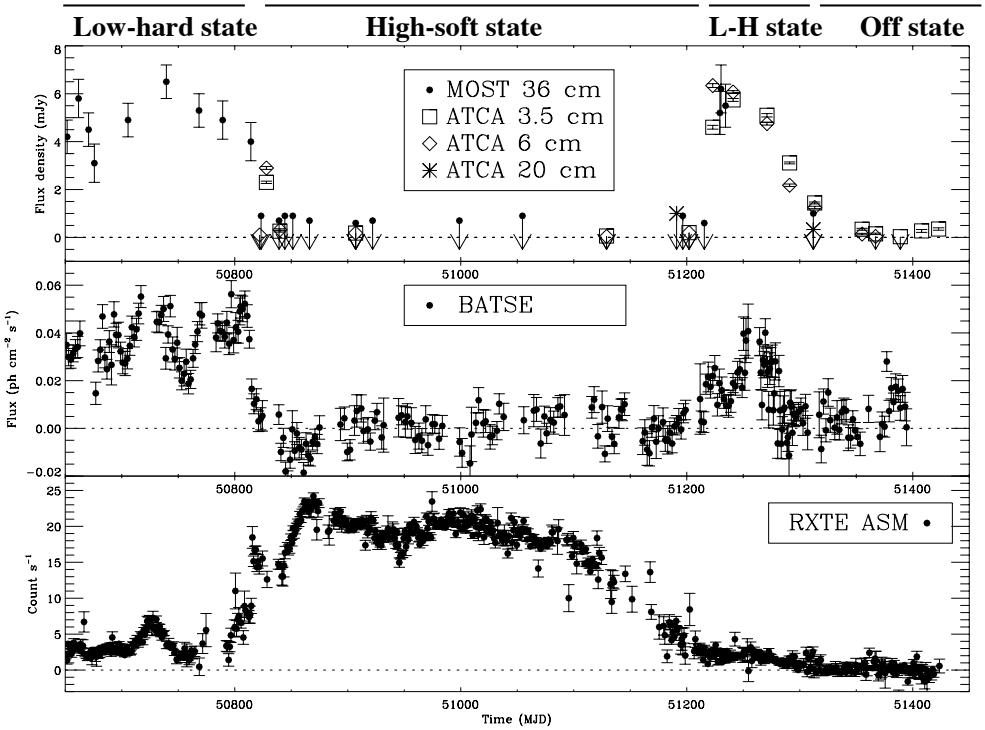

FIG. 3.3 – Suppression du jet compact de GX 339−4 lors de l'état thermique en 1998. Observations radio (haut), γ (milieu) et X (bas) de GX 339−4 lors du sursaut de 1998 correspondant aux transitions entre états dur $\Rightarrow$ mou $\Rightarrow$ dur $\Rightarrow$ repos. Figure extraite de Corbel et al. (2000).

3.2 Suppression du jet compact dans l'état thermique

Lors de l'introduction de ce manuscrit (chapitre 1), nous avions présenté les observations historiques (Figure 1.1) de Cyg X−1 en 1971 par Tananbaum et al. (1972) et Hjellming et al. (1975), qui auraient déjà pu être considérées comme précurseurs de certains aspects de nos travaux. En effet, il est observé, lors d'une transition de l'état thermique vers l'état dur, l'apparition progressive de la contrepartie radio de Cyg X−1, impliquant donc son absence lors de l'état thermique. De façon similaire, Zhang et al. (1997) observent partiellement un phénomène identique en 1997. Néanmoins, compte tenu des connaissances de l'époque, aucune caractéristique particulière ne se détachait quant aux propriétés de l'état thermique, dont le spectre d'émission à haute énergie est dominé par le disque d'accrétion. Dans les années 1970, la communauté des chercheurs "hautes énergies" s'attachaient à l'étude des propriétés X et γ de ces sources et non pas aux observations multi-longueurs d'onde. De nouveau, le trou noir GX 339−4 va apporter un éclairage important sur cet état spectral.

En effet jusqu'à la fin de l'année 1997, GX 339−4 était quasi persistant en X et demeurait dans l'état dur. Néanmoins, GX 339−4 entra dans une phase éruptive majeure en décembre 1997 et transita vers l'état thermique où il demeura pendant toute l'année 1998. Un retour vers l'état dur se produisit début 1999, puis vers une phase de repos de juin 1999 à avril 2002 (voir chapitre 2). Nous avons effectué un grand nombre d'observations radio de GX 339−4 avec ATCA et MOST de 1997 à 1999 et nous remarquons alors une suppression du rayonnement radio – d'un facteur 25 – lors de la transition de l'état dur vers l'état thermique (Fender et al.

1999a; Corbel et al. 2000). Aucune détection radio n'est effectuée pendant l'état thermique de 1998. De plus, l'émission radio réapparait lors du retour à l'état dur à la fin du sursaut (Figure 3.3).

Ces observations constituèrent la première contrainte observationnelle forte indiquant l'absence de rayonnement radio pendant l'état thermique. Aucun mécanisme physique (pertes adiabatiques, par effet synchrotron ou par effet Compton inverse) ne semble pouvoir expliquer ces observations, si ce n'est la suppression physique du jet compact dans l'état thermique (Fender et al. 1999a; Corbel et al. 2000).

Ces résultats, obtenus en 1999, ont été confirmés depuis par l'observation récurrente d'un certain nombre de trous noirs. On peut citer XTE J1550−564 pour lequel l'émission radio est réduite d'un facteur > 50 (Corbel et al. 2001b) – éventuellement ici il s'agirait plutôt d'un état intermédiaire – ou de nouveau Cyg X−1, (Tigelaar et al. 2004). De même, l'étude des corrélations radio/X semblent indiquer une suppression du rayonnement radio vers 10% de la luminosité d'Eddinton, niveau compatible avec l'état thermique (Gallo et al. 2003b). Il semblerait donc que les états thermiques ne soient donc jamais associés à un rayonnement radio fort, ce qui est cohérent avec les observations répétées de GRS 1915+105 (Klein-Wolt et al. 2002).

Meier (2001) et Meier et al. (2001) expliquent la suppression du jet compact suite à une transition d'un disque épais – type ADAF – vers un disque d'accrétion standard de type Shakura & Sunyaev (1973). En effet, la formation des jets compacts nécessiterait la présence de champs magnétiques poloïdaux relativement forts – du même ordre de grandeur que les champs magnétiques toroïdaux –. Selon ces auteurs, cette condition ne serait remplie qu'avec des disques épais – type ADAF –. Néanmoins, nous soulignons que cela est en désaccord avec les calculs de Ferreira (1997) et Casse & Ferreira (2000) qui montrent qu'un disque épais – type ADAF – ne peut pas soutenir des champs magnétiques forts et que, par conséquent la formation des jets compacts ne pourraient se faire qu'en présence d'un disque standard. Cela souligne, néanmoins, la forte incertitude au sujet du lien entre le disque et les jets.

3.3 Vision dynamique de la formation et de la destruction des jets compacts

La découverte des jets compacts résulte des observations radio fréquentes des trous noirs lors de leur réactivation, qui est habituellement repérée par *RXTE/ASM*. Ces sources étaient en général dans un état dur. Néanmoins, cet état dur est aussi observé vers la fin du sursaut après une plus ou moins longue période dans l'état thermique. Ces dernières années, nous avons donc porté un effort observationnel soutenu, afin de caractériser les propriétés à toute longueur d'onde de ces systèmes lors du retour vers l'état dur. Comment se manifeste la réapparition du jet compact sur l'ensemble de la distribution spectrale énergétique ? Tout d'abord parlons de la nature de la transition vers l'état dur, telle que décrite par les observations fréquentes réalisées par *RXTE*.

À partir des observations quotidiennes par *RXTE* de la décroissance de ces sources X, nous avons mis en évidence un certain nombre de nouvelles propriétés globales en analysant les spectres de puissance et les spectres en énergie de ces trous noirs (Tomsick et al. 2001; Kalemci 2002; Kalemci et al. 2003, 2004, 2005, 2006a). Se référer à ces publications pour les détails précis des observations. Les figures 3.4 et 3.5 illustrent ces propriétés dans le cas de H 1743−322 et de 4U 1543−47 tandis que la figure 3.6 résume les principaux points mentionnés ci-dessous.

En se basant sur l'analyse d'un certains nombres de sources – 4U 1543−47, H 1743−322 (Figures 3.4 et 3.5) et GX 339−4 ou GRO J1655−40 en cours de publication –, nous pouvons

résumer les résultats comme suit (voir la figure 3.6) :

- Une transition rapide – sur une échelle de temps d'un jour – entre l'état thermique et l'état intermédiaire dur. Cette transition est observée essentiellement à partir de la forme du spectre de puissance et de l'augmentation brusque de l'amplitude de la variabilité r.m.s.. Il ne semble pas y avoir de modification du spectre X à cette occasion, si ce n'est une augmentation du flux dans la composante en loi de puissance. Aucune coupure du spectre X à haute énergie n'est requise.
- Cinq à sept jours plus tard, l'indice de la loi de puissance du spectre de photons X commence à diminuer et en l'espace de dix jours, la source a fait la transition vers l'état dur. Durant cette période, la plupart des sources présentent une coupure du spectre X à haute énergie.

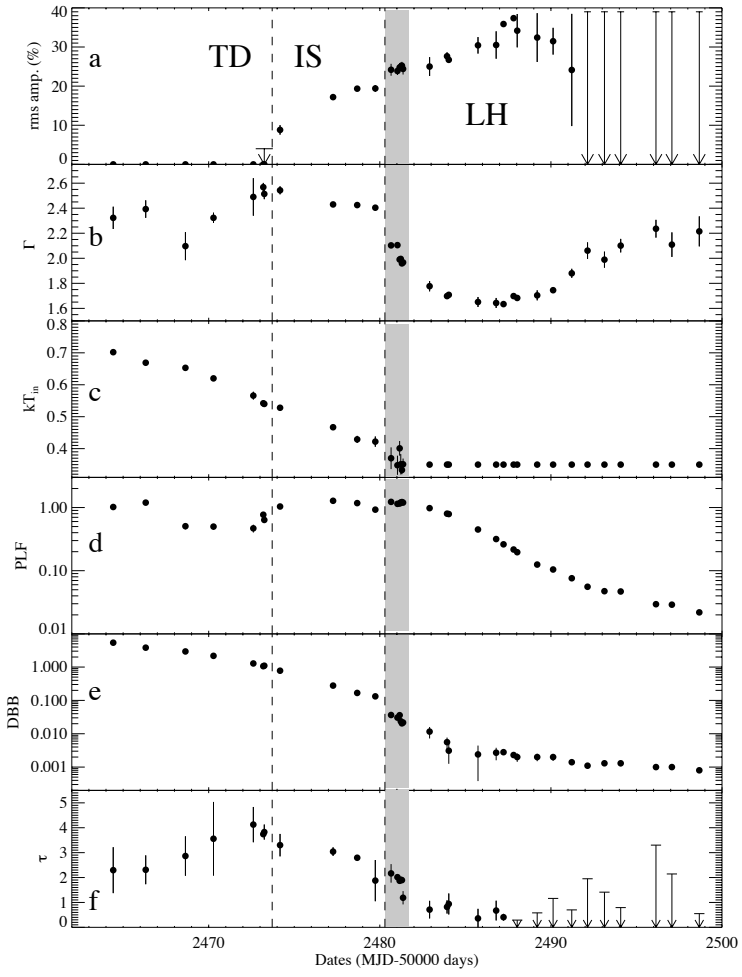

FIG. 3.4 – Décroissance du sursaut X de 4U 1543−47 en 2002 : (a) Amplitude r.m.s., (b) Indice de la loi de puissance, (c) Température interne du disque d'accrétion, (d) Contribution de la loi de puissance au flux 3–25 keV en 10^{-9} erg s^{-1} cm^{-2}, (e) Contribution du disque d'accrétion au flux 3–25 keV en 10^{-9} erg s^{-1} cm^{-2}, (f) Épaisseur optique du seuil d'absorption. Les lignes hachurées indiquent la période approximative des transitions d'état – TD : état thermique, IS : état intermédiaire, LH : état dur –. La zone grisée caractérise le moment où une coupure à haute énergie est nécessaire pour la loi de puissance. Figure extraite de Kalemci et al. (2005).

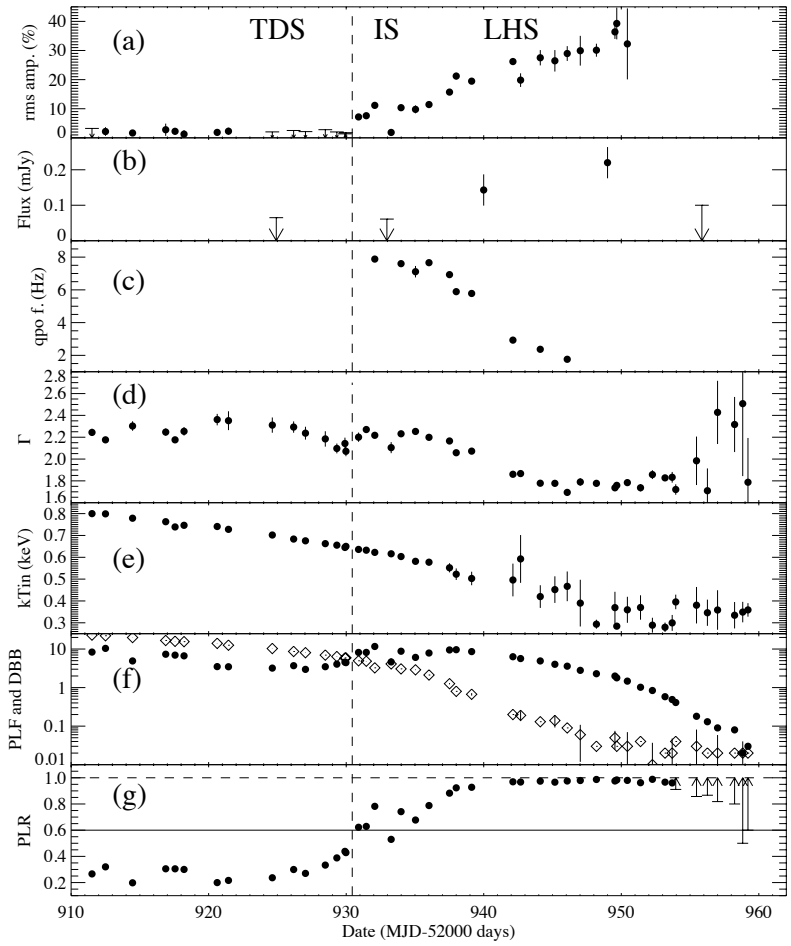

FIG. 3.5 – Décroissance du sursaut X de H 1743−322 en 2003 : (a) Amplitude r.m.s., (b) Flux radio, (c) Fréquence du QPO, (d) Indice de la loi de puissance, (e) Température interne du disque d'accrétion, (f) Contributions de la loi de puissance et du disque d'accrétion au flux 3–25 keV en 10^{-10} erg s^{-1} cm^{-2}, (g) Rapport du flux de la loi de puissance sur le flux total (PLR). Les lignes hachurées indiquent la période approximative des transitions d'état – TDS : état thermique, IS : état intermédiaire, LHS : état dur –. Figure extraite de Kalemci et al. (2006a).

- Au moment où le spectre X est le plus dur, nous assistons à la réapparition du jet compact en radio et/ou en infrarouge. La coupure du spectre X à haute énergie disparaît deux ou trois jours après l'apparition du jet compact. Il semblerait que la formation du jet compact nécessite un spectre X dominé par la loi de puissance – Rapport du flux de la loi de puissance sur le flux total, PLR > 0.99 – et un indice de photons < 1.7.
- Comme indiqué dans la section 3.1, une augmentation – en valeur absolue – de l'indice de photons X est observée pour certaines de ces sources après l'apparition du jet compact.
- Pendant toute la décroissance du sursaut, les fréquences caractéristiques – QPOs, Lorentziennes – du spectre de puissance diminuent de façon monotone.

Nous avons déjà discuté du ramollissement du spectre X – "softening" – vers lors du repos dans la section 3.1. Lors de la transition brusque de l'état thermique vers l'état intermédiaire, l'augmentation du rapport du flux de la loi de puissance sur le flux total est due à un accroissement du flux dans la loi de puissance et non pas à une décroissance de la contribution du

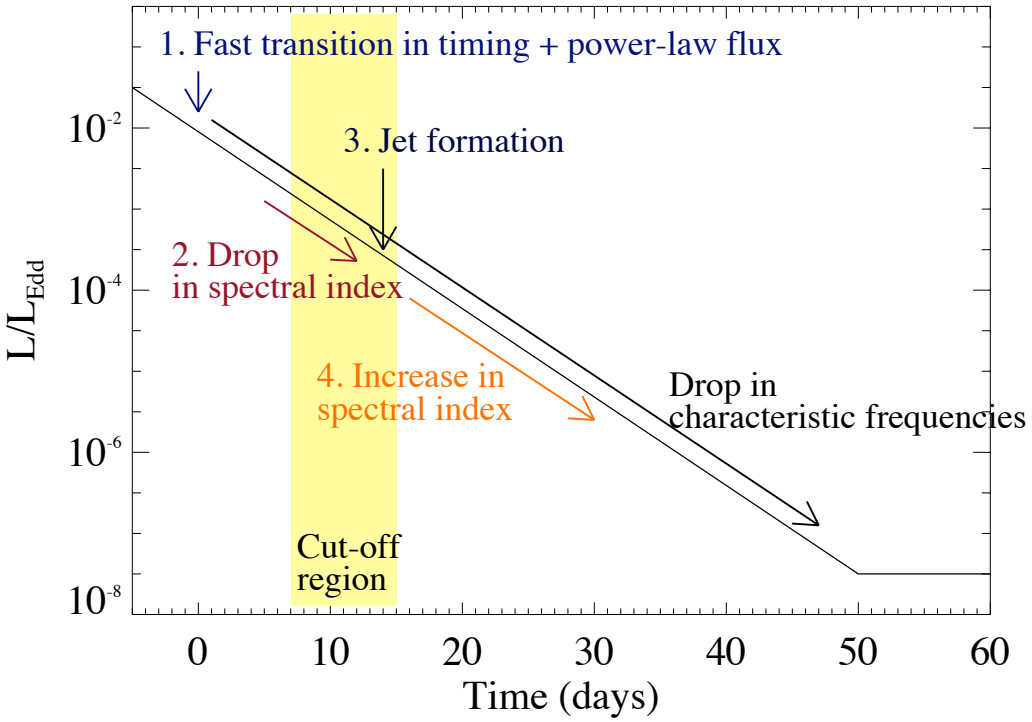

FIG. 3.6 – Propriétés X des trous noirs accrétants lors de la décroissance finale du sursaut. Le temps 0 correspond à la transition rapide entre l'état thermique et l'état intermédiaire dur. Les échelles de temps et de luminosité sont approximatives et varient de source à source. Figure extraite de Kalemci et al. (2006b).

disque d'accrétion. Après la transition vers l'état intermédiaire, le flux et la température interne du disque d'accrétion diminuent régulièrement et la source atteint finalement l'état dur. Le jet compact est détecté après la transition et non pendant l'état intermédiaire. L'évolution des fréquences caractéristiques du spectre de puissance et des paramètres du disque d'accrétion est compatible avec un disque s'éloignant du trou noir – voir par contre Miller et al. 2006b,a qui sembleraient indiquer le contraire –. L'évolution du rapport du flux de la loi de puissance sur le flux total et de l'indice de photons indique la présence d'un milieu comptonisant – soit une couronne indépendante ou la base du jet – devenant de plus en plus important.

En plus des propriétés X des trous noirs lors de la décroissance du sursaut, nos observations apportent aussi des informations complémentaires sur l'émission du jet compact (Figure 3.7). En effet, pour 4U 1543−47 nous observons que la contribution infrarouge du jet compact est maximale trois jours après la transition vers l'état dur. Lors de la croissance du rayonnement infrarouge, nous assistions déjà à la décroissance de l'émission X dure (Kalemci et al. 2005). On note aussi que la diminution de l'indice de photons X commence juste après le maximum de l'émission infrarouge. Ces courbes de lumière, tout comme l'évolution des indices spectraux – X et infrarouge-X –, sembleraient indiquer que la source majeure des X durs ne soit pas une émission synchrotron directe du jet compact, mais plutôt une émission de nature Compton inverse, probablement du Compton externe au début et ensuite du synchrotron self-compton au fur et à mesure que l'émission thermique du disque décroît (Kalemci et al. 2005).

Lors de la transition état thermique - état intermédiaire, l'indice de photons évolue peu, il

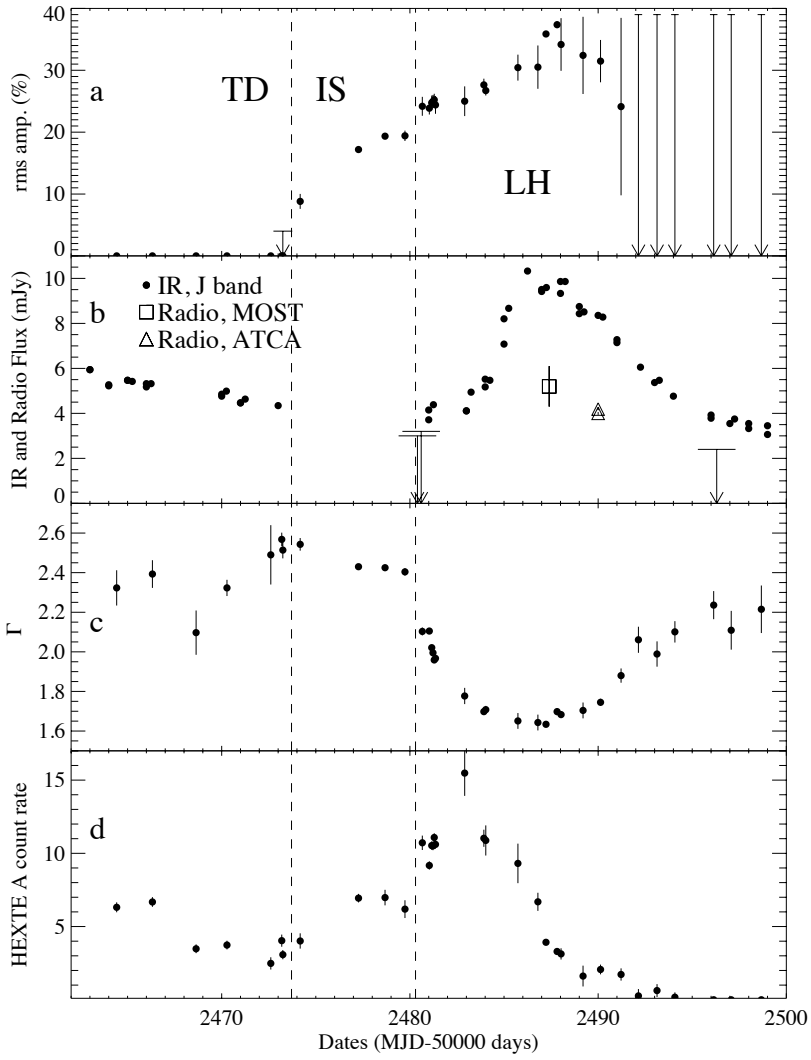

FIG. 3.7 – Évolution de (a) l'amplitude rms de la variabilité X, (b) la densité de flux infrarouge (bande J) et radio, (c) l'indice de photons et (d) le taux de comptage en X dur. Les lignes hachurées indiquent la période approximative des transitions d'état – TD : état thermique, IS : état intermédiaire, LH : état dur. Figure extraite de Kalemci et al. (2005).

s'agit d'une augmentation du flux de la loi de puissance accompagnée d'une brusque augmentation de la variabilité rms. Dans le cadre de modèle de comptonisation thermique – la couronne standard –, l'indice de photons dépend de deux paramètres : la température et l'épaisseur optique du milieu comptonisant (Sunyaev & Titarchuk 1980). Le flux de la loi de puissance, quant à lui, dépend de la source de photons X mous, de l'épaisseur optique et du taux de couverture du disque par la couronne. Une augmentation du flux du disque entraînerait aussi une augmentation de la contribution de la loi de puissance, par contre à cause des effets de refroidissement nous devrions assister aussi à une diminution de la température coronale. Nos observations n'indiquent pas un accroissement de la contribution du disque. Une expansion soudaine de la couronne – à épaisseur optique constante – pourrait expliquer le changement de la contribution de la loi de puissance.

On pourrait aussi imaginer l'émergence d'une autre source – non détectée par le PCA –

de photons mous à l'intérieur de la couronne qui pourrait aussi expliquer cette transition. Un candidat possible est la réapparition du jet compact, et son émission synchrotron associée, qui produirait un rayonnement – SSC – synchrotron self-compton (Markoff & Nowak 2004). Ainsi, la loi de puissance en X dur serait une combinaison de comptonisation thermique des photons synchrotron – source interne – et du disque – source interne et externe, dépendant de la géométrie de la couronne – ainsi que d'une émission non thermique synchrotron. Il est possible que la très forte variabilité rms est créée plus efficacement si la source est interne à la couronne. Comme les changements majeurs ne sont pas liés à la température ou à l'épaisseur optique de la couronne, cela expliquerait pourquoi l'indice de photons varie très peu pendant la transition de l'état thermique vers l'état intermédiaire.

Une autre possibilité pour augmenter le flux de la loi de puissance serait d'avoir deux mécanismes produisant des lois de puissances. Pendant la transition – TD vers IS –, la deuxième composante produisant la variabilité rms deviendrait active. Pendant l'état thermique, une comptonisation par mouvement d'ensemble – bulk-motion comptonisation – serait le mécanisme principal d'émission, tandis que la comptonisation thermique et/ou le rayonnement synchrotron prendrait le relais à partir de l'état intermédiaire

Néanmoins, la séparation de toute ces composantes d'émission, (comme dans Markoff et al. 2005) nécessiterait de faire des ajustements statistiques des distributions spectrales énergétiques de 4U 1543−47 ou des autres sources. C'est une démarche qui commence à se faire, mais il est clair que notre perception de ces changements spectraux risque d'évoluer dans les années futures.

3.4 Éjections relativistes : schéma d'unification

Pour le moment nous avons essentiellement discuté de la présence des jets compacts – de dimension de quelques dizaines d'unités astronomiques – uniquement associés à l'état dur. Il est néanmoins temps de présenter les phénomènes transitoires d'éjections massives de plasma, qui ont été à l'origine de la découverte et de la renommée des microquasars (Mirabel & Rodriguez 1994; Hjellming & Rupen 1995). Nous parlons, ici, de tailles caractéristiques des jets de l'ordre de dix milles unités astronomiques. Ces jets transitoires furent révélés par le mouvement apparemment superluminiques de bulles de plasma relativiste ayant un rayonnement de type synchrotron optiquement mince – et donc décroissant avec la fréquence, différent des jets compacts. Ils furent initialement découverts dans la source GRS 1915+105 en 1994 (Mirabel & Rodriguez 1994), puis rapidement aussi pour GRO J1655−40 (Hjellming & Rupen 1995). GRS 1915+105 est le siège d'éjections fréquentes (Fender et al. 1999b; Mirabel & Rodríguez 1999), alors que pour les autres sources transitoires (e.g. Hannikainen et al. 2001) on ne les observe en général qu'une seule fois – quand les télescopes radio sont dans la bonne configuration. Habituellement, ces phases d'activité sont observées lorsque la source X est très brillante – à priori associée à une accrétion élevée.

Comme indiqué précédemment, nous avons observé un grand nombre de sources X lors de leur phase d'activité. Certaines de ces observations ont permis de révéler des informations sur la période de ces éjections massives. En effet, on peut prendre l'exemple de GX 339−4 lors de son sursaut 2002-2003 (Gallo et al. 2004; Corbel et al. 2004). Une éjection massive a eu lieu directement pendant nos observations (Figure 3.8). Sur une période de 12h, nous avons vu (Figure 3.8) GX 339−4 passer d'un niveau moyen de $\sim$ 10 mJy avec un spectre plat à un niveau record – pour cette source – de plus de 50 mJy. Ce sursaut radio correspond à une éjection – non résolue – qui donnera naissance (voir chapitre 4) ultérieurement à un jet large (Gallo et al. 2004). Le moment précis de l'éjection est donc parfaitement déterminé.

En utilisant les données *RXTE/ASM* (Figure 3.9), nous montrons dans Corbel et al. (2004)

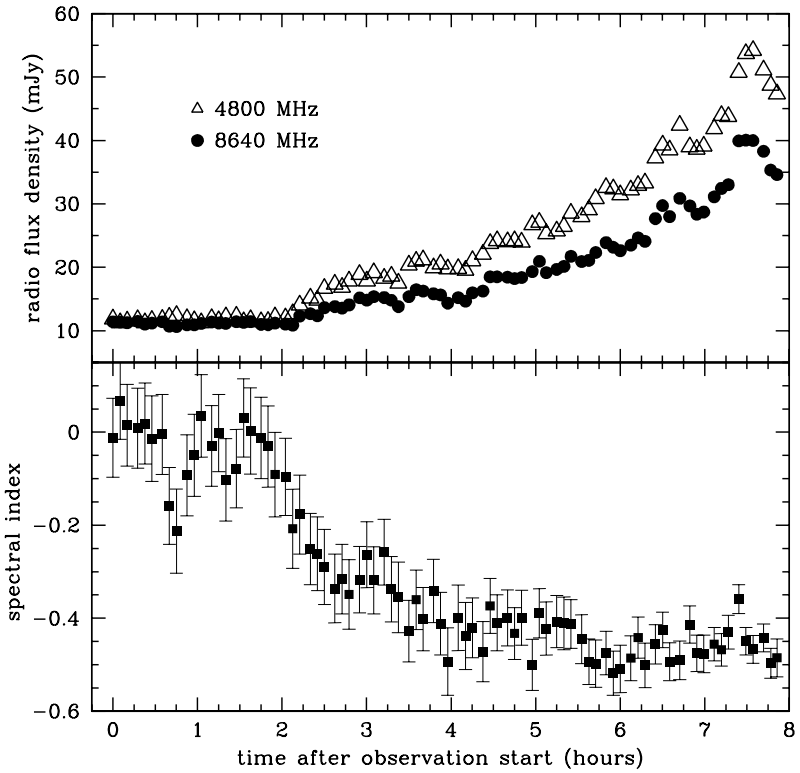

FIG. 3.8 – Sursaut radio de GX 339−4 en 2002 lors de la transition vers l'état intermédiaire mou. Haut : Courbe de lumière à 4.8 et 8.6 GHz, bas : évolution de l'indice spectral. Figure extraite de Gallo et al. (2004).

que l'éjection correspond au moment où l'indice de dureté atteint sa valeur la plus faible possible. La succession d'états spectraux s'est faite dans l'ordre suivant : état dur, état intermédiaire dur et état intermédiaire mou – quasi-équivalent au SPL de McClintock & Remillard 2006. La dureté du spectre X diminue le long de ces états – branche horizontale supérieure du HID. De plus, avant cette éjection transitoire, les caractéristiques de l'émission radio – spectre plat – implique que le jet compact persiste dans l'état intermédiaire dur (Corbel et al. 2004) et donc bien au delà de l'état dur comme supposé précédemment.

En corroborant ces résultats avec ceux d'autres sources – XTE J1650−500, XTE J1550−564 et XTE J1859+226 –, nous montrons que nous pouvons généraliser les résultats obtenus sur GX 339−4 (Corbel et al. 2004). Ces travaux – tout comme ceux de Fender et al. (2004b) – ont permis de proposer le schéma d'unification qui suit (Corbel et al. 2004).

Le jet compact existe et prend de la puissance au fur et à mesure que la source pénètre dans l'état dur. Ce jet compact persiste pendant l'état intermédiaire dur. Au moment où le disque d'accrétion atteindrait sa dernière orbite stable – correspondant au "ramollissement" maximal du spectre X et à une transition vers l'état intermédiaire mou, une éjection massive de plasma relativiste a lieu. Ensuite une fois dans cet état – SPL –, à chaque transition vers un état plus dur – et retour vers un état mou – correspondrait une éjection "mineure" de plasma relativiste. Il n'existerait pas de jet pendant l'état thermique et donc aucune émission radio ne serait détectée dans cet état – attention quand même au cas particulier où le plasma éjecté interagit avec le milieu interstellaire, Corbel et al. 2004. Le jet compact réapparaît une fois la source de retour dans l'état dur.

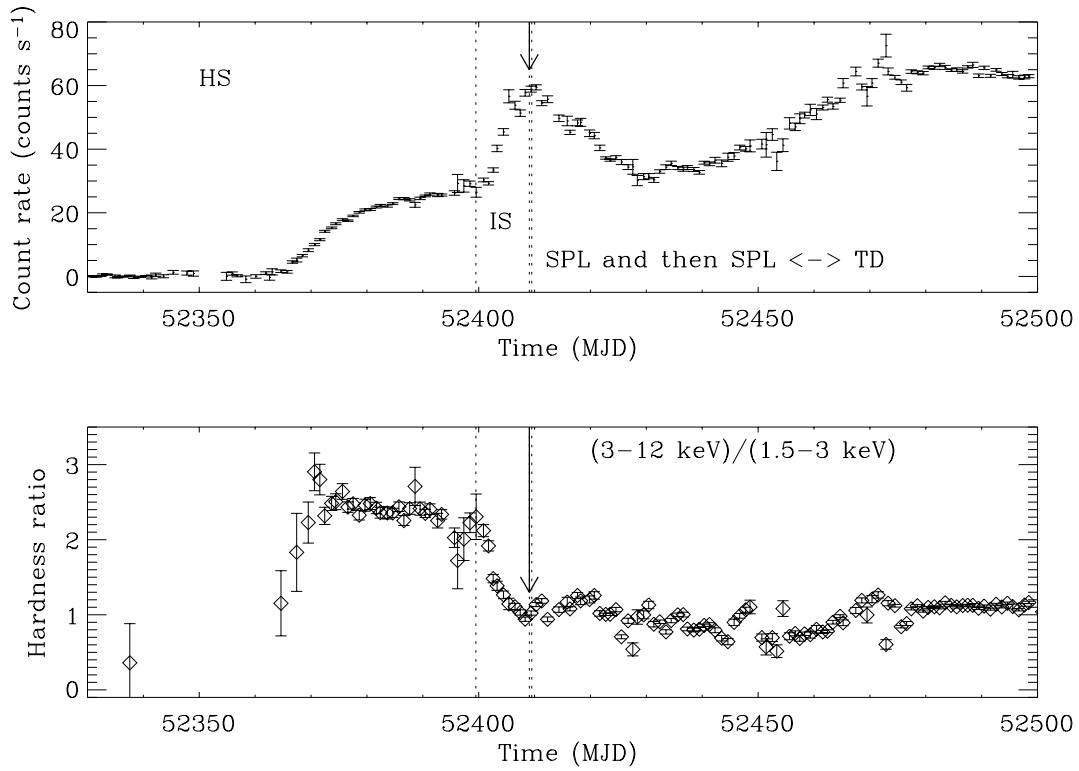

FIG. 3.9 – Courbe de lumière *RXTE/ASM* (haut) et indice de dureté de GX 339−4 pendant la phase initial de son sursaut X en 2002. La fléche représente la date précise de l'éjection massive de plasma représentée sur la figure 3.8. HS = état dur, IS = état intermédiaire dur, SPL = état intermédiaire mou et TD = état thermique. Figure extraite de Corbel et al. (2004).

Au delà de ce scénario généralisé, Fender et al. (2004b) explique de plus l'origine de l'éjection massive de la façon suivante. Ils proposent que les vitesses des jets transitoires soient plus rapides – facteur de Lorentz $\Gamma > 2$ – que pour les jets compacts – $\Gamma < 1.4$. Au fur et à mesure que le disque d'accrétion s'approcherait de l'objet compact – état intermédiaire dur – , le facteur de Lorentz du jet compact augmenterait. Il s'ensuivrait des chocs internes au niveau du jet compact qui seraient à l'origine du sursaut radio des jets transitoires – au moment de la transition vers l'état intermédiaire mou ou SPL, aussi appelé "jet line". Le jet compact étant ainsi détruit, le sursaut transitoire d'émission radio forte ne pourrait avoir lieu qu'une seule fois (Fender et al. 2004b). En effet, aucun sursaut radio n'a été observé à ce jour lors de transition état thermique – état intermédiaire. De plus, on notera que le passage – après l'état thermique – à l'état intermédiaire dur – la branche horizontale inférieure du HID entre les états thermique et dur – n'entraîne pas la formation du jet compact (voir section 3.3). Et si le jet compact est absent, il est logique de ne pas avoir une éjection massive de plasma – et donc en accord avec le scénario de chocs internes de Fender et al. 2004b – .

La présence du jet compact semblerait donc nécessaire pour observer des éjections de type superluminiques. Il est à noter que lors de leur réactivation X, la quasi-totalité des trous noirs accrétant effectuent les diverses transitions dans un ordre bien précis – mouvement dans le HID dans le sens des aiguilles d'une montre.

On notera une particularité de la source récurrente 4U 1630−47. En effet, son sursaut

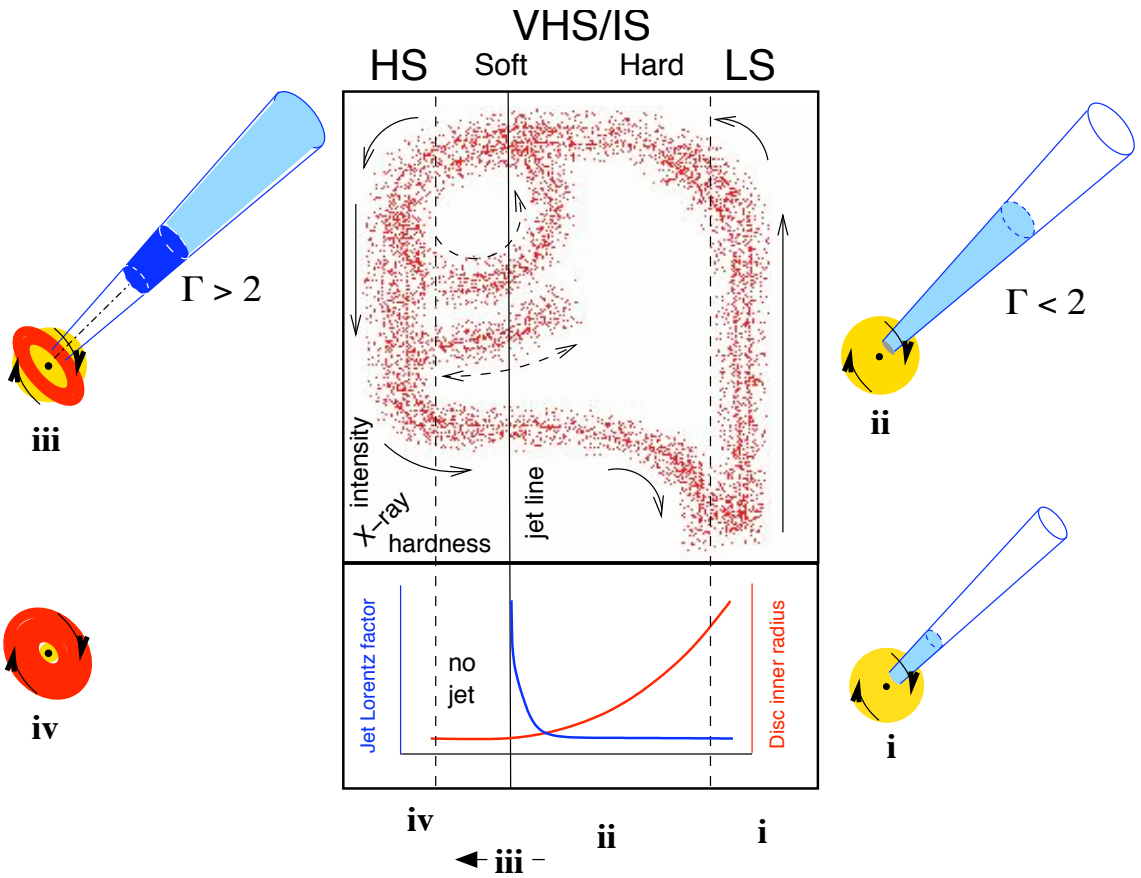

FIG. 3.10 – Schéma simplifié du couplage accrétion-éjection pour les trous noirs accrétants. Le graphe central représente le diagramme intensité–dureté X (HID) avec les initiales HS pour l'état thermique, HS pour l'état dur et VHS/IS pour l'état intermédiaire version molle – soft – ou dur – hard –. Le graphe du bas illustre les variations du facteur de Lorentz et du rayon interne du disque d'accrétion en fonction de la dureté du spectre X. Un jet compact à faible facteur de Lorentz est initialement produit – phases i et ii – pendant l'état dur. Lors de la transition vers l'état intermédiaire mou, l'augmentation du facteur de Lorentz entraînerait la création de chocs internes – phase iii – dans le jet compact qui serait à l'origine du sursaut radio observés à ce moment. Les schémas autour du graphe central représente la contribution relative de chaque composante émissive : le jet (en bleu), la couronne (jaune) et le disque d'accrétion (rouge). Figure extraite de Fender et al. (2004b).

de 1998 était similaire aux autres trous noirs, et il fut – pour la seule occasion – observé un phénomène d'éjection transitoire (Hjellming et al. 1999). Par contre, lors de son sursaut exceptionnellement long de 2002-2004, nous montrons que 4U 1630−47 a effectué son mouvement dans le HID dans le sens inverse – contrairement à 1998 – des aiguilles d'une montre (Tomsick et al. 2005; Tomsick 2006). Aucun état dur initial ne fut observé et à aucun moment de l'émission radio ne fut détectée (Tomsick et al. 2005). Ce qui semblerait indiquer que la formation du jet compact nécessiterait préalablement un certain niveau de dureté du spectre X et qu'en l'absence de celui-ci il ne serait pas possible d'observer une éjection transitoire – en accord toujours avec le scénario de Fender et al. 2004b. L'évolution du sursaut 2002-2004 de 4U 1630−47 semblerait donc mettre en évidence certaines subtilités qui échappent à notre compréhension au niveau de l'évolution des propriétés de ces sources – phénomènes

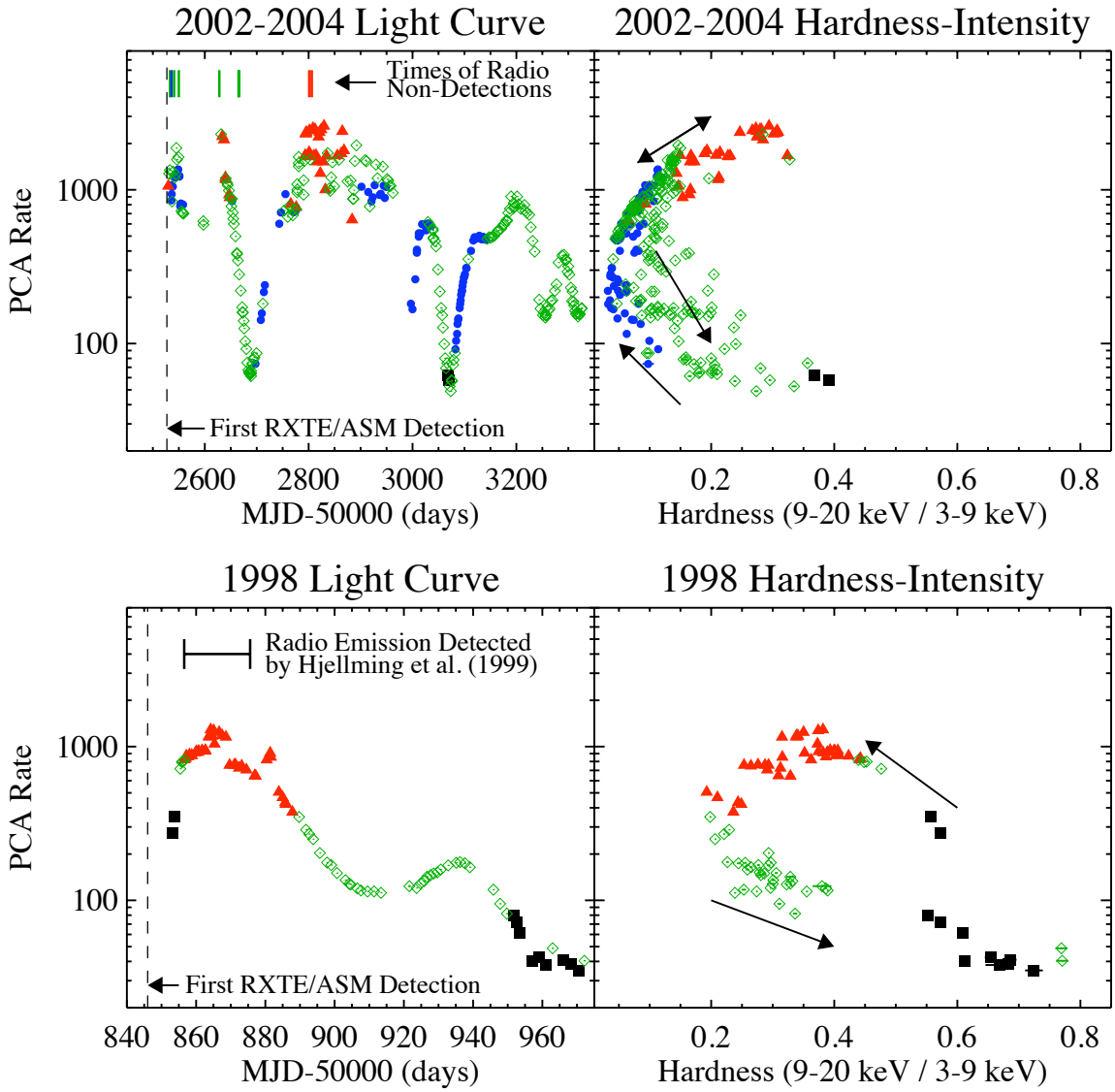

FIG. 3.11 – Propriétés X de 4U 1630−47 pendant les sursauts de 1998 (bas) et de 2002-04 (haut). Les courbes de lumière PCA sont représentées à gauche, tandis que les diagrammes intensité-dureté sont à droite. Les couleurs représentent les différents états spectraux X selon la terminologie de McClintock & Remillard (2006) : état dur (noir), état thermique (bleu), état SPL (rouge) et état intermédiaire (vert). Les flèches indiquent le sens d'évolution temporelle dans le HID lors des différents sursauts. Figure extraite de Tomsick (2006).

d'hystérésis, évolution des transitions, etc...–.

Il est intéressant de noter que Ferreira et al. (2006) propose un scénario théorique à priori en accord avec les grandes caractéristiques spectrales observationnelles de ces sources X. Les ingrédients de ce modèle sont un disque d'accrétion standard (de type Shakura & Sunyaev 1973) à l'intérieur duquel se trouve un disque faiblement radiatif –JED. Ce JED sert de réservoir de puissance alimentant la couronne standard et le jet compact, et à plus forte accrétion un jet ultra-relativiste suite à la création par le jet MHD de paires électron–positons. Il resterait à démontrer que ce modèle puisse reproduire la forme des spectres X et/ou la nature

des caractéristiques temporelles de ces objets. Néanmoins, l'approche physique unificatrice est intéressante. Pour poursuivre cette unification un peu plus loin, on peut noter que Körding et al. (2006c) propose pour les AGN des diagrammes similaires aux HID utilisés pour les trous noirs stellaires galactiques. Il s'ensuit que les diverses classes d'AGN semblent montrer des états d'accrétion variés similaires aux systèmes binaires, mais qu'en plus l'unification proposée puisse aussi leur être appliquée (Körding et al. 2006c).

3.5 Articles de recherche

3.5.1

Chandra Detections of Two Quiescent Black Hole X-Ray Transients.

Article publié dans :

Astrophys. J., 2003, 597, L133-L136

Tomsick, J. A., Corbel, S., Fender, R., Miller, J. M., Orosz, J. A., Rupen, M. P., Tzioumis, T., Wijnands, R., Kaaret, P.

THE ASTROPHYSICAL JOURNAL, 597:L133–L136, 2003 November 10

CHANDRA DETECTIONS OF TWO QUIESCENT BLACK HOLE X-RAY TRANSIENTS

JOHN A. TOMSICK,[1] STÉPHANE CORBEL,[2] ROB FENDER,[3] JON M. MILLER,[4,5] JEROME A. OROSZ,[6] MICHAEL P. RUPEN,[7] TASSO TZIOUMIS,[8] RUDY WIJNANDS,[9] AND PHILIP KAARET[4]
Received 2003 August 4; accepted 2003 September 26; published 2003 October 21

ABSTRACT

Using the *Chandra X-Ray Observatory*, we have detected the black hole transients V4641 Sgr and XTE J1859+226 in their low-luminosity quiescent states. The 0.3–8 keV luminosities are $(4.0^{+3.3}_{-2.4}) \times 10^{31}$ $(d/7 \text{ kpc})^2$ ergs s^{-1} and $(4.2^{+4.8}_{-2.2}) \times 10^{31}$ $(d/11 \text{ kpc})^2$ ergs s^{-1} for V4641 Sgr and XTE J1859+226, respectively. With the addition of these two systems, 14 out of the 15 transients with confirmed black holes (via compact object mass measurements) now have measured quiescent luminosities or sensitive upper limits. The only exception is GRS 1915+105, which has not been in quiescence since its discovery in 1992. The luminosities for V4641 Sgr and XTE J1859+226 are consistent with the median luminosity of 2×10^{31} ergs s^{-1} for the systems with previous detections. Our analysis suggests that the quiescent X-ray spectrum of V4641 Sgr is harder than for the other systems in this group, but because of the low statistical quality of the spectrum, it is not clear if V4641 Sgr is intrinsically hard or if the column density is higher than the interstellar value. Focusing on V4641 Sgr, we compare our results to theoretical models for X-ray emission from black holes in quiescence. Also, we obtain precise X-ray positions for V4641 Sgr and XTE J1859+226 via cross-correlation of the X-ray sources detected near our targets with IR sources in the Two Micron All Sky Survey catalog.

Subject headings: accretion, accretion disks — black hole physics — stars: individual (V4641 Sgr, XTE J1859+226) — stars: winds, outflows — X-rays: stars

1. INTRODUCTION

Previous measurements of black hole (BH) X-ray transients in quiescence show that the BH systems have X-ray luminosities ranging from 10^{30} to 10^{33} ergs s^{-1} (Garcia et al. 2001; Hameury et al. 2003). As in outburst, there is evidence for the presence of an accretion disk in quiescence (Orosz & Bailyn 1997; McClintock et al. 2003), but the accretion rate onto the BH itself is unclear, as is the nature of the accretion flow. Although there is currently no consensus on the origin of the quiescent X-ray emission, three emission sites are considered to be viable for at least some systems: the accretion disk, the putative outflow or jet, and the secondary star.

One picture for the quiescent accretion flow is that of an inner quasi-spherical and optically thin region surrounded by an optically thick disk as in the advection-dominated accretion flow (ADAF) model (Narayan, McClintock, & Yi 1996). This model explains the faintness of quiescent BHs as being due to advection of radiation across the BH event horizon (Garcia et al. 2001). However, it has been determined that ADAFs are convectively unstable for certain viscosity ranges, leading to convection-dominated accretion flows (CDAFs; Quataert & Gruzinov 2000). Such a model can explain the low BH luminosities without the need for advection across an event horizon. In addition, BH advection may not be necessary if outflows or jets transport the accretion energy out of the system (Blandford & Begelman 1999; Gliozzi, Bodo, & Ghisellini 1999; Fender, Gallo, & Jonker 2003). There is evidence for the presence of compact radio jets from BH systems at low X-ray luminosities (Fender 2001; Corbel et al. 2003), and these may persist in quiescence. Such jets may possibly contribute to the X-ray emission (Markoff, Falcke, & Fender 2001). Finally, Bildsten & Rutledge (2000) suggested the secondary as an X-ray emission site, but we note that this possibility has been ruled out for most systems (Kong et al. 2002b).

In this work, we describe results of observations of the BH transients V4641 Sgr and XTE J1859+226 in quiescence made using the *Chandra X-Ray Observatory* (Weisskopf et al. 2002). These systems both had major X-ray outbursts in 1999 (Wood et al. 1999; Smith, Levine, & Morgan 1999). While the XTE J1859+226 outburst was typical of BH transients, the behavior of V4641 Sgr was unusual, with a long period of low-level activity punctuated by a 12 crab flare lasting 1–2 days. From optical observations covering the 67.6 hr V4641 Sgr orbit and the (likely) 9.16 hr XTE J1859+226 orbit, the compact object masses are above 3 $M_\odot$, indicating that these systems contain BHs (Orosz et al. 2001; Filippenko & Chornock 2001). At the time of the outburst, V4641 Sgr exhibited a one-sided, rapidly evolving relativistic radio jet (Hjellming et al. 2000; Orosz et al. 2001), and there is evidence that XTE J1859+226 also produced a radio jet (Brocksopp et al. 2002). The main motivations of our *Chandra* observations are to study the BHs in quiescence and to search for large-scale X-ray jets such as those detected for XTE J1550−564 (Corbel et al. 2002) and 4U 1755−338 (Angelini & White 2003). Here, we report on the detection of the BHs in quiescence, and we will report on the X-ray jet search and the consequences of the nondetection of those jets in a future paper.

[1] Center for Astrophysics and Space Sciences, Code 0424, University of California at San Diego, La Jolla, CA 92093; jtomsick@ucsd.edu.
[2] Université Paris VII and Service d'Astrophysique, CEA Saclay, 91191 Gif sur Yvette, France.
[3] Astronomical Institute "Anton Pannekoek," University of Amsterdam and Center for High Energy Astrophysics, Kruislaan 403, NL-1098 SJ Amsterdam, Netherlands.
[4] Harvard-Smithsonian Center for Astrophysics, 60 Garden Street, Cambridge, MA 02138.
[5] National Science Foundation Astronomy and Astrophysics Fellow.
[6] Department of Astronomy, San Diego State University, San Diego, CA 92182.
[7] National Radio Astronomy Observatory, 1003 Lopezville Road, Soccoro, NM 87801.
[8] Australia Telescope National Facility, Commonwealth Scientific and Industrial Research Organization, P.O. Box 76, Epping, NSW 1710, Australia.
[9] School of Physics and Astronomy, University of St. Andrews, North Haugh, St. Andrews KY16 9SS, UK.

2. OBSERVATIONS

We obtained two *Chandra* observations of V4641 Sgr in 2002: a 4.3 ks observation on UT August 5 (observation 1a) and a 25.3 ks observation on UT October 21 (observation 1b). For both observations, we used the Advanced CCD Imaging Spectrometer (ACIS) in imaging mode, and the target was placed on one of the back-illuminated ACIS chips (S3). Observation 1a was carried out under Director's Discretionary Time and was prompted by X-ray, optical, and radio activity from the source during 2002 May and June (Markwardt & Swank 2002; Uemura et al. 2002; Rupen, Dhawan, & Mioduszewski 2002). Considering the possibility that the source might still be active in X-rays during observation 1a, we used a $\frac{1}{4}$ CCD subarray to mitigate photon pileup effects. We found that the source was not bright (Tomsick et al. 2002), and we used the full CCD for observation 1b. We also obtained a 24.8 ks *Chandra* observation of XTE J1859+226 on 2003 February 5 (observation 2) using ACIS in imaging mode. The last known X-ray activity from XTE J1859+226 was in 2000 (Tomsick & Heindl 2000). For all three observations, the background levels remain low throughout, allowing us to use the full exposure time. Very Large Array (VLA) radio observations occurred within 1 week of observations 1a and 1b and within 2 weeks of observation 2. V4641 Sgr and XTE J1859+226 showed no radio emission with rms noise levels near 0.1 mJy beam^{-1} at 4 and 6 cm.

3. SOURCE DETECTIONS AND 2MASS/*CHANDRA* CROSS-CORRELATION

We produced 0.3–8 keV ACIS images using the "level 2" event lists from the standard data processing. For the analysis described below, we used the *Chandra* Interactive Analysis of Observations (CIAO) version 2.3 software and Calibration Data Base version 2.21. To obtain the maximum sensitivity for source detection in the V4641 Sgr field, we combined the data for observations 1a and 1b. We restricted our search for sources to a 2 arcmin^2 region containing the position of V4641 Sgr. This region, which is shown in Figure 1, is fully covered by both observations giving a spatially uniform exposure time of 29.5 ks. We used the CIAO routine *wavdetect* with a detection threshold of 10^{-6} (Freeman et al. 2002) to search for sources in the combined image, leading to the detection of 12 sources with between 6 and 36 counts per source. A source with 9 counts (labeled 1 in Fig. 1) is detected at a position consistent with the V4641 Sgr radio position.

As the V4641 Sgr radio position is known to 0.″1 (Hjellming et al. 2000), it is worthwhile to obtain the best possible X-ray position in order to test whether *Chandra* source 1 is, in fact, V4641 Sgr. To register the image, we cross-correlated the *Chandra* source positions with the Two Micron All Sky Survey (2MASS) IR sources in the field. We determined that four of the 12 *Chandra* sources have 2MASS sources within the *Chandra* pointing uncertainty of 0.″6. For these four sources, the angular separations between the 2MASS and *Chandra* positions range from 0.″03 to 0.″25. Given the surface density of 2MASS sources (7×10^{-3} sources arcsec^{-2} down to $K_s \sim 14$), there is a 0.14% probability that a match with the largest separation is spurious. As source 1 (the V4641 Sgr candidate) is identified as one of the 2MASS sources (2MASS 18192163−2524258 with IR magnitudes $J = 12.532 \pm 0.029$, $H = 12.364 \pm 0.027$, and $K_s = 12.270 \pm 0.030$), we used the other three sources to register the image. For these three sources, the average 2MASS to *Chandra* differences in R.A. and decl. are $-0.″05 \pm 0.″13$ and $0.″10 \pm 0.″13$, respectively, where the uncertainties account for the *Chandra* statistical position error as well as the 0.″2 position uncertainties for 2MASS.[10] We performed the indicated shifts (0.″05 east and 0.″1 south) to complete the registration of the *Chandra* image to the 2MASS positions. The position of source 1 is R.A. = $18^h19^m21^s.641$, decl. = −25°24′25.″87 (equinox J2000.0, systematic uncertainty = 0.″13, statistical uncertainty = 0.″13). The best *Chandra* position is 0.″12 from the 2MASS position and 0.″06 from the radio position obtained from a VLA image obtained on 1999 September 17, for which Hjellming et al. (2000) interpreted the emission as coming from the BH rather than the extended jet. After registering the image, we find that all 9 ACIS counts are contained within 1″ of the radio position, while the expected number of background counts in a 1″ circle is 0.28. Thus, the Poisson probability that the detection is spurious is 2×10^{-11}.

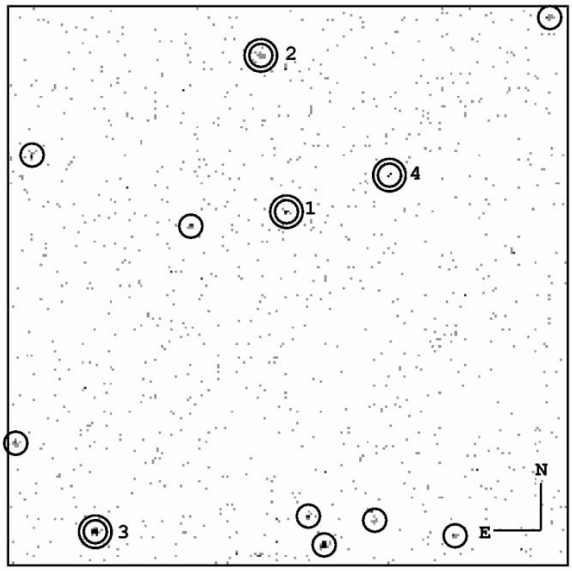

FIG. 1.—The 0.3–8 keV *Chandra* image of the V4641 Sgr field. The exposure time is 29.5 ks, and the image size is 1.968 arcmin^2. The north and east lines are 10″. The 12 detected sources are circled, and sources 1–4 (marked with two circles) have 2MASS identifications. Source 1 is V4641 Sgr.

We carried out a similar analysis for XTE J1859+226. We searched for *Chandra* sources in a 3 arcmin^2 region centered on the XTE J1859+226 radio position (Pooley & Hjellming 1999) using *wavdetect*. As shown in Figure 2, we detected five *Chandra* sources with between 6 (source 1) and 113 (source 2) counts. Source 1 is consistent with the XTE J1859+226 radio position. We cross-correlated the *Chandra* positions with the 2MASS positions and found that sources 3–5 have likely IR counterparts. For these three sources, the maximum separation between the *Chandra* and 2MASS positions is 0.″33, and there is a 0.07% probability that a match with this separation is spurious. Using the 2MASS identifications, we determined the position shifts required to register the *Chandra* image, and these are $0.″09 \pm 0.″12$ and $0.″25 \pm 0.″14$ in R.A. and decl., respectively. After shifting the *Chandra* image by 0.″09 west and 0.″25 south, the position of source 1 is R.A. = $18^h58^m41^s.485$, decl. = +22°39′29.″88 (equinox J2000.0, systematic uncer-

[10] See http://www.ipac.caltech.edu/2mass/releases/second/doc.

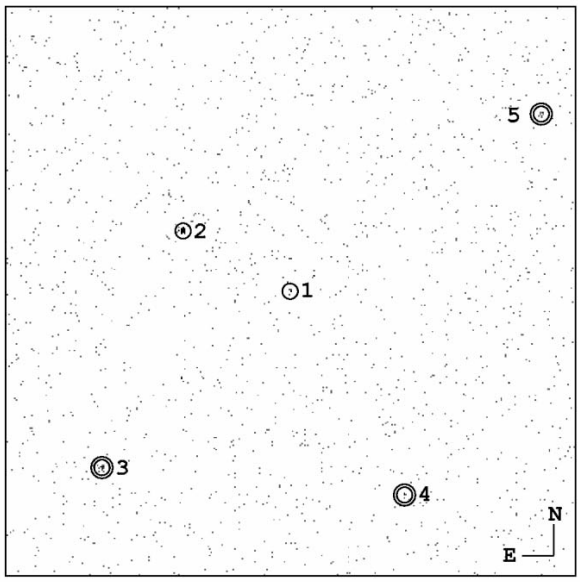

FIG. 2.—The 0.3–8 keV *Chandra* image of the XTE J1859+226 field. The exposure time is 24.8 ks, and the image size is 3 arcmin^2. The north and east lines are 10″. The five detected sources are circled, and the three sources marked with two circles have 2MASS identifications. Source 1 is XTE J1859+226.

tainty is 0.″14, statistical uncertainty is 0.″10 in R.A. and 0.″20 in decl.), which is consistent with the 0.″3 VLA radio position (Pooley & Hjellming 1999). All 6 ACIS counts are contained within 1″ of the radio position, while the expected number of background counts in a 1″ circle is 0.18. Thus, the Poisson probability that the detection is spurious is 4×10^{-8}.

4. QUIESCENT BLACK HOLE PROPERTIES

Although the number of counts detected for both V4641 Sgr and XTE J1859+226 is small, we extracted energy spectra (with 9 and 6 counts, respectively). For V4641 Sgr, the photon energies range from 0.87 to 7.0 keV, and the mean photon energy is 3.5 keV. For XTE J1859+226, the photon energies range from 0.75 to 2.7 keV, and the mean photon energy is 1.5 keV. We fitted the energy spectra with a power-law model with interstellar absorption. We used this model because this spectral shape is typically seen for quiescent BH systems (Garcia et al. 2001; Kong et al. 2002b), but we emphasize that we cannot rule out other spectral shapes. We fitted the spectra using Cash statistics (Cash 1979), and we fixed the column density ($N_{\rm H}$) to the H I values from Dickey & Lockman (1990): 2.3×10^{21} and 2.2×10^{21} cm^{-2} for V4641 Sgr and XTE J1859+226, respectively. We determined the errors on the parameters by producing and fitting 10,000 simulated spectra. We used the best-fit parameters from the fits to the actual data as input to the simulations. The power-law photon indices are $\Gamma = 0.2^{+0.9}_{-1.0}$ for V4641 Sgr and $\Gamma = 2.4^{+1.5}_{-1.3}$ for XTE J1859+226 (90% confidence errors).

The energy spectra of quiescent BHs are typically well described by an absorbed power law with a photon index of $\Gamma = 1.3$–2.3 (Kong et al. 2002b; Hameury et al. 2003; McClintock et al. 2003). Although a (much) better V4641 Sgr spectrum should be obtained to confirm its spectral shape, the best estimate of $\Gamma = 0.2$ is well outside the typical range, and even at the upper limit of $\Gamma = 1.1$, V4641 Sgr would be the hardest of the quiescent BHs. However, the uncertain column density is an important source of systematic error, and we refitted the V4641 Sgr spectrum leaving $N_{\rm H}$ as a free parameter. Our simulations indicate 90% confidence upper limits on Γ and $N_{\rm H}$ of 2.5 and 3.3×10^{22} cm^{-2}, respectively. Thus, we conclude that either the V4641 Sgr is intrinsically hard or $N_{\rm H}$ is higher than the interstellar value.

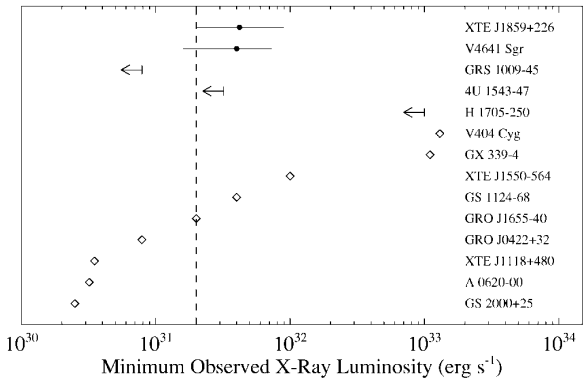

FIG. 3.—Quiescent BH X-ray luminosities. The points with error bars mark the 0.3–8 keV luminosities of XTE J1859+226 and V4641 Sgr from our *Chandra* measurements, assuming distances of 11 and 7 kpc for the two sources, respectively. The diamonds and upper limits are the minimum X-ray luminosities reported for the other 12 BH systems for which quiescent measurements have been possible (Garcia et al. 2001; Hameury et al. 2003; Sutaria et al. 2002; McClintock et al. 2003; Kong et al. 2002a; Kaaret et al. 2003; Corbel et al. 2003). The dashed line is the median luminosity for the previous detections.

We used the spectral fits to obtain flux and luminosity measurements for the sources. For V4641 Sgr, the absorbed 0.3–8 keV flux is $(6.5^{+5.7}_{-4.0}) \times 10^{-15}$ ergs cm^{-2} s^{-1} (90% confidence errors), and the unabsorbed luminosity in the same energy band is $(4.0^{+3.3}_{-2.4}) \times 10^{31}$ $(d/7\ {\rm kpc})^2$ ergs s^{-1}, where d is the source distance. Optical observations of V4641 Sgr in quiescence give a distance of 7.3 ± 1.2 kpc (J. A. Orosz et al. 2003, in preparation). For XTE J1859+226, the absorbed 0.3–8 keV flux is $(1.5^{+0.2}_{-0.7}) \times 10^{-15}$ ergs cm^{-2} s^{-1}, and the luminosity is $(4.2^{+4.8}_{-2.2}) \times 10^{31}$ $(d/11\ {\rm kpc})^2$ ergs s^{-1}. The distance estimate of 11 kpc comes from the X-ray and optical properties of the source (Zurita et al. 2002).

5. DISCUSSION

As confirmed BH systems (based on compact object mass measurements), V4641 Sgr and XTE J1859+226 represent important additions to the group of BHs that have previously been detected in X-rays in quiescence. Of the 15 confirmed (McClintock & Remillard 2003) transient BH systems, 14 now have quiescent X-ray detections or sensitive upper limits, and only GRS 1915+105, which has been in outburst since its discovery in 1992, does not. The X-ray luminosity ($L_{\rm X}$) measurements are summarized in Figure 3. We include a new low X-ray flux measurement for XTE J1550−564 (Kaaret et al. 2003), which has not been previously considered in the context of studies of quiescent BHs, and we assume a distance of 5.3 kpc (Orosz et al. 2002) to convert from flux to luminosity. We also include the lowest flux measurements for the recurrent transient GX 339−4

(Kong et al. 2002a; Corbel et al. 2003), and we assume a distance of 4 kpc. The median luminosity is 2×10^{31} ergs s^{-1} for the nine systems with previous detections, and the measured luminosities for V4641 Sgr and XTE J1859+226 are consistent with the median.

For quiescent BHs, the X-ray emission is thought to originate from the accretion flow, a jet, or the secondary star, and here we discuss how our results for V4641 Sgr may constrain theoretical models for X-ray production. The V4641 Sgr source distance (7 kpc) along with the proper motion of the one-sided radio jet seen in 1999 (0".36 per day) indicate that the angle between the jet axis and our line of sight is less than 8° (Orosz et al. 2001). Thus, if the X-ray emission originates in a fast-moving jet, one expects V4641 Sgr to be brighter because of relativistic beaming. However, the V4641 Sgr X-ray luminosity (assuming isotropic emission) is similar to the luminosities of the other BH systems, for which the jet axes either are not known or are known to be relatively far from our line of sight, indicating that the X-ray emission is not highly beamed and limiting the velocity of a putative X-ray emitting jet. For a continuous synchrotron X-ray jet (Markoff et al. 2001), it is unlikely that the bulk-motion Lorentz factor could be higher than ~1.5, as this would cause the source to be brighter than an unbeamed source by a factor of ~10 for a jet that is 8° from our line of sight (Mirabel & Rodríguez 1999). This calculation assumes a spectrum with a photon index of 1.5, which is in the range of values that can be produced within the Markoff et al. (2001) model. Assuming a photon index of 0.2 (our best estimate for V4641 Sgr) would lead to a somewhat higher limit on the Lorentz factor, but it is unclear whether such a hard spectrum could have a synchrotron origin. Also, we note that the Lorentz factor constraint is similar for models in which X-rays are produced in jets via inverse Comptonization (Georganopoulos, Aharonian, & Kirk 2002). The V4641 Sgr constraint on the Lorentz factor ($\lesssim$1.5) is consistent with recent results for BH systems in the canonical low-hard state (Gallo, Fender, & Pooley 2003; Maccarone 2003).

For accretion disk models such as the ADAF model, the quiescent X-ray luminosity depends mainly on mass accretion rate rather than on system orientation. Thus, the luminosities of V4641 Sgr and XTE J1859+226 would be expected to be similar to the other BH systems, as observed. If the hard V4641 Sgr X-ray spectrum is confirmed and is intrinsic to the source, it would suggest that another parameter besides accretion rate is important. Hard spectra can be produced by ADAFs (McClintock et al. 2003) and CDAFs (Quataert & Gruzinov 2000), but it is unclear why one system at close to the median luminosity would be intrinsically much harder than the others.

The spectral type of the V4641 Sgr secondary is B9 III (Orosz et al. 2001), making it the most luminous of the BH transients. In quiescence, the ratio of the X-ray to bolometric luminosity (L_X/L_{bol}) for V4641 Sgr is ~3×10^{-5} based on the X-ray luminosity reported here and the optical luminosity of the secondary (J. A. Orosz et al. 2003, in preparation). The V4641 Sgr ratio is higher than the average value but comparable to the highest values measured by *ROSAT* for late B-type stars (Berghoefer et al. 1997). While it is unlikely that the hard X-ray flux from V4641 Sgr comes from the secondary, we cannot rule out the possibility that the secondary makes some contribution to the soft X-ray flux below ~2 keV. The early-type secondary could also be important if it has a strong wind. The wind could collide with accretion disk material, leading to additional X-ray production, or it could cause extra X-ray absorption, explaining the hard V4641 Sgr spectrum.

We would like to thank H. Tananbaum for granting Director's Discretionary Time and the referee for very useful comments. The 2MASS is a joint project of the University of Massachusetts and IPAC/California Institute of Technology, funded by NASA and NSF. The National Radio Astronomy Observatory is a facility of the NSF operated under cooperative agreement by Associated Universities, Inc. J. A. T. acknowledges partial support from *Chandra* award number GO3-4040X. P. K. acknowledges partial support from NASA grant NAG5-7405 and *Chandra* award number GO3-4043X. J. M. M. thanks the NSF.

REFERENCES

Angelini, L., & White, N. E. 2003, ApJ, 586, L71
Berghoefer, T. W., Schmitt, J. H. M. M., Danner, R., & Cassinelli, J. P. 1997, A&A, 322, 167
Bildsten, L., & Rutledge, R. E. 2000, ApJ, 541, 908
Blandford, R. D., & Begelman, M. C. 1999, MNRAS, 303, L1
Brocksopp, C., et al. 2002, MNRAS, 331, 765
Cash, W. 1979, ApJ, 228, 939
Corbel, S., Fender, R. P., Tzioumis, A. K., Tomsick, J. A., Orosz, J. A., Miller, J. M., Wijnands, R., & Kaaret, P. 2002, Science, 298, 196
Corbel, S., Nowak, M. A., Fender, R. P., Tzioumis, A. K., & Markoff, S. 2003, A&A, 400, 1007
Dickey, J. M., & Lockman, F. J. 1990, ARA&A, 28, 215
Fender, R. P. 2001, MNRAS, 322, 31
Fender, R. P., Gallo, E., & Jonker, P. G. 2003, MNRAS, 343, L99
Filippenko, A. V., & Chornock, R. 2001, IAU Circ. 7644, 2
Freeman, P. E., Kashyap, V., Rosner, R., & Lamb, D. Q. 2002, ApJS, 138, 185
Gallo, E., Fender, R. P., & Pooley, G. G. 2003, MNRAS, 344, 60
Garcia, M. R., McClintock, J. E., Narayan, R., Callanan, P., Barret, D., & Murray, S. S. 2001, ApJ, 553, L47
Georganopoulos, M., Aharonian, F. A., & Kirk, J. G. 2002, A&A, 388, L25
Gliozzi, M., Bodo, G., & Ghisellini, G. 1999, MNRAS, 303, L37
Hameury, J.-M., Barret, D., Lasota, J.-P., McClintock, J. E., Menou, K., Motch, C., Olive, J.-F., & Webb, N. 2003, A&A, 399, 631
Hjellming, R. M., et al. 2000, ApJ, 544, 977
Kaaret, P., Corbel, S., Tomsick, J. A., Fender, R., Miller, J. M., Orosz, J. A., Tzioumis, A. K., & Wijnands, R. 2003, ApJ, 582, 945
Kong, A. K. H., Charles, P. A., Kuulkers, E., & Kitamoto, S. 2002a, MNRAS, 329, 588
Kong, A. K. H., McClintock, J. E., Garcia, M. R., Murray, S. S., & Barret, D. 2002b, ApJ, 570, 277
Maccarone, T. J. 2003, A&A, 409, 697
Markoff, S., Falcke, H., & Fender, R. 2001, A&A, 372, L25
Markwardt, C. B., & Swank, J. H. 2002, IAU Circ. 7906, 3
McClintock, J., Narayan, R., Garcia, M. R., Orosz, J. A., Remillard, R. A., & Murray, S. S. 2003, ApJ, 593, 435
McClintock, J., & Remillard, R. 2003, in Compact Stellar X-Ray Sources, ed. W. H. G. Lewin & M. van der Klis, in press (astro-ph/0306213)
Mirabel, I. F., & Rodríguez, L. F. 1999, ARA&A, 37, 409
Narayan, R., McClintock, J. E., & Yi, I. 1996, ApJ, 457, 821
Orosz, J. A., & Bailyn, C. D. 1997, ApJ, 477, 876
Orosz, J. A., et al. 2001, ApJ, 555, 489
———. 2002, ApJ, 568, 845
Pooley, G. G., & Hjellming, R. M. 1999, IAU Circ. 7278, 1
Quataert, E., & Gruzinov, A. 2000, ApJ, 539, 809
Rupen, M. P., Dhawan, V., & Mioduszewski, A. J. 2002, IAU Circ. 7928, 2
Smith, D. A., Levine, A. M., & Morgan, E. H. 1999, Astron. Telegram, 43, 1
Sutaria, F. K., et al. 2002, A&A, 391, 993
Tomsick, J. A., & Heindl, W. A. 2000, IAU Circ. 7456, 3
Tomsick, J. A., et al. 2002, Astron. Telegram, 105, 1
Uemura, M., et al. 2002, PASJ, 54, L79
Weisskopf, M. C., Brinkman, B., Canizares, C., Garmire, G., Murray, S., & Van Speybroeck, L. P. 2002, PASP, 114, 1
Wood, A., Smith, D. A., Marshall, F. E., & Swank, J. 1999, IAU Circ. 7274, 1
Zurita, C., et al. 2002, MNRAS, 334, 999

3.5.2

On the Origin of Black Hole X-Ray Emission in Quiescence : Chandra Observations of XTE J1550-564 and H1743-322.

Article publié dans :

Astrophys. J., 2006, 636, 971-978

Corbel, S., Tomsick, J. A., Kaaret, P.

The Astrophysical Journal, 636:971–978, 2006 January 10

ON THE ORIGIN OF BLACK HOLE X-RAY EMISSION IN QUIESCENCE: *CHANDRA* OBSERVATIONS OF XTE J1550−564 AND H1743−322

S. Corbel,[1] J. A. Tomsick,[2] and P. Kaaret[3]
Received 2005 July 25; accepted 2005 September 2

ABSTRACT

We report the results of observations of the black hole binaries XTE J1550−564 and H1743−322 in their quiescent state using the *Chandra X-Ray Observatory*. Both sources are detected at their faintest level of X-ray emission ever observed with a 0.5–10 keV unabsorbed luminosity of 2×10^{32} $(d/5\ \mathrm{kpc})^2$ ergs s^{-1} for XTE J1550−564 and 9×10^{31} $(d/8\ \mathrm{kpc})^2$ ergs s^{-1} for H1743−322. These luminosities are in the upper range compared to the faintest levels observed in other black hole systems, possibly related to residual accretion for these sources with frequent outbursts. For XTE J1550−564, the *Chandra* observations also constrain the X-ray spectrum, as a fit with an absorbed power-law model yields a photon index of 2.25 ± 0.08, clearly indicating a softening of the X-ray spectrum at lower luminosities compared to the standard hard state. Similar softening at low luminosity is seen for several black hole transients with orbital periods less than 60 hr. Most of the current models of accreting black holes are able to reproduce such softening in quiescence. In contrast, we find that systems with orbital periods longer than 60 hr appear to have hard spectra in quiescence, and their behavior may be consistent with hardening in quiescence.

Subject heading: accretion, accretion disks — black hole physics — stars: individual (H1743−322, XTE J1550−564) — X-rays: binaries

1. INTRODUCTION

X-ray novae (or soft X-ray transients) are compact binaries in which a neutron star or black hole (BH) primary accretes from a donor star via Roche lobe overflow. Most of these systems are usually in a quiescent state with an X-ray luminosity of 10^{30}–10^{33} ergs s^{-1}. However, they undergo episodic outbursts that last for months, with X-ray luminosities that can sometime reach or exceed the Eddington limit ($\sim 10^{39}$ ergs s^{-1} for a 10 $M_\odot$ BH). Despite the residual activity of these quiescent objects, very little is known about their emission properties at very low accretion rates (McClintock & Remillard 2006). With the sensitivity of current X-ray missions (in particular *Chandra* and *XMM-Newton*), it is now possible to study in more detail the physical processes that take place in this accretion regime.

XTE J1550−564 was discovered by the *Rossi X-Ray Timing Explorer* (*RXTE*) All Sky Monitor (ASM) on 1998 September 7 (Smith 1998). A brief and intense radio/X-ray flare, associated with a massive plasma ejection, was observed two weeks later (Hannikainen et al. 2001). Subsequent radio and X-ray observations revealed the formation of large-scale jets moving away from the XTE J1550−564 black hole over the course of several years (Corbel et al. 2002; Tomsick et al. 2003a; Kaaret et al. 2003). After its discovery outburst in 1998–1999, XTE J1550−564 had a second strong outburst in 2000, and fainter and shorter outbursts were detected in 2001, 2002, and 2003 (Fig. 1). Optical observations indicate that the compact object in XTE J1550−564 is likely a black hole of $10.5 \pm 1.0\ M_\odot$ at a distance of about 5.3 kpc (Orosz et al. 2002).

H1743−322 was discovered with *Ariel 5* in 1977 August (Kaluzienski & Holt 1977) and was precisely localized by the *High Energy Astronomical Observatory 1* (*HEAO-1*) a few weeks later (Doxsey et al. 1977). On the basis of its X-ray properties, H1743−322 has been classified as a black hole candidate (BHC; White & Marshall 1983). In 2003 March, the *International Gamma-Ray Astrophysics Laboratory* (*INTEGRAL*) detected new activity from IGR J17464−3213 (Revnivtsev et al. 2003) that was later found to correspond to H1743−322. During outburst, H1743−322 went through several X-ray states with properties typical of a BHC. The 2003 outburst ended late in 2003 November. H1743−322 was observed again in outburst from 2004 July (Swank 2004) to 2004 November. A bright radio flare (likely associated with a massive ejection event) was observed in 2003 by Rupen et al. (2003). The ejected plasma was later found to interact with the interstellar medium causing in situ particle acceleration and the formation of two large-scale, synchrotron-emitting radio and X-ray jets (Corbel et al. 2005), as in the XTE J1550−564 case.

In this paper, we present the results of 10 *Chandra* observations of the two black holes XTE J1550−564 and H1743−322 carried out during their quiescent state. These two sources have been detected at their faintest level ever observed. The high-quality *Chandra* spectra for XTE J1550−564 allow us to study and monitor the emission properties of this black hole at very low accretion rate. We then investigate the quiescent emission of black hole systems.

2. OBSERVATIONS AND DATA REDUCTION

Our *Chandra* program of monitoring X-ray jets from XTE J1550−564 and H1743−322 has also allowed us to study in great detail the black holes in these two systems. XTE J1550−564 was observed by *Chandra* on five occasions: 2002 March 11 (MJD 52344.8), 2002 June 19 (MJD 52444.5), 2002 September 24 (MJD 52542.0), 2003 January 27 (MJD 52667.3), and 2003 October 23 (MJD 52935.6). For completeness, we also include the results of two published *Chandra* observations on 2000 August 21 (MJD 51777.4) and 2000 September 11 (MJD 51798.3) that were performed during the decay of the 2000 outburst of

[1] AIM–Unité Mixte de Recherche CEA–CNRS, Université Paris VII, UMR 7158, CEA Saclay, Service d'Astrophysique, F-91191 Gif-sur-Yvette, France.
[2] Center for Astrophysics and Space Sciences, University of California at San Diego, MS 0424, La Jolla, CA 92093.
[3] Department of Physics and Astronomy, University of Iowa, Iowa City, IA 52242.

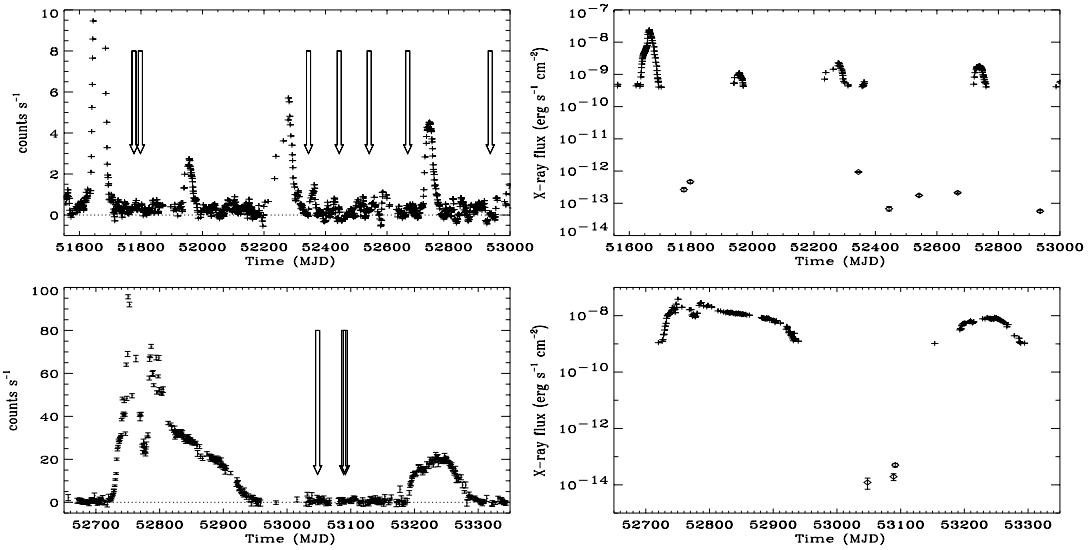

FIG. 1.—*RXTE* ASM 1.5–12 keV light curve of XTE J1550−564 (*top left*) and H 1743−322 (*bottom left*) covering the period of our *Chandra* observations. For the light curve of XTE J1550−564, the points represent 5 day averages, highlighting the weaker outbursts observed in 2001, 2002, and 2003 (*y*-axis also truncated at 10 counts s^{-1} for that purpose, the major outburst in 1998–1999 is also not shown), whereas we plot daily averages for H1743−322. The arrows mark the time of the *Chandra* observations that have all been conducted while the black holes were in (or close to) quiescence. In the panels on the right, the ASM 1.5–12 keV light curves are expressed directly (75 ASM counts s^{-1} = 1 crab = 3.0×10^{-8} ergs s^{-1} cm^{-2}) in flux units in order to allow a direct comparison with the *Chandra* 0.5–10 keV unabsorbed flux measurements (*diamonds*). The apparent ASM detection of XTE J1550−564 around MJD 52360 is likely an artifact due to the location of the source close to the solar exclusion zone.

XTE J1550−564 (Tomsick et al. 2001). The *Chandra* observations of H1743−322 were carried out on three occasions: 2004 February 12 (MJD 53048), March 24 (MJD 53089), and March 27 (MJD 53092). Figure 1 shows the *RXTE* ASM 1.5–12 keV light curves of XTE J1550−564 and H1743−322, and the arrows indicate the dates of the *Chandra* observations. This illustrates that all our observations were conducted a few months (or even up to a year for XTE J1550−564) before or after a period of significant X-ray activity (outburst). This allows us to monitor the emission properties of XTE J1550−564 and H1743−322 during their quiescent phases.

For all *Chandra* observations, we used the Advanced CCD Imaging Spectrometer spectroscopic array (ACIS-S; Bautz et al. 1998) in imaging mode, with the target placed on one of the back-illuminated ACIS Chips (S3). For the first observation of XTE J1550−564 in 2002 and the first observation of H1743−322, only the S3 chip was read out and a 1/2 subarray mode was used to limit pileup. For the later observations, the sources were known to be at lower flux, and the full ACIS-S imaging mode array was used.

We produced 0.3–8 keV ACIS images using the "level 2" event lists from the standard data processing using the *Chandra* Interactive Analysis of Observations (CIAO) software package. We constructed light curves with all valid events on the S3 chips to search for times of high background. Periods with background flares were removed using the standard CIAO script `analyse_ltcrv.sl`. We searched for X-ray sources in each 0.3–8 keV image using `wavdetect` (Freeman et al. 2002), the wavelet-based source detection routine in CIAO. For all *Chandra* observations, an X-ray source is found at the location of the black hole. With an absolute astrometric precision of 0.″6 (90% confidence level), the *Chandra* locations are consistent with the positions reported at other wavelengths (see also Corbel et al. 2005 for H1743−322). As the focus of this paper is the spectra of the two black holes in quiescence, we refer the reader to the studies of the X-ray jets presented in Corbel et al. (2002, 2005), Tomsick et al. (2003a), and Kaaret et al. (2003), as well as the Tomsick et al. (2001) black hole study for details of the *Chandra* data reduction.

3. SPECTRAL PROPERTIES OF XTE J1550−564 AND H1743−322 IN QUIESCENCE

We extracted energy spectra in the 0.3–8 keV energy range for the black holes in all *Chandra* observations using CIAO tools, and we fitted these spectra using XSPEC. We used a circular source extraction region with radii of 1.″4 and 4″ for H1743−322 and XTE J1550−564, respectively. We extracted background spectra from annuli with inner radii of 9″and 6″and outer radii of 19″and 16″ for H1743−322 and XTE J1550−564, respectively. These regions were centered on the black hole positions as given by `wavdetect`. The source aperture size is adapted to enclose most of the source counts. Background regions are adapted to cover a sufficiently large empty region. Due to the low numbers of source counts for H1743−322 (52 counts or less), we used the W statistic for fitting (Wachter et al. 1979; J. Arnaud 2006, in preparation) the unbinned spectra. This is adapted from the Cash statistic (Cash 1979) and is valid for background-subtracted spectra. For XTE J1550−564, which is brighter than H1743−322, we rebinned the spectra in order to have enough counts in each bin to be able to use the χ^2 statistic (with the exception of the *Chandra* observations on MJD 51777, 51798, and 52444, for which we used the W statistic due to the low number of counts).

These spectra are adequately fitted with a power-law model including interstellar absorption. We used this model because this spectral shape is typically seen for black holes in quiescence (Garcia et al. 2001; Kong et al. 2002), but we emphasize that we

TABLE 1

Chandra Observations of XTE J1550−564 and H1743−322: Best-Fit Spectral Parameters for a Power-Law Model

Source (Date)	Exposure (s)	Number of Counts[a]	N_H (10^{22} cm^{-2})	Photon Index	χ^2_ν/dof	Cash Monte Carlo Probability[b]	$F_{0.5-10\,keV}$[c] (10^{-14} ergs s^{-1} cm^{-2})
			XTE J1550−564				
MJD 51777.4	4985	71	0.9 (fixed)	2.6 ± 0.4	...	0.57	26.6 ± 3.5
MJD 51798.3	4572	111	0.9 (fixed)	$2.3^{+0.5}_{-0.2}$	...	0.57	46.7 ± 4.7
MJD 52344.8	26118	1206	$0.86^{+0.19}_{-0.11}$	$2.20^{+0.25}_{-0.18}$	32.8/30	...	
			0.9 (fixed)	2.25 ± 0.10	32.8/31	...	93.7 ± 2.8
MJD 52444.5	18025	58	0.9 (fixed)	$2.8^{+0.5}_{-0.9}$	...	0.55	6.8 ± 1.0
MJD 52542.0	24442	223	$0.90^{+0.53}_{-0.23}$	$2.2^{+0.7}_{-0.5}$	16.1/19	...	
			0.9 (fixed)	$2.23^{+0.25}_{-0.24}$	16.1/20	...	17.6 ± 1.2
MJD 52667.3	23683	254	$0.90^{+0.47}_{-0.22}$	$2.2^{+0.6}_{-0.4}$	13.9/19	...	
			0.9 (fixed)	$2.19^{+0.23}_{-0.21}$	13.9/20	...	21.3 ± 1.3
MJD 52935.6	47835	145	$0.69^{+0.47}_{-0.22}$	$2.2^{+0.7}_{-0.5}$	17.3/19	...	
			0.9 (fixed)	$2.5^{+0.4}_{-0.3}$	18.5/20	...	5.7 ± 0.5
Combined			$0.88^{+0.12}_{-0.09}$	$2.25^{+0.09}_{-0.13}$	137/167	...	
			0.9 (fixed)	2.25 ± 0.08	137/168	...	
			H1743−322				
MJD 53048.0	17796	6	2.3 (fixed)	$1.3^{+2.1}_{-1.7}$	...	0.33	
			2.3 (fixed)	2.0 (fixed)	...	0.48	12.2 ± 5.2
MJD 53088.9	28363	16	2.3 (fixed)	$1.6^{+1.0}_{-1.3}$	...	0.38	
			2.3 (fixed)	2.0 (fixed)	...	0.52	19.5 ± 5.3
MJD 53091.5	40037	52	2.3 (fixed)	2.2 ± 0.6	...	0.64	
			2.3 (fixed)	2.0 (fixed)	...	0.62	50.3 ± 7.3
Combined			2.3 (fixed)	1.96 ± 0.46	...	0.62	

Note.—All quoted uncertainties are 90% confidence ($\Delta\chi^2 = 2.7$ for one parameter or $\Delta\chi^2 = 4.6$ for two parameters).

[a] Number of total count within the source region in the 0.3–8 keV energy band

[b] XSPEC Monte Carlo simulations of 10,000 spectra based on the fitted model. We list the fraction of these simulated spectra that has a Cash statistic value less than the original data (for good fit, this number should be around 0.50).

[c] Unabsorbed X-ray flux in the 0.5–10 keV energy band.

cannot statistically rule out other spectral shapes. However, bremsstrahlung models provide unphysical temperatures as already mentioned in Kong et al. (2002). For H1743−322, we fixed the equivalent hydrogen absorption column density, N_H, to the constant value (2.3×10^{22} cm^{-2}) measured in *Chandra* observations of H1743−322 during its 2003 outburst (Miller et al. 2005). For XTE J1550−564, we left N_H as a free parameter in our fit. As the values obtained (Table 1) are consistent with results from previous X-ray outbursts (9×10^{21} cm^{-2}; Tomsick et al. 2001), we also fixed the column density of XTE J1550−564 to this value. This column density is inconsistent with the value inferred from the interstellar absorption lines (Sánchez-Fernández et al. 1999) but agrees with the hydrogen column density deduced from X-ray spectra of XTE J1550−564 or its associated X-ray jets (Tomsick et al. 2001, 2003a; Kaaret et al. 2003) and also with the Galactic column density along the line of sight (Jain et al. 1999). The difference when compared to the optical measurement of Sánchez-Fernández et al. (1999) may be explained in various ways. One possibility is that the X-ray absorption column density may be intrinsically higher than the optically inferred value due to additional local material covering the X-ray source. Another possibility is that the absorption column density deduced from the interstellar absorption lines are artificially lower (due, e.g., to saturation; Hynes et al. 2004). We believe that the latter is more likely, as XTE J1550−564 and its X-ray jets (which are separated by up to 30″) have similar column densities. In addition, it is interesting to point out the absence of variation of the hydrogen column density between outburst and quiescence.

For H1743−322, the best-fit photon indices are $1.3^{+2.1}_{-1.7}$, $1.6^{+1.0}_{-1.3}$, and 2.2 ± 0.6 for the observations of MJD 53048, 53089, and 53091, respectively. Refitting these three data sets simultaneously (allowing the normalization to vary) leads to a photon index of 1.96 ± 0.46 (with 90% confidence errors). As there are more frequent observations of XTE J1550−564, its X-ray spectrum is better constrained. The fit results of the individual observations are reported in Table 1. To provide the best constraint on the spectral parameters, we simultaneously fit all seven data sets simultaneously (again allowing the normalization to vary). Leaving the hydrogen column density as a free parameter leads to $N_H = (8.8 \pm 1.0) \times 10^{21}$ cm^{-2}, which is consistent with previous estimates. With N_H frozen to 9×10^{21} cm^{-2} (Tomsick et al. 2001), we obtain the best constraint on the photon index for XTE J1550−564 in quiescence, $\Gamma = 2.25 \pm 0.08$ (with 90% confidence errors). Figure 2 shows the 68%, 90%, and 99% error contours allowing two parameters (N_H and Γ) to vary. The results indicate that these parameters are very well constrained by our observations.

The photon indices in all *Chandra* observations of XTE J1550−564 (Fig. 3) are consistent with the value obtained by fitting the spectrum from the observation with the brightest flux (on MJD 52345) alone. This indicates that the X-ray spectra of XTE J1550−564 are consistent with the same spectral shape for all the observations, even though the flux varies by a factor of at least 16.

The fact that the X-ray flux varies between the observations indicates that accretion onto the black hole has not stopped in quiescence. We use the *Chandra* observations of XTE J1550−564 on MJD 52344 to construct a light curve of XTE J1550−564 with a time resolution of 1 ks (Fig. 4). A fit with a constant level leads to a χ^2 of 74 for 27 degrees of freedom, clearly indicating

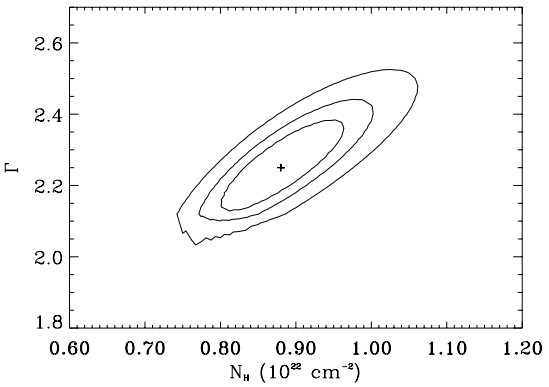

FIG. 2.—Error contours for the hydrogen column density (N_H) and the power-law index (Γ) derived from the combined *Chandra* spectrum of XTE J1550−564. The cross marks the location of the best-fit value, and 68% ($\Delta\chi^2 = 2.30$), 90% ($\Delta\chi^2 = 4.61$), and 99% ($\Delta\chi^2 = 9.21$) confidence contours are shown.

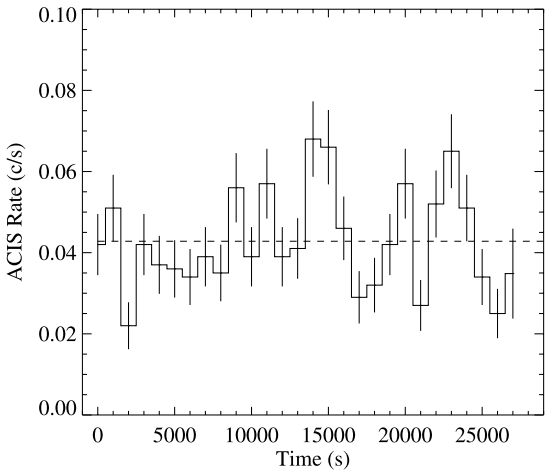

FIG. 4.— *Chandra* ACIS-S light curve of XTE J1550−564 on MJD 52344 in the 0.3−8 keV band with a time resolution of 1 ks. The dashed line illustrates the fit with a constant level.

that there is also significant X-ray variability on short (∼kilosecond) timescale.

The unabsorbed 0.5−10 keV fluxes for H1743−322 and XTE J1550−564 are reported in Table 1. For H1743−322, we fixed the power-law photon index to a value of 2.0, whereas for XTE J1550−564, the photon index was left at its fitted value. For both sources, the column densities were fixed as indicated previously. The quoted errors are based on the numbers of source and background counts and Poisson statistics.

4. DISCUSSION

4.1. *X-Ray Luminosity in Quiescence*

These *Chandra* observations represent the detection of XTE J1550−564 and H1743−322 at their faintest level of X-ray emission. The unabsorbed 0.5–10 keV luminosity of XTE J1550−564 is 1.9×10^{32} ergs s^{-1} (for a distance of 5.3 kpc; Orosz et al. 2002) and 9.3×10^{31} ergs s^{-1} for H1743−322 (at a distance of 8 kpc). For a 10 $M_\odot$ black hole, these values correspond to luminosities of $1.5 \times 10^{-7} L_{\rm Edd}$ (for XTE J1550−564) and $7.2 \times 10^{-8} L_{\rm Edd}$ (for H1743−322). We note that the mass of the compact object in H1743−322 is unknown, as well as its distance. However, the kinematic study of the large-scale jets of H1743−322, as well as its location toward the Galactic bulge, are consistent with a distance to H1743−322 of 8 kpc (Corbel et al. 2005).

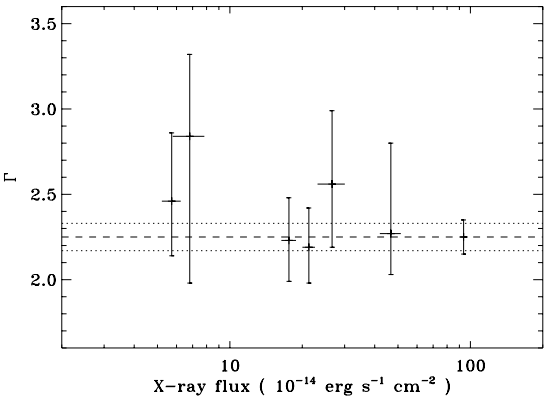

FIG. 3.—Evolution of the power-law photon index (Γ) vs. the unabsorbed 0.5−10 keV flux for all *Chandra* observations of XTE J1550−564 in quiescence. The line indicates the best-fit value for Γ. All quoted errors are at the 90% confidence level.

These quiescent luminosity levels are in the upper range compared to the faintest detected levels of other black holes (Garcia et al. 2001; Kong et al. 2002; Sutaria et al. 2002; Hameury et al. 2003; Tomsick et al. 2003b). We note that there is still the possibility that these sources were not observed in their true quiescent levels, as the *Chandra* observations were carried out between outbursts. However, we note that for XTE J1550−564, the *Chandra* observations took place during three distinct quiescent phases (Fig. 1), and a similar quiescent X-ray level is detected for two of these phases. In addition, optical observations (Jain et al. 2001) confirm that XTE J1550−564 returned to quiescence on a timescale of months. For H1743−322, we note that the last two *Chandra* observations were taken 2.5 days apart. The flux in the observation on MJD 53089 is consistent with the flux observed during the first *Chandra* observation taken 40 days before, which indicates that this is probably the quiescent level of H1743−322. Between the second and third *Chandra* observations, the flux more than doubled in less than 3 days. This may be related to continuous accretion in quiescence or possibly means that this could be the onset of the outburst that was detected by *RXTE* ASM about 90 days later (Swank 2004). Similarly, *RXTE* Proportional Counter Array (PCA) detected the X-ray activity of GX 339−4 during its 2002 outburst at least 40 days before the initial ASM detection (Homan et al. 2005). This probably indicates that the *Chandra* observations at the lowest level are likely representative of the true quiescent phase of XTE J1550−564 and H1743−322.

4.2. *X-Ray Spectra and Photon Index in Quiescence*

In addition to allowing for detection of these two black holes in quiescence, for XTE J1550−564 these observations also provide the most precise X-ray spectra of a black hole at such low luminosities (down to $\sim 10^{-7} L_{\rm Edd}$). We concentrate on the

TABLE 2
PARAMETERS OF OUR SAMPLE OF QUIESCENT BLACK HOLES: PHOTON INDEX AND ORBITAL PARAMETERS

		Quiescent[b]					
Source	Photon Index[a] (Γ)	X-Ray Flux (ergs s^{-1} cm^{-2})	Luminosity (L_{Edd})	Orbital Period (hr)	Distance[c] (kpc)	Primary Mass[d] ($M_\odot$)	Secondary Mass[c] ($M_\odot$)
XTE J1118+480	2.02 ± 0.16	8.6×10^{-15} [1]	3.9×10^{-9}	4.08	1.8 ± 0.6 [1]	6.48–7.19	0.23–0.32
A0620−00	2.26 ± 0.18	2.6×10^{-14} [1]	3.1×10^{-9}	7.75	1.16 ± 0.11 [2]	8.70–12.86	0.48–0.97
XTE J1550−564[e]	2.25 ± 0.08	5.7×10^{-14} [2]	1.4×10^{-7}	37.03	5.3 ± 2.3 [3]	9.68–11.58	0.94–1.64
GX 339−4[f]	1.99 ± 0.15	3.4×10^{-13} [3]	3.5×10^{-6}	42.00	>6 [4]	5.8	0.52
GRO J1655−40	$1.30^{+0.34}_{-0.41}$	2.8×10^{-14} [4]	4.3×10^{-8}	62.92	3.2 ± 0.2 [5]	6.03–6.57	2.23–2.74
V4641 Sgr	0.2 ± 0.9	1.0×10^{-14} [5]	1.2×10^{-7}	67.61	9.6 ± 2.4 [6]	6.82–7.42	2.85–3.34
V404 Cyg	1.55 ± 0.05	8.9×10^{-13} [6]	6.5×10^{-7}	155.28	3.0 ± 0.8 [7]	10.06–13.38	0.53–0.83

[a] 90% confidence level. References in text. See also the discussion on the influence of the hydrogen column density on the photon index.
[b] 0.5–10 keV unabsorbed X-ray flux. Adapted from quoted reference with PIMMS from Heasarc. (1) McClintock et al. 2003; (2) this work; (3) Gallo et al. 2003a; (4) Kong et al. 2002; (5) Tomsick et al. 2003b; (6) Campana et al. 2001.
[c] (1) McClintock et al. 2001; (2) Gelino et al. 2001; (3) Orosz et al. 2002; (4) Hynes et al. 2004; (5) Hjellming & Rupen 1995; (6) Orosz et al. 2001; (7) Shahbaz et al. 1994.
[d] Estimated 1 σ range from Orosz (2003) and references therein.
[e] Orbital parameters from Orosz et al. (2002), taking into account the rotational velocity of the star.
[f] Orbital parameters from Hynes et al. (2003).

power-law model, which can be representative of various emission mechanisms (see § 4.4). With a photon index of 2.25 ± 0.08, the X-ray spectra of XTE J1550−564 are significantly softer than during the standard hard state (photon index of the order of 1.5–1.7; Tomsick et al. 2001). This trend was marginally apparent in the decay of the 2000 outburst of XTE J1550−564 (Tomsick et al. 2001), but our *Chandra* observations of XTE J1550−564 clearly confirm this softening in quiescence.

In fact, this is very similar to several other black holes for which an X-ray spectrum has been measured in quiescence. For the rest of this paper, we concentrate on those systems for which the photon index has been measured with relatively high precision. We have collected results from the literature, which are presented in Table 2 (90% confidence level for the uncertainty on the photon indices) and in Figures 5 and 6. The X-ray spectrum of XTE J1118+480 ($\Gamma = 2.02 \pm 0.16$) in quiescence (McClintock et al. 2003) is also softer than during its standard hard state ($\Gamma = 1.7$; Frontera et al. 2003). When GX 339−4 is detected at very low X-ray flux (Corbel et al. 2003; Gallo et al. 2003a; C. Chapuis et al. 2006, in preparation), the X-ray spectra are again consistent with being soft ($\Gamma = 1.99 \pm 0.15$; C. Chapuis et al. 2006, in preparation) like XTE J1550−564 or XTE J1118+480. Similar conclusions can be drawn for A0620−00, which has a photon index of 2.26 ± 0.18 in quiescence (McClintock et al. 2003). However, the X-ray spectra of a subset of sources stay hard or harden significantly in quiescence compared to the standard hard state: V404 Cyg ($\Gamma = 1.55 \pm 0.07$ with N_H frozen to optical value; Kong et al. 2002) and V4641 Sgr ($\Gamma = 0.2 \pm 0.9$; Tomsick et al. 2003b). With a photon index of $1.30^{+0.34}_{-0.41}$ (Hameury et al. 2003), GRO J1655−40 may also be considered as being hard in quiescence.

It is interesting to note that the three BHs with the hardest X-ray spectra in quiescence are those with the largest orbital period (Fig. 5). From our sample, all X-ray spectra from quiescent BHs with orbital period of less than 2 days are consistent with a soft power law, whereas above this limit the power law is hard. The weighted average photon index for the four "soft" sources is $\Gamma = 2.18 \pm 0.06$, whereas $\Gamma = 1.53 \pm 0.07$ for the

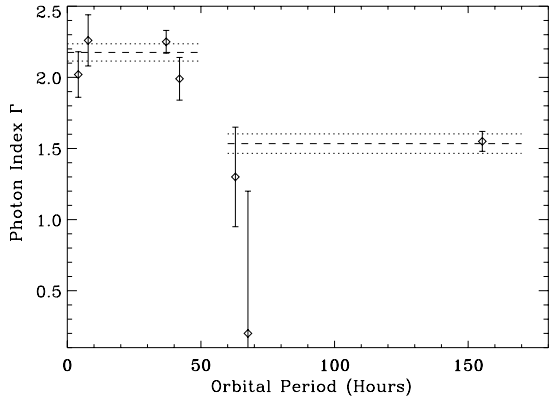

FIG. 5.—Evolution of the power-law photon index (Γ) vs. orbital period for XTE J1118+480, A 0620−00, XTE J1550−564, GX 339−4, GRO J1655−40, V4641 Sgr, and V404 Cyg (in order of increasing orbital period) in their quiescent states. The lines (with associated 1 σ error) indicate the average value of the photon index for the two groups (hard or soft; see text) of sources.

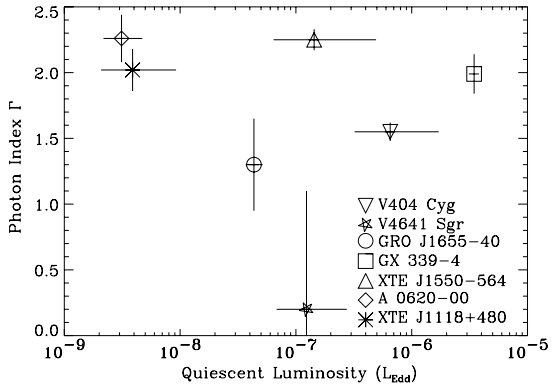

FIG. 6.—Evolution of the power-law photon index (Γ) vs. the 0.5–10 keV quiescent luminosity (in Eddington units). The uncertainty in the luminosity is based on the uncertainty in the black hole mass and distance. A distance of 8 kpc associated with a mass of 6 $M_\odot$ have been used for GX 339−4 (Hynes et al. 2003, 2004).

three "hard" sources. The difference between the two samples is significant at more than 7 σ, clearly indicating that the photon index may depend on the orbital period. However, our sample only includes seven sources with the hard sample dominated by V404 Cyg, and it needs to be confirmed by further observations of BHs in quiescence. GRS 1915+105, with an orbital period of 833 hr, would be a very good target if it returns to quiescence.

But as noted for XTE J1550−564 (§ 3), the knowledge of the interstellar absorption column density is an important parameter for fitting the X-ray spectra. Indeed, lower column density leads to harder spectra (Kong et al. 2002, Fig. 5). Some of the photon indices quoted above are deduced from X-ray spectra with a fixed column density. We should now see if fixing the interstellar absorption could lead to an artificial bias in our sample. For XTE J1550−564 (this work) and GX 339−4 (C. Chapuis et al. 2006, in preparation), the deduced $N_{\rm H}$ (as a free parameter) is consistent with previous measurements. For XTE J1118+480 and A0620−00, McClintock et al. (2003) used a fixed column density; however, as $N_{\rm H}$ is already very low for both of these sources, higher values would lead to even softer spectra. The X-ray and optical values of $N_{\rm H}$ for A0620−00 and XTE J1118+480 are consistent with each other (Kong et al. 2002; McClintock et al. 2003). For GRO J1655−40 (Hameury et al. 2003) and V404 Cyg (Kong et al. 2002), X-ray fitting may indicate a slightly higher $N_{\rm H}$ when compared to the optical measurement. With $N_{\rm H}$ free, the photon indices are softer with $\Gamma = 1.54^{+1.2}_{-0.7}$ for GRO J1655−40 and $\Gamma = 1.81 \pm 0.14$ for V404 Cyg. For V4641 Sgr, there is no independent measurement of the X-ray column density due to the very fast transient nature of the source. To summarize, if we take into account the influence of the uncertain interstellar absorption column densities on the determination of the photon indices, the difference in photon indices is significant at the 3 σ level.

If this trend is confirmed, it is of interest to understand the possible difference between the short and long orbital period systems. As outlined in Menou et al. (1999 and references therein), one of the obvious differences is the mass transfer rate between the companion star and the accretion disk. Indeed, following Frank et al. (1992), for Roche lobe overflow systems, the mass transfer rate may be driven by two separate mechanisms: loss of angular momentum through gravitational radiation and magnetic braking (*j*-driven systems) or expansion of the donor star as it evolves away from the main sequence (*n*-driven systems). The *j*-driven systems would be found preferentially in short orbital period systems. The bifurcation period between these two populations is expected to be in the range 0.5–2 days (Menou et al. 1999). Interestingly, Menou et al. (1999) have estimated the mass transfer rate for typical binary-evolution models (see their Fig. 3) driven by gravitational radiation and by secondary expansion. If we compare the orbital period of the sources in our sample (4.1 hr $< P_{\rm orb} <$ 155.3 hr), we observe that systems with orbital periods in the range 4–30 hr would have similar mass transfer rates to within a factor of a few. In any case, the systems with the longest orbital period would have a much higher mass transfer rate; therefore, this could be an origin of the possible difference in photon indices.

Taking into account the mass of the black hole (Orosz 2003 and references therein), we can further look (Fig. 6) to see if a correlation exists between the power-law photon indices and the quiescent X-ray luminosities (expressed in Eddington units). The X-ray fluxes used in this graph are from Table 2 and represent the lowest level of X-ray emission reported for these sources. This figure illustrates that the sources with the softer or harder spectra do not occur in a specific luminosity range.

4.3. *X-Ray Spectra at Intermediate Luminosities*

Most of the X-ray novae have not been observed/detected in X-rays in their quiescent state. However, we note that the softening of their X-ray spectra has been seen at a flux level well above quiescence. In the decay phase of their recent outburst, XTE J1650−500 (Corbel et al. 2004), as well as XTE J1908+094 (Jonker et al. 2004), are first observed to harden significantly in the hard state (we note that this is also the case for GX 339−4 at intermediate luminosity, possibly related to Compton reflection; Nowak et al. 2002). However, a clear softening ($\Gamma = 1.96 \pm 0.09$), as in GX 339−4, is then observed in XTE J1650−500 in the decay at a luminosity of 2×10^{34} ergs s^{-1} (Tomsick et al. 2004). No information is available on the quiescent spectra of XTE J1650−500 or XTE J1908+094, but it would be interesting to see if they also soften (as GX 339−4) in quiescence. Similarly, 4U 1543−47 gradually softened at intermediate luminosity ($\Gamma = 2.22 \pm 0.12$), whereas the hardest spectra in the hard state had $\Gamma = 1.64$ (Kalemci et al. 2005). *XMM-Newton* confirmed this softening with a photon index of $\Gamma = 1.94 \pm 0.04$ at a luminosity level of 4×10^{34} ergs s^{-1} (10^{-5} $L_{\rm Edd}$) (La Palombara & Mereghetti 2005). 4U 1543−47 was not in its true X-ray quiescence phase (at the time of the *XMM-Newton* observation), which is believed to occur below 3×10^{31} ergs s^{-1} (Garcia et al. 2001). However, the optical/infrared monitoring (Buxton & Bailyn 2004) indicates that 4U 1543−47 reached its quiescent optical level only 10 days after the *XMM-Newton* observations. It is unlikely that the X-ray flux could have decayed by 3 orders of magnitude on timescale of 10 days. This may possibly point out that the optical emission settled down to its quiescent level much before the X-rays. Other examples of similar softening at intermediate luminosity during the decay phase include XTE J1748−288 (Kotani et al. 2000) and GS 1124−68 (Ebisawa et al. 1994).

4.4. *On the X-Ray Emission of Black Holes in Quiescence*

One of the main results from our study is that a significant fraction of BHs have an X-ray spectrum that softens at lower luminosity. The emission of quiescent BHs is usually consistent with an extension of the hard-state properties to lower luminosities (Corbel et al. 2000, 2003; Kong et al. 2000; Tomsick et al. 2004), and hard-state models have been applied to explain the emission in the quiescent state.

Among these models, McClintock et al. (2003) explained the power-law photon index of $\Gamma = 2.02 \pm 0.16$ of XTE J1118+480 (one of the best-studied black holes in quiescence) with an advection-dominated accretion flow (ADAF) located inside a truncated standard thin disk. However, a pure ADAF model was insufficient to reproduce the X-ray spectrum of XTE J1118+480, and they had to reduce the mass accretion rate close to the black hole. Specifically, they assumed that the mass accretion rate varies as a function of radius as $\dot{M}(r) \propto r^p$ and obtained adequate fits only for $p \geq 0.2$. The fate of the "missing mass" is not described in McClintock et al. (2003) but could possibly take the form of an outflow (e.g., Quataert & Narayan 1999), which is then like the ADIOS model (Blandford & Begelman 1999). This is also quite similar to Yuan et al. (2005), who added a jet contribution to the standard ADAF model in order to fit the spectral energy distribution of XTE J1118+480 in the hard state. Within this context, an X-ray power-law photon index of $\sim$2 is predicted for BH in quiescence (Yuan & Cui 2005). However, at low luminosity the accretion flow is known to be convectively unstable (Igumenshchev & Abramowicz 1999; Quataert & Gruzinov 2000), and this convection-dominated accretion flow (CDAF) has a

very different structure than the standard ADAF, as convection significantly reduces the mass accretion rate (equivalent to setting the ADAF p-parameter to 1 in eq. [1] of McClintock et al. 2003). In this CDAF framework, the X-ray spectra are expected to soften significantly at very low luminosity (Ball et al. 2001) as observed in our study. Thus, it is likely that the ADAF models would be able to reproduce the soft and hard spectra described above, by tuning the amount of outflow or convection with the p-parameter. To reproduce the harder spectra of longer orbital period systems, such as V404 Cyg, larger values of the p-parameter, corresponding to stronger outflow or stronger convection, would be required.

Alternatively, in standard sphere+disk model, a softening of the X-ray spectra would also be expected due to a decrease of the coronal optical depth as the mass accretion rate decreases (see, e.g., the discussion in Tomsick et al. 2004). In the magnetic corona model, active regions above the disk are responsible for producing the hard X-ray emission and constitute the base of the outflow (Merloni & Fabian 2002). In that model, the X-ray spectrum is expected to soften at a lower accretion rate as the accretion power is carried away into the jets rather that being used to heat the electrons (Merloni & Fabian 2002). Such a model could easily explain the soft spectra of our sources in quiescence. However, in this model, the inner boundary of the accretion disk does not vary with the mass accretion rate. The characteristic frequencies of QPOs and of broadband timing noise are known to vary at state transitions and in the hard state (Tomsick et al. 2004; Kalemci et al. 2005), with lower frequencies generally occurring at lower luminosities. This is easy to understand in models in which the inner disk radius increases at low mass accretion rates but is difficult to explain in the models in which the inner disk radius is constant.

Alternatively, a new possibility for the origin of X-ray emission has emerged in recent years. Indeed, a strong correlation is observed between the radio and X-ray emission of GX 339−4, and V404 Cyg in the hard state, and this correlation seems to extend down to the quiescent level for these two sources (Corbel et al. 2003; Gallo et al. 2003b). The radio emission originates from a powerful self-absorbed compact jet (Corbel et al. 2000), and it also seems possible that this jet may contribute to the high-energy emission (Markoff et al. 2001, 2003) of BHs in the standard hard state. Furthermore, radio observations show that the compact jet (at least for V404 Cyg) is maintained in quiescence (Gallo et al. 2005). Even if the debate is still open regarding the contribution of the compact jet (Markoff & Nowak 2004; Homan et al. 2005; Markoff et al. 2006) at high energy, we can check if the jet model could explain the softening of X-ray spectra for BH in quiescence. To explain the X-ray spectra in the hard state, the electron energy distribution should have an energy index of the order of 2.2–2.4 (Markoff et al. 2003). If the electrons that could be responsible for the X-ray emission of BH in quiescence are above the cooling break due to spectral aging, then the energy index of the electron distribution (above the break) would be 3.2–3.4, therefore increasing (by 0.5) the photon index to $\Gamma \sim 2.1$ as observed in a large part of the sources from our sample. In this picture, the reason for the change would be that the particles are not sufficiently reaccelerated at low accretion rate, which is indeed quite reasonable. Alternatively, the compact jet contribution may vanish at low luminosity, giving the possibility that thermal emission from the nozzle dominates the X-ray band and therefore gives a different spectral shape. The hard spectra ($\Gamma \sim 1.6$) would easily be explained if the compact jet properties are similar to the standard hard state. This is consistent with the fact that these kind of spectra are observed for the sources (V404 Cyg, GRO J1655−40 and V4641 Sgr) that have a large accretion disk, and which may be a necessary condition to sustain a powerful compact jet. Similarly, it is of some interest to note that acceleration processes are also believed to be inefficient in the jets of the low-luminosity ($10^{-9}\,L_{\rm Edd}$) supermassive black hole, Sgr A*, located in the center of our Galaxy (Melia & Falcke 2001).

5. CONCLUSIONS

We have observed and detected XTE J1550−564 and H1743−322 during their quiescent states at their faintest level of X-ray emission with a 0.5–10 keV luminosity of 2×10^{32} $(d/5\ {\rm kpc})^2$ ergs s^{-1} for XTE J1550−564 and 9×10^{31} $(d/8\ {\rm kpc})^2$ ergs s^{-1} for H1743−322. Such levels of X-ray emission are in the upper range compared with the levels observed in other black hole systems. The *Chandra* observations also provide the best constraint on the power-law index of XTE J1550−564 with an index of 2.25 ± 0.08. We focused our analysis on the power-law model as this spectral shape is typically seen for black holes in quiescence and can represent an approximation for most theoretical emission mechanisms, but we emphasize that we cannot statistically rule out other spectral shapes. All *Chandra* spectra of XTE J1550−564 are consistent with a soft power law, therefore indicating that the X-ray spectrum softens at lower luminosity. We bring to light that all systems with short orbital period ($\sim$<60 hr) are consistent with a softening of their X-ray spectra in quiescence. However, the long orbital period systems may be consistent with a hardening of their X-ray spectra, but confirmation of this trend is required. A possible and realistic test would be to obtain *XMM-Newton* or *Chandra* observations of long orbital period systems, like V4641 Sgr or GRO J1655−40 with a long exposure during quiescence. In addition, GRS 1915+105, with an orbital period of 833 hr, may be a very good target if it returns to quiescence. Simultaneously, further observations of short orbital period systems (like XTE J1650−500, or 4U 1543−47 at lower luminosity) should be performed in order to test the softening of their spectra. We found that various classes of models (ADAF corona+jet, CDAF, sphere+disk, magnetic corona, or jet models) are able to reproduce the softening of the spectra in quiescence, but we note that most of them need the presence of powerful outflow or significant convection in order to reproduce these soft X-ray spectra. This may increase the likelihood that outflows are present in the most frequent phase (quiescence) of a black hole binary's activity and have significant influence on the physics of these systems and neighboring environment (Fender et al. 2003, 2005).

S. C. would like to thank H. Falcke, R. Fender, A. King, E. Kording, and S. Markoff for discussions on various aspects of BH emission models. *RXTE* ASM results are provided by the *RXTE* ASM team at MIT. We thank the anonymous referee for constructive comments. P. K. acknowledges partial support from NASA *Chandra* grants GO4-5038 and GO4-5039, and from a University of Iowa Faculty Scholar Award. J. A. T. acknowledges partial support from NASA *Chandra* grant GO3-4041X.

REFERENCES

Ball, G. H., Narayan, R., & Quataert, E. 2001, ApJ, 552, 221
Bautz, M. W., et al. 1998, Proc. SPIE, 3444, 210
Blandford, R. D., & Begelman, M. C. 1999, MNRAS, 303, L1
Buxton, M. M., & Bailyn, C. D. 2004, ApJ, 615, 880
Campana, S., Parmar, A. N., & Stella, L. 2001, A&A, 372, 241
Cash, W. 1979, ApJ, 228, 939
Corbel, S., Fender, R. P., Tomsick, J. A., Tzioumis, A. K., & Tingay, S. 2004, ApJ, 617, 1272
Corbel, S., Fender, R. P., Tzioumis, A. K., Nowak, M., McIntyre, V., Durouchoux, P., & Sood, R. 2000, A&A, 359, 251
Corbel, S., Fender, R. P., Tzioumis, A. K., Tomsick, J. A., Orosz, J. A., Miller, J. M., Wijnands, R., & Kaaret, P. 2002, Science, 298, 196
Corbel, S., Kaaret, P. Fender, R. P., Tzioumis, A. K., Tomsick, J. A., & Orosz, J. A. 2005, ApJ, 632, 504
Corbel, S., Nowak, M. A., Fender, R. P., Tzioumis, A. K., & Markoff, S. 2003, A&A, 400, 1007
Doxsey, R., et al. 1977, IAU Circ., 3113
Ebisawa, K., et al. 1994, PASJ, 46, 375
Fender, R. P., Gallo, E., & Jonker, P. G. 2003, MNRAS, 343, L99
Fender, R. P., Maccarone, T. J., & van Kesteren, Z. 2005, MNRAS, 360, 1085
Frank, J., King, A., & Raine, D. 1992, Accretion Power in Astrophysics (Cambridge: Cambridge Univ. Press)
Freeman, P. E., Kashyap, V., Rosner, R., & Lamb, D. Q. 2002, ApJS, 138, 185
Frontera, F., Amati, L., Zdziarski, A. A., Belloni, T., Del Sordo, S., Masetti, N., Orlandini, M., & Palazzi, E. 2003, ApJ, 592, 1110
Gallo, E., Fender, R., & Corbel, S. 2003a, ATel, 196, 1
Gallo, E., Fender, R. P., & Hynes, R. I. 2005, MNRAS, 356, 1017
Gallo, E., Fender, R. P., & Pooley, G. G. 2003b, MNRAS, 344, 60
Garcia, M. R., McClintock, J. E., Narayan, R., Callanan, P., Barret, D., & Murray, S. S. 2001, ApJ, 553, L47
Gelino, D. M., Harrison, T. E., & Orosz, J. A. 2001, AJ, 122, 2668
Hameury, J.-M., Barret, D., Lasota, J.-P., McClintock, J. E., Menou, K., Motch, C., Olive, J. F., & Webb, N. 2003, A&A, 399, 631
Hannikainen, D., Campbell-Wilson, D., Hunstead, R., McIntyre, V., Lovell, J., Reynolds, J., Tzioumis, T., & Wu, K. 2001, Astrophys. Space Sci. Supp., 276, 45
Hjellming, R. M., & Rupen, M. P. 1995, Nature, 375, 464
Homan, J., Buxton, M., Markoff, S., Bailyn, C. D., Nespoli, E., & Belloni, T. 2005, ApJ, 624, 295
Hynes, R. I., Steeghs, D., Casares, J., Charles, P. A., & O'Brien, K. 2003, ApJ, 583, L95
Hynes, R. I., et al. 2004, ApJ, 609, 317
Igumenshchev, I. V., & Abramowicz, M. A. 1999, MNRAS, 303, 309
Jain, R. K., Bailyn, C. D., Orosz, J. A., McClintock, J. E., & Remillard, R. A. 2001, ApJ, 554, L181
Jain, R. K., Bailyn, C. D., Orosz, J. A., Remillard, R. A., & McClintock, J. E. 1999, ApJ, 517, L131
Jonker, P. G., Gallo, E., Dhawan, V., Rupen, M., Fender, R. P., & Dubus, G. 2004, MNRAS, 351, 1359
Kaaret, P., Corbel, S., Tomsick, J. A., Fender, R., Miller, J. M., Orosz, J. A., Tzioumis, A. K., & Wijnands, R. 2003, ApJ, 582, 945
Kalemci, E., Tomsick, J. A., Buxton, M. M., Rothschild, R. E., Pottschmidt, K., Corbel, S., Brocksopp, C., & Kaaret, P. 2005, ApJ, 622, 508
Kaluzienski, L. J., & Holt, S. S. 1977, IAU Circ. 3099
Kong, A. K. H., Kuulkers, E., Charles, P. A., & Homer, L. 2000, MNRAS, 312, L49
Kong, A. K. H., McClintock, J. E., Garcia, M. R., Murray, S. S., & Barret, D. 2002, ApJ, 570, 277
Kotani, T., et al. 2000, ApJ, 543, L133
La Palombara, N., & Mereghetti, S. 2005, A&A, 430, L53
Markoff, S., Falcke, H., & Fender, R. 2001, A&A, 372, L25
Markoff, S., & Nowak, M. A. 2004, ApJ, 609, 972
Markoff, S., Nowak, M., Corbel, S., Fender, R., & Falcke, H. 2003, A&A, 397, 645
Markoff, S., Nowak, M., & Wilms, J. 2006, ApJ, in press
McClintock, J. E., Garcia, M. R., Caldwell, N., Falco, E. E., Garnavich, P. M., & Zhao, P. 2001, ApJ, 551, L147
McClintock, J. E., Narayan, R., Garcia, M. R., Orosz, J. A., Remillard, R. A., & Murray, S. S. 2003, ApJ, 593, 435
McClintock, J. E., & Remillard, R. A. 2006, in Compact Stellar X-Ray Sources, ed. W. H. G. Lewin & M. van der Klis (Cambridge: Cambridge Univ. Press), in press (astro-ph/0306213)
Melia, F., & Falcke, H. 2001, ARA&A, 39, 309
Menou, K., Esin, A. A., Narayan, R., Garcia, M. R., Lasota, J.-P., & McClintock, J. E. 1999, ApJ, 520, 276
Merloni, A., & Fabian, A. C. 2002, MNRAS, 332, 165
Miller, J. M., et al. 2004, ApJ, submitted (astro-ph/0406272)
Nowak, M. A., Wilms, J., & Dove, J. B. 2002, MNRAS, 332, 856
Orosz, J. A. 2003, in IAU Symp. 212, A Massive Star Odyssey: From Main Sequence to Supernova, ed. K. van der Hucht, A. Herrero, & E. César (San Francisco: ASP), 365
Orosz, J. A., et al. 2001, ApJ, 555, 489
———. 2002, ApJ, 568, 845
Quataert, E., & Gruzinov, A. 2000, ApJ, 539, 809
Quataert, E., & Narayan, R. 1999, ApJ, 520, 298
Revnivtsev, M., Chernyakova, M., Capitanio, F., Westergaard, N. J., Shoenfelder, V., Gehrels, N., & Winkler, C. 2003, ATel, 132, 1
Rupen, M. P., Mioduszewski, A. J., & Dhawan, V. 2003, ATel, 142, 1
Sánchez-Fernández, C., et al. 1999, A&A, 348, L9
Shahbaz, T., Ringwald, F. A., Bunn, J. C., Naylor, T., Charles, P. A., & Casares, J. 1994, MNRAS, 271, L10
Smith, D. A. 1998, IAU Circ. 7008
Sutaria, F. K., et al. 2002, A&A, 391, 993
Swank, J. 2004, ATel, 301, 1
Tomsick, J. A., Corbel, S., Fender, R. P., Miller, J. M., Orosz, J. A., Tzioumis, T., Wijnands, R., & Kaaret, P. 2003a, ApJ, 582, 933
Tomsick, J. A., Corbel, S., & Kaaret, P. 2001, ApJ, 563, 229
Tomsick, J. A., Kalemci, E., & Kaaret, P. 2004, ApJ, 601, 439
Tomsick, J. A., et al. 2003b, ApJ, 597, L133
Wachter, K., Leach, R., & Kellog, E. 1979, ApJ, 230, 274
White, N. E., & Marshall, F. E. 1983, IAU Circ. 3806
Yuan, F., & Cui, W. 2005, ApJ, 629, 408
Yuan, F., Cui, W., & Narayan, R. 2005, ApJ, 620, 905

3.5.3

X-Ray Observations of XTE J1550-564 during the Decay of the 2000 Outburst. I. Chandra and RXTE Energy Spectra.

Article publié dans :

Astrophys. J., 2001, 563, 229-238

Tomsick, J. A., Corbel, S., Kaaret, P.

THE ASTROPHYSICAL JOURNAL, 563:229–238, 2001 December 10

X-RAY OBSERVATIONS OF XTE J1550−564 DURING THE DECAY OF THE 2000 OUTBURST. I. *CHANDRA* AND *RXTE* ENERGY SPECTRA

JOHN A. TOMSICK
Center for Astrophysics and Space Sciences, University of California at San Diego, MS 0424, La Jolla, CA 92093; jtomsick@ucsd.edu
STÉPHANE CORBEL
Université Paris VII and Service d'Astrophysique, Centre d'Etudes de Saclay, F-91191 Gif sur Yvette Cedex, France; corbel@discovery.saclay.cea.fr
AND
PHILIP KAARET
Harvard-Smithsonian Center for Astrophysics, 60 Garden Street, Cambridge, MA 02138; pkaaret@cfa.harvard.edu
Received 2001 May 2; accepted 2001 August 7

ABSTRACT

We report on the evolution of the X-ray energy spectrum for the black hole candidate (BHC) X-ray transient XTE J1550−564 during the decay of the 2000 outburst. The *Rossi X-Ray Timing Explorer* (*RXTE*) and *Chandra* observations span nearly 5 orders of magnitude in luminosity. The *RXTE* spectra are dominated by a power-law component, and a comparatively weak soft component was also detected for the first two observations. The source made a transition to the canonical hard state near a luminosity of 9×10^{36} ergs s^{-1} over several observations, as evidenced by a drop in the flux of the soft component in the *RXTE* energy band and a hardening of the power-law component to a photon index near 1.6. The power law did not exhibit this behavior for the previous XTE J1550−564 outburst. For some observations, we detect a high-energy cutoff and find that the cutoff is more significant and at lower energy during the transition than in the hard state. The cutoff in the hard state is at higher energy than has been seen for most previous accreting BHCs. The *Chandra* spectrum provides evidence for spectral evolution after the hard-state transition. It is well, but not uniquely, described by a power law with a photon index of $2.30^{+0.41}_{-0.48}$ (90% confidence) and interstellar absorption. Advection-dominated accretion flow models predict gradual spectral softening as the luminosity drops, but our observations do not allow us to determine whether the spectral evolution is gradual or sudden. The lowest luminosity we measure for XTE J1550−564 with *Chandra* is 5×10^{32} ergs s^{-1} (0.5–7 keV, for a distance of 4 kpc). Although this is probably not the true quiescent luminosity, it represents a useful upper limit on this quantity.

Subject headings: accretion, accretion disks — black hole physics — stars: individual (XTE J1550−564) — X-rays: bursts — X-rays: stars

1. INTRODUCTION

The energy spectra of accreting black hole candidates (BHCs), while complex, are dominated by two emission components: a soft thermal component peaking below 10 keV and a hard component that extends to hundreds of keV (Grove et al. 1998). For most BHC X-ray transients, both components are present in the X-ray band when the source is bright during the outburst, and the source is said to be in the soft state or the very high state depending on the details of the spectral and timing properties (see van der Klis 1995 for a review of spectral states). There is strong evidence that the soft component is optically thick blackbody emission from the accretion disk. As the X-ray luminosity drops, significant changes in the spectral and timing properties are observed as sources enter the hard state. The soft component becomes undetectable at energies above 1 keV, and the spectrum is dominated by a hard power law or breaking power-law component. An increase in the strength of the timing noise is also characteristic of the transition to the hard state. It is likely that the high-energy emission is due to inverse Comptonization of soft photons by energetic electrons, but there is uncertainty about the system geometry, the electron energy distribution, and the mechanism for transferring energy to the electrons. One possibility is that a quasi-spherical, optically thin region forms in the inner portion of the accretion disk as predicted by advection-dominated accretion flow (ADAF) models (Narayan, Garcia, & McClintock 1997). Another possibility that implies a different site for hard X-ray production is that the hard X-ray emission is due to magnetic flares above the disk (Galeev, Rosner, & Vaiana 1979). The source behavior during the decay from the hard state into quiescence is not well established. Here we present a study of the evolution of the energy spectrum for the BHC X-ray transient XTE J1550−564 spanning nearly 5 orders of magnitude in luminosity during outburst decay.

XTE J1550−564 was first detected by the *Rossi X-Ray Timing Explorer* (*RXTE*) All-Sky Monitor (ASM) in 1998 September (Smith 1998). It was identified as a probable black hole system based on its X-ray spectral (Sobczak et al. 1999) and timing properties. The source shows strong aperiodic variability including low- (0.08–18 Hz) and high- (100–285 Hz) frequency quasi-periodic oscillations (Cui et al. 1999; Remillard et al. 1999; Homan, Wijnands, & van der Klis 1999; Remillard et al. 2001; Homan et al. 2001; Miller et al. 2001b). The optical (Orosz, Bailyn, & Jain 1998) and radio (Campbell-Wilson et al. 1998) counterparts were identified, and recent optical observations confirm that the system contains a black hole (Orosz et al. 2001). A superluminal ejection was observed in the radio (Hannikainen et al. 2001), establishing that the source is a microquasar similar to GRO J1655−40 and GRS 1915+105. XTE

J1550−564 became active in X-rays again in 2000 April (Smith et al. 2000), making it one of the few BHC X-ray transients for which multiple outbursts have been observed. X-ray observations during the 2000 outburst were made by us as well as by another group (Miller et al. 2001a). A radio study of the 2000 outburst (Corbel et al. 2001) showed evidence for a compact jet when the source was in the hard state and that this jet is quenched during the intermediate/very high state (see Homan et al. 2001 for a discussion of spectral states in XTE J1550−564). In 2001 January, the source flared again and was detected in the X-ray (Tomsick et al. 2001), optical (Jain, Bailyn, & Tomsick 2001), and radio, but this flare did not develop into a full outburst.

In this paper, we focus on the properties of the energy spectrum during the decay of the 2000 outburst. The *RXTE* and *Chandra* observations used for this paper include a study of a transition to the hard state and spectral evolution at low luminosities. A study of the timing properties using the *RXTE* data is presented in a companion paper (Kalemci et al. 2001, hereafter Paper II).

2. OBSERVATIONS AND LIGHT CURVE

During the XTE J1550−564 outburst, we obtained two *Chandra* observations of the BHC at low flux and several observations with *RXTE* during the decay of the outburst. The *RXTE* observations were made under a program to study BHC X-ray transients during outburst decay, and the *Chandra* observations were granted from Director's Discretionary Time, motivated by our *RXTE* observations. Figure 1 shows the 1.5–12 keV light curve for the outburst, including data from the *RXTE*/ASM and our pointed observations. Table 1 provides information about the observations that we used for spectral analysis.

When observing sources near the Galactic plane with *RXTE*, one must be aware of contributions from the Galactic ridge emission (Valinia & Marshall 1998) and the possibility of source confusion. XTE J1550−564 is 1°.8 from the Galactic plane, and the Galactic ridge emission is significant for our fainter observations. To estimate the level of Galactic ridge emission, we used public *RXTE* observations of the XTE J1550−564 position that were made when the source was in quiescence. The observations were made on 1999 August 13 and consist mostly of scans used to study the nearby supernova remnant G326.3–1.8. Although the observations include only 128 s on the XTE J1550−564 position, this is sufficient to determine the X-ray flux. Assuming an absorbed Raymond-Smith plus power-law model with the parameter values found by Valinia & Marshall (1998) for the central ridge but with the overall normalization left as a free parameter, the Galactic ridge flux is 1.68×10^{-11} ergs cm^{-2} s^{-1} (1.5–12 keV) at the XTE J1550−564 position.

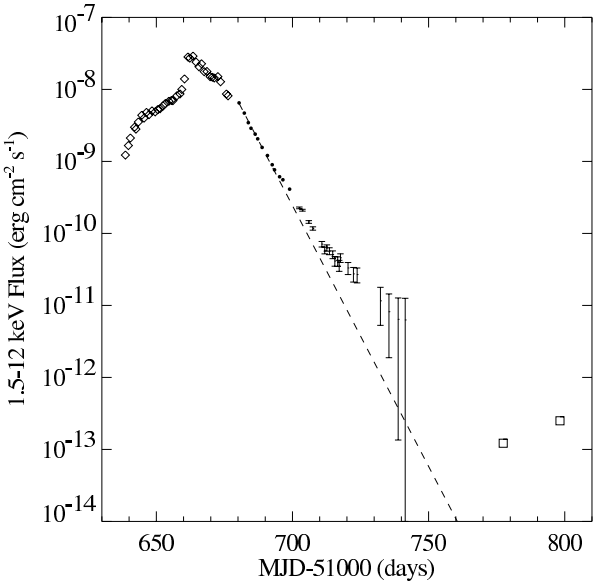

FIG. 1.—The X-ray light curve for the 2000 outburst from XTE J1550−564, including data from the *RXTE*/ASM (*diamonds*), *RXTE* pointed observations (*filled circles and error bars*), and *Chandra* observations (*squares*). Dashed line is an exponential decay with an *e*-folding time of 6.0 days.

TABLE 1

RXTE OBSERVATIONS OF XTE J1550−564

Observation	MJD[a]	Integration Time (s)	PCUs[b]	PCA Count Rate[c] (counts s^{-1})	HEXTE Count Rate[d] (counts s^{-1})	Flux[e]
1	51,680.391	2032	2, 3, 4	1992	36	5.6×10^{-9}
2	51,682.316	1712	2, 3, 4	1575	40	4.7×10^{-9}
3	51,683.786	2688	2, 3, 4	1278	40	4.0×10^{-9}
4	51,684.769	848	1, 2, 3, 4	1145	38	3.5×10^{-9}
5	51,686.302	1520	1, 2, 3, 4	955	33	3.0×10^{-9}
6	51,687.229	1408	2, 3	855	30	2.7×10^{-9}
7	51,688.846	1712	2, 3	663	24	2.1×10^{-9}
8	51,690.807	1760	2, 3	508	17	1.6×10^{-9}
9	51,692.562	1728	2	380	13	1.2×10^{-9}
10	51,693.411	1168	2	330	12	1.0×10^{-9}
11	51,695.271	1136	2, 3	258	9	8.1×10^{-10}
12	51,696.483	1712	2, 3, 4	218	8	7.1×10^{-10}
13	51,698.948	1152	2	165	6	5.0×10^{-10}

[a] Modified Julian Date (MJD = JD−2,400,000.5) at the midpoint of the observation.
[b] The Proportional Counter Units (other than PCU 0) that were on during the observation.
[c] The 3–25 keV count rate normalized to the rate for 5 PCUs (all three layers) after background subtraction.
[d] The 18–150 keV count rate for HEXTE (cluster A only) after background subtraction.
[e] Absorbed 3–25 keV flux in units of ergs cm^{-2} s^{-1}.

Source confusion is also an issue for our *RXTE* observations. The transient pulsar XTE J1543−568 (Marshall, Takeshima, & in't Zand 2000), which is 0.°966 from the XTE J1550−564 pointing position (Kaptein, in't Zand, & Heise 2001), was in outburst during our observations. We analyzed the ASM data for XTE J1543−568 to determine the flux this source contributed during our observations. For ten 15 day intervals during the XTE J1550−564 outburst, the ASM count rate for the pulsar was between 0.15 and 0.90 counts s^{-1}. At the maximum count rate and given the 3% response that is expected for the angular separation, we estimate that XTE J1543−568 contributed a flux of 1.08×10^{-11} ergs cm^{-2} s^{-1} (1.5–12 keV) during our observations. The level of emission observed during our last two *RXTE* observations is consistent with the emission coming from the Galactic ridge and XTE J1543−568 with little or no contribution from XTE J1550−564. The emission properties observed for our last several observations confirm that we are seeing significant contributions from the Galactic ridge and XTE J1543−568. We find a strong iron line at 6.7 keV for our last several observations, which is a property of the Galactic ridge emission (Valinia & Marshall 1998). Also, we detect pulsations at 27 s, which is the known pulse period for XTE J1543−568 (Marshall, Takeshima, & in't Zand 2000).

For the light curve shown in Figure 1 we assume that the flux contribution to the *RXTE* observations from the Galactic ridge emission and XTE J1543−568 is between 1.68×10^{-11} ergs cm^{-2} s^{-1} and the value we find for our last observation, 2.94×10^{-11} ergs cm^{-2} s^{-1} (1.5–12 keV). For the first 13 *RXTE* observations, the level of contamination is not significant. These observations are shown as filled circles in Figure 1, and we use only these observations for the spectral analysis described below. Error bars are shown for the other *RXTE* observations. Fitting an exponential to the first 13 *RXTE* observations gives 6.0 days for the *e*-folding time for the decay, which is a very fast decay compared to other BHC X-ray transients (Chen, Shrader, & Livio 1997; Tomsick & Kaaret 2000). A deviation from the exponential decay first occurs on MJD 51,695 during observation 11. It is interesting that a flare is seen in the near-IR light curves for XTE J1550−564 that peaks at this time (Jain et al. 2001) and that the radio observation indicating the presence of a compact jet was made soon after on MJD 51,697 (Corbel et al. 2001). A fractionally larger deviation from the exponential decay in the X-ray light curve occurs between MJD 51,710 and 51,730. Generally, the X-ray light curve for XTE J1550−564 is similar to those of other BHC X-ray transients, which typically show reflares, glitches, and secondary maxima (Chen et al. 1997). We note that the ASM data for XTE J1543−568 indicates that it is unlikely that features in the XTE J1550−564 light curve are due to flux variations from the pulsar.

The *Chandra* observations were made on MJD 51,777.405 (2000 August 21) and MJD 51,798.245 (2000 September 11) using the Advanced CCD Imaging Spectrometer (ACIS). We used one of the back-illuminated ACIS chips (S3) to obtain the best low-energy response. For the first observation, a 1.5–12 keV flux of 1.2×10^{-13} ergs cm^{-2} s^{-1} is inferred (assuming an absorbed power-law model), while the flux was 2.5×10^{-13} ergs cm^{-2} s^{-1} for the second observation. The fact that the flux increased by a factor of more than 2 between the observations indicates that the main part of the decay had ended by the time the *Chandra* observations were made. This is consistent with the optical behavior of the source. XTE J1550−564 reached optical quiescence by MJD 51,750 and remained at its quiescent level during both of our *Chandra* observations (Jain et al. 2001).

3. *CHANDRA* ANALYSIS AND RESULTS

We analyzed the data from the *Chandra* observations using the CIAO v2.1 and XSPEC v11.0 software packages. XTE J1550−564 is clearly detected in both observations at R.A. = $15^h50^m58^s.65$, decl. = $-56°28'35''.2$ (equinox 2000.0) with an uncertainty of 1″, which is consistent with the optical and radio positions previously reported (Jain et al. 1999; Corbel et al. 2001). We extracted source spectra for each observation from a circular region with a radius of 5″ and background spectra from an annulus with an inner radius of 5″ and an outer radius of 18″ centered on the source. The outer radius is constrained by the presence of a nearby source. For the first observation, there are brief time segments where excess background is observed. Removing these causes a drop in the exposure time from 5099 to 4985 s. Periods of high background are not seen in the second observation, allowing us to use the entire 4572 s. In the energy band used for spectral analysis (0.5–7 keV), 71 and 111 counts were collected in the source region for the first and second observations, respectively. We determined that the expected background levels in the source extraction region in the 0.5–7 keV energy band are 1.2 and 1.3 counts for the first and second observations, respectively, indicating that background subtraction is unnecessary. The CIAO routine *psextract* was used to extract the spectra and create response matrices. It is important to note that the response matrices created by this routine do not account for the energy dependence of the High-Resolution Mirror Array (HRMA) point-spread function (PSF). This leads to underestimating the source flux, especially at higher energies where the PSF is broader. To correct the response matrix for this effect, we used the HRMA calibration data from Table 4.2 of the *Chandra* Proposer's Guide (10″ diameter case). The data was interpolated to obtain a value for the encircled energy fraction for each energy bin in the ACIS response matrix, and the correction was applied by multiplying the effective areas used for the response matrix by these fractions. For our 5″ extraction radius, the correction causes an increase of the 0.5–7 keV energy flux (and thus the quoted luminosities) by 5%. It should be noted that this correction becomes significantly larger if small extraction radii are used.

We began by fitting each spectrum with a power-law model, which is commonly used for fitting BHC X-ray transients at low flux levels (e.g., Asai et al. 1998). We included interstellar absorption and left the column density as a free parameter. Although the flux is different by a factor of 2 between observations, the spectral parameters obtained are not significantly different, and we carried out further spectral analysis after combining the data for the two observations. The increase in flux for the second observation is rather surprising, and we made light curves for the two observations with four and eight time bins to determine whether the flux increase was caused by a short-timescale phenomenon (e.g., a flare). We found no statistically significant variability in either observation.

We rebinned the spectrum for the two observations combined as shown in Figure 2 and fitted the spectrum using χ^2

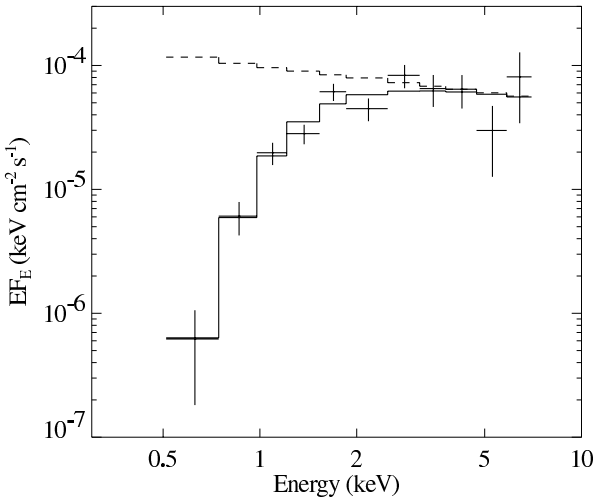

FIG. 2.—The *Chandra*/ACIS energy spectrum for the two *Chandra* observations combined. Solid line is a power law with interstellar absorption, and dashed line is a power law with $\Gamma = 2.3$ without absorption.

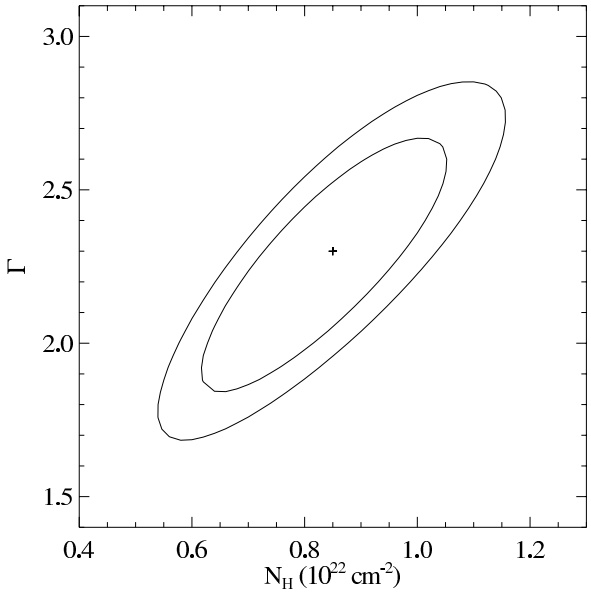

FIG. 3.—Error contours for the column density (N_H) and the power-law index (Γ) derived from the *Chandra* spectrum. The cross marks the location of the best-fit values, and the 68% ($\Delta\chi^2 = 2.30$) and 90% ($\Delta\chi^2 = 4.61$) confidence contours are shown.

minimization first with a power-law model and then with a simple blackbody (both with absorption). The fit is somewhat better for the power-law model ($\chi^2/\nu = 9.5/8$) than for the blackbody model ($\chi^2/\nu = 12.8/8$). In addition, a blackbody temperature of 0.7 keV is obtained, which is considerably higher than typical values seen for quiescent neutron star transients (Asai et al. 1998). The distance for XTE J1550−564 has been estimated at between 2.5 kpc (Sánchez-Fernández et al. 1999) and 6 kpc (Sobczak et al. 1999). For the flux observed during the *Chandra* observations, a blackbody temperature of 0.7 keV implies a blackbody radius of between 0.06 and 0.15 km for distances of 2.5 and 6 kpc, respectively, indicating that it is unlikely that a blackbody interpretation could be physically meaningful. These findings are consistent with the identification of XTE J1550−564 as a black hole rather than as a neutron star system, and in the following we focus on the power-law model.

We refitted the spectrum for the two observations combined with a power-law model with interstellar absorption using the Cash statistic (Cash 1979). This maximum likelihood method allows for the determination of errors and confidence intervals for parameters and does not require that the data be rebinned in energy. This is desirable since rebinning data necessarily removes spectral information. We obtain values of $\Gamma = 2.30^{+0.41}_{-0.48}$ for the power-law photon index and $N_H = (8.5^{+2.2}_{-2.4}) \times 10^{21}$ cm^{-2} for the column density (90% confidence errors are given in both cases). We note that the correction for the energy dependence of the PSF described above changes Γ by only 2%, which is insignificant compared to the statistical errors. Figure 3 shows the 68% and 90% error contours for the two parameters. The column density is consistent with 9×10^{21} cm^{-2}, which is the value for the Galactic column density along the line of sight (Jain et al. 1999), but it is only marginally consistent with the value inferred from the optical work of Sánchez-Fernández et al. (1999). From optical spectra of XTE J1550−564 taken during outburst, they find that $E(B-V) = 0.70 \pm 0.10$, which corresponds to a column density of $(3.9 \pm 0.6) \times 10^{21}$ cm^{-2} (Predehl & Schmitt 1995). The value of N_H measured by *Chandra* could indicate that the distance to the source is somewhat greater than 2.5 kpc, which is the distance estimate obtained from the measured value of $E(B-V)$. The significance of the value we find for Γ is discussed below.

4. *RXTE* SPECTRAL ANALYSIS AND RESULTS

We produced Proportional Counter Array (PCA) and High-Energy X-Ray Timing Experiment (HEXTE) energy spectra for each observation (see Bradt, Rothschild, & Swank 1993 for instrument descriptions). We used the PCA in the 3–25 keV energy band and HEXTE in the 18–150 keV energy band. For the PCA, we used standard-mode data consisting of 129 bin spectra with 16 s time resolution, included the photons from all three anode layers, and estimated the background using the "Sky-VLE" model. For each observation, data was combined from Proportional Counter Units (PCUs) 1–4 that were turned on. For most of the observations, at least one of the PCUs was turned off. Damage to PCU 0 prevented us from using data from this detector. We produced HEXTE energy spectra using standard-mode data, consisting of 64 bin spectra with 16 s time resolution. We used the 1997 March response matrices and applied the necessary dead-time correction (Rothschild et al. 1998). For the spectral fits, the normalization was left free between HEXTE and the PCA. The HEXTE background subtraction is performed by alternating between observations of source and background fields. Each cluster has two background fields, and we checked the background subtraction by comparing the count rates for the two fields.

For the PCA, we used the 2001 February response matrices and tested them by combining spectra from all the available Crab observations from 2000 May 14 to 2001 January 28, where PCUs 1–4 were turned on, resulting in a Crab spectrum with an exposure time of 17,584 s. We fitted the spectrum with a model consisting of two power-law

components, representing the contributions from the nebula and the pulsar, with interstellar absorption. We fixed the column density to 3.2×10^{21} cm^{-2} (Massaro et al. 2000) and the photon index for the pulsar component to 1.8 (Knight 1982). We restricted the bandpass to 3–25 keV since very large residuals (near or above the 5% level) are present outside this range. Even when only the 3–25 keV range is used, we obtain a reduced χ^2 well above 1.0 due to the small statistical errors. The Crab residuals are larger below 8 keV than above this energy, and including 0.8% systematic errors from 3–8 keV and 0.4% systematic errors from 8–25 keV leads to a drop in the reduced χ^2 to 1.0. We added these systematic errors to the XTE J1550−564 spectra to account for uncertainties in the PCA response.

We determined which spectral model to use by fitting the PCA plus HEXTE energy spectrum for observation 1. A power law alone (with interstellar absorption) provides a very poor fit with $\chi^2/\nu = 1118/90$. Large positive residuals are seen near 6–7 keV, and a broad minimum centered near 10 keV is present in the residuals. Models with cutoffs at high energies, such as the Comptonization model of Titarchuk (1994), give even worse fits ($\chi^2/\nu = 1649/88$) since the spectrum extends to high energies without a clear cutoff. We obtain a significant improvement in the fit to $\chi^2/\nu = 135/87$ by adding a smeared iron edge (Ebisawa et al. 1994) to the power law. The smeared edge has been used by other authors to fit XTE J1550−546 spectra (Sobczak et al. 2000) and also for other BHC transients during outburst decay (Tomsick & Kaaret 2000). Even with the smeared edge, large residuals are present below 4 keV, suggesting the presence of a soft component. The addition of a disk-blackbody model (Makishima et al. 1986) with a temperature near 0.5 keV improves the fit significantly to $\chi^2/\nu = 71/85$. Finally, the addition of a Gaussian iron line improves the fit to $\chi^2/\nu = 59/82$, which is significant at the 99.8% level based on an F-test. Although we left all the model parameters free for these fits, the data is not adequate to provide good constraints on the column density, the width of the smeared edge, the line energy or the line width, and, for subsequent fits, we fixed these parameters as follows. We used a value of 9×10^{21} cm^{-2} for the column density, which is the Galactic column density along the line of sight to XTE J1550−564 and is also consistent with the value found using *Chandra*. Following Sobczak et al. (2000), we fixed the width of the smeared edge to 7 keV and the width (σ) of the iron line to 0.5 keV. Also, we fixed the line energy to 6.5 keV, which is consistent with the Kα line for moderately ionized iron. We note that all these values fall within the 68% confidence error regions for the parameters when they are left free and that we obtain $\chi^2/\nu = 63/86$ when the parameters are fixed. Figure 4 shows the observation 1 spectrum and the residuals for a model consisting of a power law, a disk-blackbody, a smeared edge, and an iron line with the parameters fixed as specified above.

We used the same model to fit the other XTE J1550−564 observations. The model provides a good description of the spectrum in each case, with reduced χ^2 values between 0.56 and 1.26 for between 54 and 87 degrees of freedom. We include results only for observations 1–13 because the contamination from the Galactic ridge and the pulsar XTE J1543−568 provides a significant source of uncertainty in parameter estimation for later observations. F-tests indicate that the disk-blackbody is detected only at extremely high

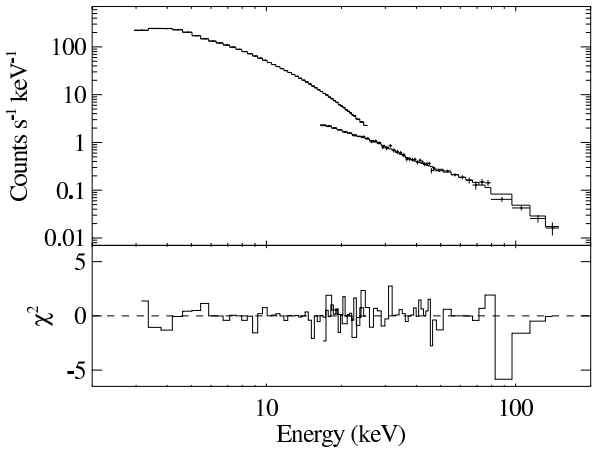

FIG. 4.—*RXTE* energy spectrum for observation 1, including the PCA from 3 to 25 keV and HEXTE from 18 to 150 keV. *Bottom panel*: The residuals in the form of the contribution to the value of χ^2 for each energy bin.

significance [$1-(2 \times 10^{-15})$] for the first observation. It is marginally detected at 98% confidence for the second observation, and is not statistically significant for the other observations. Inner disk temperatures ($kT_{\rm in}$) of 0.70 and 0.62 keV are obtained for observations 1 and 2, respectively. Although the statistical error on the temperature measurements is 0.05 keV, there is also a systematic uncertainty related to the fact that $kT_{\rm in}$ depends on the column density. We estimate that the total error on the temperature measurements for observations 1 and 2 is near 0.1 keV. The disk-blackbody normalizations[1] are 533^{+202}_{-147} and 355^{+1145}_{-210} for observations 1 and 2, respectively. As for the temperature, the 68% confidence statistical errors reported here underestimate the true normalization uncertainties. Although the disk-blackbody component is not detected at high significance for observations 3–13, we obtain values of $kT_{\rm in}$ near 0.35 keV for observations 3 and 4 with this component in the model. In fitting the spectra for observations 3–13, we included a disk-blackbody component with the temperature fixed to 0.35 keV. At such a low temperature, this component contributes only to the lowest two or three PCA energy bins and does not significantly change the values for the other fit parameters. For observations 3–5, we calculate 90% confidence upper limits on N between 9000 and 15,000, and for observations 6–13, the upper limits are between 1000 and 2100.

The smeared edge is detected at greater than 99% confidence for all observations except for 11 and 13. The edge energies are consistent with neutral or moderately ionized iron and the optical depth of the edge (Ebisawa et al. 1994) drops over time from 0.9 for observation 1 to about 0.4 for observations 8, 9, 10, and 12. However, we emphasize that the smeared edge model is phenomenological, and physical significance should not be attached to its parameters. The feature itself is clearly present in most of the spectra and may be related to Compton reflection (Lightman & White 1988). For most of the observations, the iron line equivalent

[1] The disk-blackbody normalization is $N = \cos i (R_{\rm in}/d_{10})^2$, where i is the binary inclination, $R_{\rm in}$ is the accretion disk inner radius in units of km, and d_{10} is the source distance in units of 10 kpc.

TABLE 2

RXTE MEASUREMENT OF POWER-LAW PHOTON INDEX (Γ)

Observation	PCA[a]	HEXTE[a]	PCA+HEXTE[a] (No Cutoff)	PCA+HEXTE[a] (With Cutoff)	Consensus[b]
1	2.047 ± 0.012	1.997 ± 0.022	2.053 ± 0.010	...	2.05 ± 0.04
2	1.864 ± 0.013	1.849 ± 0.020	1.878 ± 0.011	1.852 ± 0.014	1.85 ± 0.04
3	1.717 ± 0.005	1.698 ± 0.013	1.720 ± 0.005	1.714 ± 0.004	1.71 ± 0.04
4	1.698 ± 0.006	1.674 ± 0.023	1.700 ± 0.006	1.696 ± 0.005	1.70 ± 0.04
5	1.669 ± 0.005	1.580 ± 0.021	1.665 ± 0.005	...	1.67 ± 0.04
6	1.640 ± 0.008	1.597 ± 0.025	1.637 ± 0.007	...	1.64 ± 0.04
7	1.606 ± 0.007	1.578 ± 0.023	1.606 ± 0.007	...	1.61 ± 0.04
8	1.609 ± 0.008	1.601 ± 0.027	1.609 ± 0.007	...	1.61 ± 0.04
9	1.591 ± 0.013	1.634 ± 0.041	1.598 ± 0.012	...	1.60 ± 0.04
10	1.599 ± 0.018	1.469 ± 0.053	1.581 ± 0.016	...	1.58 ± 0.05
11	1.640 ± 0.018	1.559 ± 0.070	1.632 ± 0.017	...	1.63 ± 0.05
12	1.620 ± 0.012	1.627 ± 0.065	1.620 ± 0.012	...	1.62 ± 0.05
13	1.718 ± 0.021	1.629 ± 0.171	1.726 ± 0.033	...	1.73 ± 0.06

[a] The 68% confidence errors are given.

[b] Measured value for Γ with PCA and HEXTE after accounting for the high-energy cutoffs detected for observations 2, 3, and 4. The error given includes the systematic error (see text).

widths are between 15 and 75 eV; the highest equivalent width of 110 eV occurs for observation 13. The detection significance for the line is greater than 99% for six of the observations.

One of our main results is the evolution of the power-law index during the decay of the outburst. Table 2 shows the photon index for the 13 observations using the PCA alone, the HEXTE alone, and both instruments combined. In all cases, the photon index is near 2.0 for observation 1, but it gradually drops to about 1.6 during the next few observations. We fitted the spectra for the two instruments separately to obtain an estimate of the systematic error due either to the model we are using for the low-energy portion of the spectrum or to uncertainty in the cross calibration between PCA and HEXTE. Although the differences between the PCA and HEXTE are only statistically significant for a few observations, it is clear that there is a systematic effect since the index measured by the PCA is softer than the index measured by HEXTE in 11 of the 13 observations. We estimate the systematic error in the measurement of the photon index by calculating the weighted average of the differences between the PCA and HEXTE. This gives a value of 0.03, which we adopt as the systematic error on the measurement of the power-law index.

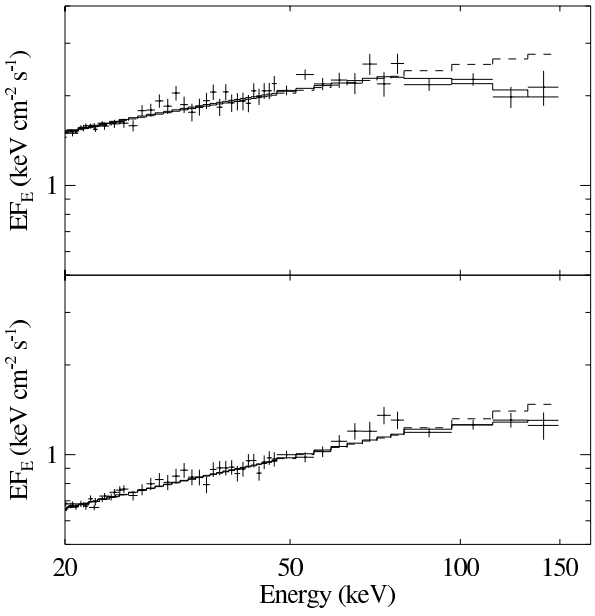

FIG. 5.—High-energy portions of the *RXTE* spectra for observation 3 (*top panel*) and observations 5–12 combined (*bottom panel*). In both cases, the dashed line shows the fit to the spectrum using a power law with no high-energy cutoff, and the solid line shows the fit using a power law with a high-energy cutoff. It is clear that a more significant cutoff is present for observation 3, during the state transition, than for observations 5–12, when the source was in the hard state.

Although the spectral model described above provides satisfactory fits to the energy spectra, for a few of the observations the spectra appear to break in the HEXTE band. To determine whether the breaks are statistically significant, we added a high-energy cutoff to our model and refit the PCA/HEXTE energy spectra. We used the XSPEC model *highecut*, which has two free parameters and has been used previously by several authors to model spectral breaks (e.g., Grove et al. 1998). Including this model modifies the power law for energies above $E_{\rm cut}$, producing an exponential cutoff with an *e*-folding energy $E_{\rm fold}$, but does not alter the spectrum for energies below $E_{\rm cut}$. For observations 2, 3, and 4, *F*-tests show that the cutoff is significant at 99.8% confidence or greater, but the cutoff is less significant for the other observations. The cutoff is detected at extremely high

TABLE 3

BREAK PARAMETERS FOR THE *RXTE* SPECTRA

Observation	$E_{\rm cut}$[a] (keV)	$E_{\rm fold}$[a] (keV)
2	40^{+8}_{-7}	338^{+91}_{-83}
3	72^{+8}_{-9}	194^{+71}_{-48}
4	73^{+10}_{-18}	175^{+110}_{-57}
5–12	78^{+23}_{-11}	462^{+342}_{-241}

[a] The 68% confidence errors are given.

significance [$1-(2.6 \times 10^{-8})$] only for observation 3. Table 2 includes the measurement of the photon index when the break is included for observations 2, 3, and 4. The change in photon index is not significant for any of the observations. We combined the data from observations 5–12, all of which have the same value for Γ within errors, and refitted the PCA/HEXTE spectrum with and without a cutoff. Adding a cutoff provides a marginally significant (98% confidence) improvement, indicating that the break is weak in this case if it is present. The best-fit values for $E_{\rm cut}$ and $E_{\rm fold}$ are given in Table 3 for observations 2, 3, 4, and 5–12. Figure 5 shows the high-energy portion of the spectrum for observation 3, where the most significant cutoff is detected, and for observations 5–12.

5. DISCUSSION

5.1. *Transition to the Hard State*

The spectral evolution we observe during the *RXTE* observations shows that XTE J1550−564 was in the process of making a transition to the hard state as our observations began. Figure 6 shows the evolution of the power-law photon index (Γ) for the *RXTE* and *Chandra* observations. The drop in Γ during the first few *RXTE* observations along with the timing properties reported in Paper II indicate that the source made a transition to the hard state. In addition, the drop in temperature and eventual nondetection of the soft component is common when such transitions occur (see Tomsick & Kaaret 2000 and references therein). Although our observations do not provide information about the state of the source before the transition, Corbel et al. (2001) indicate that XTE J1550−564 was in the intermediate/very high state before the transition since relatively strong hard X-ray emission

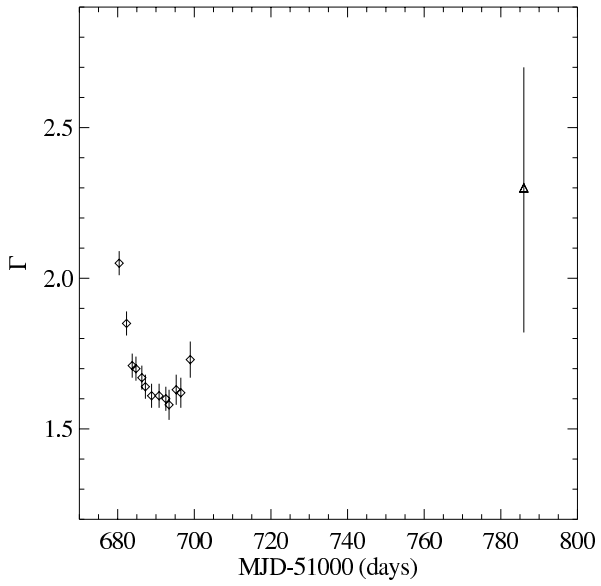

FIG. 6.—The evolution of the power-law index (Γ) for the pointed *RXTE* observations (*diamonds*) and the combination of the two *Chandra* observations (*triangle*). The *RXTE* values come from the last column of Table 2, and the error bars shown include the systematic error discussed in the text. For the *Chandra* point, a 90% ($\Delta\chi^2 = 2.71$) confidence error bar is shown.

was observed by the Burst and Transient Source Experiment (BATSE) on board the *Compton Gamma-Ray Observatory* (*CGRO*) throughout the outburst. Observations of XTE J1550−564 made during the rise of the 1998–1999 outburst indicate also that the source made a transition from the hard state to the intermediate/very high state (Cui et al. 1999; Wilson & Done 2001).

XTE J1550−564 is one of the few BHC X-ray transients that has had multiple outbursts, allowing us to compare the source behavior during the 2000 decay to that of the previous outburst. For the 2000 outburst, the transition to the hard state occurred when the source was still relatively bright. The flux for the second *RXTE* observation, which is probably near the midpoint of the transition, is 5×10^{-9} ergs cm^{-2} s^{-1} (3–25 keV). The previous outburst was observed with *RXTE* to a flux level over an order of magnitude lower (Sobczak et al. 2000). Although the behavior of the soft component shows some similarities between the two outbursts, the evolution of the power-law component was completely different. In contrast to the 2000 decay, Γ remained at between 2.2 and 2.6 down to a 2–20 keV flux level of 5×10^{-10} ergs cm^{-2} s^{-1} for the previous outburst. The subsequent observations showed some hardening of the power-law component, but the energy spectrum did not show clear evidence for a transition to the hard state. For both outbursts, a disk-blackbody component with an inner disk temperature of 0.6–0.7 keV was present when the source flux was near 6×10^{-9} ergs cm^{-2} s^{-1}, and in both cases, a drop in temperature occurred as the source decayed. As discussed by Sobczak et al. (2000), the evolution of the soft component could indicate an increase in the inner radius of the accretion disk. If this is the case, it is likely that the inner radius increased more rapidly with flux for the 2000 decay than for the previous decay since the soft component was detected down to very low flux levels during the 1998–1999 decay, while we did not detect the soft component after observation 2.

We also used *RXTE* to monitor the BHC X-ray transient 4U 1630−47 during the decay of its 1998 outburst (Tomsick & Kaaret 2000). The source made a transition to the hard state, and we observed 4U 1630−47 several times during the transition, making it interesting to compare its behavior to that of XTE J1550−564. For 4U 1630−47, Γ hardened from 2.3 to 1.8 over a period of 8 days, and the soft component became undetectable during the transition. Although our observations did not include the beginning of the XTE J1550−564 transition, Γ changed from 2.05 to 1.67 in 3.4 days, suggesting that the transition timescale is similar for the two sources. The estimated transition luminosities are similar for the two sources. Taking the second XTE J1550−564 observation as the midpoint of the transition and assuming isotropic X-ray emission gives a transition luminosity of 9×10^{36} ergs s^{-1} (3–25 keV, unabsorbed). As mentioned above, distance estimates for XTE J1550−564 range from 2.5 to 6 kpc, and here we adopt a distance of 4 kpc. For 4U 1630−47, we estimated a transition luminosity of 7×10^{36} ergs s^{-1} (2.5–20 keV).

5.2. *Spectral Evolution after the Hard-State Transition*

After the source made a transition to the hard state, Figure 6 shows that the power-law index remained very close to 1.6 until the last *RXTE* observation, where Γ showed a marginally significant increase to 1.73 ± 0.06. Although statistical significance of the change is not high,

spectral softening at low luminosities is predicted if an ADAF is present (Esin, McClintock, & Narayan 1997) since the X-ray emission is dominated by inverse Comptonization from the thermal distribution of electrons in the ADAF region. As the mass accretion rate drops, the predicted spectrum gradually softens since the optical depth of the ADAF region decreases, leading to a decrease in the Compton y-parameter. The *Chandra* spectrum provides evidence for further softening at low luminosities, which is also a prediction of the ADAF model. As shown in Figure 6, the lower limit on Γ for the *Chandra* observation is 1.82 based on the 90% confidence error bars, representing reasonably good evidence for spectral softening.

Although there is evidence that spectral evolution occurred for XTE J1550−564 between the *RXTE* observations and the *Chandra* observations, it is not clear whether this evolution occurred gradually (as predicted by ADAF models) or suddenly as the source flux decayed. In fact, not many X-ray observations of BHC systems have been made in the luminosity gap between our last *RXTE* observation, where the 3–25 keV luminosity was 9.6×10^{35} ergs s^{-1}, and our *Chandra* observations, where the mean unabsorbed 0.5–7 keV luminosity was 6.7×10^{32} ergs s^{-1}, and only a few of these observations have produced useful energy spectra. *BeppoSAX* observations of the BHC GX 339−4 at 7×10^{33} ergs s^{-1} indicate that it remains relatively hard ($\Gamma = 1.64 \pm 0.13$) at low luminosity (Kong et al. 2000). Similarly, an *Advanced Satellite for Cosmology and Astrophysics* (*ASCA*) observation of XTE J1748−288 at a luminosity of 4×10^{35} ergs s^{-1} (assuming a distance of 8.5 kpc) gave $\Gamma = 1.56^{+0.34}_{-0.31}$ (Kotani et al. 2000). However, *Ginga* observations of GS 1124−68 show some evidence for spectral softening. A power-law index of $\Gamma = 1.84^{+0.03}_{-0.04}$ was measured at a source luminosity of 5×10^{34} ergs s^{-1} (assuming a distance of 2.5 kpc), even though $\Gamma = 1.5$ was obtained when the source was brighter. V404 Cyg is the one BHC X-ray transient with a quiescent luminosity higher than the XTE J1550−564 luminosity during our *Chandra* observations (Garcia et al. 2001). This source has been observed in quiescence at a luminosity near 10^{33} ergs s^{-1} by both *ASCA* and *BeppoSAX*, and power-law indices of $2.1^{+0.5}_{-0.3}$ (Narayan, Barret, & McClintock 1997), $1.7^{+0.3}_{-0.2}$ (Asai et al. 1998), and $1.9^{+0.6}_{-0.5}$ (Campana, Parmar, & Stella 2001) have been reported. This provides some evidence for spectral softening at low luminosities since values of Γ between 1.3 and 1.5 were observed for V404 Cyg during outburst (Tanaka & Lewin 1995).

The results discussed in the previous paragraph appear to indicate that the evolution of Γ as the luminosity decreases is not consistent from source to source. Spectral softening is observed for GS 1124−68 and is probably observed for XTE J1550−564 and V404 Cyg, while the observations show that the spectra of GX 339−4 and XTE J1748−288 remain hard down to relatively low luminosities. The latter type of behavior is difficult to explain with the ADAF model, but such behavior can be explained if the X-ray emission is due to magnetic flares above the disk (Galeev et al. 1979; di Matteo, Celotti, & Fabian 1999). In fact, a magnetic flare model has been used to explain the spectral evolution of GX 339−4 (di Matteo et al. 1999). A sharp transition to a quiescent state would be expected if the emission in the hard state is due to magnetic flares. This is because the MHD turbulence that is responsible for the magnetic flares (Balbus & Hawley 1991) is expected to turn off when the accretion disk temperature drops (Gammie & Menou 1998). Other accretion physics may also be important at low luminosities that will alter the X-ray emission properties. For low-viscosity accretion flows, theory and simulations show that convection plays an important role (Narayan, Igumenshchev, & Abramowicz 2000). In the X-ray band, convection-dominated accretion flows (CDAFs) produce most of their emission via thermal bremsstrahlung in contrast to the mechanisms at work for the ADAF and magnetic flare models. Rather than being a pure power law, CDAF models predict that a peak will be observed in the X-ray band (Ball, Narayan, & Quataert 2001). Although the XTE J1550−564 *Chandra* spectrum does not show evidence for such a peak, the statistical quality of the data does not allow us to rule this out either.

The radio observations of XTE J1550−564 during the 2000 outburst give evidence for the presence of a compact jet only after the transition to the hard state (Corbel et al. 2001). An inverted radio spectrum was observed on MJD 51,697.14 within a day of observation 12. Multiwavelength observations suggest that the synchrotron emission from the jet extends from the radio to at least the near-IR and optical range, indicating a very powerful compact jet (Corbel et al. 2001). None of the models discussed here (ADAF, CDAF, and magnetic flares) include outflows required to produce such a jet. Further theoretical modeling, including outflows, would be of great interest to allow a comparison with the broadband (radio, IR, optical, and X-ray) behavior of the source. This is currently under investigation for BHC systems in the hard state (e.g., Markoff, Falcke, & Fender 2001).

5.3. *XTE J1550−564 and X-Ray Transients at Low Luminosities*

X-ray observations of transient systems in quiescence suggest that, for a given mass accretion rate, black hole systems are significantly less luminous than neutron star systems (Garcia et al. 2001). Since the ADAF model interprets this as being due to the presence of an event horizon for the black hole systems (Narayan et al. 1997), it is important to establish this trend using as many systems as possible, and it is interesting to compare the minimum luminosity we observe for XTE J1550−564 to the quiescent luminosities of other transients. During our first *Chandra* observation, the unabsorbed 0.5–7 keV luminosity was between 2×10^{32} and 1.2×10^{33} ergs s^{-1} based on the 2.5–6 kpc distance range. Although XTE J1550−564 is an established black hole system, this range of luminosities is comparable to neutron star systems and is 25–150 times brighter than the median quiescent black hole luminosity for detections given in Garcia et al. (2001). While this could have important implications for the question of whether the quiescent luminosities of black holes and neutron stars are different, we believe that it is unlikely that the system was in true quiescence during our *Chandra* observations. The luminosity increase observed for our second *Chandra* observation and the minioutburst that occurred about 4 months later both suggest the continuation of significant variability in the mass accretion rate. Perhaps XTE J1550−564 will prove to be similar to GRO J1655−40, which was detected at relatively high X-ray luminosity between two outbursts but was later observed by *Chandra* with an order of magnitude lower luminosity. Since our observations provide only an upper limit on the true quiescent luminosity, future

X-ray observations of XTE J1550−564 are necessary to determine this quantity.

The *Chandra* spectrum for XTE J1550−564 provides an opportunity for comparison to the neutron star system Cen X-4. This comparison is especially useful because Cen X-4 was observed with the same instrument (ACIS back-illuminated chip) at a luminosity within a factor of a few of XTE J1550−564 (Rutledge et al. 2001). A soft component and a power law are necessary to fit the Cen X-4 spectrum in contrast to XTE J1550−564, where the spectrum requires only one component. It is very likely that the Cen X-4 soft component is thermal emission from the surface of the neutron star, and it can be modeled as a blackbody with a temperature of 0.175 keV. Using fit parameters from Rutledge et al. (2001), the blackbody component contributes 62% of the total 0.5–7 keV unabsorbed flux for Cen X-4. Although a two-component model does not improve the fit for XTE J1550−564, we fitted the spectrum with a blackbody plus power-law model to make a more direct comparison with Cen X-4. The blackbody parameters are not well constrained for XTE J1550−564, and we fixed the temperature to 0.175 keV to calculate an upper limit on the blackbody flux. The 90% confidence upper limit on the ratio of the blackbody flux to the total 0.5–7 keV unabsorbed flux is 32%, which is significantly lower than the measured value for Cen X-4. Finally, we note that the Cen X-4 power-law component has a photon index of $1.2^{+0.4}_{-0.5}$, which is considerably harder than the power law observed for XTE J1550−564. We conclude that the Cen X-4 and XTE J1550−564 spectra are significantly different and speculate that this is related to the fact that one contains a neutron star while the other contains a black hole.

5.4. *High-Energy Cutoff*

Our results indicate that the high-energy cutoff for XTE J1550−564 is stronger in the HEXTE band during the state transition (observations 2, 3, and 4) than after the source reaches the hard state (observations 5–12). It may be possible to explain this in the context of the standard picture that the hard X-ray emission is due to inverse Comptonization of soft photons by thermal electrons where the measured folding energy ($E_{\rm fold}$) is close to the electron temperature. In this picture, the lower value of $E_{\rm fold}$ during the transition indicates a lower electron temperature during the transition than in the hard state. The temperature change could be related to the observed drop in the strength of the soft component during the transition to the hard state since a drop in soft-photon cooling would lead to a higher temperature for the Comptonizing electrons. However, the lack of a significant cutoff for observation 1 is a problem for this picture since the strongest soft component is seen in this case. A different mechanism, such as bulk-motion Comptonization (Chakrabarti & Titarchuk 1995), may be necessary to explain the hard X-ray emission seen during observation 1. The possibility that both these mechanisms may operate in accreting BHCs has been discussed previously by several authors (e.g., Ebisawa, Titarchuk, & Chakrabarti 1996).

The folding energy we obtain for observations 5–12 ($E_{\rm fold} = 462^{+342}_{-241}$ keV, 68% confidence errors) is high compared to the folding energies reported by Grove et al. (1998) for accreting BHCs in the hard state, which are between 87 and 132 keV. Since it is thought that the high-energy emission in the hard state is produced via thermal Comptonization, this raises the question of whether realistic accretion disk models can be constructed with high enough electron temperatures to give the values of $E_{\rm fold}$ we observe for XTE J1550−564. Detailed comparisons between ADAF predictions and the XTE J1550−564 spectra will be a subject of future work, but a preliminary result is that the ADAF model underpredicts the level of high-energy emission (Esin & Tomsick 2001). Emission mechanisms other than thermal Comptonization may be required to explain the high-energy emission such as Comptonization from a nonthermal electron distribution or possibly synchrotron emission (Markoff, Falcke, & Fender 2001). Since the compact jet is a possible source of high-energy emission, correlations between hard X-ray emission and radio or IR emission (such as those mentioned in § 2) are especially interesting.

6. SUMMARY AND CONCLUSIONS

We report on spectral analysis of *RXTE* and *Chandra* observations made during the decay of the 2000 outburst from the BHC XTE J1550−564. A rapid and approximately exponential drop in flux was observed early in the decay with an *e*-folding time of 6.0 days. The evolution of the energy spectrum during this time indicates that the system made a transition to the hard state with a drop in the flux of the soft component in the *RXTE* energy band and a hardening of the power law used to model the hard component. The transition occurred near a luminosity of 9×10^{36} ergs s^{-1} assuming a source distance of 4 kpc. The spectral changes, the transition luminosity, and the timescale for the transition are similar to those we have previously observed for another BHC, 4U 1630−47. However, we note that the XTE J1550−564 hard-component behavior was significantly different during the decay of the 1998–1999 outburst.

The mean luminosity during the *Chandra* observations is within a factor of a few of the quiescent luminosity of the neutron star system Cen X-4. In contrast to Cen X-4 (Rutledge et al. 2001), the XTE J1550−564 spectrum is well described by a single power-law component with a photon index (Γ) of $2.30^{+0.41}_{-0.48}$ (90% confidence). Since we measured a value of 1.6 for Γ in the hard state, the *Chandra* spectrum provides reasonably good evidence for spectral softening at low luminosities. ADAF models predict gradual spectral softening as the luminosity drops, but our observations do not allow us to determine whether the spectral evolution is gradual or sudden. Future observations to measure the spectral evolution at intermediate luminosities are important and may allow us to distinguish between ADAF models and magnetic flare models. The lowest luminosity we measure for XTE J1550−564 with *Chandra* is 5×10^{32} ergs s^{-1}. This is probably not the true quiescent luminosity, but it represents a useful upper limit on this quantity.

Although a highly significant break is seen in the HEXTE band for observation 3 during the state transition, the break becomes weaker once the source reaches the hard state. For XTE J1550−564, the hard-state cutoff energy is higher than those found for other BHCs (Grove et al. 1998), and this may indicate the presence of nonthermal emission. More theoretical and observational work is necessary to understand the mechanism responsible for the high-energy emission. Observations of BHC X-ray transients in their hard state with the *International Gamma-Ray Astrophysics Laboratory* (*INTEGRAL*) will be especially useful.

We would like to thank *Chandra* director Harvey Tananbaum for granting Director's Discretionary Time and Jean Swank for assistance with *RXTE* observations. We also thank Raj Jain for providing optical and IR results prior to publication. J. A. T. acknowledges useful discussions with Ann Esin. This material is based upon work supported by the National Aeronautics and Space Administration under grant NAG 5-10886. P. K. acknowledges partial support from NASA grant NAG 5-7405.

REFERENCES

Asai, K., Dotani, T., Hoshi, R., Tanaka, Y., Robinson, C. R., & Terada, K. 1998, PASJ, 50, 611
Balbus, S. A., & Hawley, J. F. 1991, ApJ, 376, 214
Ball, G. H., Narayan, R., & Quataert, E. 2001, ApJ, 552, 221
Bradt, H. V., Rothschild, R. E., & Swank, J. H. 1993, A&AS, 97, 355
Campana, S., Parmar, A. N., & Stella, L. 2001, A&A, 372, 241
Campbell-Wilson, D., McIntyre, V., Hunstead, R., Green, A., Wilson, R. B., & Wilson, C. A. 1998, IAU Circ. 7010
Cash, W. 1979, ApJ, 228, 939
Chakrabarti, S., & Titarchuk, L. G. 1995, ApJ, 455, 623
Chen, W., Shrader, C. R., & Livio, M. 1997, ApJ, 491, 312
Corbel, S., et al. 2001, ApJ, 554, 43
Cui, W., Zhang, S. N., Chen, W., & Morgan, E. H. 1999, ApJ, 512, L43
di Matteo, T., Celotti, A., & Fabian, A. C. 1999, MNRAS, 304, 809
Ebisawa, K., Titarchuk, L., & Chakrabarti, S. K. 1996, PASJ, 48, 59
Ebisawa, K., et al. 1994, PASJ, 46, 375
Esin, A. A., McClintock, J. E., & Narayan, R. 1997, ApJ, 489, 865
Esin, A. A., & Tomsick, J. A. 2001, AAS Meeting, 198, 1001
Galeev, A. A., Rosner, R., & Vaiana, G. S. 1979, ApJ, 229, 318
Gammie, C. F., & Menou, K. 1998, ApJ, 492, L75
Garcia, M. R., McClintock, J. E., Narayan, R., Callanan, P., Barret, D., & Murray, S. S. 2001, ApJ, 553, L47
Grove, J. E., Johnson, W. N., Kroeger, R. A., McNaron-Brown, K., Skibo, J. G., & Phlips, B. F. 1998, ApJ, 500, 899
Hannikainen, D., et al. 2001, in Proc. 4th *INTEGRAL* Workshop, in press (Noordwijh: ESA)
Homan, J., Wijnands, R., & van der Klis, M. 1999, IAU Circ. 7121
Homan, J., et al. 2001, ApJS, 132, 377
Jain, R., Bailyn, C., & Tomsick, J. 2001, IAU Circ. 7575
Jain, R. K., Bailyn, C. D., Orosz, J. A., McClintock, J. E., & Remillard, R. A. 2001, ApJ, 554, L181
Jain, R. K., Bailyn, C. D., Orosz, J. A., Remillard, R. A., & McClintock, J. E. 1999, ApJ, 517, L131
Kalemci, E., Tomsick, J., Rothschild, R., Pottschmidt, K., & Kaaret, P. 2001, ApJ, 563, 239 (Paper II)
Kaptein, R., in't Zand, J. J. M., & Heise, J. 2001, IAU Circ. 7588
Knight, F. K. 1982, ApJ, 260, 538
Kong, A. K. H., Kuulkers, E., Charles, P. A., & Homer, L. 2000, MNRAS, 312, L49
Kotani, T., et al. 2000, ApJ, 543, L133
Lightman, A. P., & White, T. R. 1988, ApJ, 335, 57
Makishima, K., et al. 1986, ApJ, 308, 635
Markoff, S., Falcke, H., & Fender, R. 2001, A&A, 372, L25
Marshall, F. E., Takeshima, T., & in't Zand, J. 2000, IAU Circ. 7363
Massaro, E., Cusumano, G., Litterio, M., & Mineo, T. 2000, A&A, 361, 695
Miller, J., et al. 2001a, MNRAS, submitted
———. 2001b, ApJ, submitted
Narayan, R., Barret, D., & McClintock, J. E. 1997, ApJ, 482, 448
Narayan, R., Garcia, M. R., & McClintock, J. E. 1997, ApJ, 478, L79
Narayan, R., Igumenshchev, I. V., & Abramowicz, M. A. 2000, ApJ, 539, 798
Orosz, J., Bailyn, C., & Jain, R. 1998, IAU Circ. 7009
Orosz, J. A., van der Klis, M., McClintock, J. E., Jain, R. K., Bailyn, C. D., & Remillard, R. A. 2001, Astron. Telegram, 70, 70
Predehl, P., & Schmitt, J. H. M. M. 1995, A&A, 293, 889
Remillard, R. A., McClintock, J. E., Sobczak, G. J., Bailyn, C. D., Orosz, J. A., Morgan, E. H., & Levine, A. M. 1999, ApJ, 517, L127
Remillard, R. A., Sobczak, G. J., Muno, M. P., & McClintock, J. E. 2001, ApJ, submitted
Rothschild, R. E., et al. 1998, ApJ, 496, 538
Rutledge, R. E., Bildsten, L., Brown, E. F., Pavlov, G. G., & Zavlin, V. E. 2001, ApJ, 551, 921
Sánchez-Fernández, C., et al. 1999, A&A, 348, L9
Smith, D. A. 1998, IAU Circ. 7008
Smith, D. A., et al. 2000, IAU Circ. 7399
Sobczak, G. J., McClintock, J. E., Remillard, R. A., Levine, A. M., Morgan, E. H., Bailyn, C. D., & Orosz, J. A. 1999, ApJ, 517, L121
Sobczak, G. J., et al. 2000, ApJ, 544, 993
Tanaka, Y., & Lewin, W. H. G. 1995, X-Ray Binaries (Cambridge: Cambridge Univ. Press)
Titarchuk, L. 1994, ApJ, 434, 570
Tomsick, J. A., & Kaaret, P. 2000, ApJ, 537, 448
Tomsick, J. A., Smith, E., Swank, J., Wijnands, R., & Homan, J. 2001, IAU Circ. 7575
Valinia, A., & Marshall, F. E. 1998, ApJ, 505, 134
van der Klis, M. 1995, X-Ray Binaries (Cambridge: Cambridge Univ. Press)
Wilson, C. D., & Done, C. 2001, MNRAS, 325, 167

3.5.4

Multiwavelength Observations of the Galactic Black Hole Transient 4U 1543-47 during Outburst Decay : State Transitions and Jet Contribution.

Article publié dans :

Astrophys. J., 2005, 622, 508-519

Kalemci, E., Tomsick, J. A., Buxton, M. M., Rothschild, R. E., Pottschmidt, K., Corbel, S., Brocksopp, C., Kaaret, P.

The Astrophysical Journal, 622:508–519, 2005 March 20

MULTIWAVELENGTH OBSERVATIONS OF THE GALACTIC BLACK HOLE TRANSIENT 4U 1543−47 DURING OUTBURST DECAY: STATE TRANSITIONS AND JET CONTRIBUTION

E. Kalemci,[1] J. A. Tomsick,[2] M. M. Buxton,[3] R. E. Rothschild,[2] K. Pottschmidt,[4,5] S. Corbel,[6] C. Brocksopp,[7] and P. Kaaret[8]

Received 2004 September 3; accepted 2004 November 24

ABSTRACT

Multiwavelength observations of Galactic black hole (GBH) transients during state transitions and in the low/hard state may provide detailed information on the accretion structure of these systems. The object 4U 1543−47 is a GBH transient that was covered exceptionally well in X-rays and the infrared (daily observations) and reasonably well in the optical and radio during its outburst decay in 2002. When all the available information is gathered from the intermediate and the low/hard states, 4U 1543−47 makes an important contribution to our understanding of state transitions and the role of outflows in the high-energy emission properties of black hole binaries. The evolution of the X-ray spectral and temporal properties and the infrared light curve place strong constraints on different models to explain the overall emission from accreting black holes. The overall spectral energy distribution is consistent with a synchrotron origin for the optical and infrared emission; however, the X-ray flux is above the power-law continuation of the optical and infrared flux. The infrared light curve, the HEXTE light curve, and the evolution of the X-ray photon index indicate that the major source of hard X-rays cannot be direct synchrotron radiation from an acceleration region in a jet for most of the outburst decay.

Subject headings: accretion, accretion disks — binaries: close — black hole physics — stars: individual (4U 1543−47) — X-rays: binaries

1. INTRODUCTION

Galactic black hole (GBH) transients are binary systems that can show orders-of-magnitude increases in luminosity during outbursts caused by sudden, dramatic increases of mass accretion onto compact objects. During an outburst, a GBH transient often follows a specific sequence of X-ray spectral states; it is in the "hard" or "low/hard" (LH) state at the beginning and also during the decay of an outburst. Between the rise and the decay, when the 2–10 keV luminosity is high, the system is usually in the "thermal-dominant" (TD) state (historically this was called the high/soft state), and sometimes in the "steep power-law" state (historically, the very high state; see McClintock & Remillard 2003 for a detailed discussion of spectral states). They can also be found in an intermediate state (IS), where source characteristics do not fit into the TD or LH state but show various combinations of these states, especially close to state transitions (McClintock & Remillard 2003). The sequence of spectral states may be complicated, or it may be very simple, as some sources stay in the LH state throughout their outbursts (Kalemci 2002; Brocksopp et al. 2004; references therein). However, the systems are almost always found in the LH state during outburst decay (Kalemci 2002), before they return to quiescence (perhaps a continuation of the LH state at very low luminosities; Corbel et al. 2000; Kong et al. 2002; Tomsick et al. 2004).

In terms of timing, the TD state is characterized by a lack or very low level of variability (a few percent rms between 0.04 and 4 Hz), whereas the LH state shows strong variability (∼30% rms in the same band) along with quasi-periodic oscillations (QPOs) in the power density spectrum. Other Fourier analysis–related timing tools, such as "coherence" and "lag" behavior, are also different in each state (see Vaughan & Nowak 1997 and Nowak et al. 1999 for detailed definitions of these quantities). The mean coherence is very high (∼1) in the LH state, and the mean lag is either zero or very low between the 3–6 keV and 6–15 keV bands in the 1–10 Hz frequency range. During the IS and during transitions, however, the coherence is lower and the lag is higher in the same frequency band and between the same energy bands (Pottschmidt et al. 2000; Kalemci 2002).

The relation between the radio emission and the X-ray states has been well established (McClintock & Remillard 2003; see also Corbel et al. 2004 and the recent review by Fender [2005]). In the TD state, the radio emission is often quenched (Fender et al. 1999; Corbel et al. 2000). Optically thin outflows are sometimes detected during state transitions (Fender & Kuulkers 2001; Corbel et al. 2001), and powerful, compact jets are always observed in the LH state (Fender 2001). In addition, there exists a global correlation between the X-ray flux and the radio flux for different sources at different luminosities in the LH state (Corbel et al. 2003; Gallo et al. 2003). The base of the jet might provide the energetic electrons that would create the X-ray power law in the spectrum, establishing the link between the radio and the X-ray flux (Fender 2001). The fact that the lags are higher during state transitions, when the optically thin, large outflows are observed, may also point to a relation between the radio jet and energetic electrons (Pottschmidt et al. 2000; Kalemci et al. 2003). An alternative model is that the X-ray emission is synchrotron in

[1] Space Sciences Laboratory, 7 Gauss Way, University of California at Berkeley, Berkeley, CA 94720-7450.
[2] Center for Astrophysics and Space Sciences, University of California, San Diego, 9500 Gilman Drive, La Jolla, CA 92093-0424.
[3] Department of Astronomy, Yale University, New Haven, CT 06511-8101.
[4] Max-Planck-Institut für Extraterrestrische Physik, Giessenbachstrasse 1, D-85748 Garching, Germany.
[5] *INTEGRAL* Science Data Centre, Chemin d'Ecogia 16, CH-1290 Versoix, Switzerland.
[6] Université Paris VII and Service d'Astrophysique, CEA Saclay, F-91191 Gif-sur-Yvette, France.
[7] Mullard Space Science Laboratory, Holmbury St. Mary, Dorking, Surrey RH5 6NT, UK.
[8] Department of Physics and Astronomy, University of Iowa, Iowa City, IA 52242-1479.

nature and comes directly from a shock region in the jet (Falcke & Biermann 1999; Markoff et al. 2001). This model can explain the radio–X-ray flux correlation naturally; however, it fails to make any predictions about the details of the X-ray spectrum.[9]

The daily observations of transients in the optical and the infrared by the YALO consortium (Bailyn et al. 1999) provide another dimension in the study of GBH transients. A secondary maximum in the *V*, *B*, *I*, *J*, and *K* bands has been observed during the outburst decay of 4U 1543−47 (Buxton & Bailyn 2004). A similar secondary maximum was also observed in the *V*, *I*, and *H* bands during the outburst decay of XTE J1550−564 in 2000 (Jain et al. 2001a). The properties of the optical emission during the secondary maximum of the 2000 outburst of XTE J1550−564 indicate a synchrotron origin from a jet (Corbel et al. 2001), rather than X-ray reprocessing at the outer parts of the accretion disk, which was suggested to explain the optical light curves of the same source in its 1998 outburst (and also other GBH transients; Jain et al. 2001a, 2001b). X-ray reprocessing as the origin of optical emission has also been questioned by Brocksopp et al. (2004) because of a lack of correlation between the X-ray and optical light curves of V404 Cyg, GRO J1719−24, GRO J0422+32, GS 1354−64, and XTE J1118+480. The observations of GX 339−4 in the optical and the near-infrared (NIR) in the LH state show a nonthermal, optically thin synchrotron component that can be extrapolated down to the X-ray spectrum (Corbel & Fender 2002). A very recent study of GX 339−4 with good optical, infrared, and X-ray monitoring points out that in the LH state, the NIR emission has a synchrotron origin in a jet; however, the source of the optical emission may be a combination of a jet, the disk, and possibly a compact corona in this source (Homan et al. 2005). In addition, the LH state during the rise of the 2002 outburst of GX 339−4 showed a strong correlation between X-ray flux and optical/NIR, similar to the radio–X-ray flux correlation (Homan et al. 2005).

One of the most interesting epochs of an outburst is its decay, because it is almost guaranteed that there will be a transition to the LH state that provides additional information about the system through various timing-analysis techniques, and also through strong radio emission. Analysis of state transitions helps us probe the accretion dynamics of these systems. Our group has been observing GBH transients during outburst decays in X-rays with the *Rossi X-Ray Timing Explorer* (*RXTE*) and in radio to understand the evolution before, during, and after the transition to the LH state (Kalemci et al. 2001; Tomsick et al. 2001; Kalemci et al. 2003; Tomsick et al. 2003). A uniform analysis of all GBH transients observed with approximately daily coverage with *RXTE* between 1996 and 2001 resulted in a better understanding of the evolution of spectral and temporal parameters during the outburst decay (Kalemci et al. 2004). The most striking of all the results is that the sharpest change indicating a state transition is observed in the timing properties (usually a jump in the rms amplitude of variability from less than a few percent to tens of percent in less than a day). This change in the rms amplitude is often (but not always) accompanied by a sharp increase in the power-law flux. Such sharp changes in the rms amplitude of variability were noted as the times of state transition in Kalemci et al. (2004), and the same convention is applied here.

In this work, we will try to obtain a coherent picture of changes in the physical properties of a GBH transient, 4U 1543−47, around state transitions and also deep in the LH state, using multiwavelength observations. This object was discovered by the *Uhuru* satellite on 1971 August 17 (Matilsky et al. 1972). The source was observed again in outburst in 1983, in 1992, and also in 2002 (Kitamoto et al. 1984; Harmon et al. 1992; Miller & Remillard 2002; Brocksopp et al. 2004). The optical counterpart was found by Pedersen (1983). Initial dynamical mass measurements during quiescence established this source as a black hole binary system with a compact-object mass between 2.7 and 7.5 $M_{\odot}$ (Orosz et al. 1998). A more accurate value of 9.4 ± 2.0 $M_{\odot}$ is given by Park et al. (2004) based on a work in preparation by J. Orosz. The 2002 outburst was first detected by the All-Sky Monitor (ASM) on *RXTE* on MJD 52,442 (Miller & Remillard 2002; Park et al. 2004). Around a month later, as the outburst was decaying, our group started its daily monitoring campaign with *RXTE* and caught the transition to a harder state on MJD 52,479 (Kalemci et al. 2002), although subsequent analysis in this work indicates that the transition started earlier. An analysis of the *RXTE* data before the LH state, with an emphasis on broad iron reflection lines, is given by Park et al. (2004). Figure 1 shows the ASM light curve of the overall outburst, the epoch we analyzed, and the dates of pointed observations used in this work. The source was also detected and observed in the radio and optical bands (see Park et al. 2004, Buxton & Bailyn 2004, and §§ 2.2 and 2.3 in this work for more details).

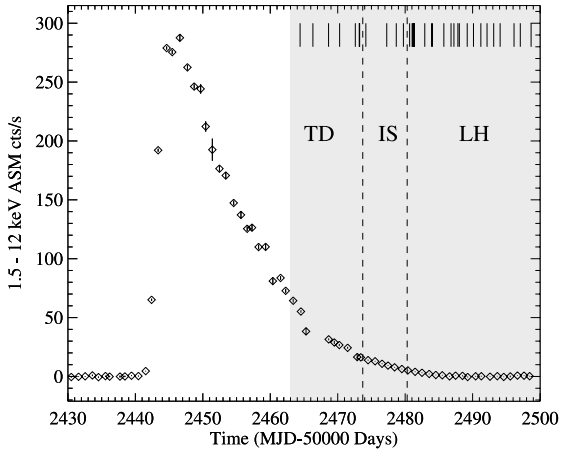

FIG. 1.—The 1.5–12 keV ASM light curve of the 2002 outburst of 4U 1543−47. We worked on the decay part of the outburst and analyzed *RXTE* data shown in the gray region. The vertical bars indicate pointed PCA observations. The dashed lines indicate approximate times of state transitions.

Here we report on the *RXTE* observations during outburst decay and combine the results with the optical, infrared, and radio information to understand jet formation and its effects on the spectral and temporal properties of 4U 1543−47.

2. OBSERVATIONS AND ANALYSIS

2.1. *RXTE Observations*

We triggered our monitoring program (P70124, PI: J. A. T.) with *RXTE* after the source's ASM count rate dropped below 15 counts s^{-1}, and the first observation took place on MJD 52,478.7. The source was already in transition from the TD to the LH state, showing broadband variability and QPOs (Kalemci et al. 2002). While the nearly daily 1–3 ks monitoring from program P70124 was going on, we triggered P70128 (PI: E. K.),

[9] Only recently, the reflection from the disk has been incorporated into the synchrotron jet model by Markoff & Nowak (2004). See also Körding & Falcke (2004) for a recent work on timing properties from this model.

TABLE 1
SPECTRAL PARAMETERS

Obs.[a]	MJD	Γ	T_{in} (keV)	Flux (10^{-10} ergs cm^{-2} s^{-1})		Notes
				Power-Law	DBB	
Thermal-dominant State						
1A.....	52,464.42	2.32 ± 0.09	0.70 ± 0.01	10.19 ± 0.97	53.92 ± 0.47	
2A.....	52,466.32	2.39 ± 0.07	0.67 ± 0.01	11.96 ± 0.91	38.20 ± 0.43	
3A.....	52,468.64	2.10 ± 0.11	0.65 ± 0.01	5.06 ± 0.68	29.44 ± 0.28	
4A.....	52,470.28	2.32 ± 0.04	0.62 ± 0.01	4.99 ± 0.59	21.72 ± 0.24	
5A.....	52,472.61	2.49 ± 0.15	0.57 ± 0.01	4.69 ± 0.50	12.84 ± 0.14	
6A.....	52,473.19	2.57 ± 0.03	0.54 ± 0.01	7.69 ± 0.58	10.62 ± 0.14	
7A.....	52,473.25	2.51 ± 0.04	0.54 ± 0.01	6.36 ± 0.52	10.99 ± 0.16	
Intermediate State						
8A.....	52,474.17	2.54 ± 0.03	0.53 ± 0.01	10.38 ± 0.29	7.781 ± 0.103	Variability, state transition
9A.....	52,477.27	2.43 ± 0.01	0.47 ± 0.01	12.78 ± 0.27	2.783 ± 0.074	QPO
10B.....	52,478.68	2.43 ± 0.01	0.43 ± 0.01	11.75 ± 0.32	1.676 ± 0.058	QPO
11B.....	52,479.74	2.40 ± 0.02	0.42 ± 0.02	9.26 ± 0.12	1.324 ± 0.041	QPO
Low/Hard State						
12B.....	52,480.66	2.10 ± 0.02	0.37 ± 0.03	12.29 ± 0.10	0.365 ± 0.026	Spectral hardening, QPO
13C.....	52,481.03	2.10 ± 0.01	0.33 ± 0.03	11.44 ± 0.11	0.305 ± 0.018	High-energy cutoff, QPO
14C.a.....	52,481.16	2.02 ± 0.01	0.40 ± 0.02	11.56 ± 0.09	0.360 ± 0.028	High-energy cutoff, QPO
14C.b.....	52,481.23	2.00 ± 0.01	0.35 ± 0.03	12.01 ± 0.11	0.237 ± 0.019	High-energy cutoff, QPO
14C.c.....	52,481.29	1.96 ± 0.01	0.33 ± 0.01	12.20 ± 0.11	0.205 ± 0.012	High-energy cutoff, QPO
14C.d.....	52,481.36	1.97 ± 0.01	0.35 ± 0.02	11.97 ± 0.21	0.217 ± 0.018	High-energy cutoff (?), QPO
15B.....	52,482.91	1.78 ± 0.04	0.35	9.77 ± 0.09	0.116 ± 0.036	Smedge optical depth begins to drop; the disk temperature is fixed from this observation on
16B.....	52,483.93	1.70 ± 0.02	0.35	8.00 ± 0.09	0.056 ± 0.015	Infrared flux begins to rise
17B.....	52,484.03	1.71 ± 0.02	0.35	7.88 ± 0.16	0.031 ± 0.016	
18B.....	52,485.74	1.65 ± 0.04	0.35	4.49 ± 0.06	0.024 ± 0.016	
19B.....	52,486.80	1.64 ± 0.04	0.35	3.17 ± 0.03	0.027 ± 0.008	
20C.....	52,487.23	1.63 ± 0.01	0.35	2.62 ± 0.01	0.028 ± 0.004	MOST radio detection
21C.....	52,487.82	1.70 ± 0.02	0.35	2.17 ± 0.03	0.023 ± 0.002	
22B.....	52,488.03	1.68 ± 0.02	0.35	1.96 ± 0.03	0.020 ± 0.004	Smedge is not required; Galactic ridge emission (<5% of the total flux) is included
23B.....	52,489.20	1.70 ± 0.04	0.35	1.25 ± 0.03	0.020 ± 0.005	
24B.....	52,490.13	1.75 ± 0.02	0.35	1.05 ± 0.01	0.020 ± 0.005	Only PCA used from this observation on; ATCA radio detection
25B.....	52,491.22	1.88 ± 0.04	0.35	0.76 ± 0.02	0.014 ± 0.001	
26B.....	52,492.14	2.06 ± 0.07	0.35	0.56 ± 0.02	0.011 ± 0.002	No timing after this observation, poor statistics
27B.....	52,493.13	1.99 ± 0.06	0.35	0.47 ± 0.02	0.013 ± 0.002	Galactic ridge emission less than 15% of the total flux
28B.....	52,494.08	2.10 ± 0.05	0.35	0.47 ± 0.02	0.013 ± 0.002	
29B.....	52,496.14	2.24 ± 0.07	0.35	0.30 ± 0.01	0.010 ± 0.001	Galactic ridge emission less than 25% of the total flux
30B.....	52,497.07	2.11 ± 0.10	0.35	0.29 ± 0.01	0.010 ± 0.002	
31B.....	52,498.67	2.22 ± 0.12	0.35	0.22 ± 0.01	0.008 ± 0.002	

[a] "A" for observations from P70133 (PI: J. McClintock), "B" for observations from P70124 (PI: J. A. T.), and "C" for observations from P70128 (PI: E. K.). Observation 14 from P70128 is divided into four.

which provided longer exposures (∼20 ks) to investigate the spectral and temporal properties of the source in greater detail than possible with the daily monitoring observations. For this work, we use the long observations and the first 18 observations of the monitoring program that provided high-quality spectral information. A very interesting part of the outburst, the onset of state transition, occurred before our monitoring observations had begun. To characterize this part, we use archival *RXTE* observations from P70133 (PI: J. McClintock). Table 1 shows the list of the observations used in this work.

2.1.1. *X-Ray Spectral Analysis*

For the major part of the outburst, we used both the PCA and the HEXTE instruments on *RXTE* for the spectral analysis (see Bradt et al. 1993 for instrument descriptions). For the PCA, the 3–25 keV band was used, and the response matrix and the background model were created using the standard FTOOLS (version 5.3) programs. We added 0.8% up to 7 keV and 0.4% above 7 keV as systematic errors based on fits to Crab observations close to ours (for the details of how we estimate systematic uncertainties, see Tomsick et al. 2001). We used all available PCUs for each observation, choosing the combination that would provide the maximum number of counts.

The 15–200 keV band was used for the HEXTE data. We used the response created by FTOOLS and applied the necessary dead-time correction (Rothschild et al. 1998). The HEXTE background subtraction is performed by alternating between observations of source and background fields. The relative normalization between the PCA and HEXTE is kept free. The HEXTE data were included in the spectral analysis until MJD 52,489.

After this date, the statistical quality of the HEXTE data was poor and they were not included in the analysis. We are presenting the first analysis of the HEXTE data for this source.

For all the observations, our first spectral model consisted of absorption (model "phabs" in XSPEC), a smeared edge ("smedge" in XSPEC; Ebisawa et al. 1994), a multicolor disk-blackbody ("diskbb" in XSPEC; Makishima et al. 1986), a power law ("pegpower" in XSPEC), and a narrow Gaussian to model the iron line. This model has been commonly used for the spectral analysis of GBHs in the LH state (Tomsick & Kaaret 2000; Sobczak et al. 2000). A difference between our analysis and that of Park et al. (2004) is the modeling of the iron line. For most of our observations, the statistical quality of the data is not sufficient for reliable iron-line studies, and including a narrow line instead of a broadened Laor-model iron line (Laor 1991) yielded acceptable fits. For consistency and simplicity, we left the iron line narrow, and we did not deduce any physical results from the iron-line fits. The hydrogen column density was fixed to 4×10^{21} cm^{-2}, as used by Park et al. (2004). The width of the smeared edge was fixed to 7 keV. Once we fitted the observations with this model, we added a high-energy cutoff ("highecut" in XSPEC) to the model and refitted. We include the high-energy cutoff in the overall model if an F-test indicates that adding this component significantly improves the fit.

At very low flux levels, the Galactic ridge emission becomes important. Although 4U 1543−47 is not very close to the plane ($b = +5.^{\circ}43$), there was some contribution from the ridge, evident from the detection of a narrow iron line at 6.7 keV. However, even during the observations when 4U 1543−47 was at its faintest (after MJD 52,500), it was still detectable by the PCA. We obtained a scanning observation on MJD 52,547 that showed an increase in the count rate when the *RXTE* pointing position reached the position of 4U 1543−47. Therefore, we were not able to use any of our observations as background for Galactic ridge emission. Instead, we model the ridge emission using the description given by Revnivtsev (2003). We also utilized an *XMM-Newton* observation on MJD 52,504.54 that is close to our faint *RXTE* observations (Miller et al. 2004). We fitted our PCA observation close to the *XMM-Newton* observation with a model consisting of interstellar absorption, a power law to represent 4U 1543−47 with *XMM-Newton* parameters, a second power law, and a narrow Gaussian to represent the ridge emission. We fixed the second power-law index to 2.15, consistent with Revnivtsev (2003), which resulted in a 1.2×10^{-11} erg cm^{-2} s^{-1} Galactic ridge contribution in the 3–25 keV band. If the index is not fixed, it results in harder ridge emission.

2.1.2. *X-Ray Temporal Analysis*

For each observation, we computed the power density spectra (PDSs) and the cross spectra from the PCA data using IDL programs developed at the University of Tübingen (Pottschmidt 2002) for three energy bands: 3–6, 6–15, and 15–30 keV. We also computed a PDS for the combined band of 3–30 keV. Above 30 keV, the source is not significantly above the background for timing analysis. The PDS was normalized as described by Miyamoto & Kitamoto (1989) and corrected for dead-time effects according to Zhang et al. (1995), with a dead time of 10 μs per event. Using 256 s time segments, we investigated the low-frequency QPOs and the timing properties of the continuum up to 256 Hz. We fitted all our PDSs with Lorentzians of the form

$$L_i(f) = \frac{R_i^2 \Delta_i}{2\pi[(f - f_i)^2 + (\frac{1}{2}\Delta_i)^2]}, \quad (1)$$

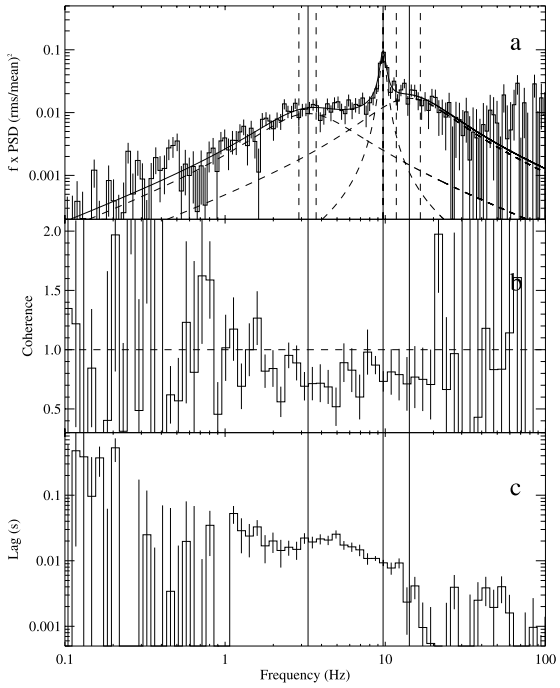

FIG. 2.—(*a*) Power spectrum of observation 9A in the 3–6 keV band, in the form of PDS times frequency. The Lorentzians shown with dashed curves are individual components producing the overall fit, shown with the solid curve. The solid vertical lines are peak frequencies, and the dashed lines show the 1 σ errors on the peak frequencies. (*b*) Coherence function for the same observation between the 3–6 keV band and the 6–15 keV band. (*c*) Fourier lag between the 3–6 keV and the 6–15 keV bands for the same observation.

where subscript i denotes each Lorentzian component in the fit, R_i is the rms amplitude of the Lorentzian in the frequency band from $-\infty$ to $+\infty$, Δ_i is the full width at half-maximum, and f_i is the resonance frequency. A useful property of the Lorentzian is the "peak frequency" at which the Lorentzian contributes maximum power per logarithmic frequency interval:

$$\nu_i = f_i \left(\frac{\Delta_i^2}{4 f_i^2} + 1 \right)^{1/2}. \quad (2)$$

An example power spectrum of 4U 1543−47 in the form of PDS multiplied by frequency is shown in Figure 2*a*. The PDS consists of broad and narrow Lorentzian fit components. In this figure the Lorentzians peak at ν_i, demonstrating the easy identification of characteristic frequencies as peak frequencies of Lorentzian components. The peak frequencies are shown with solid vertical lines in Figure 2*a*. A Lorentzian with quality value $Q_i = f_i/\Delta_i > 2$ is denoted a QPO (such as the narrow feature in the middle in Fig. 2*a*). The rms amplitudes are calculated over a frequency band from zero to infinity.

The cross spectrum leading to the coherence function and time lag constitutes another tool that is available as part of Fourier analysis. The coherence function is a Fourier frequency–dependent measure of the degree of linear correlation between two concurrent light curves measured simultaneously in two energy bands (Nowak et al. 1999). The Fourier time lag is a Fourier frequency–dependent measure of the time delay between two

concurrent time series (Miyamoto & Kitamoto 1989; Nowak et al. 1999). It is related to the phase of the average cross power spectrum between the soft- and hard-band light curves. We use the convention that the sign of the lag is positive when hard photons lag soft photons. Observations of hard lags in GBHs have often been interpreted as evidence of Compton upscattering in a hot electron gas (Payne 1980); however, simple Comptonization models have difficulty explaining the magnitude of the lags (Ford et al. 1999).

We calculated the coherence and lag spectrum between the 3–6 keV and 6–15 keV band light curves for all observations. Not all observations yielded meaningful coherence measurements, and the lag measurements are only meaningful when the coherence is well defined (Nowak et al. 1999). Figure 2 shows the coherence spectrum in the middle panel (Fig. 2*b*) and the lag spectrum in the bottom panel (Fig. 2*c*) for observation 9A. For observations close to the transition (such as the one in Fig. 2), meaningful (not noisy) coherence and lag values were observed between 1 and 10 Hz. To understand the trends in the amplitude of these quantities, we calculated the mean lag and the mean coherence, similar to what was done in Kalemci et al. (2003).

2.2. *Optical and Infrared Observations*

The optical/infrared (OIR) data sets were taken directly from Buxton & Bailyn (2004), and therefore we give only a short summary of how these observations were obtained. The details can be found in Buxton & Bailyn (2004). Daily *V*- and *J*- band images were taken using the YALO 1.0 m telescope from MJD 52,423. Daily *K*-band observations were initiated on MJD 52,440. The optical observations with *B*, *V*, and *I* filters were conducted between MJD 52,442.9 and MJD 52,500.8 using the 74 inch (1.9 m) telescope at Mount Stromlo Observatory. In this work, only the *J*-band light curve is shown, as the important features are most visible in the infrared. The light curves of the remaining bands can be found in Buxton & Bailyn (2004).

2.3. *Radio Observations*

The source was also observed at radio frequencies, and the details of the Molonglo Observatory Syntheses Telescope (MOST) and Giant Metrewave Radio Telescope (GMRT) observations are discussed by Park et al. (2004). Here we give a summary of these observations. The source was detected in radio several times between MJD 52,443 and MJD 52,447 by MOST and GMRT. After MJD 52,447, the source was radio-quiet until MJD 52,487. The upper limits for MOST and GMRT observations on MJD 52,480 are 3.0 and 3.2 mJy, respectively. On MJD 52,487, in the LH state, MOST detected the source at 5.2 ± 0.9 mJy. The final observation by MOST, on MJD 52,496.33, did not detect the source, with an upper limit of 2.4 mJy (Park et al. 2004).

We observed 4U 1543−47 five times during 2002 June and August with the Australia Telescope Compact Array (ATCA). In each case the primary calibrator was PKS 1934−638 and the secondary calibrator was PMN J1603−4904. Observations took place at 4.80 and 8.64 GHz with a bandwidth of 128 MHz. The data were reduced in the standard way with (minimal) flagging, flux and phase calibration, and finally mapping using MIRIAD (Sault et al. 1995). A point source was fitted to the detected emission and the flux density measured. A radio source was detected twice, first on MJD 52,445 at 3.18 ± 0.19 mJy (4.80 GHz) and 2.76 ± 0.07 mJy (8.64 GHz), and second on MJD 52,490 at 4.00 ± 0.05 mJy (4.80 GHz) and 4.19 ± 0.06 mJy (8.64 GHz). On MJD 52,450, 52,451, and 52,453, during the TD state, the source was radio-quiet, with upper limits ranging between 0.2 and 3.0 mJy.

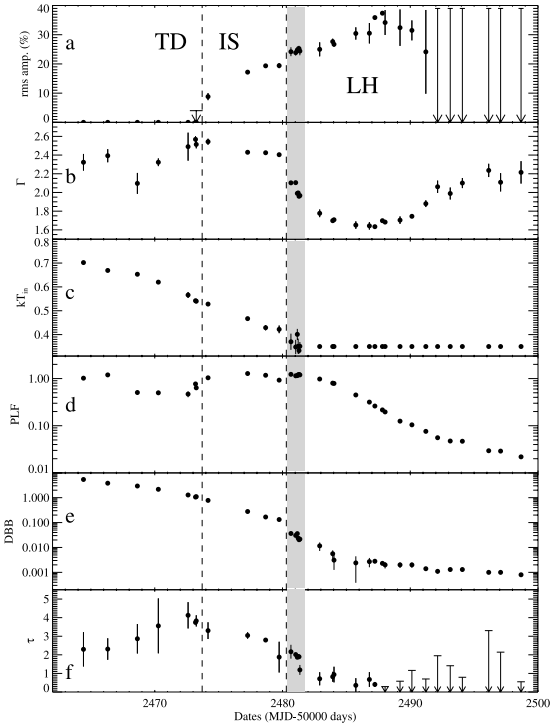

FIG. 3.—Evolution of (*a*) the total rms amplitude of variability in the 3–30 keV band, (*b*) the photon index (Γ), (*c*) the inner disk temperature $kT_{\rm in}$, (*d*) the power-law flux in the 3–25 keV band in units of 10^{-9} ergs cm^{-2} s^{-1}, (*e*) the disk-blackbody flux in the 3–25 keV band in units of 10^{-9} ergs cm^{-2} s^{-1}, and (*f*) the optical depth of the smeared-edge component in the fit. Unabsorbed fluxes were used. For most of the flux measurements, the 1 σ uncertainties are smaller than the plot symbols; 2 σ upper limits are shown with arrows. The dashed lines indicate approximate times of state transitions. The gray area shows the observations during the transition to the LH state.

3. RESULTS

3.1. *Evolution in the X-Ray Regime*

To be able to determine the sequence of events during the decay of the outburst, we investigated the evolution of several spectral and temporal fit parameters, as well as the infrared and radio fluxes. To establish the times of state transitions, we use a plot of several parameters as a function of time (Fig. 3). The main spectral fit parameters are also tabulated in Table 1.

3.1.1. *States and Transitions*

In Figure 3, we marked the time of the first state transition at MJD ∼52,474 (between observations 7A and 8A in Table 1), when the source showed a sharp increase in the rms amplitude of variability accompanied by a sharp increase in the power-law flux. Before this date, the spectra were dominated by the disk component (more than 80% of the total flux in the 3–25 keV band), and hence the source was in the TD state. Within a few days, the power law became the dominant component in the spectrum, and the rms amplitude of variability increased to ∼18%. A QPO appeared in the PDS (see Fig. 4). Note that during this time, while the rms amplitude of variability and the power-law flux were changing rapidly, the photon index remained almost constant, and the inner disk temperature ($T_{\rm in}$) and the disk-blackbody (DBB) flux decayed smoothly, consistent with the observations

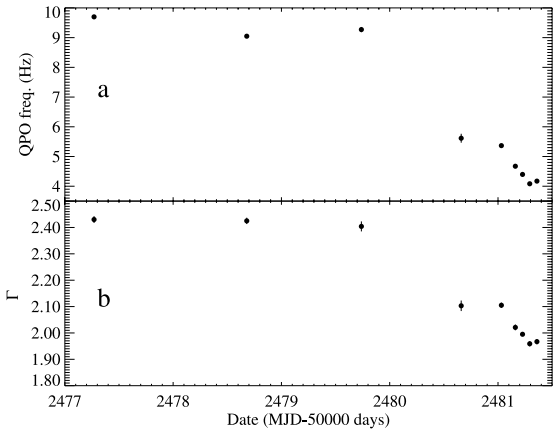

FIG. 4.—(*a*) QPO frequency (for the times when the QPO is observed); (*b*) photon index of 4U 1543−47 in the IS and during the transition to the LH state.

reported in Kalemci et al. (2004). The source was in the IS during this time, based on the softness of the photon index and the relatively comparable contributions of the hard and the soft components to the spectrum.

Around MJD 52,480 (observation 12B in Table 1), another set of sharp changes occurred; the rms amplitude of variability jumped to the ∼24% level, accompanied by a sharp hardening of the photon index and rapid cooling of the inner disk temperature. The power-law flux increased slightly, and the DBB flux decreased, still smoothly but more rapidly. The overall effect was total dominance of the power-law flux over the whole spectrum. After all these rapid changes (shown by the gray area in Fig. 3), the source was in the LH state. In this state, the rms amplitude of variability continued to increase before leveling off at ∼35%. The photon index stayed around 1.7 and then increased slightly after MJD 52,490. The power-law flux decayed smoothly. We fixed $T_{\rm in}$ to 0.35 keV, as the fit did not produce meaningful errors when we let $T_{\rm in}$ vary. The disk component was only affecting the first spectral bin in our fit. As long as the $N_{\rm H}$ value was fixed, the DBB component was required by the *F*-test in the fit, although its relative contribution to the overall flux is less than 5% (see Table 1).

The evolution of the smeared-edge component in the spectral fits is also worth mentioning (see Fig. 3*f* for the evolution of the optical depth). This component was required in the fit until MJD 52,488, although its effects are less and less pronounced after MJD 52,481. For observation 14C.d, the optical depth (which may be related to reflection fraction) in the "smedge" component was ∼2. It dropped down to ∼0.8 on MJD 52,483 and stayed between 0.5 and 0.7 for the next six observations. This evolution may indicate that the reflection fraction dropped as the source went into the LH state. After MJD 52,488, the smedge component was not required in the fit, although the reduced quality of the spectra prevented us from placing strong upper limits on the optical depth of the component after MJD 52,492.

3.1.2. *Short-Timescale Evolution*

The first long observation in program P70128 was well timed, in that it was conducted when the source was in transition to the LH state, while changes were happening rapidly. In order to quantify these changes, we divided the long observation into five sections (naturally separated by occultations, with each piece having three PCUs on). Including these pieces, we show that the QPO frequency and the photon index are strongly correlated (with linear correlation coefficient of 0.995) in the IS and during the transition (see Fig. 4). Note that the last six observations are only 2–3 hours apart! A QPO frequency–photon index correlation has previously been recognized (Kalemci 2002; Vignarca et al. 2003), but we have shown for the first time that it holds on timescales as short as hours.

TABLE 2
HIGH-ENERGY CUTOFF PARAMETERS

Observation	MJD	$E_{\rm cut}$ (keV)	$E_{\rm folding}$ (keV)
13C	52,481.03	56 ± 15	98 ± 53
14C.a	52,481.16	56 ± 10	79 ± 32
14C.b	52,481.23	38 ± 15	197 ± 88
14C.c	52,481.29	45 ± 7	86 ± 28
14C.d	52,481.36	34 ± 13	320^{+410}_{-130}

Another very important result that came out from the long observation is the presence of a high-energy cutoff in the HEXTE spectrum during the state transition. The cutoff is only detected significantly during the observations in which the power-law index was changing rapidly and the transition was taking place (Fig. 3, *gray area*). The cutoff and the folding energies for those observations are given in Table 2. Errors are too large to establish a pattern in the folding energy, except for observation 14C.d, for which the folding energy increased. This increase is probably a sign of a return to regular power-law shape. After this observation, the fit values for the folding energy are far beyond the HEXTE energy range, and a cutoff component is not required by the *F*-test. This is not the first time that the existence of a high-energy cutoff has been observed during a state transition. XTE J1550−564 during its decay in 2000 outburst showed similar behavior: the cutoff was only significant during the transition (Tomsick 2001; Rodriguez 2003).

3.1.3. *Evolution in Temporal Parameters*

The evolution of the total rms amplitude of variability and the QPO frequencies is shown in Figures 3 and 4. The QPO was detected only for the IS and during the transition to the LH state. In the LH state, the PDS can usually be characterized with two broad Lorentzians. Therefore, to understand the evolution of characteristic frequencies, we used the broad Lorentzian with the lowest peak frequency, which is present for all observations (ν_1; see eq. [2]). This evolution is shown in Figure 5*b*. In this figure we also show the evolution of the photon index (Fig. 5*a*), which is known to correlate with the temporal parameters that are discussed in this section. There is a good correlation between the photon index and ν_1, something that has also been observed for other sources (Kalemci 2002; Pottschmidt et al. 2003). The decrease of characteristic frequencies in time after the transition to the LH state is also a known effect (Kalemci et al. 2004). Note that the characteristic frequency levels off as the photon index also levels off at low flux levels.

We also include the evolution of mean coherence and lags in the 1–10 Hz band in Figure 5. It was necessary to merge the light curves of the five observations in the LH state (15B–19B in Table 1) to improve statistics. In the IS, the coherence is relatively low, whereas the lags are high. As the source enters the LH state, the coherence increases and approaches unity, and the lag decreases. In the LH state, the coherence is high and the mean lag is low. These results are in agreement with the analysis

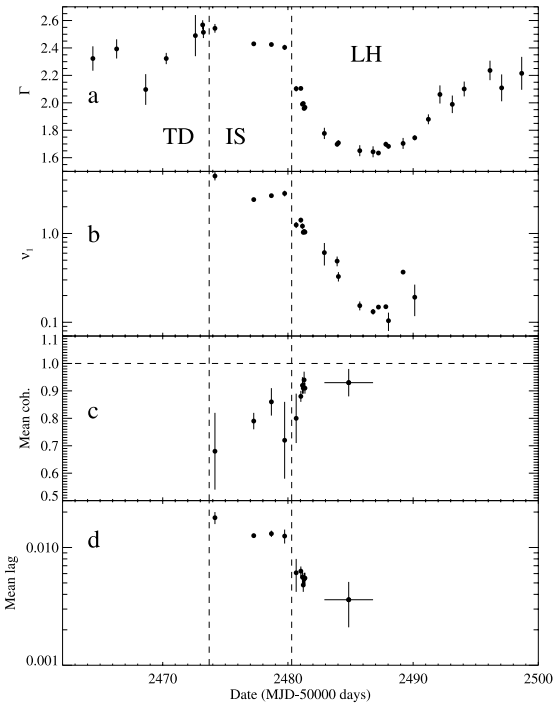

FIG. 5.—Evolution of (*a*) the photon index (same as Fig. 3*b*), (*b*) the lowest peak frequency (ν_1), (*c*) the mean coherence in the 1–10 Hz band between the 3–6 keV and the 6–15 keV bands, and (*d*) the mean lag in the 1–10 Hz band between the 3–6 keV and the 6–15 keV bands. The dashed lines represent approximate times of state transitions. Five LH-state observations were merged to obtain the last point.

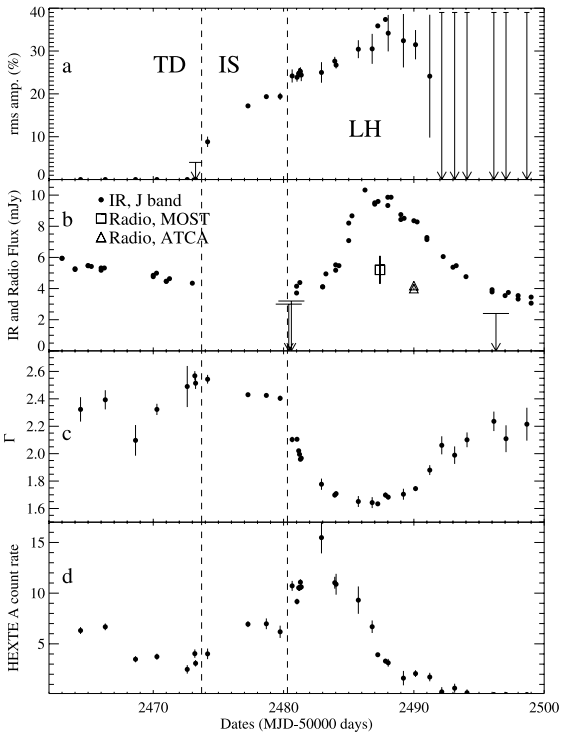

FIG. 6.—Evolution of (*a*) the rms amplitude of variability, (*b*) the *J*-band infrared fluxes from Buxton & Bailyn 2004 (*circles*) along with radio fluxes from our observations (*triangles*) and Park et al. (2004; *upper limits and square*), (*c*) the photon index, and (*d*) the HEXTE cluster A count rate in the 16–100 keV band. Note that (*a*) and (*c*) were shown before in Fig. 3. The gap in the infrared light curve during the IS is due to lack of coverage.

of other black hole transients: high lag and low coherence during the IS, and high coherence and low (usually consistent with zero) lag in the LH state, along with a correlation between photon index and the 1–10 Hz mean lag when they are measurable (Kalemci 2002).

3.2. *Multiwavelength Observations*

Although some of the radio, optical, and infrared data from this source were presented before (Park et al. 2004; Buxton & Bailyn 2004), additional information is available when they are combined with the data from pointed *RXTE* observations. The evolution of the *J*-band fluxes, along with the radio information, is shown in Figure 6*b*. In Figure 6 we also show the rms amplitude of variability and the photon index (same as Figs. 3*a* and 3*b*, respectively), as well as the HEXTE cluster A count rate in the 16–100 keV band. The *J*-band flux decreased steadily in the TD state as the source flux was decaying. Unfortunately, there was no coverage during the first transition, making it impossible for us to determine if there was a response in the OIR emission. On the other hand, there was strong response after the transition to the LH state, such that the *J*-band flux started to increase sharply ~3 days after the time of transition and peaked in 3 days. A two-sided Gaussian fit to the *J*-band light curve during the secondary maximum results in a peak time of MJD $52{,}486.3^{+1.5}_{-1.8}$ (Buxton & Bailyn 2004). After staying at the peak for a few days, it started to decay and reached the pre–secondary-peak levels in 7 days. As shown by Buxton & Bailyn (2004), both the optical (*B*, *V*, *I*) and the infrared light curves show this peak. It is most pronounced in the *J* and the *K* bands, as the strength of emission increases with wavelength. The spectrum of the OIR points is best fitted by a power law rather than a blackbody or a DBB model (Buxton & Bailyn 2004). This strongly suggests that the origin of the OIR emission is optically thin synchrotron. From the beginning of our observations on MJD 52,464 to MJD 52,487, there was only one radio observation that resulted in no detection. The detections occurred in the LH state, during the secondary maximum. The radio emission most likely originates from an outflow, possibly a compact jet given the inverted spectrum of observation 24B (see Fig. 8 below).

While the *J*-band flux increased, the rms amplitude of variability (Fig. 6*a*) also increased slightly. It is not clear what happened to the rms amplitude of variability after MJD 52,492, as the count rate was too low to constrain the timing properties. The photon index (Fig. 6*c*), on the other hand, seemed to show an anticorrelation with the *J*-band flux. There is a ~2 day time lag between the time at which the photon index began to harden and when the *J*-band flux began to increase. As the *J*-band flux decreased, the photon index began to soften.[10]

Another interesting change with respect to the changes in the OIR is the evolution of the hard flux. This is represented by the

[10] When not fixed in the fit, the indices of the Galactic ridge emission were consistently harder than 2.15 for the last two points. We fixed the ridge power-law index to 2.15 so that the fit resulted in a harder index for the source. The actual photon indices for these two points were probably higher.

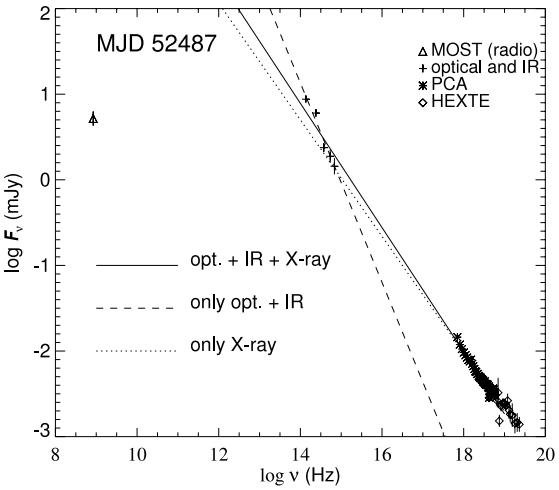

FIG. 7.—Spectral energy distribution of 4U 1543−47 at MJD 52,487. The lines represent power-law fits to different subsets of data (see Table 3).

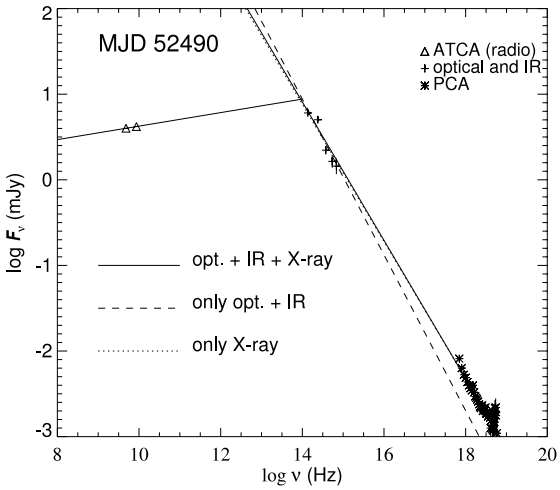

FIG. 8.—Spectral energy distribution of 4U 1543−47 at MJD 52,490. The lines passing through the optical, infrared, and X-ray points represent power-law fits to different subsets of data (see Table 3). Another line is drawn that passes through the radio points and intersects the power-law fits.

HEXTE cluster A count rate in the 16–100 keV band in Figure 6*d*. First of all, there was a sharp increase in the count rate right at the transition (probably caused by sharp hardening of the X-ray spectrum). By the time the HEXTE count rate peaked, the power-law index had dipped and the *J*-band flux started to rise. The lag between the time that hard X-rays peaked and the OIR peaked was about 2 days.

3.3. *Spectral Energy Distribution*

We have constructed two spectral energy distributions (SEDs) close to the peak of the infrared maximum for the dates of the MOST (MJD ∼52,487) and ATCA (MJD ∼52,490) observations. We first corrected the OIR magnitudes for interstellar extinction using $E(B-V) = 0.50 \pm 0.05$ (Orosz et al. 1998), $A_V = 3.2E(B-V) = 1.60 \pm 0.16$ (Zombeck 1990), $A_B/A_V = 1.324$, $A_I/A_V = 0.482$, $A_J/A_V = 0.282$, and $A_K/A_V = 0.112$ (Rieke & Lebofsky 1985). There were no *B*, *V*, or *I* observations on MJD 52,487 (Buxton & Bailyn 2004). The source was observed in the *B*, *V*, and *I* bands on MJD 52,486 and again on MJD 52,490. We used linear interpolation to estimate the peak fluxes on MJD 52,487. For each band, we fitted a line to the underlying magnitudes using the points before and after the peak to estimate the underlying flux during the secondary maximum. We converted the peak and underlying magnitudes into fluxes using the irradiation factors and description given by Zombeck (1990) and then subtracted the underlying flux from the peak flux to obtain the residual flux representing the emission from the peak only (similar to what was done in Buxton & Bailyn 2004). We used a measurement error of 0.05 mag in each band. In addition, we calculated the error due to uncertainty in extinction using the uncertainty in $E(B-V)$. We also obtained 0.05 and 0.08 mag uncertainties in determining the baseline fluxes for *JK* and *BVI* bands, respectively, from the fitting process. For MJD 52,487, an additional 0.05 mag uncertainty is estimated in *B*, *V*, and *I* due to interpolation in finding the peak flux. All the error components were added in quadrature to estimate the total uncertainty in the measurements. The unabsorbed PCA and HEXTE fluxes for MJD 52,487 and the unabsorbed PCA fluxes for MJD 52,490 were converted into millijanskys to complete the SEDs shown in Figures 7 and 8.

For each case, we fitted a power law to three sets of data: OIR set only, X-ray set only, and OIR and X-ray (overall) set. Figure 7 shows the SED at MJD 52,487, which includes the MOST observation, the OIR data, and the PCA and HEXTE data, as well as the power-law fits (see Table 3 for fit parameters). Statistically, the OIR points are not a continuation of the power law for the X-ray data, as the high-quality PCA and HEXTE data have a photon index of −1.63 with reduced χ^2 value of 0.64 (XSPEC fit, including all other model components). The OIR points alone result in a much steeper power-law index of 2.16.

Although the OIR points again do not follow the power-law fit of the X-ray data for the SED of MJD 52,490 shown in Figure 8, the discrepancy is much less compared with the MJD 52,487 observation. The X-ray and OIR power-law indices are consistent within 2 σ uncertainty. Unlike the first case, this SED provides the break point in the spectrum, as there are two radio points. The turnover is around 10^{14} Hz. This value is similar to the observed values for other sources (Corbel & Fender 2002; Homan et al. 2005).

For the *B*, *V*, and *I* bands, the largest contribution to the error estimate is from the reddening factor. We investigated whether an underestimated error in the reddening could cause the discrepancy between the OIR slope and the X-ray slope for our SEDs.

TABLE 3
SED POWER-LAW FIT PARAMETERS

Data Set	Photon Index	χ^2/dof
MJD 52,487:		
Optical and IR only	−2.16 ± 0.10	8.74/3
X-ray only[a]	−1.63 ± 0.01	39.78/62
Optical, IR, and X-ray	−1.73 ± 0.01	164.30/64
MJD 52,490:		
Optical and IR only	−1.91 ± 0.10	14.66/3
X-ray only[a]	−1.75 ± 0.02	47.68/43
Optical, IR, and X-ray	−1.80 ± 0.02	80.39/42

[a] X-ray–only fits for both dates are from XSPEC fits, with all other model components.

For the SED on MJD 52,490, an uncertainty of 15% in A_V instead of the quoted 10% is enough to make the OIR slope and the X-ray slope be consistent within 1 σ uncertainty. However, for the SED on MJD 52,487, the uncertainty of the reddening factor must be as high as 60% to make OIR slope and X-ray slope consistent, which is highly unlikely.

3.4. *Summary of Results*

In this section we summarize our main results, which are discussed in detail in § 4.

1. The source 4U 1543−47 showed two state transitions during its decay in the 2002 outburst:

   a) The first transition was from the TD state to the IS on MJD ∼52,474 and was marked by a jump in the rms amplitude of variability and power-law flux; and

   b) The second transition was from the IS to the LH state and was marked by a sharp hardening of the X-ray spectrum and an increase in the rms amplitude of variability.

2. During the IS and the transition to the LH state, a QPO was detected. The resonance frequency (see eq. [1]) of the QPO shows a very strong correlation with the photon index on timescales of hours.

3. A high-energy cutoff was detected in the X-ray spectrum only during the transition to the LH state, whereas after the transition and during the LH state, the cutoff was either absent or beyond the HEXTE detection range.

4. The spectrum softened at very low flux levels in the LH state.

5. The characteristic frequencies decreased during the transition and in the LH state before they leveled off. The characteristic frequencies and the photon index show a good correlation.

6. The mean coherence was low during the IS and then increased and approached unity as the source made the transition to the LH state. The mean lag, on the other hand, was high in the IS and decreased during the transition.

7. The OIR light curves started peaking ∼3 days after the transition to the LH state. The radio detections occurred during the OIR secondary maximum.

8. The HEXTE 16–100 keV light curve increased during the transition to the LH state, while the photon index hardened. It did decay, however, while the infrared flux was rising.

9. The SEDs show that the OIR part of the spectrum can be represented by a power law. For the SED on MJD 52,487, the hard X-ray points are not a continuation of the OIR points and have a different index. For the SED on MJD 52,490, the difference is less, and the X-ray and OIR power-law indices are consistent within 2 σ uncertainty.

4. DISCUSSION

The multiwavelength observations of the 2002 outburst of 4U 1543−47 have provided a wealth of information on the physical processes that operate during state transitions and the LH state of GBH transients. In this section, using our observational results, previous experience from other sources, and some theoretical models, we try to place constraints on the X-ray emission geometry and the hard X-ray emission mechanism (the power-law part of the X-ray spectrum), and we try to identify the origin of the seed photons (if seed photons are required). These three properties constitute the fundamental differences between various models of X-ray emission from GBHs (Tomsick 2004).

One set of models considers a corona (which could be in the form of an advection-dominated accretion flow, or ADAF) inside a transition radius (which can move) as the accretion geometry (see, e.g., Esin et al. 1997). In this case, the base of the jet may be the whole corona, or the base may be small compared with the overall size of the corona (Fender 2001; Markoff & Nowak 2004). We note that the jet has not been incorporated into the ADAF or "sphere plus disk" models in a self-consistent way. In the "magnetic corona" model, active, optically thin regions above the disk are responsible for the hard X-ray emission and the outflow formation (Merloni & Fabian 2002). In this model, the position of the inner edge of the accretion disk does not necessarily change significantly. For these cases in which the main hard X-ray–producing mechanism is Compton scattering, the seed photons could be produced either in the accretion disk as blackbody radiation or in the corona as synchrotron radiation (synchrotron self-Compton; Markoff & Nowak 2004). On the other hand, the main hard X-ray emission mechanism may be not Compton scattering but synchrotron radiation originating in the optically thin shock region in the jet (Falcke & Biermann 1999; Markoff et al. 2001; Markoff & Nowak 2004). A combination of emission mechanisms is also possible (see, e.g., Rodriguez et al. 2004); synchrotron radiation and Compton scattering may contribute simultaneously, and the seed photons for Compton scattering might also be a combination of synchrotron at the base of a jet or accretion disk. However, unless these mechanisms conspire to result in very similar observational properties, it may still be possible to determine the major emission mechanism and major contributor of seed photons.

The transition of 4U 1543−47 to the IS from the TD state shows characteristics that many other sources also show, namely, a strong jump in the rms amplitude of variability (from less than 4% to ∼9%) accompanied by an increase in the power-law flux on a timescale of a few days. Note that during this transition, the change in the power-law photon index is smooth. Based on the similar evolution of spectral and temporal parameters of other GBH transients, in Kalemci et al. (2004) it was concluded that a threshold volume for a hot corona is required in order to observe variability. The second transition, during which the photon index and the inner disk temperature decrease very rapidly, and the multiwavelength observations in the LH state provide more insight into the hard X-ray emission mechanism for this source. Below, we describe how the sequence of observational changes may be explained by different hard X-ray emission mechanisms and geometries.

4.1. *Compton Scattering: Recessing Accretion Disk*

In the IS, the inner edge of the disk is close to the black hole, the high reflection fraction indicates that the disk and the corona have some overlap, and there is strong cooling of coronal electrons by the accretion disk seed photons. The electron distribution is most likely not Maxwellian (Coppi 1999), as no cutoff is detected in the HEXTE spectrum. It is possible that an outflow may already be present in this state that provides an "elongated" and variable corona structure at its base, which could explain large lags and small coherence values, as well as the nonthermal nature of the electron population (Pottschmidt et al. 2000; Kalemci et al. 2003).

At some critical combination of physical parameters (the mass accretion rate has been shown not to be the only parameter determining when the transition occurs; Homan et al. 2001; Kalemci et al. 2004), the inner parts of the disk evaporate rapidly into a hot corona and the transition radius moves outward. During this process, the optical thickness of the corona increases and thermal electrons dominate the system, causing a harder spectrum with a cutoff in the HEXTE band. As the disk moves outward, the hardening of the spectrum continues

because of a lower level of cooling by the disk (the cutoff becomes undetectable), and the disk temperature decreases as the hotter inner parts of the disk evaporate. Recession of the disk could also explain the evolution of the QPO frequency and ν_1 if they are related to some dynamical timescale of the inner disk. This model may further explain the correlation between the photon index and the QPO if the hardening is a direct result of less cooling due to an increasing inner disk radius, to which the QPO frequency is linked. Similar arguments have been put forward to explain the well-established correlation between photon index and reflection fraction in GBHs and active galactic nuclei (Zdziarski et al. 2002 and references therein). The relation between the photon index and the QPO frequency could also be due to increasing optical depth of the corona as it expands (Titarchuk & Fiorito 2004).

The detection of an inverted radio spectrum, and also the infrared peak, indicates that a compact jet is present deep in the LH state. The high coherence and low lag values, and the indication of a low reflection fraction, may point to the size of the jet now being small compared with the transition radius. According to Meier et al. (2001), the production region for an MHD-driven compact jet is $(7–8)R_g$ for a Schwarzschild hole, and even smaller for a Kerr hole. A decrease by more than 1 order of magnitude in characteristic frequency between the IS and the deep LH state may also indicate that the transition radius is away from the jet production region. The detection of the QPO and the photon index–QPO frequency correlation point to an accretion disk as the major source of seed photons in the IS and during the transition. Also, once the spectrum reaches its hardest point, on MJD ~52,483, the HEXTE count rate starts to decrease, in parallel with the decrease in the DBB flux, again indicating that the major source of seed photons is the accretion disk. However, the source of seed photons deep in the LH state is unclear, and synchrotron self-Compton may be contributing to the hard X-ray emission after MJD ~52,487. The spectral softening at the end of the outburst may be due to a decrease of the optical thickness of the Comptonizing medium as the mass accretion rate decreases, and the energetic electrons either advectively accrete onto the black hole or leave the vicinity of the black hole in the form of an outflow (Esin et al. 1997). We note that this type of softening is observed in many sources (Tomsick et al. 2001; Kalemci 2002).

4.2. *Compton Scattering: Stable Inner Disk* (*Magnetic Flares*)

The fits to the PCA spectrum, even at very low flux levels, require a disk component to be able to fit the first bin. However, we cannot reliably constrain disk parameters after MJD 52,485 with PCA observations when only one bin is affected. The *XMM-Newton* observation that took place on MJD 52,504.5 indicates that a disk component is required in the fit at the ~3 σ level with a temperature of 0.19 keV. After converting the normalization of the DBB fit to an inner disk radius, Miller et al. (2004) claimed that the disk may still be very close to the last stable orbit. If the disk is not moving, as in the magnetic-flares model, the explanation of the spectral evolution is different from the case of a moving disk. In the stable-disk case, after the transition to the IS the active regions increase in number as compared with before the transition, and the observed variability is due to short-lived flares in the active regions (Merloni & Fabian 2001). A non-Maxwellian distribution of electrons in the corona is again required in the IS. During the transition to the LH state, a larger and larger portion of the accretion energy is used to buoy the magnetic flux tubes and to heat the corona. This results in cooling of the disk and a hardening photon index. At lower mass accretion rates, the accretion energy might be channeled into launching and sustaining the jet rather than heating the electrons, which may explain the softening at the end of the outburst (Merloni & Fabian 2002). The decrease in the reflection fraction could be explained if the surface of the disk becomes ionized, which would wash away the features (Nayakshin & Dove 2001). However, a recent study has shown that the magnetic-flares model cannot explain the high-energy emission of Cygnus X-1, even with the ionization effect (Barrio et al. 2003). It is also not clear what determines the QPO frequency, what causes the temporal evolution, why the characteristic frequencies decrease in time, or what causes the QPO frequency–photon index correlation.

4.3. *Direct Synchrotron Radiation*

It is hard to explain the sequence of events in this source if the main hard X-ray emission mechanism is direct synchrotron from a shock region (first acceleration zone) in a jet for most of the outburst decay. The origin of the OIR peak emission is probably synchrotron from a shock region in the jet (where the hard X-rays would also originate), as indicated by the SEDs (Buxton & Bailyn 2004). The infrared peak shows that the shock region has formed after the transition to the LH state. Even though there is no coverage in the OIR during the IS, the infrared emission between MJD 52,480 and MJD 52,483 is the continuation of the decay in infrared before the IS, and it is unlikely that another infrared peak is present in the IS. The outflow may be present after the first transition to the IS; however, the formation of the shock region did not take place before the source was in the LH state. If the above assessment is correct, the synchrotron X-ray emission from the jet region could not have been produced before the source was deep in the LH state. But it is possible that the synchrotron emission becomes the dominant X-ray emission mechanism after the formation of the shock region. The synchrotron model results in a very low reflection fraction (~3%; Markoff & Nowak 2004). There is a sharp drop in smeared-edge optical depth just before the infrared flux begins to rise. It is also intriguing that the QPO disappears and the structure of the power spectrum changes as the reflection decreases. However, there is also evidence against the synchrotron interpretation even after the infrared flux begins to rise. The SEDs indicate that, even without an exponential cutoff, the X-ray contribution from synchrotron is below the observed levels. More importantly, the HEXTE light curve does not follow the infrared light curve, decreasing while the infrared is still rising and the photon index is hardening between MJD 52,483 and MJD 52,487 (see Fig. 6). This is very hard to explain in the synchrotron model when the infrared and optical emission comes from the optically thin part of the SED as in 4U 1543−47 (see Figs. 7 and 8). We emphasize that the synchrotron radiation from the jet may still be contributing to the overall X-ray emission, but it cannot be the dominant emission mechanism until about MJD 52,490. It is hard to make a claim about the dominant emission mechanism after this date. Note that the discrepancy in the power-law index of the OIR points and X-ray points on MJD 52,490 is also much less than that on MJD 52,487 (see Figs. 7 and 8).

4.4. *Comparison with GX 339−4*

When only the evolution of X-ray properties is considered, 4U 1543−47 is a very typical source, showing characteristics seen in many other GBH transients (Kalemci et al. 2004). However, this does not translate easily into generalizing the results from this work to all GBH transients, as few objects have had nearly daily simultaneous infrared and X-ray coverage such that one could compare the details of spectral evolution. GX 339−4

had such coverage during its 2002 outburst. It is also a very typical GBH transient in its spectral and timing properties. In fact, its 2002 outburst decay shows spectral and temporal characteristics in X-rays very similar to the decay of 4U 1543−47 (E. Kalemci et al., in preparation). However, in the LH state during the outburst rise, GX 339−4 showed a correlation between the X-ray flux and the OIR flux (Homan et al. 2005), whereas 4U 1543−47 shows an anticorrelation in the LH state during the decay. Although somewhat speculative, the main difference between the behavior in 4U 1543−47 and in GX 339−4 could be the origin of seed photons for Compton upscattering. For 4U 1543−47, the decay part of the HEXTE light curve seems to have two slopes: a sharp decay until MJD 52,486 and a more gradual decay after this date. This could be a sign of the major seed photon emission mechanism changing from DBB from the accretion disk to synchrotron self-Compton at the base of the jet after MJD 52,489, as the infrared and X-rays correlate after this date. Complete multiwavelength analysis (including OIR data) of other black hole transients is necessary to generalize the relation between the OIR and X-ray flux.

5. SUMMARY AND CONCLUSION

Using X-rays, optical/infrared, and radio observations, we have characterized the outburst decay of the Galactic black hole transient 4U 1543−47 and placed constraints on several emission models. A large, nonthermal, and radiatively inefficient outflow could explain the spectral and temporal evolution in the intermediate state. The presence of a high-energy cutoff in the X-ray spectra during the transition to the low/hard state is indicative of a thermal electron distribution. In general, our observations are consistent with a recessing accretion disk plus hot corona plus "compact" jet geometry, with the main hard X-ray emission mechanism being Compton upscattering of soft accretion disk seed photons by energetic electrons in the corona. Here we use the word "compact" to also emphasize the size of the base of the jet, which most likely is small compared with the overall size of the corona. This interpretation can reasonably explain all aspects of our observations until deep in the LH state.

Our results do not strongly rule out the possibility of the accretion disk always being close to the last stable orbit, as in the magnetic-flares model; however, the QPO frequency–photon index correlation and the decrease of characteristic frequencies with time are two results from this and other sources that need to be understood for this model (Zdziarski et al. 2003; Tomsick 2004).

Our observations disfavor synchrotron from a shock region in the jet as the major source of hard X-rays until deep in the LH state. We cannot place constraints on different emission models after MJD 52,490.

E. K. acknowledges NASA grant NAG 5-13142 and partial support from TÜBİTAK. The authors thank Sera Markoff, Jeroen Homan, and Juri Poutanen for useful discussion and comments. E. K. thanks all the scientists who contributed to the Tübingen Timing Tools. The authors thank Charles Bailyn, who (along with M. M. Buxton) provided access to the OIR data prior to publication. J. A. T. acknowledges partial support from NASA grant NAG 5-13055. M. B. gratefully acknowledges support from the National Science Foundation through grant AST 00-98421. R. E. R. acknowledges NASA grant NAS 5-30270. K. P. acknowledges support from the Deutsches Zentrum für Luft- und Raumfahrt, grant 50 OG 95030. The authors also would like to thank Jean Swank and Evan Smith for all their scheduling efforts, especially scheduling the first P70128 observation as early as possible; that observation could not have taken place at a better time. We also would like to thank Rob Fender for his help coordinating the radio observations, and Steven Tingay for conducting the ATCA observations. The Australia Telescope Compact Array is part of the Australia Telescope, which is funded by the Commonwealth of Australia for operation as a National Facility managed by CSIRO. This work has made use of data obtained through the High Energy Astrophysics Science Archive Research Center online service, provided by the NASA Goddard Space Flight Center.

REFERENCES

Bailyn, C. D., DePoy, D., Agostinho, R., Méndez, R., Espinoza, J., & González, D. 1999, BAAS, 31, 1502
Barrio, F. E., Done, C., & Nayakshin, S. 2003, MNRAS, 342, 557
Bradt, H. V., Rothschild, R. E., & Swank, J. H. 1993, A&AS, 97, 355
Brocksopp, C., Bandyopadhyay, R. M., & Fender, R. P. 2004, NewA, 9, 249
Buxton, M. M., & Bailyn, C. D. 2004, ApJ, 615, 880
Coppi, P. S. 1999, in ASP Conf. Ser. 161, High Energy Processes in Accreting Black Holes, ed. J. Poutanen & R. Svensson (San Francisco: ASP), 375
Corbel, S., & Fender, R. P. 2002, ApJ, 573, L35
Corbel, S., Fender, R. P., Tomsick, J. A., Tzioumis, A. K., & Tingay, S. 2004, ApJ, 617, 1272
Corbel, S., Fender, R. P., Tzioumis, A. K., Nowak, M., McIntyre, V., Durouchoux, P., & Sood, R. 2000, A&A, 359, 251
Corbel, S., Nowak, M. A., Fender, R. P., Tzioumis, A. K., & Markoff, S. 2003, A&A, 400, 1007
Corbel, S., et al. 2001, ApJ, 554, 43
Ebisawa, K., et al. 1994, PASJ, 46, 375
Esin, A. A., McClintock, J. E., & Narayan, R. 1997, ApJ, 489, 865 (erratum 500, 523 [1998])
Falcke, H., & Biermann, P. L. 1999, A&A, 342, 49
Fender, R. 2005, in Compact Stellar X-Ray Sources, ed. W. H. G. Lewin & M. van der Klis (Cambridge: Cambridge Univ. Press), in press (astro-ph/0303339)
Fender, R., et al. 1999, ApJ, 519, L165
Fender, R. P. 2001, MNRAS, 322, 31
Fender, R. P., & Kuulkers, E. 2001, MNRAS, 324, 923
Ford, E. C., van der Klis, M., Méndez, M., van Paradijs, J., & Kaaret, P. 1999, ApJ, 512, L31
Gallo, E., Fender, R. P., & Pooley, G. G. 2003, MNRAS, 344, 60
Harmon, B. A., Wilson, R. B., Finger, M. H., Paciesas, W. S., Rubin, B. C., & Fishman, G. J. 1992, IAU Circ. 5510
Homan, J., Buxton, M., Markoff, S., Bailyn, C. D., Nespoli, E., & Belloni, T. 2005, ApJ, in press (astro-ph/0501349)
Homan, J., Wijnands, R., van der Klis, M., Belloni, T., van Paradijs, J., Klein-Wolt, M., Fender, R., & Méndez, M. 2001, ApJS, 132, 377
Jain, R. K., Bailyn, C. D., Orosz, J. A., McClintock, J. E., & Remillard, R. A. 2001a, ApJ, 554, L181
Jain, R. K., Bailyn, C. D., Orosz, J. A., McClintock, J. E., Sobczak, G. J., & Remillard, R. A. 2001b, ApJ, 546, 1086
Kalemci, E. 2002, Ph.D. thesis, Univ. California, San Diego
Kalemci, E., Tomsick, J., Rothschild, R., Corbel, S., Kaaret, P., & McClintock, J. 2002, Astron. Telegram, No. 103
Kalemci, E., Tomsick, J. A., Rothschild, R. E., Pottschmidt, K., Corbel, S., Wijnands, R., Miller, J. M., & Kaaret, P. 2003, ApJ, 586, 419
Kalemci, E., Tomsick, J. A., Rothschild, R. E., Pottschmidt, K., & Kaaret, P. 2001, ApJ, 563, 239
———. 2004, ApJ, 603, 231
Kitamoto, S., Miyamoto, S., Tsunemi, H., Makishima, K., & Nakagawa, M. 1984, PASJ, 36, 799
Körding, E., & Falcke, H. 2004, A&A, 414, 795
Kong, A. K. H., Charles, P. A., Kuulkers, E., & Kitamoto, S. 2002, MNRAS, 329, 588
Laor, A. 1991, ApJ, 376, 90
Makishima, K., Maejima, Y., Mitsuda, K., Bradt, H. V., Remillard, R. A., Tuohy, I. R., Hoshi, R., & Nakagawa, M. 1986, ApJ, 308, 635
Markoff, S., Falcke, H., & Fender, R. 2001, A&A, 372, L25
Markoff, S., & Nowak, M. A. 2004, ApJ, 609, 972

Matilsky, T. A., Giacconi, R., Gursky, H., Kellogg, E. M., & Tananbaum, H. D. 1972, ApJ, 174, L53
McClintock, J. E., & Remillard, R. A. 2003, in Compact Stellar X-Ray Sources, ed. W. H. G. Lewin & M. van der Klis (Cambridge: Cambridge Univ. Press), in press (astro-ph/0306213)
Meier, D. L., Koide, S., & Uchida, Y. 2001, Science, 291, 84
Merloni, A., & Fabian, A. C. 2001, MNRAS, 321, 549
———. 2002, MNRAS, 332, 165
Miller, J. M., Fabian, A. C., & Lewin, W. H. G. 2004, Astron. Telegram, No. 212
Miller, J. M., & Remillard, R. A. 2002, IAU Circ. 7920
Miyamoto, S., & Kitamoto, S. 1989, Nature, 342, 773
Nayakshin, S., & Dove, J. B. 2001, ApJ, 560, 885
Nowak, M. A., Vaughan, B. A., Wilms, J., Dove, J. B., & Begelman, M. C. 1999, ApJ, 510, 874
Orosz, J. A., Jain, R. K., Bailyn, C. D., McClintock, J. E., & Remillard, R. A. 1998, ApJ, 499, 375
Park, S. Q., et al. 2004, ApJ, 610, 378
Payne, D. G. 1980, ApJ, 237, 951
Pedersen, H. 1983, Messenger, 34, 21
Pottschmidt, K. 2002, Ph.D. thesis, Univ. Tübingen
Pottschmidt, K., Wilms, J., Nowak, M. A., Heindl, W. A., Smith, D. M., & Staubert, R. 2000, A&A, 357, L17
Pottschmidt, K., et al. 2003, A&A, 407, 1039
Revnivtsev, M. 2003, A&A, 410, 865
Rieke, G. H., & Lebofsky, M. J. 1985, ApJ, 288, 618
Rodriguez, J., Corbel, S., Hannikainen, D. C., Belloni, T., Paizis, A., & Vilhu, O. 2004, ApJ, 615, 416
Rodriguez, J., Corbel, S., & Tomsick, J. A. 2003, ApJ, 595, 1032
Rothschild, R. E., et al. 1998, ApJ, 496, 538
Sault, R. J., Teuben, P. J., & Wright, M. C. H. 1995, in ASP Conf. Ser. 77, Astronomical Data Analysis Software and Systems IV, ed. R. A. Shaw, H. E. Payne, & J. J. E. Hayes (San Francisco: ASP), 433
Sobczak, G. J., McClintock, J. E., Remillard, R. A., Cui, W., Levine, A. M., Morgan, E. H., Orosz, J. A., & Bailyn, C. D. 2000, ApJ, 544, 993
Titarchuk, L., & Fiorito, R. 2004, ApJ, 612, 988
Tomsick, J. A. 2004, in AIP Conf. Proc. 714, X-Ray Timing 2003, ed. P. Kaaret, F. K. Lamb, & J. H. Swank (Melville, NY: AIP), 71
Tomsick, J. A., Corbel, S., & Kaaret, P. 2001, ApJ, 563, 229
Tomsick, J. A., & Kaaret, P. 2000, ApJ, 537, 448
Tomsick, J. A., Kalemci, E., Corbel, S., & Kaaret, P. 2003, ApJ, 592, 1100
Tomsick, J. A., Kalemci, E., & Kaaret, P. 2004, ApJ, 601, 439
Vaughan, B. A., & Nowak, M. A. 1997, ApJ, 474, L43
Vignarca, F., Migliari, S., Belloni, T., Psaltis, D., & van der Klis, M. 2003, A&A, 397, 729
Zdziarski, A. A., Lubiński, P., Gilfanov, M., & Revnivtsev, M. 2003, MNRAS, 342, 355
Zdziarski, A. A., Poutanen, J., Paciesas, W. S., & Wen, L. 2002, ApJ, 578, 357
Zhang, W., Jahoda, K., Swank, J. H., Morgan, E. H., & Giles, A. B. 1995, ApJ, 449, 930
Zombeck, M. V. 1990, Handbook of Space Astronomy and Astrophysics (2nd ed.; Cambridge: Cambridge Univ. Press)

3.5.5

The Galactic Black Hole Transient H1743-322 during Outburst Decay : Connections between Timing Noise, State Transitions, and Radio Emission.

Article publié dans :

Astrophys. J., 2006, 639, 340-347

Kalemci, E., Tomsick, J. A., Rothschild, R. E., Pottschmidt, K., Corbel, S., Kaaret, P.

The Astrophysical Journal, 639:340–347, 2006 March 1

THE GALACTIC BLACK HOLE TRANSIENT H1743−322 DURING OUTBURST DECAY: CONNECTIONS BETWEEN TIMING NOISE, STATE TRANSITIONS, AND RADIO EMISSION

E. Kalemci,[1,2] J. A. Tomsick,[3] R. E. Rothschild,[3] K. Pottschmidt,[3] S. Corbel,[4] and P. Kaaret[5]

Received 2005 July 8; accepted 2005 October 28

ABSTRACT

Multiwavelength observations of Galactic black hole transients during outburst decay are instrumental for our understanding of the accretion geometry and the formation of outflows around black hole systems. H1743−322, a black hole transient observed intensely in X-rays and also covered in the radio band during its 2003 decay, provides clues about the changes in accretion geometry during state transitions and also the general properties of X-ray emission during the intermediate and low-hard states. In this work, we report on the evolution of spectral and temporal properties in X-rays and the flux in the radio band, with the goal of understanding the nature of state transitions observed in this source. We concentrate on the transition from the thermal dominant state to the intermediate state that occurs on a timescale of 1 day. We show that the state transition is associated with a sudden increase in power-law flux. We determine that the ratio of the power-law flux to the overall flux in the 3–25 keV band must exceed 0.6 for us to observe strong timing noise. Even after the state transition, once this ratio was below 0.6, the system transited back to the thermal dominant state for 1 day. We show that the emission from the compact radio core does not turn on during the transition from the thermal dominant state to the intermediate state but does turn on when the source reaches the low-hard state, as seen in 4U 1543−47 and GX 339−4. We find that the photon index correlates strongly with the QPO frequency and anticorrelates with the rms amplitude of variability. We also show that the variability is more likely to be associated with the power-law emission than the disk emission.

Subject headings: accretion, accretion disks — binaries: close — black hole physics — stars: individual (H1743−322) — X-rays: binaries — X-rays: stars

1. INTRODUCTION

The Galactic black hole transients show several correlated spectral and temporal variability properties during outbursts, denoted as spectral states. During the initial rise and at the end of the decay before quiescence, these transients are usually in the "low-hard" state (LHS). In this state, a hard power-law component dominates the X-ray spectrum, and strong variability (>20% rms amplitude) and quasi-periodic oscillations (QPOs) are often observed. In between the rise and the decay, the source may evolve through a combination of "thermal dominant" and "steep power-law" states. In the thermal dominant state (TDS), the soft disk component dominates the spectrum, and the timing noise is very low or absent. In the steep power-law state, the power-law flux in the 2–20 keV band accounts for more than 50% of the flux and has a photon index (Γ) greater than 2.4. Moderate variability and QPOs are observed in this state. There also exist intermediate states (IS) in which source characteristics do not fit into the steep power law, TDS, or LHS, but show various combinations of these states (see McClintock & Remillard 2006 for detailed discussion of spectral states). Throughout this work, we use the name IS for the particular intermediate state between the TDS and the LHS during the outburst decay. Even though these states were historically characterized using X-ray observations, changes in other bands occur as well. In the TDS, the radio emission from the compact core is quenched (Fender et al. 1999; Corbel et al. 2000). Optically thin outflows are sometimes detected during state transitions (Fender & Kuulkers 2001; Corbel et al. 2001), and powerful, compact jets are always observed in the LHS (Fender 2001). The optical and infrared emission also show state-dependent properties (Kalemci et al. 2005; Homan et al. 2005a; Corbel & Fender 2002).

The multiwavelength observations made during the decaying portion of the outbursts provide valuable information about black hole transients because of the very high probability of observing transitions from the TDS to the IS, and eventually to the LHS (Kalemci 2002). The changes during the transitions can reveal the geometry and physical environment of these systems before and after the transitions (Esin et al. 1997; Zdziarski et al. 2002). The LHS contains additional information due to strong variability and strong radio emission, both correlating with spectral parameters. Our group has been observing these transients during outburst decay in X-rays with the *Rossi X-Ray Timing Explorer* (*RXTE*) and in radio to understand the evolution before, during, and after the state transitions (Kalemci et al. 2001, 2003, 2005; Tomsick et al. 2001, 2003). Our emphasis is on state transitions, and especially on understanding the changes in X-rays while the radio jet is turning on. A uniform analysis of all black hole transients observed with approximately daily coverage with *RXTE* during outburst decay between 1996 and 2001 provided important information on the evolution of spectral and temporal parameters during the decay (Kalemci et al. 2004a). The sharpest change indicating a state transition is observed to be a jump in the rms amplitude of variability from less than a few percent to more than tens of percent in less than 1 day. This change in the rms amplitude is almost always accompanied by a sharp increase in the power-law flux. There is also evidence that the strong rms noise is only observed when the power-law flux from the source is above a

[1] Space Sciences Laboratory, 7 Gauss Way, University of California, Berkeley, CA 94720-7450.
[2] Current address: Sabancı University, Orhanlı-Tuzla 34956, İstanbul, Turkey.
[3] Center for Astrophysics and Space Sciences, Code 0424, University of California at San Diego, La Jolla, CA 92093-0424.
[4] AIM-Unité Mixte de Recherche CEA-CNRS-Université Paris VII-UMR 7158, CEA Saclay, Service d'Astrophysique, F-91191 Gif sur Yvette, France.
[5] Department of Physics and Astronomy, University of Iowa, Van Allen Hall, Iowa City, IA 52242.

certain percentage of the total flux. This sharp change in rms amplitude of variability is noted as the time of state transition from the TDS to a harder state in Kalemci et al. (2004a), and the same definition is applied here. During the outburst decay, the photon index, disk temperature, and disk flux usually decrease slowly. Often, late in the outburst, the disk flux becomes undetectable. After the transition, characteristic frequencies of the power-density spectrum also decrease with time.

H1743−322 was discovered with the *Ariel 5* (Kaluzienski & Holt 1977) and *HEAO 1* (Doxsey et al. 1977) satellites in 1977 August. After a couple of detections in 1984 with *EXOSAT* (Reynolds 1999), and in 1996 with the TTM/COMIS telescope on *Mir-Kvant* (Emelyanov et al. 2000), the source was detected in outburst again in 2003 March with *INTEGRAL* (Revnivtsev et al. 2003) and *RXTE* (Markwardt & Swank 2003). The radio (Rupen et al. 2003a), infrared (Baba et al. 2003), and optical (Steeghs et al. 2003) counterparts were quickly identified during the 2003 outburst. The radio observations revealed relativistic jets ($v/c \simeq 0.8$; Rupen et al. 2004b; Corbel et al. 2005). Large-scale jets were also detected in X-rays with *Chandra* at the end of the outburst (Corbel et al. 2005). The X-ray observations with *RXTE* and *INTEGRAL* indicate that the source went through several spectral states before fading at the end of 2003 (Markwardt & Swank 2003; Homan et al. 2003; Kretschmar et al. 2003; Grebenev et al. 2003; Tomsick & Kalemci 2003; Parmar et al. 2003; Joinet et al. 2005). Even though there is no mass measurement of the compact object, the X-ray spectral and temporal properties and a high-frequency QPO pair with frequencies similar to those of other black hole sources (Homan et al. 2005b) establish this source as a very likely black hole.

In this work we characterize the X-ray and radio properties of H1743−322 during the outburst decay in 2003, compare these properties to the general properties of black hole transients, and discuss the unique properties of this source in detail. We especially concentrate on the triggering mechanism for the state transitions during the outburst decay.

2. OBSERVATIONS AND ANALYSIS

2.1. *The RXTE Observations*

The *RXTE* All-Sky Monitor (ASM) light curve of H1743−322 in the 2003 outburst is shown in Figure 1. Our daily monitoring campaign with *RXTE* (under observation ID 80137, each pointing 2–3 ks long) started on MJD 52,906 after the source's ASM count rate dropped below 15 counts s^{-1}. The source was in the TDS until MJD 52,930, when a transition to the IS occurred (Tomsick & Kalemci 2003). After MJD 52,938, the source was in the LHS (Kalemci et al. 2004b). In the LHS, we also obtained longer exposure observations (10–15 ks; see Table 1) to investigate spectral and temporal properties of the source in greater detail than the daily monitoring observations. The monitoring program has very good coverage of the transitions and evolution during the outburst decay (see Fig. 1). Table 1 shows the list of the observations we used in this work.

2.1.1. *X-Ray Spectral Analysis*

For most of the observations, we used both the Proportional Counter Array (PCA) and the High-Energy X-Ray Timing Experiment (HEXTE) instruments on *RXTE* for the spectral analysis (see Bradt et al. [1993] for instrument descriptions). For the PCA, the 3–25 keV band was used, and the response matrix and background model were created using the standard FTOOLS (version 5.3.1) programs. We added 0.8% up to 7 keV and 0.4% above 7 keV as systematic error (for the details of how we estimated systematic uncertainties, see Tomsick et al. 2001). We used all available proportional counter units (PCUs) for each observation, choosing the combination that would give the maximum number of counts per pointing.

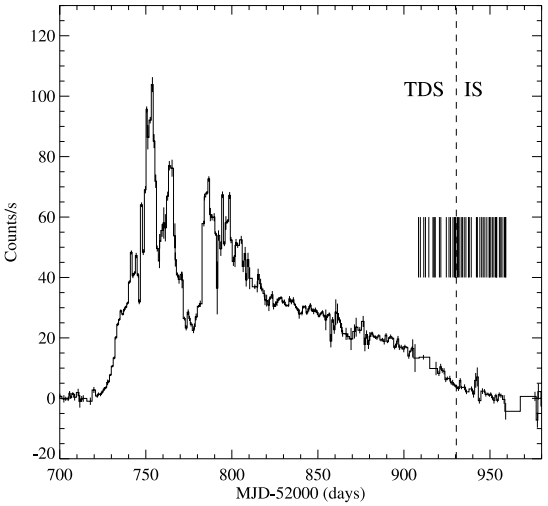

FIG. 1.—The 2–12 keV ASM light curve of the 2003 outburst of H1743−322. The vertical lines indicate the times for *RXTE* pointings that we analyzed. The dashed line indicates the approximate time of state transitions from the TDS to the IS.

The 15–200 keV band was used for the HEXTE data. We used the response matrix created by FTOOLS and applied the necessary dead-time correction (Rothschild et al. 1998). The HEXTE background is measured throughout the observation by alternating between the source and background fields every 32 s. As H1743−322 is close to the plane ($b = -1.^{\circ}83$), both the source confusion and the Galactic ridge emission are important for determining the HEXTE background. By using the HEXTEROCK utility and Galactic bulge scans and comparing the rates between "positive" and "negative" off-source cluster positions, we determined that for both clusters, positive background pointing provides a better estimate of the background for our observations. For cluster A, the negative pointing is in the Galactic plane, with very strong ridge contribution, and background sources are contributing in the cluster B negative position. The relative normalization between the PCA and the HEXTE is kept free, and varies between 0.9 and 1. The HEXTE data were included in the spectral analysis until MJD 52,950. After this date, including HEXTE data did not improve the fits due to low fluxes and short observation times.

The Galactic ridge emission was a factor for all of the observations discussed here because of the proximity of the source to the Galactic plane. We determined that our last nine observations in 2004 (MJD 53,021–53,055) had a constant flux that represented the ridge emission with a power-law index of 2.325 and an iron line at 6.62 keV. The 3–25 keV unabsorbed flux from the ridge emission is 1.08×10^{-10} ergs cm^{-2} s^{-1}. These numbers are consistent with expectations from the Galactic ridge (Revnivtsev 2003). To make sure, we also analyzed the *RXTE* Galactic bulge scans before and after the outburst. We determined that the model described above fits them as well. For all observations, we fixed the ridge parameters as given above. After MJD 52,960, our monitoring observations did not detect the source significantly above the Galactic ridge emission.

TABLE 1
OBSERVATIONAL PARAMETERS

Observation No.[a]	Date (MJD)	Exposure[b] (ks)	Γ	T_{in}	PL Flux[c]	DBB Flux[d]	rms (%)[e]	Notes
01-00	52908.49	2.40	2.73 ± 0.07	0.82 ± 0.01	5.06	24.63	<3.25	
02-00	52909.53	3.00	2.40 ± 0.05	0.81 ± 0.01	6.03	23.86	<3.25	
03-00	52911.52	3.54	2.24 ± 0.03	0.80 ± 0.01	8.34	23.00	<3.23	
04-00	52912.50	3.54	2.18 ± 0.03	0.800 ± 0.01	10.4	22.11	2.17 ± 1.48	
05-00	52914.47	2.40	2.30 ± 0.04	0.780 ± 0.01	4.91	19.87	1.66 ± 0.99	
11-00	52916.88	3.48	2.25 ± 0.03	0.76 ± 0.01	7.33	16.69	2.78 ± 2.10	
07-00	52917.56	3.48	2.18 ± 0.03	0.74 ± 0.01	6.95	15.84	2.24 ± 1.11	
08-00	52918.21	2.94	2.25 ± 0.04	0.75 ± 0.01	6.66	15.53	1.28 ± 1.33	
09-00	52920.62	2.52	2.36 ± 0.05	0.74 ± 0.01	3.50	14.02	1.86 ± 0.80	
10-00	52921.44	2.28	2.35 ± 0.09	0.73 ± 0.01	3.47	12.57	2.28 ± 1.16	
13-00	52924.62	2.70	2.31 ± 0.07	0.70 ± 0.01	3.20	10.32	<2.04	Radio (VLA) observation with no detection.
14-00	52926.18	3.48	2.29 ± 0.05	0.68 ± 0.01	3.70	8.65	<2.53	
15-00	52927.04	3.42	2.24 ± 0.06	0.68 ± 0.01	2.97	8.03	<2.15	
16-00	52928.48	1.86	2.18 ± 0.07	0.66 ± 0.01	3.48	6.96	<2.80	Galactic ridge ∼10% of the overall flux.
17-00	52929.32	3.54	2.01 ± 0.05	0.66 ± 0.01	4.05	6.38	<2.03	
18-00	52929.91	1.56	2.14 ± 0.05	0.65 ± 0.01	4.58	5.87	<1.37	
18-01	52929.98	2.04	2.07 ± 0.05	0.65 ± 0.01	4.44	5.92	<1.77	Still in the TD state.
19-01	52930.90	1.56	2.20 ± 0.04	0.64 ± 0.01	8.17	4.96	7.18 ± 0.27	Timing noise, transition to the IS.
19-00	52931.46	1.98	2.27 ± 0.03	0.63 ± 0.01	8.18	4.83	7.60 ± 0.52	
20-00	52932.07	3.30	2.22 ± 0.02	0.62 ± 0.01	11.66	3.25	11.15 ± 0.46	No radio detection at MJD 52932.96. QPO at 7.8 Hz.
21-00	52933.27	3.42	2.10 ± 0.05	0.62 ± 0.01	4.63	4.11	1.85 ± 0.26	Timing noise reduces substantially for this observation only!
22-00	52933.99	3.48	2.23 ± 0.02	0.60 ± 0.01	8.77	3.06	10.35 ± 1.10	QPO at 7.6 Hz.
23-00	52935.04	2.88	2.25 ± 0.03	0.58 ± 0.01	6.07	2.89	9.77 ± 1.36	QPO at 7.1 Hz.
24-00	52936.02	2.28	2.20 ± 0.02	0.58 ± 0.01	7.88	2.12	11.44 ± 0.56	QPO at 7.7 Hz.
25-00	52937.51	3.48	2.17 ± 0.02	0.55 ± 0.02	9.47	1.26	15.71 ± 0.91	QPO at 6.9 Hz.
26-00	52938.00	2.10	2.06 ± 0.02	0.52 ± 0.03	9.61	0.80	21.22 ± 1.13	LHS according to McClintock & Remillard (2006). QPO at 5.9 Hz.
27-00	52939.12	2.04	2.07 ± 0.02	0.50 ± 0.03	8.58	0.67	19.47 ± 0.78	Radio (VLA) detection! QPO at 5.8 Hz.
28-00	52942.12	1.98	1.86 ± 0.02	0.50 ± 0.08	6.31	0.20	26.21 ± 1.08	QPO at 2.9 Hz.
29-00	52942.68	1.62	1.87 ± 0.03	0.59 ± 0.11	5.66	0.19	19.82 ± 2.34	QPO at 2.4 Hz.
L01-00.....	52944.10	10.08	1.78 ± 0.01	0.42 ± 0.05	4.91	0.13	27.51 ± 2.63	QPO at 1.8 Hz.
30-00	52945.17	1.80	1.78 ± 0.02	0.45 ± 0.06	4.02	0.14	26.46 ± 3.69	
L01-01.....	52946.07	10.62	1.69 ± 0.02	0.47 ± 0.07	3.59	0.09	28.96 ± 2.54	
31-00	52947.02	1.08	1.79 ± 0.03	0.39 ± 0.10	2.80	0.06	29.93 ± 5.11	
32-00	52948.19	5.22	1.78 ± 0.02	0.29 ± 0.02	2.29	0.03	30.11 ± 2.23	
33-00	52949.53	3.54	1.74 ± 0.02	0.37 ± 0.07	1.99	0.05	36.40 ± 2.41	Last radio (VLA) detection.
L01-02.....	52949.67	10.38	1.76 ± 0.01	0.28 ± 0.01	1.79	0.03	39.29 ± 5.45	
34-00	52950.44	2.04	1.78 ± 0.03	0.36 ± 0.06	1.47	0.03	32.27 ± 12.20	Only PCA is used from this observation on.
35-00[f]	52951.39	3.72	1.74 ± 0.03	0.37 ± 0.06	1.02	0.04	...	Galactic ridge is as strong as the source.
36-00	52952.26	1.56	1.86 ± 0.04	0.29 ± 0.03	0.84	0.01	...	
L02-00.....	52953.18	14.28	1.83 ± 0.02	0.28 ± 0.02	0.58	0.02	...	
L02-01.....	52953.69	3.96	1.83 ± 0.05	0.30 ± 0.04	0.49	0.02	...	
L02-02.....	52953.96	8.76	1.72 ± 0.05	0.40 ± 0.03	0.41	0.04	...	
37-00	52955.46	1.74	1.98 ± 0.22	0.38 ± 0.08	0.18	0.03	...	
38-00	52956.26	3.06	1.71 ± 0.20	0.35 ± 0.06	0.13	0.02	...	Radio (ATCA) observation with no detection.
39-00	52957.00	1.44	2.43 ± 0.29	0.36 ± 0.09	0.09	0.02	...	
40-00	52958.23	3.66	2.32 ± 0.25	0.33 ± 0.06	0.08	0.02	...	
L03-0x[g]	52958.82	12.12	2.51 ± 0.66	0.35 ± 0.05	0.02	0.02	...	
L03-01.....	52959.21	14.64	1.79 ± 0.41	0.36 ± 0.03	0.03	0.02	...	

[a] Full observation ID is, e.g., 80137-01-Obs for observations that do not start with L, and 80137-02-Obs for those that start with L, denoting "long."
[b] Exposure time.
[c] Unabsorbed power-law flux in the 3–25 keV band, in units of 10^{-10} ergs cm^{-2} s^{-1}
[d] Unabsorbed disk-blackbody flux in the 3–25 keV band, in units of 10^{-10} ergs cm^{-2} s^{-1}.
[e] rms amplitude of variability in the 3–30 keV band after ridge correction.
[f] Observations 34-01, 35-00, and 35-01 were merged.
[g] Observations L03-00, L03-02, and L03-03 were merged.

For all the observations, our first spectral model consisted of absorption (`phabs` in XSPEC), smeared edge (`smedge` in XSPEC; Ebisawa et al. 1994), a multicolor disk blackbody (`diskbb` in XSPEC; Makishima et al. 1986), a power law (`pegpwrlw` in XSPEC), a narrow Gaussian to model the iron line, and the ridge emission (as described above). This model has been commonly used for the spectral analysis of black holes in the LHS (Tomsick & Kaaret 2000; Sobczak et al. 2000; Kalemci et al. 2005). The hydrogen column density was fixed to $N_{\rm H} = 2.3 \times 10^{22}$ cm^{-2} based on the *Chandra* results (Miller et al. 2004). The smeared edge width was fixed to 10 keV. Once we fit the observations with this model, we added a high-energy cutoff (`highecut` in XSPEC) to the model. None of the observations showed a significant decrease in χ^2, which would indicate a high-energy cutoff.

2.1.2. *X-Ray Temporal Analysis*

For each observation, we computed the power density spectra (PDS) from the PCA data using IDL programs developed at the University of Tübingen (Pottschmidt 2002) for three energy bands, 3–6 keV, 6–15 keV, and 15–30 keV. We also computed the PDS for the combined band of 3–30 keV. The source flux above 30 keV is too low for timing analysis. The PDS was normalized as described in Miyamoto & Kitamoto (1989) and corrected for the dead-time effects according to Zhang et al. (1995), with a dead time of 10 μs per event. Using 256 s time segments, we investigated the low-frequency QPOs and the timing properties of the continuum up to 256 Hz for different energy bands. We fit all our PDSs with broad and narrow Lorentzians with our standard timing analysis techniques (Kalemci et al. 2005; Kalemci 2002; Pottschmidt 2002).

In the PDS fits, Lorentzians with quality value (centroid frequency divided by the width) $Q > 2$ are denoted as QPOs. The rms amplitudes are calculated over a frequency band from zero to infinity. We multiplied the rms amplitude of variability with $T^2/[T - (R + B)]^2$, where T is the overall count rate, B is the background rate determined using `pcabackest`, and R is the count rate due to the Galactic ridge, to obtain the variability inherent to the source (Berger & van der Klis 1994).

2.2. *Radio Observations*

We obtained Very Large Array (VLA) radio information (observations conducted by M. Rupen) for dates between MJD 52,920 and 52,949. The "core" was not detected in 4.86 and 8.64 GHz frequencies on MJD 52,924.9 and 52,933.0. Another radio component (from an earlier discrete plasma ejection) away from the core was detected during this time (Rupen et al. 2004c). The first detection of the core during the decay occurred on MJD 52,940.0, with a flux density of 0.14 ± 0.04 mJy beam^{-1} (M. Rupen 2003, private communication). The last detection of the core with the VLA occurred on MJD 52,949, with a flux density of 0.22 ± 0.04 mJy at 4.86 GHz (Rupen et al. 2004a).

Toward the end of the 2003 outburst, the source was observed with the Australia Telescope Compact Array (ATCA). The source was not detected on MJD 52,955.86, 52,973.72, 52,983.45, 52,994.49, or 53,049.40, with the highest rms value of 0.10 mJy at 4.8 GHz (Corbel et al. 2005). The evolution of the radio fluxes during the outburst decay is given in Figure 2*b*.

3. RESULTS

We investigated the evolution of several spectral and temporal fit parameters during the decay of H1743−322 to establish the time of state transitions. Some of the important parameters are shown in Figure 2, and some of the spectral fit parameters are tabulated in Table 1.

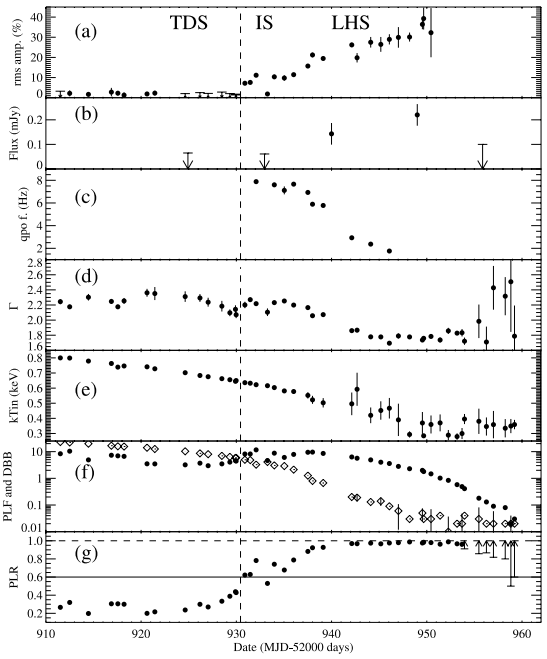

FIG. 2.—Evolution of (*a*) the total rms amplitude of variability in the 3–30 keV band, (*b*) the radio flux density at 4.86 GHz, (*c*) the QPO frequency, (*d*) the photon index (Γ), (*e*) the inner disk temperature $T_{\rm in}$, (*f*) the power-law flux (*circles*) and the disk-blackbody flux (*diamonds*) in the 3–25 keV band in units of 10^{-10} ergs cm^{-2} s^{-1}, and (*g*) the ratio of the power-law flux to the total flux in the 3–25 keV band. The dashed line indicates the case for which all the emission comes from the power-law component. The solid line shows the threshold for observing timing noise. Unabsorbed fluxes are shown. For most of the measurements, the 1 σ uncertainties are smaller than the plot symbols. The vertical dashed line indicates the approximate time of transition from the TDS to the IS. The first four data points in (*b*) are from VLA, and the final point is from ATCA.

3.1. *States and Transitions*

Until MJD 52,930, the spectral and temporal properties of the source indicated a TDS. When the noise was detected in the PDS, it was characterized by a weak power law typically observed in the TDS (see Fig. 3*a*). The rms amplitude of variability was less than 3%. On MJD 52,930, the power-law flux doubled, while the power-law ratio (PLR, the ratio of the power-law flux to the total flux in the 3–25 keV band) exceeded 0.6, and the PDS showed detectable timing noise, with an rms amplitude of ~7%. The spectral and temporal properties (see Figs. 3*b* and 3*d*) indicate an IS right after this transition. During the transition, the photon index increased slightly. The evolutions of $T_{\rm in}$ and the disk-blackbody (DBB) flux were smooth.

A QPO appeared on MJD 52,932 as the PLR reached 0.8. Just after this date, for one observation, the power-law flux and the PLR dropped. The strong timing signature also disappeared, and the PDS only showed a weak power-law component. The source properties were similar to those of the TDS. This single observation is called "TD-like" for this reason. Within half a day, the power-law flux increased to the IS levels, and the timing noise reappeared, along with the QPO (see Fig. 3). Based on the TDS observations and the TD-like observation, we set a PLR threshold

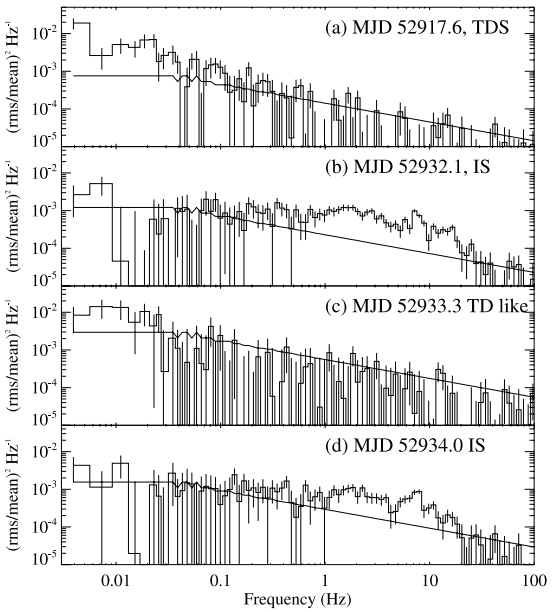

FIG. 3.—Power spectra (*a*) in the TDS, (*b*) after the transition to the IS, (*c*) during the TD-like observation, and (*d*) right after the TD-like observation, again in the IS. PDSs in (*b*), (*c*), and (*d*) are approximately 1 day apart. The solid line shows the effective Poisson noise level (uncertainty in Poisson noise subtraction after merging segments and binning the data; Nowak et al. 1999).

of variability of ∼0.6 for H1743−322. The duration for the TD-like case is of the order of 1 day. Interestingly, the photon index decreased during the TD-like observation, returning to the value measured right before the transition to the IS.

QPOs with decreasing frequency were observed in 10 observations after the transition. After MJD 52,933, the rms amplitude of variability increased, the photon index hardened, and the inner disk temperature and DBB flux decreased smoothly. At the end of this evolution, the source was in the LHS. The transition to the LHS was smooth, and it is difficult to determine when the source left the IS. Based on the McClintock & Remillard (2006) criteria (spectrum dominated by the power-law component, $1.5 < \Gamma < 2.1$, rms amplitude of variability >10%), the transition happened around MJD 52,938. In the LHS the photon index hovered between 1.7 and 1.9 until MJD 52,956. The rms amplitude of variability increased until MJD 52,950. After this date, the statistical quality of the data was not good enough to determine the rms amplitude of variability.

3.2. *Correlations between Spectral and Temporal Parameters*

It has been well established that the black hole transients show several correlations between spectral and temporal parameters (Kalemci 2002, and references therein). During outburst decays, the photon index shows the strongest correlations (or anticorrelations) with the QPO frequency and the rms amplitude of variability (Vignarca et al. 2003; Kalemci 2002). We plotted these parameters as a function of photon index in Figure 4. We also included the PLR as a function of photon index, as it shows a strong correlation with the rms amplitude of variability in the IS. Figure 4 shows that the rms amplitude of variability is strongly anticorrelated (linear correlation coefficient of −0.949), and the QPO frequency is strongly correlated (linear correlation coefficient of 0.987) with the photon index. Notice that there might be

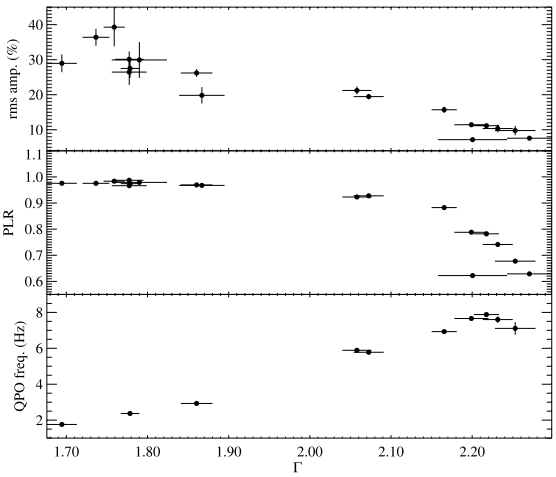

FIG. 4.—Correlation between the photon index and the rms amplitude of variability (*top*), the PLR (*middle*), and the QPO frequency (*bottom*) for observations taken between MJD 52,930.9 and 52,949.7, excluding the TD-like observation.

a turnover (or a saturation) in the QPO-Γ relation, as seen earlier for other sources by Vignarca et al. (2003). The TD-like observation is not shown. Obviously, it does not obey the anticorrelation between the rms amplitude of variability and Γ.

Another interesting relation is between the rms amplitude of variability and the disk flux. It is well known that the rms amplitude of variability increases with energy for systems with significant disk emission (Kalemci 2002), but once this disk component is not significant, the relation between rms amplitude of variability and energy is not predictable (Kalemci et al. 2004a). In Figure 5, we show the rms amplitude of variability for two energy bands, their ratio, and the PLR. The presence of DBB emission clearly reduces the rms amplitude of variability in the 3–6 keV

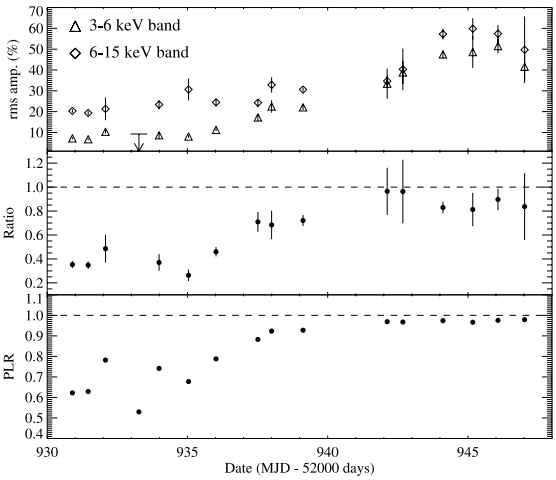

FIG. 5.—*Top*: Evolution of the rms amplitude of variability in the 3–6 keV (*triangles*) and 6–15 keV (*diamonds*) bands. The 3 σ upper-limit rms amplitude of variability for the TD-like observation in the 6–15 keV band (9.25%) is shown with an arrow. The 3–6 keV band upper limit of 3.28% is not shown for clarity. *Middle*: The ratio of the rms variability in the 3–6 keV and 6–15 keV bands. *Bottom*: The PLR.

band. For most of the observations during which the DBB emission is not significant, the ratio between rms amplitudes of variability is consistent with unity. But when the last six observations are grouped, it is clear that the 6–15 keV band rms amplitude of variability is higher than that of the 3–6 keV band.

4. DISCUSSION

4.1. *Evolution of Spectral and Temporal Properties during Outburst Decay*

In general, the evolution of the spectral and temporal parameters of H1743−322 show very similar characteristics to the evolution of other black hole systems during outburst decay. The transition from the TDS to the IS is sharp, and is marked by a jump in the rms amplitude of variability, the power-law flux, and the PLR (Kalemci et al. 2004a, 2005). We note that, during the transition, both the power-law flux and the PLR increase substantially. But the sudden increase in the PLR is always due to a sudden increase in the power-law flux, and not to a sudden decrease in DBB emission. Therefore, the physical change that causes the state transition is associated with a sudden increase in the power-law flux. On the other hand, the PLR provides a threshold for strong variability. After the transition from the TDS to the IS, the DBB flux and inner disk temperature steadily decrease, and finally the source reaches the LHS.

A detailed discussion of several scenarios that could result in such evolution during the decay is given for 4U 1543−47 in Kalemci et al. (2005). H1743−322 shows spectral and temporal evolution in X-rays quite similar to those of 4U 1543−47. In addition, for both cases, the radio core was only detected after the sources reached their hardest levels, and not detected right after the transition to the IS. For H1743−322, the fits never require a high-energy cutoff in the spectrum, while for 4U 1543−47, a cutoff is observed only during the transition to the LHS. It is possible that a portion of electrons are nonthermal for both sources, at least in the TDS and IS (Coppi 1999). For H1743−322, the evolution of $T_{\rm in}$ is consistent with an accretion disk receding away from the black hole (and the drop in QPO frequency may also be an indication of this). The evolutions of the PLR and Γ indicate a Comptonizing medium (either an independent corona or the base of a jet) getting stronger as the decay progresses. The lack of adequate multiwavelength coverage does not allow us to strongly constrain the details of different models, as we were able to do for 4U 1543−47.

Even though most of the properties of H1743−322 are generic to the black hole transients during decay, it also showed two unexpected behaviors. The first one is the TD-like observation on MJD 52,932. Once the transition to a harder state occurs, it is unusual for a system to go back to the previous, softer state just for 1 day during the outburst decay. (Short branchings to harder states are common, such as branching seen in the 1998 outburst of XTE J1550−564; Homan et al. 2001). For the 14 outburst decays analyzed in Kalemci 2002, only XTE J1859+226 showed a similar behavior in its outburst decay in 1999. After the transition to the IS at MJD 51,524, XTE J1859+226 transited back to the TDS twice for a short time (Kalemci 2002). A recent report indicates that during the decay of the 2002–2003 outburst of GX 339−4, the source transited back to the TDS for 3 days after the transition to the IS (Belloni et al. 2005). We note that these branchings with timescales of a few days may be more common, as frequent monitoring is required to catch them. If we examine the cases source by source, rather than outburst by outburst, from the seven transients that have been observed with daily monitoring, three sources showed this behavior. The IS is a transitional state between the TDS and the LHS, but these branchings imply that the evolution is not monotonic. Transitions back and forth to the TDS can occur on a timescale of days. In contrast, once the source is in the hard state and the X-ray luminosity keeps decreasing, the process is irreversible; there is no example (to the best of our knowledge) of a transition back to the IS or the TDS.

A second unexpected behavior is the slight increase in photon index (∼6%) during the transition to the IS (see Fig. 2). The only other case that showed an increase in photon index during a transition from the TDS to the IS is the 2000 outburst of XTE J1550−564 (Kalemci et al. 2004a; Rodriguez et al. 2003). During such transitions, the power-law index usually does not change, or decreases somewhat (Kalemci et al. 2004a). For both H1743−322 and XTE J1550−564, the power-law flux and the PLR showed a sudden increase, while the photon index also increased. However, for H1743−322, this transition resulted in an increase in rms amplitude of variability, whereas for XTE J1550−564, it resulted in a decrease of rms amplitude of variability. Note that the conditions for these two transitions were not the same. For H1743−322, the transition was from the TDS to an IS, whereas for XTE J1550−564, the transition was from a soft IS to a harder IS, en route to the LHS.

4.2. *Emission Mechanisms during the State Transition from the TDS to the IS*

In the TDS, the bulk of the emission comes from the disk as multicolor blackbody radiation. The evolution of the DBB component during the transition to the IS is smooth. On the other hand, the power-law component in the X-ray spectrum shows a sudden change, and is perhaps associated with the state transition. For the power-law component, the two important observations are (1) a sudden (less than 1 day) and strong (100%) increase in the flux, and (2) a small change (6% increase) in the photon index. We note that an increase in the power-law flux with only little or no change in the power-law index is a universal property of the state transitions that coincide with the appearance of timing noise and QPOs for most of the black hole systems (Kalemci et al. 2004a). In this section, we discuss various scenarios that may explain the evolution of the power-law component during the transition to the IS.

For thermal Comptonization, the photon index depends on two parameters of the corona: the temperature and the optical depth of the Comptonizing medium (Sunyaev & Titarchuk 1980). The power-law flux depends on the input soft flux, the optical depth, and the covering fraction of the Comptonizing medium. Increasing the soft input flux would result in a larger power-law flux and also may cause a lower coronal temperature due to cooling. Our observations do not indicate an increase in the DBB flux. A sudden expansion of the corona (while keeping the optical depth constant) could explain the change in power-law flux if the volume increase corresponds to an increase in the covering fraction. Before the transition, the rms amplitude of variability is less than 1.8%; therefore, there is at least a factor of 4 increase in the rms amplitude of variability, whereas there is only a factor of 2 increase in the power-law flux. Therefore, the volume increase should have a nonlinear relation to the variability amplitude to explain the strong increase. Emergence of another soft photon source inside the corona (with a spectrum not contributing in the PCA range) is another possible explanation for the transition. One candidate is synchrotron radiation inside the corona, causing synchrotron self-Compton emission (Markoff & Nowak 2004). In this case, the hard power-law emission would be created by a combination of thermal Comptonization of synchrotron and disk photons and nonthermal synchrotron self-Compton emission. For the case

of synchrotron, the seed photons come from inside, while for the DBB, the seed photons come from both the outside and the inside of the corona, depending on the assumed geometry. It is possible that the strong variability is created more efficiently if the source is inside the corona. Since the major change is not related to the temperature and optical depth of the corona, it could also explain why the photon index varies little during the transition. The small change in the index may be due to additional cooling (if the increase in the secondary soft flux is more than the decrease in the DBB flux), or the effect of additional nonthermal Comptonization. If the strong variability in the IS and the LHS is due to an additional soft component such as the synchrotron radiation, then the origin of low-frequency QPOs will not be the accretion disk (Lee & Miller 1998; Titarchuk & Fiorito 2004). One can also envision a combination of scenarios, such as an expansion of the corona while the synchrotron self-Compton contribution is increasing.

Another way to increase the power-law flux is to have two emission mechanisms producing power-law spectra. During the transition, the second component, which also produces the timing noise, may become active. One possibility is that during the TDS the bulk motion (dynamical) Comptonization (Laurent & Titarchuk 1999; Titarchuk & Fiorito 2004) may be the main mechanism, whereas in the IS, thermal Comptonization starts to operate. This requires that both components produce very similar power-law spectra right at the transition. The secondary component in the IS may also be direct synchrotron emission from a jet (Falcke & Biermann 1999; Markoff et al. 2001). This, again, requires that both emission mechanisms produce a similar spectrum at the transition. There is another argument against this second possibility. The radio observations indicate that the emission from the compact jet began sometime between MJD 52,933 and 52,940, well after the transition to the IS. (Since there was no optical or infrared monitoring of the source during the transition, we were not able to pinpoint the time of jet formation.) Based on the comparison between the optical and IR light curves and the X-ray and radio properties of GX 339−4 (Homan et al. 2005a) and 4U 1543−47 (Kalemci et al. 2005), one can argue that the compact jet does not turn on before the source is settled in the LHS. H1743−322 seems to support this argument, as the compact radio jet was first detected after the source was in the LHS, according to McClintock & Remillard (2006). We note that, during the rise, a compact radio core was observed, even after the transition from the LHS to the IS (Joinet et al. 2005; Rupen et al. 2003). This shows that, even though the *formation* of the compact jet requires the LHS with almost no soft emission in the PCA band, it can be *sustained* for a while in the presence of soft emission (Corbel et al. 2004).

4.3. *The Correlations*

There is a very strong correlation between the photon index and the QPO frequency up to a photon index of 2.2. At high photon indices, the relation seems to be turning over. XTE J1550−564 and GRO J1655−40 are two other sources that show a turnover in the QPO frequency–photon index relation (Vignarca et al. 2003). Relativistic effects may cause this turnover, if the QPO has an "accretion ejection instability" origin (Varnière et al. 2002; Vignarca et al. 2003). We note that we cannot conclusively claim that the relation turns over for H1743−322, because the evidence for a turnover is based on a single data point (see Fig. 4). A saturation QPO frequency with photon index could be a sign of a system dominated by a converging inflow (Titarchuk & Fiorito 2004).

There is a strong anticorrelation between the photon index and the rms amplitude of variability. This is a global relation that is valid for most black hole transients during outburst decay (Kalemci et al. 2003). One can also observe a strong correlation between the PLR and the rms amplitude of variability at high spectral indices (see Fig. 4). This shows the diminishing effect of the DBB radiation on the rms amplitude of variability. Another way to investigate the effect of DBB on the rms amplitude of variability is to compare the energy dependence of variability. Figure 5 shows that for the observations with strong DBB emission, the rms amplitude of variability is much stronger in the higher energy band than in the lower energy band. One can see a correlation between the ratio of the rms amplitude of variability in two bands and the PLR. Once the DBB emission is negligible (PLR $\sim$ 1), the relation between the rms amplitude of variability and energy is not that clear. The correlations between the PLR and both the rms amplitude of variability and the variability ratio indicate that the variability is generated in the power-law component, and that the DBB component regulates the rms amplitude of variability by changing the mean flux (Churazov et al. 2001; Kalemci 2002).

5. SUMMARY AND CONCLUSIONS

We analyzed the *RXTE* X-ray observations of H1743−322 during its outburst decay in 2003. In addition to the X-ray observations, we also obtained radio fluxes and discussed their evolution with respect to the state transitions. The evolution of the spectral and temporal fit parameters show similar properties to those of other sources. The transition from the TDS to the IS is marked by a strong increase in the rms amplitude of variability and power-law flux. This transition may correspond to the emergence of a secondary soft component, such as synchrotron radiation, or a secondary power-law component. Future multiwavelength observations of these transients may help in making the distinction. At the time of this transition, the radio core was not detected. Three days after the transition, the source went back to the TDS for 1 day, indicating that the IS is not stable. After the source returned to the IS, it gradually reached the low-hard state. The core is detected in the radio band when the X-ray spectrum is totally dominated by the power-law emission.

There is a strong correlation between the photon index and the QPO frequency. At high QPO frequencies and photon indices, the correlation shows a turnover (or saturates). The threshold PLR for the state transition and the correlation between the PLR and the ratio of rms amplitude of variability in the 6–15 keV and 3–6 keV bands show that the DBB emission dilutes the amplitude of variability. When the DBB emission is absent, the rms amplitude of variability in two bands is similar. This may indicate that the origin of the variability and the QPO is the corona itself, rather than the disk.

E. K. acknowledges NASA grant NAG5-13142 and the partial support of TÜBİTAK. E. K. thanks all scientists who contributed to the Tübingen Timing Tools. The authors thank Michael Rupen for the valuable VLA data. E. K. thanks Lev Titarchuk for his remarks on state transition and evolution. This work made use of the Galactic bulge scans of Craig Markwardt. J. A. T. acknowledges partial support from NASA grant NNG04GB19G. R. E. R. acknowledges NASA grant NAS5-30720. P. K. acknowledges partial support from a University of Iowa Faculty Scholar Award. The authors also thank the anonymous reviewer for his comments, which significantly improved the scientific quality of the paper. The Australia Telescope is funded by the Commonwealth of Australia for operation as a national facility managed by CSIRO.

REFERENCES

Baba, D., Nagata, T., Iwata, I., Kato, T., & Yamaoka, H. 2003, IAU Circ., 8112, 2
Belloni, T., Homan, J., Casella, P., van der Klis, M., Nespoli, E., Lewin, W. H. G., Miller, J. M., & Mendez, M. 2005, A&A, 440, 207
Berger, M., & van der Klis, M. 1994, A&A, 292, 175
Bradt, H. V., Rothschild, R. E., & Swank, J. H. 1993, A&AS, 97, 355
Churazov, E., Gilfanov, M., & Revnivtsev, M. 2001, MNRAS, 321, 759
Coppi, P. S. 1999, in ASP Conf. Ser. 161, High Energy Processes in Accreting Black Hole, ed. J. Poutanen & R. Svensson (San Francisco: ASP), 375
Corbel, S., & Fender, R. P. 2002, ApJ, 573, L35
Corbel, S., Fender, R. P., Tomsick, J. A., Tzioumis, A. K., & Tingay, S. 2004, ApJ, 617, 1272
Corbel, S., Fender, R. P., Tzioumis, A. K., Nowak, M., McIntyre, V., Durouchoux, P., & Sood, R. 2000, A&A, 359, 251
Corbel, S., Kaaret, P., Fender, R. P., Tzioumis, A. K., Tomsick, J. A., & Orosz, J. A. 2005, ApJ, 632, 504
Corbel, S., et al. 2001, ApJ, 554, 43
Doxsey, R., et al. 1977, IAU Circ., 3113, 1
Ebisawa, K., et al. 1994, PASJ, 46, 375
Emelyanov, A. N., Aleksandrovich, N. L., & Sunyaev, R. A. 2000, Astron. Lett., 26, 297
Esin, A. A., McClintock, J. E., & Narayan, R. 1997, ApJ, 489, 865
Falcke, H., & Biermann, P. L. 1999, A&A, 342, 49
Fender, R., et al. 1999, ApJ, 519, L165
Fender, R. P. 2001, MNRAS, 322, 31
Fender, R. P., & Kuulkers, E. 2001, MNRAS, 324, 923
Grebenev, S. A., Lutovinov, A. A., & Sunyaev, R. A. 2003, Astron. Tel., 189
Homan, J., Buxton, M., Markoff, S., Bailyn, C., Nespoli, E., & Belloni, T. 2005a, ApJ, 624, 295
Homan, J., Miller, J. M., Wijnands, R., Steeghs, D., Belloni, T., van der Klis, M., & Lewin, W. H. G. 2003, Astron. Tel., 162
Homan, J., Miller, J. M., Wijnands, R., van der Klis, M., Belloni, T., Steeghs, D., & Lewin, W. H. G. 2005b, ApJ, 623, 383
Homan, J., Wijnands, R., van der Klis, M., Belloni, T., van Paradijs, J., Klein-Wolt, M., Fender, R., & Méndez, M. 2001, ApJS, 132, 377
Joinet, A., Jourdain, E., Malzac, J., Roques, J. P., Schönfelder, V., Ubertini, P., & Capitanio, F. 2005, ApJ, 629, 1008
Kalemci, E. 2002, Ph.D. thesis, Univ. California, San Diego
Kalemci, E., Tomsick, J. A., Buxton, M. M., Rothschild, R. E., Pottschmidt, K., Corbel, S., Brocksopp, C., & Kaaret, P. 2005, ApJ, 622, 508
Kalemci, E., Tomsick, J. A., Rothschild, R. E., Pottschmidt, K., Corbel, S., Wijnands, R., Miller, J. M., & Kaaret, P. 2003, ApJ, 586, 419
Kalemci, E., Tomsick, J. A., Rothschild, R. E., Pottschmidt, K., & Kaaret, P. 2001, ApJ, 563, 239
———. 2004a, ApJ, 603, 231
———. 2004b, in AIP Conf. Proc. 714, X-ray Timing 2003: Rossi and Beyond, ed. P. Kaaret, F. K. Lamb, & J. H. Swank (New York: AIP), 52
Kaluzienski, L. J., & Holt, S. S. 1977, IAU Circ., 3106, 1
Kretschmar, P., Chenevez, J., Capitanio, F., Orr, A., Palumbo, G., & Grebenev, S. 2003, Astron. Tel., 180
Laurent, P., & Titarchuk, L. 1999, ApJ, 511, 289
Lee, H. C., & Miller, G. S. 1998, MNRAS, 299, 479
Makishima, K., Maejima, Y., Mitsuda, K., Bradt, H. V., Remillard, R. A., Tuohy, I. R., Hoshi, R., & Nakagawa, M. 1986, ApJ, 308, 635
Markoff, S., Falcke, H., & Fender, R. 2001, A&A, 372, L25
Markoff, S., & Nowak, M. A. 2004, ApJ, 609, 972
Markwardt, C. B., & Swank, J. H. 2003, Astron. Tel., 133
McClintock, J. E., & Remillard, R. A. 2006, in Compact Stellar X-Ray Sources, ed. W. H. G. Lewin & M. van der Klis (Cambridge: Cambridge Univ. Press), in press (astro-ph/0306213)
Miller, J. M., et al. 2004, ApJ, submitted (astro-ph/0406272)
Miyamoto, S., & Kitamoto, S. 1989, Nature, 342, 773
Nowak, M. A., Vaughan, B. A., Wilms, J., Dove, J. B., & Begelman, M. C. 1999, ApJ, 510, 874
Parmar, A. N., Kuulkers, E., Oosterbroek, T., Barr, P., Much, R., Orr, A., Williams, O. R., & Winkler, C. 2003, A&A, 411, L421
Pottschmidt, K. 2002, Ph.D. thesis, Univ. Tübingen
Revnivtsev, M. 2003, A&A, 410, 865
Revnivtsev, M., Chernyakova, M., Capitanio, F., Westergaard, N. J., Shoenfelder, V., Gehrels, N., & Winkler, C. 2003, Astron. Tel., 132
Reynolds, P. S. 1999, Astrophys. Lett. Commun., 38, 425
Rodriguez, J., Corbel, S., & Tomsick, J. A. 2003, ApJ, 595, 1032
Rothschild, R. E., et al. 1998, ApJ, 496, 538
Rupen, M. P., Dhawan, V., & Mioduszewski, A. J. 2003a, Astron. Tel., 210
———. 2004a, Astron. Tel., 304
Rupen, M. P., Mioduszewski, A. J., & Dhawan, V. 2003b, Astron. Tel., 139
———. 2004b, BAAS, 8, 17.06
———. 2004c, Astron. Tel., 314
Sobczak, G. J., McClintock, J. E., Remillard, R. A., Cui, W., Levine, A. M., Morgan, E. H., Orosz, J. A., & Bailyn, C. D. 2000, ApJ, 544, 993
Steeghs, D., Miller, J. M., Kaplan, D., & Rupen, M. 2003, Astron. Tel., 146
Sunyaev, R., & Titarchuk, L. 1980, A&A, 86, 121
Titarchuk, L., & Fiorito, R. 2004, ApJ, 612, 988
Tomsick, J. A., Corbel, S., & Kaaret, P. 2001, ApJ, 563, 229
Tomsick, J. A., & Kaaret, P. 2000, ApJ, 537, 448
Tomsick, J. A., & Kalemci, E. 2003, Astron. Tel., 198
Tomsick, J. A., Kalemci, E., Corbel, S., & Kaaret, P. 2003, ApJ, 592, 1100
Varnière, P., Rodriguez, J., & Tagger, M. 2002, A&A, 387, 497
Vignarca, F., Migliari, S., Belloni, T., Psaltis, D., & van der Klis, M. 2003, A&A, 397, 729
Zdziarski, A. A., Poutanen, J., Paciesas, W. S., & Wen, L. 2002, ApJ, 578, 357
Zhang, W., Jahoda, K., Swank, J. H., Morgan, E. H., & Giles, A. B. 1995, ApJ, 449, 930

3.5.6

On the Origin of Radio Emission in the X-Ray States of XTE J1650-500 during the 2001-2002 Outburst.

Article publié dans :

Astrophys. J., 2004, 617, 1272-1283

Corbel, S., Fender, R. P., Tomsick, J. A., Tzioumis, A. K., Tingay, S.

The Astrophysical Journal, 617:1272–1283, 2004 December 20

ON THE ORIGIN OF RADIO EMISSION IN THE X-RAY STATES OF XTE J1650−500 DURING THE 2001–2002 OUTBURST

S. Corbel,[1] R. P. Fender,[2] J. A. Tomsick,[3] A. K. Tzioumis,[4] and S. Tingay[5]
Received 2004 June 11; accepted 2004 August 13

ABSTRACT

We report on simultaneous radio and X-ray observations of the black hole candidate XTE J1650−500 during the course of its 2001–2002 outburst. The scheduling of the observations allowed us to sample the properties of XTE J1650−500 in different X-ray spectral states, namely, the hard state, the steep power-law state, and the thermal dominant state, according to the recent spectral classification of McClintock & Remillard. The hard state is consistent with a compact jet dominating the spectral energy distribution at radio frequencies; however, the current data suggest that its contribution as direct synchrotron emission at higher energies may not be significant. In that case, XTE J1650−500 may be dominated by Compton processes (either inverse Comptonization of thermal disk photons and/or synchrotron self-Compton radiation from the base of the compact jet) in the X-ray regime. We surprisingly detect a faint level of radio emission in the thermal dominant state that may be consistent with the emission of previously ejected material interacting with the interstellar medium, similar (but on a smaller angular scale) to what was observed in XTE J1550−564 by Corbel and coworkers. Based on the properties of radio emission in the steep power-law state of XTE J1650−500 and taking into account the behavior of other black hole candidates (namely, GX 339−4, XTE J1550−564, and XTE J1859+226) while in the intermediate and steep power-law states, we are able to present a general pattern of behavior for the origin of radio emission in these two states that could be important for understanding the accretion-ejection coupling very close to the black hole event horizon.

Subject headings: accretion, accretion disks — black hole physics — ISM: jets and outflows — radio continuum: stars — stars: individual (GX 339−4, XTE J1550−564, XTE J1650−500, XTE J1859+226)

1. INTRODUCTION

XTE J1650−500 is a soft X-ray transient discovered on 2001 September 5 (MJD 52,157; Remillard 2001) by the All-Sky Monitor on board the *Rossi X-Ray Timing Explorer* (*RXTE* ASM). On the next day, pointed *RXTE* PCA (Proportional Counter Array) observations confirmed the ASM detection of XTE J1650−500 with an X-ray spectrum typical of a black hole candidate (BHC) in the hard state (HS) (Markwardt et al. 2001). This was confirmed by further analysis of the power density spectra (Revnivtsev & Sunyaev 2001; Wijnands et al. 2001). During the course of the outburst, XTE J1650−500 went into all the canonical X-ray spectral states (Rossi et al. 2004) that are typical of the population of BHCs (Belloni 2004; McClintock & Remillard 2004). High-frequency quasi-periodic oscillations (QPOs) have been reported by Homan et al. (2003). The possible detection of a broad iron Kα emission (e.g., Miller et al. 2002) may suggest that XTE J1650−500 is a maximal Kerr black hole. In addition, short ($\sim$100 s) X-ray flares and long-timescale oscillations have been reported by Tomsick et al. (2003b) during the decay to quiescence.

The optical counterpart was discovered by Castro-Tirado et al. (2001) with the 0.6 m optical telescope at Lake Tekapo, New Zealand. The identification was later confirmed by Groot et al. (2001) and Augusteijn et al. (2001). The radio counterpart was discovered with the Australia Telescope Compact Array (ATCA) located in Narrabri, Australia (Groot et al. 2001). Further optical observations of XTE J1650−500 in quiescence with the 6.5 m Magellan telescope and the 8 m Very Large Telescope revealed the orbital parameters of this system (Orosz et al. 2004). The companion star is of spectral type K3 V–K5 V, and the orbital period of the system is 0.3205 days. The mass function of $2.73 \pm 0.56\ M_{\odot}$ and the lower limit on the inclination angle of $50^{\circ} \pm 3^{\circ}$ (in contradiction to what was originally proposed by Sanchez-Fernandez et al. [2002]) give an upper limit of $7.3\ M_{\odot}$ for the mass of the compact object. The primary in the XTE J1650−500 system is likely a black hole, and in fact, the existing data suggest that it could be a black hole with a mass of only $4\ M_{\odot}$ (Orosz et al. 2004).

In this paper we report on X-ray and radio observations of XTE J1650−500 spread over the entire outburst. In § 2 we describe the observations and the outburst evolution. We then discuss the properties of the radio emission from XTE J1650−500 in each of the states covered by our observations, including the HS, the steep power-law (SPL) state (we also discuss the nature of the intermediate state [IS]), the thermal dominant (TD) state, and the state transitions. Our conclusions are summarized in § 4. Our X-ray state definitions are nearly the same as the new definitions described in the review by McClintock & Remillard (2004). In this work we follow McClintock & Remillard (2004) by using the names HS and TD state rather than the previous names (low-hard state and high-soft state, respectively) to designate the two best-known X-ray states. The

[1] Université Paris 7, Denis Diderot, and Service d'Astrophysique, UMR AIM, CEA Saclay, F-91191 Gif-sur-Yvette, France.
[2] Astronomical Institute 'Anton Pannekoek' and Center for High Energy Astrophysics, University of Amsterdam, Kruislaan 403, 1098 SJ Amsterdam, Netherlands.
[3] Center for Astrophysics and Space Sciences, University of California at San Diego, MS 04-24, La Jolla, CA 92093.
[4] Australia Telescope National Facility, CSIRO, P.O. Box 76, Epping, NSW 1710, Australia.
[5] Center for Astrophysics and Supercomputing, Swinburne University of Technology, Mail Number 31, P.O. Box 218, Hawthorn, VIC 3122, Australia.

TABLE 1
OBSERVING LOG AND RESULTS

PARAMETER	OBSERVATION							
	1	2	3	4	5	6	7	8
Date (MJD)[a]	52159.94	52160.81	52177.01	52187.67	52195.85	52204.25	52241.52	52247.63
Calendar date	2001 Sep 7	2001 Sep 8	2001 Sep 24	2001 Oct 5	2001 Oct 13	2001 Oct 21	2001 Nov 27	2001 Dec 4
Time on source (hr)[b]	0.66, 1.09	1.16, 0.99	1.29	4.10	3.75	1.80	6.56	2.73
Array configuration	6B	6B	0.750D	EW352	EW352	EW352	6D	6D
Flux density (mJy):								
1384 MHz	2.7 ± 0.3	4.08 ± 0.20	...	...	...	...	...	...
2496 MHz	2.3 ± 0.2	5.30 ± 0.15	...	...	...	...	...	...
4800 MHz	...	5.28 ± 0.10	0.83 ± 0.10	<0.21	1.29 ± 0.07	0.78 ± 0.10	1.21 ± 0.06	0.75 ± 0.10
8640 MHz	...	4.48 ± 0.10	0.77 ± 0.10	<0.18	0.91 ± 0.10	0.34 ± 0.09	1.15 ± 0.06	<0.30
Spectral index	−0.27 ± 0.31	−0.29 ± 0.04[c]	−0.13 ± 0.86	...	−0.59 ± 0.56	−1.41 ± 1.36	−0.09 ± 0.18	<−1.3
X-ray state	HS	HS	SPL	SPL	TD	TD	HS	HS
X-ray flux[d]	10.40 ± 0.10	10.96 ± 0.11	10.47 ± 0.10	10.31 ± 0.10	10.04 ± 0.10	7.25 ± 0.07	1.75 ± 0.08	1.13 ± 0.06

NOTE.—Upper limits are given at the 3 σ confidence level.
[a] Radio observation midpoint.
[b] The first number is for the observations at 1384 and 2496 MHz (if noted); otherwise, it is related to the observations at 4800 and 8640 MHz.
[c] Spectral index obtained if we fit the radio spectrum with a power law and thermal free-free absorption. If we use the two higher frequencies, a spectral index of -0.28 ± 0.14 is deduced.
[d] Unabsorbed 2–11 keV flux in units of 10^{-9} ergs s^{-1} cm^{-2}.

difference between our definitions and those of McClintock & Remillard (2004) concerns the intermediate and very high states, which could possibly be various instances of the same state (e.g., Homan et al. 2001; Belloni 2004). McClintock & Remillard (2004) divided these two flavors of the intermediate/very high state as follows: First is the soft (i.e., photon index >2.4) flavor, which has a steep power-law spectrum and was therefore called the SPL state. In the SPL state, low- and high-frequency QPOs are usually detected. The interpretation of the IS in McClintock & Remillard (2004) is more ambiguous, as it is defined in terms of combinations of the other spectral states. In this work we define the IS as having properties between the HS and SPL state, so that the IS is essentially a hard flavor of the intermediate/very high state mentioned previously.

2. OBSERVATIONS AND OUTBURST OVERVIEW

2.1. *Radio Observations*

During the X-ray outburst of XTE J1650−500, we conducted eight continuum radio observations with ATCA, located in Narrabri, New South Wales, Australia. The ATCA synthesis telescope is an east-west array consisting of six 22 m antennas. The ATCA uses orthogonal polarized feeds and records full Stokes parameters. We carried out observations mostly at 4800 MHz (6.3 cm) and 8640 MHz (3.5 cm) with the exception of the first two observations, for which we also made measurements at 1384 MHz (21.7 cm) and 2496 MHz (12.0 cm). For the first observation, because of the large uncertainty in the X-ray position at that time, the radio counterpart of XTE J1650−500 was outside the primary beam of the telescope at 4800 and 8640 MHz. We performed observations in various array configurations: 6B (baselines ranging from 214 to 5969 m), 6D (77–5878 m), 0.750D (31–4469 m), and EW352 (31–4438 m), in order of decreasing spatial resolution. An additional observation (6A configuration) was conducted on 2003 December 21 while XTE J1650−500 was in quiescence. We did not detect XTE J1650−500 with a 3 σ upper limit of 0.3 mJy at 4800 and 8640 MHz.

The amplitude and bandpass calibrator was PKS 1934−638, and the antenna's gain and phase calibration, as well as the polarization leakage, were derived from regular observations of the nearby (less than a degree away) calibrator PMN 1646−50. The editing, calibration, Fourier transformation, deconvolution, and image analysis were performed using the MIRIAD software package (Sault & Killeen 1998). An observing log, as well as the ATCA flux densities of XTE J1650−500, can be found in Table 1. The dates of our ATCA observations are indicated in Figures 1 and 2 in order to illustrate how they are related to the X-ray states of XTE J1650−500.

2.2. *X-Ray Observations*

In order to have a long-term view of the X-ray behavior of XTE J1650−500, we used the publicly available X-ray data from the *RXTE* ASM (Levine et al. 1996). The 1.5–12 keV ASM light curve is plotted in Figure 1. In addition, we also used PCA and HEXTE data from our pointed observations, as well as observations available from the *RXTE* archive. The procedure for reduction of these data can be found in Tomsick et al. (2003b, 2004). We used these data to extract count rates in the 3–200 keV band as a function of time. We define a hard color as the ratio of the HEXTE count rate (20–200 keV) to the 3–20 keV PCA count rate. We then constructed a hardness-intensity diagram (HID), similarly to Homan et al. (2003) and Rossi et al. (2004). We conducted a more detailed analysis of the X-ray energy spectrum for the *RXTE* observations closest in time to the eight radio observations. Using the XSPEC (ver. 11) software for spectral analysis, we fitted the PCA+HEXTE spectra, primarily to determine the fluxes in several energy bands (see Table 1, Figs. 5 and 6). In all cases, the spectral continuum is well described by a disk-blackbody (Makishima et al. 1986) plus power-law or cutoff power-law model, which is typical of BHC systems. We also accounted for interstellar absorption, and we fixed the column density to the value of $N_{\rm H} = 6 \times 10^{21}$ cm^{-2} measured by the *Chandra X-Ray Observatory* (Tomsick et al. 2004). For some observations, this continuum model left significant residuals near the iron Kα complex (6–10 keV), but we obtained acceptable fits with reduced $\chi^2 < 1.0$ after including an iron emission line and a smeared iron edge (Ebisawa et al. 1994). The final model we used to determine the

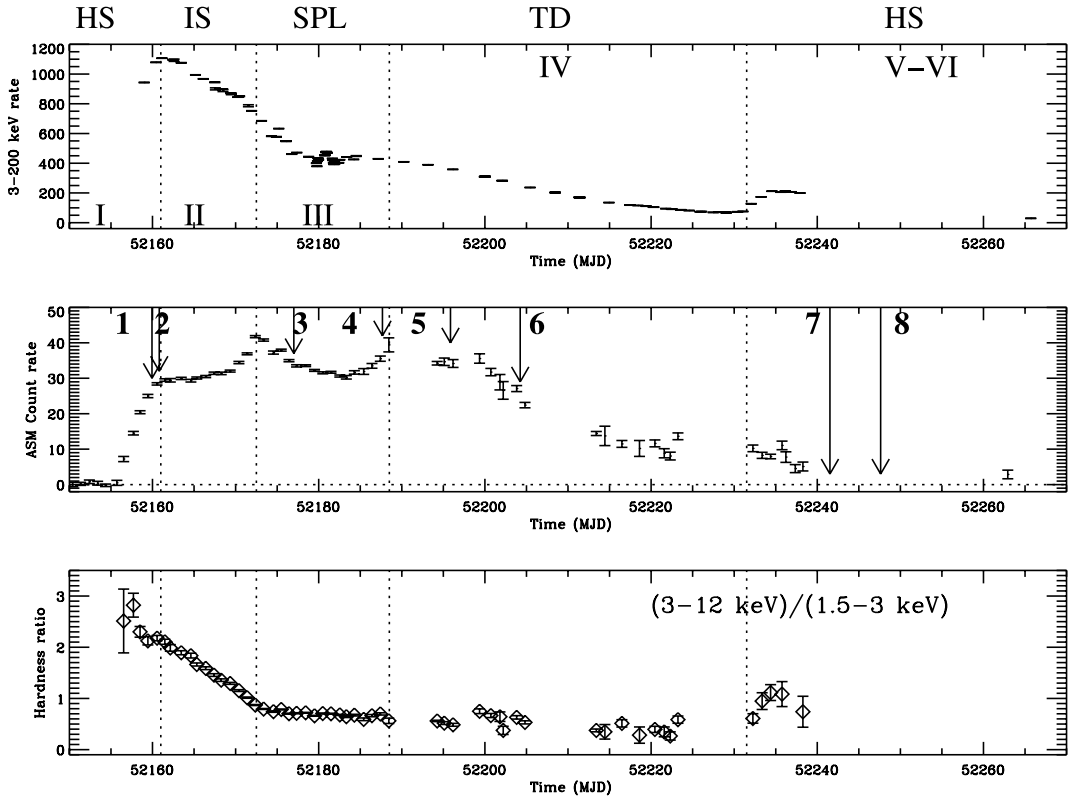

FIG. 1.—*Top*: *RXTE* (PCA+HEXTE) 3–200 keV count rate light curve (daily average) of XTE J1650−500 during its 2001–2002 outburst. *Middle*: *RXTE* ASM 1.5–12 keV count rate light curve. *Bottom*: Evolution of the ASM hardness ratio (3–12 keV/1.5–3 keV) during the whole outburst. The vertical dotted lines indicate the transition between the various X-ray states: HS (hard state), IS (intermediate state), SPL (steep power-law state), and TD (thermal dominant state). The roman numerals in the top panel illustrate the various time intervals used by Homan et al. (2003) and Rossi et al. (2004) for their X-ray analysis. The arrows (with a number) indicate when our radio observations were performed. We note that the high-frequency QPOs have been detected only in interval III (Homan et al. 2003).

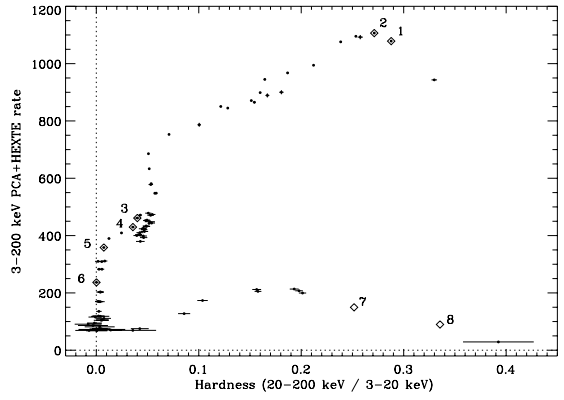

FIG. 2.—HID for the outburst of XTE J1650−500, similar to the one used by Homan et al. (2003). The diamonds (with associated number) indicate the period of simultaneous radio and X-ray observations. For observations 7 and 8, the position is only indicative, as XTE J1650−500 could not be observed by *RXTE* because of its proximity to the Sun. However (see text and Fig. 5), their positions are likely to be approximately correct.

X-ray fluxes is also described in detail in, e.g., Tomsick et al. (2001).

2.3. *The 2001–2002 X-Ray Outburst of XTE J1650−500*

To fully understand the radio properties of XTE J1650−500 during its outburst, we first need to characterize the X-ray states of XTE J1650−500 as a function of time. For that purpose, Figure 1 shows the *RXTE* ASM 1.5–12 keV and *RXTE* PCA+HEXTE 3–200 keV light curves, as well as the evolution of the *RXTE* ASM (3–12 keV/1.5–3 keV) hardness ratio; the arrows indicate the dates of the ATCA radio observations. In addition, the HID in Figure 2 adds complementary information on the outburst evolution; the diamonds highlight the radio observations. XTE J1650−500 moved counterclockwise in the HID during the whole outburst. As can be seen from these two figures, the scheduling of the radio observations provides a sampling of very different X-ray states of XTE J1650−500. In Figure 1 we indicate the time intervals used by Homan et al. (2003) and Rossi et al. (2004) with Roman numerals.

After its discovery on 2001 September 5 (MJD 52,157) by *RXTE* ASM (Remillard 2001), the first *RXTE* pointed observation occurred on 2001 September 6. The *RXTE* observations (up to September 9) are consistent with a BHC in the HS with a strong band-limited noise component in the power density

spectra and energy spectra dominated by a power-law component of photon index ∼1.6 and exponential cutoff (Revnivtsev & Sunyaev 2001; Wijnands et al. 2001). The rest of the bright outburst phase has been described by Rossi et al. (2004; S. Rossi 2004, private communication) and Homan et al. (2003), and we outline their conclusions below (for the decay phase, see Kalemci et al. [2003] and Tomsick et al. [2003b, 2004]). Starting around September 9, a gradual softening of the spectrum occurs up until October 5 (MJD 52,187). From September 9 to 20 (MJD 52,161–52,172), XTE J1650−500 is characterized by a smooth softening of its energy spectrum (with an evolution of the power-law photon index from 1.5 to 2.2), and the frequency of the QPO increases from ∼1 to 9 Hz. During the period from September 20 to October 5 (MJD 52,172–52,187), the photon index of the power-law component saturates to a value of ∼2.2. The rms variability and the frequency of the QPO become more erratic, with oscillations around their maxima. The high-frequency QPOs are observed only during this portion of the outburst (Homan et al. 2003). The accretion disk and power-law flux components give similar contributions to the total flux, which makes this interval very typical of the SPL state. We note that the photon index does not exactly fulfill the criteria (not greater than 2.4) of McClintock & Remillard (2004) for an SPL state, but as it is the part of the outburst with the steepest power law, we consider it as an SPL state for the rest of the paper. The properties of XTE J1650−500, between September 9 and 20, would then be consistent with an IS as defined above. From October 5 to November 19 (MJD 52,187–52,232), the contribution from the accretion disk dominates the energy spectra, and the level of rms variability is very low, as is typical of the TD state. XTE J1650−500 returned back to the HS after November 19 (MJD 52,232), as illustrated by the hardening of the spectrum and the increased rms variability (Kalemci et al. 2003; Rossi et al. 2004).

To summarize, after a brief (but we cannot exclude that the outburst was ongoing for many days before the discovery of the source) initial HS, XTE J1650−500 underwent a smooth transition to the IS, followed by transitions to the SPL state, the TD state, and then back to the HS. Our radio observations occurred as follows: observations 1 and 2 during the initial HS (however, observation 2 is very close to the transition to the IS), observations 3 and 4 during the SPL state (however, observation 4 is very close to the transition to the TD state), observations 5 and 6 during the TD state, and observations 7 and 8 during the final HS. A ninth observation was performed later, when XTE J1650−500 was back in quiescence. We now describe the properties of XTE J1650−500 within these X-ray states.

3. RADIO EMISSION FROM XTE J1650−500: RESULTS AND DISCUSSION

We now focus on the properties of the radio emission. We obtained radio coverage during the initial and final HSs, the SPL state, and the TD state. By looking at Table 1 and Figure 3, in which the radio light curve of XTE J1650−500 is plotted, we note that radio emission from XTE J1650−500 is detected during the first radio observation on September 7 with a spectrum consistent with being flat between 1384 and 2496 MHz. The day after, the radio flux density increased by almost a factor of 2 and had similar spectral characteristics. On September 24 we observed the source at a much fainter radio flux (∼0.8 mJy), and the source disappeared below the sensitivity level on October 5 with 3 σ upper limits of 0.21 and 0.18 mJy at 4800 and 8640 MHz, respectively. Compared to the brightest

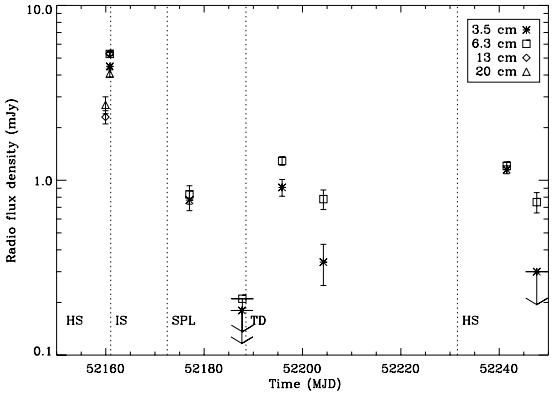

FIG. 3.—Radio light curve of XTE J1650−500 during its outburst in 2001. The vertical lines define the state transitions (see also Fig. 1). Upper limits are plotted at the 3 σ confidence level.

level of radio emission observed on September 8, this indicates a significant quenching (of more than a factor of 25) of the radio emission. Surprisingly, radio emission is again observed (observations 5 and 6) at the millijansky level in the TD state (contrary to expectations based on observations of other BHCs; e.g., Fender et al. 1999; Corbel et al. 2000). During the final two radio observations, the behavior of the source may be consistent with the behavior during the first two observations. For the rest of the paper, we define the radio spectral index α with $S_\nu \propto \nu^\alpha$, where S_ν is the radio flux density and ν is the frequency.

The best position of the radio counterpart to XTE J1650−500 (with the radio source fitted as a pointlike source) is $\alpha(\mathrm{J2000.0}) = 16^{\mathrm{h}}50^{\mathrm{m}}00^{\mathrm{s}}.96$, $\delta(\mathrm{J2000.0}) = -49^\circ 57' 44''.60$, with an absolute positional uncertainty of $0''.25$, mostly due to the uncertainty on the phase calibrator position. All radio observations (when the radio source is detected) are consistent with a location of the radio counterpart at this position. This constitutes the most accurate position for XTE J1650−500 and is in agreement with the one derived from optical observations (Castro-Tirado et al. 2001) and *Chandra* observations (Tomsick et al. 2004).

3.1. *The Initial and Final Hard States*

3.1.1. *Radio Emission from a Compact Jet*

Radio observations 1, 2, 7, and 8 were performed while XTE J1650−500 was in the HS. Both the initial and final hard X-ray states are therefore covered. Once again, the overall properties of the HS radio emission are broadly consistent with those that have been observed in other BHCs in a similar X-ray state (Corbel et al. 2000; Fender 2001): a level of radio emission of a few millijanskys with a radio spectrum that is almost flat. Such characteristics are believed to originate from a self-absorbed conical outflow or compact jet (e.g., Blandford & Königl 1979; Hjellming & Johnston 1988), similar to the one directly resolved from Cyg X-1 by Stirling et al. (2001). We do not detect linear polarization from the compact jet of XTE J1650−500, with our best 3 σ upper limit of 4.0% or 4.7% at 4800 or 8640 MHz, respectively. Such limits are consistent with previous detections at lower levels (e.g., Corbel et al. 2000 for GX 339−4).

For the purpose of our discussion, we have calculated the radio spectral indices, and these are included in Table 1.

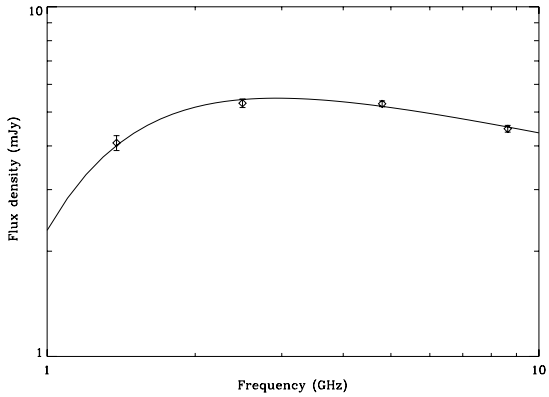

FIG. 4.—Radio spectrum of XTE J1650−500 for observation 2 on 2001 September 8. The solid line is the fit to a spectrum with a power law and thermal free-free absorption.

Despite being consistent with being flat ($\alpha \sim 0$), the radio spectrum (e.g., Fig. 4) seems less inverted at high radio frequencies than is typical for BHC systems.

Below, we come back to the last observation on December 4, which shows a very unusual spectrum. It is interesting to note that the radio spectrum on September 8 (observation 2: Fig. 4) shows a turnover at lower frequencies. This could be due to free-free absorption by a thermal plasma, and, indeed, a fit to the spectrum with a power law and free-free absorption [$S_\nu = S_0\nu^\alpha \exp(-\tau\nu^{-2.1})$, where S_0 is the amplitude at 1 GHz, α is the spectral index of the unabsorbed spectrum, and τ is the free-free optical depth at 1 GHz] describes the data sufficiently well, with $S_0 = 8.59 \pm 0.07$ mJy, $\alpha = -0.29 \pm 0.04$, and $\tau = 1.32 \pm 0.02$. The opacity is in the range of values obtained by Fender (2001) for the 1989 outburst of V404 Cyg (GS 2023+338). We note that similarly, during the first detection of XTE J1859+226 in 1999, the radio spectrum also shows absorption at low frequencies (Brocksopp et al. 2002) while in the HS. If the radio emission arises from a compact jet (as is usually observed in the HS), then it is unlikely that synchrotron self-absorption is responsible for the observed absorption at low frequencies, as this emission originates from large-scale regions (see Fender 2001). The nature of the putative thermal absorbing plasma is unclear (higher interstellar medium [ISM] density, remnant of past activity, etc.). Alternatively (but probably less plausibly), the radio spectrum could be caused by two components: a flat component from the compact jet, as well as a second component from an optically thick ejection event. This may be a possibility, as radio observation 2 occurred very close to the hard to intermediate state transition. However, this is not favored by the fact that the radio spectra are all consistent with having the same intrinsic spectral index, even during the final HS (with the exception of observation 8). In addition, as discussed below, if an ejection event occurred for XTE J1650−500, it probably took place during the intermediate to SPL state transition (§ 3.2).

We note that the radio spectrum in observation 8 is very steep ($\alpha \leq -1.3$), and this is unusual for a black hole in the HS. It is not clear if this is related to the jet/ISM interaction mentioned below (likely not, as the spectrum in observation 7 looks similar to the initial HS) or possibly to the X-ray oscillation behavior observed 10 days later (Tomsick et al. 2003b).

As discussed above, we obtained the best constraint on the spectral index during the September 8 observation, with $\alpha = -0.29 \pm 0.04$. The reason the radio spectrum may have been less inverted than usual is still unclear. This may be related to the inclination angle of the jet, as usually lower inclination angles lead to flatter spectra (e.g., Falcke 1996). For example, the radio to millimeter spectrum of the compact jet of Cyg X-1 (a low-inclination system) is almost flat, i.e., $\alpha \sim 0$ (Fender et al. 2000). However, even with a low inclination angle for the jet, it is almost impossible to obtain such a negative spectral index. Furthermore, optical observations indicate that the inclination angle of the orbital plane in XTE J1650−500 is at least 50° (Orosz et al. 2004), so this explanation does not work for XTE J1650−500 unless the compact jets are strongly misaligned with the orbital plane (as might be the case in few systems; Maccarone 2002). In addition, we note that even in a system such as 4U 1543−47 with a low inclination angle ($20.^\circ7 \pm 1.^\circ0$; J. A. Orosz et al. 2005, in preparation), the radio spectrum of the compact jet (e.g., $\alpha = 0.08 \pm 0.04$) is still slightly inverted (Kalemci et al. 2004b). We also note that the spectral index also varies within a single source (e.g., GX 339−4; Corbel et al. 2000), so it is unlikely that the inclination angle is responsible for this less inverted radio spectrum.

According to Hjellming & Johnston (1988), a less inverted radio spectrum would also be expected in the case of lateral expansion slowed by an external medium (i.e., a compact jet with a narrower opening angle). In addition, because of the longitudinal pressure gradient, the bulk Lorentz factor would increase along the jet axis. If observers were looking into the jet boosting cone, they would expect to see an increase in low-frequency radio emission (which originates far from the base of the jet) and therefore possibly a much less inverted radio spectrum (e.g., Falcke 1996). Obscuration of part of the receding jet may also contribute to the nature of the spectrum. In any case, a combination of all these effects may be in place in XTE J1650−500. It is also clear that future studies of the evolution of the radio spectral index of the compact jets in BHC systems are important, as they may shed light on the geometry of the system.

If the measured spectral index is correct, then it is likely that the contribution from the compact jet at higher frequencies will not be significant. As illustrated in GX 339−4 and XTE J1550−564, the spectrum of the compact jet extends to shorter wavelengths, with a transition to the optically thin regime in the near-infrared (Corbel et al. 2001; Corbel & Fender 2002). In that case, it is unlikely that an infrared reflare would have been detected during the soft to hard state transition, as in XTE J1550−564, GX 339−4, or 4U 1543−47 (Jain et al. 2001; Buxton & Bailyn 2004). The contribution in X-ray, as direct synchrotron emission (e.g., Markoff et al. 2001, 2003), may also be negligible (see § 3.1.2); however, a contribution from synchrotron self-Compton (SSC) emission from the base of the compact jet (e.g., Markoff & Nowak 2004) cannot be ruled out at this stage.

3.1.2. *On the Radio/X-Ray Correlation*

While in the HS, BHCs display a strong correlation between their radio and X-ray emission. This was first observed in GX 339−4 (Corbel et al. 2000, 2003) over more than 3 orders of magnitude in X-ray flux and almost down to its quiescence level. Gallo et al. (2003) found a similar correlation for GS 2023+338 (V404 Cyg), but, interestingly, they show that all BHCs in the HS behave similarly, i.e., their data are consistent with a universal relation between radio and X-ray luminosities. They also observed a relatively small scatter of approximately

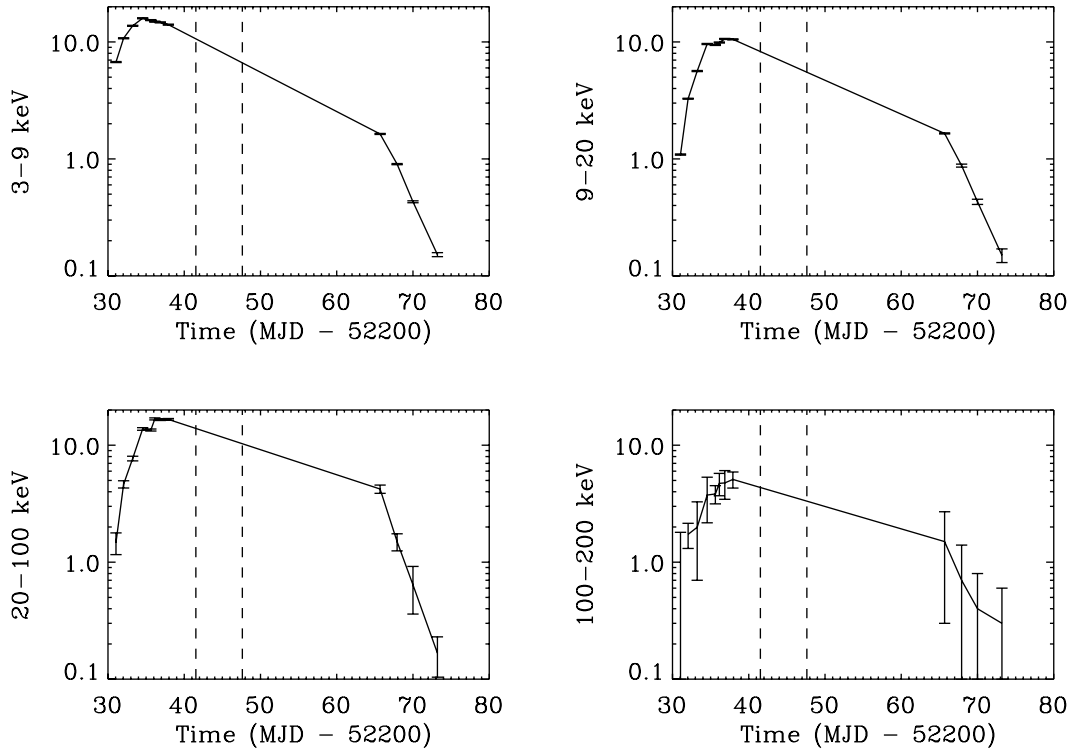

FIG. 5.—Evolution of the X-ray flux (in units of 10^{-9} ergs s^{-1} cm^{-2}) in various energy bands during the decay phase. The transition from the TD state to the HS occurred on MJD 52,232. The dashed vertical lines indicate when radio observations 7 and 8 were performed. These figures give a feeling for the precision of our X-ray flux estimates (for radio observations 7 and 8) based on an interpolation of the decay trend.

1 order of magnitude in radio power. In fact, the scatter could be even smaller if we account for the recent distance estimate, in the range between 6 and 15 kpc, for GX 339−4 by Hynes et al. (2004), as this will bring GX 339−4 closer to GS 2023+338, and the small scatter could imply low bulk Lorentz factors (<2) for the compact jets. Interestingly, this correlation also seems to hold for a large sample of supermassive black holes if one takes into account the mass of the black hole as an additional correction (Merloni et al. 2003; Falcke et al. 2004).

In order to see if XTE J1650−500 fits into this picture, we looked at the relationship between the X-ray and radio flux levels for XTE J1650−500. Despite our efforts to get quasi-simultaneous X-ray and ATCA observations (see Table 1), this was not possible for the final HS, as XTE J1650−500 was in the solar exclusion zone for *RXTE*. In Figure 5 we plot the X-ray flux in various bands during a portion of the decay of the 2001 outburst (see also Tomsick et al. 2003b, 2004). After the transition to the HS (on MJD 52,232; Kalemci et al. 2004a), the decay is smooth enough that interpolation of the X-ray flux at the time of the radio observation is sufficient to obtain an estimate. We note that an increase of the decay rate is observed at the end of the outburst (Fig. 5), with a spectrum that gets harder with time (a smooth variation of the photon index: 1.91 ± 0.02 on MJD 52,235.6 to 1.35 ± 0.23 on MJD 52,267.9), very similar to the decay of XTE J1908+094 during its 2003 outburst (Jonker et al. 2004).

In Figure 6 we have plotted the radio flux density at 4.8 GHz versus the unabsorbed 2–11 keV X-ray flux (in Crab units) scaled to a distance of 1 kpc (similar to Gallo et al. 2003),

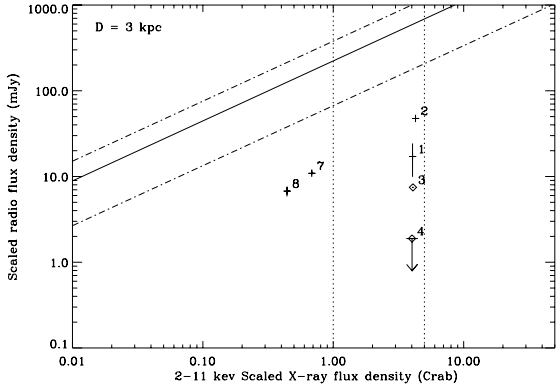

FIG. 6.—Radio flux density (mJy) at 4.8 GHz of XTE J1650−500 during the HS and SPL state vs. the unabsorbed 2–11 keV X-ray flux (in Crab units) scaled to a distance of 1 kpc (this assumes that XTE J1650−500 is located at 3 kpc from the Earth). As described in the text, the X-ray fluxes for observations 7 and 8 are from an interpolation of the decay trend. The best-fit function (*solid line*) with its associated error (*dot-dashed lines*), obtained by Gallo et al. (2003) for GX 339−4 and GS 2023+338, are also plotted. The vertical dotted lines indicate the level of 2% and 10% Eddington luminosity for a 4 $M_{\odot}$ black hole.

assuming a distance of 3 kpc for XTE J1650−500. This distance gives luminosity estimates during the state transition consistent with other BHCs (Maccarone 2003). In Figure 6 we have also plotted the best-fit function obtained by Gallo et al. (2003) using their data sets, i.e., $S_{\rm radio} = k(S_x)^{+0.7}$, with $k = 223 \pm 156$ mJy. Although we have a sample of only four data points, we can clearly see that they all lie significantly below (by a factor 20) the best-fit line of Gallo et al. (2003). The determination of the slope of the power-law function linking the radio and X-ray emission is very uncertain because of our limited sample of data points (as well as the unusual radio spectrum in observation 8 and the fact that two observations took place very close to state transitions). The reason that the normalization in XTE J1650−500 is significantly lower (the source is less radio loud or more X-ray loud) than in other BHCs (Gallo et al. 2003) is still unclear. It may be related to the fact that direct synchrotron X-ray emission (and possibly even SSC) from the compact jets is likely not dominant in the case of XTE J1650−500 for a reason that still remains to be explained. The lower normalization in XTE J1650−500 could be related to the fact that the X-ray regime may be dominated by thermal Comptonization of disk photons in the corona. We note that the distance to XTE J1650−500 may be larger than 3 kpc, but this will only make XTE J1650−500 more anomalous relative to the other BHCs.

3.2. *Radio Emission in the Intermediate and Steep Power-Law States*

3.2.1. *The Steep Power-Law State of XTE J1650−500*

As outlined above, after a few days in the HS, XTE J1650−500 entered the IS and then went into the SPL state. In the IS, the X-ray spectrum softens gradually until the photon index reaches a value of ∼2.2 (Rossi et al. 2004), whereas the QPO frequency increases from 1 to 8.5 Hz. Then (SPL state), the photon index and the QPO frequency (it is not clear if this is the same type of QPO) oscillate around their saturation value. This behavior is more pronounced for the QPO frequency, as it fluctuates along with the broadband variability. The slow variations of the photon index could be related to cooling of the corona by an increase in the number of soft disk photons (the inner accretion disk could get closer to the black hole). Significant variations are also observed in the total disk flux contribution (Rossi et al. 2004) and may indicate that the accretion disk has reached the innermost stable circular orbit (ISCO) and is oscillating around this value. This interval (SPL state) also corresponds to the period over which high-frequency QPOs are detected and therefore confirms that the disk is very close to the black hole (Homan et al. 2003).

We conducted two radio observations during the SPL state of XTE J1650−500 in 2001. The first one resulted in the detection of XTE J1650−500 at a faint level of ∼0.8 mJy (the spectral index is not well constrained: $\alpha = -0.13 \pm 0.86$). The second observation did not result in a detection of XTE J1650−500, with 3 σ upper limits of 0.18 mJy at 8640 MHz and 0.21 mJy at 4800 MHz, indicating a significant (more than a factor of 25) quenching of radio emission compared to the initial HS.

3.2.2. *The Steep Power-Law State of XTE J1550−564 and XTE J1859+226*

Very few soft X-ray transients have been observed at radio frequencies during the intermediate or SPL states. Moreover, when these states have been observed, the radio emission has usually been dominated by the decaying optically thin synchrotron emission arising from jet ejections that occur at or near state transitions prior to the source entering the intermediate or SPL state. Thus, when the emission from the jet ejections is detected, it is decoupled from the black hole system, implying that the observed radio emission is not an intrinsic property of the intermediate or SPL states, as the emitting electrons are already far from the system.

There is only one case for which the radio observations sampled the intrinsic properties of the intermediate or SPL states: XTE J1550−564 during its reactivation in 2000 (Corbel et al. 2001). Interestingly, the properties of the radio emission from XTE J1550−564 were quite similar to what we observe now in XTE J1650−500; indeed, for XTE J1550−564 the first detection showed an optically thin spectrum with a well-constrained spectral index of $\alpha = -0.45 \pm 0.05$, while later, the radio emission was quenched. The optically thin component was interpreted as synchrotron emission arising from relativistic plasma during the state transition. Such small ejection events are frequently observed during state transitions (e.g., see Fender et al. [1999] or Corbel et al. [2000] for the 1998 outburst of GX 339−4 or Brocksopp et al. [2005] for the 2003 outburst of XTE J1720−318). We note that the spectacular massive ejection events (with bright radio emission and a radio core that is usually resolved on a timescale of weeks; e.g., Mirabel & Rodríguez [1994] for GRS 1915+105) may be related to sharper state transitions, possibly related to a huge increase in the accretion rate in the inner part of the accretion disk or maybe to a different black hole parameter, such as the spin.

Furthermore, we highlight the fact that during the 1999 outburst of XTE J1859+226, Brocksopp et al. (2002) reported the detection of flaring radio emission from this black hole in a soft state, which is unexpected in the canonical high/soft (or TD) state (e.g., Fender et al. 1999). In that case, the radio flaring emission was clearly associated with spectral hardening of the X-ray spectrum. However, their definition of a soft state is not clear. Indeed, the hard X-ray light curve in Brocksopp et al. (2002) revealed a very significant level of hard X-ray emission up to at least MJD 51,490, which is very uncommon for a TD state (e.g., McClintock & Remillard 2004). In addition, Cui et al. (2000) reported the detection of high-frequency QPOs around MJD 51,468, which is a characteristic of the SPL state (McClintock & Remillard 2004); this is also favored by the large fraction of X-ray flux in the power-law component (Hynes et al. 2002), which is also quite steep. Kalemci (2002), analyzing the *RXTE* PCA data of XTE J1859+226 after MJD 51,515, describes the spectral state evolution as a TD state from MJD 51,515 up to 51,524, after which the system was found in the IS for the remaining PCA observations. Based on the above, it seems likely that the TD state in XTE J1859+226 did not start before MJD 51,490. This is confirmed by Markwardt (2001), as this work indicates that the disk component became dominant only after MJD 51,487. Therefore, the X-ray state in which Brocksopp et al. (2002) detected flaring radio emission from XTE J1859+226 was most likely the SPL state (or less probably an IS) and not a TD state. Therefore, the observed radio flaring behavior in XTE J1859+226 must be related to the behavior of BHCs while in the SPL state. This conclusion has also been drawn by Fender et al. (2005).

3.2.3. *XTE J1650−500 and the Origin of Radio Emission in the Steep Power-Law State*

With our new observations, XTE J1650−500 is therefore the third source for which the intrinsic radio properties of the SPL state have been sampled, and the observed behavior is consistent with what has been found in XTE J1550−564 (Corbel

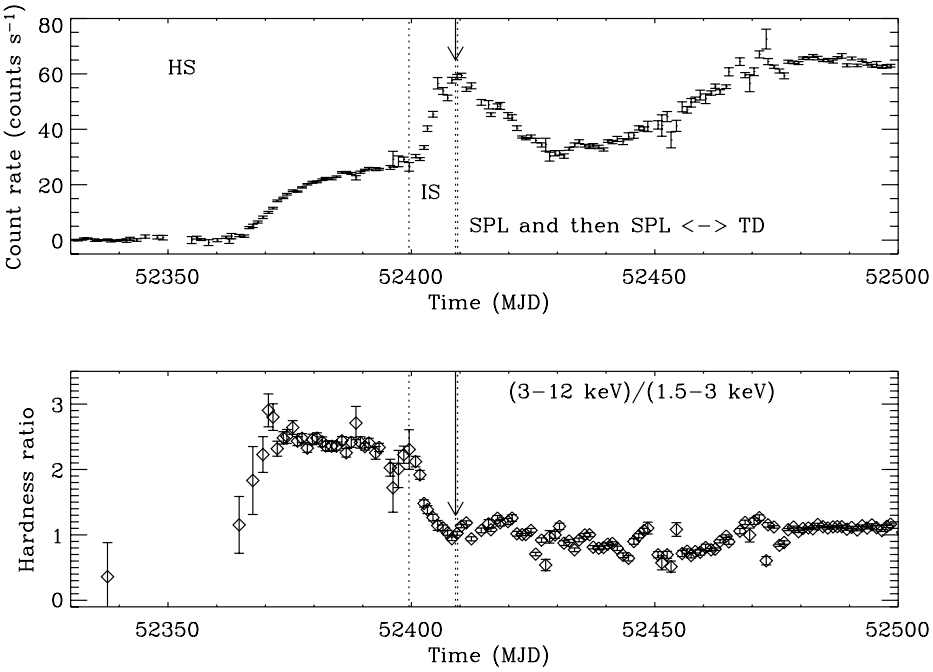

FIG. 7.—Evolution of the *RXTE* ASM count rate and hardness ratio (similar to Fig. 1) for the initial part of the 2002 outburst of GX 339−4. Again, the X-ray spectral states sampled (T. Belloni 2004, private communication) are indicated. The arrow marks the time of the major radio flare observed by Gallo et al. (2004) in 2002 May.

et al. 2001). The detection of the faint radio component in the SPL state on September 24 (observation 3) may be related to an ejection event at the time of the transition from the hard to intermediate states (on September 9). However, as there is significant time (15 days) between the transition and the detection of the faint radio component, we consider two alternative explanations.

First, an interesting comparison can be made with the 2002–2003 outburst of GX 339−4, as a strong radio flare has been observed with ATCA (Gallo et al. 2004). In Figure 7 we have plotted the ASM light curve and hardness ratio (similar to Fig. 1 for XTE J1650−500) for the initial part of the outburst. As GX 339−4 and XTE J1650−500 have similar hydrogen column densities (e.g., Miller et al. 2004), we can directly compare their hardness ratios, which are indeed very similar (Figs. 1 and 7). After an initial HS, GX 339−4 makes a transition to an IS around MJD 52,400. Then, the spectrum softens up to approximately MJD 52,409, when GX 339−4 is found in the SPL state. The evolution of the states becomes more complicated later on in the outburst (T. Belloni 2004, private communication). The spectral state evolution (during the beginning of the outburst) in GX 339−4 is therefore identical to that of XTE J1650−500. The radio flare observed by Gallo et al. (2004) started on 2002 May 14 around 13:00 (MJD 52,409.042), reaching its maximum 6 hr later. The arrow in Figure 7 indicates that the radio flare started once the softening of the X-ray spectrum ended, i.e., it corresponds to the transition from the IS to the SPL state. Based on the above, and comparing their hardness ratios, we can say that if a radio flare (and hence massive plasma ejection) occurred in XTE J1650−500, then this happened at the transition between the IS and SPL state. In that case, the observed radio emission on September 24 would have been at the end of the decay of this flare. This could correspond to the ejected materials that later interacts with the ISM (§ 3.3), as in GX 339−4 (Gallo et al. 2004).

Alternatively, an equally plausible explanation is the following. The transition from the IS to the SPL state seems to correspond to a period over which the inner radius of the accretion disk reaches the ISCO, and this would be valid for most of the SPL state, as outlined above in § 3.2.1. As the X-ray properties of the SPL state favor an "unstable" accretion disk (Rossi et al. 2004), they may suggest that the optically thin synchrotron component observed on September 24 could be related to an ejection of a very small portion of the inner accretion disk or corona. In that case, it would be very similar to the radio flaring behavior observed in XTE J1859+226 during its SPL state in 1999 or to the behavior observed in GRS 1915+105 (but at a much slower rate). The comparison of GRS 1915+105 with BHCs in canonical X-ray states is not straightforward, but the X-ray states A, B (soft), and C (hard) may be similar to intermediate and very high states (Reig et al. 2003). Oscillations between states A, B, and C are correlated with radio flaring activity (e.g., Klein-Wolt et al. 2002), with stronger radio emission in the spectrally hard state C, whereas the soft states are never associated with bright radio emission.

These two possible explanations for the origin of radio emission in the IS and SPL state could be combined as follows: For GX 339−4 and probably for XTE J1650−500, the transition from the IS to the SPL state is associated with an ejection event (with a radio spectrum characteristic of optically thin synchrotron emission) that decays on a timescale of hours. After the transition, the accretion disk settles down close to the ISCO. At that time, as the spectrum hardens, accretion disk or coronal material can be ejected from the system (as in XTE J1859+226), resulting in weak radio flares. If the radio observation takes place between two flares, then no radio emission will be observed. Indeed, this

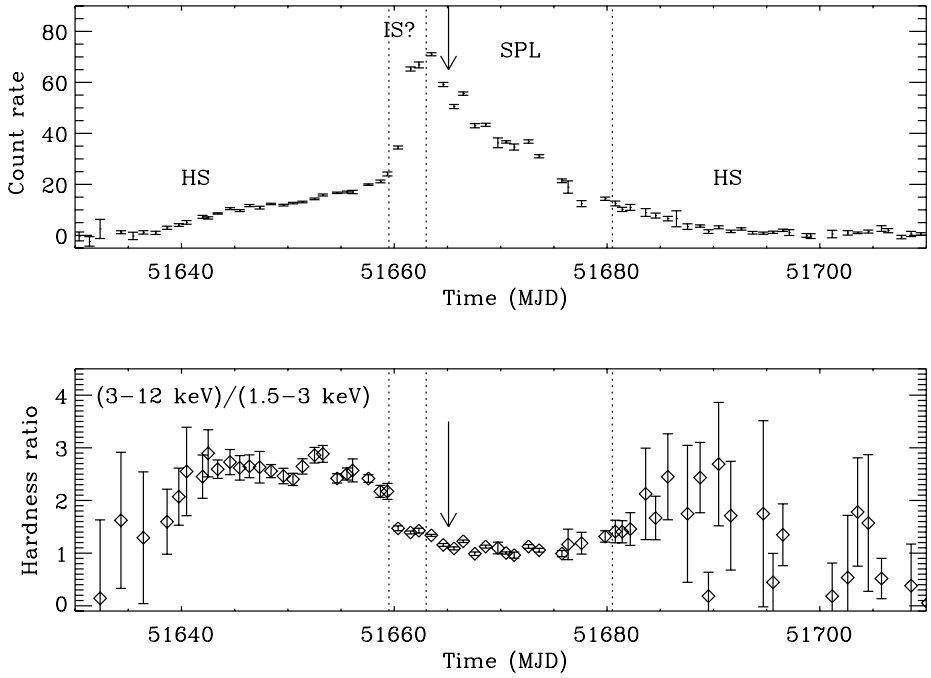

FIG. 8.—Same as Fig. 7, but for the 2000 outburst of XTE J1550−564. The arrow indicates the date of the radio observations performed by Corbel et al. (2001), during which they probably detected the end of the radio flare associated with the state transition. The high-frequency QPOs are detected only during the SPL state.

was also the case for GX 339−4: after the major radio flare associated with the IS to SPL state transition, several radio flares were observed during the SPL state (Gallo et al. 2004), and, interestingly, for at least one SPL state radio observation (on 2002 June 9 [MJD 52,434]), the radio emission was quenched (by a factor of more than 45 compared to the initial HS).

Indeed, we can now try to see if the 2000 radio observations of XTE J1550−564 fit into this framework. For that purpose, we have plotted in Figure 8 the ASM hardness ratio and light curve for the 2000 outburst. Similarly, after an initial HS (e.g., Rodriguez et al. 2003, 2004), the source went into the SPL state with gradual softening of the X-ray spectrum in between (very similar to the IS of XTE J1650−500 and GX 339−4 mentioned above). The radio flare was observed again after the softening was over (Corbel et al. 2001). Again, the high-frequency QPOs (Miller et al. 2001) were reported in only the SPL state (between MJD 51,663 and 51,672), i.e., after the end of the softening. The second radio observation of XTE J1550−564 occurred later in the SPL state and showed that the radio emission was quenched, so that either the observation occurred between two flares or perhaps there was no flare at all. The X-ray spectral evolution (Rodriguez et al. 2003) may even suggest that the ejected material could be originating from the corona. The outburst evolution of XTE J1859+226 (Fig. 9) could again be included in this picture in this way: after an initial HS and a softening, a massive radio flare occurred, and then, as the source became spectrally harder, several weaker flares took place.

3.2.4. *On the Nature of Radio Emission in the Intermediate State*

At this stage, it is not clear if the general pattern presented in § 3.2.3 concerns only the SPL state. Perhaps the IS, with slower evolution and a significant level of hard X-ray emission (like the IS in XTE J1650−500), is not associated with radio emission. In fact, it is interesting to note that before the major radio flare observed in 2002 (see Fig. 2 in Gallo et al. 2004), a stable level of radio emission with a flux of ∼12 mJy and a flat spectrum (between 4.8 and 8.6 GHz) was observed in GX 339−4. Therefore, as GX 339−4 was in the IS at that time, this would indicate that the compact jet could possibly survive during the IS but could be destroyed very quickly, i.e., on a timescale of hours. Similarly, a nonzero level of radio emission with a flat spectrum is also observed in XTE J1859+226 prior to its major radio flare in 1999 (Brocksopp et al. 2002). Again, this detection would be consistent with the presence of the compact jet in the IS of XTE J1859+226. If this interpretation is correct (i.e., that the compact jet exists in the IS), this would be an important clue for understanding the inflow-outflow coupling close to the event horizon of a black hole. For that purpose, it would be very important to monitor the radio properties of BHCs during the IS or SPL state in order to constrain the geometry of these BHC systems during the various X-ray states. In any case, this suggestion seems to be confirmed by Fender et al. (2005), who studied similar data sets (including also GRS 1915+105 but not XTE J1650−500) and drew similar conclusions regarding the nature of radio emission in the IS and SPL state.

3.2.5. *Quenched Radio Emission at a Few Percent Eddington Luminosity*

As a final remark, in Figure 6 we observe that the radio observations in the initial HS and in the SPL state occurred at the same unabsorbed X-ray flux, which corresponds to a level of 4 Crab (∼8% of the Eddington luminosity for a 4 $M_{\odot}$ black hole at 3 kpc; if we used an upper limit of 7 $M_{\odot}$, then it would correspond to about 4.6% of the Eddington luminosity). This

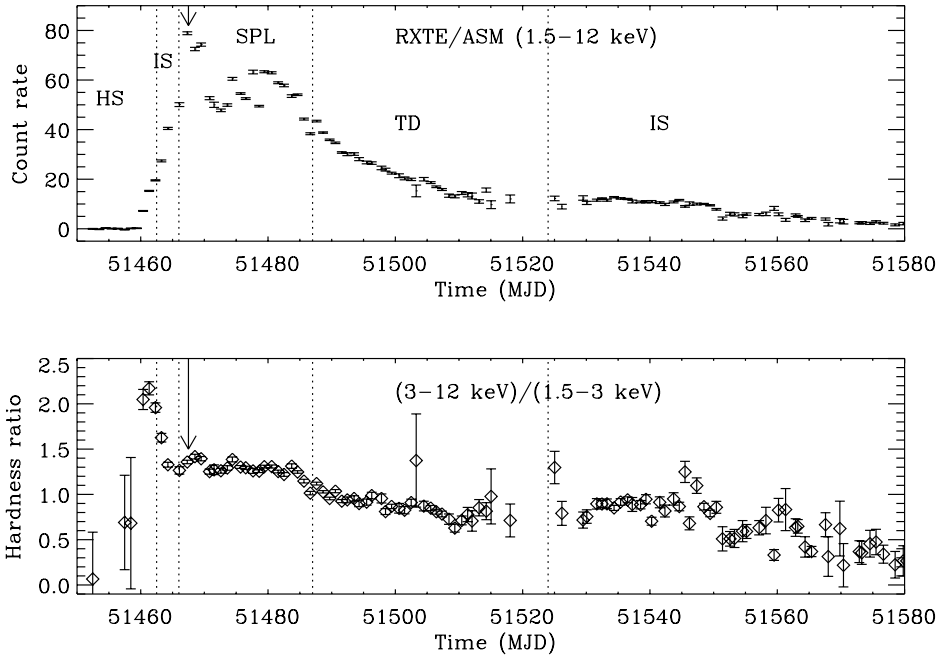

FIG. 9.—Same as Fig. 7, but for the 1999 outburst of XTE J1859+226. The arrow indicates the date of the major radio flare detected by Brocksopp et al. (2002). The first two vertical lines, for the HS and IS, are approximately indicative of the period of state transitions.

picture is qualitatively consistent with the behavior of GX 339−4, Cyg X-1, and GS 2023+338 (Gallo et al. 2003), indicating that the quenching of the compact jet occurs at an almost fixed fraction (a few percent) of the Eddington luminosity, so that there is a correlation between the mass of the black hole and the X-ray flux where the transition occurs. We note that if the mass of a black hole is known, then a measurement of the X-ray flux for which quenching occurs could constitute an independent distance estimate (or vice versa).

3.3. *Surprising Detection of Radio Emission in a Thermal Dominant State*

The last radio observations that we discuss in this paper are those (5 and 6) that were conducted during the TD state. Radio emission is observed (Figs. 3 and 10) at a level of ∼1 mJy, with a spectrum that is consistent with optically thin synchrotron emission (but the spectral index is not well constrained). These detections are contrary to what would have been expected in the TD state, which has always (in previous observations of BHCs) been associated with quenched radio emission: e.g., GX 339−4 (Fender et al. 1999; Corbel et al. 2000) and Cyg X-1 (Gallo et al. 2003; Tigelaar et al. 2004). Therefore, these detections do not fit with the standard view, and they constitute a certain surprise. As discussed in § 3.2, the radio flaring emission observed in the soft state of XTE J1859+226 (Brocksopp et al. 2002) has to be related to the behavior of the BHC while in the SPL state. Regarding the case of XTE J1650−500, the HID (Fig. 2) indicates that the detection of radio emission in the TD state is not related to spectral hardening at all, as the X-ray emission stays very soft during this period, with no hard component. Therefore, an alternative explanation must be found, and we concentrate on two possibilities.

First, we consider the possibility that the radio emission is still related to the compact jet. As demonstrated in the case of GX 339−4 (Fender et al. 1999; Corbel et al. 2000), the TD state is associated with a quenching of the compact jet by at least a factor of 25. According to Meier et al. (2001), the quenching would be the result of a weaker poloidal magnetic field in a geometrically thin accretion disk. Migliari et al. (2004) reported the detection of radio emission in two atoll-type neutron star

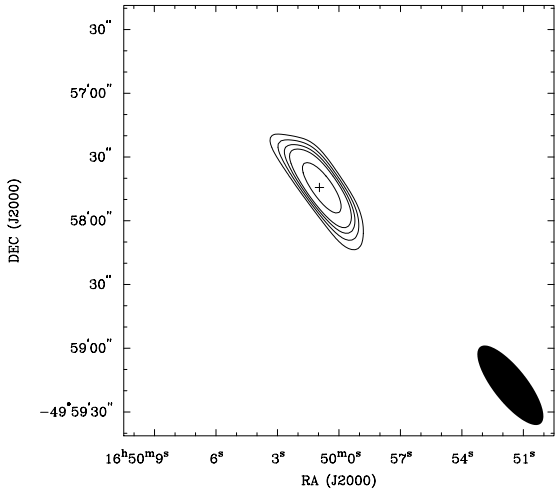

FIG. 10.—Radio emission at 8640 MHz during an observation performed on MJD 52,195 (observation 5) in a TD state. Contours are at 3, 4, 5, 7, and 9 times the rms level of 0.10 mJy beam^{-1}.

TABLE 2
PROPERTIES OF RADIO EMISSION ALONG THE VARIOUS X-RAY STATES IN XTE J1650−500 AND IN BLACK HOLE BINARY SYSTEMS IN GENERAL

X-RAY STATE	ORIGIN OF THE RADIO EMISSION	
	XTE J1650−500	Black Hole Candidates
HS	Self-absorbed compact jet	Self-absorbed compact jet
IS	No radio observation	Self-absorbed compact jet
IS to SPL state transition	No radio observation	Massive ejection event
SPL state	Decay of massive ejection event or small ejection event and quenching	Small ejection events and/or quenched radio emission
TD state	Interaction jet/ISM?	Quenched radio emission

NOTES.—See also Fender et al. (2005) for the general case. We note that in any state observed after the IS to SPL state transition, radio emission from the interaction of the massive ejection event with the ISM may contribute to the observed level of radio emission (if unresolved).

X-ray binaries while they were in a soft (banana) X-ray state. They suggested that this could be related to an interaction of the magnetic field of the neutron star with the accretion disk. However, such an explanation does not work in the case of XTE J1650−500, which is likely a black hole, based on its X-ray properties and also its mass function (Orosz et al. 2004). Perhaps the mass of the black hole in XTE J1650−500 (which may be smaller than a typical stellar-mass black hole) is an important parameter that could set the level of quenching when the spectrum gets soft. However, as the compact jet was quenched by a factor of more than 25 in the SPL state (observation 4), similar to other BHCs (e.g., GX 339−4; Fender et al. 1999), it seems likely that the observed radio emission in the TD state of XTE J1650−500 does not originate from the compact jet.

The second possibility that we consider now is that the observed radio emission is the result of the interaction of material previously ejected from the system with the ISM, similarly to what has been observed for XTE J1550−564 (Corbel et al. 2002; Tomsick et al. 2003a; Kaaret et al. 2003) and for GX 339−4 (Gallo et al. 2004). The observed radio spectrum would be consistent with this interpretation (optically thin synchrotron emission, but it should be kept in mind that the spectral index is not well constrained). In addition, we have also observed that within an observation, the flux is varying (decaying) on a timescale of hours. For example, in observation 5, the radio flux density drops (during the observation) from 1.74 ± 0.11 to 0.85 ± 0.11 mJy at 4800 MHz and from 1.09 ± 0.11 to 0.80 ± 0.15 mJy at 8640 MHz. There also seems to be some variations for observation 6.

This is contrary to what has been found previously in XTE J1550−564, with the slow decay of radio emission (on a timescale of a week) due to the jet/ISM interaction (Corbel et al. 2002; S. Corbel et al. 2005, in preparation). However, the variations of radio emission in the large-scale jet of GX 339−4 were much faster than in the case of XTE J1550−564. The origin of the ejected material could be related to the flaring behavior in the SPL state, or more likely during the IS to SPL state transition (as discussed in § 3.2), similarly to GX 339−4. If this interpretation were correct, the contribution to the X-ray spectrum of the interaction of the jet with the ISM (as in XTE J1550−564) would not be detectable, as the X-ray spectrum would likely be dominated by the thermal emission from the accretion disk. In any case, this may suggest that the reactivation of particle acceleration during collisions with the ISM may be a common occurrence in microquasars.

4. CONCLUSIONS

XTE J1650−500 was discovered in 2001 September and then underwent transitions between various X-ray spectral states while we observed the source at radio frequencies. We can summarize our conclusions as follows: In the HS, the radio emission of XTE J1650−500 can be interpreted (like other BHCs) as arising from a self-absorbed compact jet. However, there seems to be some indication that the radio spectrum is less inverted than in other sources. In addition, XTE J1650−500 seems to be more X-ray loud when compared to other black hole candidates observed at similar radio flux density. This could possibly indicate that XTE J1650−500 is dominated in the X-ray regime by Comptonization of the disk photons in the corona with negligible (if any) contribution from the compact jet at high energies (X-ray, optical, and possibly even in the infrared). With the observations performed in the SPL state and using the existing data from other BHCs, we conclude that the transition from the IS to the SPL state is likely associated with a (more or less) massive ejection event that decays on a timescale of hours. In addition, weaker radio flares (and hence ejection events) may be observed in the SPL state associated with X-ray spectral hardening. If a radio observation took place between two flares or if no flare occurred at all, then no radio emission would be detected. For the IS itself, the detection of radio emission (with a flat spectrum) prior to the major flare of XTE J1859+226 in 1999 and of GX 339−4 in 2002 (associated with an IS to SPL state transition) may suggest that the compact jet can survive in the IS, and perhaps this is due to the fact that the flux of soft X-rays is lower in the IS than in the SPL state. In the TD state, we have surprisingly detected a significant amount of varying radio emission, which we interpret as the interaction of previously ejected materials with the neighboring environment (ISM or a remnant of past activity), similar to what has been observed in XTE J1550−564. In that case, such events may be more common than previously thought. Our conclusions regarding the nature of radio emission within the various spectral states of XTE J1650−500 and a possible extension to BHCs in general are summarized in Table 2. All of this points to the fact that it is extremely important to intensively monitor the radio properties of BHCs along the various X-ray states in order to shed light on the accretion-ejection coupling close to the black hole event horizon.

The Australia Telescope is funded by the Commonwealth of Australia for operation as a national facility managed by CSIRO. *RXTE* ASM results are provided by the *RXTE* ASM team at the Massachusetts Institute of Technology. We thank Bob Sault, Dave McConnell, and the ATCA time allocating committee for allowing these observations at the right times to sample various X-ray states. S. C. acknowledges useful and

interesting discussions with Heino Falcke, Elena Gallo, Sera Markoff, Mike Nowak, and Jerry Orosz. S. C. would like to thank Dick Hunstead and Duncan Campbell-Wilson for providing information on the *MOST* observations, which helped to schedule the ATCA observations, and Bryan Gaensler and Jim Lovell for conducting some of the radio observations. We also warmly thank Sabrina Rossi and Tomaso Belloni for providing information on their PCA data analysis of XTE J1650−500 and GX 339−4, which helped in defining the state evolution. J. A. T. acknowledges partial support from NASA grant NAG5-13055.

REFERENCES

Augusteijn, T., Coe, M., & Groot, P. 2001, IAU Circ. 7710
Belloni, T. 2004, in The Restless High-Energy Universe, ed. E. P. J. van den Heuvel, J. J. M. in 't Zand, & R. A. M. J. Wijers (Amsterdam: North-Holland) (astro-ph/0309028)
Blandford, R. D., & Königl, A. 1979, ApJ, 232, 34
Brocksopp, C., Corbel, S., Fender, R. P., Rupen, M., Sault, R., Tingay, S. J., Hannikainen, D., & O'Brien, K. 2005, MNRAS, in press (astro-ph/0410353)
Brocksopp, C., et al. 2002, MNRAS, 331, 765
Buxton, M., & Bailyn, C. 2004, in AIP Conf. Proc. 714, X-Ray Timing 2003: Rossi and Beyond, ed. P. E. Kaaret & F. Lamb (New York: AIP), 146
Castro-Tirado, A. J., Kilmartin, P., Gilmore, A., Petterson, O., Bond, I., Yock, P., & Sanchez-Fernandez, C. 2001, IAU Circ. 7707
Corbel, S., & Fender, R. P. 2002, ApJ, 573, L35
Corbel, S., Fender, R. P., Tzioumis, A. K., Nowak, M., McIntyre, V., Durouchoux, P., & Sood, R. 2000, A&A, 359, 251
Corbel, S., Fender, R. P., Tzioumis, A. K., Tomsick, J. A., Orosz, J. A., Miller, J. M., Wijnands, R., & Kaaret, P. 2002, Science, 298, 196
Corbel, S., Nowak, M. A., Fender, R. P., Tzioumis, A. K., & Markoff, S. 2003, A&A, 400, 1007
Corbel, S., et al. 2001, ApJ, 554, 43
Cui, W., Shrader, C. R., Haswell, C. A., & Hynes, R. I. 2000, ApJ, 535, L123
Ebisawa, K., et al. 1994, PASJ, 46, 375
Falcke, H. 1996, ApJ, 464, L67
Falcke, H., Körding, E., & Markoff, S. 2004, A&A, 414, 895
Fender, R. P. 2001, MNRAS, 322, 31
Fender, R. P., Belloni, T., & Gallo, E. 2005, ApJ, in press (astro-ph/0409360)
Fender, R. P., Pooley, G. G., Durouchoux, P., Tilanus, R. P. J., & Brocksopp, C. 2000, MNRAS, 312, 853
Fender, R. P., et al. 1999, ApJ, 519, L165
Gallo, E., Corbel, S., Fender, R. P., Maccarone, T. J., & Tzioumis, A. K. 2004, MNRAS, 347, L52
Gallo, E., Fender, R. P., & Pooley, G. G. 2003, MNRAS, 344, 60
Groot, P., Tingay, S., Udalski, A., & Miller, J. 2001, IAU Circ. 7708
Hjellming R. M., & Johnston K. J. 1988, ApJ, 328, 600
Homan, J., Klein-Wolt, M., Rossi, S., Miller, J. M., Wijnands, R., Belloni, T., van der Klis, M., & Lewin, W. H. G. 2003, ApJ, 586, 1262
Homan, J., Wijnands, R., van der Klis, M., Belloni, T., van Paradijs, J., Klein-Wolt, M., Fender, R., & Méndez, M. 2001, ApJS, 132, 377
Hynes, R. I., Haswell, C. A., Chaty, S., Shrader, C. R., & Cui, W. 2002, MNRAS, 331, 169
Hynes, R. I., Steeghs, D., Casares, J., Charles, P. A., & O'Brien, K. 2004, ApJ, 609, 317
Jain, R. K., Bailyn, C. D., Orosz, J. A., McClintock, J. E., & Remillard, R. A. 2001, ApJ, 554, L181
Jonker, P. G., Gallo, E., Dhawan, V., Rupen, M., Fender, R. P., & Dubus, G. 2004, MNRAS, 351, 1359
Kaaret, P., Corbel, S., Tomsick, J. A., Fender, R., Miller, J. M., Orosz, J. A., Tzioumis, A. K., & Wijnands, R. 2003, ApJ, 582, 945
Kalemci, E. 2002, Ph.D. thesis, Univ. California, San Diego
Kalemci, E., Tomsick, J. A., Rothschild, R. E., Pottschmidt, K., Corbel, S., Wijnands, R., Miller, J. M., & Kaaret, P. 2003, ApJ, 586, 419
Kalemci, E., Tomsick, J. A., Rothschild, R. E., Pottschmidt, K., & Kaaret, P. 2004a, ApJ, 603, 231
Kalemci, E., et al. 2004b, ApJ, submitted (astro-ph/0409092)
Klein-Wolt, M., Fender, R. P., Pooley, G. G., Belloni, T., Migliari, S., Morgan, E. H., & van der Klis, M. 2002, MNRAS, 331, 745
Levine, A. M., Bradt, H., Cui, W., Jernigan, J. G., Morgan, E. H., Remillard, R., Shirey, R. E., & Smith, D. A. 1996, ApJ, 469, L33
Maccarone, T. J. 2002, MNRAS, 336, 1371
———. 2003, A&A, 409, 697
Makishima, K., Maejima, Y., Mitsuda, K., Bradt, H. V., Remillard, R. A., Tuohy, I. R., Hoshi, R., & Nakagawa, M. 1986, ApJ, 308, 635
Markoff, S., Falcke, H., & Fender, R. 2001, A&A, 372, L25
Markoff, S., & Nowak, M. 2004, ApJ, 609, 972
Markoff, S., Nowak, M., Corbel, S., Fender, R., & Falcke, H. 2003, A&A, 397, 645
Markwardt, C. 2001, Ap&SS Suppl., 276, 209
Markwardt, C., Swank, J., & Smith, E. 2001, IAU Circ. 7707
McClintock, J. E., & Remillard, R. A. 2004, in Compact Stellar X-Ray Sources, ed. W. H. G. Lewin & M. van der Klis (Cambridge: Cambridge Univ. Press), in press
Meier, D., Koide, S., & Uchida, Y. 2001, Science, 291, 84
Merloni, A., Heinz, S., & di Matteo, T. 2003, MNRAS, 345, 1057
Migliari, S., Fender, R. P., Rupen, M., Wachter, S., Jonker, P. G., Homan, J., & van der Klis, M. 2004, MNRAS, 351, 186
Miller, J. M., et al. 2001, ApJ, 563, 928
———. 2002, ApJ, 570, L69
———. 2004, ApJ, 601, 450
Mirabel, I. F., & Rodríguez, L. F. 1994, Nature, 371, 46
Orosz, J. A., McClintock, J. E., Remillard, R. A., & Corbel, S. 2004, ApJ, 616, 376
Reig, P., Belloni, T., & van der Klis, M. 2003, A&A, 412, 229
Remillard, R. 2001, IAU Circ. 7707
Revnivtsev, M., & Sunyaev, R. 2001, IAU Circ. 7715
Rodriguez, J., Corbel, S., Kalemci, E., Tomsick, J. A., & Tagger, M. 2004, ApJ, 612, 1018
Rodriguez, J., Corbel, S., & Tomsick, J. A. 2003, ApJ, 595, 1032
Rossi, S., Homan, J., Miller, J. M., & Belloni, T. 2004, in The Restless High-Energy Universe, ed. E. P. J. van den Heuvel, J. J. M. in 't Zand, & R. A. M. J. Wijers (Amsterdam: North-Holland) (astro-ph/0309129)
Sanchez-Fernandez, C., Zurita, C., Casares, J., Castro-Tirado, A. J., Bond, I., Brandt, S., & Lund, N. 2002, IAU Circ. 7989
Sault R. J., & Killeen N. E. B. 1998, The Miriad User's Guide (Sydney: Australia Telescope National Facility)
Stirling, A. M., Spencer, R. E., de la Force, C. J., Garrett, M. A., Fender, R. P., & Ogley, R. N. 2001, MNRAS, 327, 1273
Tigelaar, S. P., Fender, R. P., Tilamus, R. P. J., Gallo, E., & Pooley, G. 2004, MNRAS, 352, 1015
Tomsick, J. A., Corbel, S., Fender, R., Miller, J. M., Orosz, J. A., Tzioumis, T., Wijnands, R., & Kaaret, P. 2003a, ApJ, 582, 933
Tomsick, J. A., Corbel, S., & Kaaret, P. 2001, ApJ, 563, 229
Tomsick, J. A., Kalemci, E., Corbel, S., & Kaaret, P. 2003b, ApJ, 592, 1100
Tomsick, J. A., Kalemci, E., & Kaaret, P. 2004, ApJ, 601, 439
Wijnands, R., Miller, J. M., & Lewin, W. H. G. 2001, IAU Circ. 7715

3.5.7

X-Ray Observations of the Black Hole Transient 4U 1630-47 during 2 Years of X-Ray Activity.

Article publié dans :

Astrophys. J., 2005, 630, 413-429

Tomsick, J. A., Corbel, S., Goldwurm, A., Kaaret, P.

The Astrophysical Journal, 630:413–429, 2005 September 1

X-RAY OBSERVATIONS OF THE BLACK HOLE TRANSIENT 4U 1630−47 DURING 2 YEARS OF X-RAY ACTIVITY

John A. Tomsick,[1] Stéphane Corbel,[2] Andrea Goldwurm,[3] and Philip Kaaret[4]

Received 2005 March 8; accepted 2005 May 11

ABSTRACT

The black hole candidate (BHC) X-ray transient 4U 1630−47 continuously produced strong X-ray emission for more than 2 years during its 2002–2004 outburst, which is one of the brightest and longest outbursts ever seen from this source. We use more than 300 observations made with the *Rossi X-Ray Timing Explorer* (*RXTE*) to study the source throughout the outburst, along with hard X-ray images from the *International Gamma-Ray Astrophysics Laboratory* (*INTEGRAL*), which are critical for interpreting the *RXTE* data in this crowded field. The source exhibits extreme behaviors, which can be interpreted as an indication that the system luminosity approaches the Eddington limit. For 15 observations, fitting the spectral continuum with a disk-blackbody plus power-law model results in measured inner disk temperatures between 2.7 and 3.8 keV, and such temperatures are only rivaled by the brightest BHC systems, such as GRS 1915+105 and XTE J1550−564. If the high temperatures are caused by the dominance of electron scattering opacity in the inner regions of the accretion disk, it is theoretically required that the source luminosity be considerably higher than 20% of the Eddington limit. We detect a variety of high-amplitude variability, including hard 10–100 s flares, which peak at levels as much as 2–3 times higher than nonflare levels. This flaring occurs at the highest disk luminosities in a regime in which the source deviates from the $L_{\rm disk} \propto T_{\rm in}^4$ relationship that is seen at lower luminosities, possibly suggesting that we are seeing transitions between a Shakura & Sunyaev disk and a "slim" disk, which is predicted to occur at very high mass accretion rates. The X-ray properties in 2002–2004 are significantly different from those seen during the 1998 outburst, which is the only outburst with detected radio jet emission. Our results support the "jet line" concept recently advanced by Fender and coworkers. Our study allows for a test of the quantitative McClintock & Remillard spectral state definitions, and we find that these definitions alone do not provide a complete description of the outburst. Finally, for several of the observations, the high-energy emission is dominated by the nearby sources IGR J16320–4751 and IGR J16358–4726, and we provide information on when these sources were bright and on the nature of their energy spectra.

Subject headings: accretion, accretion disks — black hole physics — stars: individual (4U 1630−47, IGR J16320−4751, IGR J16358−4726) — X-rays: stars

Online material: color figures

1. INTRODUCTION

The X-ray (∼1–10 keV) luminosities from Galactic black hole candidate (BHC) transients range from values below 10^{30} ergs s^{-1} when the sources are in quiescence (Garcia et al. 2001) to values that can approach or exceed 10^{39} ergs s^{-1} for some sources (Done et al. 2004). During outbursts, luminosities above $\sim 10^{34}$ ergs s^{-1} are usually seen for at least several months (Chen et al. 1997), and significant changes in the X-ray properties occur over time. We do not have a detailed understanding of all the physical changes that lead to changes in the X-ray emission properties, but the physics involves the structure of the accretion disk around the black hole, as well as the connection between the accretion disk and the steady or impulsive jets that can be launched from these systems. The changes in the X-ray emission properties are partially caused by changes in the mass accretion rate onto the black hole; however, it has been demonstrated that other physical parameters must also be important for determining those properties (Homan et al. 2001; Tomsick 2004b).

The emission properties of accreting black holes are often classified in terms of "spectral states." Recently, efforts have been made to make the state definitions more quantitative and to connect these definitions directly to the continuum spectral components (McClintock & Remillard 2003). The spectra can often be described as the combination of a soft, thermal component along with a hard component that can fall off more or less steeply with energy. The thermal component is almost certainly blackbody emission from an accretion disk, as in Shakura & Sunyaev (1973), but the mechanism for producing the hard component is less clear. Accreting black holes can be highly variable, sometimes with quasi-periodic oscillations (QPOs); spectral and timing properties are both incorporated in the following spectral state definitions from McClintock & Remillard (2003).

In the thermal-dominant (TD) state, the thermal component accounts for >75% of the total 2–20 keV flux. In this state, no or weak QPOs are seen with rms levels below 1%, and the 0.1–10 Hz continuum rms is $\lesssim$6%. In the steep power-law (SPL) state, the hard component is a power law with $\Gamma > 2.4$, where Γ is the power-law photon index. A source is said to be in the SPL state if QPOs are present and the hard component contributes >20% of the 2–20 keV flux or if, regardless of the timing properties, the hard component contributes >50% of the 2–20 keV flux. Finally, in the hard state, the hard component is much less steep, at $1.5 < \Gamma < 2.1$, the hard component contributes more than 80% of the 2–20 keV flux, the 0.1–10 Hz continuum rms is between 10% and 30%, and the presence of radio emission

[1] Center for Astrophysics and Space Sciences, Code 0424, University of California at San Diego, La Jolla, CA 92093; jtomsick@ucsd.edu.
[2] Université Paris VII and Service d'Astrophysique, CEA Saclay, 91191 Gif sur Yvette, France.
[3] Service d'Astrophysique, CEA Saclay, 91191 Gif sur Yvette; and APC, 11 place M. Berthelot, 75231 Paris, France.
[4] Department of Physics and Astronomy, University of Iowa, Iowa City, IA 52242.

TABLE 1
RXTE Observations

Proposal ID	Number of Observations	Range of Exposure Times (s)	Mean Exposure Time (s)
P70417	53	96–7504	1745
P70113	55	288–11,216	2756
P80117	53	96–7376	1849
P80417	1	1072–1072	1072
P80420	55	320–2320	1144
P90128	54	256–3392	1635
P90410	47	464–3264	1775

signals the presence of a compact jet (Fender 2001). As discussed in McClintock & Remillard (2003), systems also exhibit intermediate states, with properties that are usually some combination of the three main states (TD, SPL, and hard).

The X-ray activity from the BHC transient 4U 1630−47 over more than 2 years during 2002–2004, along with good high-energy coverage of the source by the *Rossi X-Ray Timing Explorer* (*RXTE*) and the *International Gamma-Ray Astrophysics Laboratory* (*INTEGRAL*), provides an opportunity to study the long-term evolution of the source as it enters different spectral states and exhibits different emission properties. Among BHC transients 4U 1630−47 is one of the most active, and it has produced strong hard X-ray emission during its 17 detected outbursts (Trudolyubov et al. 2001; Tomsick & Kaaret 2000; Oosterbroek et al. 1998; Kuulkers et al. 1997; Parmar et al. 1997). The source has a quasi-periodic ∼600–700 day outburst recurrence time (Kuulkers et al. 1997), which is unusually short for systems of this type, probably indicating a higher time-averaged mass accretion rate from its companion (Chen et al. 1997). Highly polarized radio emission was detected from 4U 1630−47 during its 1998 outburst (Hjellming et al. 1999), indicating the presence of jets, and the source is often compared to microquasars such as GRS 1915+105 and GRO J1655−40. The compact object mass has not been measured for 4U 1630−47, but McClintock & Remillard (2003) classify it as a very likely "category A" BHC. Also, the binary orbital period is not known, and our lack of knowledge is due to the difficulty in performing optical and infrared studies of the source due to its high column density (but see Augusteijn et al. [2001] for the likely identification of the source's infrared counterpart).

The current outburst from 4U 1630−47, which began in 2002 September (Wijnands et al. 2002), is one of the brightest and longest recorded outbursts from this system. A new high-amplitude flaring behavior has been reported at different times during this outburst (Homan & Wijnands 2002; Tomsick 2003), and in this work we study this behavior in more detail. Also, transitions between spectral states have been observed during this outburst (Tomsick et al. 2004b; Tomsick 2004a). In addition to the high level of recent activity from 4U 1630−47 and the recent work on defining spectral states, our study comes at a time when *INTEGRAL* is providing high-quality hard X-ray images. Images of the 4U 1630−47 field, which we present in this work and in Tomsick et al. 2004b, are extremely useful for avoiding source confusion. In the following, we present X-ray spectral and timing studies of 4U 1630−47.

2. OBSERVATIONS

RXTE regularly monitored 4U 1630−47 in outburst with pointed observations between 2002 September 12 (MJD 52,529) and 2005 January 4 (MJD 53,375). Here we study the evolution of the X-ray properties throughout the outburst by analyzing data from the 318 *RXTE* observations that occurred during this time. With the exception of five 22–36 day observing gaps caused mainly by Sun angle constraints, pointed observations occurred, on average, approximately every other day for 2.3 years. The observations were made under seven different proposals (see Table 1 for the proposal IDs): In three cases (P70113, P80117, and P90128) we observed 4U 1630−47 in conjunction with our *INTEGRAL* program; and in the other four cases (P70417,

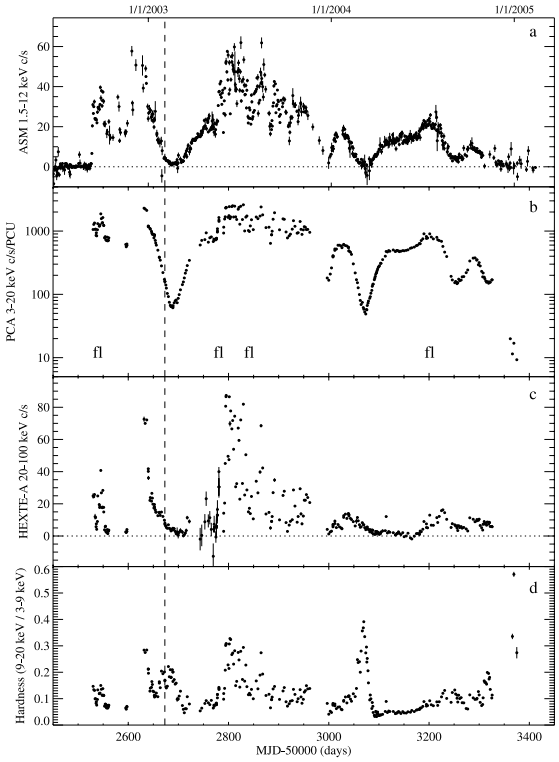

Fig. 1.—X-ray light curves and hardness vs. time for 4U 1630−47 from 2002 September to 2005 January. (*a*) *RXTE* ASM 1.5–12 keV rates (daily averages). (*b*) 3–20 keV PCA light curve for the 318 pointed observations. (*c*) 20–100 keV HEXTE light curve. (*d*) 9–20/3–9 keV hardness ratio using the PCA count rates. The vertical dashed line marks the time of the *INTEGRAL* observation. In (*b*) "fl" marks the examples of the flaring behavior shown in Fig. 4. Also, the PCA count rates for the final four observations (see [*b*]) are consistent with little or no contribution to the emission from 4U 1630−47.

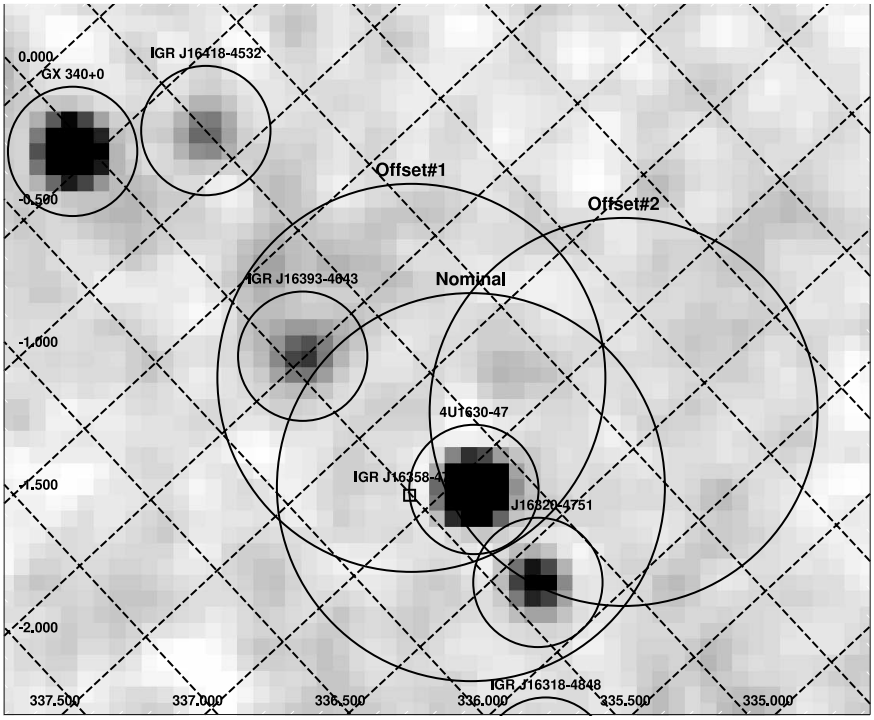

FIG. 2.—A 20–40 keV image (significance map) using the IBIS instrument on *INTEGRAL* taken on UT 2003 February 1.2–5.3. The small circles mark detected sources, and the position of the undetected transient IGR J16358−4726 is marked with a square. The large circles (labeled nominal, offset 1, and offset 2) show the three pointing positions used during the *RXTE* campaign. The circles have a 2° diameter, corresponding to the FWZI collimator response. We used different *RXTE* pointing positions in an attempt to minimize contamination of 4U 1630−47 by nearby sources. [*See the electronic edition of the Journal for a color version of this figure.*]

P80417, P80420, and P90410) the observations were made under a public Target of Opportunity program, and we analyzed data from the public archive. The Proportional Counter Array (PCA) and High-Energy X-Ray Timing Experiment (HEXTE) light curves shown in Figure 1 indicate the times of the *RXTE* observations.

After the launch of the European Space Agency (ESA) satellite *INTEGRAL* (Winkler et al. 2003) in 2002 October, we triggered our Target of Opportunity to observe 4U 1630−47 when the source became observable during outburst in early 2003. We obtained a 293 ks exposure between UT 2003 February 1.2 and UT 2003 February 5.3, and the time of this observation is marked in Figure 1. We previously used the data from this observation for studies of the obscured X-ray source IGR J16320−4751 (AX J1631.9−4752), which is a hard and persistent (though highly variable) source that is close to 4U 1630−47 (Tomsick et al. 2003; Rodriguez et al. 2003; Foschini et al. 2004), and we used these data to report detections of two other new *INTEGRAL* sources (Tomsick et al. 2004a). In addition, the 20–40 keV images from this observation can be found in Tomsick et al. (2004b) along with information about the sources in the *INTEGRAL* field of view (FOV), including an initial look at the hard X-ray and gamma-ray properties of 4U 1630−47. Although we do not present a full analysis of the *INTEGRAL* data here, the hard X-ray *INTEGRAL* images are important for interpreting the *RXTE* data.

3. DATA ANALYSIS

We extracted energy spectra and light curves from the *RXTE* data using scripts developed at the University of California, San Diego, and the University of Tübingen that incorporate the standard software for *RXTE* data reduction (FTOOLS). We processed the data using the most recent *RXTE* calibration files, which were released on 2003 July 7, and performed extractions using FTOOLS versions 5.3 and 5.3.1. The *RXTE* routines are identical for these two versions of FTOOLS. We performed time filtering for the 330 observations using data from times during which the following criteria are satisfied: the *RXTE* pointing is within 0.°1 of the nominal pointing position, the nominal pointing position is more than 10° above the limb of the Earth, a South Atlantic Anomaly (SAA) passage has not occurred within the previous 30 minutes, Proportional Counter Unit (PCU) 2 is turned on, and the PCU 2 electron ratio is less than 0.25. We chose PCU 2 because, in normal *RXTE* operation, this unit is programmed to have a very high duty cycle to allow for the most precise observation-to-observation comparisons. Our filtering led to zero exposure time for only 12 out of 330 observations (3.6%), leaving us with 318 observations for further study. As shown in Table 1, we typically obtained 1–3 ks of exposure time per observation, but exposure times vary greatly, from 96 s up to 11 ks. For all 318 observations, the mean exposure time is 1.8 ks.

We extracted the following information for each observation: the 3–20 keV PCU 2 count rate, the 3–9 keV PCU 2 count rate, the 9–20 keV PCU 2 count rate, the 20–100 keV HEXTE-A count rate, the 3–200 keV PCA+HEXTE energy spectrum, and the 3–20 keV PCA light curve with 16 s time bins. We took the PCA information from the standard 2 data, which includes 129 channel energy spectra taken with 16 s time resolution. We used the sky-VLE model to estimate and subtract off the background.

For HEXTE, we used event list data, and we used the normal HEXTE rocking mode to estimate and subtract off the background. As described below in § 7, we also selected five observations for more detailed study, and for these, we used the higher time resolution PCA data to produce power spectra. For four of the observations, we used a PCA mode with 64 energy channels and 2^{-13} s (= 122 μs) time resolution. In the fifth case, we combined the data from two PCA modes: a mode with 2^{-7} s (7.8 ms) time resolution, covering the lower energy portion of the spectrum; and a second mode with higher time resolution, containing an event list for the higher energy photons. We used data from all the active PCUs when producing the power spectra.

INTEGRAL hard X-ray images from the observation described above show that 4U 1630−47 lies in a region of the Galaxy that has a high density of hard X-ray sources, including a source, IGR J16320−4751, that is 0.°58 from 4U 1630−47. The 20–40 keV IBIS (Imager On-board the *INTEGRAL* Satellite) image, produced using the Off-line Scientific Analysis (OSA version 4.2) software (Goldwurm et al. 2003), is shown in Figure 2. When we realized that there is another hard X-ray source within the *RXTE* FOV for the nominal 4U 1630−47 pointing position, we requested a change in the pointing position to avoid IGR J16320−4751. From MJD 52,691 to 52,722, we used the pointing position labeled offset 1 in Figure 2. However, the presence of IGR J16393−4643 (Combi et al. 2004) and a third X-ray transient, IGR J16358−4726 (Patel et al. 2004), prompted another change in pointing position to offset 2, and we used this pointing position from MJD 52,722 to 52,781. The PCA and HEXTE collimators have a triangular response with an FWHM FOV of 1° and a full-width at zero-intensity (FWZI) FOV of 2°. Where necessary in the work described below, we corrected for the collimator response when producing light curves or response matrices for spectral analysis.

4. FLUX AND HARDNESS EVOLUTION DURING THE OUTBURST

Figure 1*a* shows the *RXTE* All-Sky Monitor (ASM) 1.5–12 keV light curve for 4U 1630−47 with the source in outburst from 2002 September to the end of 2004. In addition to being the longest outburst during the *RXTE* lifetime, at its peak its ASM flux is ∼800 mcrab (1 crab = 74 ASM counts s^{-1}), which is ∼50% brighter than any previous outburst observed by the ASM. Below we divide the outburst into the various spectral states the source entered, but in general the ASM light curve shows two very bright and highly variable periods: the first occurred for ∼120 days between MJD 52,530 and ∼52,650, and the second occurred for ∼200 days in 2003 between MJD 52,750 and 52,950. The source was also bright for much of 2004, but it did not become as bright as the previous two periods of very high activity. Twice in 2003 and once in early 2004 the source flux was low enough to be only marginally detected by the ASM. The source became undetectable again in late 2004, and it appears that the source has remained in quiescence into 2005.

Figure 1*b* shows the count rates measured in the 3–20 keV band by the PCA during the pointed *RXTE* observations. For the observations made at the offset pointing positions, the count rates are corrected using the PCA collimator response. The *RXTE* monitoring program began soon after the source was detected by the ASM. While the source flux was at the ASM sensitivity limit at times, the PCA, with its better sensitivity, shows continuous activity until 2004 November 16 (MJD 53,326). After this date there was a 36 day gap in coverage, and we obtained four more PCA measurements after this gap. For these observations, the PCA rates are consistent with Galactic ridge emission and flux from IGR J16320−4751, with little or no emission from 4U 1630−47. They are not included in the spectral and timing analysis in the next two sections (leaving 314 observations). Figure 1*c* shows the HEXTE-A 20–100 keV count rate, and Figure 1*d* shows the source hardness, defined as the ratio of the 9–20 keV PCA rate to the 3–9 keV PCA rate.

5. ENERGY SPECTRA

For the 314 observations, we used the XSPEC version 11.3.1t software to perform χ^2-minimization spectral fits to the PCA+HEXTE 3–200 keV energy spectra. For the PCA spectra, we included systematic errors at a level of 0.6% for 3–8 keV and at a level of 0.3% for 8–25 keV, and these numbers are derived by fitting energy spectra of the Crab nebula as described in Tomsick et al. (2001). For many of the observations, the standard two component model—disk-blackbody (Makishima et al. 1986) plus power law with interstellar absorption—provides acceptable fits, but for 31 observations, we obtain $\chi^2_\nu > 2.0$ for 63 degrees of freedom (dof), and for the 314 observations, the mean χ^2_ν is 1.51. By examining the residuals for several of the spectra with statistically poor fits, we found two main reasons for the poor fits. First, in many cases, large residuals (positive and negative) are present around the iron Kα complex. Second, negative residuals are sometimes seen at high energies, above 50 keV, indicating the presence of a cutoff in the spectrum. The presence of iron features and high-energy cutoffs is not surprising, as they have been seen previously for 4U 1630−47 as well as for other black hole sources (Tomsick & Kaaret 2000; Zdziarski et al. 1996).

Thus, we refitted all the energy spectra after adding a narrow iron Kα emission line and a smeared iron edge (Ebisawa et al. 1994) in a similar manner to that described in Tomsick & Kaaret (2000). We restricted the line energies to between 6.4 and 7.1 keV, spanning the possible iron Kα range for nonredshifted lines. Similarly, we restricted the edge energy to between 7.1 and 9.3 keV. Sample fits to several spectra show that the width of the smeared edge is not well constrained in most cases, and we fixed the width to 10 keV (Ebisawa et al. 1994; Tomsick & Kaaret 2000). We also added a high-energy cutoff allowing the model to exponentially turn over above an energy $E_{\rm cut}$ with an e-folding energy of $E_{\rm fold}$. Finally, although the column density ($N_{\rm H}$) has been fixed to values close to 10^{23} cm^{-2} in some previous studies (e.g., Tomsick & Kaaret 2000), the results for this *RXTE* data set indicate significant changes during the outburst. Thus, we have left $N_{\rm H}$ as a free parameter, except that we have restricted the column density to be greater than 6×10^{22} cm^{-2}, which is the lowest value that has been measured for 4U 1630−47 by a soft X-ray instrument (Parmar et al. 1997). This value may represent the interstellar value along the line of sight.

These additions to the spectral model produce significant improvements in the quality of the fits. For the 314 spectra, the mean χ^2_ν is 1.15 for 57 dof, and only 13 have $\chi^2_\nu > 2.0$. We examined the spectral residuals as well as the 16 s light curves for the cases in which the worst fits are obtained. In most of these cases, the light curves show a high degree of variability, suggesting that spectral variability during the observation degrades the quality of the fits. However, in several cases, the level of variability is not particularly high, and in four of these observations significant positive residuals are present at high energies, above ∼40 keV. Although it is possible that these residuals indicate a high-energy excess from 4U 1630−47, the observations for which the excess is present occurred at the nominal pointing position for 4U 1630−47, so that the *RXTE* FOV includes the persistent hard X-ray source IGR J16320−4751 (see Fig. 2). Using

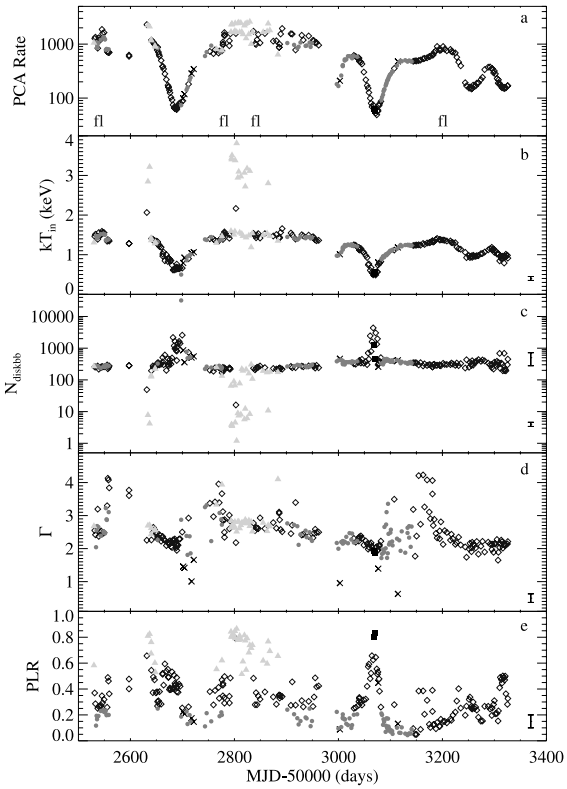

FIG. 3.—Evolution of the spectral properties of 4U 1630−47 during the 2002–2004 outburst. The 314 observations have been divided into spectral states using the spectral parameters and the quantitative definitions of McClintock & Remillard (2003). The symbols correspond to states as follows: triangles: steep power-law; open diamonds: intermediate state; circles: thermal-dominant; squares: hard. The crosses indicate observations that we believe are contaminated by the nearby sources IGR J16320−4751 or IGR J16358−4726. (*a*) 3–20 keV PCA light curve, and "fl" marks the examples of the flaring behavior shown in Fig. 4. (*b*) and (*c*) Disk-blackbody parameters. (*d*) Power-law photon index. (*e*) Power-law ratio (see text for definition). In panels (*b*) through (*e*), an average-sized error bar is shown, although it should be noted that there is some variation in the error-bar size from observation-to-observation (see Table 2). [*See the electronic edition of the Journal for a color version of this figure.*]

INTEGRAL flux measurements and *RXTE* pointings at the 4U 1630−47 position during times when 4U 1630−47 was not active, we demonstrate in Appendix A that the positive high-energy residuals are very likely caused by IGR J16320−4751. The four observations with positive high-energy residuals occurred between MJD 52,560 and 52,596, and as the spectra for these four observations are likely contaminated, we do not consider them in the following analysis.

Figure 3 shows the PCA rates and spectral parameters versus time. The spectral parameters shown include the temperature of the disk-blackbody component ($kT_{\rm in}$), the normalization of this component [$N_{\rm diskbb} = (R_{\rm in}/d_{10})^2 \cos i$, where $R_{\rm in}$ is the inner radius of the accretion disk in kilometers, d_{10} is the source distance in units of 10 kpc, and i is the disk inclination], the power-law photon index (Γ), and the ratio of the unabsorbed 2–20 keV power-law flux to the total flux (PLR). When the entire outburst is considered, the range of $kT_{\rm in}$ values is 0.49–3.81 keV, while the range is 0.63–4.13 for Γ. We use the spectral parameters and the McClintock & Remillard (2003) state definitions to divide the observations into different spectral states, and the classifications are indicated in Figure 3. The steep power-law (SPL) observations have $\Gamma > 2.4$ and PLR > 0.5. Those in the thermal-dominant (TD) state have PLR < 0.25. The source was only in the hard state with $1.5 < \Gamma < 2.1$ and PLR > 0.80 for two observations near MJD 53,069. The remainder of the observations do not fit into any of the spectral states as defined by McClintock & Remillard (2003), and we say that the source was in one or more intermediate states (ISs) during these observations. It should be noted that we have divided the observations into spectral states using only spectral and not timing information. While timing information is important to the study of spectral states and is part of the full McClintock & Remillard (2003) definitions, our results for a sample of the power spectra (see § 7) show that the timing properties are in line with the McClintock & Remillard (2003) criteria for the various states. If we had included timing information in dividing up the spectral states, it is possible that some TD observations with higher noise levels would be reclassified as IS and that if some of the IS or TD observations have QPOs, they might be reclassified as SPL. However, such reclassifications would not change the results or conclusions of this work.

There are seven observations with distinctly different spectra. For these observations, the power law is very hard, with values of Γ between 0.6 and 1.7, and it is sharply cut off, with *e*-folding energies between 10 and 50 keV. While such a spectrum would represent the discovery of a new black hole state, we strongly suspect that these observations are contaminated by emission from the hard X-ray transient IGR J16358−4726. Although IGR J16358−4726 was not detected during our 2003 February *INTEGRAL* observation (see Fig. 2), four of the observations for which we see the very hard X-ray spectrum occurred during the time period from MJD 52,701 to 52,722, when the source was known to be active (Revnivtsev 2003; Revnivtsev et al. 2003; Patel et al. 2004). During this time period, we used the offset 1 pointing position, so the FOV included IGR J16358−4726 but not IGR J16320−4751. In addition, the hard spectrum is not detected for any of the observations for which we used the offset 2 pointing position, which does not include IGR J16358−4726 in the FOV. In Appendix B, we include details about the hard spectra, as they provide useful information on IGR J16358−4726. Other than in Appendix B, we do not consider these observations further.

6. HIGH-AMPLITUDE VARIABILITY

An inspection of the 3–20 keV 16 s PCA light curves for all 314 observations indicates that in addition to the observation-to-observation variability that is clearly seen in Figures 1 and 3, many of the light curves show high-amplitude variability during the observations. To quantify the level of variability, we calculated the peak-to-peak amplitude for each observation, $A_{\rm pp}$, defined simply as the maximum PCA count rate minus the minimum rate divided by the mean rate for the observation. The errors on $A_{\rm pp}$ depend on the uncertainties in the count rates for the individual maximum and minimum 16 s time bins as well as the error in the mean rate. For the 314 observations, the mean value of $A_{\rm pp}$ is 0.26 and the standard deviation is 0.20. While the majority of the observations have some form of significant variability, we focus on the observations with high-amplitude variability, defined as the observations during which $A_{\rm pp}$ minus the 2 σ error on $A_{\rm pp}$ is greater than 0.3. With this definition, there are 72 observations with high-amplitude variability.

A more careful examination of the 72 light curves with high-amplitude variability indicates that there are at least four types of high-amplitude variability, and examples of the most common type are shown in Figure 4, while the other three types are

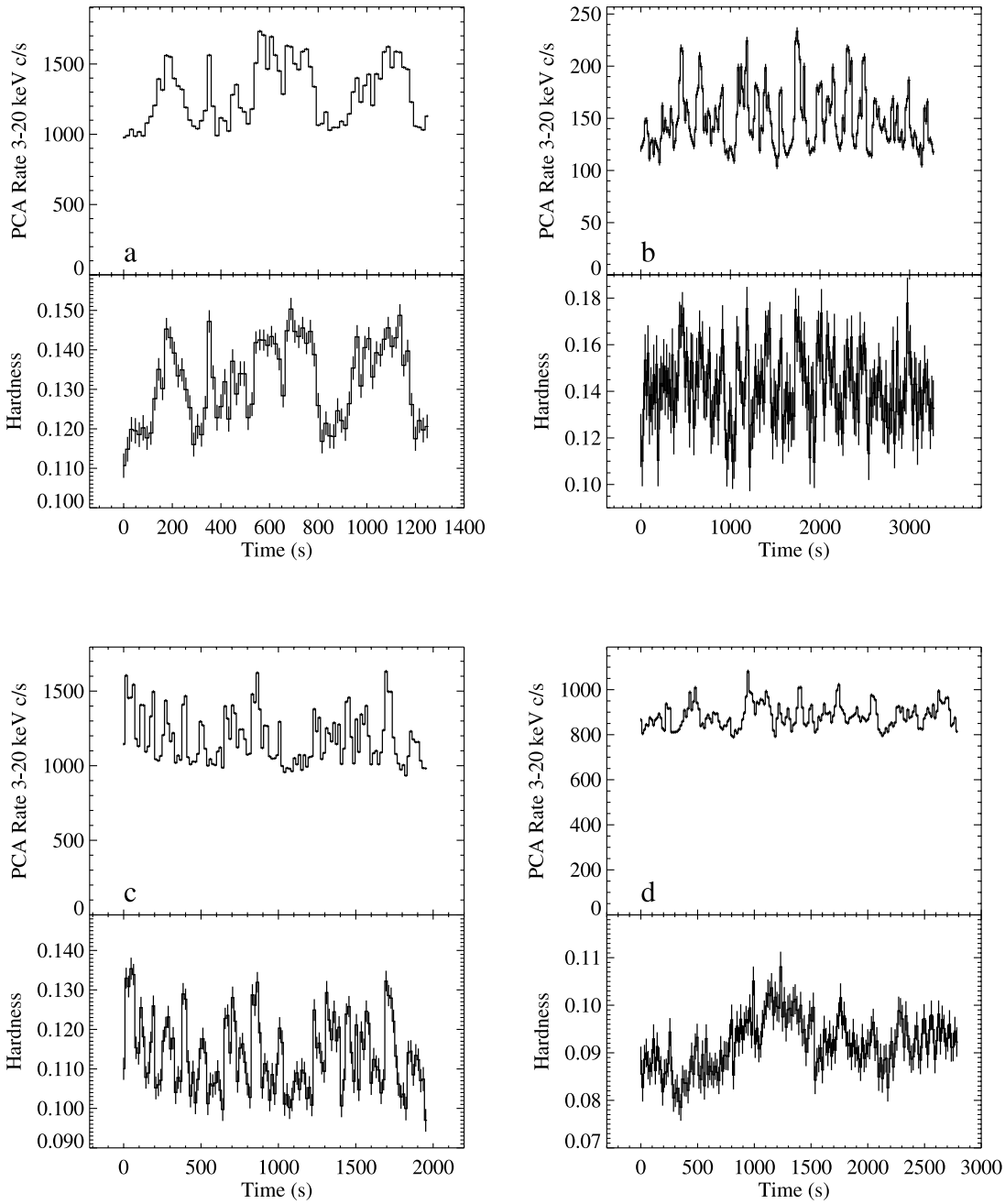

FIG. 4.—PCA light curves and 9–20/3–9 keV hardnesses vs. time with 16 s time bins for four IS observations that exhibit the flaring behavior. The times and Observation IDs for these observations are (*a*) MJD 52,539.094 and 70417-01-04-02, (*b*) MJD 52,780.746 and 70113-01-43-00, (*c*) MJD 52,843.379 and 80117-01-13-02, and (*d*) MJD 53,201.305 and 90410-01-13-01. These are also marked on Figs. 1 and 3. Note that the observations for (*a*), (*c*), and (*d*) were made in the nominal pointing position, while the observation for (*b*) was made in one of the offset pointing positions.

shown in Figure 5. The light curves shown in Figure 4 can be interpreted as a series of 10–100 s flares; however, in some of the light curves the flares occur so often that it is difficult to distinguish the individual flares. We refer to this as "flaring" behavior below, and we chose the examples to illustrate that flaring occurs over a wide range of times during the outburst, as shown in Figures 1 and 3. While all of the examples shown in Figure 4 are from IS observations, flaring also sometimes occurs during observations classified as TD and SPL. Figure 4 also shows the 9–20/3–9 keV hardness as a function of time. For the observations

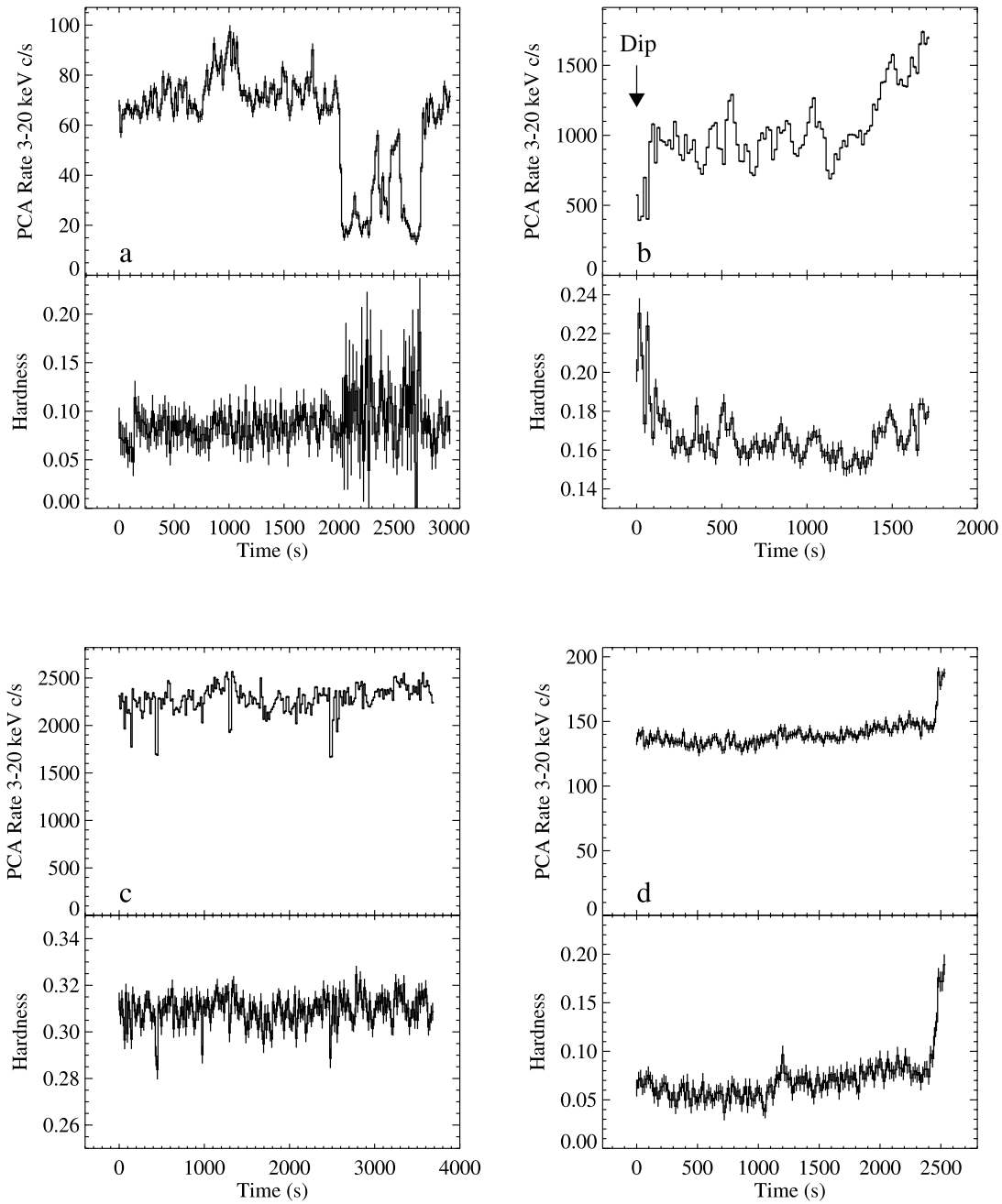

FIG. 5.—PCA light curves and 9–20/3–9 keV hardnesses vs. time with 16 s time bins showing three other types of high-amplitude variability. (*a*) and (*b*) Examples in which absorption is likely the cause of the dips. (*c*) Example of short dips seen in three of the SPL observations. (*d*) An unusually hard flare that is probably from 4U 1630−47. The times and Observation IDs for these observations are (*a*) MJD 52,759.672 and 70113-01-36-00, (*b*) MJD 52,795.340 and 80117-01-03-00, (*c*) MJD 52,832.188 and 80117-01-12-00, and (*d*) MJD 53,087.832 and 90128-01-05-00. Note that the observations for (*b*), (*c*), and (*d*) were made in the nominal pointing position, while the observation for (*a*) was made in one of the offset pointing positions.

shown in panels (*a*), (*b*), and (*c*), the hardness is tightly correlated with the total 3–20 keV rate (i.e., these are hard flares). However, this correlation is not seen for the panel (*d*) observation.

Even more extreme variability, with $A_{pp} > 1.0$, is seen in the two light curves shown in Figures 5*a* and 5*b*. These light curves exhibit deep dips that are clearly different from the other types of variability observed. The dip shown in Figure 5*a* is very similar to the dip observed from 4U 1630−47 during its 1996 outburst (Tomsick et al. 1998; Kuulkers et al. 1998). Spectral analysis of the 1996 dip indicates that it is likely caused by

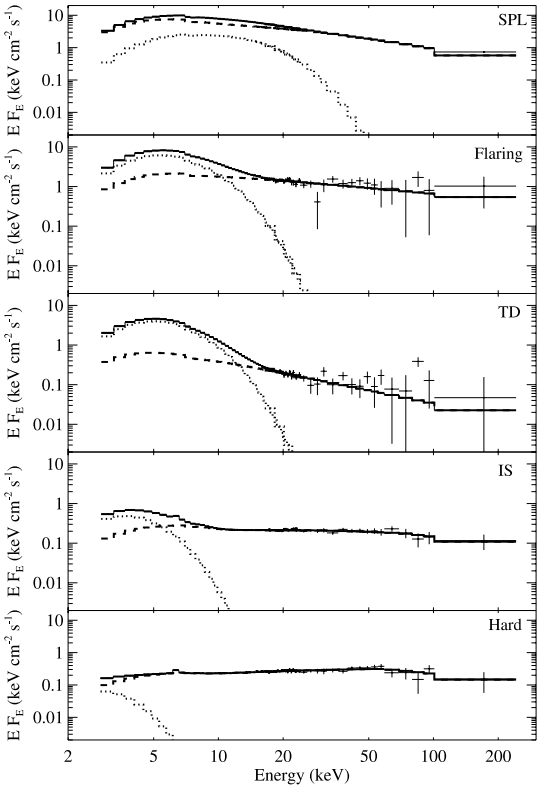

FIG. 6.—Five example *RXTE* energy spectra fitted with the model described in the text. In addition to the total model (*solid line*), the *dotted line* shows the disk-blackbody component and the *dashed line* shows the power-law component. From top to bottom, the spectra are ordered by decreasing 3–200 keV flux and disk-blackbody temperature and illustrate examples of the following states or behaviors: SPL, flaring, TD, IS, and hard. See Table 2 for details such as Observation IDs, observation times, and parameter values.

absorption, perhaps from accretion disk material, but the fact that the dip is not spectrally hard indicates partial covering of the X-ray source (Tomsick et al. 1998; Kuulkers et al. 1998). Similarly, the dip shown in Figure 5*a* shows, at most, only a moderate level of hardening.

A third type of variability is illustrated in Figure 5*c* and can be described as short, 10–20 s dips, and similar dips have been reported during the 1998 outburst from 4U 1630−47 (Tomsick & Kaaret 2000; Dieters et al. 2000). The hardness ratio indicates that the spectrum becomes softer during the dips. During this outburst, we only see these short, soft dips during the three observations from MJD 52,794.289, 52,795.340, and 52,801.445, and a total of seven or eight short dips are seen in the 19 ks of exposure time accumulated for these three observations, which are all classified as SPL.

The final type of high-amplitude variability is shown in Figure 5*d* and consists of a single, very hard flare that occurred at the end of the observation performed on MJD 53,087.832, at which time the source was in the TD state. The flare did not occur close to the time of any SAA passage, and we checked that the PCA electron ratio was not high during the time of the flare, indicating that the flare did not have any instrumental or environmental cause. In addition, we checked for solar flares using the X-ray data from the Solar X-Ray Imager (SXI) on the *Geostationary Operational Environmental Satellites* (*GOES-12*), but the Sun did not flare during the *RXTE* observation. Finally, we extracted a 16 s HEXTE light curve, and we see that HEXTE also detected the hard flare. Thus, we conclude that origin of the flare was an astronomical source in the *RXTE* FOV. It is likely that the flare came from 4U 1630−47, but we cannot rule out the possibility that it came from one of the other sources in the FOV, such as IGR J16358−4726 or IGR J16320−4751.

7. EXAMPLES OF ENERGY AND POWER SPECTRA

We selected representative observations for more detailed spectral and timing analysis. The selected observations include one observation from each of the spectral states (SPL, TD, and hard) and two observations from the IS state: one that exhibits the flaring behavior described above and one that does not. The energy spectra from these observations are shown in Figure 6, and the parameters from the spectral fits are given in Table 2. From the SPL state to the hard state, the spectra are ordered according to decreasing $kT_{\rm in}$ and 3–200 keV flux, as shown in Table 2. While $kT_{\rm in}$ is correlated with the flux, the disk-blackbody normalization is anticorrelated with the flux. The changes for Γ and PLR do not have a simple relationship with the total flux. The PLR is the highest at the highest flux and the lowest flux, but the thermal, disk-blackbody component contributes a higher fraction of the flux at intermediate flux levels. Table 2 also provides the measured values for the column density ($N_{\rm H}$). The values, with

TABLE 2
SPECTRAL PARAMETERS

Observation ID	MJD[a]	$N_{\rm H}$[b]	$kT_{\rm in}$[c] (keV)	$N_{\rm diskbb}$[d]	Γ[e]	PLR[f]	Flux[g]	Spectral State[h]
70417-01-09-00.....	52,636.852	$11.03^{+0.28}_{-0.21}$	$3.22^{+0.10}_{-0.05}$	$4.2^{+0.4}_{-0.8}$	$2.71^{+0.03}_{-0.02}$	$0.835^{+0.014}_{-0.009}$	3.90×10^{-8}	SPL
70113-01-43-00.....	52,780.746	$9.76^{+0.69}_{-0.36}$	$1.58^{+0.02}_{-0.03}$	230 ± 20	$2.50^{+0.22}_{-0.20}$	$0.34^{+0.10}_{-0.05}$	2.50×10^{-8}	Flaring
70417-01-06-00.....	52,558.188	$9.67^{+1.13}_{-0.17}$	$1.39^{+0.01}_{-0.02}$	278^{+11}_{-20}	$3.10^{+0.50}_{-0.10}$	$0.21^{+0.16}_{-0.04}$	1.16×10^{-8}	TD
70113-02-04-00.....	52,675.941	$7.13^{+1.07}_{-0.68}$	$0.84^{+0.05}_{-0.06}$	437^{+308}_{-132}	$2.24^{+0.06}_{-0.04}$	0.40 ± 0.01	2.35×10^{-9}	IS
80117-01-21-01.....	53,068.789	<8.9	$0.50^{+0.15}_{-0.05}$	1246^{+4254}_{-846}	$1.92^{+0.05}_{-0.06}$	$0.80^{+0.02}_{-0.14}$	1.75×10^{-9}	Hard

[a] Modified Julian Date.
[b] Hydrogen column density in units of 10^{22} cm^{-2}. For all the parameters, 90% confidence errors are given.
[c] The inner disk temperature measured with the disk-blackbody (diskbb) model.
[d] The normalization for the disk-blackbody component; $N_{\rm diskbb} = (R_{\rm in}/d_{10})^2 \cos i$, where $R_{\rm in}$ is the disk inner radius in units of km, d_{10} is the distance to the source in units of 10 kpc, and i is the disk inclination.
[e] Power-law photon index.
[f] Ratio of the unabsorbed 2–20 keV flux in the power-law component to the total 2–20 keV flux.
[g] Unabsorbed 3–200 keV flux in ergs cm^{-2} s^{-1}.
[h] SPL, TD, IS, and hard state label the spectral state of the observation. The observation labeled "flaring" is an IS observation that exhibits the flaring behavior.

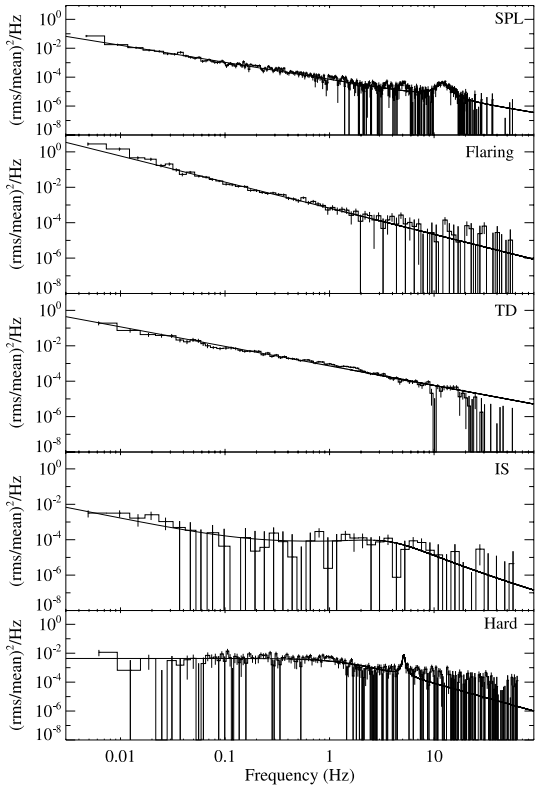

FIG. 7.—*RXTE* power spectra for each of the five observations shown in Fig. 6, illustrating examples of the following states or behaviors: SPL, flaring, TD, IS, and hard. The solid lines represent model fits, and the parameters for these models are given in Table 3.

90% confidence error bars, indicate that the column density drops significantly with flux.

The 0.005–64 Hz rms-normalized power spectra for the same five observations are shown in Figure 7. In fitting the power spectra, we considered various combinations of three different components, which we also previously used to fit the 4U 1630−47 spectra from the 1998 outburst (Tomsick & Kaaret 2000): a power-law function (PL); a band-limited noise component (BL), which we modeled as a zero-centered Lorentzian; and a QPO, which we modeled using a Lorentzian. For the SPL state, the 0.005–10 Hz continuum is well described by the PL model. In addition, a QPO is present at 12.15 ± 0.15 Hz with a quality factor of $Q = 4.4 \pm 0.7$ and a fractional rms of $1.30\% \pm 0.07\%$ (see Table 3). Above this QPO, the power drops much more rapidly than the extrapolation of the PL. For the IS observation with flaring, nearly the entire 0.005–64 Hz range is well described by the PL. There are no QPOs in this case, but there is excess power below ~0.02 Hz due to the flaring. The TD state power spectrum has approximately a power-law shape from 0.005 to 10 Hz. There appears to be a narrow dip in the power at 10 Hz, and the power drops off more rapidly than the extrapolation of the power law above 20 Hz. In the IS state, there is evidence for BL and PL components, although the statistics are rather poor for this state due to a lower count rate and a lower rms noise level. There is no evidence for the presence of QPOs in the IS state. Finally, in the hard state, the continuum is well described by only the BL component, and a QPO is present at 5.13 ± 0.01 Hz with $Q = 21 \pm 5$ and a fractional rms level of $5.4\% \pm 0.3\%$. The other hard state observation exhibited a very similar power spectrum but with the QPO at 4.03 ± 0.01 Hz.

The power spectra for the observations we previously identified as being in the TD, SPL, and hard states based on their spectral properties are consistent with the typical power spectra expected for these states as described by McClintock & Remillard (2003). TD power spectra typically have 0.1–10 Hz rms values $\lesssim 6\%$ with weak or no QPOs and a power-law shape, and these properties are consistent with our example TD power spectrum. For SPL power spectra, the continuum often (but not always) has a power-law shape, and low-frequency (1–15 Hz) QPOs are usually present. Our example SPL power spectrum exhibits similar properties. Based on the fact that the QPO in our SPL example is relatively broad, it would be classified as type A or B (depending on its phase lag properties) using the QPO classifications given in Remillard et al. (2002), and the combination of a power-law continuum and type A or B QPOs is typical (Casella et al. 2004).

The power spectra for the two observations identified as being in the hard state have relatively strong band-limited noise, which is a characteristic of hard state power spectra. The 0.1–10 Hz rms values for these two observations are $9.6\% \pm 0.4\%$ and $9.0\% \pm 0.6\%$, lying just below the 10%–30% range that is typical for the hard state. While this could indicate that the source was close to but not quite in the hard state, it is important to note that these are the only two observations for which we found strong band-limited noise. We produced power spectra for the five IS observations closest in time to the two hard state observations. We fitted them with a power-law model and obtained reduced-χ^2 values between 0.4 and 2.1 for 17 dof. The

TABLE 3
TIMING PARAMETERS

Observation ID	Spectral State[a]	Model[b]	Continuum rms (0.1–10 Hz) (%)	ν_{QPO} (Hz)	Q[c]	QPO rms (%)	A_{pp}[d]
70417-01-09-00	SPL	PL+QPO	1.8 ± 0.2	12.15 ± 0.15	4.4 ± 0.7	1.30 ± 0.07	0.25 ± 0.01
70113-01-43-00	Flaring	PL	6.1 ± 0.5	...	...	...	0.86 ± 0.03
70417-01-06-00	TD	PL	5.8 ± 0.7	...	...	...	0.26 ± 0.01
70113-02-04-00	IS	PL+BL	3.5 ± 1.3	...	...	...	0.31 ± 0.04
80117-01-21-01	Hard	BL+QPO	9.6 ± 0.4	5.13 ± 0.01	21 ± 5	5.4 ± 0.3	0.20 ± 0.05

[a] SPL, TD, IS, and hard state label the spectral state of the observation. The observation labeled "flaring" is an IS observation that exhibits the flaring behavior.
[b] Components used in modeling the power spectra, where PL = power law, BL = band limited, and QPO = quasi-periodic oscillation.
[c] The quality factor of the QPO, defined as ν_{QPO} divided by the QPO's FWHM.
[d] The peak-to-peak amplitude of the noise (see the text for a precise definition.)

power-law fits give 0.1–10 Hz rms values between 1% and 4%, indicating that the noise level is much lower for these observations than for the two observations identified as hard state observations. Thus, these two observations distinguish themselves from the other observations on the basis of their spectral and timing properties, which appears to indicate that the source did briefly enter the hard state.

The properties of the QPOs seen for the two hard state power spectra are also different from the QPO seen in the SPL. In addition to being at lower frequency, 4–5 Hz, the hard state QPOs are much narrower, and they would be classified as type C QPOs. The combination of type C QPOs and band-limited noise is typical (Casella et al. 2004). It is also notable that the hard state power spectra are very similar to those seen at the end of the 1998 outburst from 4U 1630−47 (Tomsick & Kaaret 2000). As the source declined in 1998, the QPO was first detected at 3.4 Hz and then gradually dropped to 0.2 Hz. Thus, the 4–5 Hz QPO we see in the 2002–2004 outburst likely indicates that a similar phenomenon began to occur but was stopped, perhaps by an increase in the mass accretion rate.

8. DISCUSSION

Good X-ray coverage of 4U 1630−47 during the 2002–2004 outburst has allowed us to study its source properties throughout the outburst in detail, and here we discuss these properties in the context of previous outbursts from 4U 1630−47, as well as in the context of accreting black holes in general. The 2002–2004 outburst is by far the longest and brightest that has occurred during the *RXTE* era, and in § 8.1 we make comparisons to historical outbursts. In our study, we have found several extreme and unusual source properties, and in § 8.2 we discuss our measurements of the soft component, including the extremely high inner disk temperatures that occur for some of the steep power-law state observations. In § 8.3 we extend the analysis described above to constrain the nature of the high-amplitude flaring. In § 8.4 we compare the X-ray and radio properties of the 2002–2004 outburst to those of the 1998 outburst and discuss radio–X-ray connections. Finally, our study has provided a test of the quantitative McClintock & Remillard (2003) state definitions, and in § 8.5 we discuss some of the pros and cons of these definitions.

8.1. *Comparison of the 2002–2004 Outburst to Previous Outbursts*

Prior to the 2002–2004 outburst from 4U 1630−47, four outbursts from this source had been observed by the *RXTE* ASM during the *RXTE* era (1996–present). The mean duration of these four outbursts as measured by the *RXTE* ASM is 140 days, and the mean peak ASM count rate is 28 counts s^{-1} (0.38 crab). From the ASM light curve (Fig. 1*a*), the duration of the 2002–2004 outburst is 825 days, and the peak ASM rate is 62 counts s^{-1} (0.84 crab), making it longer by a factor of nearly 6 and brighter by a factor of 2.2 than the mean values for the first four outbursts.

While the current outburst is unusual compared to the 4U 1630−47 outbursts of the past decade, it is not unprecedented in duration or in brightness when compared to the entire group of outbursts going back to 1969. Although there are many cases in which poor X-ray coverage makes it difficult to tell whether outbursts were extended or not, the clearest example of an extended outburst occurred when the *Ginga* All-Sky Monitor detected the source for 2.4 years between 1988 October and 1991 March (Kuulkers et al. 1997). The *Ginga* light curve shows that the 1988–1991 outburst had many similarities to the current outburst, including flares in which the flux reached ∼0.6 crab, as well as multiple time periods of low flux during the outburst. For the 1988–1991 outburst, the low-flux periods are separated by ∼220 days (Kuulkers et al. 1997). The ASM light curve for the 2002–2004 outburst has local minima at MJD 52,685, 53,000, 53,075, and 53,250, indicating separations of 315, 75, and 175 days; thus, they are the same order of magnitude as the 220 day separations, but they are clearly different.

With a peak flux of 0.84 crab (1.5–12 keV), the 2002–2004 outburst is somewhat brighter than the 0.6 crab (1–20 keV) flares detected during the 1988–1991 outburst. However, at a 3–6 keV flux of 1.4 crab (Chen et al. 1997), the 1977 outburst, which lasted for about 0.3 yr, was brighter than the current outburst. In summary, while the 2002–2004 outburst is one of the longest and brightest outbursts ever detected from 4U 1630−47, it is not unprecedented in either category. On the other hand, no previous outburst was both brighter and longer than the current outburst, so it is very likely that the total mass accreted is higher for the 2002–2004 outburst than for any previous outburst.

The high level of recent activity from 4U 1630−47 strengthens the argument made by Chen et al. (1997) that the mass accretion rate from the binary companion ($\dot{M}_c$) is unusually high for this source. Furthermore, Chen et al. (1997) point out that this implies a very long binary orbital period ($P_{orb} > 12$ days) for 4U 1630−47 based on the calculations of van Paradijs (1996), which show that for a given P_{orb}, an X-ray binary will only be transient if $\dot{M}_c$ is smaller than a critical value.

8.2. *The Soft Component: Disk Temperatures and Luminosities*

In BHC energy spectra the presence of a strong soft component is a clear indication that we are seeing thermal emission from an optically thick accretion disk. The basic physical properties that determine the shape of the soft component include the mass accretion rate, the mass of the black hole, the inner radius of the disk, and the binary inclination. If we could assume a standard Shakura & Sunyaev (1973) accretion disk, at least some of these parameters might be directly measurable by modeling the shape of the soft component; however, in practice, other physical processes can be important and can complicate the interpretation of any derived parameters.

For 4U 1630−47, we detect the soft component over a wide range of luminosities and mass accretion rates. While we have modeled the soft component using the disk-blackbody (diskbb) model, the limitations of this model must be understood when interpreting the parameters. For example, the shape of the soft component can be drastically changed if the disk opacity is dominated by electron scattering rather than free-free absorption (Shimura & Takahara 1995). It has been shown that this effect can cause measurements of inner disk radii to be underestimated by a factor of 5 or more (Merloni et al. 2000). In addition, at high mass accretion rates, additional cooling mechanisms may cause a change from the thin Shakura & Sunyaev (1973) disk solution to a geometrically thicker "slim" disk (Abramowicz et al. 1988). This can lead to significantly more material, and thus emission, at small radii and can also produce a much flatter radial temperature profile ($T \propto R^{-p}$), with a change in p from 0.75 to ∼0.5 (Watarai et al. 2000). As a final example of the limitations of the diskbb model, it has been shown that assumptions about the boundary conditions at the inner radius of the disk can be important. The nonzero torque boundary condition assumed (basically for computational convenience) in the diskbb model can lead to an overestimation of the inner disk radius by a factor of more than 2 (Zimmerman et al. 2005).

Using observations of BHC systems XTE J1550−564, GRO J1655−40, and LMC X-3 and observations from previous

outbursts of 4U 1630−47, Kubota and coworkers show how effects of electron scattering and changes in the radial temperature profile can manifest themselves (Kubota & Makishima 2004; Kubota et al. 2001; Abe et al. 2004). Following these studies, we plot in Figure 8 the disk temperature ($kT_{\rm in}$) versus the bolometric disk luminosity ($L_{\rm disk}$) as derived from the 4U 1630−47 diskbb parameters. In deriving the luminosity, we assume a source distance of 10 kpc and a binary inclination of 60°, but these are highly uncertain. In Figure 8, we plot a solid line representing the slope of the $L_{\rm disk} \propto T_{\rm in}^4$ relationship that is expected for a standard Shakura & Sunyaev (1973) accretion disk with a constant inner radius ($R_{\rm in}$). A large number of mostly TD and IS points at disk luminosities between 3×10^{37} and 3×10^{38} ergs s^{-1} lie close to the line of constant $R_{\rm in}$, and for these observations, we may be seeing a standard disk with a relatively stable inner radius. However, many of the points also deviate from this line, and we identify three regions of deviation that likely have distinct explanations. First, several IS and hard state observations at the lower luminosities ($\lesssim 10^{38}$ ergs s^{-1}) show disk temperatures well below values that would be consistent with the line of constant $R_{\rm in}$. These are cases for which the overall source luminosity and presumably also the mass accretion rate are low, and these are likely cases in which the inner disk radius increases or at least in which the inner part of the disk is radiatively inefficient.

A second region of deviation includes TD, IS, and some of the SPL observations and occurs at the highest disk luminosities. This flattening of the $L_{\rm disk}$-$kT_{\rm in}$ relationship may be similar to what has been seen for XTE J1550−564 at high $L_{\rm disk}$ (Kubota & Makishima 2004). For XTE J1550−564, Kubota & Makishima (2004) showed that the relationship flattened to a slope close to $L_{\rm disk} \propto T_{\rm in}^2$, which, based on the work of Watarai et al. (2000), could be an indication of a transition to a slim disk. In 4U 1630−47, it is clear from Figure 8 that the source leaves the solid line above $\sim 2 \times 10^{38}$ ergs s^{-1}, and it appears that it may begin to follow the $T_{\rm in}^2$ relationship (Fig. 8, *dotted line*) for at least some luminosity range. However, the source appears to deviate from the $T_{\rm in}^2$ relationship at the very highest values of $L_{\rm disk}$, and it is possible that the source recovers the $T_{\rm in}^4$ relationship (Fig. 8, *dashed line*). Although the exact evolution is not completely clear, it is interesting that the observations at the highest values of $L_{\rm disk}$ that deviate from the solid line are also the observations for which the high-amplitude flaring occurred (see Fig. 8*b*). For transitions between the standard disk and the slim disk, theory predicts a limit cycle with a region of instability in between the two solutions. Thus, the flaring may be a consequence of the limit cycle, and this is a possibility we explore further below.

A third region of deviation from the line of constant $R_{\rm in}$ is contains mostly SPL observations for which $kT_{\rm in}$ is extremely high, including 15 observations with $kT_{\rm in}$ between 2.7 and 3.8 keV. Along with extremely high temperatures, the spectra exhibit very low values of $N_{\rm diskbb}$, in the range of 1.2–12.3, implying values of $R_{\rm in}$ that are unphysical. As an example, for a source distance of 10 kpc and a binary inclination of 60° (as assumed above), this range of normalizations indicates inner radii between 1.5 and 5.0 km; the former being an order of magnitude lower than the gravitational radius of a $10\,M_\odot$ black hole. Rather than extremely small inner disk radii, these high temperatures and luminosities are much more likely to be caused by spectral hardening due to the dominance of electron scattering in the inner region of the accretion disk.

Although the explanation for the high SPL state values of $kT_{\rm in}$ is very likely electron scattering, it is notable that the extremely high temperatures are seen for such a large number of observations. During its 1998 outburst, 4U 1630−47 entered

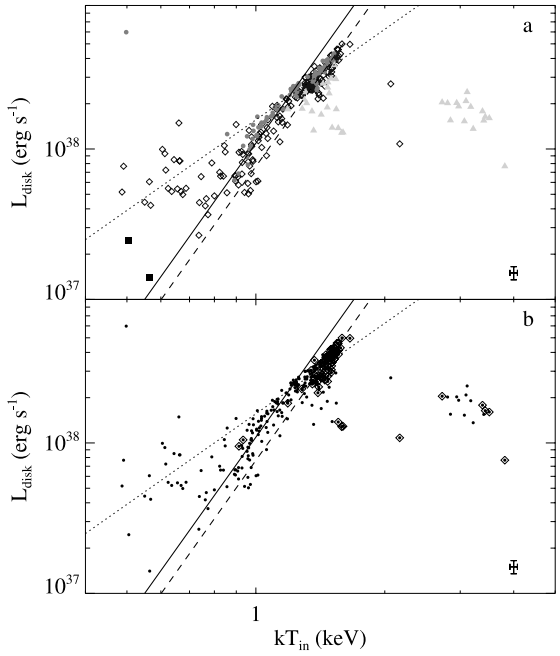

FIG. 8.—For each *RXTE* observation, (*a*) and (*b*) show $L_{\rm disk}$, the bolometric disk luminosity derived from the diskbb parameters assuming a distance of 10 kpc and a binary inclination of 60° vs. the inner disk temperature, $kT_{\rm in}$. The symbols in (*a*) represent the different spectral states (*triangles*: SPL; *open diamonds*: IS; *circles*: TD; *squares*: hard). Representative errors are shown in the bottom right-hand corner of the plots. In (*b*), the observations with high-amplitude variability are marked with diamonds. In (*a*) and (*b*), the solid and dashed lines are lines of constant $R_{\rm in}$ ($L_{\rm disk} \propto T_{\rm in}^4$), while the dotted line indicates a $L_{\rm disk} \propto T_{\rm in}^2$ relationship (see text for a discussion of the physical significance of these relationships). [*See the electronic edition of the Journal for a color version of this figure.*]

the SPL state, and fits to *RXTE* spectra gave $kT_{\rm in} = 1.6$–1.7 keV and $N_{\rm diskbb} = 46$ (Tomsick & Kaaret 2000; McClintock & Remillard 2003), which are considerably less extreme when compared to the 2002–2004 values. Very high values of $kT_{\rm in}$ have been seen for other accreting BHCs, although they are not common. For the 10 SPL spectra of accreting black holes studied by McClintock & Remillard (2003), only XTE J1550−564 and GRO J1655−40 have $kT_{\rm in} > 2.0$ keV. In 1998, the XTE J1550−564 spectrum showed $kT_{\rm in} = 3.3$ keV and $N_{\rm diskbb} = 7.8$ (Sobczak et al. 2000; McClintock & Remillard 2003), which are within the range of values we see for 4U 1630−47; however, for XTE J1550−564, this spectral shape was only seen for a single *RXTE* observation, which occurred during a remarkable 6 crab flare during which powerful superluminal jets were ejected (Hannikainen et al. 2001). For GRO J1655−40, another superluminal jet source, McClintock & Remillard (2003) give a SPL example where the disk-blackbody temperature is 2.2 keV, and this source showed temperatures of ~2 keV for a few other observations (Sobczak et al. 1999). However, for the other eight McClintock & Remillard (2003) SPL systems, $kT_{\rm in}$ is in the range 0.5–1.7 keV. Although not discussed in McClintock & Remillard (2003), very high disk-blackbody temperatures have also been seen for GRS 1915+105. For six of the 1996–1997 observations made when the GRS 1915+105 luminosity was very high, Muno et al. (1999) report values of $kT_{\rm in}$ in the range 2.6–4.8 keV. Based on the McClintock & Remillard (2003) definitions

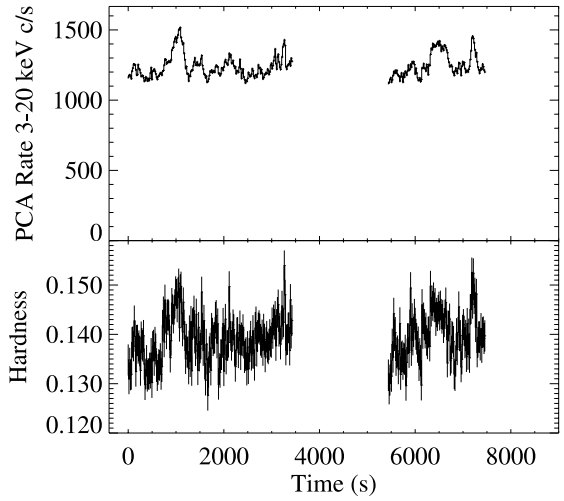

FIG. 9.—PCA light curve and 9–20/3–9 keV hardnesses vs. time with 16 s time bins, showing that flaring was also seen during one of the previous 4U 1630−47 outbursts. These data come from an *RXTE* observation made on 2000 November 18 (MJD 51,866.9) during the 2000–2001 outburst (observation ID 50120-01-04-00).

and the parameters reported in Muno et al. (1999), GRS 1915+105 was in the SPL state during these observations, but it should be noted that the properties of GRS 1915+105 make it difficult to classify its behaviors into the canonical spectral states (Reig et al. 2003).

Concerning 4U 1630−47, we can conclude that the extremely high disk-blackbody temperatures that we measure during the 2002–2004 outburst are rare and may be a new phenomenon for this source. When compared to other BHC sources, the 4U 1630−47 temperatures are only matched by XTE J1550−564 and GRS 1915+105. For 4U 1630−47 and XTE J1550−564, the high temperatures are only measured during observations for which the sources are at their very brightest, and for GRS 1915+105, the high temperatures occur when the source is at or close to its brightest level (Muno et al. 1999; Done et al. 2004). It is possible that these high temperatures are an indication of the highest accretion rates that are possible from these systems. As described above, the cause of these high temperatures may be electron scattering in the inner disk. This causes the observed temperature, $kT_{\rm in}$, to be higher than the effective temperature, $kT_{\rm eff}$, by a factor of f. For the highest values of $kT_{\rm in}$ that occur for 4U 1630−47 and GRS 1915+105 ($\sim$4 keV), f would need to be $\sim$3 to obtain the temperatures expected for a Shakura & Sunyaev (1973) disk around a 10 $M_{\odot}$ black hole. Although this is higher than the value of $f = 1.7$ theoretically expected for luminosities around 10% of the Eddington luminosity (Shimura & Takahara 1995), these authors also find that much higher values of f can occur for luminosities approaching the Eddington limit.

8.3. *Flaring Behavior*

Flaring from accreting BHC systems is seen on a wide range of timescales and may have various physical origins, including (but not limited to) accretion of clumps of matter or magnetically powered particle acceleration. While black hole variability is common, the flaring we see for 4U 1630−47, with amplitudes as high as $A_{\rm pp} = 1.0$ on timescales of 10–100 s, is extreme. The 4U 1630−47 amplitudes are comparable to the wild variability seen for GRS 1915+105 (e.g., Belloni et al. 2000); however, the 4U 1630−47 light curves do not show the distinctive repeating patterns seen for GRS 1915+105. Recently, high-amplitude variability at relatively long timescales has been seen for the black hole systems XTE J1859+226 (Casella et al. 2004) and H1743−322 (Miller et al. 2004; Homan et al. 2005). Although the flares in these systems are not as extreme as we see in 4U 1630−47, they may be related.

To determine if the flaring is unique to the 2002–2004 outburst from 4U 1630−47, we inspected the 16 s light curves for the nearly 300 pointed *RXTE* observations made during the four previous outbursts. Similar flaring only occurred for three of the observations, and these observations were made during the 2000–2001 outburst over the time period 2000 November 16–18. Figure 9 shows the 16 s light curve and hardness ratio versus time for the November 18 observation, and it is notable that the PCA count rates and hardness levels are similar to those seen during the 2002–2004 flaring observations. For the November 18 observation, we extracted a PCA plus HEXTE energy spectrum and fitted the spectrum as described above for the 2002–2004 observations. The spectral parameters are remarkably similar to those seen for the 2002–2004 flaring observations. The measured inner disk temperature is $kT_{\rm in} = 1.450^{+0.007}_{-0.010}$ keV and $L_{\rm disk} = 3.2\times10^{38}$ ergs s^{-1}, putting it in the same region as the other flaring observations in Figure 8. Also, $\Gamma = 2.59^{+0.04}_{-0.02}$ and $PLR = 0.43$, so the observation would be classified as IS.

For the observations with light curves shown in Figure 4*b* (70113-01-43-00) and Figure 4*c* (80117-01-13-02), we performed spectral fits to study the spectral evolution as a function of PCA count rate. In both cases, we divided the 16 s time-resolution data into different PCA count rate ranges. We separated the full range from minimum rate to maximum rate into four subranges of equal size and produced four PCA spectra. We did not use HEXTE for this analysis because the HEXTE rocking would complicate the analysis. We fitted the four spectra simultaneously, leaving the parameters for the iron features free, but requiring that they be the same for all four spectra. We did not include a high-energy cutoff, as a cutoff was not required for either observation. Originally, for both observations we allowed the column density to be different for the four spectra. For 70113-01-43-00, when we forced $N_{\rm H}$ to be the same for all four spectra, the quality of the fit changed from $\chi^2/\nu = 187.8/174$ to 189.4/177. For 80117-01-13-02, the change was from $\chi^2/\nu = 208.8/174$ to 209.7/177, indicating that the spectra are consistent with a constant $N_{\rm H}$ for both observations. Figure 10 shows the evolution of the spectral parameters with count rate. For both observations, clear trends are seen with $kT_{\rm in}$ increasing and Γ hardening with count rate. The results indicate that both the soft and hard components are affected. In light of the above standard/slim disk discussion above, perhaps the most important result is the clear and strong increase in $kT_{\rm in}$. The temperature increase is expected if the disk solution changes from a standard disk at low count rates to a slim disk at high count rates. This, along with the fact that the flaring may be a consequence of the zone of instability between the standard and slim disk solutions, make this explanation attractive. However, from the spectral evidence alone we cannot rule out that the disk temperature rises because of an increase in the mass accretion rate.

Although the spectral analysis indicates that changes in the accretion disk are important in producing the flaring, one might also ask whether the flaring behavior could have any physical connection to outflows or jets in the system. For example, in the case of the BHC H1743−322, from which spectrally hard flares were also recently detected, the flaring was accompanied by the

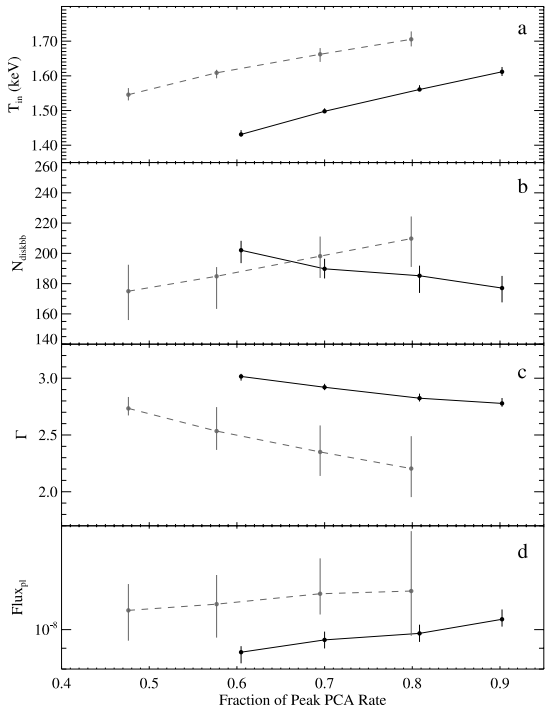

FIG. 10.—Spectral parameters measured for two of the flaring observations as a function of the PCA count rate divided by the peak PCA count rate. The points connected with dashed lines and the points connected with solid lines are for Observation IDs 70113-01-43-00 and 80117-01-13-02, respectively, and the light curves for these observations are shown in Fig. 4. (*a*) and (*b*) show the disk-blackbody parameters, while (*c*) and (*d*) show the power-law parameters, including the flux of the power-law component in units of ergs cm^{-2} s^{-1}. For both observations, the two clear trends are an increase in kT_{in} and a hardening of Γ with rate. [*See the electronic edition of the Journal for a color version of this figure.*]

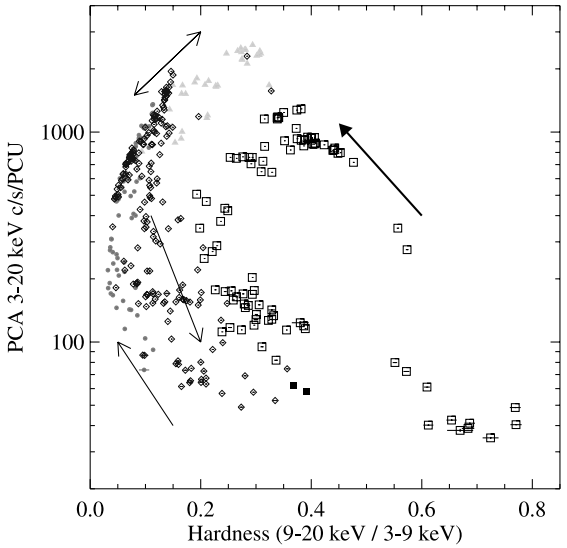

FIG. 11.—Hardness-intensity diagram showing the 3–20 keV PCA count rates vs. the 9–20/3–9 keV hardness ratio for the *RXTE* observations from the 2002–2004 and 1998 outbursts. The 1998 outburst is the only time when radio emission was detected from 4U 1630−47. The 2002–2004 observations are marked using the same symbols as described in the captions of Figs. 6 and 8. The 1998 observations are marked with open squares. The thick-lined arrow with the filled arrowhead shows the counter-clockwise motion seen for the 1998 outburst. For the 2002–2004 outburst, the pattern of the motion is complicated as shown by the thin-lined arrows with the open arrowheads. [*See the electronic edition of the Journal for a color version of this figure.*]

presence of blue-shifted absorption lines detected in spectra taken with the *Chandra X-Ray Observatory* (Miller et al. 2004). As these authors point out, the blue-shifting of the lines strongly suggest the presence of an outflow. In addition, Miller et al. (2004) find that the line strength varies during the ∼300 s variations seen in H1743−322, and Homan et al. (2005) suggest the possibility that if the outflow is energetic enough, it may be able to produce hard emission via up scattering. For 4U 1630−47, we do not have information about the presence of absorption lines, but as our spectral analysis indicates that the flaring is connected to the accretion disk, a link between the flaring and an outflow would represent an important disk/jet connection.

One might expect that an outflow energetic enough to lead to strong flares would also lead to a high level of radio emission. However, for H1743−322, the radio flux is actually lower during *Chandra* observations when the absorption lines are detected than when they are not detected (Miller et al. 2004). For 4U 1630−47, Hannikainen et al. (2002) observed the source in the radio band on three occasions (2002 September 16, 19, and 24) when the source was exhibiting flaring, and they obtained upper limits on the 3 and 6 cm radio flux of 95, 180, and 180 μJy, respectively, for the three dates. This does not preclude the presence of an outflow, but it does place limits on how strong any outflow might be. We note that several other radio observations of 4U 1630−47 occurred during various parts of the 2002–2004 outburst (including times of other flaring episodes and when the source was in the SPL state), but no radio detections were reported.

8.4. *A Connection between X-Ray Properties and Radio Jet Emission*

The absence of radio emission during the 2002–2004 outburst is also interesting when comparing the X-ray properties during this outburst to those seen during the 1998 outburst, which is the only time radio emission has been detected from 4U 1630−47. In Figure 11, for both the 2002–2004 and 1998 outbursts, we show the hardness, defined as the ratio of the 9–20 keV PCA count rate to the 3–9 keV PCA count rate, versus the source intensity (the 3–20 keV PCA count rate). For the 2002–2004 outburst, we divide the observations into the different spectral states. All of the 1998 observations are marked with open squares. There are potentially important differences between the X-ray properties for the two outbursts in light of the fact that radio jet emission was only present for the 1998 outburst. Although both outbursts have C-shaped hardness-intensity diagrams, as is relatively typical for BHC systems (Fender et al. 2004; Homan & Belloni 2005), the 1998 outburst is shifted in hardness, indicating that the spectrum was harder in 1998 than in 2002–2004. Also, as marked in Figure 11, 4U 1630−47 traveled through the hardness-intensity diagram in a counter-clockwise fashion during its 1998 outburst, while in 2002–2004, the source often moved in the clockwise direction. A related fact is that 4U 1630−47 entered a hard and bright state at the beginning of its 1998 outburst, whereas in 2002–2004 there is no evidence that this occurred. Although it is likely that 4U 1630−47 did enter a hard state during the 2002–2004 rise as this is the common pattern in BHC systems, the combination of the ASM and pointed *RXTE* observations (see Fig. 1) indicate that such a state would

have had to last a very short time and be limited to a time period when the source was dim.

These patterns are especially interesting in light of recent work on connections between black hole X-ray states, a source's position in the hardness-intensity diagram, and radio jet ejections (Homan & Belloni 2005; Corbel et al. 2004; Fender et al. 2004; Fender & Belloni 2004). A general pattern seen in a number of BHC outbursts is that the systems will evolve from the hard state to an intermediate state and then a radio ejection will occur during the subsequent transition to the SPL state (Corbel et al. 2004). Fender et al. (2004) use the hardness-intensity diagram to quantify this effect, and it should be noted that they follow Homan & Belloni (2005) by using somewhat different terminology, describing the transition from the IS to the SPL states as a transition from the "hard intermediate" state to the "soft intermediate" state. Fender et al. (2004) suggest that each BHC system has a threshold hardness and that major jet ejections are only produced when the source crosses this "jet line" from a high to a low hardness level. If this is the case, Figure 11 suggests that the jet line for 4U 1630−47 may be around a hardness of 0.4. Our results for 4U 1630−47 provide evidence in favor of the jet line concept; however, based on the behavior of 4U 1630−47, it is not entirely clear if the presence of a radio jet in 1998 occurred because the outburst was harder overall or if the source simply entering a bright hard state led to the jet ejection.

8.5. *Notes on Spectral States*

Our analysis of this data also provides a test of the quantitative spectral state definitions of McClintock & Remillard (2003). In some ways, these definitions are quite successful. For example, it is impressive that the only two observations with spectral parameters meeting the hard state requirements are also the only two we found with power spectra that include a strong band-limited noise component. Also, looking at the hardness-intensity diagram in Figure 11, these two observations lie at the extreme end of the C-shaped pattern. However, in other areas, the definitions appear to be less satisfactory. Although most of the observations labeled as SPL lie at the other end of the C-shaped pattern in the hardness-intensity diagram, the SPL observations have a extremely wide variety of properties. For example, for about half of the SPL observations $kT_{\rm in}$ lies in the 2.7–3.8 keV range, while the other half have temperatures <1.8 keV. We argue above that there are important physical differences between these two groups. Also, it is notable that over half of the observations made during the 2002–2004 outburst are put in the IS, meaning that a large fraction of the observations have X-ray properties that do not meet the requirements for any of the McClintock & Remillard (2003) states. Overall, while the McClintock & Remillard (2003) criteria appear to be useful for classifying the observations at the extremes of BHC behavior, it should be recognized that they, by themselves, do not provide a complete description of a BHC outburst due to significant variations in properties within states and the large fraction of IS observations.

9. SUMMARY AND CONCLUSIONS

Outstanding *RXTE* coverage of 4U 1630−47 during its 2002–2004 outburst has allowed us to study the detailed evolution of its X-ray spectral and timing properties over a period of more than 2 years. Historically, this outburst is among the longest and brightest seen in 36 years of observing 4U 1630−47, and it is very likely that it is the largest ever observed in terms of total mass transfer.

The X-ray properties during this outburst were also extreme, including 15 observations with very high disk-blackbody inner disk temperatures between 2.7 and 3.8 keV. The inner disk radii inferred from these fits are unphysically small, and it is likely that the high temperatures and small radii are caused by electron scattering. This explanation requires a spectral hardening factor of $f \sim 3$, implying a source luminosity that is considerably higher than 20% of the Eddington limit (Shimura & Takahara 1995), which is not unreasonable, as we measure 3–200 keV luminosities of 5×10^{38} ergs s^{-1} (d/10 kpc)^2.

At the highest disk luminosities, we detect a deviation from the $L_{\rm disk} \propto T_{\rm in}^4$ relationship (line of constant $R_{\rm in}$) seen at lower luminosities as well as high-amplitude flaring. The deviation may be a sign of a transition from a standard disk to a slim disk as suggested by Kubota and coworkers. The flaring behavior of 4U 1630−47 may be consistent with this interpretation, as a zone of instability is expected between the two disk solutions. Also, our spectral analysis of flaring observations, showing that $kT_{\rm in}$ is correlated with PCA count rate is consistent with a change from a standard disk to a slim disk.

Although sensitive radio observations occurred during the 2002–2004 outburst, no strong radio emission that would indicate the presence of radio jets was detected. This is interesting in light of the fact that the X-ray properties were very different during the 1998 outburst when radio jet emission was detected. Compared to the 2002–2004 outburst, the 1998 outburst hardness-intensity diagram was shifted to a higher hardness level, and in 1998 the source entered into a bright and hard state, while it did not in 2002–2004. These findings support the connections between radio jets and spectral states found by Corbel et al. (2004) and the jet line idea recently proposed by Fender et al. (2004).

Finally, our analysis of a large number of *RXTE* observations has provided a good test of the quantitative McClintock & Remillard (2003) spectral state definitions. While the hard state appears to be well defined, the spectral and timing properties of the observations selected as SPL are highly nonuniform. Also, it is notable that over half of the observations are put in the IS because they do not meet the requirements of any of the McClintock & Remillard (2003) definitions. The results show that 4U 1630−47 exhibits many properties not encompassed by the McClintock & Remillard (2003) definitions that are likely to be physically important.

J. A. T. would like to thank Tomaso Belloni, Ken Ebisawa, Joern Wilms, Rick Rothschild, and Katja Pottschmidt for useful discussions. J. A. T. thanks Jerome Rodriguez, Luigi Foschini, and Katja Pottschmidt for help with the *INTEGRAL* data analysis. J. A. T. acknowledges partial support from NASA grants NAG5-12703 and NNG04GA49G. We thank the referee, Tomaso Belloni, for a useful report that helped us to improve the manuscript.

APPENDIX A

As described in § 5 above, there are four *RXTE* observations for which we see strong positive residuals at high energies ($\gtrsim$30 keV) after fitting the PCA plus HEXTE spectra with our standard spectral model. These occur for observations made at the nominal pointing position, and during these observations IGR J16320–4751 was in the FOV, 0.°58 from 4U 1630−47 and the center of the FOV. Due to the high level of activity from IGR J16320–4751, its known hard spectrum, and its known strong variability (see

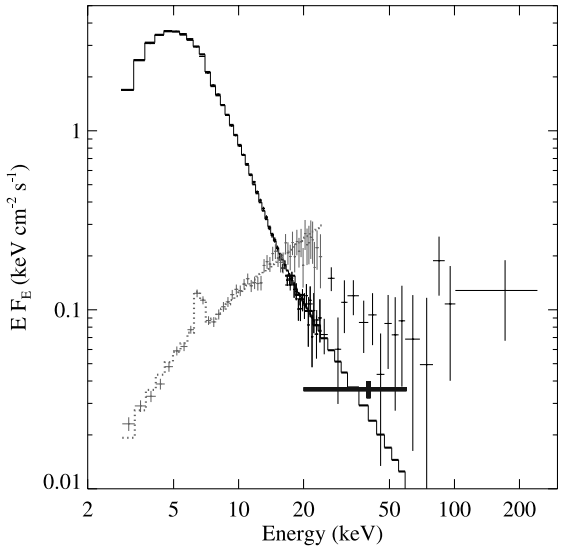

FIG. 12.—Energy spectra and flux measurements demonstrating that it is likely that the high-energy excess seen for some of the *RXTE* observations comes from the nearby source IGR J16320−4751. The spectrum (*solid histogram*) demonstrates the presence of a high-energy excess in the *RXTE* observation 70417-01-07-02. The thick, solid point (20−60 keV) represents the IGR J16320−4751 flux measured by *INTEGRAL* in 2003 February. The PCA spectrum (*dotted histogram*) comes from an *RXTE* observation pointed at 4U 1630−47 during a time in early 2000 (observation ID 40112-01-31-00) when 4U 1630−47 was in quiescence. [*See the electronic edition of the Journal for a color version of this figure.*]

Foschini et al. 2004 and references therein), we suspect that this source may be producing much of the high-energy emission that we see in the four observations with strong positive residuals. As a test, we compare the flux of the high-energy emission seen in one of these observations (observation ID 70417-01-07-02 taken on MJD 52,539.094) to measurements of IGR J16320−4751 taken at other times.

Our 2003 February *INTEGRAL* observation provides the cleanest measurement of the high-energy flux from IGR J16320−4751. From the Foschini et al. (2004) analysis of the ISGRI spectrum, the peak 20–60 keV flux during this observation is 2×10^{-10} ergs cm^{-2} s^{-1}, and the energy spectrum is consistent with a power law with Γ between 2.6 and 3.1. In Figure 12, we plot the *RXTE* spectrum for observation ID 70417-01-07-02 and the 20–60 keV flux measured by *INTEGRAL* ∼135 days later. We reduced the *INTEGRAL* flux appropriately to account for the *RXTE* collimator response at the location of IGR J16320−4751. Although the measured *INTEGRAL* flux at the time of the *INTEGRAL* observation is a factor of ∼2–3 too low to explain the strong residuals, long-term variability at higher levels than this has been reported from IGR J16320−4751 (Rodriguez et al. 2003), making it probable that the source gets bright enough to explain the strong residuals at times.

Further evidence that IGR J16320−4751 is sometimes bright enough to explain the strong residuals comes from *RXTE* observations made of 4U 1630−47 between 1999 December 25 and 2000 January 14. These observations were made when 4U 1630−47 was in quiescence in an effort to observe 4U 1630−47 as it turned on; however, it did not turn on during this sequence of 36 very short (typically 500 s) observations. During this sequence of observations (Observation IDs 40112-01-01-00 to 40112-01-36-00) the PCA count rate varied significantly between 8 and 26 counts s^{-1} PCU^{-1}. Although some of the detected emission is probably Galactic ridge emission, the high level of variability indicates that a compact source is producing much of the flux, and IGR J16320−4751 is the most likely candidate. In Figure 12, we show the PCA spectrum from the observation with the highest count rate, which was made on 2000 January 11 (Observation ID 40112-01-31-00). We note that no collimator response correction is necessary because the pointing position is approximately the same for this observation and for 70417-01-07-02. Another technical note is that although we attempted to also use HEXTE, with such short observations in a crowded field, this was not straightforward. Figure 12 indicates that the source was very hard $\Gamma\sim1.3$, and the extension of this spectrum is more than bright enough to explain the high-energy residuals, even if the spectrum breaks above 20 keV. In summary, this analysis provides strong evidence that IGR J16320−4751 is the cause of the high-energy residuals.

APPENDIX B

In addition to the four observations discussed in Appendix A, there are seven other observations for which it is likely that the high-energy emission is dominated by a source other than 4U 1630−47. The spectral parameters for these seven observations are shown in Figure 3, and these are the extremely hard observations with Γ in the 0.6–1.7 range. As discussed in § 5 above, four of the seven observations (70113-01-20-00, 70113-01-21-00, 70113-01-25-00, and 70113-01-28-00) occurred during a time period when IGR J16358−4726 was active according to reports from *INTEGRAL*, *Chandra*, and other *RXTE* observations (Revnivtsev 2003; Revnivtsev et al. 2003; Patel et al. 2004). As was the case for IGR J16320−4751, *INTEGRAL* provides the cleanest measurement of the high-energy flux due to its imaging capabilities, and Revnivtsev et al. (2003) report a 15–40 keV flux of 50 mcrab ($\sim2\times10^{-9}$ ergs cm^{-1} s^{-1}) and a 40–100 keV flux of 20 mcrab ($\sim3\times10^{-10}$ ergs cm^{-1} s^{-1}) on MJD 52,727.4. Our observation 70113-01-25-00 occurred on the

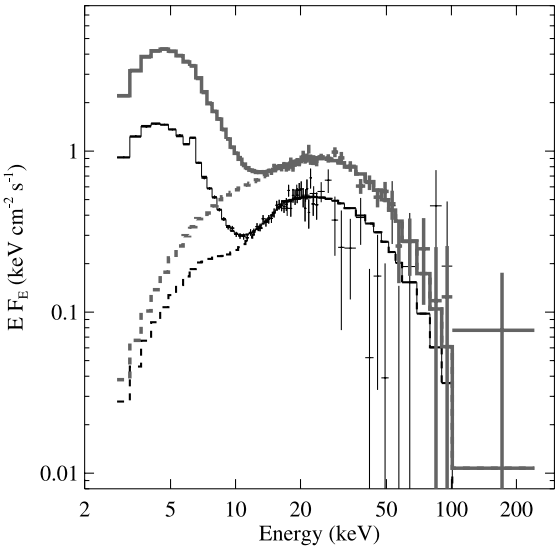

FIG. 13.—*RXTE* spectra demonstrating the high-energy contribution from other sources. The soft component comes from 4U 1630−47, but the emission above ∼15 keV is dominated by another source. The *RXTE* spectrum (*thin histogram*) from observation ID 70113-01-25-00 was taken on the same day as an *INTEGRAL* observation of the region, and we argue in the text that it is very likely that the high-energy flux comes from IGR J16358−4726. The *RXTE* spectrum (*thick histogram*) comes from much later (observation ID 90410-01-01-01 taken on MJD 53,114.410), but the two spectra are very similar, suggesting that they may be from the same source. [*See the electronic edition of the Journal for a color version of this figure.*]

same day (MJD 52,727.633), and after correcting the *RXTE* collimator response for the position of IGR J16358–4726, which is 0.°61 from the center of the offset 1 FOV, we measure 15–40 and 40–100 keV fluxes of 7.5×10^{-10} and 2.5×10^{-10} ergs cm^{-1} s^{-1}, respectively. The 15–40 keV flux is a factor of 2.7 lower than the *INTEGRAL* measurement, and the 40–100 keV is nearly the same in the two cases. Although the 15–40 keV flux measured by *RXTE* is somewhat low, the difference is consistent with a report by Revnivtsev et al. (2003) that the flux varies by a factor of ∼2 on a timescale of hours. More importantly, the flux comparison confirms our suspicion that the 4U 1630−47 spectrum is contaminated by the flux from IGR J16358–4726 at high energies.

Although it is clear that we are seeing emission from IGR J16358–4726 in four of the seven observations with low values of Γ, it is less clear whether the high-energy emission for the other three observations (80420-01-15-00 made on MJD 53,002.863; 80117-01-24-00 made on MJD 53,076.664; 90410-01-01-01 made on MJD 53,114.410) is also dominated by IGR J16358–4726, because no *INTEGRAL* detections of IGR J16358–4726 were reported and also because IGR J16320–4751 was in the *RXTE* FOV for these three observations. In Figure 13, we compare the PCA plus HEXTE spectrum from 90410-01-01-01 to that of 70113-01-25-00, where we know the emission is from IGR J16358–4726, and the spectra are remarkably similar. After correcting for the *RXTE* collimator response, the 15–40 and 40–100 keV fluxes for 90410-01-01-01 are about a factor of 1.8 higher than for 70113-01-25-00. Even though this may be considered an argument in favor of the emission being from IGR J16358–4726, IGR J16320–4751 is also known to produce very hard ($\Gamma < 1.0$) spectra at times (Tomsick et al. 2003).

REFERENCES

Abe, Y., Fukazawa, Y., & Kubota, A. 2004, Prog. Theor. Phys. Suppl., 155, 303
Abramowicz, M. A., Czerny, B., Lasota, J. P., & Szuszkiewicz, E. 1988, ApJ, 332, 646
Augusteijn, T., Kuulkers, E., & van Kerkwijk, M. H. 2001, A&A, 375, 447
Belloni, T., Klein-Wolt, M., Méndez, M., van der Klis, M., & van Paradijs, J. 2000, A&A, 355, 271
Casella, P., Belloni, T., Homan, J., & Stella, L. 2004, A&A, 426, 587
Chen, W., Shrader, C. R., & Livio, M. 1997, ApJ, 491, 312
Combi, J. A., Ribó, M., Mirabel, I. F., & Sugizaki, M. 2004, A&A, 422, 1031
Corbel, S., Fender, R. P., Tomsick, J. A., Tzioumis, A. K., & Tingay, S. 2004, ApJ, 617, 1272
Dieters, S. W., et al. 2000, ApJ, 538, 307
Done, C., Wardziński, G., & Gierliński, M. 2004, MNRAS, 349, 393
Ebisawa, K., et al. 1994, PASJ, 46, 375
Fender, R. P. 2001, MNRAS, 322, 31
Fender, R., & Belloni, T. 2004, ARA&A, 42, 317
Fender, R. P., Belloni, T. M., & Gallo, E. 2004, MNRAS, 355, 1105
Foschini, L., Tomsick, J., Rodriguez, J., Walter, R., Goldwurm, A., Corbel, S., & Kaaret, P. 2004, in The INTEGRAL Universe, ed. V. Schoenfelder, G. Lichti, & C. Winkler (ESA SP-552; Noordwijk: ESA), 247
Garcia, M. R., McClintock, J. E., Narayan, R., Callanan, P., Barret, D., & Murray, S. S. 2001, ApJ, 553, L47
Goldwurm, A., et al. 2003, A&A, 411, L223
Hannikainen, D., Campbell-Wilson, D., Hunstead, R., McIntyre, V., Lovell, J., Reynolds, J., Tzioumis, T., & Wu, K. 2001, Ap&SS, 276, 45
Hannikainen, D., Sault, B., Kuulkers, E., Wu, K., Jones, P., & Hunstead, R. 2002, Astron. Telegram, 108
Hjellming, R. M., et al. 1999, ApJ, 514, 383
Homan, J., & Belloni, T. 2005, in From X-ray Binaries to Quasars: Black Hole Accretion on All Mass Scales, ed. T. J. Maccarone, R. P. Fender, & L. C. Ho (Dordrecht: Kluwer), in press (astro-ph/0412597)
Homan, J., Miller, J. M., Wijnands, R., van der Klis, M., Belloni, T., Steeghs, D., & Lewin, W. H. G. 2005, ApJ, 623, 383
Homan, J., & Wijnands, R. 2002, Astron. Telegram, 109
Homan, J., Wijnands, R., van der Klis, M., Belloni, T., van Paradijs, J., Klein-Wolt, M., Fender, R., & Méndez, M. 2001, ApJS, 132, 377
Kubota, A., & Makishima, K. 2004, ApJ, 601, 428
Kubota, A., Makishima, K., & Ebisawa, K. 2001, ApJ, 560, L147
Kuulkers, E., Parmar, A. N., Kitamoto, S., Cominsky, L. R., & Sood, R. K. 1997, MNRAS, 291, 81
Kuulkers, E., Wijnands, R., Belloni, T., Mendez, M., van der Klis, M., & van Paradijs, J. 1998, ApJ, 494, 753
Makishima, K., Maejima, Y., Mitsuda, K., Bradt, H. V., Remillard, R. A., Tuohy, I. R., Hoshi, R., & Nakagawa, M. 1986, ApJ, 308, 635

McClintock, J., & Remillard, R. 2003, in Compact Stellar X-Ray Sources, ed. W. H. G. Lewin & M. van der Klis (Cambridge: Cambridge Univ. Press), preprint (astro-ph/0306213)
Merloni, A., Fabian, A. C., & Ross, R. R. 2000, MNRAS, 313, 193
Miller, J. M., et al. 2004, ApJ, submitted (astro-ph/0406272)
Muno, M. P., Morgan, E. H., & Remillard, R. A. 1999, ApJ, 527, 321
Oosterbroek, T., Parmar, A. N., Kuulkers, E., Belloni, T., van der Klis, M., Frontera, F., & Santangelo, A. 1998, A&A, 340, 431
Parmar, A. N., Williams, O. R., Kuulkers, E., Angelini, L., & White, N. E. 1997, A&A, 319, 855
Patel, S. K., et al. 2004, ApJ, 602, L45
Reig, P., Belloni, T., & van der Klis, M. 2003, A&A, 412, 229
Remillard, R. A., Sobczak, G. J., Muno, M. P., & McClintock, J. E. 2002, ApJ, 564, 962
Revnivtsev, M. G. 2003, Astron. Lett., 29, 644
Revnivtsev, M., Tuerler, M., Del Santo, M., Westergaard, N. J., Gehrels, N., & Winkler, C. 2003, IAU Circ., 8097, 2
Rodriguez, J., Tomsick, J. A., Foschini, L., Walter, R., Goldwurm, A., Corbel, S., & Kaaret, P. 2003, A&A, 407, L41
Shakura, N. I., & Sunyaev, R. A. 1973, A&A, 24, 337
Shimura, T., & Takahara, F. 1995, ApJ, 445, 780
Sobczak, G. J., McClintock, J. E., Remillard, R. A., Cui, W., Levine, A. M., Morgan, E. H., Orosz, J. A., & Bailyn, C. D. 2000, ApJ, 531, 537
Sobczak, G. J., McClintock, J. E., Remillard, R. A., Levine, A. M., Morgan, E. H., Bailyn, C. D., & Orosz, J. A. 1999, ApJ, 517, L121
Tomsick, J. A. 2003, Astron. Telegram, 161
———. 2004a, Astron. Telegram, 247
———. 2004b, in AIP Conf. Proc. 714, X-Ray Timing 2003: Rossi and Beyond, ed. P. Kaaret, F. K. Lamb, & J. H. Swank (Melville: AIP), 71
Tomsick, J. A., Corbel, S., & Kaaret, P. 2001, ApJ, 563, 229
Tomsick, J. A., & Kaaret, P. 2000, ApJ, 537, 448
Tomsick, J. A., Lapshov, I., & Kaaret, P. 1998, ApJ, 494, 747
Tomsick, J. A., Lingenfelter, R., Corbel, S., Goldwurm, A., & Kaaret, P. 2004a, Astron. Telegram, 224
———. 2004b, in Proc. 5th *INTEGRAL* Workshop, ed. V. Schoenfelder, G. Lichti, & C. Winkler (ESA SP-552; Noordwijk: ESA), 413
Tomsick, J. A., Lingenfelter, R., Walter, R., Rodriguez, J., Goldwurm, A., Corbel, S., & Kaaret, P. 2003, IAU Circ., 8076, 1
Trudolyubov, S. P., Borozdin, K. N., & Priedhorsky, W. C. 2001, MNRAS, 322, 309
van Paradijs, J. 1996, ApJ, 464, L139
Watarai, K., Fukue, J., Takeuchi, M., & Mineshige, S. 2000, PASJ, 52, 133
Wijnands, R., Remillard, R., & Miller, J. M. 2002, Astron. Telegram, 106
Winkler, C., et al. 2003, A&A, 411, L1
Zdziarski, A. A., Gierlinski, M., Gondek, D., & Magdziarz, P. 1996, A&AS, 120, 553
Zimmerman, E. R., Narayan, R., McClintock, J. E., & Miller, J. M. 2005, ApJ, 618, 832

Chapitre 4
Interactions des jets avec le milieu interstellaire

Le plus timide bourgeon est la preuve qu'il n'y a pas de mort réelle.
— William Blake

4.1 Introduction

Après une présentation des jets compacts, pendant l'état spectral dur (chapitre 2), et une description des éjections impulsives associées aux transitions d'état (section 3.4), il fallait s'attendre à ce que ces formes diverses de jets aient un impact sur le milieu environnant à un moment donné. Il faut d'ailleurs noter qu'historiquement, le terme microquasar ne provient pas des éjections apparemment superluminiques de GRS 1915+105 (Mirabel & Rodriguez 1994), mais plutôt de la découverte de lobes radio – ou jets larges – autour des sources 1E 1740.7−2942 ou GRS 1758−258 (Mirabel et al. 1992; Martí et al. 2002). Ces lobes résulteraient de l'impact du plasma relativiste – jets compacts ou éjections impulsives – de ces sources sur le milieu interstellaire (ISM).

Peut être que l'image la plus spectaculaire de telles interactions est celle de la nébuleuse radio W50 (Dubner et al. 1998) englobant la source particulière SS 433 (Figure 4.1). En effet, cette nébuleuse est déformée de chaque coté par l'impact des jets en provenance de SS 433. On peut, de plus, y déceler le mouvement de précession de ces jets. À ce niveau, on pourrait aussi citer la nébuleuse radio de Cir X−1 (Stewart et al. 1993) qui fut une des sources radio les plus brillantes des années 70. Au vu des caractéristiques du jet associé (Fender et al. 2004a), il serait possible d'imaginer, que nous possédions déjà, avec cette source, l'exemple du premier microblazar Galactique... Mais il s'agit là d'une autre histoire qui pourrait faire partie des perspectives futures.

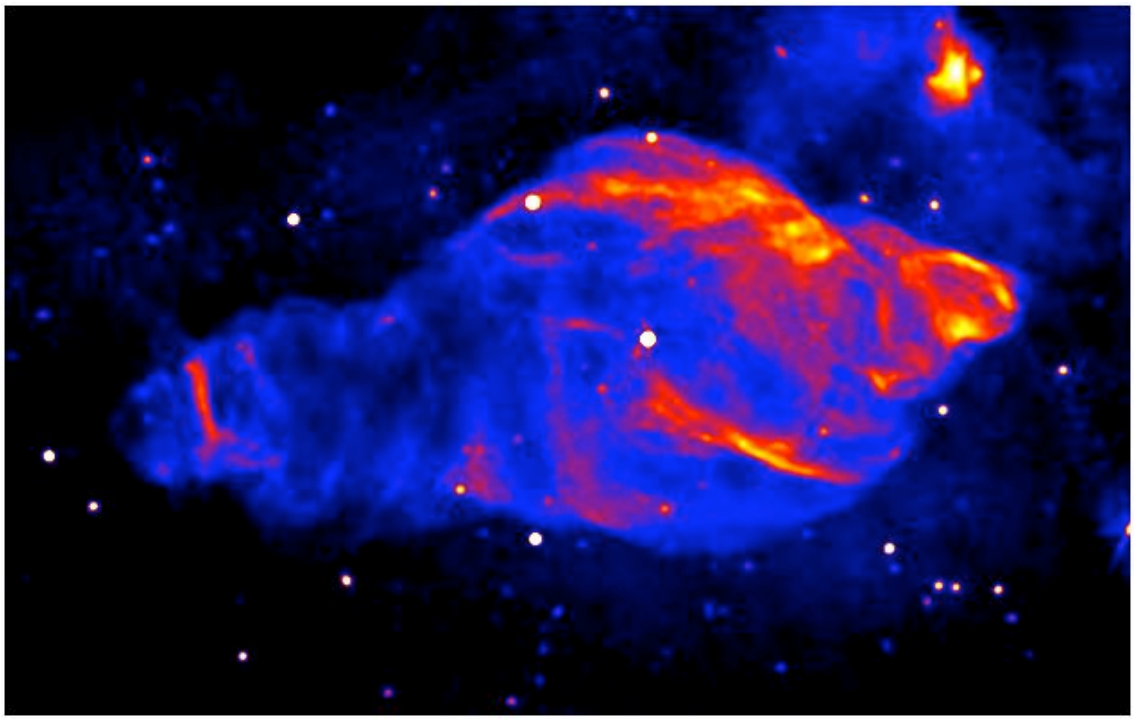

FIG. 4.1 – La nébuleuse radio W50 autour de SS 433 est déformée par l'impact récurrent des jets de l'objet compact depuis des milliers d'années. Figure extraite de Dubner et al. (1998).

4.2 XTE J1550−564 : un accélérateur cosmique

XTE J1550−564 est une source X transitoire découverte originellement en septembre 1998 par *RXTE/ASM* (Smith 1998). Peu de temps après, elle eut un énorme sursaut X bref – un jour – dont l'intensité atteignit au moins huit fois celle de la nébuleuse du Crabe (Sobczak et al. 2000; Homan et al. 2001). À cette occasion furent observés – par interférométrie à très longue ligne de base $\sim$ VLBI – des jets relativistes ayant une vitesse apparente au moins deux fois supérieure à celle de la lumière (Hannikainen et al. 2001).

La masse de l'objet compact au sein de XTE J1550−564 est de 10.5 ± 1.0 $M_\odot$, indiquant qu'il s'agit d'un trou noir. Ce système se trouve à une distance probable de 5.3 kpc (Orosz et al. 2002). Après ce premier sursaut en 1998-99, il est entré de nouveau en éruption en 2000 (e.g. Corbel et al. 2001b; Rodriguez et al. 2003, 2004), 2001, 2002 et 2003 (Corbel et al. 2006).

Lors de sa réactivation en 2002, nous constatons (Corbel et al. 2002a) la réapparition du jet compact (c.f. chapitre 2) associé à l'état dur. À cela s'ajoute la présence (Figure 4.2) d'une autre source radio 22″ à l'ouest du trou noir (Corbel et al. 2002a) et ayant le même angle de position que celui de l'éjection transitoire – le jet VLBI – de 1998 (Hannikainen et al. 2001). En réanalysant les archives de nos observations passées – e.g. le sursaut X de 2000 –, nous constatons la présence quasi-symétrique d'une autre source radio à l'est de XTE J1550−564 (Figure 4.2) et alignée avec l'axe du jet VLBI de septembre 1998.

L'analyse des données d'archive *Chandra* nous montre que la source radio à l'Est est associée (Figure 4.3) avec une source X se déplaçant sur le plan du ciel (Corbel et al. 2002b). Au vu des résultats obtenus avec les archives radio et X, nous avons obtenu du temps avec le directeur de *Chandra* en 2002. Cela a conduit à la découverte d'une contrepartie X associée à

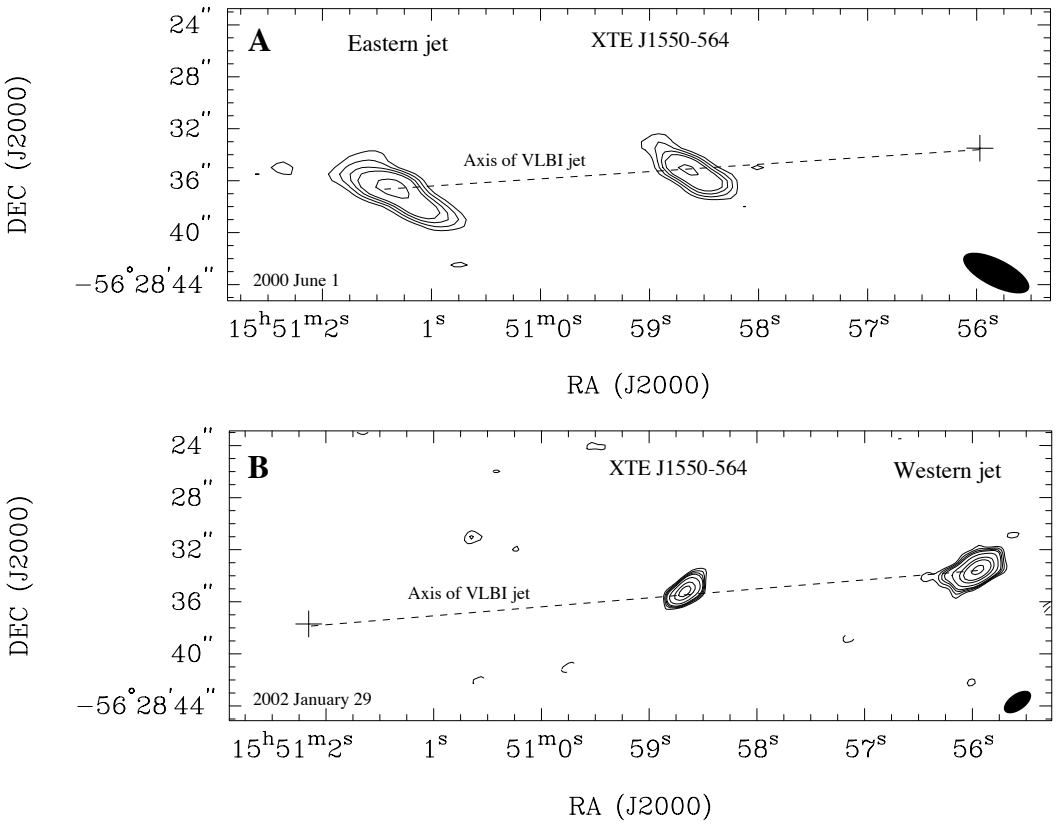

FIG. 4.2 – Images radio de la région autour de XTE J1550−564. A : le 1er juin 2000 à 4.8 GHz, B : le 29 janvier 2002 à 8.6 GHz. La ligne pointillée indique l'axe du jet transitoire observé par interférométrie à très longue base (VLBI) en septembre 1998 par Hannikainen et al. 2001. Figure extraite de Corbel et al. (2002b).

la source radio à l'ouest de XTE J1550−564 (Corbel et al. 2002b).

Des observations optiques VLT furent aussi obtenues le 11 mars 2002 mais ne permirent pas de détecter les contreparties optiques de ces sources. Néanmoins, le spectre (Figure 4.4) de la source à l'ouest de XTE J1550−564 est compatible avec une loi de puissance de la radio jusqu'aux X et d'indice spectral de -0.660 $\pm$ 0.005 (Corbel et al. 2002b). Les morphologies radio et X sont en excellent accord. L'alignement de ces nouvelles sources X et radio avec l'axe du jet VLBI de septembre 1998 favoriserait donc une origine commune.

Nous pensons que ces sources représentent l'interaction des éjecta de septembre 1998 avec le milieu interstellaire en formant des lobes, de manière similaire aux noyaux actifs de galaxie. Le mouvement propre du lobe Est étant plus élevé, cela indiquerait qu'il est lié au jet pointant vers l'observateur. La morphologie des lobes, et surtout la distribution spectrale énergétique (Figure 4.4), indiquent que le rayonnement de ces lobes est du à l'émission synchrotron de particules énergétiques. Un calcul d'équipartition indique que le champ magnétique serait de l'ordre de 0.3 mG, mais surtout que le facteur de Lorentz des électrons rayonnant en X serait d'environs 2×10^7, équivalent à une énergie de $\sim$ 10 TeV.

C'est la première fois que de tels jets énergétiques sont observés dans un trou noir galactique. À la distance de XTE J1550−564, ces lobes auraient une longueur – projetée sur le plan du ciel – de 0.6 et 0.8 pc. Cette taille est intermédiaire entre la dimension caractéristique des éjections transitoires – type GRS 1915+105 – et celle des lobes radio de microquasars – comme 1E 1740.7−2942. Ces lobes radio pourraient donc résulter de l'accumulation d'impacts

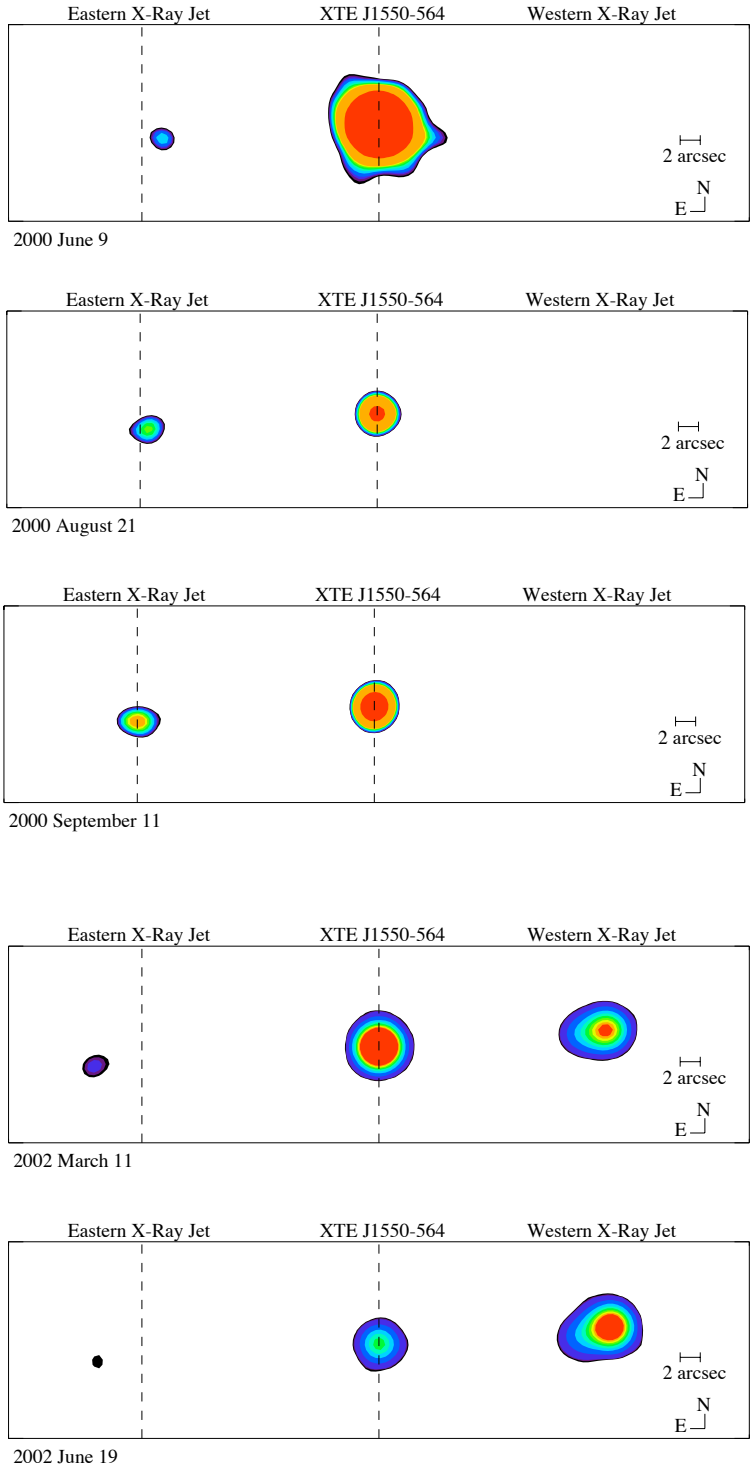

FIG. 4.3 – Séquence d'observations par *Chandra* dans la bande 0.3 – 8 keV des jets larges de XTE J1550−564 de 2000 à 2002. Les images CCD originelles de *Chandra* ont été convoluées par une gaussienne à deux dimensions ayant une largeur de deux pixels. Figure adaptée de Corbel et al. (2002b).

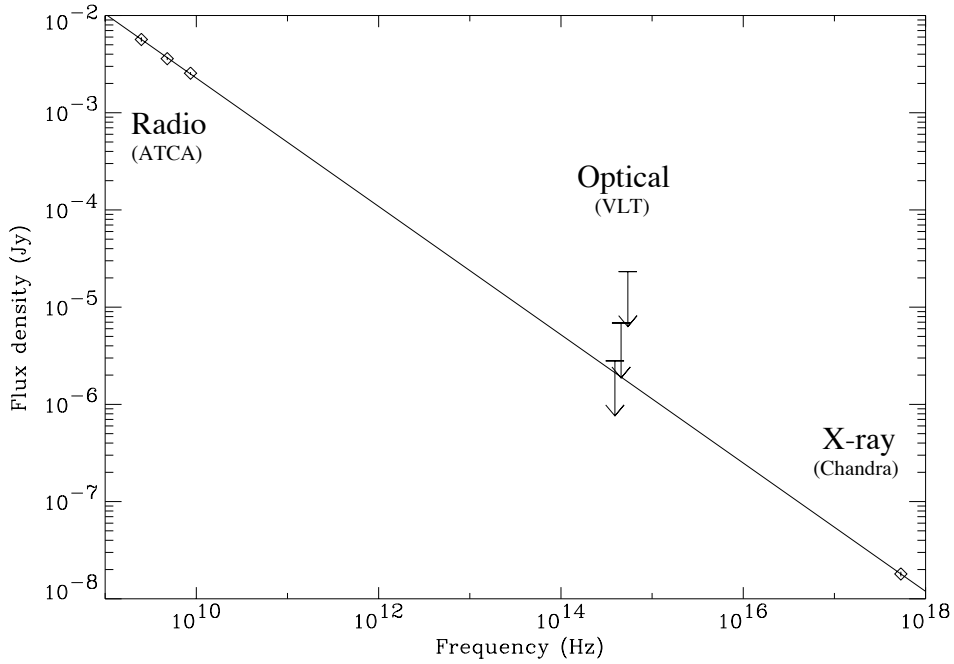

FIG. 4.4 – Distribution spectrale énergétique du jet Ouest de XTE J1550−564 vers le 11 mars 2002. Figure extraite de Corbel et al. (2002b).

d'évènements impulsifs au fil du temps.

La présence d'électrons si énergétiques nécessite très probablement des collisions très fortes. Ces chocs pourraient résulter d'instabilités internes dans les jets (Hardee 2000), voire de collisions entre différentes bulles de plasma éjectés – ou de flots à vitesse variable – lors du sursaut bref de septembre 1998 (Rees & Meszaros 1994; Kaiser et al. 2000).

Néanmoins, il est plus probable que l'accélération de particules se fasse lors des collisions avec le milieu interstellaire. En effet, une ou – plus probablement – plusieurs bulles de plasma ont été éjectées le 20 septembre 1998 (Hannikainen et al. 2001). Elles ont continué à se propager dans le MIS, tout en ayant un rayonnement radio s'affaiblissant à cause de leur expansion adiabatique. Leur "voyage" dans le MIS s'est fait incognito, jusqu'au moment où elles sont entrées en collision avec des phases plus denses du MIS, phases associées au "rallumage" des jets.

Le mouvement propre des deux lobes est détecté et indique pour la première fois une décélération graduelle au sein de jets relativistes (Corbel & Fender 2002; Tomsick et al. 2003b; Kaaret et al. 2003b). La décélération des éjecta lors de la rencontre avec le MIS entraîne une perte d'énergie cinétique d'ensemble, compatible avec le gain en énergie interne des particules rayonnantes. Des détails plus précis – mouvement propre, morphologie, flux – pourront être trouvés dans les publications associées à ce chapitre (Corbel & Fender 2002; Tomsick et al. 2003b; Kaaret et al. 2003b).

4.3 Un jet large transitoire au sein du système GX 339−4

Comme nous l'avions vu lors des chapitres 2 et 3, GX 339−4 a été une source essentielle pour comprendre la nature du couplage accrétion-éjection au sein des trous noirs. On peut

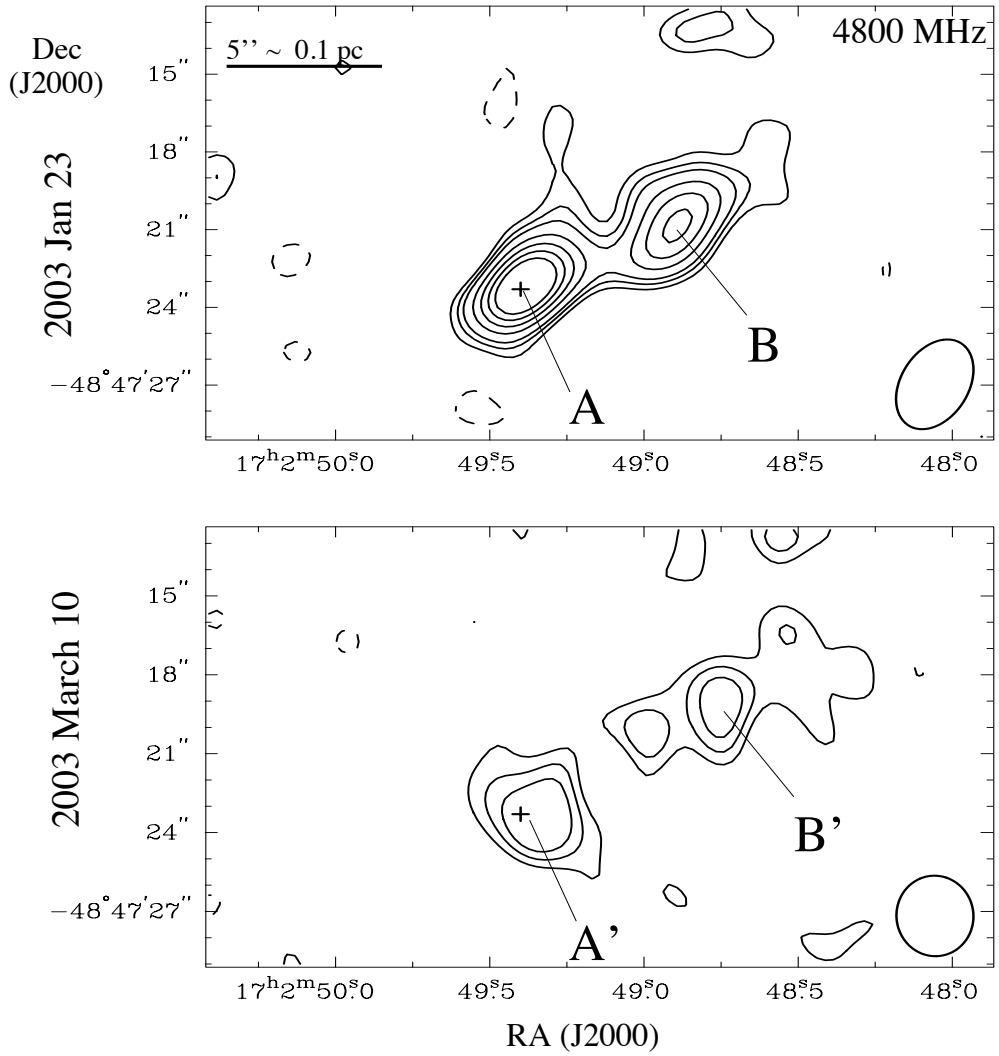

FIG. 4.5 – Images ATCA à 4.8 GHz de GX 339−4 le 23 janvier 2003 (haut) et le 10 mars 2003 (bas). Figure extraite de Gallo et al. (2004).

citer la mise en évidence des jets compacts ou l'unification des propriétés des jets lors des différents états spectraux. Lors de sa réactivation en 2002 (section 3.4), nous avons assisté en direct à une phase d'éjection massive de plasma (Figure 3.8) lors d'une transition d'état. Par la suite, les données radio montrent plusieurs phases d'éjections mineures. Dès fin août 2002, nous remarquons (Gallo et al. 2004) que la position de la source radio, associée à GX 339−4, n'est plus compatible avec celle du trou noir. Les observations de janvier à mai 2003 montrent le développement d'un jet large (Figure 4.5) dont l'intensité radio décroît très rapidement, pour devenir indétectable en mai 2003. Les observations *Chandra* réalisées – trop tard – en octobre 2003 ne permirent pas de détecter de contrepartie X aux jets radio.

Les cartes radio sont compatibles avec la présence de deux coeurs principaux dans le jet, avec un spectre radio très pentu – indice spectral de –1. En mars 2003, ce jet large s'étire sur plus de 12″, ce qui à la distance minimale – 4 kpc – de GX 339−4 correspondrait à une longueur – projetée sur le ciel – d'au moins 0.23 pc. En faisant l'hypothèse raisonnable que le moment de l'éjection correspond à la période du sursaut massif du 14 mai 2002 (Figure 3.8), nous en déduisons une vitesse apparente superluminique d'au moins 1.3 c – voire 1.8 c.

La composante la plus proche du trou noir – A et A' – est toujours plus brillante que celle – B et B' – qui est éloignée. Une fois que ces composantes apparaissent, leurs émissions diminuent au fil du temps, tandis que leurs positions ne semblent pas varier – contrairement à XTE J1550−564, mais l'échelle de temps est aussi plus courte. Contrairement aux éjections de GRS 1915+105 (Rodríguez & Mirabel 1999; Fender et al. 1999a) pour lesquelles les observations sont compatibles avec un mouvement balistique de bulles de plasma, le jet large de GX 339−4 pourrait s'expliquer par la propagation d'onde de choc à l'intérieur du jet ou/et par l'interaction d'un flot relativiste invisible avec le milieu environnant.

4.4 Découverte de lobes X transitoires autour de H 1743−322

Suite à la découverte des jets en X – et radio – pour XTE J1550−564 et en radio pour GX 339−4, mais surtout aussi à cause de la décroissance rapide de l'émission radio des lobes de GX 339−4, nous avons mis en place avec ATCA un programme nous permettant d'observer n'importe quelle source ayant été active dans le passé. Nous espérions ainsi pouvoir détecter toute nouvelle source apparaissant dans le champ de vue d'un trou noir, et pouvant résulter de l'interaction d'un éjecta passé avec le milieu interstellaire. Plusieurs transitoires ont été observées depuis 2003 et nous allons abordé ici le cas particulièrement intéressant de H 1743−322
.

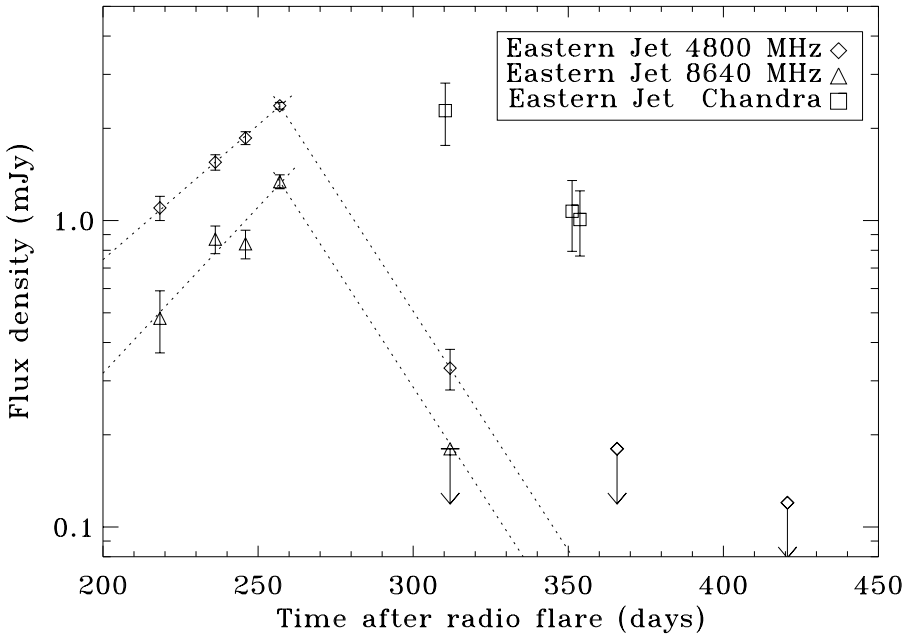

FIG. 4.6 – Courbes de lumière à 4.8 et 8.6 GHz du lobe Est de H 1743−322 . Figure extraite de Corbel et al. (2005).

H 1743−322, initialement découvert en 1977, est entré de nouveau en éruption en mars 2003 (Revnivtsev et al. 2003). Un important sursaut radio fut détecté par le VLA, ce qui traduisait très probablement une éjection massive de plasma relativiste (Rupen et al. 2003). Le sursaut X s'est terminé vers la fin novembre 2003, période à partir de laquelle nous avons détecté une nouvelle source radio à 4.6″ à l'est de H 1743−322. L'intensité radio de cette

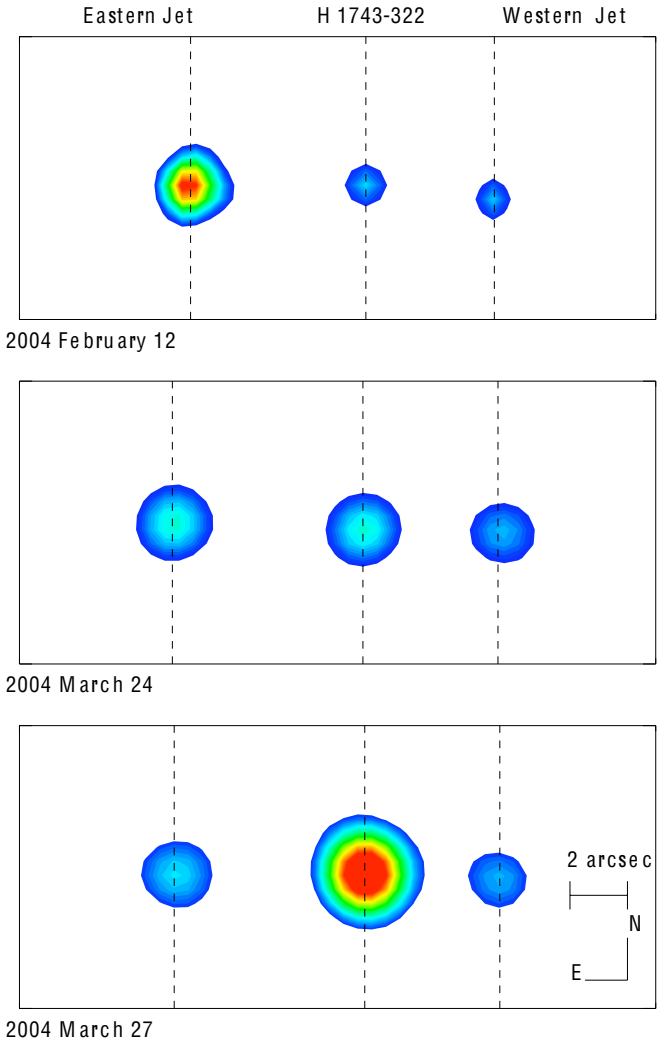

FIG. 4.7 – Séquence d'observations par *Chandra* dans la bande 0.3 – 8 keV des jets larges de H 1743−322 en 2004. Les images CCD originelles de *Chandra* ont été convoluées par une gaussienne à deux dimensions ayant une largeur de deux pixels. Figure extraite de Corbel et al. (2005).

source (Figure 4.6), tout comme la distance angulaire au trou noir, ont augmenté jusqu'à fin décembre 2003, période à laquelle nous avons déclenché nos observations *Chandra*. À cause de contraintes solaires, elles n'ont pu avoir lieu qu'en février et juin 2004. Il est à noter qu'à ce moment là l'émission radio s'est mise à décroître très rapidement. On notera aussi la présence en février 2004 d'une autre source radio, de faible intensité, localisée de façon symétrique à l'ouest de H 1743−322.

Comme nous l'espérions, nous détectons une contrepartie X à chacune des sources radio (Figure 4.7), ainsi que le trou noir H 1743−322 en quiescence. Les trois sources X sont alignées, ce qui semble favoriser une connexion physique entres elles. De façon similaire à XTE J1550−564, nous pouvons interpréter les deux sources X/radio se déplaçant comme étant le résultat de l'impact des éjecta de mars 2003 (Rupen et al. 2003) sur le milieu interstellaire. Le mouvement propre de ces lobes (Figure 4.8) implique la présence d'un flot de particules dans H 1743−322 demeurant relativiste au moins un an après l'évènement déclencheur (Corbel

et al. 2005).

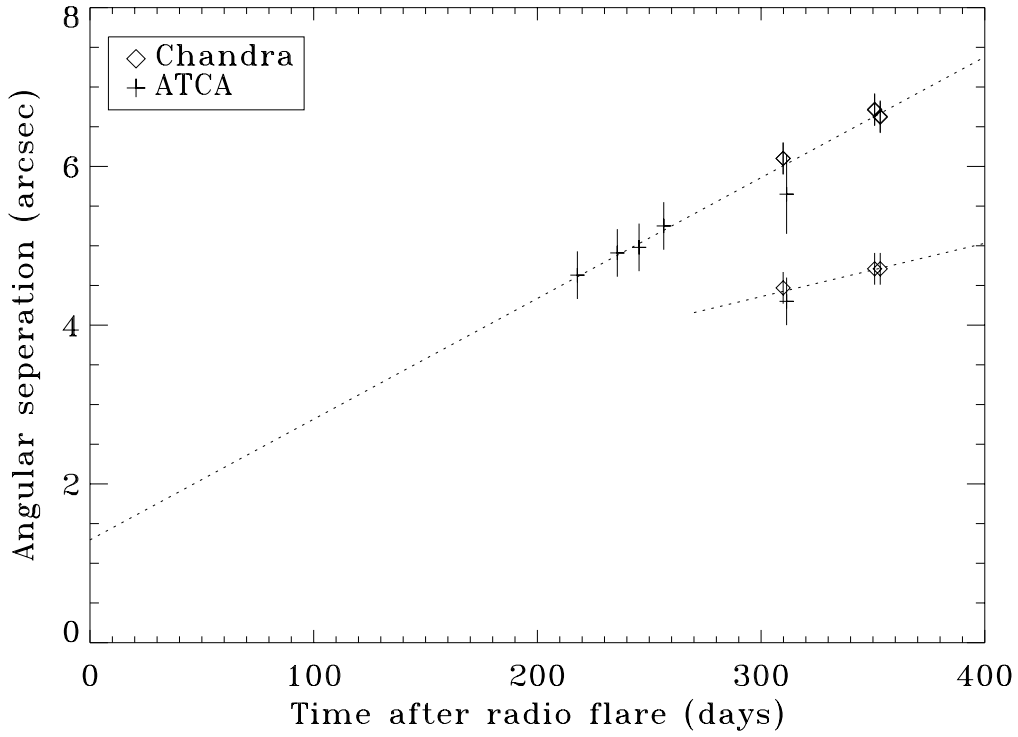

FIG. 4.8 – Séparation angulaire entre H 1743−322 et ses lobes en fonction du temps écoulé depuis le sursaut radio d'avril 2003. Figure extraite de Corbel et al. (2005).

Le spectre X est compatible avec une extension de la loi de puissance – d'indice spectral de –0.64 ± 0.02 – provenant du domaine radio. Le mécanisme physique favorisé pour expliquer l'émission de ces deux lobes est le rayonnement synchrotron de particules énergétiques. Les calculs, supposant l'équipartition, donnent des paramètres similaires à XTE J1550−564, c'est-à-dire des électrons ayant des facteurs de Lorentz de l'ordre de 2×10^7 et donc une énergie supérieure au TeV.

On notera que pendant la phase "d'allumage" des lobes, le spectre radio était très pentu avec un indice spectral moyen de $\sim$ –1. Cela traduit donc une propriété intrinsèque du processus accélérant les particules du jet. On peut penser que la phase d'allumage des lobes traduirait la propagation d'un jet à travers un milieu dense, tandis que la phase de décroissance serait liée au mouvement des lobes formés dans un milieu moins dense et cela sans nouvelle accélération des particules (Corbel et al. 2005).

4.5 Évolution des jets X persistants de 4U 1755−33

Peu de temps après notre découverte de l'émission X des jets relativistes de XTE J1550−564, Angelini & White (2003) ont mis en évidence la présence d'un jet large (Figure 4.9) en X avec *XMM–Newton* au sein du système 4U 1755−33 . Il s'agit d'une structure linéaire s'étendant sur plus de 3′ de part et d'autre de la position de cette source. Pour une distance de 4 à 9 kpc, cette extension angulaire correspond à une taille apparente de 3 à 8 pc.

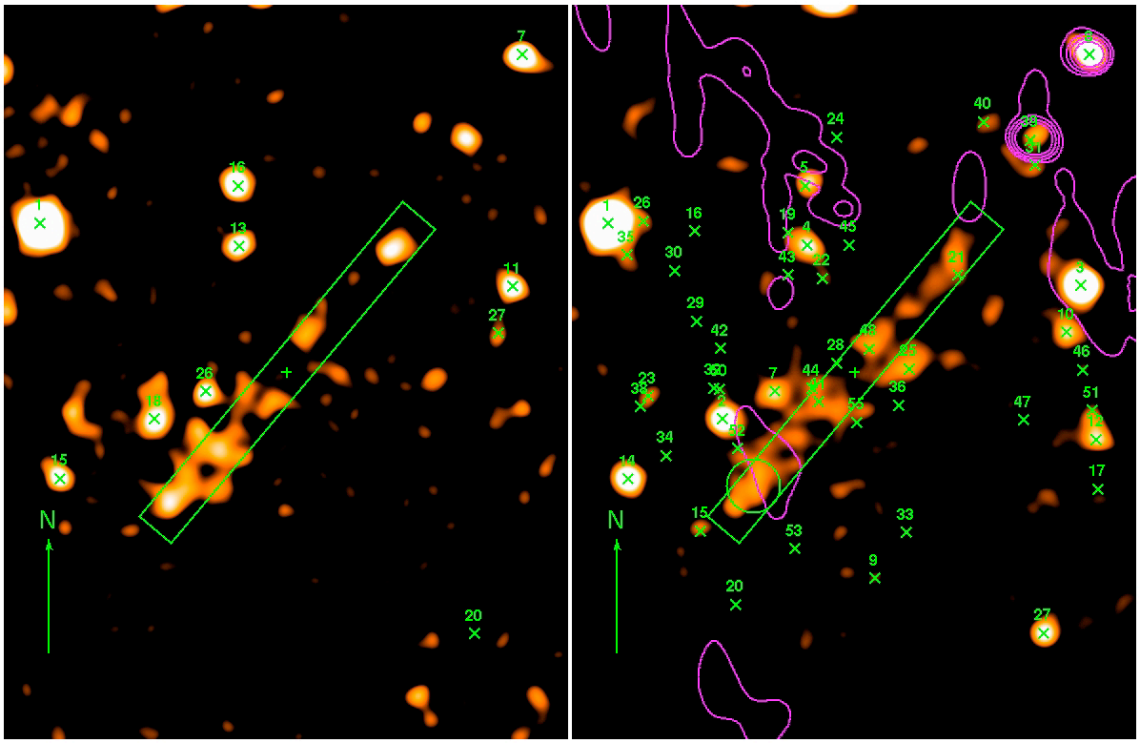

FIG. 4.9 – Observations *XMM–Newton* de 4U 1755−33 le 8 mars 2001 (gauche) et le 18 septembre 2004 (droite). La croix verte indique la position de 4U 1755−33 et les rectangles verts correspondent aux positions des jets larges. La flèche verte indique le Nord et a une longueur de 2′. Les contours magenta (droite) traduisent les niveaux d'intensité radio à 13 cm, telle que mesurée par ATCA. Les images *XMM–Newton* ont été lissées par une gaussienne de largeur 8″. Figure extraite de Kaaret et al. (2006).

Pour former une telle structure, le jet doit avoir eu, au moins, une durée de vie de 10 à 30 ans (Kaaret et al. 2006). 4U 1755−33, découverte en 1970 par *Uhuru* (Jones 1977), fut active à plusieurs occasions jusqu'en 1996, où elle entra en quiescence (e.g. Roberts et al. 1996; Church & Balucinska-Church 1997). Elle fut donc active pendant au moins une période de 26 ans, ce qui est compatible avec la dimension du jet. Des observations *Chandra* ne détectèrent pas de sources ponctuelles le long des jets. Par contre, elles montrent un excès d'émission sur la surface du jet, ce qui indique que l'émission détectée par *XMM–Newton* est diffuse et ne constitue pas un alignement de sources ponctuelles (Park et al. 2005).

Au delà de l'observation 2001 d'Angelini & White (2003) (partie gauche de la figure 4.9), nous avons obtenu une nouvelle observation – 2.5 fois plus longue – avec *XMM–Newton* en 2004 pour étudier une éventuelle évolution du jet de 4U 1755−33. Le profil selon l'axe du jet pour les deux observations *XMM–Newton* est représenté sur la figure 4.10. La morphologie du jet apparaît similaire entre les deux observations. Il existe des correspondances entre les noeuds, mais l'extraction du mouvement propre est difficile car la morphologie individuelle des noeuds a changé. Le flux total du jet dans la bande 0.5–10 keV est passé de 15×10^{-13} erg s^{-1} cm^{-2} à 20×10^{-14} erg s^{-1} cm^{-2} en l'espace de 3 ans. Le temps caractéristique, dans le cas d'une décroissance exponentielle, serait de l'ordre de 11 ans. Nos observations radio avec ATCA ne permettent pas de détecter une contrepartie à 1384 ou 2368 MHz.

Le mécanisme d'émission le plus probable est de nouveau le rayonnement synchrotron

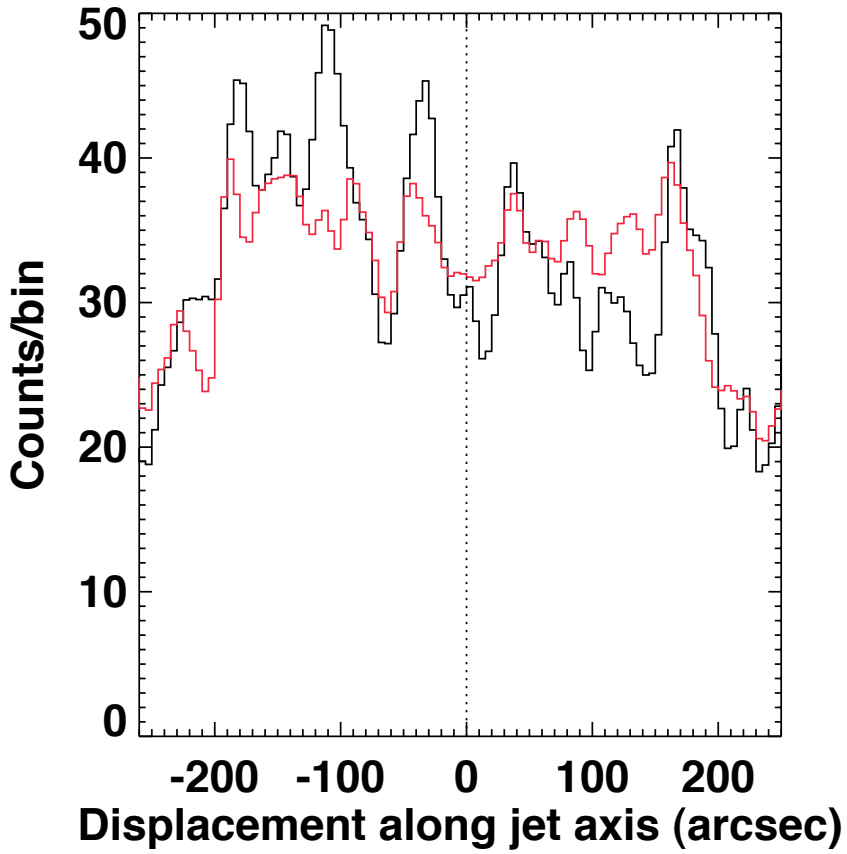

FIG. 4.10 – Profil du nombre du photons par canaux le long de l'axe du jet de 4U 1755−33 (noir = 2001 ; rouge = 2004). La différence du temps d'observation est prise en compte. La ligne pointillée marque la position de 4U 1755−33. Figure extraite de Kaaret et al. (2006).

d'électrons relativistes. Des arguments énergétiques invalideraient des mécanismes physiques tels que le bremstrahlung thermique ou la diffusion Compton inverse. Dans l'hypothèse d'une interprétation synchrotron, il en résulte de nouveau une nécessité d'accélération d'électrons jusqu'à des énergies extrêmes – $>$ 60 TeV. La durée de vie de tels électrons est de l'ordre de quelques centaines d'années, donc bien au delà du temps de décroissance observé. L'extrapolation du spectre X vers les basses énergies est compatible avec les limites supérieures en radio, si l'indice spectral entre la radio et les X est inférieur à –0.65, ce qui est conforme aux observations d'autres lobes radio comme SS 433 (Dubner et al. 1998).

4.6 Microquasars : accélérateurs extrêmes de particules

La mise en place de notre programme de recherche systématique de zones d'interaction des jets relativistes avec le MIS, et associées à une accélération extrême de particules, a permis de montrer que ce genre de phénomène n'était pas rare. Après XTE J1550−564 et H 1743−322 – voire GX 339−4–, il est probable qu'il s'agisse d'un processus fréquent dans notre Galaxie. Par exemple, l'émission radio de XTE J1650−500 pendant son état thermique (Corbel et al. 2004) pourrait être liée à l'impact d'une éjection majeure avec le MIS. D'une manière similaire, il fut observé en 1998 dans XTEJ1748−288 un rallumage des jets, probablement lors de collisions avec le milieu interstellaire (Kotani et al. 2000, Hjellming non publié). L'émission infrarouge

résolue de GRS 1915+105 – résultat très contreversé à l'époque – pourrait, elle aussi, avoir la même origine (Sams et al. 1996). La recherche de lobes autour de cette source s'est révélée infructueuse à ce jour (Rodriguez & Mirabel 1998; Chaty et al. 2001; Kaiser et al. 2004, 2005).

On peut noter aussi que SS 433 (Figure 4.1) présente au niveau de ses lobes terminaux une émission X non-thermique et stationnaire, qui pourrait éventuellement être liée à une interaction avec des phases plus denses du MIS (Seward et al. 1980; Dubner et al. 1998; Safi-Harb & Petre 1999). À proximité de l'objet compact, il est intéressant de signaler que de l'émission X thermique est observée par Migliari et al. (2002). Elle est associée au réchauffage du contenu baryonique du jet, qui pourrait être lié à la présence d'un flot ultra-rapide invisible au sein de cette source (Migliari et al. 2005).

La similarité est forte avec Sco X−1, où le mouvement balistique de deux lobes radio est observé de part et d'autre de ce système à étoile à neutrons (Fomalont et al. 2001b,a). De nouveau, un flot ultra-relativiste invisible donnerait de la puissance aux lobes terminaux mobiles.

Mais la comparaison de SS 433 ou de Sco X−1 avec les autres microquasars présentés précédemment s'arrête ici. En effet, le phénomène observé pour SS 433 et Sco X−1 serait lié à une injection continue de plasma – sans doute liée à un taux d'accrétion (très ?) supérieure à la limite d'Eddington – dans des lobes mobiles, tandis que pour les autres objets, il s'agit d'un évènement de nature impulsive – lié à une transition d'état – qui se propage incognito dans le MIS jusqu'à former des lobes lors d'une rencontre avec une phase dense de ce MIS.

Gallo et al. (2005a) détecte une structure annulaire large proche du trou noir Cyg X−1 (Figure 4.11). Le jet compact de Cyg X−1 gonfle un lobe radio en surpression par rapport

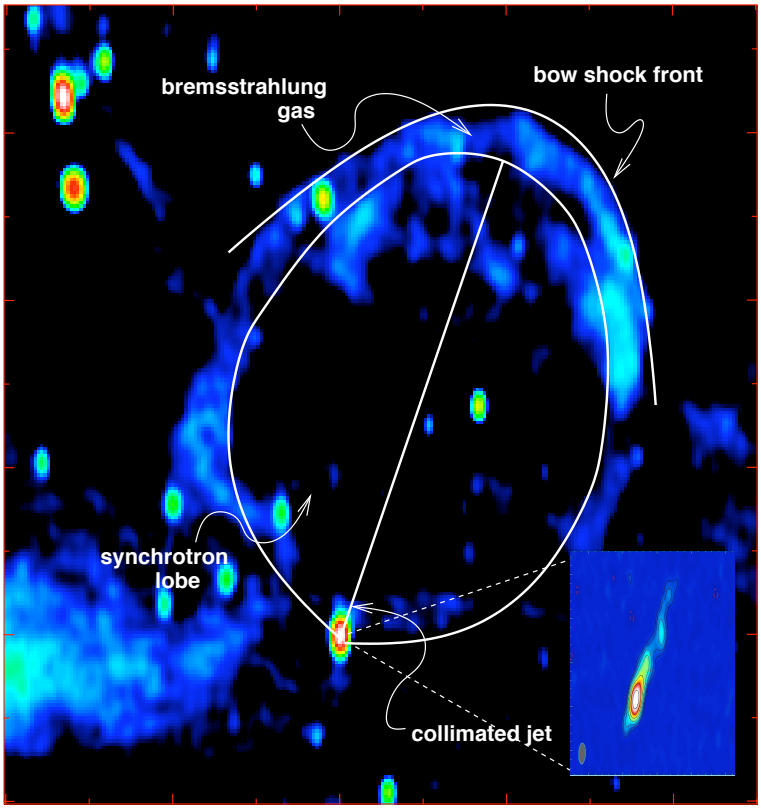

FIG. 4.11 – Émission bremstrahlung à 1.4 GHz associée au choc d'étrave de Cyg X−1, due à la propagation du jet compact dans le MIS. Figure extraite de Gallo et al. (2005a).

au milieu environnant. Ce lobe en expansion compresse le MIS et crée une onde de choc à l'origine de l'émission bremstrahlung observée. En utilisant le MIS comme un calorimètre, il est possible de mesurer l'énergie totale associée aux jets de Cyg X−1. Il en résulte que ces jets sont très puissants et pourraient emporter l'intégralité de la puissance d'accrétion (Gallo et al. 2005a; Russell et al. 2007).

Une simple application de la loi d'échelle des propriétés dynamiques des AGN, les microquasars pourraient se trouver dans des milieux de faible densité et de faible pression, avec pour corollaire une brillance de surface très faible. Cela expliquerait la rareté des lobes radio larges autour de telles sources (Heinz 2002, mais voir aussi Kaiser et al. 2004). Grâce à *Chandra*, la détection de jets résolus spatialement en X est devenue fréquente au sein des noyaux actifs de galaxie (Harris & Krawczynski 2006). Il est probable que la détection de jets similaires dans les microquasars va apporter certains éclaircissements quant aux propriétés des jets d'AGN, au vu de l'évolution dynamique des jets de microquasars – et de celle de la vie d'un chercheur.

On peut noter aussi qu'il pourrait être réaliste d'imaginer que cela puisse apporter certaines informations sur les propriétés des chocs des sursauts gamma (voir par exemple l'application de modèle de choc en retour pour XTE J1550−564 dans Wang et al. 2003). Avec ces nouvelles observations, nous assistons en direct au ralentissement du plasma relativiste sur le MIS et à la formation de lobes radio larges associée à l'accélération de particules jusqu'à des énergies insoupçonnées à ce jour. Il est possible qu'un suivi très détaillé de tels évènements nous donne accès à des informations précieuses sur la physique des chocs relativistes.

4.7 Articles de recherche

4.7.1

Large-Scale, Decelerating, Relativistic X-ray Jets from the Microquasar XTE J1550-564.

Article publié dans :

Science, 2002, 298, 196-199

Corbel, S., Fender, R. P., Tzioumis, A. K., Tomsick, J. A., Orosz, J. A., Miller, J. M., Wijnands, R., Kaaret, P.

REPORTS

Large-Scale, Decelerating, Relativistic X-ray Jets from the Microquasar XTE J1550−564

S. Corbel,[1]* R. P. Fender,[2] A. K. Tzioumis,[3] J. A. Tomsick,[4] J. A. Orosz,[5] J. M. Miller,[6] R. Wijnands,[6] P. Kaaret[7]

We have detected, at x-ray and radio wavelengths, large-scale moving jets from the microquasar XTE J1550−564. Plasma ejected from near the black hole traveled at relativistic velocities for at least 4 years. We present direct evidence for gradual deceleration in a relativistic jet. The broadband spectrum of the jets is consistent with synchrotron emission from high-energy (up to 10 tera–electron volts) particles that were accelerated in the shock waves formed within the relativistic ejecta or by the interaction of the jets with the interstellar medium. XTE J1550−564 offers a rare opportunity to study the dynamical evolution of relativistic jets on time scales inaccessible for active galactic nuclei jets, with implications for our understanding of relativistic jets from Galactic x-ray binaries and active galactic nuclei.

Collimated relativistic jets produced by active galactic nuclei (*1*) (AGN) and by accretion-powered stellar compact objects in sources called microquasars (*2*) are commonly observed at radio wavelengths. Such jets are produced close to black holes (supermassive ones in AGN and stellar-mass ones in microquasars) and may help probe the dynamics of matter being accreted in intense gravitational fields. The unprecedented sub–arc second resolution of the Chandra x-ray observatory has recently allowed the detection of x-ray jets in many AGN. Whereas the radio emission of AGN jets is thought to originate from synchrotron emission, the nature of the x-ray emission is still under debate; but synchrotron or inverse Compton radiation is likely involved (*3*). Jets produced by Galactic black holes such as XTE J1550−564 should evolve much more rapidly than AGN jets and, therefore, could provide insights into the dynamical evolution of relativistic outflows and also into the processes of particle acceleration. Here, we present the detection of large-scale, moving, relativistic jets ejected from a Galactic black hole binary.

The x-ray transient XTE J1550−564 (Galactic longitude and latitude l = 325.88°, b = −1.83°) was discovered by the All-Sky Monitor (ASM) aboard the Rossi X-ray Timing Explorer (RXTE) on 7 September 1998 (*4*). Shortly afterward, a strong and brief (about 1 day) x-ray flare was observed on 20 September 1998 (*5*, *6*), and radio jets with apparent superluminal velocities (>2 c, where c is the speed of light) were observed beginning 24 September 1998 (*7*). Subsequent optical observations showed that the dynamical mass of the compact object is 10.5 ± 1.0 stellar masses, indicating that the compact object in XTE J1550−564 is a black hole; revealed the binary companion to be a low-mass star; and led to a distance estimate of about 5.3 kpc (*8*).

After the reappearance of x-ray emission from XTE J1550−564 in early 2002 (*9*), we initiated a series of radio observations with the Australia Telescope Compact Array (ATCA). Observations on 16 January 2002 showed renewed activity at radio wavelengths from the XTE J1550−564 black hole binary (*10*). These observations also revealed a previously unknown radio source ~22 arc sec to the west of the black hole binary. ATCA observations performed on 29 January 2002 (Fig. 1), in an array configuration allowing higher spatial resolution imaging, showed that the western source had a possible extension pointed toward XTE J1550−564. The position angle of this radio source relative to XTE J1550−564 was −85.8° ± 1.0°, which is consistent with the position angle [−86.1° ± 0.8° (*11*)] of the western component of the superluminal jet observed during the September 1998 radio flare with long baseline interferometry (*7*).

Prompted by the detection of the western source along the axis of the jet from XTE J1550−564, we searched Chandra archival data taken in 2000 for x-ray sources located along the jet axis of XTE J1550−564. The field of view of XTE J1550−564 was imaged by Chandra on 9 June, 21 August, and 11 September of 2000. Examination of the 0.3- to 8-keV images (Fig. 2) revealed an x-ray source ~23 arc sec to the east of XTE J1550−564 at a position angle of 93.8° ± 0.9° from XTE J1550−564, lying along the axis of the eastern components of the radio superluminal jets (*7*) [at a position angle of 93.9° ± 0.8° (*11*)]. The angular separation between this eastern source and XTE J1550−564 increased from 21.3 ± 0.5 arc sec on 9 June 2000 to 23.4 ± 0.5 arc sec on 11 September 2000, implying that the eastern source moved with an average proper motion of 21.2 ± 7.2 milli–arc sec (mas) day^{-1} between these two observations. Thus, we were able to obtain an x-ray jet proper-motion measurement, something not previously done for any accretion-powered Galactic or extragalactic source. Our radio observations (Fig. 1), performed with ATCA between April 2000 and February 2001, showed a weak, decaying, and moving radio source consistent with the position of the eastern x-ray source. It was not detected in February 2002 (Fig. 1) with a 3σ upper limit of 0.18 mJy (1 Jy = 10^{-26} W m^{-2} Hz^{-1}) at 3.5 cm.

With the detection of the western radio source in early 2002, we obtained a 30-ks Chandra observation on 11 March 2002. In the resulting 0.3- to 8-keV image (Fig. 2), three sources were detected along the axis of the jet: the x-ray binary XTE J1550−564, an extended x-ray source at the position of the western radio source, and a faint source 29.0 ± 0.5 arc sec east of XTE J1550−564. This weak x-ray source was the eastern source that had smoothly decayed and moved by 5.7 ± 0.7 arc sec since September 2000. The eastern source was active during a period of at least 2 years (from April 2000 to March 2002).

The most remarkable feature of this Chandra observation is the x-ray emission associated with the western radio source. Both the radio and x-ray emissions of the western source appeared extended toward XTE J1550−564, and the morphology matched well between the two wavelengths. Most (70%) of the x-ray emission was concentrated in the leading peak, which has a full width at half maximum (FWHM) of 1.2 arc sec. A trailing tail, pointed back toward XTE J1550−564, gave a full width at 10% of maximum intensity of 5 arc sec.

The alignment of the eastern and western sources with the axis of the jet observed on 24 September 1998 (*7*), as well as the proper motion of the eastern source, imply that both

[1]Université Paris VII and Service d'Astrophysique, Commissariat à l'Energie Atomique CE-Saclay, 91191 Gif sur Yvette, France. [2]Astronomical Institute Anton Pannekoek, University of Amsterdam, and Center for High Energy Astrophysics, Kruislaan 403, 1098 SJ Amsterdam, Netherlands. [3]Australia Telescope National Facility, Commonwealth Scientific and Industrial Research Organization (CSIRO), Post Office Box 76, Epping NSW 1710, Australia. [4]Center for Astrophysics and Space Sciences, University of California at San Diego, MS 0424, La Jolla, CA 92093, USA. [5]Astronomical Institute, Utrecht University, Postbus 80000, 3508 TA Utrecht, Netherlands. [6]Center for Space Research, Massachusetts Institute of Technology, NE80-6055, 77 Massachusetts Avenue, Cambridge, MA 02139−4307, USA. [7]Harvard-Smithsonian Center for Astrophysics, 60 Garden Street, Cambridge, MA 02138, USA.

*To whom correspondence should be addressed. E-mail: corbel@discovery.saclay.cea.fr

sources are related to the jets of XTE J1550–564. In addition, both sources are likely to be connected with the apparently superluminal ejecta from the brief and intense flare of 20 September 1998 (*7*). Indeed, large-scale ejections of relativistic plasma (from XTE J1550–564) have been observed and resolved only during this occasion; the radio emission detected at other epochs has been associated with the compact jet of the low-hard x-ray spectral state (*12*). Also, the RXTE-ASM has not detected any other x-ray flares similar to the large flare of 20 September 1998 in subsequent monitoring. The fact that the eastern source apparently moves faster than the western source is consistent with the interpretation in which the eastern source constitutes the jet that is pointing toward Earth (the approaching jet) and the western source constitutes the receding jet.

With the positions of the eastern (and approaching) jet on 9 June 2000 and that of the western (and receding) jet on 16 January 2002, we find average proper motions of 32.9 ± 0.7 mas day^{-1} and 18.3 ± 0.7 mas day^{-1}, respectively. At a distance of 5.3 kpc (*8*), this corresponds to average apparent velocities on the plane of the sky of 1.0 *c* and 0.6 *c* for the eastern and western jets, respectively. The proper motion of 21.2 ± 7.2 mas day^{-1} measured by Chandra for the eastern jet between 9 June 2000 and 11 September 2000 is significantly smaller than its corresponding average proper motion, which indicates that the ejecta decelerated after the ejection. This is confirmed by the Chandra detection of the eastern jet in March 2002, implying an average proper motion of 10.4 ± 0.9 mas day^{-1} between 11 September 2000 and 11 March 2002. The relativistic plasma was originally ejected at greater velocities, because the relative velocity was initially greater than 2 *c* [the initial proper motion was greater than 57 mas day^{-1} for the approaching jet (*7*)]. These observations provide direct evidence for gradual deceleration of relativistic materials in a jet. Previous observations of other microquasars are consistent with purely ballistic motions [for example (*2*, *13*)], except for the system called XTE J1748–288, where after ballistic ejections, the jet was observed to stop suddenly, presumably after a collision with environmental material (*14*, *15*).

The eastern and western jets have been detected up to angular separations from XTE J1550–564 of 29 and 23 arc sec, respectively, which correspond to projected physical separations of 0.75 and 0.59 pc, respectively, for a distance of 5.3 kpc (*8*). These are large distances for moving relativistic ejecta [in GRS 1915+105, the ejecta have been observed to travel up to a projected distance of 0.08 pc and on a maximum time scale of 4 months (*2*)]. Persistent large-scale (1 to 3 pc) jets have previously been observed only at radio wavelengths, for example, 1E 1740.7–2942 and GRS 1758–258 (*16*, *17*), but without indication of associated moving ejecta. Our observations reveal that the relativistic ejecta of a Galactic black hole have been able to travel over parsec-scale distances at relativistic velocities during several years. An important aspect of our study is that it provides direct evidence for a large-scale, moving x-ray jet from a black hole (Galactic or in AGN).

SS 433 is the only other x-ray binary for which large-scale (up to ~40 arc min, i.e., several tens of parsecs), nonthermal x-ray emission has been previously observed, probably associated with interactions of the jets with the interstellar medium (ISM) (*18*–*22*). The helical pattern observed in the lobes at radio wavelengths indicates a connection between the lobes and the corkscrew pattern associated with plasma ejection close to (on an arc sec scale) the core of the SS 433/W50 system (*23*). However, relativistic motion at large scales has not been observed in SS 433. We note that thermal x-ray emission arising from moving relativistic ejecta, but only out to ~0.05 pc from the compact object, has been reported in SS 433 (*24*, *25*).

Our results demonstrate that the emission from relativistic ejecta of Galactic black holes can be observed at wavelengths extending up to x-rays. Future sensitive, high-resolution observations of other Galactic black hole jets in the infrared (*26*), optical, and x-ray bands may reveal that broadband emission from relativistic ejecta of Galactic black holes is more common than previously thought and may offer an exciting way to probe the physics of the jets. AGN jets, which were previously detected at radio and optical wavelengths, are now known, with the advent of the Chandra observatory, to often produce x-rays. Whereas the radio emission of AGN jets is thought to originate from synchrotron emission, the nature of the x-ray emission has

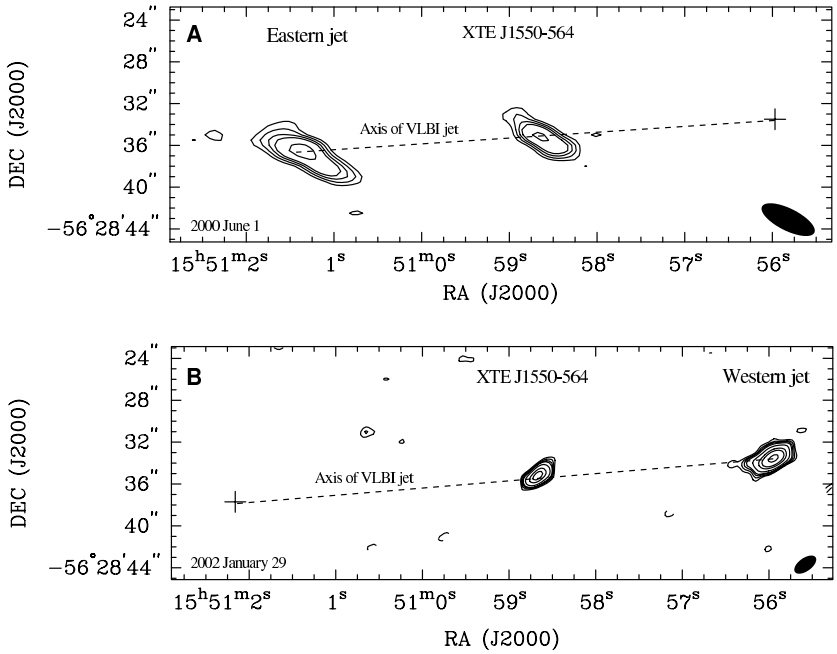

Fig. 1. Uniform weighted maps of the field of view around the black hole candidate XTE J1550–564 on 1 June 2000 (A) and 29 January 2002 (B) showing the radio counterpart to the eastern and western jets (when detected). RA, right ascension; DEC, declination. The stationary black hole binary XTE J1550–564 is at the center of the images and has a radio spectrum typical of the self-absorbed compact jet (*33*, *34*) that is observed during the x-ray low-hard spectral state (*12*). (**A**) 1 June 2000 map at 4800 MHz (6 cm). The position of the eastern radio jet is α(J2000) = 15h 51m 01s.30 and δ(J2000) = –56°28′ 36.9″, with a total uncertainty of 0.3 arc sec; that is, at a position angle of 93.8° ± 0.9° from XTE J1550–564. The synthesized beam (in the lower right corner) is 5.5 × 2.1 arc sec, with the major axis in a position angle of 63.1°. The peak brightness in the image is 1.1 mJy per beam. Contours are plotted at –3, 3, 4, 5, 6, and 9 times the root mean squared (rms) noise equal to 0.1 mJy per beam. The cross marks the position of the western jet as measured on 29 January 2002. (**B**) 29 January 2002 map at 8640 MHz (3.5 cm). The position of the western radio jet is α(J2000) = 15h 50m 55s.94 and δ(J2000) = –56°28′ 33.5″, with a total uncertainty of 0.3 arc sec. The synthesized beam is 2.4 × 1.3 arc sec with the major axis in a position angle of –54.6°. The peak brightness in the image is 1.79 mJy per beam. Contours are plotted at –3, 3, 4, 5, 6, 9, 15, 20, and 30 times the rms noise equal to 0.05 mJy per beam. The cross marks the position of the eastern jet as measured on 11 March 2002 during the Chandra observation.

not always been clearly identified. Although it is thought to be nonthermal, it is not always known whether synchrotron or inverse Compton radiation predominates for a particular object (*3*, *27*–*29*).

The nature of the physical mechanism producing the emission from the relativistic jets of XTE J1550−564 can be understood by looking at the broadband spectrum, for example, for the western jet on 11 March 2002 (Fig. 3). The position and morphology of the radio and x-ray counterparts of the western jet are consistent with each other (Figs. 1 and 2), and the spectral energy distribution is consistent with a single power law (of spectral index −0.660 ± 0.005). These facts favor a scenario in which the broadband emission from the jets is synchrotron emission from high-energy particles. Similar conclusions could be drawn for the eastern jet in 2000, because the overall radio flux was also consistent with an extrapolation of the x-ray spectrum with a spectral index of −0.6. The detection of x-ray synchrotron emission would imply a large Lorentz factor, on the order of 2×10^7 (corresponding to an energy of ~10 TeV), for the x-ray–emitting electrons (under the equipartition assumption giving a magnetic field of ~0.3 mG).

Acceleration in a shock wave is the most likely origin for the very high energies required. Shock waves could be produced by internal instabilities (*30*) or by varying flow speeds within the jet, as has been proposed to occur in some models of gamma-ray bursts or AGN (*31*, *32*). If several relativistic plasmoids were ejected around 24 September 1998 (*7*) and their velocities were slightly different, then it would have taken several months (maybe years) for them to collide. Such a collision would have produced shock waves, particle acceleration, and the brightening of the jets.

A more plausible alternative is that the shock waves are produced when the jet material, moving with bulk relativistic speed, interacts with the ISM (producing an external shock). In fact, the gradual deceleration we observed for the eastern jet would be easily explained by such interactions. Inhomogeneities in the ISM could also be at the origin of the brightening of the eastern and western jet at different epochs. The origin of the western jet is less clear because no proper motion has been observed yet. Continuous observations of XTE J1550−564 will show whether or not the western jet is still moving and, together with high spatial resolution observations and broadband spectra, will be important in deciding between the models (internal or external shocks). Also, regular observation of the jets of XTE J1550−564 would map the propagation of the shocks and allow estimation of the energy dissipated in the jets when decelerating in the ISM. XTE J1550−564 offers a unique opportunity to study the dynamical evolution of relativistic jets on time scales inaccessible for AGN jets and has implications not only for the study of jets from Galactic x-ray binaries but also for our understanding of relativistic jets from AGN.

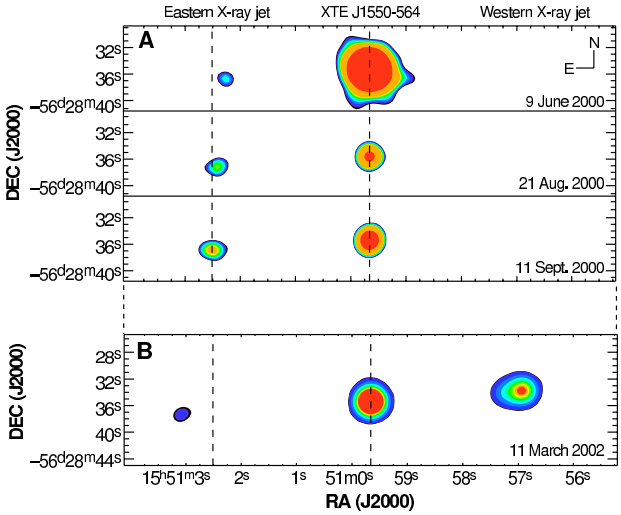

Fig. 2. Chandra 0.3- to 8-keV images (using the Advanced Charged-Coupled Device Imaging Spectrometer spectroscopy array ACIS-S), which show the black hole binary XTE J1550−564 (center), the approaching eastern x-ray jet (left), and the receding western x-ray jet (right). The observations are ordered chronologically from top to bottom, and each image is labeled with the observation date. These filled contour plots have been produced by convolving the original Chandra image with a two-dimensional Gaussian with a width of 2 pixels in both directions. In 2000 (**A**), there are 11 contours between the lowest contour of 1.33×10^{-3} count s^{-1} $pixel^{-1}$ and the highest contour of 8.16×10^{-3} count s^{-1} $pixel^{-1}$. The same contour levels are used in all three 2000 images, but it should be noted that the flux levels for 9 June 2000 are not directly comparable to those for the other two observations because a grating was inserted for the 9 June observation. For the 2002 image (**B**), there are 11 contours between 0.33×10^{-3} count s^{-1} $pixel^{-1}$ and 8.16×10^{-3} count s^{-1} $pixel^{-1}$. The dashed lines mark the positions of XTE J1550−564 and the eastern x-ray jet on 11 September 2000, when the sources were separated by 23″.4. The proper motion of the x-ray jet is 21.2 ± 7.2 mas day^{-1} between 9 June 2000 and 11 September 2000 and averages 10.4 ± 0.9 mas day^{-1} between 11 September 2000 and 11 March 2002, indicating deceleration of the jet. Assuming a power-law spectral shape with a photon index of 1.7 and interstellar absorption of $N_H = 9 \times 10^{21}$ cm^{-2}, a count rate of 1.33×10^{-3} count s^{-1} corresponds to a flux of 7.71×10^{-14} erg cm^{-2} s^{-1} in the 0.3- to 8-keV band for the 9 June 2000 observation (with the grating) and to 1.66×10^{-14} erg cm^{-2} s^{-1} for other observations.

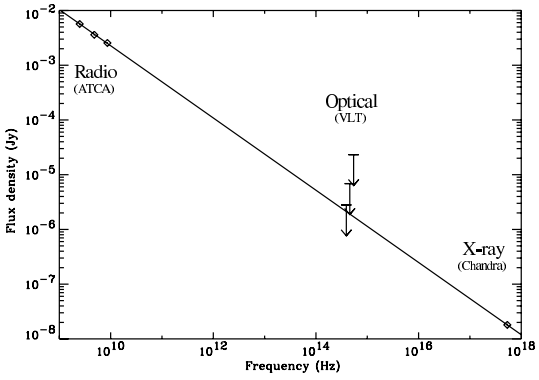

Fig. 3. The spectral energy distribution of the western jet around 11 March 2002. The radio points near 10^{10} Hz are ACTA measurements from 6 March. The radio flux densities were 5.7 ± 0.3, 3.60 ± 0.08, and 2.55 ± 0.07 mJy at 2496, 4800, and 8640 MHz, respectively, giving a spectral index of −0.63 ± 0.05 in the radio range. The x-ray measurement near 5×10^{17} Hz is the Chandra measurement from 11 March. X-ray spectral fitting of the Chandra data for the western source, assuming a power-law form with interstellar absorption fixed to the total Galactic atomic hydrogen column density ($N_H = 9.0 \times 10^{21}$ cm^{-2}), gives a spectral index of −0.70 ± 0.15 (90% confidence level). The spectrum may be somewhat steeper if there is additional absorption near the source. The unabsorbed 0.3- to 8-keV flux is 3.8×10^{-13} ergs cm^{-2} s^{-1} (i.e., 18 nJy at 2.2 keV). The optical upper limits (99% confidence level) in between are derived from deep observations carried out with the 8.2-m unit 3 telescope at the ESO, Paranal. The source was observed with the FORS1 instrument in the Bessel *V* and *R* filters on 10 March, with limiting magnitudes for point sources of 25.2 and 25.5 mag., respectively, and on 18 March with FORS1 and the Bessel *I* filter, with a limiting magnitude for point sources of 25.5 mag. We assumed an optical extinction of $A_V = 4.75$ mag (*8*). The broadband spectral energy distribution is consistent with a single power law of spectral index of −0.660 ± 0.005.

References and Notes

1. A. H. Bridle, R. A. Perley, *Annu. Rev. Astron. Astrophys.* **22**, 319 (1984).
2. I. F. Mirabel, L. F. Rodríguez, *Annu. Rev. Astron. Astrophys.* **37**, 409 (1999).
3. D. E. Harris, H. Krawczynski, *Astrophys. J.* **565**, 244 (2002).
4. D. A. Smith, *Int. Astron. Union Circ. No. 7008* (1998).
5. G. J. Sobczak *et al.*, *Astrophys. J.* **544**, 993 (2000).

6. J. Homan *et al.*, *Astrophys. J. Suppl. Ser.* **132**, 377 (2001).
7. D. Hannikainen *et al.*, *Astrophys. Space Sci. Rev.* **276**, 45 (2001).
8. J. A. Orosz *et al.*, *Astrophys. J.* **568**, 845 (2002).
9. J. Swank, E. Smith, C. Markwardt, *Int. Astron. Union Circ. No. 7792* (2002).
10. S. Corbel, R. P. Fender, A. K. Tzioumis, *Int. Astron. Union Circ. No. 7795* (2002).
11. D. Hannikainen, personal communication.
12. S. Corbel *et al.*, *Astrophys. J.* **554**, 43 (2001).
13. R. P. Fender *et al.*, *Mon. Not. R. Astron. Soc.* **304**, 865 (1999).
14. T. Kotani *et al.*, *Astrophys. J.* **543**, L133 (2000).
15. M. Rupen, personal communication.
16. I. F. Mirabel, L. F. Rodríguez, B. Cordier, J. Paul, F. A. Lebrun, *Nature* **358**, 215 (1992).
17. L. F. Rodríguez, I. F. Mirabel, J. Martí, *Astrophys. J.* **401**, L15 (1992).
18. F. Seward, J. Grindlay, E. Seaquist, W. Gilmore, *Nature* **287**, 806 (1980).
19. M. G. Watson, R. Willingale, J. E. Grindlay, F. D. Seward, *Astrophys. J.* **273**, 688 (1983).
20. W. Brinkmann, B. Aschenbach, N. Kawai, *Astron. Astrophys.* **312**, 306 (1996).
21. S. Safi-Harb, H. Oegelman, *Astrophys. J.* **483**, 868 (1997).
22. S. Safi-Harb, R. Petre, *Astrophys. J.* **512**, 784 (1999).
23. G. M. Dubner, M. Holdaway, W. M. Goss, I. F. Mirabel, *Astron. J.* **116**, 1842 (1998).
24. H. L. Marshall, C. R. Canizares, N. S. Schulz, *Astrophys. J.* **564**, 941 (2002).
25. S. Migliari, R. P. Fender, M. Méndez, *Science* **297**, 1673 (2002).
26. B. J. Sams, A. Eckart, R. Sunyaev, *Nature* **382**, 47 (1996).
27. A. S. Wilson, A. J. Young, P. L. Shopbell, *Astrophys. J.* **547**, 740 (2001).
28. R. M. Sambruna *et al.*, *Astrophys. J.* **549**, L161 (2001).
29. R. M. Sambruna *et al.*, *Astrophys. J.* **571**, 206 (2002).
30. P. E. Hardee, *Astrophys. J.* **533**, 176 (2000).
31. M. J. Rees, P. Meszaros, *Astrophys. J.* **430**, L93 (1994).
32. C. R. Kaiser, R. Sunyaev, H. C. Spruit, *Astron. Astrophys.* **356**, 975 (2000).
33. R. M. Hjellming, K. J. Johnston, *Astrophys. J.* **328**, 600 (1988).
34. R. P. Fender, *Mon. Not. R. Astron. Soc.* **322**, 31 (2001).

35. S.C. and J.A.T. acknowledge useful conversations with A. Celotti, S. Heinz, and V. Dhawan. P.K. acknowledges useful discussions with H. Falcke and D. Harris. S.C. thanks C. Bailyn, S. Chaty, D. Hannikainen, and D. Hunstead for providing information before publication; F. Mirabel for a careful reading of this manuscript; and R. Ekers, D. McConnell, R. Norris, B. Sault, and the ATCA Time Allocating Committee for allowing the radio observations. We thank H. Tananbaum for granting Director's Discretionary Time for the Chandra observations and J. Nichols for rapid processing of the data. We have made use of observations performed with the European Southern Observatory (ESO) Melipal Telescope at the Paranal Observatory under Director's Discretionary Time program 268.D-5771. The Australia Telescope is funded by the Commonwealth of Australia for operation as a National Facility managed by CSIRO.

8 July 2002; accepted 26 August 2002

4.7.2

X-Ray Jet Emission from the Black Hole X-Ray Binary XTE J1550-564 with Chandra in 2000.

Article publié dans :

Astrophys. J., 2003, 582, 933-944

Tomsick, J. A., Corbel, S., Fender, R., Miller, J. M., Orosz, J. A., Tzioumis, T., Wijnands, R., Kaaret, P.

THE ASTROPHYSICAL JOURNAL, 582:933–944, 2003 January 10

X-RAY JET EMISSION FROM THE BLACK HOLE X-RAY BINARY XTE J1550−564 WITH *CHANDRA* IN 2000

JOHN A. TOMSICK,[1] STÉPHANE CORBEL,[2] ROB FENDER,[3] JON M. MILLER,[4] JEROME A. OROSZ,[5] TASSO TZIOUMIS,[6] RUDY WIJNANDS,[4,7] AND PHILIP KAARET[8]

Received 2002 June 12; accepted 2002 September 12

ABSTRACT

We have discovered an X-ray jet due to material ejected from the black hole X-ray transient XTE J1550−564. The discovery was first reported in 2002 by Corbel and coworkers, and here we present an analysis of the three *Chandra* observations made between 2000 June and September. For these observations, a source is present that moves in an eastward direction away from the point source associated with the compact object. The separation between the new source and the compact object changes from 21″.3 in June to 23″.4 in September, implying a proper motion of 21.2 ± 7.2 mas day^{-1}, a projected separation of 0.31–0.85 pc, and an apparent jet velocity between 0.34 ± 0.12 and 0.93 ± 0.32 times the speed of light for a source distance range of $d = 2.8$–7.6 kpc. These observations represent the first time that an X-ray jet proper-motion measurement has been obtained for any accretion-powered Galactic or extragalactic source. While this work deals with the jet to the east of the compact object, the western jet has also been detected in the X-ray and radio bands. The most likely scenario is that the eastern jet is the approaching jet and that the jet material was ejected from the black hole in 1998. Along with a 1998 VLBI proper-motion measurement, the *Chandra* proper motion indicates that the eastern jet decelerated between 1998 and 2000. There is evidence that the eastern jet is extended by ±2″–3″ in the direction of the proper motion. The upper limit on the source extension in the perpendicular direction is ±1″.5, which corresponds to a jet opening angle of less than 7°.5. The X-ray jet energy spectrum is well but not uniquely described by a power law with an energy index of $\alpha = -0.8 \pm 0.4$ ($S_\nu \propto \nu^\alpha$) and interstellar absorption. The eastern jet was also detected in the radio band during an observation made within 7.4 days of the June *Chandra* observation. The overall radio flux level is consistent with an extrapolation of the X-ray power law with $\alpha = -0.6$. The 0.3–8 keV X-ray jet luminosity is in the range $(3$–$24) \times 10^{32}$ ergs s^{-1} for the June observation using the distance range above but is a factor of ∼2–3 lower for the later observations. We cannot definitively determine the X-ray emission mechanism, but a synchrotron origin is viable and may provide the simplest explanation for the observations.

Subject headings: acceleration of particles — accretion, accretion disks — black hole physics — stars: individual (XTE J1550−564) — stars: winds, outflows — X-rays: stars

1. INTRODUCTION

Outflows are observed in active galactic nuclei (AGNs) and for some Galactic compact objects containing relativistic particles that are accelerated away from the compact objects in collimated jets. At least three types of radio jets are observed in Galactic X-ray binaries. In 1992, double-sided radio lobes were detected for two accreting black hole candidates: GRS 1758−258 (Rodríguez, Mirabel, & Marti 1992) and 1E 1740.7−2942 (Mirabel et al. 1992). For these sources, the compact object/radio lobe separations are 1–3 pc, and the lobes are stationary. Because of observational and likely physical similarities to AGNs, the name microquasar was given to these sources. The number of X-ray binaries in the group of microquasars was greatly increased with the discovery of relativistic radio jets on much smaller size scales (0.02–0.06 pc). The two best known systems are GRS 1915+105 (Mirabel & Rodríguez 1994) and GRO J1655−40 (Tingay et al. 1995; Hjellming & Rupen 1995). For both of these systems, apparently superluminal jet velocities are observed, and the actual jet velocities inferred are greater than $0.9c$. Although not as relevant for this work, the third type of radio jet is often called a "compact jet" and has been detected for a relatively large number of X-ray binaries. Despite their small size (∼10^{-4} pc), compact jets have been resolved for GRS 1915+105 (Dhawan, Mirabel, & Rodríguez 2000) and Cyg X-1 (Stirling et al. 2001).

The jets are usually detected at radio wavelengths, but, in AGNs, optical and X-ray jets are also frequently seen. With the exception of the large-scale (∼40 pc) diffuse X-ray emission detected from the X-ray binary SS 433 with the *Einstein Observatory* (Seward et al. 1980), X-ray jets were not seen for Galactic systems prior to the launch of the *Chandra X-Ray Observatory* (Weisskopf et al. 2002) in 1999. With a large improvement in angular resolution over previous missions, *Chandra* detected arcsecond (∼0.025 pc) X-ray jets in

[1] Center for Astrophysics and Space Sciences, Code 0424, University of California at San Diego, La Jolla, CA 92093; jtomsick@ucsd.edu.
[2] Université Paris VII and Service d'Astrophysique, Centre d'Etudes de Saclay, F-91191 Gif-sur-Yvette, France.
[3] Astronomical Institute "Anton Pannekoek," University of Amsterdam and Center for High Energy Astrophysics, Kruislaan 403, 1098 SJ Amsterdam, Netherlands.
[4] Department of Physics and Center for Space Research, Massachusetts Institute of Technology, Cambridge, MA 02139.
[5] Astronomical Institute, Utrecht University, Postbus 80000, 3508 TA Utrecht, Netherlands.
[6] Australia Telescope National Facility, Commonwealth Science and Industrial Research Organisation, P.O. Box 76, Epping, NSW 1710, Australia.
[7] Chandra Fellow.
[8] Harvard-Smithsonian Center for Astrophysics, 60 Garden Street, Cambridge, MA 02138.

SS 433 (Marshall, Canizares, & Schulz 2002), but similar jets have not previously been reported for other accretion-powered Galactic sources.

XTE J1550−564 was first detected by the *Rossi X-Ray Timing Explorer* (*RXTE*) All-Sky Monitor (ASM) in 1998 September (Smith 1998). It was identified as a probable black hole system based on its X-ray spectral and timing properties, and optical observations of the source in quiescence indicate a compact object mass near 10 $M_{\odot}$, confirming that the system contains a black hole (Orosz et al. 2002). Soon after the discovery of the source, a jet ejection with an apparent separation velocity greater than $2c$ was observed in the radio band using very long baseline interferometry (VLBI), establishing that the source is a microquasar (Hannikainen et al. 2001). The VLBI observations followed a very bright radio and X-ray flare that was likely related to the ejection event (Sobczak et al. 1999; Wu et al. 2002). XTE J1550−564 has shown a high degree of X-ray activity over the last few years, having a major outburst in 2000 (Tomsick, Corbel, & Kaaret 2001a and references therein) and mini-outbursts in 2001 and 2002 (Tomsick et al. 2001b; Swank, Smith, & Markwardt 2002). Bright radio and X-ray flares like the 1998 flare have not been observed during these outbursts, but unresolved radio emission was detected, indicating the presence of a compact jet (Corbel et al. 2001).

During the 2002 X-ray outburst, radio observations of XTE J1550−564 were made with the Australia Telescope Compact Array (ATCA). The detection of a variable radio source 22″ west of XTE J1550−564 (Corbel, Fender, & Tzioumis 2002a) prompted us to examine *Chandra* observations of the source that were made in 2000. As reported by Corbel et al. (2002b), we discovered an X-ray source that is at approximately the same angular distance from XTE J1550−564 as the variable radio source and is to the east. In this paper we present an analysis of the *Chandra* observations. The three sources (XTE J1550−564, the western radio source, and the eastern X-ray source) are aligned with each other and with the VLBI radio jets that were detected in 1998. The alignment strongly suggests that the X-ray and radio sources are jets from XTE J1550−564. The jet size scale that we infer is in between those of the previously detected radio jets, providing an important connection between these two types of jets.

2. OBSERVATIONS

Seven XTE J1550−564 *Chandra* observations occurred in May and June during the 2000 outburst from this source, and two observations were made near the end of the outburst on 2000 August 21 and September 11. These observations were described in previous work where results for the XTE J1550−564 point source were presented (Tomsick et al. 2001a; Miller et al. 2001). Modes with two-dimensional imaging were used for the observations made on June 9, August 21, and September 11 (henceforth observations 1, 2, and 3), and here we focus on these observations. The rest of the May and June observations were grating observations made in "continuous clocking mode," providing only one-dimensional imaging. In addition, a filter was used to block the zeroth order as a result of the high XTE J1550−564 flux level. Thus, with the exception of the June 9 observation, the May and June observations are not suitable for our search for extended emission from the source.

Table 1 provides information about observations 1, 2, and 3, including the observation time, the exposure time, and the instrument configuration. All three observations were made using the Advanced CCD Imaging Spectrometer (ACIS). In each case, XTE J1550−564 was placed on one of the back-illuminated ACIS chips (S3), providing the best low-energy response. Observation 1 differs from the other two observations in that the High Energy Transmission Grating (HETG) was inserted. Although grating observations provide two-dimensional imaging, the sensitivity is reduced. In addition, observation 1 includes data taken with two different ACIS CCD configurations with longer (1.1 s) and shorter (0.3 s) individual frame exposure times ("alternating exposure mode"). We carried out our analysis using the data from all exposures with a total exposure time of 4957 s. We made background light curves for all three observations and found that, for observation 2, there are brief time segments where excess background is observed. Removing these causes a drop in the exposure time from 5099 to 4985 s. Periods of high background are not seen for the other observations. For observation 3, we used data from the entire 4572 s exposure time.

While a detailed analysis of the XTE J1550−564 energy spectrum is presented for observations 2 and 3 in Tomsick et al. (2001a), similar results for observation 1 have not been reported. Thus, we extracted the ACIS grating spectrum for observation 1. We fitted 0.8–8 keV Medium Energy Grating (MEG) and 2–10 keV High Energy Grating (HEG) energy spectra with a model consisting of a power law with interstellar absorption. A reasonably good (but not formally acceptable) fit is obtained ($\chi^2/\nu = 94/71$) with a column density of $N_{\rm H} = (8.4 \pm 0.8) \times 10^{21}$ cm^{-2}, which is consistent with the Galactic value in the direction of XTE J1550−564, and a power-law photon index of $\Gamma = 1.58 \pm 0.08$ (90% confidence errors). The fit is not significantly improved by the addition of a soft "disk blackbody" component (Makishima et al. 1986), and no obvious emission or absorption lines are present in the residuals. The 0.3–8 keV source flux for observation 1 is 9.3×10^{-11} ergs cm^{-2} s^{-1}. For observations 2 and 3, we obtain 0.3–8 keV source fluxes of 1.2×10^{-13} and 2.4×10^{-13} ergs cm^{-2} s^{-1}, respectively, using the spectral parameters from Tomsick et al. (2001a).

TABLE 1
XTE J1550−564 *Chandra* Observations

Observation	MJD[a] (days)	UT Date	Exposure Time (s)	Instrument Configuration
1	51704.538	2000 Jun 9	4957	ACIS-S/HETG
2	51777.405	2000 Aug 21	4985	ACIS-S
3	51798.245	2000 Sep 11	4572	ACIS-S

[a] Modified Julian Date (JD −2,400,000.5) at exposure midpoint.

This paper also includes a reanalysis of a 5 hr radio band observation made with ATCA on 2000 June 1, which is close in time to *Chandra* observation 1. The ATCA observation was carried out in the high spatial resolution 6B array configuration, and flux measurements were obtained at central frequencies of 1384, 2496, 4800, and 8640 MHz with a total bandwidth of 128 MHz. More details can be found in a previous publication where these observations were used (Corbel et al. 2001).

3. RESULTS

We searched for X-ray sources in the 0.3–8 keV images for all three *Chandra* observations using the *wavdetect* program (Freeman et al. 2002) in Version 2.2 of the *Chandra* Interactive Analysis of Observations (CIAO) software package. We only included photons with energies up to 8 keV as the ACIS effective area drops off rapidly above this energy. We used data from the ACIS chip containing XTE J1550−564 (ACIS-S3). For observation 1, we restricted the search to a square region of dimension 1.′5 centered on XTE J1550−564 to avoid regions that include the dispersed spectrum, while we searched over the entire S3 chip for observations 2 and 3.

For observation 1, only one other source besides XTE J1550−564 is detected at a significance level of 4.8 σ. The source is $\sim$21″ east of XTE J1550−564, while the new radio transient is $\sim$22″ west of XTE J1550−564. For observation 2, there are seven sources detected at greater than 3 σ significance, excluding XTE J1550−564. Although none of the sources have positions consistent with that of the new radio transient (see Kaaret et al. 2002 for flux limits), the most significantly detected source (at 8.3 σ) is located $\sim$23″ east of XTE J1550−564. For observation 3, there are two sources detected at greater than 3 σ significance, excluding XTE J1550−564. Similarly to observation 2, the most significantly detected source (at 9.1 σ) is located $\sim$23″ east of XTE J1550−564, but we do not detect a source at the position of the new radio transient.

Figure 1 shows the portion of the 0.3–8 keV raw (i.e., unsmoothed) images for the three observations containing XTE J1550−564 and the source to the east of XTE J1550−564 that is detected in all three observations. For observation 3, the position of the eastern source is R.A. = $15^{h}51^{m}01\overset{s}{.}47$, decl. = −56°28′36.″7 (equinox J2000.0). We calculated this position using the XTE J1550−564 radio position, which is known to 0.″3 (Corbel et al. 2001), and the separations between XTE J1550−564 and the X-ray jet in the *Chandra* images. The separation measurement is good to about 0.″5 (see § 3.2), indicating an error of less than 0.″8 on the X-ray jet position. While we do not detect an X-ray source in these observations coincident with the western radio source, it is notable that the three sources (XTE J1550−564, the western radio source, and the eastern X-ray source) are aligned (see Corbel et al. 2002b for a clear illustration of the alignment). In addition, it is remarkable that they are aligned with the radio jets that were resolved during the bright 1998 X-ray outburst from XTE J1550−564 (Hannikainen et al. 2001). This provides evidence for a connection between the radio jets, the eastern

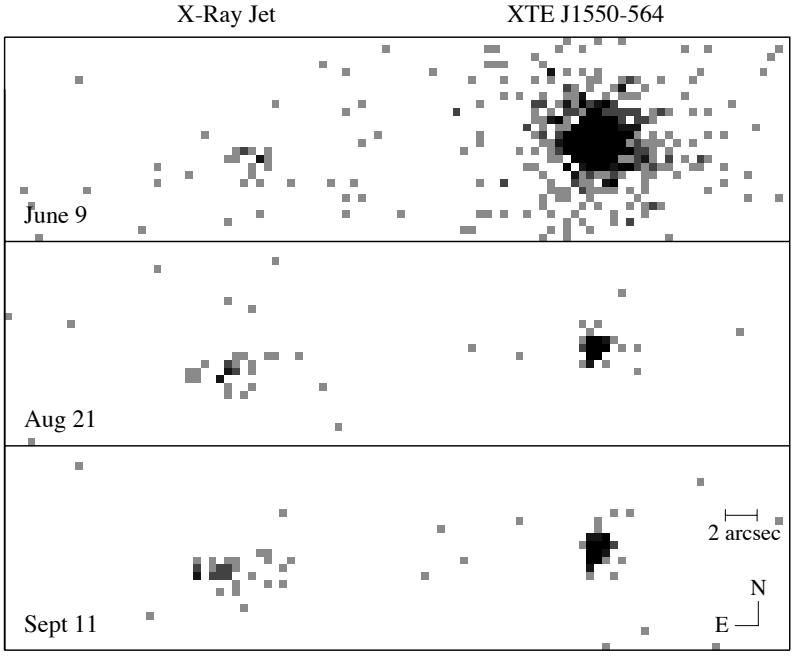

FIG. 1.—Three *Chandra* 0.3–8 keV images showing XTE J1550−564 and an X-ray jet. The observations were made in 2000 on June 9, August 21, and September 11, and exposure times of 4957, 4985, and 4572 s were obtained, respectively. The gray scale is logarithmic based on the number of counts detected per pixel. To provide a scale where XTE J1550−564 and the X-ray jet are both visible, we set a saturation level of 12 counts. We used the same scale in all three images, but it should be noted that the levels for June 9 are not directly comparable to those for the other two observations since a grating was inserted for the June 9 observation. The pixel size is 0.″492 × 0.″492.

X-ray source, and the western radio source, and the results presented below support this interpretation. Henceforth, we refer to the eastern X-ray source as the X-ray jet.

3.1. *Proper Motion of the X-Ray Jet*

We determined the separation between XTE J1550−564 and the X-ray jet for each observation. While an inspection of the images indicates that we obtain reasonable X-ray jet positions with *wavdetect*, we used a second measurement technique to obtain an estimate of the systematic error. For each observation, we determined the positions for XTE J1550−564 and the X-ray jet by calculating the source centroid using the 0.3–8 keV events from a 16×16 pixel ($7\farcs9 \times 7\farcs9$) region centered on the *wavdetect* position. An inspection of the images (see Fig. 1) indicates that this region contains all or nearly all of the events that are likely related to the source along with a small number of background events. We estimate that the number of background events in the 16×16 pixel regions is 4.0, 1.2, and 0.7 for observations 1, 2, and 3, respectively. Our technique for estimating the background surface brightness is described in § 3.3. Compared to the *wavdetect* positions, the recalculated XTE J1550−564 positions change by less than $0\farcs1$, and the X-ray jet positions change by less than $0\farcs5$. For observations 1 and 2, the recalculated source separations are $0\farcs45$ and $0\farcs27$ larger, respectively, and for observation 3, the recalculated source separation is $0\farcs38$ smaller. Based on these changes, we estimate that the error on the source separation is approximately $0\farcs5$ and is dominated by systematics.

The angular separations between XTE J1550−564 and the X-ray jet are given in Table 2 and are plotted versus time in Figure 2. The separations show that the X-ray jet is moving away from XTE J1550−564, and the data are well described by a linear increase in the separation. The linear fit shown in the figure corresponds to a proper motion of 21.2 ± 7.2 mas day^{-1}, and an extrapolation of the linear fit predicts zero separation on MJD $50,699 \pm 278$. MJD 50,699 corresponds to 1997 September 8, which is nearly a year before the first reported X-ray and radio activity for XTE J1550−564 in 1998 September. We obtained the *RXTE*/ASM light curve for the full *RXTE* mission to check for X-ray activity between early 1996 and 1998 September. XTE J1550−564 was not detected during this time with a 3 σ upper limit of 1×10^{-9} ergs cm^{-2} s^{-1} for daily 1.5–12 keV flux measurements. The largest gap in ASM coverage during this time was 14 days, which is much shorter than the duration of a typical outburst. Thus, it is most likely that the material responsible for the X-ray jet was ejected during the large 1998 September radio and X-ray flare (Wu et al. 2002). We note that the errors on the linear fit parameters are dominated by the systematic errors on the individual separations and thus do not correspond to 68% confidence statistical errors.

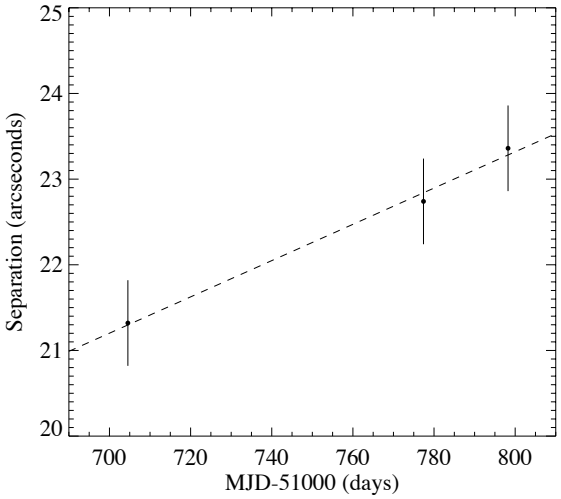

FIG. 2.—Angular separation between XTE J1550−564 and the X-ray jet for the June 9, August 21, and September 11 *Chandra* observations. The dashed line shows a linear fit corresponding to a proper motion of 21.2 ± 7.2 mas day^{-1}, and an extrapolation of the linear fit predicts zero separation on MJD $50,699 \pm 278$.

3.2. *Source Morphology*

We produced the contour plots shown in Figure 3 for the three observations after convolving the raw images (from Fig. 1) with a two-dimensional Gaussian with a width (σ) of 2 pixels in both directions. In addition to illustrating that the X-ray jet moves away from XTE J1550−564 over time, the contour plots for observations 2 and 3 suggest that the X-ray jet is elongated in the direction of the proper motion (roughly east to west).

To study the jet morphology for observations 2 and 3, we produced source profiles showing the number of counts as a function of position along and perpendicular to the jet axis.

TABLE 2
X-RAY JET RESULTS

Observation	Rate[a] (counts s^{-1})	Separation[b] (arcsec)	Γ[c]	Flux[d]
1	3.0×10^{-3}	21.3 ± 0.5	$1.7^{+0.7}_{-1.0}$	$(20 \pm 6) \times 10^{-14}$
2	5.0×10^{-3}	22.7 ± 0.5	1.8 ± 0.6	$(6.1 \pm 1.3) \times 10^{-14}$
3	6.9×10^{-3}	23.4 ± 0.5	1.9 ± 0.8	$(8.2 \pm 1.5) \times 10^{-14}$

[a] 0.3–8 keV count rate after background subtraction.
[b] Separation between the XTE J1550−564 point source and the X-ray jet.
[c] Power-law photon index (with 90% confidence errors) obtained with the column density fixed to the Galactic value of $N_H = 9 \times 10^{21}$ cm^{-2}.
[d] Absorbed 0.3–8 keV X-ray flux in ergs cm^{-2} s^{-1} obtained from a simultaneous power-law fit to all three observations. We fixed N_H to the Galactic value and found a photon index of $\Gamma = 1.8 \pm 0.4$.

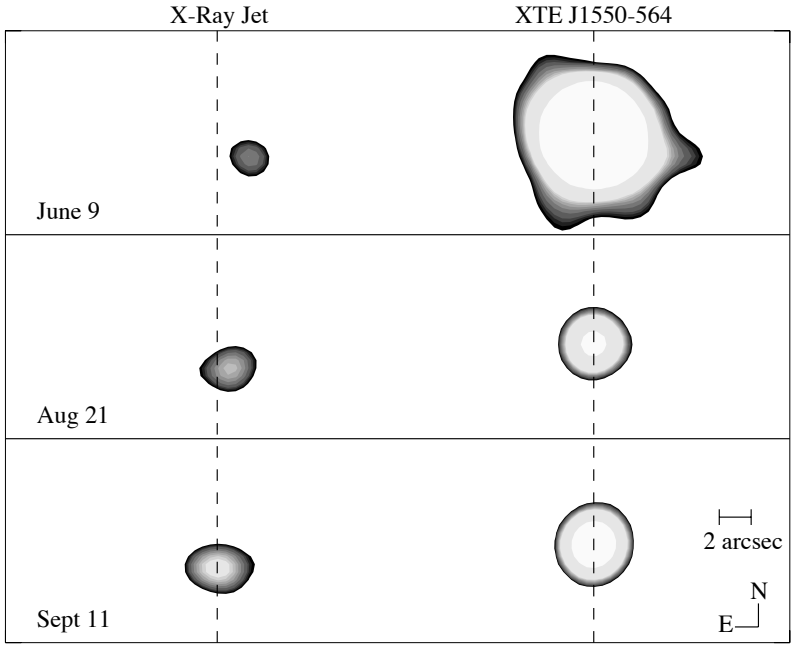

FIG. 3.—Contour plots produced by convolving the 0.3–8 keV images shown in Fig. 1 with a two-dimensional Gaussian with a width (σ) of 2 pixels in both directions. The same contour levels are used for all three images. The vertical dashed lines clearly demonstrate the X-ray jet motion relative to XTE J1550−564. In addition, the August 21 and September 11 images suggest that the X-ray jet is elongated in the direction of the proper motion.

We determined the jet axis using the source positions obtained above. For observations 2 and 3, the jet position angles are $93\overset{\circ}{.}9 \pm 1\overset{\circ}{.}3$ and $93\overset{\circ}{.}7 \pm 1\overset{\circ}{.}3$, respectively. Here we use a value of $93\overset{\circ}{.}8$, which is consistent with the position angle of $93\overset{\circ}{.}9 \pm 0\overset{\circ}{.}8$ derived for the VLBI radio jets (D. Hannikainen 2002, private communication). In producing the source profiles, we used the source counts from a 16×16 pixel ($7\overset{''}{.}9 \times 7\overset{''}{.}9$) region centered on the jet position and oriented so that the resampled pixels run along and perpendicular to the jet axis. We then binned the counts in 1 pixel strips in both directions. Each strip is expected to contain 0.07 and 0.05 background counts for observations 2 and 3, respectively, and we neglected this low background level for this analysis. We repeated the analysis for XTE J1550−564 to provide a comparison to the jet profiles. Figures 4 and 5 show the results for observations 2 and 3, respectively. In each case, panels (*a*) and (*b*) are the profiles along and perpendicular to the jet axis, respectively. The solid lines with Poisson error bars are the jet profiles, and the dotted lines are the XTE J1550−564 profiles after renormalizing so that the peak bin has the same number of counts for the jet and XTE J1550−564.

We performed Kolmogorov-Smirnov (K-S) tests (Press et al. 1992) on the unbinned counts to obtain a formal comparison of the profiles. Using the K-S statistic, we calculated the probability that the X-ray jet profiles along and perpendicular to the jet axis are taken from the same parent distribution as the XTE J1550−564 profiles (i.e., the probability that the X-ray jet is not extended in a direction). In addition, we compared the X-ray jet profiles to the profiles for the source PG 1634+706 (observation ID 1269), which is used to calibrate the ACIS point-spread function (PSF). The results shown in Table 3 indicate that it is unlikely that the X-ray jet profile for observation 3 is the same as the XTE J1550−564 and PG 1634+706 profiles along the jet axis with probabilities of 1.8% and 0.2% for the respective comparison sources. The

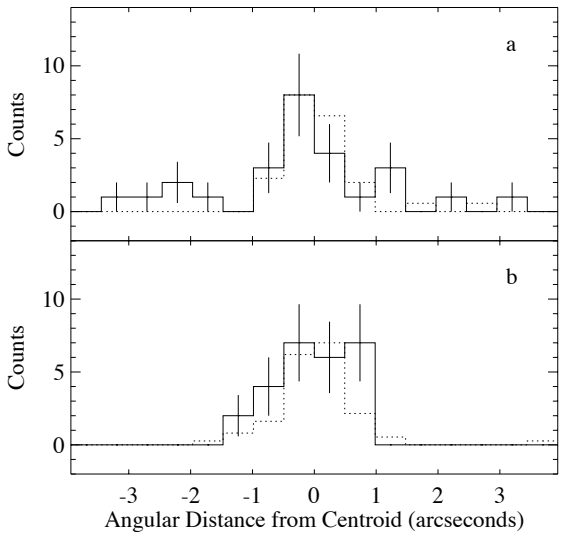

FIG. 4.—Spatial profiles showing the number of counts as a function of position (*a*) along the jet axis and (*b*) perpendicular to the jet axis for the observation 2 X-ray jet. In both panels, the solid lines with Poisson error bars are the jet profiles and the dotted lines are the XTE J1550−564 profiles after renormalizing to facilitate comparison to the X-ray jet profiles.

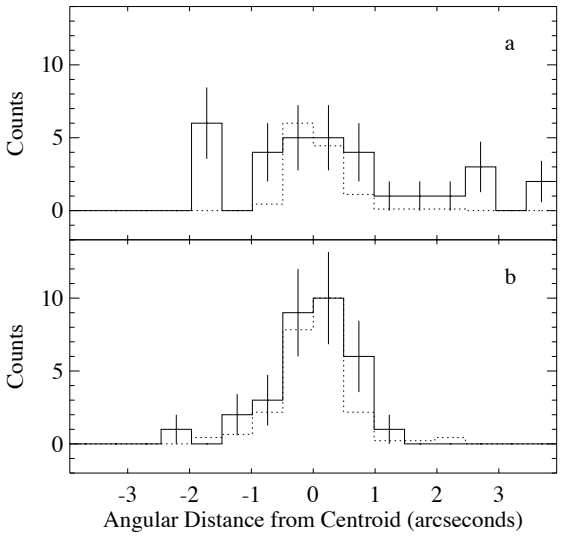

FIG. 5.—Spatial profiles showing the number of counts as a function of position (*a*) along the jet axis and (*b*) perpendicular to the jet axis for the observation 3 X-ray jet. The line designations are the same as for Fig. 4.

extension along the jet axis is not significant for observation 2 with probabilities of 21% and 6.3% for XTE J1550−564 and PG 1634+706, respectively. In the direction perpendicular to the jet axis, the probabilities that the X-ray jet profiles are the same as the comparison source profiles are in the range 21%–71%. Thus, there is no evidence that the X-ray jet is extended in this direction.

In summary, the K-S tests show that it is likely (at least for observation 3) that the X-ray jet is extended along the jet axis. From Figures 4*a* and 5*a*, we estimate that the jets are extended by $\pm 2''$–$3''$ along the jet axis but by less than $\pm 1\farcs5$ in the perpendicular direction. At an angular separation of $23''$ from XTE J1550−564, the upper limit of $\pm 1\farcs5$ corresponds to a jet opening angle of less than 7°.5.

3.3. *X-Ray Jet Energy Spectrum and Flux*

We extracted energy spectra for each observation. For observations 2 and 3, we used a circular source extraction region with a radius of $4''$, and we extracted background spectra from an annulus with an inner radius of $5''$ and an outer radius of $18''$. The source and background regions were both centered on the X-ray jet. For observation 1, the background count rate near the X-ray jet is several times higher than the rates for the other observations. It is likely that this is partly due to the XTE J1550−564 dust-scattering halo, but measurements of the observation 1 background rate far from XTE J1550−564 show count rates that are still about a factor of 2 higher than the other observations, indicating that the intrinsic observation 1 background rate is somewhat higher. Thus, we used a smaller circular source extraction region with a radius of $2\farcs5$ for observation 1 to minimize contamination. In addition, as the XTE J1550−564 X-ray halo contributes to the background near the X-ray jet, we estimated the background level using the counts in an annulus centered on XTE J1550−564 with an inner radius of $18\farcs8$ and an outer radius of $23\farcs8$ ($\pm 2\farcs5$ from the angular separation between XTE J1550−564 and the X-ray jet). We removed the parts of the annulus containing the X-ray jet and the readout strip. In the 0.3–8 keV energy band, 17, 26, and 32 counts were collected in the source regions for observations 1, 2, and 3, respectively. In the same energy band, we estimate background levels of 1.3, 1.0, and 0.6 counts in the source extraction regions for observations 1, 2, and 3, respectively. We used the CIAO routine *psextract* to extract the spectra and create response matrices.

Although the low numbers of source counts do not provide high-quality spectra, we fitted the spectra in an attempt to distinguish between models. As the same instrumental configuration was used for observations 2 and 3, we combined the data from these two observations to improve the statistics. For these initial fits, we rebinned the spectrum after combining the data from the two observations and fitted the spectra using χ^2 minimization. We used a power-law model, appropriate for nonthermal emission, and also a thermal bremsstrahlung model ("bremss" in XSPEC v11.1) and included interstellar absorption. These two models provide fits of nearly identical quality, and in both cases the reduced χ^2 value is 0.9 for 7 degrees of freedom. The parameter constraints are poor with both models giving a column density ($N_{\rm H}$) range of approximately $(2\text{–}14) \times 10^{21}$ cm^{-2} (90% confidence, $\Delta\chi^2 = 2.7$). With $N_{\rm H}$ left as a free parameter, the range of possible values for the power-law photon index is $\Gamma = 0.6$–2.5, and the bremsstrahlung temperature is only constrained to be greater than 2.8 keV. The

TABLE 3
K-S TEST RESULTS FOR COMPARING ONE-DIMENSIONAL PROFILES

		PROBABILITY	
OBSERVATION	COMPARISON SOURCE[a]	Along Jet Axis[b]	Perpendicular to Jet Axis[c]
2.....	XTE J1550−564	0.208	0.465
2.....	PG 1634+706	0.063	0.207
3.....	XTE J1550−564	0.018	0.707
3.....	PG 1634+706	0.0024	0.378

[a] The X-ray jet profiles along the jet axis and perpendicular to the jet axis are compared to the one-dimensional profiles for the comparison sources.
[b] K-S test probability that the X-ray jet profile along the jet axis is the same as the comparison profile.
[c] K-S test probability that the X-ray jet profile perpendicular to the jet axis is the same as the comparison profile.

column density range quoted above is consistent with the Galactic value in the direction of XTE J1550−564 ($N_{\rm H} = 9 \times 10^{21}$ cm^{-2}); thus, we fixed $N_{\rm H}$ to this value for the fits described below. Detecting iron line emission would provide evidence that the X-ray emission has a thermal origin. No clear excess is observed in the X-ray jet spectrum at iron line energies, but the upper limit on the equivalent width of such a line is high (several keV).

We fitted the 0.3–8 keV spectra for each observation separately with a power-law model and interstellar absorption with the column density fixed to the Galactic value. Rather than χ^2 minimization, we used the Cash statistic (Cash 1979), which does not require that the data be rebinned in energy. This is desirable since rebinning data necessarily removes spectral information. We did not perform background subtraction as the background levels are low enough to neglect. As shown in Table 2, we obtain $1.7^{+0.7}_{-1.0}$, 1.8 ± 0.6, and 1.9 ± 0.6 (with 90% confidence errors) for the power-law photon index (Γ) for observations 1, 2, and 3, respectively. We conclude that there is no evidence for spectral variability. Thus, we refitted the three spectra simultaneously and obtained a value of $\Gamma = 1.8 \pm 0.4$ (energy index $\alpha = -0.8 \pm 0.4$, $S_\nu \propto \nu^\alpha$). Although we take this as our best estimate of the power-law photon index, we note that it was obtained with $N_{\rm H}$ fixed to the Galactic value and that uncertainties in $N_{\rm H}$ represent a possible source of systematic error.

We used the simultaneous power-law fit to the three spectra to obtain measurements of the X-ray jet flux. We obtain 0.3–8 keV absorbed fluxes of $(20 \pm 6) \times 10^{-14}$, $(6.1 \pm 1.3) \times 10^{-14}$, and $(8.2 \pm 1.5) \times 10^{-14}$ ergs cm^{-2} s^{-1} for observations 1, 2, and 3, respectively, indicating that the flux dropped by a factor of ~2–3 between the June observation and the August and September observations. The quoted errors are based on the numbers of source and background counts and Poisson statistics, and the observation 1 flux is corrected for the reduction of sensitivity due to insertion of the grating. A source of systematic error (not included in the quoted errors) comes from the fact that a smaller source extraction region was used for observation 1. For observations 2 and 3, 15% and 19% of the counts within the source regions lie outside a radius of 2″.5 (the observation 1 extraction radius), indicating that the observation 1 flux could be higher than the quoted value by 15%–20%. Even if this source of systematic error is considered, the data are not strongly inconsistent with a smooth exponential or power-law decay (see also Kaaret et al. 2002). Based on the XTE J1550−564 source distance ($d = 2.8$–7.6 kpc; Orosz et al. 2002), the intrinsic 0.3–8 keV X-ray jet luminosity for observation 1 is in the range $(3$–$24) \times 10^{32}$ ergs s^{-1}.

We reanalyzed the 2000 June 1 ATCA radio band observations and found a radio source coincident with the eastern jet. We measured flux levels of 3.0 ± 0.3, 1.58 ± 0.25, 1.30 ± 0.10, and 0.38 ± 0.13 mJy at frequencies of 1384, 2496, 4800, and 8640 MHz, respectively. We fitted the radio spectrum with a power-law model and obtained an energy index of $\alpha = -0.82 \pm 0.15$ and a flux density of 1.1 ± 0.1 mJy at 5000 MHz (90% confidence errors in both cases). The power-law fit is not formally acceptable with a reduced χ^2 near 5 for 2 degrees of freedom, but the overall radio spectrum is consistent with being an optically thin synchrotron spectrum in the sense that $\alpha < 0$.

Figure 6 shows the four radio flux measurements along with the power-law fits to the *Chandra* energy spectra.

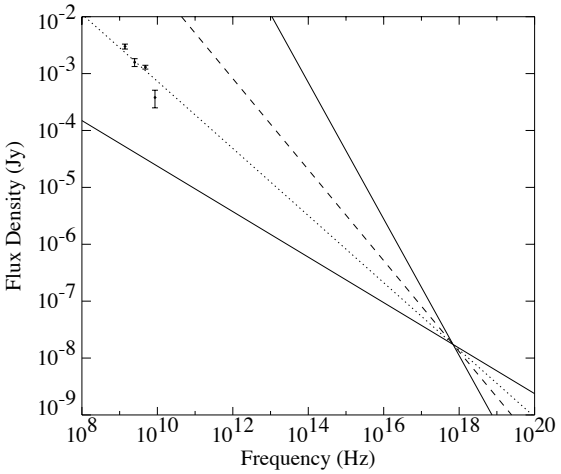

FIG. 6.—Energy spectrum showing the power-law fits to the *Chandra* data (all four lines) for different assumed values of α and the radio flux measurements made on 2000 June 1 with ATCA. We use the normalization appropriate for observation 1 for the power-law fits as it occurred within 7.4 days of the radio observation. The solid lines correspond to $\alpha = -0.4$ and -1.2 (90% confidence lower and upper limits from the *Chandra* fits). The dashed and dotted lines correspond to $\alpha = -0.8$ and -0.6, respectively.

We obtained the power-law fits to the *Chandra* data by fixing the power-law index to various values and fitting for the normalization. The normalization appropriate for observation 1 is used as it occurred closest in time to the radio observations. The power-law fits shown in the figure include the 90% confidence lower and upper limits on α (-0.4 and -1.2), the best-fit value from the *Chandra* data (-0.8), and the value that is most consistent with the radio data (-0.6). The "pivot point" for the power-law fits occurs at 2.9 keV, and the flux density is 17 nJy at that point. The overall radio flux level is consistent with an extrapolation of the X-ray spectrum with $\alpha = -0.6$, and it is possible that the radio and X-ray emissions are part of the same spectral component, which would provide evidence for a synchrotron X-ray emission mechanism. We note that $\alpha = -0.6$ lies slightly outside the error region for α found from fitting the radio spectrum alone. Although the X-ray and radio observations were not strictly simultaneous, observation 1 and the radio observation were only separated by 7.4 days, and it is unlikely that the flux levels could change significantly over this time.

We also fitted the X-ray spectra for the three *Chandra* observations simultaneously using the thermal bremsstrahlung model. We used the Cash statistic and fixed the column density to 9×10^{21} cm^{-2}. The 90% confidence lower limit on the bremsstrahlung temperature is 3.8 keV, and the only other free parameter in the fit is the normalization, which is related to physical parameters according to $N = 2.4 \times 10^{-16} d^{-2} \int n_e n_i \, dV$ cm^{-5} (Rybicki & Lightman 1979; Arnaud 1996), where d is the source distance and n_e and n_i are, respectively, the electron and ion number densities within the volume V. From the simultaneous fit, $N = (4$–$10) \times 10^{-5}$ cm^{-5} (90% confidence) for observation 1.

4. DISCUSSION

These results demonstrate that the eastern X-ray source detected in the 2000 *Chandra* observations is, in fact, X-ray jet emission from XTE J1550−564. In addition to the alignment between the XTE J1550−564 point source, the western radio source, and the eastern X-ray source and the fact that these sources are aligned with the 1998 radio jets (Corbel et al. 2002b), the *Chandra* images indicate motion of the eastern X-ray source away from XTE J1550−564 along the jet axis, and there is evidence that the eastern X-ray source is elongated in the direction of this motion. This is only the second Galactic X-ray binary, after SS 433 (Seward et al. 1980; Marshall et al. 2002), where X-ray jet emission has been resolved, and these observations represent the first time that an X-ray jet proper-motion measurement has been obtained for any accretion-powered Galactic or extragalactic source.

4.1. *Jet Kinematics*

Our proper-motion measurement of 21.2 ± 7.2 mas day^{-1} for the eastern X-ray jet and the source distance range of 2.8–7.6 kpc, determined from optical observations of XTE J1550−564 in X-ray quiescence (Orosz et al. 2002), indicate an apparent jet velocity ($\beta_{\rm app} = v_{\rm app}/c$) between 0.34 ± 0.12 and 0.93 ± 0.32. To make progress in estimating the actual jet velocity (β), it is necessary to determine what constraints we can place on the source geometry. As jet emission is detected on both sides of XTE J1550−564, we adopt the usual picture of a bipolar outflow with one approaching jet and one receding jet. Although perfect symmetry between the two jets is not critical to the discussion we present here, we note that the fact that one of the jets was detected first in X-rays and the other was detected first in the radio band should not be taken as evidence for a lack of symmetry. In fact, another *Chandra* observation made in 2002 March indicates that there is X-ray emission coincident with the western jet (Kaaret et al. 2002).

The main evidence that the eastern jet is the approaching jet is that the X-ray and radio observations made in 2000 and 2002 indicate that the mean proper motion relative to XTE J1550−564 is greater for the eastern jet. We determine the mean proper motions assuming that the material for both jets was ejected during the large 1998 September radio and X-ray flare (Wu et al. 2002; Sobczak et al. 1999). Corbel et al. (2002b) present arguments for this interpretation. In addition, as mentioned above, an extrapolation of the linear fit to the X-ray jet/XTE J1550−564 separations predicts zero separation prior to 1998 September. Since the first detected activity from XTE J1550−564 occurred in 1998 September, it is very unlikely that the ejection time was earlier. We assume an ejection time of MJD 51,078, which corresponds to the peak of the 1998 September radio flare (Wu et al. 2002) and is 2 days before the resolved radio jets were detected (Hannikainen et al. 2001). For the western jet, the separation between the jet and XTE J1550−564 was 22″.43 on MJD 52,307 (Corbel et al. 2002b), implying a mean proper motion of 18.3 mas day^{-1}. Based on the linear fit to the three X-ray jet measurements, the X-ray jet reached 22″.43 on MJD 51,759, which implies a mean proper motion of 32.9 mas day^{-1}. The larger mean proper motion for the eastern jet indicates that it is the approaching jet.

Although there is strong evidence that the eastern jet is the approaching jet, the actual jet velocity (β) depends on the exact angle the jet axis makes with the line of sight (θ), which cannot be determined from the jet observations presented in this work. Here we derive a lower limit on the value of β during 2000 June–September when the X-ray jet proper-motion measurement was made. The lower limit is independent of θ but depends on the distance range given above. In general, for an approaching jet, the minimum value of β occurs when $\theta_{\rm min} = \tan^{-1}(1/\beta_{\rm app})$. Using the minimum apparent velocity for the X-ray jet ($\beta_{\rm app} = 0.34 \pm 0.12$) and the equation $\beta = \beta_{\rm app}/(\sin\theta_{\rm min} + \beta_{\rm app}\cos\theta_{\rm min})$, which relates the apparent velocity to the actual velocity for an approaching jet, we obtain a minimum value for β of 0.32 ± 0.10 for $\theta_{\rm min} = 71°$. Thus, we conclude that the X-ray jet is moving at a velocity of at least 22% of the speed of light.

4.2. *X-Ray Emission Mechanism*

For the X-ray jets in AGNs, three emission mechanisms are commonly considered: thermal bremsstrahlung, synchrotron, and inverse Compton (Harris & Krawczynski 2002). For most AGN jets, observations rule out thermal bremsstrahlung. When high-quality X-ray jet spectra have been obtained for AGNs (e.g., Marshall et al. 2001), thermal emission lines have not been detected. Further, the very large amount of hot gas necessary to explain the emission via thermal bremsstrahlung is inconsistent with radio polarization measurements (Harris & Krawczynski 2002). In fact, the detection of radio polarization indicates that the synchrotron mechanism is operating in the radio band. In some cases, the broadband (radio to X-ray) energy spectra can be fitted with a single power law or a power law with one break (Marshall et al. 2001; Hardcastle, Birkinshaw, & Worrall 2001; Hardcastle et al. 2002), supporting a model where the broadband jet spectrum is dominated by synchrotron emission. However, inverse Compton emission in the form of synchrotron self-Compton (SSC) is known to dominate the X-ray emission for some AGN jets (Harris & Krawczynski 2002).

Other than XTE J1550−564, the only X-ray binary where X-ray jet spectra have been obtained is the well-known system SS 433 that resides in the radio nebula W50. The large-scale SS 433 X-ray jets extend up to 1° from the X-ray binary, and the energy spectrum of the jet shows significant spatial variation. On scales of arcseconds and smaller, the jets exhibit X-ray emission lines, indicating that thermal bremsstrahlung contributes to the X-ray emission (Marshall et al. 2002; Migliari, Fender, & Méndez 2002). However, on larger angular scales (15′–45′), emission lines are not detected with *ASCA* in the X-ray band (Yamauchi, Kawai, & Aoki 1994), and *RXTE* observations indicate that the spectrum extends to 100 keV (Safi-Harb & Petre 1999), indicating a nonthermal mechanism.

To study the implications of the various emission mechanisms for the XTE J1550−564 jets, it is necessary to estimate the volume of the emitting region. We assume that the shape of the emitting region is a section of a cone with its vertex at the compact object. The base of the conical section is at a distance of $d \tan\alpha_b$ from the compact object, where α_b is equal to the angular source separation given in Table 2 plus 2″.5. The value of 2″.5 comes from our estimate of the source extension obtained in § 3.2. Although there is some uncertainty associated with the size of the extension for the eastern jet, we obtained a *Chandra* image of the western jet with

much better statistics and measured a similar extension (Kaaret et al. 2002). The top of the conical section is at a distance of $d \tan \alpha_t$ from the compact object, where α_t is equal to the angular source separation minus 2.″5. As the opening angle of the cone is not well constrained, we consider values for the full opening angle of 7.°5 (our upper limit for the eastern jet obtained in § 3.2) and also 1°. The latter may be more realistic, as the upper limit on the opening angle for the western jet is 2° (Kaaret et al. 2002). In addition, we considered the distance range of $d = 2.8$–7.6 kpc in determining the volume. A caveat is that the volume could be somewhat larger if θ (the angle between the jet axis and the line of sight) is small; however, the fact that the VLBI jets were two-sided and similar in brightness (Hannikainen et al. 2001) makes this unlikely. We obtain a minimum volume of 3.8×10^{49} cm^3 for a distance of 2.8 kpc and an opening angle of 1° and a maximum volume of 4.3×10^{52} cm^3 for $d = 7.6$ kpc and an opening angle of 7.°5.

The volume estimates allow for a calculation of the mass implied by the thermal bremsstrahlung fits to the energy spectrum (see § 3.3) for observation 1. Assuming that the plasma consists of electrons and protons (i.e., $n_e = n_i$) and that n_e is constant over the emitting volume gives $n_e = (6.5 \times 10^7) d (N/V)^{1/2}$ cm^{-3}. We obtain a minimum mass of 4×10^{28} g for $d = 2.8$ kpc, $V = 3.8 \times 10^{49}$ cm^3, and $N = 4 \times 10^{-5}$ cm^{-5} and a maximum mass of 5×10^{30} g for $d = 7.6$ kpc, $V = 4.3 \times 10^{52}$ cm^3, and $N = 1 \times 10^{-4}$ cm^{-5}. It is difficult to devise a scenario in which the jet could contain such large masses. Even at the lower end of the mass range, it would take the black hole more than 1000 yr to accumulate this much mass through accretion at a rate of 10^{18} g s^{-1}, corresponding to the accretion rate for a luminosity of 10^{38} ergs s^{-1} and an accretion efficiency of 10%. It would also be difficult for the jet to start out with much less mass and then to entrain most of its mass from the interstellar medium (ISM) gradually as it moves away from the compact object because momentum conservation would lead to rapid deceleration of the jet. However, we probably cannot rule out a scenario in which the jet suddenly collides with a large amount of material that is far from the compact object such as material that is left from previous ejections. Thermal bremsstrahlung may still be a possible X-ray emission mechanism if the jet has sufficient kinetic energy associated with its bulk motion to heat such material to X-ray temperatures.

Here we assume that the X-ray and radio spectra can be described by a single power law with an index of $\alpha = -0.6$ as shown in Figure 6 to study the implications of a synchrotron X-ray emission mechanism. A lower limit on the strength of the magnetic field in the jet, $B_{\rm eq}$, comes from the assumption of equipartition between the magnetic and electron energy densities (Burbidge 1956). We derive the equipartition magnetic field using

$$B_{\rm eq} = \left(\frac{19 C_{12} L}{V} \right)^{2/7} \quad (1)$$

(Pacholczyk 1970), where L is the integrated luminosity and C_{12} is an expression, given in Pacholczyk (1970), that depends on the lower and upper frequency limits and the spectral index (α). For both parameters, we used the frequency range from 1.384×10^9 to 1.9×10^{18} Hz and $\alpha = -0.6$. We calculated L using a flux density of 17 nJy at 7×10^{17} Hz (appropriate for observation 1) and the range of distances and volumes derived in the previous paragraphs. Considering these distance and volume ranges, the lowest value of $B_{\rm eq}$ we obtain is 134 μG for $d = 7.6$ kpc and $V = 4.3 \times 10^{52}$ cm^3, and the highest value of $B_{\rm eq}$ we obtain is 566 μG for $d = 2.8$ kpc and $V = 3.8 \times 10^{49}$ cm^3. These values for $B_{\rm eq}$ are somewhat higher than the values found from radio observations of other Galactic objects (e.g., Rodríguez et al. 1992). This is at least in part due to the fact that the equipartition energy is higher because the spectrum for the XTE J1550−564 jet extends to the X-ray band.

While it is important to keep in mind that the value for $B_{\rm eq}$ assumes equipartition, we can use our result to obtain estimates of other physical jet quantities such as the Lorentz factor (γ) and lifetime (t_s) of the X-ray–emitting electrons, the number of electrons in the jet, and the total mass of material in the jet. From $\gamma(\nu) \sim (\nu/\nu_{\rm L})^{1/2}$ (Begelman, Blandford, & Rees 1984), where $\nu_{\rm L}$ is the Larmor frequency, we obtain values of γ at 1 keV between 1.2×10^7 and 2.5×10^7, and we obtain synchrotron lifetimes of 6–60 yr at 1 keV using $t_s = 8 \times 10^8 B_{\rm eq}^{-2} \gamma^{-1}$ s (Begelman et al. 1984), which is longer than the lifetime of the XTE J1550−564 X-ray jet. We note that if the flux decay by a factor of 2–3 that we observe over a period of about 4 months during the *Chandra* observations is due to synchrotron losses, this would imply a significantly shorter lifetime and probably a magnetic field strength above the equipartition value. Following Fender et al. (1999), the number of electrons in the jet can be calculated from the parameters of the energy spectrum (α and luminosity) and $B_{\rm eq}$, and we obtain a range of values from 4×10^{44} to 1×10^{46} electrons. Assuming one proton per electron gives values between 7×10^{20} and 2×10^{22} g for the mass of material in the jet. For a mass accretion rate of 10^{18} g s^{-1}, this amount of material could be accumulated in 700 and 2×10^4 s for the two masses, respectively. These times fit with the likely ejection time as the large X-ray and radio flare occurred 2 days before the jets were resolved using VLBI.

Although we have shown that a synchrotron mechanism is viable for the X-ray jet emission from XTE J1550−564, we cannot immediately rule out inverse Compton or SSC. However, we can determine how much emission these mechanisms are likely to contribute by comparing the photon energy density to the magnetic energy density. We calculate the magnetic energy density assuming that only the radio emission has a synchrotron origin, and we use the parameters from the power-law fits to the radio emission ($\alpha = -0.82$ and a flux density of 1.1 mJy at 5000 MHz) described in § 3.3. Using the same distance and volume ranges as above, we obtain $B_{\rm eq} = 82$–344 μG and a magnetic energy density ($B_{\rm eq}^2/8\pi$) range of (3–50) $\times 10^{-10}$ ergs cm^{-3}. We determine the photon energy density (u) due to the source itself using $u = 3LR/4cV$ (Wilson, Young, & Shopbell 2000), where R is the linear size of the source, and we use the approximation $R = (3V/4\pi)^{1/3}$. It should be noted that u is distance independent, and the main uncertainty in its determination is the opening angle of the cone that is used to estimate V. For opening angles of 1° and 7.°5, respectively, u is 6×10^{-12} and 4×10^{-13} ergs cm^{-3}. As these values are considerably less than the magnetic energy density, SSC should not be important. Inverse Compton from the interstellar radiation field (ISRF) and the cosmic microwave background (CMB) are also possibilities. However, the maximum ISRF photon energy density in the Galaxy is 2×10^{-11} ergs cm^{-3} (Strong, Moskalenko, & Reimer 2000),

and the CMB photon energy density is 3×10^{-13} ergs cm^{-3}, which are both considerably less than the magnetic energy density.

4.3. *Jet Deceleration*

The mean proper motion for the eastern jet between its ejection in 1998 September and the *Chandra* detections in 2000 of 32.9 mas day^{-1} derived above is greater than the proper motion of 21.2 ± 7.2 mas day^{-1} that we measure during 2000 June–September, indicating a reduction in the jet velocity. The 1998 September VLBI observations of the radio jets provide information consistent with a higher initial ejection velocity. Hannikainen et al. (2001) find that the separation between the two radio jets increases at a rate of 115 mas day^{-1}. Thus, with no additional information, we conclude that the initial proper motion for the eastern, approaching jet is at least 57.5 mas day^{-1}, indicating that the apparent jet velocity decreased by a factor of at least 2.7 ± 0.9. This also implies a drop in the actual jet velocity; however, the size of this drop depends on the distance to the source (d) and the angle between the jet axis and the line of sight (θ), and these quantities are not well constrained.

Although the jet does decelerate, the fact that we detect a proper motion for the X-ray jet is in contrast to the apparently stationary radio lobes that are seen in GRS 1758−258 (Rodríguez et al. 1992) and 1E 1740.7−2942 (Mirabel et al. 1992). However, the projected separation between XTE J1550−564 and the X-ray jet (0.31–0.85 pc for $d = 2.8$–7.6 kpc) is a reasonable fraction of the compact object/radio lobe separations in the other two sources (2.5 pc in GRS 1758−258 and 1.1 pc in 1E 1740.7−2942, assuming $d = 8.5$ kpc in both cases). Thus, the XTE J1550−564 X-ray jet may represent an intermediate stage in the evolution of the jet as the bulk motion velocity decreases from relativistic velocities to zero velocity.

Observations of AGNs suggest that their initially relativistic jets also decelerate as they move away from the core of the galaxy (Bridle et al. 1994). A model has been developed to explain jet deceleration where material in the ISM or intergalactic medium (IGM) is entrained into the jet (Bicknell 1994; Bowman, Leahy, & Komissarov 1996). As a consequence of momentum conservation, mass entrainment leads to deceleration of the jet. It is not clear if the XTE J1550−564 jet is entraining material, but even if it is not, elastic collisions between the jet and the ISM material will cause the jet to decelerate. The level of mass entrainment depends on how the jet pressure compares to the ISM gas pressure. The equipartition jet pressure ($p_{\rm eq} = B_{\rm eq}^2/4\pi$) for the XTE J1550−564 X-ray jet is between 10^{-9} and a few times 10^{-8} ergs cm^{-3} for the range of $B_{\rm eq}$ values derived above (134–566 μG assuming that the X-rays have a synchrotron origin). These values for $p_{\rm eq}$ are considerably larger than the values typically measured for the ISM, which are between 10^{-13} and 10^{-12} ergs cm^{-3} (Jenkins & Tripp 2001), and this may suggest that elastic collisions are more important than entrainment in causing the jet to decelerate. A related question is whether we are observing the motion of the bulk flow of material in the jet or the motion of a shock front. Although the latter is a possibility, further deceleration of the eastern X-ray jet is reported in Kaaret et al. (2002), indicating that a mechanism would be necessary to explain the deceleration of the shock.

It is also possible to derive the total internal energy for the X-ray–emitting electrons under the equipartition assumption. For the range of source distances and jet opening angles used above, we obtain energies between 5×10^{41} (for $d = 2.8$ kpc and an opening angle of 1°) and 3×10^{43} ergs (for $d = 7.6$ kpc and an opening angle of 7°.5). With the deceleration of the jet, it is interesting to consider whether the change in the bulk motion kinetic energy can account for the internal energy of the electrons. From the *Chandra* proper-motion measurement in 2000, the VLBI proper-motion lower limit in 1998, and the total mass of protons in the jet of 7×10^{20} g derived above for an assumed distance of 2.8 kpc and an assumed opening angle of 1°, we obtain a lower limit on the change in bulk motion kinetic energy (ΔKE) of 2×10^{41} ergs for $\theta = 43°$. For larger values of θ, which are probably more likely for XTE J1550−564, the lower limit on ΔKE increases gradually to 9×10^{41} ergs, which is nearly a factor of 2 larger than the internal electron energy. Although the internal electron energy estimates increase significantly with source distance and opening angle, for $d > 3$ kpc, there are nonzero values for θ that give initial jet velocities of c, leading to arbitrarily large values for ΔKE. We conclude that, for certain values of θ, the bulk motion kinetic energy is sufficient to power the observed X-ray emission for most, if not all, of the allowed distance range. However, it is important to note that this calculation assumes that the total mass of protons in the jet is constant. A significant level of entrainment from the ISM would invalidate this assumption.

4.4. *Observations of Quiescent Black Hole Transients*

The discovery of X-ray jets from XTE J1550−564 has implications for X-ray observations of black hole transients at low flux levels or in quiescence using observatories without sufficient angular resolution to separate the black hole flux from the jet flux. For example, if XTE J1550−564 was observed with *ASCA* or *BeppoSAX* during the times of our *Chandra* observations 2 and 3, the X-ray jet flux would significantly contaminate the black hole flux, but the X-ray jet would not be resolved as a result of the 1′–3′ angular resolution provided by these satellites. For XTE J1550−564, the measured X-ray jet fluxes are between 6×10^{-14} and 20×10^{-14} ergs cm^{-2} s^{-1} (0.3–8 keV), which is considerably brighter than five of the six black hole systems observed by *Chandra* in quiescence (Garcia et al. 2001). For the 1996 March *ASCA* observation of the microquasar GRO J1655−40 (Asai et al. 1998), it is conceivable that an X-ray jet was responsible for at least part of the detected flux. The *ASCA* observation was made about 1.5 yr after the discovery of powerful radio jets from this source (Tingay et al. 1995; Hjellming & Rupen 1995). In addition, although it was thought that GRO J1655−40 was in quiescence during the *ASCA* observation, the source flux was an order of magnitude lower during an observation made by *Chandra* in 2000 (Garcia et al. 2001). Finally, we note that if X-ray jet fluxes in other sources are similar to the level we observe for XTE J1550−564, they will not significantly contaminate the nonimaging measurements made by *RXTE* as the quality of the Proportional Counter Array background subtraction limits observations to sources brighter than a few times 10^{-12} ergs cm^{-2} s^{-1} (3–20 keV).

5. SUMMARY AND CONCLUSIONS

In this paper we present an analysis of *Chandra* observations and an ATCA radio observation of XTE J1550−564 made in 2000 where an X-ray jet is detected to the east of the black hole in the X-ray and radio bands. The discovery of the jet was first reported by Corbel et al. (2002b). The jet axis is aligned with the relativistic bipolar radio jets detected with VLBI in 1998 (Hannikainen et al. 2001). We argue that the material for the 2000 jet was likely ejected during the large X-ray and radio flare that occurred in 1998 (Wu et al. 2002) and that we detect the eastern jet (but not the western jet) during the 2000 observations because the eastern jet is the approaching jet. Although we do not detect a western jet for the 2000 observations, it is detected in the radio band (Corbel et al. 2002a) and X-ray (Kaaret et al. 2002) during observations made in 2002. In fact, this paper is a result of a reanalysis of the 2000 *Chandra* data that was prompted by the radio detection of the western jet.

A main result of this work is the measurement of the proper motion of the X-ray jet using three *Chandra* observations made between 2000 June and September. The X-ray jet moves away from XTE J1550−564 with a proper motion of 21.2 ± 7.2 mas day^{-1}, and these observations represent the first time that an X-ray jet proper-motion measurement has been obtained for any accretion-powered Galactic or extragalactic source. Comparing this value to the lower limit on the proper motion of the eastern jet from the 1998 VLBI observations of 57.5 mas day^{-1} indicates that the jet has decelerated since its initial ejection. Assuming that the source distance is in the range $d = 2.8$–7.6 kpc, the apparent jet velocity ($\beta_{\rm app}$) is between 0.34 ± 0.12 and 0.93 ± 0.32, and we obtain a lower limit on the actual X-ray jet velocity in 2000 of $\beta = 0.32 \pm 0.10$ that is independent of the angle between the jet axis and the line of sight (θ). There is evidence that the eastern jet is extended by $\pm 2''$–$3''$ in the direction of the proper motion. The upper limit on the source extension in the perpendicular direction is $\pm 1\farcs5$, which corresponds to a jet opening angle of less than $7\fdg5$.

We consider thermal bremsstrahlung, synchrotron, SSC, and inverse Compton mechanisms to explain the X-ray jet emission from XTE J1550−564. Assuming equipartition between the magnetic and electron energy densities, we derive a range of jet magnetic field strengths ($B_{\rm eq}$) between 134 and 566 μG, depending on the source distance and jet opening angles between 1° and $7\fdg5$. From $B_{\rm eq}$, the range of Lorentz factors (γ) for the electrons responsible for the 1 keV X-rays is $(1.2$–$2.7) \times 10^7$, and the range of synchrotron lifetimes (at 1 keV) is 6–60 yr. The mass of material required by a synchrotron mechanism could be accumulated in the likely jet ejection time of less than 2 days, while the mass required by a thermal bremsstrahlung mechanism is about 8 orders of magnitude higher, requiring mass from a very large number of ejection events. A comparison between the magnetic energy density in the jet and estimates for the photon density suggests that synchrotron emission should dominate over SSC and inverse Compton mechanisms. We conclude that a synchrotron mechanism is viable and appears to provide the simplest explanation for the observations. The synchrotron hypothesis can be tested via constraints on the optical or IR flux from the jet or by obtaining better constraints on X-ray emission line strengths.

With a projected separation of 0.31–0.85 pc between XTE J1550−564 and the jet in 2000, the XTE J1550−564 jet is intermediate in size to the 0.02–0.06 pc relativistic radio jets that have been detected in several sources (e.g., GRS 1915+105 and GRO J1655−40) and the stationary 1–3 pc radio lobes that have been seen in GRS 1758−258 and 1E 1740.7−2942. Further, the fact that the XTE J1550−564 jets decelerated between 1998 and 2000 provides an additional connection between the two types of jets that have been observed previously. It is likely that the deceleration occurs when the jet collides with the ISM. However, the jet pressure we derive from equipartition suggests that the pressure is too high to entrain material and that elastic collisions of the jet with ISM material may be a better way to model the jet evolution. More work is necessary to understand the details of the deceleration. Finally, studying the evolution of the XTE J1550−564 jet underscores the fact that jets in Galactic X-ray binaries can provide useful information about jets in AGNs. In XTE J1550−564, the timescale for material to travel the length of the jet is several years, while this process takes tens of thousands of years for a typical AGN.

J. A. T. and S. C. acknowledge useful conversations with participants of the 4th Microquasar Workshop in Corsica, especially A. Celotti, S. Heinz, and V. Dhawan. J. A. T. acknowledges useful conversations with G. Fossati, D. Fox, W. Heindl, R. Rothschild, and G. Burbidge. We thank *Chandra* director H. Tananbaum for granting Director's Discretionary Time for the August and September observations described in this work. R. W. was supported by NASA through Chandra Postdoctoral Fellowship grant PF9-10010 awarded by CXC, which is operated by SAO for NASA under contract NAS8-39073. P. K. acknowledges partial support from NASA grant NAG5-7405 and *Chandra* grant G01-2034X. J. A. T. acknowledges partial support from NASA grant NAG5-10886.

REFERENCES

Arnaud, K. A. 1996, in ASP Conf. Ser. 101, Astronomical Data Analysis Software and Systems V, ed. G. H. Jacoby & J. Barnes (San Francisco: ASP), 17
Asai, K., Dotani, T., Hoshi, R., Tanaka, Y., Robinson, C. R., & Terada, K. 1998, PASJ, 50, 611
Begelman, M. C., Blandford, R. D., & Rees, M. J. 1984, Rev. Mod. Phys., 56, 255
Bicknell, G. V. 1994, ApJ, 422, 542
Bowman, M., Leahy, J. P., & Komissarov, S. S. 1996, MNRAS, 279, 899
Bridle, A. H., Hough, D. H., Lonsdale, C. J., Burns, J. O., & Laing, R. A. 1994, AJ, 108, 766
Burbidge, G. R. 1956, ApJ, 124, 416
Cash, W. 1979, ApJ, 228, 939
Corbel, S., Fender, R., & Tzioumis, A. 2002a, IAU Circ. 7795
Corbel, S., et al. 2001, ApJ, 554, 43
———. 2002b, Science, 298, 196
Dhawan, V., Mirabel, I. F., & Rodríguez, L. F. 2000, ApJ, 543, 373
Fender, R. P., Garrington, S. T., McKay, D. J., Muxlow, T. W. B., Pooley, G. G., Spencer, R. E., Stirling, A. M., & Waltman, E. B. 1999, MNRAS, 304, 865
Freeman, P. E., Kashyap, V., Rosner, R., & Lamb, D. Q. 2002, ApJS, 138, 185
Garcia, M. R., McClintock, J. E., Narayan, R., Callanan, P., Barret, D., & Murray, S. S. 2001, ApJ, 553, L47
Hannikainen, D., Campbell-Wilson, D., Hunstead, R., McIntyre, V., Lovell, J., Reynolds, J., Tzioumis, T., & Wu, K. 2001, Ap&SS Supp., 276, 45
Hardcastle, M. J., Birkinshaw, M., & Worrall, D. M. 2001, MNRAS, 326, 1499
Hardcastle, M. J., Worrall, D. M., Birkinshaw, M., Laing, R. A., & Bridle, A. H. 2002, MNRAS, 334, 182
Harris, D. E., & Krawczynski, H. 2002, ApJ, 565, 244
Hjellming, R. M., & Rupen, M. P. 1995, Nature, 375, 464
Jenkins, E. B., & Tripp, T. M. 2001, ApJS, 137, 297

Kaaret, P., Corbel, S., Tomsick, J., Fender, R., Miller, J., Orosz, J., Tzioumis, T., & Wijnands, R. 2002, ApJ, 582, 945
Makishima, K., Maejima, Y., Mitsuda, K., Bradt, H. V., Remillard, R. A., Tuohy, I. R., Hoshi, R., & Nakagawa, M. 1986, ApJ, 308, 635
Marshall, H. L., Canizares, C. R., & Schulz, N. S. 2002, ApJ, 564, 941
Marshall, H. L., et al. 2001, ApJ, 549, L167
Migliari, S., Fender, R. P., & Méndez, M. 2002, Science, 297, 1673
Miller, J. M., et al. 2001, MNRAS, in press
Mirabel, I. F., & Rodríguez, L. F. 1994, Nature, 371, 46
Mirabel, I. F., Rodríguez, L. F., Cordier, B., Paul, J., & Lebrun, F. 1992, Nature, 358, 215
Orosz, J. A., et al. 2002, ApJ, 568, 845
Pacholczyk, A. G. 1970, Radio Astrophysics: Nonthermal Processes in Galactic and Extragalactic Sources (San Francisco: Freeman)
Press, W. H., Teukolsky, S. A., Vetterling, W. T., & Flannery, B. P. 1992, Numerical Recipes in FORTRAN: The Art of Scientific Computing (2d ed.; Cambridge: Cambridge Univ. Press)
Rodríguez, L. F., Mirabel, I. F., & Marti, J. 1992, ApJ, 401, L15
Rybicki, G. B., & Lightman, A. P. 1979, Radiative Processes in Astrophysics (New York: Wiley)
Safi-Harb, S., & Petre, R. 1999, ApJ, 512, 784
Seward, F., Grindlay, J., Seaquist, E., & Gilmore, W. 1980, Nature, 287, 806
Smith, D. A. 1998, IAU Circ. 7008
Sobczak, G. J., McClintock, J. E., Remillard, R. A., Levine, A. M., Morgan, E. H., Bailyn, C. D., & Orosz, J. A. 1999, ApJ, 517, L121
Stirling, A. M., Spencer, R. E., de la Force, C. J., Garrett, M. A., Fender, R. P., & Ogley, R. N. 2001, MNRAS, 327, 1273
Strong, A. W., Moskalenko, I. V., & Reimer, O. 2000, ApJ, 537, 763
Swank, J., Smith, E., & Markwardt, C. 2002, IAU Circ. 7792
Tingay, S. J., et al. 1995, Nature, 374, 141
Tomsick, J. A., Corbel, S., & Kaaret, P. 2001a, ApJ, 563, 229
Tomsick, J. A., Smith, E., Swank, J., Wijnands, R., & Homan, J. 2001b, IAU Circ. 7575
Weisskopf, M. C., Brinkman, B., Canizares, C., Garmire, G., Murray, S., & Van Speybroeck, L. P. 2002, PASP, 114, 1
Wilson, A. S., Young, A. J., & Shopbell, P. L. 2000, ApJ, 544, L27
Wu, K., et al. 2002, ApJ, 565, 1161
Yamauchi, S., Kawai, N., & Aoki, T. 1994, PASJ, 46, L109

4.7.3

X-Ray Emission from the Jets of XTE J1550-564.

Article publié dans :

Astrophys. J., 2003, 582, 945-953

Kaaret, P., Corbel, S., Tomsick, J. A., Fender, R., Miller, J. M., Orosz, J. A., Tzioumis, A. K., Wijnands, R..

The Astrophysical Journal, 582:945–953, 2003 January 10

X-RAY EMISSION FROM THE JETS OF XTE J1550−564

P. Kaaret,[1] S. Corbel,[2] J. A. Tomsick,[3] R. Fender,[4] J. M. Miller,[5,6] J. A. Orosz,[7] A. K. Tzioumis,[8] and R. Wijnands[5,6]

Received 2002 June 14; accepted 2002 September 3

ABSTRACT

We report on X-ray observations of the large-scale jets recently discovered in the radio and detected in X-rays from the black hole candidate X-ray transient and microquasar XTE J1550−564. On 2002 March 11, X-ray emission was detected 23″ to the west of the black hole candidate and was extended along the jet axis with an FWHM of 1.″2 and a full width at 10% of maximum intensity of 5″. The morphology of the X-ray emission matched well to that of the radio emission at the same epoch. The jet moved by $0.''52 \pm 0.''13$ between 2002 March 11 and June 19. The apparent speed during that interval was 5.2 ± 1.3 mas day^{-1}. This is significantly less than the average apparent speed of 18.1 ± 0.4 mas day^{-1} from 1998 to 2002, assuming that the jet was ejected in 1998 September, and indicates that the jet has decelerated. The X-ray spectrum is adequately described by a power law with a photon index near 1.8 subject to interstellar absorption. The unabsorbed X-ray flux was 3.4×10^{-13} ergs cm^{-2} s^{-1} in the 0.3–8 keV band in 2002 March and decreased to 2.9×10^{-13} ergs cm^{-2} s^{-1} in June. We also detect X-rays from the eastern jet in 2002 March and show that it has decelerated and dimmed since the previous detections in 2000.

Subject headings: black hole physics — stars: individual (XTE J1550−564) — stars: winds, outflows — X-rays: binaries

1. INTRODUCTION

Jets are a ubiquitous facet of accretion in systems ranging from young stellar objects, to Galactic X-ray binaries, to active galactic nuclei (AGNs). Many important questions regarding jet formation and propagation remain unanswered, and new data will likely be required to resolve them. Observations of systems within the Galaxy hold the great advantage that their evolution is rapid. Processes requiring millions of years in AGNs can unfold in a few years for stellar mass scale systems, so that the dynamics can be studied directly.

Corbel, Fender, & Tzioumis (2002a) and Corbel et al. (2002b) recently discovered a large-scale, relativistic radio and X-ray–emitting jet from the X-ray transient XTE J1550−564. The source is a Galactic black hole candidate, and the mass of the compact object is constrained to be 8–12 $M_\odot$ (Orosz et al. 2002). A superluminal jet ejection event had been previously observed from this source in the radio in 1998 September (Hannikainen et al. 2001) during a very bright X-ray outburst (Sobczak et al. 1999). Detection of the large-scale radio jet to the west of XTE J1550−564 led to a reanalysis of archival *Chandra* data and discovery of an X-ray jet to the east of XTE J1550−564 (Corbel et al. 2002b; Tomsick et al. 2002). This X-ray jet exhibits proper motion directly away from XTE J1550−564. Based on the angular separations and the measured proper motion, the most likely epoch of origin of these large-scale jets is near the major X-ray outburst that peaked on 1998 September 20 (Sobczak et al. 1999), and we adopt this date as the origin of the currently observed jets (Corbel et al. 2002b).

Discovery of the large-scale radio jet also led to new observations of XTE J1550−564 made with the *Chandra X-Ray Observatory* (Weisskopf et al. 2002), which are described here. The subarcsecond resolution of *Chandra* delivered by the High-Resolution Mirror Assembly (van Speybroeck et al. 1997) has allowed us to detect and resolve X-ray emission from the western jet. In addition, we have again detected the eastern jet. In the following, § 2 presents the new observation and source detections, § 3 contains our results on the spectrum, morphology, motion, and variability of the eastern jet, § 4 describes our new data on the western jet, and § 5 includes a few comments on the implications of these results.

[1] Harvard-Smithsonian Center for Astrophysics, 60 Garden Street, Cambridge, MA 02138; pkaaret@cfa.harvard.edu.
[2] Université Paris VII and Service d'Astrophysique, Centre d'Etudes de Saclay, F-91191 Gif-sur-Yvette, France.
[3] Center for Astrophysics and Space Sciences, Code 0424, University of California at San Diego, La Jolla, CA 92093-0424.
[4] Astronomical Institute "Anton Pannekoek," University of Amsterdam and Center for High Energy Astrophysics, Kruislaan 403, 1098 SJ Amsterdam, Netherlands.
[5] Center for Space Research, Massachusetts Institute of Technology, 77 Massachusetts Avenue, Cambridge, MA 02139.
[6] Chandra Fellow.
[7] Astronomical Institute, Utrecht University, Postbus 80000, 3508 TA Utrecht, Netherlands.
[8] Australia Telescope National Facility, Commonwealth Science and Industrial Research Organisation, P.O. Box 76, Epping, NSW 1710, Australia.

2. OBSERVATIONS AND SOURCE DETECTION

XTE J1550−564 was observed on 2002 March 11 and June 19 with the *Chandra X-Ray Observatory* (Weisskopf et al. 2002) using the Advanced CCD Imaging Spectrometer spectroscopy array (ACIS-S; Bautz et al. 1998) using Director's Discretionary Time in response to a Target of Opportunity request based on the discovery of the western radio jet (Corbel et al. 2002a) and a follow-up request made after discovery of X-ray emission from the western jet. For the March observation (observation ID [ObsID] 3448), a total of 26,118 s of useful exposure were obtained with the ACIS-S operated in a 1/4 subarray mode with only the S3 chip read out to minimize pileup

for XTE J1550−564, which was in the decay phase of a recent X-ray outburst and expected to be relatively bright during the observation. The roll angle of 68° placed the short axis of the field of view in the subarray mode nearly along the jet axis, but the useful field of view along that axis, ∼120″, was still adequate to image both jets. For the June observation (ObsID 3672), a total exposure of 18,025 s was obtained with the ACIS-S operated in the full array mode with six ACIS chips read out.

The data were subjected to the standard data processing (ASCDS v6.6.0 using CALDB v2.12), and then customary event processing and filtering procedures, from the Chandra Interactive Analysis of Observations (CIAO) software package v2.2.1, were applied to produce a level 2 event list. Light curves including all valid events on the S3 chip were constructed to search for times of high background. In both observations, the count rate appears uniform with no obvious flares.

Images of the region around XTE J1550−564 extended 120″ along the jet axis and 60″ perpendicular to the jet axis were constructed using photons in the energy band 0.3–7 keV. We searched for sources using *wavdetect* (Freeman et al. 2002), the wavelet-based source detection routine in CIAO. Four sources were detected at significances greater than 4 σ. One source is coincident with XTE J1550−564, and two others lie along the jet axis. The western jet was detected in both March and June, while the eastern jet was detected only in March. The fourth source, at R.A. = $15^{h}50^{m}53\overset{s}{.}05$, decl. = −56°29′02″.0 (J2000.0), does not lie along the jet axis and is identified with a relatively nearby K/M dwarf present in optical images of the field. A portion of the March image along the jet axis and containing XTE J1550−564 and its two jets is shown in Figure 1.

We adjusted the astrometry of each image so that the position of the source coincident with XTE J1550−564 matches the accurately measured radio position. A shift of 0″.76 was required for the March observation and a shift of 0″.22 for June. Both shifts are within the absolute astrometric accuracy of *Chandra*. The statistical error on the source positions is less than 0″.22 (1 σ) in all cases and less than 0″.1 for XTE J1550−564. However, care must be taken in comparing positions of the jet sources due to their finite extent as discussed below.

We defined source regions using ellipses with radii 4 times the radius of 50% encircled energy calculated from the observed photons for each source by *wavdetect*. The diameter of the ellipse for XTE J1550−564 is 3″.9, which is consistent with that expected for an on-axis point source (8 times the ∼0″.5 half-power radius for ACIS-I). We extracted counts for each source region and a corresponding background region. The exposure was calculated for a monochromatic beam of 1.5 keV. The exposure over the regions including XTE J1550−564 and the western jet is uniform to within 2%. The region including the eastern jet lies over a CCD node boundary, and the exposure is up to 15% lower. We translated the count rates to photon fluxes using the exposure, then to energy fluxes in the 0.3–7 keV band assuming a power-law spectrum with a photon index of 1.8 and a column density equal to the total Galactic column in the direction of XTE J1550−564, which we take to be $N_{\rm H} = 9.0 \times 10^{21}$ cm^{-2} based on radio measurements of the H I column density (Dickey & Lockman 1990) along the line of sight. This $N_{\rm H}$ value is consistent with the one measured by high-resolution X-ray spectroscopy of XTE J1550−564 by Miller et al. (2002). The properties of the three sources along the jet axis are listed in Table 1.

Below, we also include results from archival *Chandra* data. Observations with two-dimensional imaging are available for 2000 June 9, August 21, and September 11. These data and the analysis of the eastern jet are described in Tomsick et al. (2002). Each observation is brief with an exposure of no more than 5200 s. The 2000 June observation had a grating in place, while the others did not.

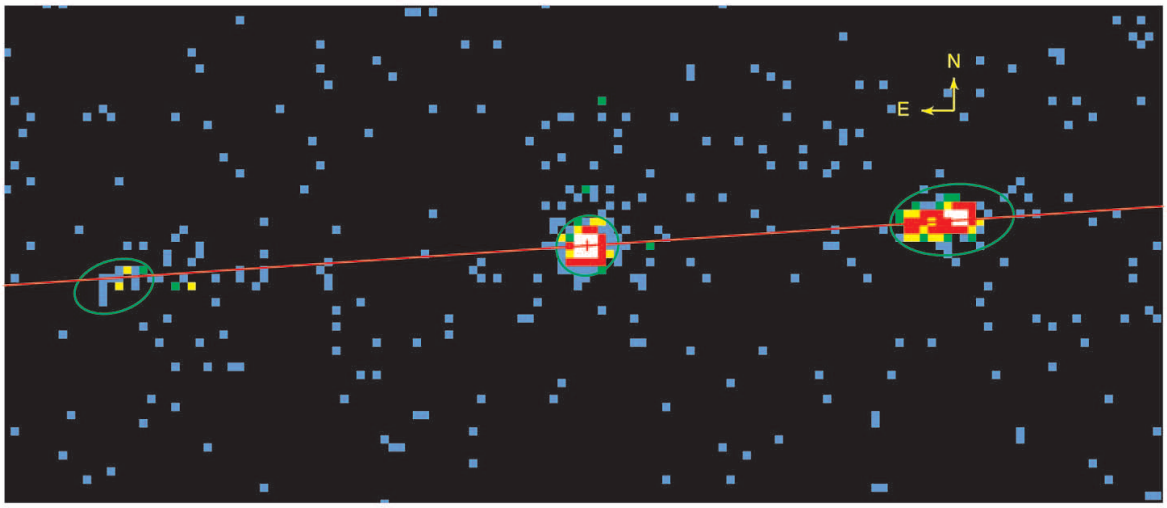

FIG. 1.—X-ray image of XTE J1550−564 for the 0.3–7 keV band taken on 2002 March 11. The color of each pixel represents the number of X-ray counts: black = 0 counts, blue = 1, green = 2, yellow = 3–4, red = 5–20, white = 21–330. The green ellipses are source regions and indicate detection of the western and eastern jets in addition to XTE J1550−564 itself. The red line is the axis of the superluminal jet emission at a position angle of −86°.1 (D. Hannikainen 2002, private communication). The arrows indicating north and east are 2″ long.

TABLE 1
X-RAY SOURCES NEAR XTE J1550−564

Date (1)	R.A. (2)	Decl. (3)	S/N (4)	Counts (5)	Flux (6)	Comments (7)
March	15 50 58.66	−56 28 35.2	334.3	1163.4	4.64	XTE J1550−564
June	15 50 58.66	−56 28 35.2	26.3	54.5	0.31	
March	15 50 55.97	−56 28 33.6	122.5	409.1	1.64	Western jet
June	15 50 55.90	−56 28 33.6	87.4	238.2	1.36	
March	15 51 02.16	−56 28 37.7	4.9	18.4	0.08	Eastern jet
June	...	...	...	...	...	Not detected

NOTE.—Units of right ascension are hours, minutes, and seconds, and units of declination are degrees, arcminutes, and arcseconds. Col. (1): Date of observation. Cols. (2) and (3): Position of the source in J2000.0 coordinates. Col. (4): Significance of the source detection as calculated by *wavdetect*. Col. (5): Net counts in the 0.3–7 keV band. Col. (6): Observed (absorbed) source flux in units of 10^{-13} ergs cm^{-2} s^{-1} in the 0.3–7 keV band calculated assuming a power-law spectrum with photon index of 1.8 and Galactic absorption. Col. (7): Comments on the sources. There are two rows for each source: one for the March observation and one for the June observation.

3. WESTERN JET

3.1. *Spectrum*

We extracted a spectrum for the western jet from the March observation using CIAO tools and applied the recent correction for the low-energy quantum efficiency degradation of the ACIS. We fitted the spectrum using XSPEC (see Fig. 2). The spectrum is adequately fitted with a power-law model with absorption by material with solar abundances. With the equivalent hydrogen absorption column density fixed to $N_{\rm H} = 9.0 \times 10^{21}$ cm^{-2}, the best-fit photon index is $\Gamma = 1.77$ and the allowed range at 90% confidence is 1.61–1.93 ($\Delta\chi^2 = 2.7$ for one parameter). The absorbed flux is $(1.9 \pm 0.1) \times 10^{-13}$ ergs cm^{-2} s^{-1} in the 0.3–8 keV band, and unabsorbed flux would then be 3.4×10^{-13} ergs cm^{-2} s^{-1} in the same band.

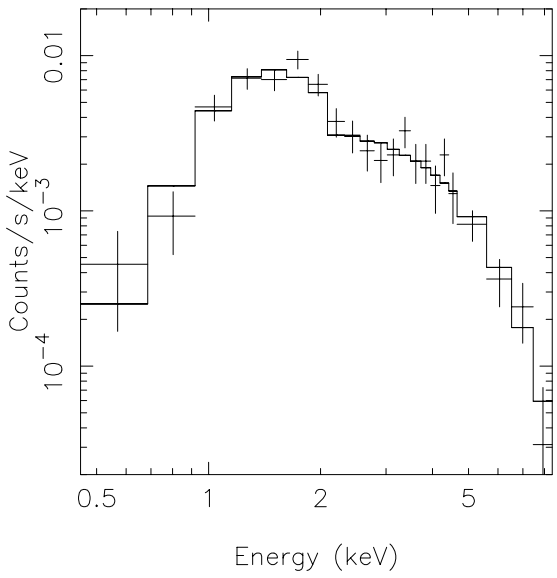

FIG. 2.—X-ray spectrum of emission from the western jet in the March observation. The curve is the best-fit power-law model with absorption fixed to the Galactic value.

Allowing the absorption column density to vary leads to an allowed range of $N_{\rm H} = (7.9\text{–}14.7) \times 10^{21}$ cm^{-2} at 90% confidence ($\Delta\chi^2 = 4.6$ for two parameters) and a corresponding range of 1.58–2.37 for the photon index. The best-fit values are $N_{\rm H} = 10.9 \times 10^{21}$ cm^{-2} and $\Gamma = 2.00$. The allowed $N_{\rm H}$ range includes the Galactic H I value. We cannot exclude extra absorption using the X-ray data.

For the June observation, the spectrum is, again, adequately fitted with a power-law model with absorption. With $N_{\rm H} = 9.0 \times 10^{21}$ cm^{-2}, the best-fit photon index is $\Gamma = 1.77$ and the allowed range at 90% confidence is 1.52–2.02. The spectrum in June appears consistent with that measured in March. The absorbed flux is $(1.6 \pm 0.1) \times 10^{-13}$ ergs cm^{-2} s^{-1} in the 0.3–8 keV band, and the unabsorbed flux is 2.9×10^{-13} ergs cm^{-2} s^{-1} in the same band.

Since there is no evidence of spectral variability, we fitted the two data sets simultaneously to obtain better constraints on the fit parameters. With $N_{\rm H} = 9.0 \times 10^{21}$ cm^{-2}, the best-fit photon index is $\Gamma = 1.77$ and the allowed range at 90% confidence is 1.64–1.90. Allowing the absorption column density to vary leads to $N_{\rm H} = (9.9^{+2.9}_{-2.2}) \times 10^{21}$ cm^{-2} and $\Gamma = 1.87 \pm 0.31$ at 90% confidence ($\Delta\chi^2 = 4.6$ for two parameters).

In addition to the nonthermal power-law model, we also fitted the combined data with the MEKAL model, which is appropriate for thermal emission from hot diffuse gas. With $N_{\rm H}$ fixed to the Galactic value, an adequate fit was obtained with $kT = 5.6^{+2.2}_{-1.1}$ keV. A simple thermal bremsstrahlung model gives a similar temperature range, $kT = 6.1^{+2.5}_{-1.5}$ keV. No prominent line emission is observed. However, the limits on the equivalent width are not strongly constraining (varying from 100 eV to 1.3 keV at 90% confidence [$\Delta\chi^2 = 2.7$] for a narrow line with energy in the range 3–7 keV).

3.2. *Morphology and Motion*

The X-ray counterpart of the western jet appears extended. Figure 3 shows the X-ray images from both *Chandra* observations with radio contours obtained from observations made on 2002 January 29 using the Australian Telescope Compact Array (ATCA; Corbel et al. 2002b) superimposed on the 2002 March 11 *Chandra* data. The ATCA image of the compact source XTE J1550−564 appears extended along a northwest-southeast axis as a result of partial synthesis caused by the limited parallactic

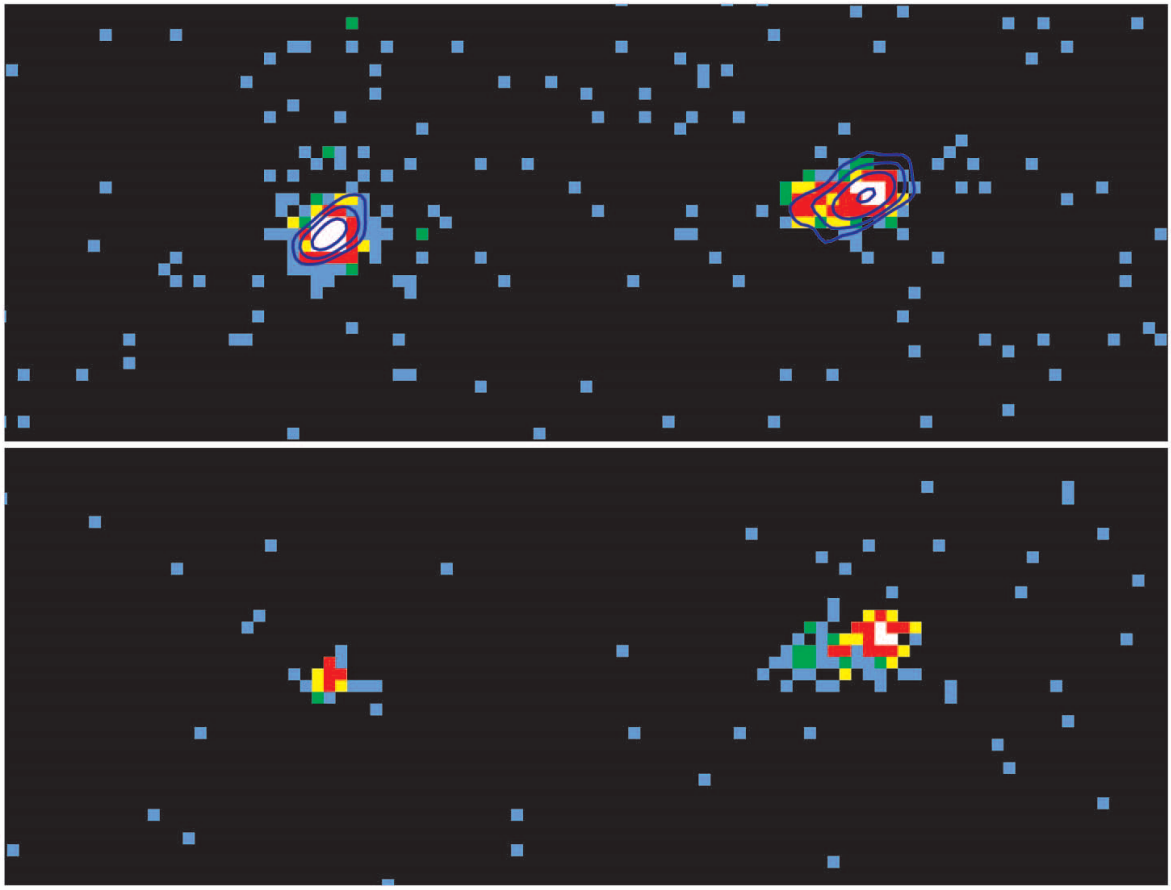

FIG. 3.—X-ray images of XTE J1550−564 (on the left) and the western jet (on the right). The top panel is from the 2002 March 11 observation, and the bottom panel is from the 2002 June 19 observation. The X-ray data are for the 0.3–7 keV band, and the color scale and orientation are the same as in Fig. 1. The top panel has radio contours (*dark blue curves*) from an observation on 2002 January 29 superimposed. The contour levels are 0.2, 0.4, 0.8, and 1.6 mJy.

angle coverage with the linear ATCA array. However, in addition to the extent caused by partial synthesis, there is a true, physical extent to the western radio jet. The peak of the jet emission is toward the west (away from XTE J1550−564), and there is lower intensity emission extending to the east, back toward XTE J1550−564. The morphology of the X-ray source closely matches that of the radio source.

We define the jet axis using the positions of the X-ray sources corresponding to XTE J1550−564 and the western jet, as reported in Table 1. The resulting position angle is $-85\overset{\circ}{.}9 \pm 1\overset{\circ}{.}3$, in good agreement with the position angle of $-86\overset{\circ}{.}1 \pm 0\overset{\circ}{.}8$ reported for the superluminal jets (D. Hannikainen 2002, private communication) and with the position angle of $-85\overset{\circ}{.}8 \pm 1\overset{\circ}{.}0$ reported for the radio western jet (Corbel et al. 2002b). To determine if the jet tails lie along the jet axis, we calculated the average azimuthal angle for events between 2″ and 6″ from the western jet position and within ±40° in azimuth of a vector pointing back to XTE J1550−564. The average azimuthal angle is $2\overset{\circ}{.}2 \pm 1\overset{\circ}{.}9$ for the March data and $7\overset{\circ}{.}4 \pm 3\overset{\circ}{.}2$ for the June data. The tail of the western jet appears aligned with the jet axis in the March data but may be slightly skewed to the south in the June data. However, the skew is only marginally statistically significant and may be affected by uncertainty in the true position of the jet peak, discussed below.

To study the morphology and motion of the X-ray jet, we decomposed the image along axes parallel and perpendicular to the jet axis (as defined above). We calculated the displacement of each X-ray event parallel and perpendicular to this axis. Figure 4 shows the profile of X-ray counts along the jet axis from the two observations. All photons with energies in the range 0.3–7 keV and within 2″ of the jet axis in the perpendicular direction are included. In the March data, both jets are clearly present. In the June data, there is no strong source at the location of the eastern jet, but there may be some diffuse emission above the background level. The western jet appears to have moved away from XTE J1550−564.

For the March observation, the peak of the X-ray emission of the western jet is displaced by 0″.6 (along the jet axis and away from XTE J1550−564) from the position reported in Table 1, which is the centroid over the region containing 50% of the encircled energy (Freeman et al. 2002). Hence,

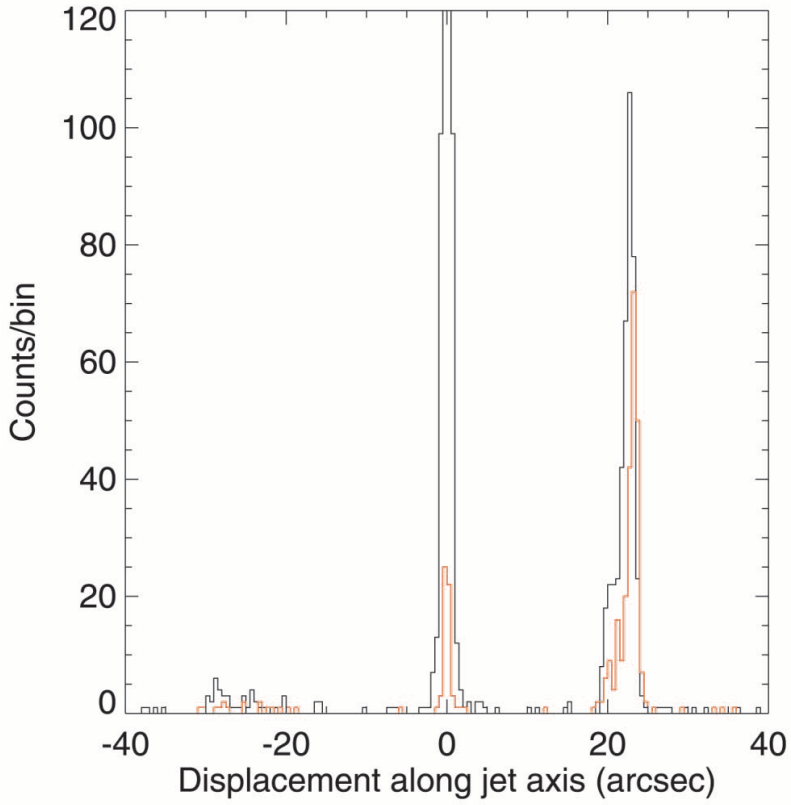

FIG. 4.—Distribution of X-ray counts along the jet axis. The black line is for the March observation, and the red line is for the June observation. The bin size is 0″.5.

caution is warranted when comparing the jet position to positions found in other observations.

To measure the relative position of the western jet in the March and June observations, we used a Kolmogorov-Smirnov (K-S) test to permit comparison of unbinned position data. We used the position along the jet axis for each event calculated above. We added an offset, in the range from $-1''$ to $+1''$, to the June event positions and then compared the offset positions with the March event positions within $\pm 8''$ of the western jet peak. The best match occurred for an offset of 0″.52. Given this offset, the K-S test gives a 61% probability that the two samples are drawn from the same parent distribution. To evaluate the uncertainty in the offset, we integrated the K-S test probability distribution as a function of offset and found the offsets corresponding to 5% and 95% of the full integral (i.e., the 90% confidence interval). These are 0″.39 and 0″.60. The hypothesis that the two distributions are the same with zero offset is rejected at the level of 5×10^{-13}. The western jet moved by $0''.52 \pm 0''.13$ between the March and June observations.

The morphology of the western jet does not appear to have changed, even though it moved. Figure 5 shows the western jet profiles along the jet axis from the March and June observations, with the June data shifted by 0″.52 and scaled so that the peaks match. As noted above, a K-S test is consistent with the two profiles being the same.

The figure also shows the data for XTE J1550−564 itself from the March observation, rescaled and displaced to match the peak at the western jet. From its time variability, we know that the X-ray emission from XTE J1550−564 must arise from what is effectively a point source for the angular resolution of *Chandra*. Hence, we use XTE J1550−564 as a calibration of the point-spread function for the observation to determine the spatial extent of the emission from the western jet. This procedure accounts for any aspect jitter during the observation and also for any source extent induced by scattering of the X-rays in the interstellar medium (ISM) between us and the source. The spectrum of XTE J1550−564 during the March observation is quite similar to that found for the western jet, so effects due to the energy dependence of the *Chandra* point-spread function should be negligible. Both sources are sufficiently close to the aim point so that the degradation of the *Chandra* point-spread function off-axis should also be negligible.

Comparison of the rescaled profile of XTE J1550−564 with the profile of the X-ray emission from the western jet in the March observation shows that the western jet is extended. The leading edge of the X-ray source (the edge away from XTE J1550−564) is approximately consistent with the profile of a point source. The trailing edge is clearly extended. The FWHM of the source is 1″.2, and the full width at 10% of maximum intensity is 5″.

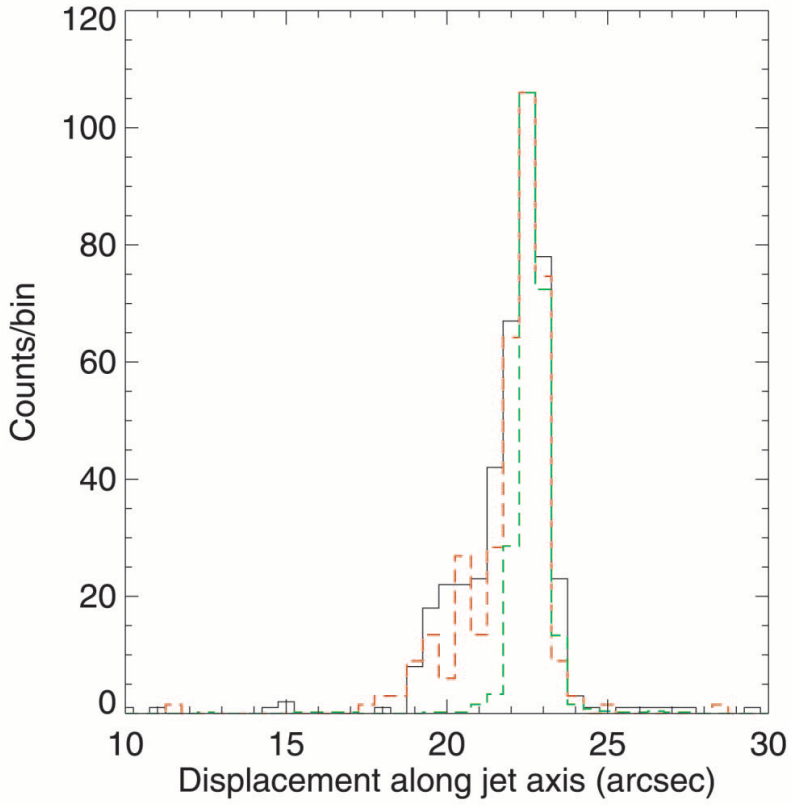

FIG. 5.—Distribution of X-ray counts in the western jet along the jet axis. The black solid line is for the March observation, the red dashed line is for the June observation, and the green dashed line is the profile of XTE J1550−564 from March. The latter two profiles have been shifted and rescaled to match the peak of the first. The bin size is 0.″5.

Figure 6 shows the distribution of X-ray counts perpendicular to the displacement axis for the western jet and XTE J1550−564 in the March data. We used X-rays with energies in the range 0.3–7 keV and with displacements along the jet axis of up to ±5″ from the respective source position as reported in Table 1. A K-S test shows that the two distributions are inconsistent at the 97% confidence level (2.2 σ). The western jet may be slightly extended perpendicular to the jet axis, but the evidence is weak. Deconvolving, assuming that the physical width adds in quadrature with the instrumental width, we place an upper limit of 0.″8 (FWHM) on the extent of the X-ray western jet perpendicular to the jet axis. The perpendicular distribution of the western jet found from the June data is consistent with that in the March data. The X-ray western jet is clearly much more extended along the jet axis than perpendicular to it.

3.3. *Variability*

To investigate the variability of the X-ray western jet, we examined archival *Chandra* data on XTE J1550−564 from 2000 June, August, and September. Using a large region extending ±4″ perpendicular to the jet axis and covering the full extent of the western jet beginning 11″ from XTE J1550−564 and extending 2″ beyond its position in 2002, we find no evidence for X-ray emission from the western jet in any of the archival observations with upper limits (2 σ) on the ACIS counting rate, which are fractions of 0.10–0.16 of the counting rate in our 2002 March data. Combining the 2000 August and September observations, in which the ACIS was not partially blocked by a grating, we find 6 counts in a total exposure of 9557 s. Given a mean of 6, the 90% confidence upper bound from a Poisson distribution is 9 counts, leading to a 90% confidence upper bound on the count rate from the western jet of 0.00094 counts s^{-1}. This is 6% of the rate in the 2002 March observation, corresponding to an upper bound on the absorbed flux (assuming identical spectral parameters) of 1.1×10^{-14} ergs cm^{-2} s^{-1} in the 0.3–8 keV band. This analysis assumes that none of the counts are due to background. Performing a background subtraction would reduce this limit.

During 2002, the flux decayed between March and June. Using the two flux measurements to calculate the $1/e$-folding time for an exponential decay, we find 327 ± 95 days. However, two data points are insufficient to determine the shape of light-curve decay.

4. EASTERN JET

The new *Chandra* observations add one additional detection to the results presented in Tomsick et al. (2002). The

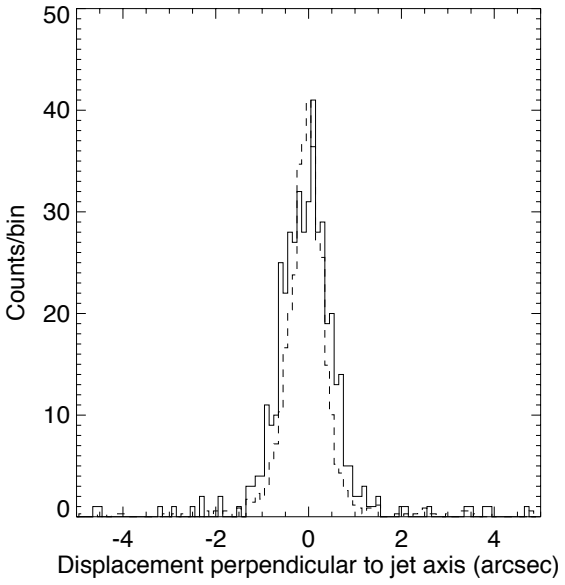

FIG. 6.—Distribution of X-ray counts perpendicular to the jet axis from the 2002 March observation. The solid line is for the western jet. The dashed line is the profile of XTE J1550−564 rescaled to match the peak of emission in the western jet. The bin size is 0″.1.

source contains far fewer counts than the western jet, and so we concentrate on the position and flux of the source.

The proper motion of the eastern jet is shown in Figure 7. The figure includes the three data points from Tomsick et al. (2002) and our new data point for 2002 March 11. Tomsick et al. (2002) showed that the apparent velocity of the eastern jet in 2000 was lower than the minimum velocity allowed during the superluminal ejection (Hannikainen et al. 2001), thus indicating that the eastern jet has decelerated. The 2002 March point is inconsistent with an extrapolation of the velocity measured from the 2000 data and indicates that this deceleration has continued.

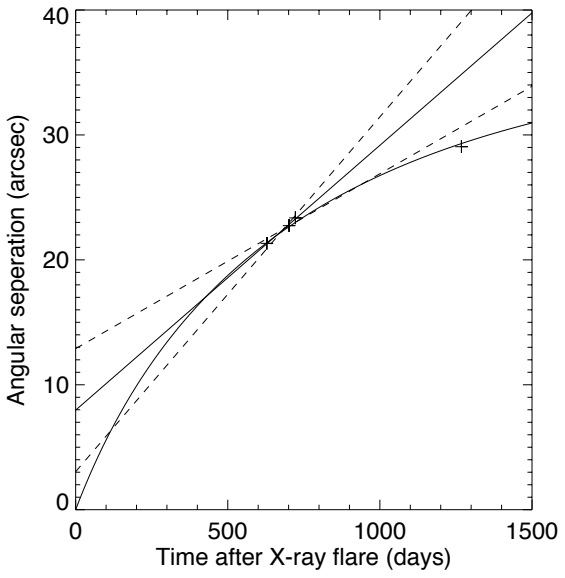

FIG. 7.—Position of the centroid of the X-ray eastern jet vs. time. The solid line is the fit to the proper motion in the 2000 data found by Tomsick et al. (2002). The dashed line indicates the uncertainty in the fit parameters. The solid curve is a decelerating jet model fit described in the text.

We fitted the proper motion data with a model in which the jet has a deceleration proportional to its velocity relative to the X-ray binary (which we assume to be roughly at rest relative to the ISM). The velocity profile is then a decaying exponential, and the observed position evolution is modified by light-travel delays. Our model has three fitted parameters: the initial jet speed divided by the speed of light β_0, the timescale ($1/e$-folding time) for the velocity decay τ, and the jet angle relative to the line of sight θ. The assumed source distance affects the fitted parameters. For a source distance of 4 kpc, we find an adequate fit (shown in Fig. 7) with $\beta_0 = 0.94$, $\tau = 1030$ days, and $\theta = 62°$. For source distances larger than 5.1 kpc, the best-fit initial speed is larger than the speed of light. However, we do not consider this a constraint on the distance as the model is rather ad hoc. For a distance of 3 kpc, the best fit is $\beta_0 = 0.82$, $\tau = 960$ days, and $\theta = 50°$. Both of these fits are consistent with the lower bound on the initial jet speed from the VLBI observations (Hannikainen et al. 2001).

Figure 8 shows the time variation of the X-ray flux of the eastern jet. The first three points are from Tomsick et al. (2002). For consistency with that analysis, we found the fluxes for the 2002 March data using a circular extraction region of 4″ radius centered on the *wavdetect* position and with an annulus with an inner radius of 5″ and an outer radius of 18″ for background estimation. We used a power-law model with photon index fixed to 1.8 and an absorption column density fixed to 9×10^{21} cm^{-2} and corrected for the degradation in the low-energy quantum efficiency of the

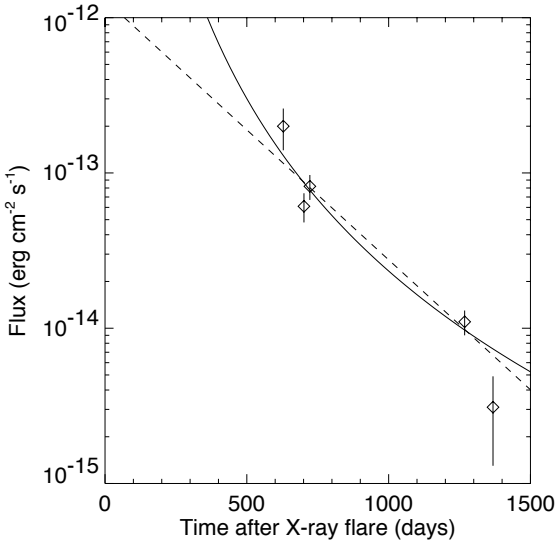

FIG. 8.—X-ray flux of the eastern jet vs. time. The curves are the power-law (*solid curve*) and exponential (*dashed curve*) decays described in the text.

ACIS. The absorbed flux in the 0.3–8 keV band was $(1.1 \pm 0.3) \times 10^{-14}$ ergs cm^{-2} s^{-1}. For June, no source was detected by *wavdetect* at the location of the western jet. We extracted counts from a circular region 4″ radius centered at the position found in March. This region is sufficiently large to include most of the diffuse emission apparent in Figure 4. With spectral parameters fixed as above, the absorbed flux in the 0.3–8 keV band is $(3 \pm 2) \times 10^{-15}$ ergs cm^{-2} s^{-1}. We interpret this number as an upper limit on the jet flux in June.

We fitted both an exponential decay and a power-law decay to the flux data. The power-law decay provides a slightly better fit, but both fits are acceptable. The index of the power-law decay is 3.7 ± 0.7. The $1/e$-folding time of the exponential decay is 260 ± 50 days. The extrapolated flux at the origin of the jet for the exponential decay would be $(1.3 \pm 0.5) \times 10^{-12}$ ergs cm^{-2} s^{-1} in the 0.3–8 keV band. This is a small fraction of the X-ray fluxes measured during the 1998 outburst. Hence, the available X-ray data are not inconsistent with an exponential decline of flux since the origin of the eastern X-ray jet.

5. DISCUSSION

The discovery of extended radio and X-ray emission from XTE J1550−564 (Corbel et al. 2002b; Tomsick et al. 2002; results reported here) represents the first detection of large-scale relativistic jets from a Galactic black hole candidate in both radio and X-rays. These large-scale jets appear to arise from a relatively brief jet injection episode (Corbel et al. 2002b) and, therefore, offer a unique opportunity to study the large-scale evolution of an impulsive jet event.

In the following, we assume that both jets were created in a single injection episode in 1998 September. The assumption is motivated by the detection of superluminal jets (Hannikainen et al. 2001) following an extremely large X-ray flare in 1998 September and the absence of any other X-ray flare of similar magnitude in continual X-ray monitoring from 1996 to 2002 (Corbel et al. 2002b). The eastern jet appears to be the approaching jet based on its larger current separation from XTE J1550−564 (Corbel et al. 2002b). The distance to XTE J1550−564 is constrained from optical observations to be in the range 2.8–7.6 kpc with a favored value of 5.3 kpc (Orosz et al. 2002).

We detected X-ray emission from the western jet on 2002 March 11 (MJD 52,344) at a separation of 23″ from the black hole candidate, implying a projected physical separation of 0.59 pc$(d/5.3$ kpc$) = 1.8 \times 10^{18}$ cm$(d/5.3$ kpc) and a mean projected speed of 18.1 ± 0.4 mas day^{-1} or $0.55c(d/5.3$ kpc). From the motion of the jet between March 11 and June 19, we calculate an average speed at that epoch of 5.2 ± 1.3 mas day^{-1} or $(0.16 \pm 0.04)c(d/5.3$ kpc). This is significantly less than the average speed from 1998 to 2002 and indicates that the jet has decelerated. Our detection of motion in the western jet argues against it having reached a termination. The jet appears to have a relativistic bulk velocity.

The angular size of the X-ray emission perpendicular to the jet axis in the western jet is quite small, less than 0.″8 (FWHM), placing an upper bound on the jet half opening angle of 1.°0. The opening angle is small, similar to the half opening angles of Fanaroff-Riley class II (FR II; Fanaroff & Riley 1974) sources, which are less than 3° (Muxlow & Garrington 1991). The angular size of the western X-ray jet perpendicular to the jet axis limits the expansion velocity to less than $0.01c(d/5.3$ kpc). At the same epoch, the eastern jet has a projected physical separation of 0.75 pc$(d/5.3$ kpc).

For comparison with the properties of the western jet, we review the properties of the eastern jet at the same angular separation. From the linear fit in Tomsick et al. (2002), we find that the eastern jet passed through a separation of 23″ on MJD $51,785 \pm 16$. Fortuitously, this is consistent with the times of the 2000 August 21 and September 11 *Chandra* observations (the separations from both of those observations are consistent with 23″). As discussed in Tomsick et al. (2002), the high proper motion of the eastern jet when at a separation of 23″ argues strongly against it having reached a termination at that point. The continued motion of the eastern jet to larger separations demonstrated here reinforces this argument. At a separation of 23″, the apparent speed of the eastern jet was 21.2 ± 7.2 mas day^{-1} and the absorbed flux was $(7.2 \pm 1.0) \times 10^{-14}$ ergs cm^{-2} s^{-1} in the 0.3–8 keV band. The western (receding) jet flux at the same separation was a factor of 2.6 ± 0.4 higher than the eastern (approaching) jet flux.

The X-ray data provide measurements of the local apparent speed at equal angular separations from the origin for the approaching and receding jets. If the jets are symmetric, in terms of their velocity profiles, then it would be possible to use relativistic kinematics (Mirabel & Rodríguez 1999) to constrain the jet true speed β, inclination to the line of sight θ, and distance d. We find that $\beta \cos\theta = 0.61 \pm 0.13$ and $d = (12.6 \pm 4.4) \tan\theta$ kpc under the assumption that the jet propagation is symmetric. This would imply that the inclination angle $\theta \leq 61°$ and the jet speed $\beta \geq 0.48$ (allowing for the uncertainty in $\beta \cos\theta$).

However, the fact that the western (receding) jet is brighter than the eastern (approaching) jet argues against symmetric jet propagation. For symmetric jet propagation, the ratio of observed flux densities measured at equal separations from the core for a twin pair of optically thin isotropically emitting jets is

$$\frac{S_a}{S_r} = \left(\frac{1 + \beta\cos\theta}{1 - \beta\cos\theta}\right)^{k-\alpha}, \qquad (1)$$

where S_a is the approaching flux density, S_r is the receding flux density, β is the jet speed divided by the speed of light, θ is the jet inclination angle, α is the spectral index of the emission defined so that $S_\nu \propto \nu^\alpha$, and k is a parameter that is 2 for a continuous jet and 3 for discrete condensations (Mirabel & Rodríguez 1999). If the exponent $k - \alpha > 0$, then the approaching jet must always be brighter than the receding jet measured at the same angular separation from the core. Given the photon index quoted above (allowing the absorption to vary) and allowing a continuous jet, the minimum allowed value for the exponent is 2.6, which is well above zero. Hence, the observed brightness ratio $S_a/S_r = 0.38 \pm 0.05$ is inconsistent with symmetric jet propagation. However, because the X-ray jet detections occurred well after the initial jet ejection, we cannot independently constrain the jet ejection, which may have been symmetric.

Large intrinsic asymmetries have been observed in the radio for the jets from the microquasar GRO J1655−40 (Hjellming & Rupen 1995). Which of the two jets was brighter differed from day to day, while the kinematics of the jet propagation appeared symmetric. Asymmetries of similar magnitude could explain the ratio of X-ray fluxes

from the jets of XTE J1550−564 if the jet inclination angle is high. In this case, the X-ray emissivity of the western jet would need to be low early on, to be consistent with the nondetection in 2000, and then increase sharply at later times, to be consistent with the flux measured in 2002. Such an X-ray emissivity profile could be produced by, e.g., internal shocks produced by a faster plasmon overtaking a slower one. This would require reacceleration of particles in the jet long after its initial ejection.

Alternatively, the emission from the jets could be produced by shocks arising from interactions of the jets with the ISM. The jets appear to be moving with speeds much greater than the sound speed of the ISM. In this case, the supersonic motion of the jet should produce a shock wave. The shock will be strongest at the head of the jet and weaken around the sides of the jet (De Young 2002). This morphology matches that observed for the eastern jet. In this case, the asymmetry between the two jets may reflect nonuniformity in the ISM. If the western jet is propagating into a denser medium, it would be brighter and would have decelerated more than the eastern jet. Interaction of a relativistic plasmon with the ISM appears to consistently describe all of the available data on the large-scale jets of XTE J1550−564.

Continued observation of the jets of XTE J1550−564 offers an exciting opportunity to study the dynamics of relativistic jets on timescales inaccessible for AGN jets. New, deep observations of XTE J1550−564 will allow us to study the deceleration and evolution of the morphology, flux, and spectrum of the western jet. This may help determine whether the observed jets are due to the internal interactions of relativistic plasmons or to external interactions with the ISM. A deep observation may also permit a new detection of the eastern jet, which would further constrain its deceleration and decay. Finally, continued monitoring may eventually show the termination of the jets.

We thank Harvey Tananbaum for granting the DDT observations, Joy Nichols for exceptionally rapid processing of the data, and the CXC team for successfully executing the observation. P. K. thanks Heino Falcke, Dan Harris, and David De Young for useful discussions and acknowledges partial support from NASA grant NAG5-7405 and *Chandra* grant G01-2034X. R. W. was supported by NASA through *Chandra* Postdoctoral Fellowship grant PF9-10010 awarded by CXC, which is operated by SAO for NASA under contract NAS8-39073.

REFERENCES

Bautz, M. W., et al. 1998, Proc. SPIE, 3444, 210
Corbel, S., Fender, R., & Tzioumis, A. 2002a, IAU Circ. 7795
Corbel, S., Fender, R. P., Tzioumis, T., Tomsick, J. A., Orosz, J. A., Miller, J. M., Wijnands, R., & Kaaret, P. 2002b, Science, 298, 196
De Young, D. S. 2002, The Physics of Extragalactic Radio Sources (Chicago: Univ. Chicago Press)
Dickey, J. M., & Lockman, F. J. 1990, ARA&A, 28, 215
Fanaroff, B. L., & Riley, J. M. 1974, MNRAS, 167, 31P
Freeman, P. E., Kashyap, V., Rosner, R., & Lamb, D. Q. 2002, ApJS, 138, 185
Hannikainen, D., Campbell-Wilson, D., Hunstead, R., McIntyre, V., Lovell, J., Reynolds, J., Tzioumis, T., & Wu, K. 2001, Ap&SS Supp., 276, 45
Hjellming, R. M., & Rupen, M. P. 1995, Nature, 375, 464
Miller, J. M., et al. 2002, MNRAS, in press
Mirabel, I. F., & Rodríguez, L. F. 1999, ARA&A, 37, 409
Muxlow, T. W. B., & Garrington, S. T. 1991, in Beams and Jets in Astrophysics, ed. P. A. Hughes (Cambridge: Cambridge Univ. Press), 52
Orosz, J. A., et al. 2002, ApJ, 568, 845
Sobczak, G. J., McClintock, J. E., Remillard, R. A., Levine, A. M., Morgan, E. H., Bailyn, C. D., & Orosz, J. A. 1999, ApJ, 517, L121
Tomsick, J. A., Corbel, S., Fender, R. P., Miller, J. M., Orosz, J. A., Tzioumis, T., Wijnands, R., & Kaaret, P. 2002, ApJ, 582, 933
van Speybroeck, L. P., et al. 1997, Proc. SPIE, 3113, 89
Weisskopf, M. C., Brinkman, B., Canizares, C., Garmire, G., Murray, S., & Van Speybroeck, L. P. 2002, PASP, 114, 1

4.7.4

A transient large-scale relativistic radio jet from GX 339-4.

Article publié dans :

Mon. Not. R. Astron. Soc., 2004, 347, L52-L56

Gallo, E., Corbel, S., Fender, R. P., Maccarone, T. J., Tzioumis, A. K.

Mon. Not. R. Astron. Soc. **347,** L52–L56 (2004)

A transient large-scale relativistic radio jet from GX 339−4

E. Gallo,[1⋆] S. Corbel,[2] R. P. Fender,[1] T. J. Maccarone[1] and A. K. Tzioumis[3]

[1]*Astronomical Institute 'Anton Pannekoek' and Center for High Energy Astrophysics, University of Amsterdam, Kruislaan 403, 1098 SJ Amsterdam, the Netherlands*

[2]*Université Paris VII and Service d'Astrophysique (Fédération APC), CEA-Saclay, 91191 Gif-sur-Yvette, France*

[3]*Australia Telescope National Facility, CSIRO, Post Office Box 76, Epping NSW 1710, Australia*

Accepted 2003 November 18. Received 2003 November 17; in original form 2003 October 6

ABSTRACT

We report on the formation and evolution of a large-scale, synchrotron-emitting jet from the black hole candidate and X-ray binary system GX 339−4. In 2002 May, the source moved from a low/hard to a very high X-ray state, contemporaneously exhibiting a very bright optically thin radio flare. Further observations with the Australia Telescope Compact Array have tracked the formation of a collimated structure extending to about 12 arcsec, with apparent velocity greater than $0.9c$. The luminosity of the outflow seems to be rapidly decreasing; these observations confirm that transient large-scale jets are likely to be common events triggered by X-ray state transitions in black hole X-ray binaries.

Key words: accretion, accretion discs – binaries: general – ISM: jets and outflows – radio continuum: stars – X-rays: stars – X-rays: individual: GX 339−4.

1 INTRODUCTION

The X-ray binary GX 339−4 comprises a compact primary which is a strong black hole candidate (BHC), with a mass function of 5.8 $\pm$ 0.5 $M_{\odot}$ (Hynes et al. 2003) and a secondary which is likely to be an evolved low mass star (Shahbaz, Fender & Charles 2001; Chaty et al. 2002). The system has an orbital period of 1.75 d (Hynes et al. 2003) and is located at a distance of at least 4 kpc (Zdziarski et al. 1998; see also Shahbaz et al. 2001; Maccarone 2003), with an orbital inclination of less than 60° to the line of sight, as inferred from the lack of eclipses (Cowley et al. 2002). GX 339−4 has been a key source in our understanding of the relation between accretion and the production of relativistic jets. It was the first BHC to reveal a positive correlation between radio and X-ray fluxes in the low/hard X-ray state (Hannikainen et al. 1998; later quantified by Corbel et al. 2003), and to demonstrate an association between the 'quenching' of core radio emission and the transition to a high/soft X-ray state (Fender et al. 1999b; see, for example, Done 2001 for a review on X-ray states and Fender 2004 for a comparison of radio and X-ray behaviour in Galactic BHCs). After spending almost three years in 'quiescence', GX 339−4 re-brightened in X-rays at the end of 2002 March (Smith et al. 2002) and changed rapidly to a soft outburst state, undergoing a dramatic state change in 2002 May. This transition was associated with a bright radio flare (Fender et al. 2002), reaching four to five times the brightest radio level ever observed from the source (see Corbel et al. 2000 for the long-term behaviour of GX 339−4). By analogy with other systems (e.g. XTE J1550–564, Corbel et al. 2001), this flare was likely to be the signature of a powerful ejection event. Repeated radio observations of GX 339−4 have indeed confirmed this association: the 2002 radio flaring has led to the formation of a large-scale relativistic radio jet, whose morphology and dynamics will be presented in the course of this Letter.

⋆E-mail: egallo@science.uva.nl

2 ATCA OBSERVATIONS

The Australia Telescope Compact Array (ATCA) performed eight continuum observations of GX 339−4 at roughly regular intervals between 2002 April and August, simultaneously at 4800 MHz (6.3 cm) and 8640 MHz (3.5 cm). Three further observations were performed in 2003 January, March and May at four frequencies: 1384 MHz (21.7 cm), 2368 MHz (12.7 cm), 4800 and 8640 MHz.

The ATCA synthesis telescope is an east–west array of six 22-m antennas with baselines ranging from 31 m to 6 km; it uses orthogonal polarized feeds and records full Stokes parameters (I, Q, U, V). The target was systematically offset by about 10 arcsec from the array phase centre, in order to avoid possible artefacts due to system errors such as DC-offsets. In each observation, PKS 1934–638 was used for absolute flux and bandpass calibration, while either PMN 1603–4904, PMN 1650–5044 or PMN 1726–5529 was the phase calibrator for antenna gains and phases. The data reduction process and image analysis have been carried out with the Multichannel Image Reconstruction, Image Analysis and Display (MIRIAD) software package (Sault, Teuben & Wright 1995; Sault & Killeen 1998). Dates of ATCA observations are indicated in Fig. 1, superimposed on the *Rossi X-ray Timing Explorer*/All Sky Monitor (*RXTE*/ASM) 2–12 keV light curve of the system.

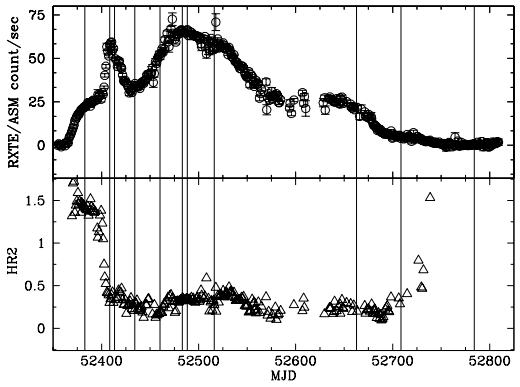

Figure 1. X-ray light curve and hardness ratio HR2 (5–12 keV/3–5 keV count rate, only plotted for fractional errors <0.25) of GX 339−4 as monitored by the *Rossi X-ray Timing Explorer*/All Sky Monitor. At the end of 2002 April, following three years of 'quiescence', the source re-brightened in X-rays, contemporaneously undergoing a very bright radio flare (on 2002 May 14, MJD 52 408). The times of our ATCA observations are indicated with solid vertical lines; the thick line marks the peak radio level of ∼55 mJy.

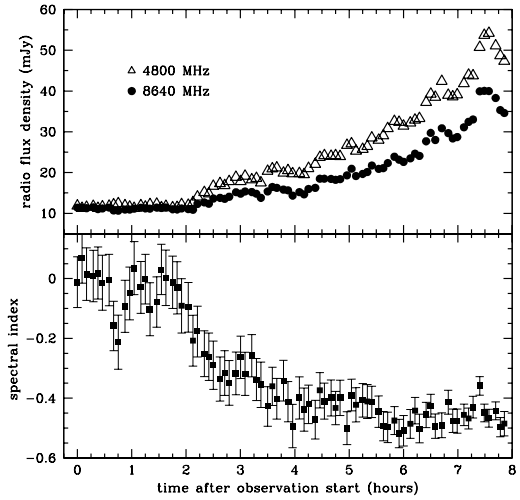

Figure 2. Radio light curves (5-min averages) of GX 339−4 on 2002 May 14 (MJD 52 408) at 8640 and 4800 MHz are plotted in the upper panel (the typical error bar is smaller than the marker size); the flux density at 4800 MHz rose from ∼12 to ∼55 mJy – four to five times the brightest radio level ever observed from the source – in 5.5 h. Temporal evolution of the spectral index α (where $S_\nu \propto \nu^\alpha$) is shown in the lower panel: as the flux density starts to rise, 2 h after the beginning of the observation, the spectral index starts to decrease.

2.1 Outburst and optically thin core radio flare

Smith et al. (2002) reported an increase in the X-ray flux from GX 339−4, which had been in quiescence for almost three years (Kong et al. 2000), on 2002 March 26 (MJD 52 360). The source reached a peak flux (2–12 keV) of ∼0.8 Crab on 2002 May 15 (MJD 52 410), followed by a decrease to ∼0.4 Crab, and a secondary rise to ∼0.9 Crab around MJD 52 500, after which GX 339−4 started a slow return to 'quiescence' (reached by the time of writing). The hardness ratio HR2 suggests that a rapid transition from a low/hard to a softer X-ray state took place a few days before the (first) outburst peak, although colour and timing analysis of the *RXTE* Proportional Counter Array data indicates a smooth transition from a low/hard to a very high state in the rising phase, followed by a high/soft state (or possibly an 'oscillating' very high state) after the peak (Belloni et al. 2002; Nespoli et al. 2003).

ATCA observations performed between 2002 April and June have detected the brightest radio flare ever observed by the system, which reached a peak flux density of about 55 mJy on May 14 (MJD 52 408), almost contemporaneously with the (first) X-ray peak.

The radio flare light curves at 4800 and 8640 MHz are shown in Fig. 2 together with the temporal evolution of the spectral index, which decreased from $\alpha \sim 0$ down to ~ -0.5 (where $\alpha = \Delta\log S_\nu/\Delta\log\nu$). As the spectral index does not significantly decrease during the last two hours prior to the flare peak, the flux rise in this time interval can not be due to decreasing optical depth, as predicted by adiabatic expansion models (e.g. van der Laan 1966), but instead represents a finite phase of particle acceleration.

We can derive the minimum energy associated with the emitting component during the rise, following the formulation by Longair (1994, see also Fender 2004). Assuming an optimal jet viewing angle $\theta \sim 26°$, for which the maximum apparent velocity of the jet is achieved (i.e. a jet semi-opening angle given by $\cos\,\theta = \beta$ with $\beta = 0.9$; see next section), and a volume of the emitting region of about 9×10^{44} cm^3 [given by $(4/3\,\pi)(ct_{\rm rise})^3$, with $t_{\rm rise} = 5.5$ h], the corresponding minimum energy required is $E_{\rm min} \sim 5 \times 10^{39}$ erg; the associated magnetic field for which the energy in relativistic particles equals the magnetic energy is ∼8 mG. The kinetic energy in case of a pure e^+e^- plasma would be $E_{\rm kin} = (\Gamma - 1)\,E_{\rm min} \sim 7 \times 10^{39}$ erg. If there is one (cold) proton for each electron, then $E_{\rm kin} \sim 5 \times 10^{40}$ erg, with an associated mass of $\sim 4 \times 10^{19}$ g. In order to accumulate such mass for a 10 $M_\odot$ BH accreting at a few per cent of the Eddington rate (as indicated by the X-ray luminosity), it would have taken a few minutes. The (much longer) observed rise time of 5.5 h would be of the same order of the injection time-scale if only a few per cent of the accreted mass was loaded into the jet.

The minimum jet powers equal 3×10^{35} and 2×10^{36} erg s^{-1}, for e^+e^- and baryonic plasma, respectively. In the last 20 min of the observation, after reaching the peak level of ∼55 mJy at 4800 MHz, the flux density decreases linearly with time with the same slope at both frequencies, indicating that the main radiative cooling process is adiabatic (synchrotron and Compton cooling times scale with the frequency as $\nu^{-0.5}$); the observed decline is much shallower than that predicted by adiabatic expansion models without any additional energy injection (e.g. $S_\nu \propto t^{-4.8}$; van der Laan 1966).

The position of the radio source on 2002 April 18, when the source was in a bright, flat-spectrum radio state prior to the outburst, is consistent with the binary centre as given by Corbel et al. (2000). Radio emission from GX 339−4 dropped to undetectable levels by 2002 June 09 (<0.4 mJy at 4800 MHz), possibly corresponding to extinction of the May 14 flare.

Although further ATCA observations are consistent with a single fading radio source (see Table 1), observations at 843 MHz performed with the Molonglo Observatory Synthesis Telescope (MOST) indicate more complex behaviour over the period 2002 June–July (Campbell-Wilson & Hunstead, private communication), possibly associated with multiple ejection events. A more detailed analysis of the radio variability over this period, including the MOST data, will be presented in a future paper.

Fig. 3 shows radio maps of GX 339−4 at 8640 and 4800 MHz on 2002 July 5, July 28 and August 30. The position of the radio

Table 1. Image properties of GX 339−4 as observed by ATCA at 8640 and 4800 MHz between 2002 April and August. Fluxes and positions have been derived by fitting the knots with point-like sources; position offsets are expressed in arcsec with respect to the binary core position. Flux density errors correspond to the rms noise levels in the final, naturally weighted images; upper limits are given at a 3σ confidence level.

Date (UT time)	MJD (day)	8640 MHz flux (mJy)	offset[a] α, δ (arcsec)	lin pol P/I, PA	4800 MHz flux (mJy)	offset[a] α, δ (arcsec)	lin pol P/I, PA	α ($S_\nu \propto \nu^\alpha$)
2002:04:18	52 382.75	13.49±0.08	−0.05, +0.07	<1 per cent	12.97 ± 0.07	−0.05, +0.09	<1 per cent	+0.07 ± 0.01
2002:05:14	52 408.48	*10–40*	...	∼ 9 per cent, −47° ± 2°	*10–55*	...	∼4 per cent, −35° ± 3°	−0.52 ± 0.01[b]
2002:05:19	52 413.42	12.27±0.16	−0.12, +0.13	<3 per cent	20.39 ± 0.23	−0.12, +0.10	<2 per cent	−0.86 ± 0.03
2002:06:09	52 434.28	<0.3	...	...	<0.4	...	...	...
2002:07:05	52 460.29	10.62 ± 0.15	−0.17, −0.05	∼4 per cent, −55° ± 8°	14.89 ± 0.19	−0.22, −0.00	∼5 per cent, −21° ± 3°	−0.57 ± 0.03
2002:07:28	52 483.20	10.33 ± 0.18	−0.25, −0.02	∼5 per cent, +33° ± 6°	13.84 ± 0.29	−0.27, −0.00	∼5 per cent, +56° ± 5°	−0.50 ± 0.04
2002:08:02	52 488.28	9.45 ± 0.17	−0.22, −0.08	<1 per cent	11.98 ± 0.25	−0.30, −0.03	<2 per cent	−0.40 ± 0.05
2002:08:30	52 516.12	1.51 ± 0.13	−0.63, +0.02	<10 per cent	2.47 ± 0.07	−0.61, +0.20	<8 per cent	−0.83 ± 0.14

[a]Absolute positional uncertainty is of 0.26 arcsec between 2002:04:18 and 2002:06:09, 0.35 arcsec between 2002:07:05 and 2002:08:30.
[b]Spectral index as measured at the peak value of 55 mJy.

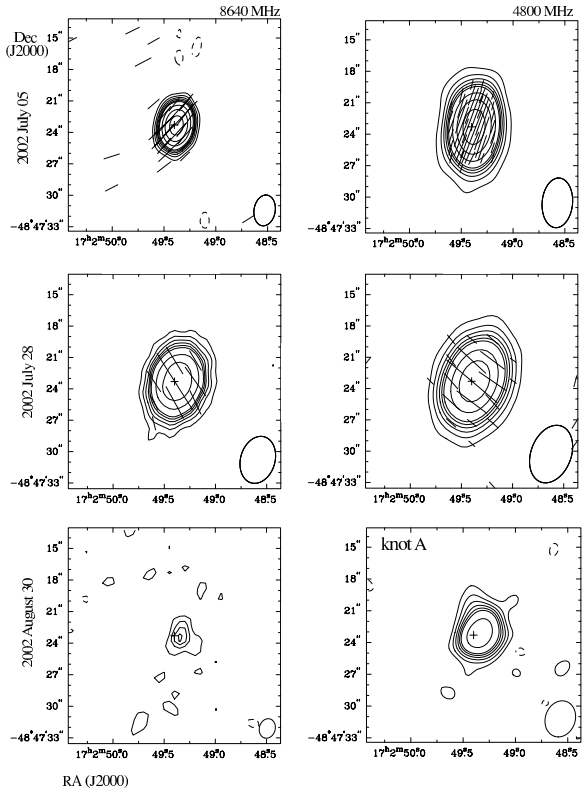

Figure 3. Naturally weighted ATCA images of GX 339−4 at 8640 and 4800 MHz (left- and right-hand panels, respectively). From top to bottom: 2002 July 5, July 28 and August 30; the array configuration was 1.5G, 1.5G and 6C, respectively. The contour interval (CI) is chosen as the rms noise in the final image (see flux density errors in Table 1), and plotted contours are at −2, 2, 4, 8, 12, 20, 32, 52, 84 and 136 times the CI. Linear polarization E vectors are superimposed upon the contour maps in the top and centre panels (where significant polarization is detected), showing a clear rotation in the position angles. Synthesized beams appear on the bottom right-hand corner of each image. The cross indicates the binary core position. By 2002 August 30, the radio source is significantly displaced from the core.

source as imaged by ATCA is displaced by about 0.2 arcsec to the western side (to the right on the maps) of the binary core on 2002 July 5, July 28 and August 2 (not shown), although, given a total positional uncertainty of 0.3 arcsec in this set of observations, these coordinates are still consistent with the binary core. By 2002 August 30, however, the displacement to the western side is of 0.6 arcsec (in position angle PA = −72° ± 32°; PA is defined positive north-east) at both frequencies, indicating the formation of a physically separated component. If this event was powered by the May 2002 flare, that would imply a proper motion of about 6 mas d^{-1}, i.e. a minimum projected velocity of 0.1*c* (for the minimum distance of 4 kpc); however, if the displacement of about 0.2 arcsec measured on August 2 was real, it would imply a separation of at least 400 mas covered in 28 d, i.e. a minimum projected velocity of 0.3*c*.

2.2 Extended radio jet

We expect the bright radio flare(s) of GX 339−4 during its 2002 outburst to be associated with powerful ejection event(s) fed by the source central engine. In fact, ATCA has been observing GX 339−4 at regular intervals again in 2003, tracking the formation of a large-scale, relativistic jet. Fig. 4 and Table 2 present the result of these observations at 4800 MHz, where the most notable structures have appeared.

By 2003 January, an extended outflow composed of two separate 'plasmons' has developed in the same direction of the western component detected on 2002 August 30: the first structure, knot A, is displaced by 0.3 arcsec north-west from the core, while the other component, knot B, is displaced by 5.5 arcsec in PA = −62° ± 2° with respect to the binary core, implying a minimum velocity of ∼0.5*c* if associated with the 2002 May flare. It is worth stressing that this value only represents a lower limit on the velocity not only because of the lower limit on the distance, but also because it is likely that the knots were energized by the outflow somewhat earlier than when they were observed (see Section 3). Both knots display steep optically thin radio spectrum, with $\alpha_A = -0.98 \pm 0.03$ and $\alpha_B = -0.96 \pm 0.08$ (probably either because we are looking above the cooling break frequency or because of resolution effects). An elongated structure is visible at 2368 MHz, too.

By 2003 March 10 (MJD 52 708), the outflow had faded; at least two components are distinguishable at 4800 MHz: knots A′ and B′,

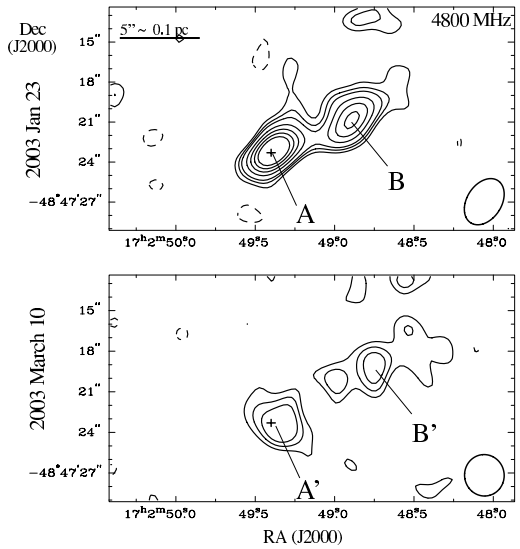

Figure 4. Naturally weighted 4800-MHz maps of the extended jet developed by GX 339–4. 2003 January 23 is on the top with a peak flux density of 0.66 mJy beam^{-1} and convolved with a Gaussian beam 3.62 × 2.24 arcsec in PA = − 22°. Contours are at −2, 2, 4, 6, 8, 10 and 12 times the rms noise level of 0.04 mJy. 2003 March 10 is on the bottom panel, with a peak flux density of 0.25 mJy beam^{-1} and convolved with a Gaussian beam 3.06 × 2.47 arcsec in PA = + 1.7°. Contours are at −2, 2, 4, 6, 8, 10 and 12 times the rms noise level of 0.02 mJy. Knot B′ is displaced by 6.9 arcsec from the binary core; if powered by the 2002 May flare, this would correspond to a projected velocity of about 28 mas d^{-1}, i.e. a jet with velocity higher than 0.6*c* (for $D \gtrsim 4$ kpc).

Table 2. Image properties of the large-scale jet developed by GX 339–4 at 4800 MHz. The absolute positional error, mainly given by the uncertainty on the phase calibrator position (here PMN 1603–4904), is of 0.26 arcsec.

Date (UT time)	MJD (day)	4800 MHz flux (mJy)	offset α, δ(arcsec)	spectral index α, ($S_\nu \propto \nu^\alpha$)
2003:01:23	52 662.67			
knot A		0.66 ± 0.04	−0.25 +0.22	−0.98 ± 0.03
knot B		0.47 ± 0.04	−4.88 +2.54	−0.96 ± 0.08
2003:03:10	52 708.56			
knot A′		0.25 ± 0.04	−0.55, −0.07	−0.98 ± 0.10
knot B′		0.21 ± 0.04	−6.28, +2.80	[a]

[a]Knot B′ is significantly detected at 4800 MHz only.

probably associated with knots A and B from January 23. They are displaced by 0.5 and 6.9 arcsec, respectively (with a relative error of 0.3 arcsec), with PA(A′) = −83° ± 26° and PA(B′) = −66° ± 2°. The spectrum remains optically thin, with $\alpha_A = -0.98 \pm 0.10$ (while knot B′ is significantly detected at 4800 MHz only). Assuming again an association with the 2002 May flare, the separation between knot B′ and the binary core (6.9 arcsec) corresponds to a velocity of 0.6*c* at 4 kpc. The jet *head* in the 4800-MHz map is about 12 arcsec away from the core, implying a projected extension of 0.23 pc at 4 kpc and a minimum velocity of 0.9*c*. If GX 339–4 was instead at a distance of at least 5.6 kpc, as estimated from the upper limit on the magnitude of the secondary star (Shahbaz et al. 2001), the jet would become *superluminal*, with apparent velocity higher than 1.3*c*; while, given a minimum distance of 7.6 kpc, as inferred by Maccarone (2003) from the typical soft-to-hard X-ray state transition luminosity of X-ray binaries, the jet apparent velocity would be higher than 1.8*c*.

Table 3. Core flux densities (mJy) from GX 339–4 on 2003 May 25 (MJD 52 784); the spectrum is optically thick, with $\alpha = 0.72 \pm 0.04$.

1384 MHz	2368 MHz	4800 MHz	8640 MHz
<0.57	0.39 ± 0.08	0.60 ± 0.04	0.94 ± 0.06

By 2003 May 25 (MJD 52 784), the isolated optically thin knots have faded below detectable levels at all wavelengths. Instead, a central component has re-brightened at the binary core position, with peak flux density of 0.9 mJy at 8640 MHz. Core emission at four frequencies is consistent with an inverted spectrum ($\alpha = +0.72 \pm 0.04$), characteristic of an optically thick synchrotron jet, indicating the source core return to a hard state. Table 3 lists core flux densities (1σ upper limits on the optically thin components of the extended jet are given by their errors, i.e. rms noise levels) at four frequencies. No counter-jet has been detected so far.

2.3 Linear polarization

Linearly polarized emission is significantly detected at three epochs. On 2002 May 14, when the powerful flare was detected, the mean polarization level is of 4 per cent at 4800 MHz and of 9 per cent at 8640 MHz, with mean polarization angles PA(4800) = −35° ± 3° and PA(8640) = −47° ± 2°. On 2002 July 5, about 5 per cent of the flux is linearly polarized at both 4800 and 8640 MHz, with electric field vectors in position angle PA(4800) = −21° ± 3° and PA(8640) = −56 ± 6°. A comparable polarization level is seen on 2002 July 28: position angles have switched to PA(4800) = +56° ± 5° and PA(8640) = +33° ± 6° (E vectors are plotted in Fig. 3, superimposed upon the contour maps). The rotations ΔPA(4800 MHz) and ΔPA(8640 MHz) are consistent between 2002 July 5 and July 28, likely reflecting an overall rotation of the projected magnetic field of the emission region. The rotation angle between the two frequencies is between 24 and 46° on July 5 and between 13 and 35° on July 28, indicative of foreground Faraday rotation; if so, we get a lower limit of about 100 rad m^2 on the rotation measure. No significant linearly polarized emission is detected in any of the other 2002 observations when the source was bright enough to detect a polarized signal at a level of a few per cent (see Table 1 for upper limits). In particular, linear polarization is lower than 1 per cent by 2002 April 18, when the optically thick core emission is seen ($\alpha = +0.07$); for comparison, Corbel et al. (2000) detected about 2 per cent of linear polarization at 8704 MHz in 1997 February, with a flux of 8–9 mJy and a similar optically thick spectrum ($\alpha = 0.11$–0.23).

3 SUMMARY AND DISCUSSION

The main result established in this work is the formation of a large-scale relativistic radio jet powered by GX 339–4 during its 2002 outburst: this association indicates that large-scale outflows are likely to be *common* following any major radio flare triggered by a hard-to-soft(er) X-ray state transition (see e.g. Harmon 1995; Fender & Kuulkers 2001).

How does the large-scale jet develop? The position of the radio source detected by ATCA is consistent with the binary core until the beginning of 2002 August. Observations between the end of 2002 August and 2003 March reveal the presence of at least two physically separated components: the first to appear, always brighter

and closer to the binary core (knot A–A′), has a mean separation of 0.5 ± 0.1 arcsec to the western side of the core, while its density flux decreases by a factor of 10 in about 220 days. The second component – always fainter – first appears in the 2003 maps (knot B–B′ in Fig 4) and is displaced by about 7 arcsec from the binary core in PA $= -64^\circ \pm 2^\circ$. Once they have appeared, both knots decline in flux while their positions remain unchanged within uncertainties, unlike, for example, in GRS 1915+105, where the observed ejecta are consistent with simple ballistic bulk motions (Rodríguez & Mirabel 1999; Fender et al. 1999b). The large-scale jet of GX 339-4 seems instead to be better explained in terms of *shock waves* formed within the jet itself and/or by the interaction of an underlying highly relativistic outflow with ambient matter. A more detailed modelling of the jet components, including maps at all four frequencies, will be presented in a forthcoming paper.

Polarization analysis at three epochs shows a significant rotation of the electric vector position angle at two frequencies, indicating a change in the projection of the magnetic field on the plane of the sky. The large-scale jet position angle (PA $= -64^\circ \pm 2^\circ$) is consistent with that of the jet-like extension in the 8640-MHz map of GX 339−4 observed by ATCA in 1996 July (Fender et al. 1997). In addition, Corbel et al. (2000), analysing the persistent radio emission of GX 339−4 while in the low/hard X-ray state, found a similar PA for the electric field vector (expected to be parallel to the magnetic field vector in case of optically thick spectrum) of the linearly polarized signal, indicating a rather stable jet orientation over the years.

Persistent large-scale radio jets observed in 1E 1740.7–2942 (Mirabel et al. 1992) and GRS 1758–258 (Rodríguez, Mirabel & Martí 1992) have been found to extend up to 1–3 pc; in the case of GRS 1915+105 instead, relativistic ejecta were tracked up a projected distance of 0.08 pc (Mirabel & Rodríguez 1999), whereas in the large-scale X-ray jet powered by XTE J1550–564 (Corbel et al. 2002), the eastern jet has been detected to a projected physical separation of 0.75 pc covered in 4 yr. The large-scale radio jet of GX 339−4 displays something, with a projected extension of 0.23 pc (at 4 kpc) covered in about 250 days (if associated with the 2002 May radio flare). Scheduled *Chandra* observation will discover if the jet is active in X-rays as well, possibly confirming the similarity with XTE J1550–564 (Corbel et al. 2002; Kaaret et al. 2003; Tomsick et al. 2003), where the X-ray jet is still capable of accelerating particles up to TeV energies four years after the main ejection event.

ACKNOWLEDGMENTS

We thank Dick Hunstead and Duncan Campbell-Wilson for kindly providing us with preliminary results of the MOST observations. The Australia Telescope is funded by the Commonwealth of Australia for operation as a National Facility managed by CSIRO. RXTE/ASM results are provided by the ASM/XTE team at MIT.

REFERENCES

Belloni T., Nespoli E., Homan J., van der Klis M., Lewin W. H. G., Miller J. M., Mendéz M., 2002, in Durouchoux Ph., Fuchs Y., Rodríguez J., eds, the Fourth Microquasars Workshop, New Views on Microquasars. Center for Space Phys., Kolkata, p. 75

Chaty S., Mirabel I. F., Goldoni P., Mereghetti S., Duc P. A., Martí J., Mignani R. P., 2002, MNRAS, 331, 1065

Corbel S., Fender R. P., Tzioumis A. K., Nowak M., McIntyre V., Durouchoux P., Sood R., 2000, A&A, 359, 251

Corbel S. et al., 2001, ApJ, 554, 43

Corbel S., Fender R. P., Tzioumis A. K., Tomsick J. A., Orosz J. A., Miller J. M., Wijnands R., Kaaret P., 2002, Sci, 298, 196

Corbel S., Nowak M. A., Fender R. P., Tzioumis A. K., Markoff S., 2003, A&A, 400, 1007

Cowley A. P., Schmidtke P. C., Hutchings J. B., Crampton D., 2002, ApJ, 123, 1741

Done C., 2001, Adv. Space Res., 28, 255

Fender R. P., 2004, in Lewin W. H. G., van der Klis M., eds, Compact Stellar X-Ray Sources. Cambridge Univ. Press, Cambridge, to appear (astro-ph/0303339)

Fender R. P., Kuulkers E., 2001, MNRAS, 324, 923

Fender R. P., Spencer R. E., Newell S. J., Tzioumis A. K., 1997, MNRAS, 286, L29

Fender R. P. et al., 1999a, ApJ, 519, L165

Fender R. P., Garrington S. T., McKay D. J., Muxlow T. W. B., Pooley G. G., Spencer R. E., Stirling A. M., Waltman E. B., 1999b, MNRAS, 304, 865

Fender R. P., Corbel S., Tzioumis A. K., Tingay S., Brocksopp C., Gallo E., 2002, The Astronomer's Telegram, 107

Hannikainen D. C., Hunstead R. W., Campbell-Wilson D., Sood R. K., 1998, A&A, 337, 460

Harmon B. A., 1995, Nat, 374, 703

Hynes R. I., Steeghs D., Casares J., Charles P. A., O'Brien K., 2003, ApJ, L583

Kaaret P., Corbel S., Tomsick J. A., Fender R. P., Miller J. M., Orosz J. A., Tzioumis A. K., Wijnands R., 2003, ApJ, 582, 945

Kong A. K. H., Kuulkers E., Charles P. A., Homer L., 2000, MNRAS, 312, L49

Longair M. S., 1994, High Energy Astrophysics. Cambridge Univ. Press, Cambridge

Maccarone T. J., 2003, A&A, 409, 697

Mirabel I. F., Rodríguez L. F., 1999, ARA&A, 37, 409

Mirabel I. F., Rodríguez L. F., Cordier B., Paul J., Lebrun F., 1992, Nat, 358, 215

Nespoli E., Belloni T., Homan J., Miller J. M., Mendéz M., van der Klis M., 2003, A&A, 412, 235

Rodríguez L. F., Mirabel I. F., 1999, 511, 398

Rodríguez L. F., Mirabel I. F., Martí J., 1992, ApJ, 401, L15

Sault R. J., Killeen N. E. B., 1998, The Miriad User's Guide. Australia Telesc. Natl. Facility, Sydney

Sault R. J., Teuben P. J., Wright M. C. H., 1995, in Shaw R. A., Payne H. E., Hayes J. J. E., eds, ASP Conf. Ser. Vol. 77, Astronomical Data Analysis Software and Systems IV. Astron. Soc. Pac., San Francisco, p. 433

Shahbaz T., Fender R. P., Charles P. A., 2001, A&A, 376, L17

Smith D. M., Swank J. H., Heindl W. A., Remillard R. A., 2002, The Astronomer's Telegram, 85

Tomsick J. A., Corbel S., Fender R. P., Miller J. M., Orosz J. A., Tzioumis A. K., Wijnands R., Kaaret P., 2003, ApJ, 582, 933

van der Laan H., 1966, Nat., 211, 1131

Zdziarski A. A., Poutanen J., Mikolajewska J., Gierlinski M., Ebisawa K., Johnson W. N., 1998, MNRAS, 301, 435

This paper has been typeset from a TEX/LATEX file prepared by the author.

4.7.5

Discovery of X-Ray Jets in the Microquasar H1743-322.

Article publié dans :

Astrophys. J., 2005, 632, 504-513

Corbel, S., Kaaret, P., Fender, R. P., Tzioumis, A. K., Tomsick, J. A., Orosz, J. A..

The Astrophysical Journal, 632:504–513, 2005 October 10

DISCOVERY OF X-RAY JETS IN THE MICROQUASAR H1743−322

S. Corbel,[1] P. Kaaret,[2] R. P. Fender,[3] A. K. Tzioumis,[4] J. A. Tomsick,[5] and J. A. Orosz[6]
Received 2005 February 14; accepted 2005 May 26

ABSTRACT

We report on the formation and evolution of two large-scale, synchrotron-emitting jets from the black hole candidate H1743−322 following its reactivation in 2003. In 2003 November, after the end of its 2003 outburst, we noticed, in observations with the Australia Telescope Compact Array, the presence of a new and variable radio source about 4″.6 to the east of H1743−322 that was later found to move away from H1743−322. In 2004 February, we detected a radio source to the west of H1743−322, symmetrically placed relative to the eastern jet. In 2004, follow-up X-ray observations with *Chandra* led to the discovery of X-ray emission associated with the two radio sources. This likely indicates that we are witnessing the interaction of relativistic jets from H1743−322 with the interstellar medium, causing in situ particle acceleration. The spectral energy distribution of the jets during the decay phase is consistent with a classical synchrotron spectrum of a single electron distribution from radio up to X-rays, implying the production of very high energy (>10 TeV) particles in those jets. We discuss the jet kinematics, highlighting the presence of a significantly relativistic flow in H1743−322 almost a year after the ejection event.

Subject headings: accretion, accretion disks — black hole physics — ISM: jets and outflows — radio continuum: stars — stars: individual (H1743−322, XTE J1550−564)

1. INTRODUCTION

Relativistic jets are now believed to be a common occurrence in black hole X-ray binaries (e.g., Corbel 2004; Fender 2005). The optically thin synchrotron spectra of the discrete ejection events (the so-called superluminal jets) imply that the emission becomes much fainter at higher frequencies. For that reason, such events were only observed at radio frequencies. However, Sams et al. (1996) reported the detection of extended infrared emission in GRS 1915+105 after a massive ejection event that could be of synchrotron nature. The most extreme case has been the detection of moving and decelerating X-ray (and radio) relativistic jets in the microquasar XTE J1550−564 a few years after the ejection event and on over large distances (Corbel et al. 2002; Tomsick et al. 2003a; Kaaret et al. 2003). The detection of optically thin synchrotron X-ray emission from discrete ejection events implies in situ particle acceleration up to several TeV. This acceleration may be caused by interaction of the jets with the interstellar medium (ISM).

It now appears that relativistic jets emit throughout the entire electromagnetic spectrum. But are the jets of XTE J1550−564 unique due to special physical conditions, or should we expect to observe similar X-ray jets in other X-ray novae (XNe)? If jets containing TeV particles are common among XNe, then there may be interesting consequences. The high-energy particles could produce a distinctive signature in the cosmic-ray flux (Heinz & Sunyaev 2002) or produce neutrinos if the jets contain protons (Distefano et al. 2002). Furthermore, the study of X-ray jets in microquasars could add an additional bridge between the physics of jets in microquasars and those from supermassive black holes. Interestingly, a connection with gamma-ray bursts has also been drawn by Wang et al. (2003), who showed that the evolution of the eastern X-ray jet of XTE J1550−564 was consistent with the emission from adiabatically expanding ejecta heated by a reverse shock following its interaction with the ISM. The sensitivity of current X-ray missions (in particular, *Chandra* and *XMM-Newton*) is sufficient to enable new discoveries in this emerging field and therefore provides further clues regarding the physical nature of these high-energy phenomena.

H1743−322 was discovered with *Ariel 5* in 1977 August (Kaluzienski & Holt 1977) and has been precisely localized by *HEAO-1* (Doxsey et al. 1977). It was originally proposed to be a black hole candidate (BHC) by White & Marshall (1983). H1743−322 has probably been active several times during the past decades with activity observed in 1984 by *EXOSAT* (Reynolds et al. 1999) and in 1996 by TTM (Emelyanov et al. 2000). In 2003 March, *INTEGRAL* detected new activity from IGR J17464−3213 (Revnivtsev et al. 2003) that was later found to correspond to H1743−322. After its reactivation in 2003, a radio counterpart was found with the Very Large Array (VLA) by Rupen et al. (2003a), and a bright radio flare (likely associated with a massive ejection event) was observed on 2003 April 8 (MJD 52,738) by Rupen et al. (2003b). During outburst, H1743−322 went through several X-ray states with properties typical of BHCs. Low- and high-frequency quasi-periodic oscillations have been detected in H1743−322 by *RXTE* (Homan et al. 2005; Remillard et al. 2004). *Chandra* observations during the 2003 outburst revealed the presence of narrow and variable absorption lines in the X-ray spectrum of H1743−322, possibly related to an ionized outflow (Miller et al. 2004). The 2003 active phase (as observed by *RXTE* ASM) ended around late November of 2003, but a new 4 month outburst started in 2004 July (Swank 2004) with a later reactivation at radio frequencies (Rupen et al. 2004).

In this paper we present an analysis of *Chandra* X-ray and Australia Telescope Compact Array (ATCA) radio observations of H1743−322 from 2003 November through 2004 June that led

[1] AIM, Unité Mixte de Recherche, CEA, CNRS, Université Paris, VII-UMR 7158, Paris, France; and Service d'Astrophysique, Centre d'Etudes Astrophysique de Saclay, F-91191 Gif-sur-Yvette, France.
[2] Department of Physics and Astronomy, University of Iowa, Iowa City, IA 52242.
[3] School of Physics and Astronomy, University of Southampton, Highfield, Southampton SO17 1BJ, England.
[4] Australia Telescope National Facility, CSIRO, P.O. Box 76, Epping, NSW 1710, Australia.
[5] Center for Astrophysics and Space Sciences, University of California at San Diego, MS 0424, La Jolla, CA 92093.
[6] Department of Astronomy, San Diego State University, 5500 Campanile Drive, PA 210, San Diego, CA 92182-1221.

TABLE 1
RADIO OBSERVATIONS OF H1743−322 AND ASSOCIATED JETS: POSITION AND ANGULAR SEPARATION

DATE	MJD	SOURCE	POSITION		ANGULAR SEPARATION (arcsec)
			R.A.	Decl.	
2003 Nov 12.....	52,955.86	Eastern jet	17 46 15.978	−32 14 01.08	4.63 ± 0.30
2003 Nov 30.....	52,973.72	Eastern jet	17 46 15.995	−32 14 00.15	4.91 ± 0.30
2003 Dec 9	52,983.45	Eastern jet	17 46 16.005	−32 14 00.83	4.98 ± 0.30
2003 Dec 20	52,994.49	Eastern jet	17 46 16.026	−32 14 00.67	5.25 ± 0.30
2004 Feb 13.....	53,049.40	Eastern jet	17 46 16.056	−32 14 00.40	5.65 ± 0.50
		Western jet	17 46 15.274	−32 14 00.78	4.30 ± 1.00
2004 Apr 7.....	53,103.22		No detection		
2004 Jun 1	53,158.15		No detection		

NOTES.—Units of right ascension are hours, minutes, and seconds, and units of declination are degrees, arcminutes, and arcseconds. MJD: Modified Julian date (observation midtime). The angular separation is based on the *Chandra* position of the black hole H1743−322.

to the discovery of large-scale radio jets on each side of the BHC H1743−322. More importantly, we also report that the discovery of X-ray emission is very reminiscent of the large-scale decelerating relativistic jets observed in XTE J1550−564 (Corbel et al. 2002). In § 2 we describe the detection and localization of the radio and X-ray sources. In § 3 we discuss the jet kinematics and the nature of the jet emission mechanism.

2. OBSERVATIONS AND SOURCE DETECTION

2.1. *Radio Observations*

Following the transition of H1743−322 to the hard X-ray state (Tomsick & Kalemci 2003) on 2003 October 20 (MJD 52,933), we initiated a series of radio observations with ATCA starting on 2003 November 12 (MJD 52,955). The ATCA synthesis telescope is located in Narrabri, New South Wales, Australia, and consists of an east-west array with six 22 m antennas. A total of seven radio observations were carried out with the ATCA, mostly at 4800 and 8640 MHz, with occasional observations at 1384 and 2496 MHz (see Tables 1 and 2 for details). The amplitude and band-pass calibrator was PKS 1934−638, and the antenna's gain and phase calibration, as well as the polarization leakage, were derived from regular observations of the nearby ($5\overset{\circ}{.}8$ away) calibrator PMN 1729−373. The editing, calibration, Fourier transformation, deconvolution, and image analysis were performed using the MIRIAD software package (Sault & Killeen 1998).

No radio emission is detected at the position of H1743−322 in any of our ATCA observations. However, we note the presence of a new radio source (Fig. 1) about $4\overset{''}{.}6$ to the east of H1743−322, immediately in the first ATCA observation. The following observations indicate that the new source increased in flux (see Tables 1 and 2 and Fig. 2). The position of the source also changed over time, moving away from the BHC H1743−322. We discuss the motion of the source in a later section, taking into account the additional constraints from the *Chandra* observations.

The light curve of this source, combining all our ATCA observations (at 4800 and 8640 MHz), is presented in Figure 2. This source was brightening from our first observations until the end of 2003. The single detection on 2004 February 13 (MJD 53,049) at a much (almost a factor of 10) fainter level points to a very fast decay. The maximum of radio emission was likely in 2004 January. The rise of radio emission at 4800 MHz is gradual, whereas there may be some variations during the rise at 8640 MHz. We fitted an exponential rise and a power-law rise to the radio data (at both frequencies) and found that both fits are equally acceptable. The timescales are consistent for both radio frequencies. The 1/*e*-folding time of the exponential rise is 49.4 ± 4.8 days at 4800 MHz and 40.0 ± 6.8 days at 8640 MHz. The index of the power-law rise is 4.9 ± 0.5 at 4800 MHz and 6.0 ± 1.0 at 8640 MHz.

Due to the fast decay of radio emission, we cannot accurately constrain its decay rate. However, we can give some limits that clearly indicate that the decay is faster than the rise. Assuming a maximum at the time when we detected the source at its brightest level (on 2003 December 20), and taking the 4800 MHz detection during the decay, we deduced a 1/*e*-folding time of the exponential decay of 27.9 ± 2.2 days or an index of the

TABLE 2
RADIO OBSERVATIONS OF H1743−322 AND ASSOCIATED JETS: FLUX DENSITY AND SPECTRAL INDEX

DATE	MJD	SOURCE	FLUX DENSITY (mJy)				SPECTRAL INDEX
			1384 MHz	2368 MHz	4800 MHz	8640 MHz	
2003 Nov 12.....	52,955.86	Eastern jet	...	...	1.10 ± 0.10	0.48 ± 0.11	−1.41 ± 0.42
2003 Nov 30.....	52,973.72	Eastern jet	...	...	1.55 ± 0.09	0.87 ± 0.09	−0.98 ± 0.20
2003 Dec 9	52,983.45	Eastern jet	...	...	1.86 ± 0.09	0.84 ± 0.09	−1.35 ± 0.20
2003 Dec 20	52,994.49	Eastern jet	...	...	2.37 ± 0.06	1.34 ± 0.07	−0.97 ± 0.10
2004 Feb 13.....	53,049.40	Eastern jet	0.62 ± 0.15	0.41 ± 0.15	0.33 ± 0.05	<0.21	−0.49 ± 0.22
		Western jet	<0.45	<0.45	0.14 ± 0.05	<0.21	N/A
2004 Apr 7.....	53,103.22	Eastern jet	...	...	<0.18	...	N/A
2004 Jun 1	53,158.15	Eastern jet	<0.45	<0.30	<0.12	...	N/A

NOTES.—MJD: Modified Julian date (observation midtime). Radio upper limits are given at the 3 σ level. Fluxes for the western jet are only given for the day of its unique ATCA detection; otherwise the upper limits can be deduced from the error bars (1 σ) or upper limits on the flux densities of the eastern jet.

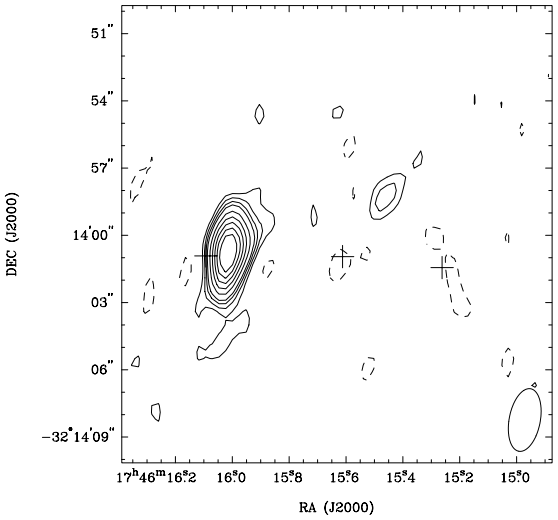

FIG. 1.—ATCA radio map at 8.64 GHz of the field near the BHC H1743−322 on 2003 December 20. Crosses (size of 1″) indicate the location of H1743−322 (*center*), the eastern and western jets, as observed during the first *Chandra* observations 2 months later (on 2004 February 12). Contours are plotted at −2, 2, 3, 4, 5, 7, 9, 11, 13, 15, 18, 21, 25, and 30 times the rms noise level of 0.07 mJy beam^{-1}. The synthesized beam (in the lower right corner) is 2.8×1.4 arcsec^2, with the major axis at a position angle of $-10\overset{\circ}{.}9$.

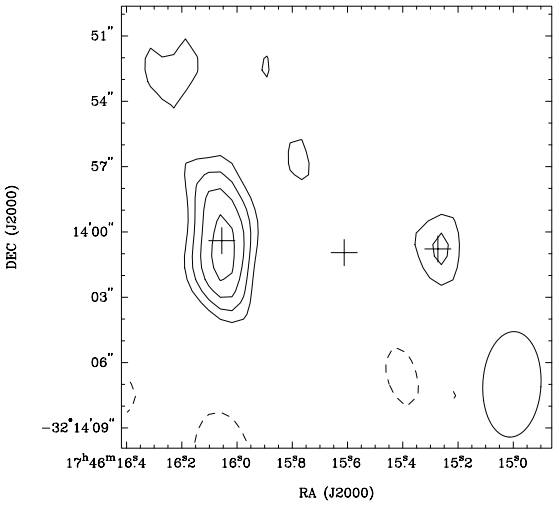

FIG. 3.—ATCA radio map at 4.8 GHz of the field near the BHC H1743−322 on 2004 February 13. Crosses indicate the location of H1743−322 (*center*), the eastern and western jets. The weak source at the position of the western jet is consistent with location the X-ray counterpart. Contours are plotted at −2, 2, 3, 4, and 5 times the rms noise level of 0.05 mJy beam^{-1}. The synthesized beam (in the lower right corner) is 4.8×2.7 arcsec^2, with the major axis at a position angle of $-3\overset{\circ}{.}0$.

power-law decay of 10.2 ± 0.8. We emphasize that these limits (an upper limit on the $1/e$-folding time and a lower limit on the index of the power law) are quite conservative and that the true decay during the early part of 2004 is likely faster than that indicated by these numbers. The light curve at 8640 MHz is consistent with that at 4800 MHz, but very few data points are available.

We searched for linearly polarized radio emission when the eastern source was at its brightest level (i.e., on 2003 December 20). Linear polarization at the level of $9.9\% \pm 2.9\%$ with a mean polarization angle of $51\overset{\circ}{.}9 \pm 8\overset{\circ}{.}3$ is detected at 4800 MHz. At 8640 MHz, we find an ($3\ \sigma$) upper limit of ∼21% on the polarization. This limit is weak because the 8640 MHz flux density is weaker than at 4800 MHz.

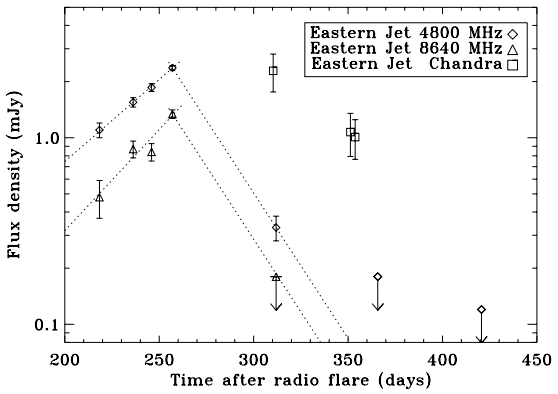

FIG. 2.—Radio light curve at 8.6 GHz (3 cm) and 4.8 GHz (6 cm) of the eastern jet of H1743−322 as measured by ATCA. Upper limits are plotted at the 3 σ level. The dotted lines illustrate the exponential fit to the rise and decay of radio emission. The *Chandra* 0.3−8 keV unabsorbed flux ($\times 10^6$) of the eastern jet is also plotted, and this indicates the dates of the X-ray observations. The *x*-axis represents the time since the major radio flare as observed by the VLA on 2003 April 8 (MJD 52,738) by Rupen et al. (2003b).

In addition to the new source to the east of H1743−322, we note that a radio source is detected to the west of H1743−322 (Fig. 3), almost symmetrically placed relative to the eastern source, only on 2004 February 13 with a flux density of 0.14 ± 0.05 mJy at 4800 MHz. Despite its weak flux density, the *Chandra* data on the same day (Figs. 4 and 5) confirm the existence of an X-ray source at this position and therefore strengthen the reality of the western radio source.

As both of these radio sources appear to be moving away from the BHC, we conclude that they are related to the H1743−322 system. The properties are very reminiscent of the large-scale relativistic radio and X-ray jets of XTE J1550−564 (Corbel et al. 2002) after 2000. It is therefore likely that these evolving radio sources represent the action of previously ejected plasma on the ISM. As discussed below, the most likely ejection date is around 2003 April 8 when a major radio flare was observed by Rupen et al. (2003b). We now refer to these sources as the eastern and western jets, based on their location with respect to H1743−322. We report in Tables 1 and 2 their positions (from radio observations) and angular separation from H1743−322, as well as their flux densities. As H1743−322 is not detected at radio frequencies, we used its *Chandra* position as defined in the next section.

2.2. *X-Ray Observations*

2.2.1. *Source Detection*

Following the detection of the eastern-moving radio source and its strong similarities with the large-scale X-ray jets in XTE J1550−564 (Corbel et al. 2002; Tomsick et al. 2003a; Kaaret et al. 2003), we triggered our target of opportunity proposal for the *Chandra X-Ray Observatory* (Weisskopf et al. 2002) to search for an X-ray counterpart to the radio jets. The *Chandra* observations were significantly delayed relative to the trigger because H1743−322 passed near the Sun and was not observable.

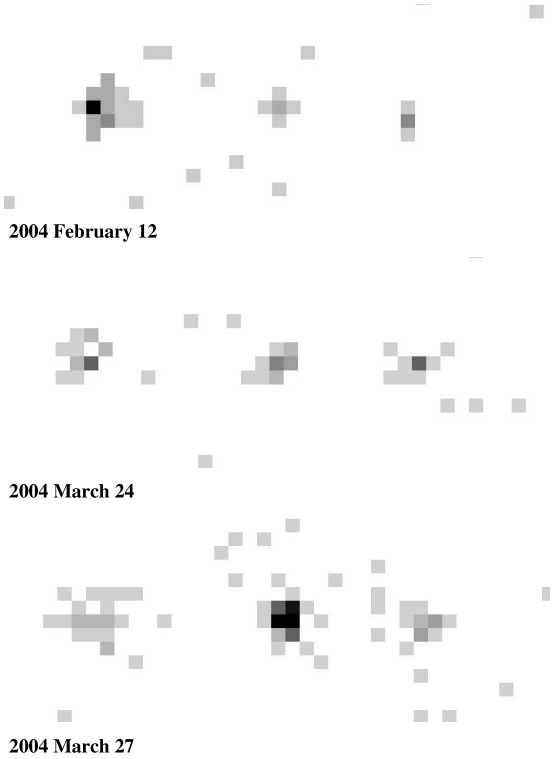

FIG. 4.—X-ray images of H1743−322 for the 0.3–8 keV band taken on 2004 February 12, March 24, and March 27. The gray scale represents the number of X-ray counts per pixel with a maximal of 6, 5, and 13 counts on 2004 February 12, March 24, and March 27, respectively. H1743−322 is located at the center of the image, whereas the eastern jet is on the left and the western jet is on the right.

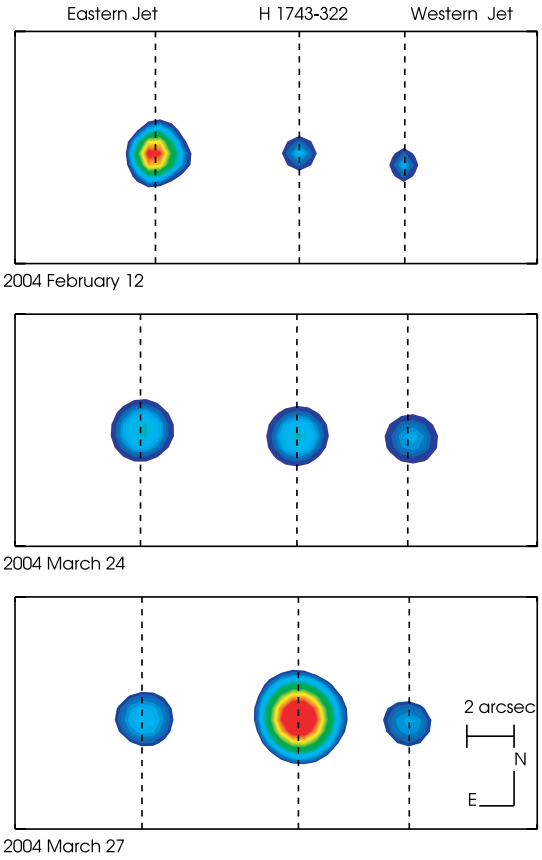

FIG. 5.—Filled contour plots produced by convolving the 0.3–8 keV images shown in Fig. 4 with a two-dimensional Gaussian with a width of 2 pixels in both directions. The vertical lines indicate the position of the X-ray sources in each observation. Each count image has been normalized by its integration time.

As indicated previously, the eastern jet was already decaying when the *Chandra* observations were performed (see Fig. 2 for their scheduling relative to the radio light curve).

H1743−322 was observed with *Chandra* on 2004 February 12 (MJD 53,048), March 24 (MJD 53,089), and March 27 (MJD 53,092) using the Advanced CCD Imaging Spectrometer spectroscopic array (ACIS-S; Bautz et al. 1998). In all observations, the target was placed on one of the back-illuminated ACIS chips (S3) with the ACIS-S operated in imaging mode. For the first observation, only the S3 chip was read out and a 1/2 subarray mode was used to limit pileup. For the latter two observations, the source was known to be a lower flux state, and the full ACIS-S imaging mode array was used.

We produced 0.3–8 keV ACIS images using the "level 2" event lists from the standard data processing (ASCDS ver. 7.2.1) using the *Chandra* Interactive Analysis of Observations (CIAO) software package version 3.0.2 and Calibration Data Base (CALDB) version 2.26. We constructed light curves with all valid events on the S3 chips to search for time of high background. Only weak background flares were found (and removed) for the February observation; otherwise, the count rate appears uniform. The total useful exposure obtained was 17,796 s on February 12 (observation 1), 28,363 s on March 24 (observation 2), and 40,037 s on March 27 (observation 3).

We searched for X-ray sources in each 0.3–8 keV image using *wavdetect* (Freeman et al. 2002), the wavelet-based source detection routine in CIAO. For all three *Chandra* observations, an X-ray source is found at the location of H1743−322, the eastern jet, and western jet (Figs. 4 and 5). All three sources appear aligned and therefore provide further evidence for a connection with H1743−322.

We check the *Chandra wavdetect* position of each source by calculating the source's centroid using the 0.3–8 keV events from a 4×4 pixel ($2'' \times 2''$) region centered on its *wavdetect* positions. This region contains all events likely related to the source, along with a small number of background events. The recalculated positions of H1743−322, the eastern and western jets, are in good agreement with the *wavdetect* positions; the differences were less than $0''.10$. The position angle of the eastern jet relative to H1743−322 is $89^\circ.0 \pm 1^\circ.5$, while the position angle of the western jet is $-91^\circ.7 \pm 1^\circ.8$.

2.2.2. *Source Localization*

To obtain the best constraint on the position of each detected source (especially H1743−322, which is not detected in our radio images), we registered the *Chandra* images with an infrared image from the Two-Micron All-Sky Survey (2MASS) following the procedure described by Tomsick et al. (2003b). We use the two longest *Chandra* observations (2 and 3) and inspected each observation separately. We restricted our search for X-ray and infrared sources within a $4'$ radius

TABLE 3
Chandra Observations of H1743−322

Observation Number	Date 2004	MJD	Exposure Time (s)	Source	Position			Angular Separation (arcsec)
					R.A.	Decl.	Uncertainty (arcsec)	
1.....	02−12	53,048.0	17,796	H1743−322	17 46 15.613	−32 14 0.95	0.10	N/A
				Eastern jet	17 46 16.094	−32 14 0.92	0.19	6.10 ± 0.20
				Western jet	17 46 15.263	−32 14 1.44	0.24	4.47 ± 0.30
2.....	03−24	53,088.9	28,363	H1743−322		See obs. 1		N/A
				Eastern jet	17 46 16.142	−32 14 0.76	0.17	6.72 ± 0.20
				Western jet	17 46 15.243	−32 14 1.05	0.16	4.70 ± 0.20
3.....	03−27	53,091.5	40,037	H1743−322		See obs. 1		N/A
				Eastern jet	17 46 16.135	−32 14 0.83	0.11	6.63 ± 0.20
				Western jet	17 46 15.243	−32 14 1.09	0.15	4.70 ± 0.20

Notes.—Units of right ascension are hours, minutes, and seconds, and units of declination are degrees, arcminutes, and arcseconds. MJD: Modified Julian date (exposure midtime). The angular separation between the jets and H1743−322 is based on the *Chandra* position of the BHC H1743−322 as estimated in observations 2 and 3 during the 2MASS/*Chandra* registration process. The uncertainties on the position include systematics due to the registration process and the statistical uncertainties on the *wavdetect* position. However, the angular separation does not depend on the image registration.

circle centered on the position of H1743−322 as reported by *wavdetect*.

We cross-correlated the *Chandra* source positions with the 2MASS sources in the field. We find that five *Chandra* sources for observation 2 and nine for observation 3 have 2MASS sources within the *Chandra* pointing uncertainty of 0.″6. The accuracy of the 2MASS source positions is 0.″2 (90% confidence). For these sources, the angular separation between the 2MASS and *Chandra* positions ranges from 0.″07 to 0.″22 for observation 2 and from 0.″06 to 0.″46 for observation 3. Given the surface density of 2MASS sources, there is a 0.11% probability that a match with the largest separation is spurious for observation 2, and 0.50% for observation 3. We used the full set of matches to register each X-ray image. The average 2MASS to *Chandra* differences are $-0.''01 \pm 0.''11$ in R.A. and $-0.''05 \pm 0.''10$ in decl. for observation 2 and $-0.''19 \pm 0.''10$ in R.A. and $-0.''09 \pm 0.''08$ in decl. for observation 3. We estimated the location of H1743−322 as the average of the positions measured in the two *Chandra* images after registration to the 2MASS positions by performing the above indicated shifts. H1743−322 is found to be located at R.A. $= 17^{h}46^{m}15^{s}.613$, decl. $= -32^{\circ}14'0.''95$, with a total uncertainty of 0.″10 (including the 0.″2 systematics due to the registration of 2MASS images and the statistical uncertainties on the *Chandra wavdetect* position). The difference in position of the eastern and western jets, after the registering process, between the two *Chandra* observations (only separated by 2.5 days) was less than 0.″10 (i.e., within the total uncertainty). This precise *Chandra* position of H1743−322 is consistent within uncertainties (a difference of 0.″25) with the recently refined VLA radio position (Rupen et al. 2004).

We used the position of H1743−322 to register *Chandra* observation 1 on the 2MASS frame, for which shifts of $-0.''25 \pm 0.''17$ (in R.A.) and $-0.''32 \pm 0.''16$ (in decl.) are needed. These shifts are smaller than the *Chandra* absolute astrometric of 0.″6 at 90% confidence. We report in Table 3 the location of H1743−322, the western and eastern jets, as well as the angular separation between the jets and the BHC for all three *Chandra* observations. We note that the angular separation does not depend on the image registration.

2.2.3. *Flux and Energy Spectra*

We extracted an energy spectrum in the 0.3–8 keV energy range for the eastern and western jets in all three *Chandra* observations using CIAO version 3.0.2 tools, and we fitted these spectra using XSPEC version 11.3.0. We used a circular source extraction region with a radius of 2.″3 and 1.″2 and we extracted background spectra from an annulus with an inner radius of 13″ and an outer radius of 22″ and 19.″5 for the eastern and western jets, respectively. These regions were centered on the jet positions as given by *wavdetect*. Due to the low numbers of source counts (at maximum of 24 counts), we used the W statistic for fitting (Wachter et al. 1979; K. Arnaud 2005, in preparation) the unbinned spectra; this is adapted from the Cash statistic (Cash 1979) and works with background-subtracted spectra and low count rate.

These spectra are adequately fitted with a power-law model including interstellar absorption. We fixed the equivalent hydrogen absorption column density, $N_{\rm H}$, to the constant value measured in *Chandra* observations of H1743−322 during its 2003 outburst (Miller et al. 2004), i.e., 2.3×10^{22} cm^{-2}. For the eastern jet, the best-fit photon index is 1.67 ± 0.90, 1.78 ± 1.10, and 2.03 ± 0.90 for *Chandra* observations 1, 2, and 3, respectively. Refitting these three data sets simultaneously (allowing the normalization to vary) led to a photon index of 1.83 ± 0.54 (with 90% confidence errors). We did the same for the western jet, giving photon indexes of 2.5 ± 2.5, 2.2 ± 1.0, and 1.6 ± 1.0 for *Chandra* observations 1, 2 and 3, respectively, and a photon index of 1.9 ± 0.8 (with 90% confidence errors) for the combined spectrum.

We fixed the power-law photon index (see § 3.2.2) to a value of 1.6 to obtain measurements of the X-ray flux. This value is extracted from the fit to the radio/X-ray spectral energy distribution (SED). We measure 0.3–8 keV absorbed fluxes for the eastern jet of $(21.3 \pm 4.9) \times 10^{-15}$, $(10.0 \pm 2.6) \times 10^{-15}$, and $(9.4 \pm 2.3) \times 10^{-15}$ ergs s^{-1} cm^{-2} for observations 1, 2, and 3, respectively. Concerning the western jet, the 0.3–8 keV absorbed fluxes are $(3.0 \pm 2.1) \times 10^{-15}$, $(6.4 \pm 2.6) \times 10^{-15}$, and $(6.2 \pm 1.8) \times 10^{-15}$ ergs s^{-1} cm^{-2} for observations 1, 2, and 3, respectively. The unabsorbed fluxes in the same band are 2.0 higher than the absorbed values quoted above. The quoted errors are based on the numbers of source and background counts and Poisson statistics.

Figure 6 shows the time variation of the 0.3–8 keV unabsorbed flux of the eastern and western jets. The X-ray emission of the eastern jet is decaying, whereas the emission from the western jet is consistent with a slightly rising source (or even constant). We

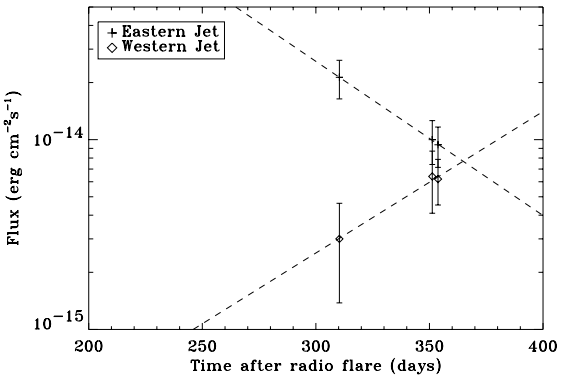

FIG. 6.—X-ray flux of the eastern (*plus sign*) and western (*diamond*) jets vs. the time after the bright radio flare on 2003 April 8. The curves represent the exponential decay (eastern jet) and "rise" (western jet) described in the text.

fitted an exponential or a power-law decay to the eastern jet, and we found that both fits are equally acceptable. The 1/*e*-folding time of the exponential decay is 53.5 ± 19.6 days, whereas the index of the power-law decay is 6.2 ± 2.3. The constraints are rather weak for the western jet; the 1/*e*-folding time of the exponential rise is 58.2 ± 46.3 days, and the index of the power-law rise is 5.7 ± 4.5.

We note that the western jet was likely detected at 4.8 GHz during the first *Chandra* observation (Fig. 3), but unfortunately no radio observation was possible during the time of the second and third *Chandra* observations. However, we did perform an ATCA observation about 2 weeks after the third *Chandra* observations but failed to detect radio emission from the western jet (with similar sensitivity to its detection in February; see Table 2). This indicates that the peak of emission from the western jet was likely sometime between 2004 February and the beginning of April, i.e., roughly 2 or 3 months after the peak of emission from the eastern jet. At this peak, the X-ray (0.3–8 keV band) luminosity (for a distance of 8 kpc) of the eastern jet was of the order of more than 3×10^{32} ergs s^{-1}, i.e., a level consistent with the X-ray emission of some BHCs while in their quiescent state (e.g., Garcia et al. 2001). Therefore, if the production of X-ray jets is more common than previously thought as we suggest here, some of the reported measurements of the quiescent X-ray emission of BHC may be contaminated by jet emission, particularly for observations made using instruments with worse angular resolution than *Chandra*.

2.2.4. *Source Morphology*

The western jet of XTE J1550−564 was clearly extended, with a leading peak and a trailing tail extended up to 5″ toward the black hole (Kaaret et al. 2003). To study the morphology of the X-ray jets in H1743−322, we decomposed the images along axes parallel and perpendicular to the jet axis defined as a line extending through the BHC and the jets. Following the procedure described in Kaaret et al. (2003), we calculated the displacement of each X-ray event parallel and perpendicular to this axis. All photons with energies in the range 0.3–8 keV and within 2″ of the jet axis in the perpendicular direction are included. For each observation, we compared the morphology of the BHC H1743−322, assumed to be pointlike, to each of the detected jets, except for observation 1 in which the western jet had too few counts for a meaningful comparison.

We carried out the morphology comparison using a Kolmogorov-Smirnov (KS) test to permit comparison of unbinned position

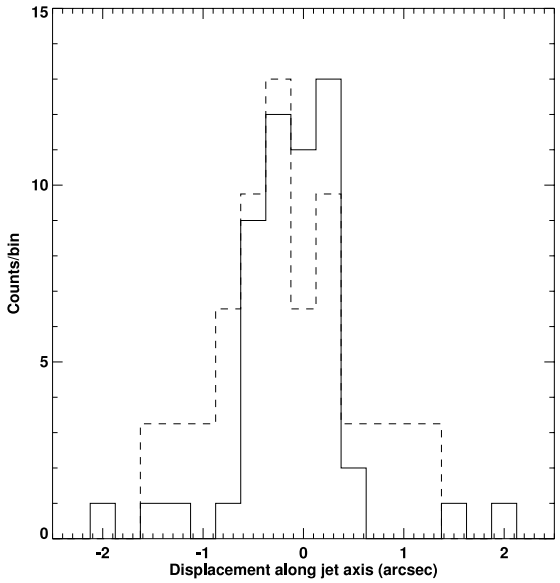

FIG. 7.—Distribution of the X-ray counts along the jet axis combining *Chandra* observations 2 and 3. The dashed line shows the profile of the eastern jet, and the solid line shows H1743−322 rescaled to match the peak of emission of the eastern jet. The bin size is 0.″25.

data. We shifted the jet positions to match the BHC position using the positions derived from *wavdetect*. We compared the morphology for events lying within 2″ along the jet axis of each source position. We find no significant evidence for spatial extent along or perpendicular to the jet axis for any jet in any observation. We also combined the data from observations 2 and 3 (Fig. 7) and still did not find any significant evidence for spatial extent of either jet. The KS-test probabilities that the black hole and jet samples are drawn from the same parent distribution range from 0.11 to 0.96. To place an upper bound on the size of the western jet along the jet axis, we calculated the standard deviation of the displacements of events along the jet axis from the *wavdetect* position of the jet. We find a value of 0.″61 ± 0.″04. This is inconsistent with the standard deviation calculated for the black hole candidate (0.″48 ± 0.″02) by only 2.7 σ, so again, there is no strong evidence for spatial extent and the value should be taken as an upper limit on the jet size.

In order to increase the statistics for the comparison source, we decided to compare the X-ray jet profiles to the profiles for the source PG 1634+706 (Obs ID 1269), which is used to calibrate the ACIS point-spread function. Again, the KS test does not indicate significantly that the BHC H1743−322 or its associated X-ray jets are extended along or perpendicular to the jet axis.

3. DISCUSSION

3.1. *Proper Motion and Jet Kinematics*

The positions of the eastern and western jets change between the various radio and X-ray observations when the jets move away from BHC H1743−322. In order to quantify this motion, we have calculated the angular separation between H1743−322 and each jet. For all *Chandra* and ATCA observations, we used the position of H1743−322 as determined in the previous section. Figure 8 shows the angular separation between H1743− 322 and each jet as a function of time. In this figure, the origin of time

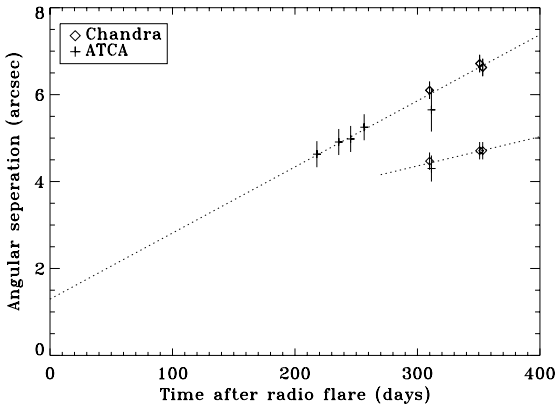

FIG. 8.—Angular separation between the BHC H1743−322 and each jet vs. time since the bright radio flare observed on 2003 April 8. This plot is based on ATCA (*plus signs*) and *Chandra* (*diamonds*) data. The western jet is the one that is moving more slowly. The dotted lines represent the linear fit to the proper motion of the jets assuming no deceleration.

(day 0) is the day (2003 April 8 = MJD 52,738) in which a major radio flare, and hence a massive plasma ejection, was observed (Rupen et al. 2003b).

This figure clearly illustrates that the eastern jet is moving away from H1743−322. The *Chandra* and ATCA positions of the eastern jet are consistent with a linear increase of the angular separation versus time, and a linear fit to the angular separation implies a proper motion of 15.2 ± 1.8 mas day^{-1}. The *Chandra* locations are consistent with a continuation of the motion from the ATCA observations. The data for the western jet are only weakly inconsistent with a fixed position. A linear fit to the angular separation for the western jet gives a proper motion of 6.7 ± 5.2 mas day^{-1}.

Extrapolation of the linear fit for the eastern jet (for which we have the best statistics) implies zero separation on MJD $52{,}652 \pm 38$ (i.e., around 2003 January 13). This date is well before the initial detection of H1743−322 by *INTEGRAL* on 2003 March 21 (MJD 52,719; Revnivtsev et al. 2003). With the *RXTE* ASM data, it is not possible to assess the X-ray activity of H1743−322 around MJD 52,652. However, observations of several black hole systems (Corbel et al. 2004; Fender et al. 2004) have revealed that the massive ejection events occurred later during the outburst at a period consistent with the transition from the intermediate state to the steep power-law state. Again, the bright radio flare observed by Rupen et al. (2003b) on 2003 April 8 (MJD 52,737) is consistent with this interpretation, as illustrated, for example, by the hardness evolution of the X-ray spectra (Capitanio et al. 2005).

For the rest of this paper, we therefore consider the time origin of the jets as the day of the bright radio flare (day 0 in Fig. 8). With the linear fit to the motion of the eastern jet, we predict an angular separation of $1''.29 \pm 0''.55$ at the time of the first bright radio flare. If the velocity of the eastern jet were constant, we should have obtained a zero separation on this day. While the deviation from zero is not highly significant ($2.4\ \sigma$ or 98% confidence level), this could imply that the jets were intrinsically more relativistic at the time of ejection and decelerated gradually later on. This would be another similarity with the X-ray jets of XTE J1550−564 (Corbel et al. 2002). More frequent radio and/or X-ray observations would have been necessary to better constrain this motion.

The proper motion of the eastern jet appears higher than that of the western jet. Also, the X-ray flux of the western jet continues to rise, and the eastern jet is decaying in both the radio and X-rays. The western jet is not detected at radio frequency during the 2004 April and June ATCA observations, despite a sensitivity similar to the 2004 February observation (Table 2). This could suggest that the rise of emission from the western jet has stopped and that the peak of its emission occurred some time between 2004 February and April, i.e., a few months after the peak observed for the eastern jet. This probably indicates that the eastern jet is approaching and the western jet is receding.

3.1.1. *Case of Ballistic Jets*

As there is no strong indication of a decelerating jet in H1743−322, we first consider the kinematics of the jets under the assumption of an intrinsically symmetric ballistic ejection (see, e.g., Fender et al. 1999 for the formalism). From the first detection of the jets (ATCA on MJD 52,956 for the eastern jet and *Chandra* on MJD 53,092 for the western jet), we estimate their average proper motions between ejection on 2003 April 8 and their first detections. We deduced an average proper motion of 21.2 ± 1.4 mas day^{-1} for the eastern jet and 13.3 ± 0.6 mas day^{-1} for the western jet. From this we derive $\beta \cos\theta = 0.23 \pm 0.05$, with $\beta = v/c$ the true bulk velocity and θ the angle between the axis of the jet and the line of sight. This immediately gives a maximum angle to the axis of the jets of $\theta_{\max} \leq 77^\circ \pm 3^\circ$ and a minimum velocity of $\beta_{\min} \geq 0.23 \pm 0.05$. We can also infer a maximum distance to H1743−322 of 10.4 ± 2.9 kpc. To date, the distance to H1743−322 is basically unknown; however, its location toward the Galactic bulge could possibly imply a Galactic center location, which would be consistent with the above upper limit. If we assume a source distance of 8 kpc (distance to the Galactic center), we derive an intrinsic velocity of the ejection of $\beta = 0.79$ and an angle of $\theta = 73^\circ$ for the axis of the jets. At this distance the apparent velocity of the eastern jet ($\beta_{\rm app} = v_{\rm app}/c$) is 0.98, and for the western jet we deduce an apparent velocity ($\beta_{\rm rec} = v_{\rm rec}/c$) of 0.61. This clearly indicates the presence of a significantly relativistic outflow in H1743−322.

3.1.2. *Case of Decelerating Jets*

If the jets have been gradually decelerated since the ejection event, the average proper motions cannot be used to constrain the jets kinematics. In that case, we can still study their properties using the 2004 measurements of the proper motions (15.2 ± 1.8 mas day^{-1} for the eastern jet and 6.7 ± 5.2 mas day^{-1} for the western jet). We again assume a source distance of 8 kpc, keeping in mind that this is a major source of uncertainty in the derived parameters. At this distance the apparent velocity of the eastern jet ($\beta_{\rm app} = v_{\rm app}/c$) is 0.71 ± 0.08, and for the western jet we deduce an apparent velocity ($\beta_{\rm rec} = v_{\rm rec}/c$) of 0.31 ± 0.24. The true bulk velocity, $\beta = v/c$, is defined as $\beta = \beta_{\rm app}/(\beta_{\rm app}\cos\theta + \sin\theta)$, with θ equal to the angle between the axis of the jet and the line of sight. This function has a minimum at $\theta_{\min} = \tan^{-1}(1/\beta_{\rm app}) = 54^\circ$ with our measured apparent velocity for the approaching jet (again for a distance of 8 kpc). This translates into a minimum true bulk velocity of $\beta_{\min} = 0.57 \pm 0.05$, still indicating the presence in 2004 of a significantly relativistic flow in H1743−322.

3.2. *Flux Evolution and Emission Mechanism*

3.2.1. *Radio Emission: Spectra*

We define the radio flux density $S_\nu \propto \nu^\alpha$, with α the radio spectral index and ν the frequency. We note a difference in the properties of radio emission during the rise versus decay phase.

The radio spectra are consistent with being optically thin (i.e., $\alpha \leq 0$) all the time. We note that the spectra are very steep during the rise ($|\alpha| \geq 1$; see Table 2), while the single radio detection during the decay is more typical of optically thin synchrotron emission ($\alpha = -0.49 \pm 0.22$). The detection of a significant level of polarization (when the sensitivity allowed it) is consistent with the radio emission being optically thin synchrotron emission. The broadband spectra (see below) accurately constrain the spectral index and are consistent with a classical synchrotron spectral index of $\alpha \sim -0.6$. This index from the broadband SED on 2004 February 12–13 is significantly different from the average radio spectral index during the rise, which is $\alpha = -1.18 \pm 0.13$.

The difference of spectral indices during the rise is probably not related to the emission being resolved out at high frequency by the ATCA, as the four radio observations during the rise were performed in various configurations of the telescope. In addition, we note that both jets are not resolved by *Chandra*, and therefore they should appear as point sources to ATCA. Whereas the synchrotron slope is almost a textbook example during the decay, the spectral index during the rise is likely an intrinsic property of the process that accelerates the emitting particles during the collision of relativistic plasma with the local medium. This can possibly be explained as follows: The rising phase represents the propagation of the jets through a dense medium associated with a mechanism that accelerate particles to high energy, whereas the decaying phase represents propagation through a less dense medium and possibly without any further reacceleration of particles in the jets. The emission properties during the decay phase would then be governed by synchrotron and/or adiabatic losses of the relativistic particles. The steep spectrum during the rise may eventually shed light on the mechanism that accelerates particles to high energies.

3.2.2. *Broadband Spectra and Emission Mechanism*

The eastern and western jets are simultaneously detected at radio and X-ray frequencies on 2004 February 12–13. Figure 9 shows the broadband SED of the eastern jet at this epoch. The radio fluxes are from Table 2, and we convert the unabsorbed 0.3–8 keV flux to a flux density at a pivot X-ray energy defined by allowing the X-ray photon index to vary (Fig. 9). A combined fit of the radio and X-ray data results in a spectral index of -0.64 ± 0.02, which is typical of synchrotron emission. The same is true for the western jet, giving a radio/X-ray spectral index of -0.70 ± 0.05 on 2004 February 12–13.

The detection of linear polarization ($\sim$10%) from the eastern jets of H1743−322, as well as the spectral index, strongly favor synchrotron emission as the physical origin of the radio emission in the jets. The fact that the X-ray emission is consistent with an extrapolation of the radio power law suggests that the synchrotron emission extends up to X-rays.

We can therefore derive the minimum energy associated with the eastern jet on 2004 February 12–13 (the jet for which we have the best constraints) under the assumption of equipartition between the magnetic and electron energy densities (Longair 1994). We assume the case of ballistic ejection (§ 3.1.1), corresponding to an angle between the jet axis and the line of sight of $\theta = 73^\circ$ and a bulk velocity $\beta = 0.79$. We use a frequency range of 1.4×10^9 to 2×10^{18} Hz with a spectral index of -0.6 and a flux density of 2.4 nJy at the pivot energy (Fig. 9) of 2.7 keV.

The major uncertainty for this calculation is the estimate of the volume of the emitting region. For that purpose, we use the same method as in Tomsick et al. (2003a), by assuming that the emitting region is a section of a cone with its vertex at the compact object. An upper limit can be obtained using the *Chandra* constraint on the source size (FWHM $\leq 1\farcs4$) as calculated in § 2.2.4. The opening angle of the cone is not well constrained, so we consider the upper limit from the *Chandra* observations of 12° and also 1°, as in XTE J1550−564 (Kaaret et al. 2003), giving a volume of the emitting region of about 4×10^{51} cm^3 (for an opening angle of 12°) or 3×10^{49} cm^3 (for 1°).

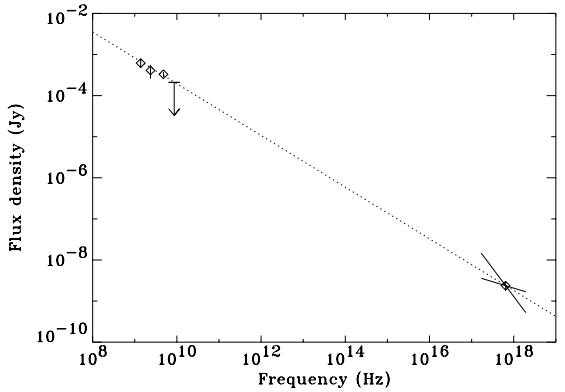

FIG. 9.—SED of the eastern jet on 2004 February 13 as observed by ATCA and *Chandra*. The "bow tie" represents the *Chandra* constraints on the flux and spectral index of the X-ray emission. The spectral index error lines are at 90% confidence level with the column density frozen to value measured for the black hole H1743−322.

For this volume range, the corresponding minimum energy required is about 1.6×10^{42} to 1.4×10^{43} ergs, and the associated magnetic field for which the energy in relativistic particles equals the magnetic energy is in the range 0.2–0.8 mG. The kinetic energy of a pure electron/positron plasma is $(1–9) \times 10^{42}$ ergs. If there is one proton per electron, then the kinetic energy of the electron/proton plasma is about 2×10^{42} to 1.1×10^{43} ergs. The associated mass of this electron/proton plasma would be of the order of $(1–4) \times 10^{21}$ g. For a typical mass accretion rate of 10^{18} g s^{-1}, this amount of material could be accumulated in 1000–4000 s. As the mass outflow rate is likely much lower, an accumulation time of the order of 1 day would be obtained if we assume a few percent efficiency; this could be consistent with the timescale of the initial radio flare.

The Lorentz factor of the X-ray synchrotron-emitting electrons would then be of the order of $(1–3) \times 10^7$ (taking a pivot energy of 2.7 keV and assuming equipartition), giving synchrotron lifetime cooling of the order of 2–50 yr, i.e., much longer than the lifetime of the X-ray jets of H1743−322. It is interesting to note (keeping in mind the limitation on the volume estimate) that all the above-derived quantities are of the same order of magnitude as those derived for XTE J1550−564 (Corbel et al. 2002; Tomsick et al. 2003a; Kaaret et al. 2003).

In the above, the X-ray emission seems consistent with an extrapolation of the synchrotron radio spectrum. However, it is of some interest to see whether some other emission mechanism, such as inverse Compton or synchrotron self-Compton (SSC), could also be viable at high energy. Assuming that only the radio emission is of synchrotron origin leads to an equipartition magnetic field of 0.2–0.7 mG; from this we deduce a range for the magnetic energy density of the order of 2×10^{-9} to 2×10^{-8} ergs cm^{-3}. The synchrotron photon energy density is then estimated, similar to the case of XTE J1550−564 (Tomsick et al. 2003a), to be of the order of 6×10^{-17} to 2×10^{-15} ergs cm^{-3}. The synchrotron photon density is well below the magnetic energy density, implying that SSC is very likely not important at X-ray

frequencies. As argued in Tomsick et al. (2003a), inverse Compton emission from the interstellar radiation field and the cosmic microwave background are unlikely because the associated energy density is well below the magnetic energy density. All of these considerations point to a coherent picture, which is that the X-ray emission associated with the jets of H1743−322 is synchrotron emission and therefore very high energy (>10 TeV) particles are produced in those jets.

3.3. *A Comparison with Other X-Ray Jets*

With this discovery of transient X-ray jets in H1743−322, we can now come to the idea that such events may be a common occurrence associated with any X-ray binary in outburst. Indeed, after the original discovery of X-ray jets in XTE J1550−564 (Corbel et al. 2002), a relativistic ejection in GX 339−4 has also been observed to later develop into a large-scale jet, possibly related to the interaction with the ISM (Gallo et al. 2004). However, the western large-scale jet of GX 339−4 has only been observed at radio frequencies (E. Gallo 2005, private communication), possibly due its fast decay rate. Indeed, taking the radio flux density quoted in Gallo et al. (2004), we can estimate the timescale associated with the two knots in the large-scale jets of GX 339−4 assuming an exponential or a power-law decay. The $1/e$-folding times of the exponential decays are 47.3 ± 8.3 and 57.0 ± 14.7 days, while the indices of the power-law decays are 5.9 ± 1.0 and 4.9 ± 1.0, respectively, for knot A and knot B. These timescales are consistent with those of H1743−322 but much faster than those of XTE J1550−564 (Kaaret et al. 2003). The X-ray observation of GX 339−4 was 6 months after the last detection of the western large-scale jet at radio frequencies (Gallo et al. 2004), and any X-ray emission likely decayed away before the observation.

It is unclear why the decay could be faster in some sources, but this may be related to local ISM conditions. Also, as outlined by Wang et al. (2003), the (already) fast decay of the X-ray emission from the eastern X-ray jet in XTE J1550−564 was not consistent with a forward shock propagating through the ISM. On the contrary, if the emission was driven by a reverse shock following the interaction of the ejecta with the ISM, then the rapidly fading X-ray emission could be the synchrotron emission from adiabatically expanding ejecta. With a "much" faster decay in H1743−322 or even GX 339−4, it may also be possible that the emission in these two cases is also related to a reverse shock moving back into the ejecta. In that case, it would be interesting to see whether a reverse shock model (as in Wang et al. 2003) could also reproduce the flux and spectral evolution that we observed during the rise of emission of the jets of H1743−322. Also, the fast transition between the rising and fading phases should also be explained.

In addition, we would like to mention the strong similarities with the neutron star system Sco X-1, which shows the ballistic motion of two radio lobes located on each side of the compact star (Fomalont et al. 2001a, 2001b). However, the Sco X-1 lobes are powered by a continuous and unseen ultrarelativistic beam of energy (Fomalont et al. 2001a, 2001b), possibly related to the fact that Sco X-1 is always close to the Eddington luminosity for a neutron star. Similarly, as discussed before, the bright radio flare in H1743−322 on 2003 April 8 took place around the transition to a steep power-law state, i.e., the state that is believed to be close to the Eddington luminosity. Otherwise, H1743−322, like most X-ray transients, is usually believed to be in a state of low accretion rate (quiescence), and even if a large fraction of the accretion energy could be carried out by an outflow (compact jet) in this accretion regime (Fender 2005), the total amount of energy would still be much less than in the brighter X-ray state. Therefore, as we do not have any indication for a continuous and persistent powerful beam of energy in H1743−322, we believe that the evolution of the large-scale jets in H1743−322 and XTE J1550−564 is the result of one (or several in a short period) impulsive ejection event(s) that later interact with the ISM.

As we have calculated above, many of the parameters (magnetic field, particle energy, etc.) derived for H1743−322 are consistent with those obtained for XTE J1550−564, and therefore strengthen the similarities between these two sources. Here we point to another similarity. When first detected, both jets in H1743−322 were at the same angular distance ($\sim 4'' = 0.16$ pc for a distance of 8 kpc) from the black hole (however, we note that the eastern jets may have been active some time before our first ATCA observations); i.e., the plasma originally ejected (probably around 2003 April 8) by the black hole has traveled the same distance before brightening again, possibly due to the collision with denser ISM. Similarly, in XTE J1550−564 the jets were observed to brighten at the same angular distance ($\sim 22'' = 0.5$ pc for a distance of 5.3 kpc) from the black hole. This could indicate that these two black holes lie in a cavity or that the jets propagate through an evacuated channel preexisting to the outburst (e.g., Heinz 2002) and that they "turn on" again when they hit a denser ISM phase.

Whereas either the ejection or the ISM was not symmetric or homogeneous in the case of XTE J1550−564 (Kaaret et al. 2003), the evolution of the radio emission of both jets may also suggest a similar case in H1743−322. Indeed, on 2004 February 13, the western jet was at an angular separation of $4\farcs47 \pm 0\farcs30$ and with the kinematics of the jets as outlined previously, it should have passed through the $4\farcs63$–$5\farcs25$ region during the last two radio observations. If the ejection were symmetric and the ISM homogeneous, the western jet should have been brighter at radio frequencies in 2004 April–June than in February. The nondetection of the western jet in the last two ATCA observation may therefore suggest a hint of asymmetry in the ISM density or in the ejection. However, a more detailed light curve would have been necessary to confirm this.

The Australia Telescope is funded by the Commonwealth of Australia for operation as a national facility managed by CSIRO. *RXTE* ASM results are provided by *XTE* ASM team at MIT. This publication makes use of data products from the Two-Micron All Sky Survey, which is a joint project of the University of Massachusetts and the Infrared Processing and Analysis Center/California Institute of Technology, funded by the National Aeronautics and Space Administration and the National Science Foundation. We thank the referee for constructive comments. S. C. acknowledges useful discussions with S. Heinz. P. K. acknowledges partial support from NASA *Chandra* grant GO4-5039X. J. A. T. acknowledges partial support from NASA *Chandra* grant GO3-4040X.

REFERENCES

Bautz, M. W., et al. 1998, Proc. SPIE, 3444, 210
Capitanio, F., et al. 2005, ApJ, 622, 503
Cash, W. 1979, ApJ, 228, 939
Corbel, S. 2004, in AIP Conf. Ser. 714, X-Ray Timing 2003: Rossi and Beyond, ed. P. Kaaret, F. K. Lamb, & J. H. Swank (New York: AIP), 127

Corbel, S., Fender, R. P., Tomsick, J. A., Tzioumis, A. K., & Tingay, S. 2004, ApJ, 617, 1272
Corbel, S., Fender, R. P., Tzioumis, A. K., Tomsick, J. A., Orosz, J. A., Miller, J. M., Wijnands, R., & Kaaret, P. 2002, Science, 298, 196
Distefano, C., Guetta, D., Waxman, E., & Levinson, A. 2002, ApJ, 575, 378
Doxsey, R., et al. 1977, IAU Circ. 3113
Emelyanov, A. N., Aleksandrovich, N. L., & Sunyaev, R. A. 2000, Astron. Lett., 26, 297
Fender, R. P. 2005, in Compact Stellar X-Ray Sources, ed. W. H. G. Lewin & M. van der Klis (Cambridge: Cambridge Univ. Press), in press (astro-ph/0303339)
Fender, R. P., Belloni, T. M., & Gallo, E. 2004, MNRAS, 355, 1105
Fender, R., Garrington, S. T., McKay, D. J., Muxlow, T. W. B., Pooley, G. G., Spencer, R. E., Stirling, A. M., & Waltman, E. B. 1999, MNRAS, 304, 865
Fomalont, E. B., Geldzahler, B. J., & Bradshaw, C. F. 2001a, ApJ, 553, L27
———. 2001b, ApJ, 558, 283
Freeman, P. E., Kashyap, V., Rosner, R., & Lamb, D. Q. 2002, ApJS, 138, 185
Gallo, E., Corbel, S., Fender, R. P., Maccarone, T. J., & Tzioumis, A. K. 2004, MNRAS, 347, L52
Garcia, M. R., McClintock, J. E., Narayan, R., Callanan, P., Barret, D., & Murray, S. S. 2001, ApJ, 553, L47
Heinz, S. 2002, A&A, 388, L40
Heinz, S., & Sunyaev, R. 2002, A&A, 390, 751
Homan, J., Miller, J. M., Wijnands, R., van der Klis, Belloni, T., Steeghs, D., & Lewin, W. H. G. 2005, ApJ, 623, 383
Kaaret, P., Corbel, S., Tomsick, J. A., Fender, R., Miller, J. M., Orosz, J. A., Tzioumis, A. K., & Wijnands, R. 2003, ApJ, 582, 945
Kaluzienski, L. J., & Holt, S. S. 1977, IAU Circ. 3099
Longair, M. S. 1994, High Energy Astrophysics (2nd ed.; Cambridge: Cambridge Univ. Press)
Miller, J. M., et al. 2004, ApJ, submitted (astro-ph/0406272)
Remillard, R. A., McClintock, J. E., Orosz, J. A., & Levine, A. M. 2004, ApJ, submitted (astro-ph/0407025)
Revnivtsev, M., Chernyakova, M., Capitanio, F., Westergaard, N. J., Shoenfelder, V., Gehrels, N., & Winkler, C. 2003, ATel, 132, 1
Reynolds, A. P., Parmar, A. N., Hakala, P. J., Pollock, A. M. T., Williams, O. R., Peacock, A., & Taylor, B. G. 1999, A&AS, 134, 287
Rupen, M. P., Mioduszewski, A. J., & Dhawan, V. 2003a, ATel, 137, 1
———. 2003b, ATel, 142, 1
———. 2004, ATel, 314, 1
Sams, B. J., Eckart, A., & Sunyaev, R. 1996, Nature, 382, 47
Sault, R. J., & Killeen, N. E. B. 1998, The MIRIAD User's Guide (Sydney: Australia Telescope National Facility)
Swank, J. 2004, ATel, 301, 1
Tomsick, J. A., Corbel, S., Fender, R., Miller, J. M., Orosz, J. A., Tzioumis, T., Wijnands, R., & Kaaret, P. 2003a, ApJ, 582, 933
Tomsick, J. A., & Kalemci, E. 2003, ATel, 198, 1
Tomsick, J. A., et al. 2003b, ApJ, 597, L133
Wachter, K., Leach, R., & Kellogg, E. 1979, ApJ, 230, 274
Wang, X. Y., Dai, Z. G., & Lu, T. 2003, ApJ, 592, 347
Weisskopf, M. C., Brinkman, B., Canizares, C., Garmire, G., Murray, S., & Van Speybroeck, L. P. 2002, PASP, 114, 1
White, N. E., & Marshall, F. E. 1983, IAU Circ. 3806

4.7.6

Evolution of the X-Ray Jets from 4U 1755-33.

Article publié dans :

Astrophys. J., 2006, 641, 410-417

Kaaret, P., Corbel, S., Tomsick, J. A., Lazendic, J., Tzioumis, A. K., Butt, Y., Wijnands, R.

The Astrophysical Journal, 641:410–417, 2006 April 10

EVOLUTION OF THE X-RAY JETS FROM 4U 1755−33

P. Kaaret,[1] S. Corbel,[2] J. A. Tomsick,[3] J. Lazendic,[4] A. K. Tzioumis,[5] Y. Butt,[6] and R. Wijnands[7]

Received 2005 October 12; accepted 2005 December 7

ABSTRACT

We report on new X-ray observations of the large-scale jets recently discovered in X-rays from the black hole candidate 4U 1755−33. Our observations in 2004 show that the jets found in 2001 are still present in X-rays. However, sensitive radio observations in 2004 failed to detect the jets. We suggest that synchrotron radiation is a viable emission mechanism for the jets and that thermal bremsstrahlung and inverse Compton emission are unlikely on energetic grounds. In the synchrotron interpretation, the production of X-rays requires acceleration of electrons up to ∼60 TeV, the jet power is $\sim 4 \times 10^{35}$ ergs s^{-1}, and the radio nondetection requires a spectral index $\alpha > -0.65$ ($S_\nu \propto \nu^\alpha$), which is similar to the indexes found in lobes surrounding some other compact objects. We find an upper limit on the flux of 4U 1755−33 in quiescence of 5×10^{-16} ergs cm^{-2} s^{-1} in the 0.3–8 keV band.

Subject headings: black hole physics — stars: individual (4U 1755−33) — stars: winds, outflows — X-rays: binaries

Online material: machine-readable tables

1. INTRODUCTION

Relativistic jets are often produced by accreting compact objects, including both stellar-mass X-ray binaries and active galactic nuclei. Jets appear to be important in the dynamics of the overall accretion flow in such systems, and a substantial fraction of the accretion energy of X-ray binaries may be dissipated in jets. Understanding the properties and production of jets is important for our understanding of the energetics and dynamics of the accretion process. Further, the jets from X-ray binaries in the Milky Way are a potentially significant source of energy input to the Galactic ISM and, if hadronic, a likely source of cosmic rays (Heinz & Sunyaev 2002) and a possible source of Galactic light-element nucleosynthesis (Butt et al. 2003).

Recent *XMM-Newton* observations have led to the discovery of a large-scale X-ray jet from the long-term X-ray transient and black hole candidate 4U 1755−33 (Angelini & White 2003). The X-ray source 4U 1755−33 was discovered with *Uhuru* (Jones 1977) and was, therefore, active in 1970 and may have been active earlier. It was later found to have an unusually soft spectrum (White & Marshall 1984; White et al. 1984) and a hard X-ray tail (Pan et al. 1995) suggesting a black hole candidate. The source shows X-rays dips that indicate that the system has a high inclination and an orbital period of 4.4 days (White et al. 1984; Mason et al. 1985). The source was still active in 1993 (Church & Balucinska-Church 1997) and then found in quiescence in 1996 (Roberts et al. 1996). The source was active for at least 23 years. The distance to the source is poorly constrained. It is likely greater than 4 kpc, because the optical counterpart (identified during outburst; McClintock et al. 1978) was not detected in quiescence (Wachter & Smale 1998), but less than 9 kpc because of the low level of visual extinction (Mason et al. 1985).

Angelini & White (2003) found a linear X-ray structure that is roughly symmetric about the position of 4U 1755−33 extending about 3′ to the northwest and 3′ to the southeast of the black hole candidate. There appear to be multiple knots in the jets. For estimated distances of 4–9 kpc, the angular size corresponds to jet lengths of 3–8 pc. Therefore, the jet must have taken at least 10–30 years to form. The source was active for at least 23 years, which appears sufficient to have formed the jet. *Chandra* observations do not show point sources along the jet but do detect emission over the area of the jet (Park et al. 2005). This indicates that the jet emission seen with *XMM-Newton* is truly diffuse and not an alignment of point sources.

The primary questions concerning the jet are what is the X-ray emission mechanism, how is the jet powered, and what is the total energy in the jet? We obtained new observations of 4U 1755−33 using *XMM-Newton* and the Australia Telescope Compact Array (ATCA) to attempt to measure a multiwavelength spectrum and observe the evolution of the jet. We describe the X-ray observations and analysis in § 2 and the radio observations and analysis in § 3, and we draw conclusions regarding the properties of the jet in § 4.

2. *XMM-NEWTON* OBSERVATIONS AND ANALYSIS

We observed 4U 1755−33 using *XMM-Newton* beginning on 2004 September 18 for 45.9 ks (ObsID 0203750101). We refer to this observation as "B." We also analyzed an archival observation obtained by Angelini & White (2003) beginning on 2001 March 8 with a duration of 19.4 ks (ObsID 0032940101). We refer to this observation as "A." Our observation was designed to have the same pointing and instrument modes as the earlier observation in order to facilitate comparison. The EPIC detectors were operated in full frame mode so that a large field could be imaged.

We reduced the data using the standard procedures described in the *XMM-Newton* User's Handbook and the *XMM-Newton*

[1] Department of Physics and Astronomy, University of Iowa, Van Allen Hall, Iowa City, IA 52242; philip-kaaret@uiowa.edu.
[2] AIM-Unité Mixte de Recherche CEA-CNRS-Université Paris VII-UMR 7158, CEA Saclay, Service d'Astrophysique, F-91191 Gif-sur-Yvette, France.
[3] Center for Astrophysics and Space Sciences, University of California at San Diego, La Jolla, CA 92093-0424.
[4] Kavli Institute for Astrophysics and Space Research, Massachusetts Institute of Technology, 77 Massachusetts Avenue, Cambridge, MA 02139.
[5] Australia Telescope National Facility, CSIRO, P.O. Box 76, Epping, NSW 1710, Australia.
[6] Harvard-Smithsonian Center for Astrophysics, 60 Garden Street, Cambridge, MA 02138.
[7] Astronomical Institute "Anton Pannekoek," University of Amsterdam, Kruislaan 403, 1098 SJ Amsterdam, Netherlands.

TABLE 1
XMM-Newton X-Ray Sources near 4U 1755−33

Source Number	R.A. (J2000.0)	Decl. (J2000.0)	Error[a] (arcsec)	Flux A[b] (10^{-14} ergs cm^{-2} s^{-1})	Flux B[c] (10^{-14} ergs cm^{-2} s^{-1})	Counterparts[d]
1	17 59 00.86	−33 45 48.1	0.2	243.9 ±10.0	171.9 ± 4.0	AW2003 1, 2MASS
2	17 57 58.88	−33 46 24.9	0.4	218.4 ±12.1	45.1 ± 2.7	2MASS
3	17 59 21.83	−33 53 15.6	0.7	77.1 ± 7.1	14.9 ± 1.9	AW2003 3
4	17 58 26.89	−33 59 53.8	0.8	76.2 ± 9.7	...	...
5	17 58 42.02	−33 41 48.8	0.3	29.3 ± 3.8	71.6 ± 2.9	1WGA J1758.6−3341
6	17 59 22.79	−33 50 25.2	0.7	63.8 ± 7.0	24.4 ± 2.3	1WGA J1759.3−3350, 2MASS
7	17 58 20.25	−33 42 51.8	0.6	63.4 ± 7.7	33.7 ± 2.2	...
8	17 58 49.48	−33 41 40.8	0.5	56.6 ± 5.7	42.7 ± 2.7	2MASS
9	17 58 36.67	−33 40 27.3	0.6	...	55.0 ± 5.7	...
10	17 58 38.88	−33 57 00.3	0.4	...	49.0 ± 2.5	...
11	17 58 21.03	−33 46 54.7	0.3	34.1 ± 4.3	41.8 ± 1.9	2MASS
12	17 59 27.97	−33 49 10.3	1.5	37.0 ± 4.5	...	...
13	17 58 44.04	−33 46 13.0	0.5	29.2 ± 3.4	11.7 ± 1.2	...
14	17 57 40.65	−33 45 53.9	0.6	...	25.4 ± 2.3	...
15	17 58 59.19	−33 50 16.3	0.5	25.3 ± 3.2	20.4 ± 1.5	...
16	17 58 44.16	−33 45 09.5	0.6	24.5 ± 3.2	12.2 ± 1.4	...
17	17 59 03.24	−33 59 18.1	0.9	...	17.8 ± 2.2	...
18	17 58 51.23	−33 49 13.8	0.7	...	17.1 ± 1.4	...
19	17 58 25.56	−33 57 46.8	2.8	...	15.8 ± 1.7	...
20	17 58 24.23	−33 52 58.8	0.5	...	14.8 ± 1.3	...
21	17 58 49.58	−33 57 14.0	0.6	...	14.1 ± 1.6	2MASS
22	17 58 12.44	−33 43 56.6	0.9	...	14.0 ± 1.7	...
23	17 58 14.22	−33 49 08.7	0.8	...	11.7 ± 1.2	...
24	17 58 43.37	−33 58 17.8	1.0	...	11.6 ± 1.5	...
25	17 59 08.17	−33 46 47.7	0.7	...	9.5 ± 1.3	...
26	17 58 46.92	−33 48 44.7	1.0	...	8.0 ± 1.1	...
27	17 58 22.29	−33 47 43.7	1.0	...	7.9 ± 1.0	...

Notes.—Units of right ascension are hours, minutes, and seconds, and units of declination are degrees, arcminutes, and arcseconds. Table 1 is also available in machine-readable form in the electronic edition of the *Astrophysical Journal*.

[a] Statistical error on the source position. Note that this does not include errors in the overall astrometry.

[b] Source flux for observation A in the 0.3–10 keV band calculated assuming a power-law spectrum with photon index of 1.5 and corrected for the Galactic absorption column density of 3.1×10^{21} cm^{-2}.

[c] The same for observation B.

[d] Indicates counterparts in Angelini & White (2003) (AW2003), the 2MASS catalog (2MASS), or the WGA catalog (WGA).

ABC Guide. We used SAS version 6.1.0. Calibration files were obtained using the online version of `cifbuild` available at *XMM-Newton* Science Operations Centre home page[8] on 2005 January 11. There were no obvious background flares in observation A and only a few small flares of less than 15% of the total count rate in observation B, so we decided not to filter the events on count rate, as is often necessary to remove background flares. In our analysis, we used only the EPIC MOS detectors because there are sizable chip gaps in the PN in the region covered by the jet. We extracted single, double, and triple events (PATTERN ≤ 12) for the MOS data and filtered according to standard procedures to eliminate events in bad pixels or rows or frames, in flickering pixels, identified as cosmic rays, outside the pulse height thresholds, near the CCD boundary, or outside the nominal field of view (specifically, we required FLAG equal to #XMMEA_EM).

2.1. *Point Sources*

We created images in sky coordinates in the 0.3–10 keV band and used `edetect_chain` to search for sources in the two MOS images for each observation. Our primary interest in source detection is the alignment of the two images, so we considered only sources with very high significance (likelihood parameter ≥ 50, equivalent to a single trial significance of 17 σ) because these sources give the most accurate positions. A list of high-significance sources is presented in Table 1. Many sources of lower significance are present in the images. The fluxes are for the 0.3–10 keV band and calculated from the count rate in this band assuming a power-law spectrum with a photon index of 1.5 and interstellar absorption with $N_{\rm H} = 3.1 \times 10^{21}$ cm^{-2} equal to the hydrogen column density along the line of sight in the Milky Way.

We searched for spatial coincidences between the source list from observation B and the catalog of 2MASS point sources. The astrometric accuracy of sources in the 2MASS catalog is 0.″2. We considered only sources with J magnitudes brighter than 12.5 to limit the source density. We find 1290 sources within 10′ of 4U 1755−33 for a source density of 0.0011 arcsec^{-2}. There are four matches between X-ray and 2MASS sources within 0.″9 and one additional match with an offset of 1.″1. Given the source density quoted above, the probability of a chance coincidence within 0.″9 between a 2MASS source and a given X-ray source is 0.3%. We conclude that the absolute astrometry of the *XMM-Newton* image is good to within 1.″0. We aligned observation A to observation B by matching 11 sources detected in both observations. The needed shift was 0.″15 in right ascension and 1.″3 in declination. After the shift, the average magnitude of offset in source positions between the two observations

[8] See http://xmm.vilspa.esa.es.

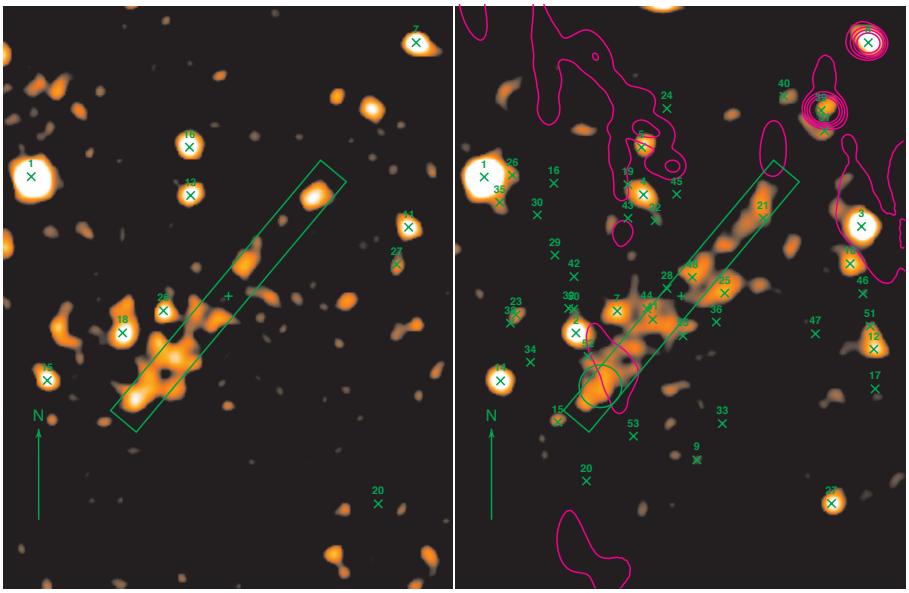

FIG. 1.—*XMM-Newton* images of 4U 1755−33. The image on the left is observation A (2001 March 8); on the right is observation B (2001 September 18). The green cross indicates the position of 4U 1755−33. The green rectangle encloses the jet and has a size of 44″ × 430″. On the left image, the green crosses mark the positions of *XMM-Newton* point sources reported in Table 1. On the right image, the green crosses mark the positions of *Chandra* point sources reported in Table 3. The green arrow indicates north and is 2′ long. Radio contours are superimposed on the image on the right in magenta. The radio contours represent the flux density at 13 cm at levels of 0.3, 0.6, 1.2, and 2.4 mJy. Also, on the right image, the green circle indicates the extraction region used to find the spectrum of the jet bright spot described in the text.

is 1.″4, which is about twice the typical statistical uncertainty in the positions as calculated by the SAS routine `emldetect`. We take 1.″4 as an estimate of the typical uncertainty in the relative *XMM-Newton* source positions between the two observations. Adding in the uncertainty in the absolute astrometry, we estimate the typical total uncertainty in the *XMM-Newton* source positions as 1.″7.

2.2. *Jet Morphology*

Images of the region around 4U 1755−33 are shown in Figure 1. The images are for the 0.3–10 keV band. Each image is the summed MOS1+MOS2 data in the 0.3–10 keV band and has been smoothed with a Gaussian filter with $\sigma = 8''$. The jet extends to the northwest (up and to the right) and southeast (down and to the left) from 4U 1755−33. The positions of point sources reported in Table 1 are marked on the image. Note that the image shown covers only a portion of the field of view, so several sources listed in the Tables are not present on the image.

Figure 2 shows the profiles of counts along the jet axis. The numbers of counts for observation A were multiplied by a factor of 2.51 to compensate for the shorter exposure time. Each profile represents the counts in the 0.5–10 keV band integrated in bins that extend 2″ along the jet axis and have a full width of 44″ perpendicular to the jet axis (the width is the same as the rectangular region shown in Fig. 1). The profiles were smoothed with a Gaussian with $\sigma = 6''$.

The morphology of the jet appears similar in the two observations. There appears to be some correspondence between knots found in the two observations, but extraction of knot motions is ambiguous because the morphologies of the individual knots have changed. With this caveat, we consider the morphology of the jet close to 4U 1755−33. Assuming that the black hole candidate (BHC) is no longer feeding the jet, one might expect the gap around the BHC to widen if the jets are moving away from the BHC. The knot to the southwest closest to the BHC (at a displacement of −30″ in Fig. 2) does appear to have shifted away from the BHC by 12″ if we compare the peaks of the two profiles in Figure 2. This corresponds to a speed of ∼0.2*c* for a

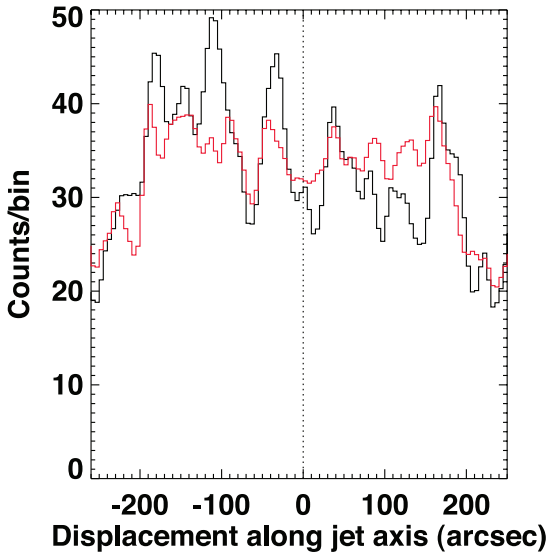

FIG. 2.—Profile of counts along the jet. The black line is for observation A, and the red line is for observation B. The counts for observation A were multiplied by a factor of 2.51 to compensate for the shorter observation time of that observation. The dotted line marks the position of 4U 1755−33.

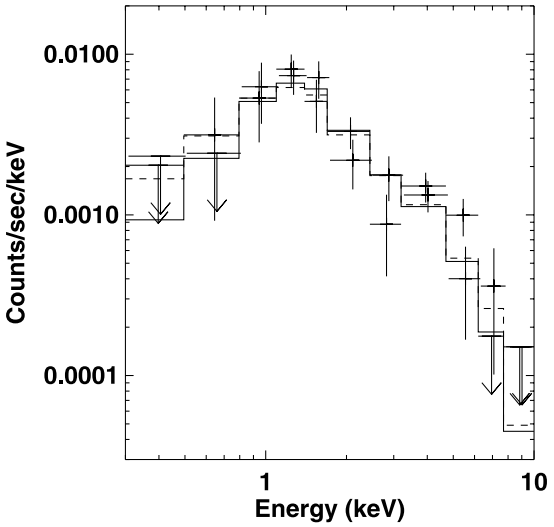

FIG. 3.—X-ray spectrum of jet emission for observation A. The data from the two MOS units are shown. The energy bins for MOS2 are artifically shifted up by 2% for clarity. The fit of a power-law model with absorption with $N_{\rm H} = 3.1 \times 10^{21}$ cm^{-2} is shown as a solid line. The fit of a MEKAL model with the same absorption is shown as a dashed line.

distance of 4 kpc ($\sim$0.4c for 9 kpc). However, on the northeast side of the jet, the closest knot appears to have remained stationary. We stress that any conclusions regarding physical motion of the jets is ambiguous. In particular, it is unclear whether these changes are really secular or merely random changes of flux over time, perhaps associated with interactions of the jet with the ISM.

2.3. *Jet Spectrum and Evolution*

We extracted spectra of the jet emission for each observation using the rectangular regions shown in Figure 1. Background spectra were extracted from a region with identical size and orientation displaced to a source-free region to the southwest of the jet. We used both MOS cameras for each observation and fit the two MOS spectra simultaneously using XSPEC 11.3.1.

We found adequate fits to the spectra with a power law subject to interstellar absorption and with a MEKAL thermal plasma emission model with solar abundances, again, subject to interstellar absorption (see Fig. 3). The fit results are presented in Table 2. We performed fits both with the interstellar absorption hydrogen column density, $N_{\rm H}$, fixed to the value found along the line of sight in H I maps (Dickey & Lockman 1990) and also allowing $N_{\rm H}$ to vary. We used the absorption model of Wilms et al. (2000), which is `tbabs` in XSPEC. We calculated the errors on the parameters using $\Delta\chi^2 = 2.71$ corresponding to 90% confidence for one free parameter of interest for the fits with $N_{\rm H}$ fixed, and $\Delta\chi^2 = 4.61$ corresponding to 90% confidence for two free parameters of interest for the fits with $N_{\rm H}$ allowed to vary. In the table, we report both the observed flux in the 0.5–10 keV band and the flux corrected for the effects of interstellar absorption.

Both the power law and the MEKAL thermal plasma model provide adequate fits to the spectra. Allowing $N_{\rm H}$ to be a free parameter widens the allowed ranges of the fit parameters. The preferred values for $N_{\rm H}$, when free, tend to be below the column density along the line of sight toward the source but include the line-of-sight density within the error interval.

No line emission is apparent. The upper bounds on line emission depend on the assumed line parameters. For line parameters similar to those found for SS 433 (Watson et al. 1986), we find 90% confidence upper bounds on the equivalent widths of Fe K emission lines of 0.6–2 keV. These are in the range of the equivalent width measured for the inner jets of SS 433 (Migliari et al. 2002) and are not constraining.

We also fit a spectrum for a region enclosing a bright spot toward the southeast end of the jet for observation B. The region is shown in Figure 1 and has a radius of 28″. This radius was selected to allow comparison with the radio beam, discussed below. The region was located to maximize the X-ray flux within that radius. We find an adequate fit with an absorbed power-law model with the absorption column density fixed to $N_{\rm H} = 3.1 \times 10^{21}$ cm^{-2}. We find a photon index $\Gamma = 1.78 \pm 0.52$, a flux of 2.8×10^{-14} ergs cm^{-2} s^{-1} in the 0.5–10 keV band, and a flux corrected for absorption of 3.6×10^{-14} ergs cm^{-2} s^{-1}.

TABLE 2
X-RAY SPECTRAL FITS TO JET EMISSION X-RAY SPECTRAL FITS TO JET EMISSION

Model[a]	$N_{\rm H}$[b] (10^{21} cm^{-2})	Γ[c]	kT (keV)	χ^2/dof	Flux[d] (10^{-13} ergs cm^{-2} s^{-1})	Unabsorbed Flux[e] (10^{-13} ergs cm^{-2} s^{-1})
Observation A: 2001 Mar 8						
Power-law	3.1	1.7 ± 0.3	...	19.3/20	2.0	2.5
	$2.4^{+2.1}_{-1.3}$	1.6 ± 0.4	...	18.8/19	2.1	2.5
MEKAL	3.1	...	>3.7	22.5/20	1.9	2.4
	$1.4^{+2.4}_{-1.3}$	...	>4.5	20.3/19	2.1	2.3
Observation B: 2004 Sep 18						
Power-law	3.1	1.5 ± 0.3	...	13.9/20	1.6	1.9
	$1.9^{+1.9}_{-1.3}$	1.4 ± 0.4	...	12.5/19	1.7	1.9
MEKAL	3.1	...	>5.2	13.8/20	1.6	1.9
	$1.8^{+1.7}_{-1.3}$	...	>6.1	12.2/19	1.7	1.8

[a] Model name (note all models include photoelectric absorption).
[b] Column density for photoelectric absorption.
[c] Photon index Γ for power-law models.
[d] Source flux in the 0.5–10 keV band.
[e] Source flux in the 0.5–10 keV band corrected for interstellar absorption.

From our two observations, we can make a crude estimate of the decay time of the jet. To minimize the dependence on the fitted spectral model, we refitted the data using a power-law model with the photon index fixed to 1.73 (the best-fit value for observation A) with interstellar absorption with $N_{\rm H} = 3.1 \times 10^{21}$ cm^{-2}. Adequate fits were found in all cases. We repeated the same procedure using a MEKAL model with fixed parameters and found that the fluxes differ by less than 5%. The uncertainty in the flux measurement is dominated by the uncertainty in the background subtraction. We find fluxes of $(20.0 \pm 2.2) \times 10^{-14}$ ergs cm^{-2} s^{-1} in the 0.5–10 keV band for observation A and $(14.6 \pm 1.4) \times 10^{-13}$ ergs cm^{-2} s^{-1} for observation B. For an exponential decay, the 1/*e* folding time is 11^{+24}_{-4} yr. We also considered the evolution of the northern and southern halves of the jet independently. For the southern half of the jet, the flux is $(12.5 \pm 1.7) \times 10^{-14}$ ergs cm^{-2} s^{-1} in the 0.5–10 keV band for observation A and $(7.8 \pm 1.0) \times 10^{-13}$ ergs cm^{-2} s^{-1} for observation B. The 1/*e* folding time of is $7.6^{+2.2}_{-1.3}$ yr. The flux from the northern part of the jet in observation B is consistent within the uncertainties with that in observation A. Therefore, we can place only a lower bound on the decay time of the northern jet of 8 years.

3. RADIO OBSERVATIONS AND ANALYSIS

On 2004 April 27, we obtained continuum radio observations of 4U 1755−33 using the Australia Telescope Compact Array (ATCA) located in Narrabri, New South Wales, Australia. This is 153 days before our *XMM-Newton* observations but still reasonably contemporaneous given the long life-time of the jet. The ATCA synthesis telescope consists of five 22 m antennas, which can be positioned along an east-west track with a short north-south spur, and a sixth antenna at a fixed location. The ATCA uses orthogonal polarized feeds and records full Stokes parameters. We observed with the ATCA for 10 hr at 1384 MHz (21.7 cm) and 2368 MHz (12.7 cm) simultaneously, with the array in the EW367 compact configuration that has baselines ranging from 46 to 4408 m. Because an interferometer acts as a filter for low spatial scales, the maximum angular size that can be imaged with the ATCA in this configuration is of the order of 5′ at 2368 MHz (8′ at 1384 MHz). Since the X-ray jets in 4U 1755−33 are diffuse hot spots, rather than a continuous smooth structure, radio imaging of the jets is possible with this ATCA configuration. The amplitude and band-pass calibrator was PKS 1934−638, and the antenna's gain and phase calibration, as well as the polarization leakage, were derived from regular observations of the nearby (6° away) calibrator PMN 1729−37. The editing, calibration, Fourier transformation, deconvolution, and image analysis were performed using the MIRIAD software package (Sault & Killeen 1998).

An image of the radio emission at 2.4 GHz (13 cm) is shown as contours in the right panel of Figure 1. Strong radio sources were detected in the northwest region of the field, but there is no significant detection of emission over the region of the X-ray jet. The rms sensitivity is 0.2 mJy beam^{-1}. There is a slight hint of emission toward the southeast end of the jet, but the flux density is always below 0.6 mJy and does not constitute a detection. The image at 1.4 GHz also shows no evidence for a significant detection of emission over the area of the jet.

4. *CHANDRA* OBSERVATIONS AND ANALYSIS

To determine if the features found in the *XMM-Newton* X-ray image are point sources or truly diffuse emission, we analyzed two *Chandra* observations obtained of the same field. The observations are a 22 ks exposure obtained on 2003 September 25 (ObsID 3510; PI S. Murray) and a 45 ks exposure obtained on 2004 June 25 (ObsID 4586; PI L. Angelini). The 2003 observation is the one analyzed by Park et al. (2005).

The *Chandra* data were subjected to the usual data processing and event screening and analyzed using the CIAO version 3.1 data analysis package (e.g., Kaaret 2005). We constructed images using all valid events on the S2 and S3 chips for ObsID 3510 and all events on the S3 and S4 chips for ObsID 4586. We computed exposure maps for each image for a power-law spectrum with photon index of 1.5 absorbed by a column density of $N_{\rm H} = 3.1 \times 10^{21}$ cm^{-2}. We used the `wavdetect` tool to search for X-ray sources. The sources with detection significance of 4 σ or higher are listed in Table 3.

We aligned the *Chandra* observations with sources in the 2MASS point-source catalog, as done for the *XMM-Newton* image above. We restricted the sources to have *J* magnitudes brighter than 12.5 to limit the source density. After applying a shift of 0.″3 to the *Chandra* astrometry, there are four matches within 0.″2 between *Chandra* sources in ObsID 4586 and 2MASS sources. We conclude that our corrected *Chandra* astrometry for ObsID 4586 is good to within 0.″2. We aligned ObsID 3510 to ObsID 4586 using several X-ray sources present in both images.

Summing the flux from all of the sources within the jet, as defined by the region shown in Figure 1, we find that discrete point sources contribute less than 10% of the total jet flux in each observation. Hence, we confirm the results of Park et al. (2005) that the X-ray jet from 4U 1755−33 is truly diffuse. We note that there are *Chandra* point-source counterparts to the two radio sources beyond the jet to the northwest. Therefore, these two radio sources are not associated with the diffuse X-ray emission of the jet.

To investigate the flux from 4U 1755−33 itself, we extracted counts from a circular region with a radius of 2″ at the position of the optical counterpart. We find a total of 3 counts in the 0.3–8 keV band in the two images. Using a 15″ radius region, we estimated the background in the source extraction region to be 3.0 counts. Therefore, we detect zero net counts from 4U 1755−33. Allowing for a Poisson distribution of counts, a 95% confidence upper limit on the number of source counts is 3.0. For a power-law spectrum with photon index of 1.5 absorbed by a column density of $N_{\rm H} = 3.1 \times 10^{21}$ cm^{-2}, this corresponds to an upper limit on the source flux of 5×10^{-16} ergs cm^{-2} s^{-1}. The upper limit on the unabsorbed flux is 6×10^{-16} ergs cm^{-2} s^{-1}. For distances of 4–9 kpc, this corresponds to a limit on the luminosity of $(1–6) \times 10^{30}$ ergs s^{-1}. This is similar to the quiescent luminosities of other short orbital period black hole X-ray binaries, such as XTE J1118+480 and A 0620−00 (Corbel et al. 2006).

5. DISCUSSION

There is now known to exist a broad range of jets from stellar-mass X-ray binaries. Persistent compact jets with lengths of tens of AU are produced in the low/hard X-ray spectral state. Impulsive jets produced at state transitions have been detected on lengths scales from hundreds of AU out to parsecs. Stationary lobes have been found in the radio at separations of several parsecs for sources such as 1E1740.7−2942 and GRS 1758−258 and in the X-ray with separations up to 70 pc from SS 433 (Watson et al. 1983).

The jet size of 3–8 pc in 4U 1755−33 is larger than the transient large-scale moving jets of XTE J1550−564 (Corbel et al. 2002) and H1743−322 (Corbel et al. 2005) but is similar

TABLE 3
Chandra X-Ray Sources near 4U 1755−33

Source Number	R.A. (J2000.0)	Decl. (J2000.0)	Error[a] (arcsec)	Flux 2003[b] (10^{-15} ergs cm^{-2} s^{-1})	Flux 2004[c] (10^{-15} ergs cm^{-2} s^{-1})	Counterparts[d]
1	17 59 00.859	−33 45 48.67	0.1	...	168 ± 7	AW2003 1, 2MASS
2	17 58 51.181	−33 49 13.96	0.1	57 ± 6	43 ± 4	XMM 18
3	17 58 21.041	−33 46 53.66	0.1	64 ± 6	169 ± 9	XMM 11
4	17 58 44.051	−33 46 12.00	0.1	34 ± 5	47 ± 4	XMM 13
5	17 58 44.259	−33 45 09.68	0.1	47 ± 5	33 ± 3	XMM 16
6	17 57 58.976	−33 46 25.94	0.1	...	217 ± 12	XMM 2
7	17 58 46.824	−33 48 45.02	0.1	26 ± 4	19 ± 2	XMM 26
8	17 58 20.343	−33 42 51.82	0.1	171 ± 16	98 ± 7	XMM 7
9	17 58 38.416	−33 52 00.99	0.3	10 ± 3	19 ± 2	...
10	17 58 22.234	−33 47 42.75	0.2	41 ± 5	26 ± 3	XMM 27
11	17 58 12.455	−33 43 56.47	0.2	...	44 ± 6	XMM 22
12	17 58 19.725	−33 49 35.24	0.2	...	21 ± 3	...
13	17 58 38.734	−33 57 00.24	0.1	57 ± 9	...	...
14	17 58 59.146	−33 50 16.97	0.2	22 ± 4	...	...
15	17 58 53.104	−33 51 11.25	0.2	11 ± 3	7.0 ± 1.5	...
16	17 58 53.508	−33 45 56.84	0.2	...	9.9 ± 1.8	...
17	17 58 19.579	−33 50 27.36	0.2	...	14 ± 2	...
18	17 58 05.137	−33 46 07.22	0.2	...	26 ± 4	...
19	17 58 45.698	−33 45 58.70	0.2	...	8.4 ± 1.7	...
20	17 58 50.079	−33 52 28.71	0.2	...	6.7 ± 1.5	...
21	17 58 31.416	−33 46 42.77	0.3	12 ± 3	...	...
22	17 58 42.817	−33 46 46.27	0.1	...	5.6 ± 1.3	...
23	17 58 57.504	−33 48 49.89	0.2	...	5.3 ± 1.3	...
24	17 58 41.580	−33 44 18.61	0.2	13 ± 4	...	...
25	17 58 35.470	−33 48 21.62	0.2	5.8 ± 1.9	6.4 ± 1.4	...
26	17 58 57.877	−33 45 46.42	0.1	15 ± 3	5.2 ± 1.4	XMM 22
27	17 58 24.178	−33 52 58.22	0.1	13 ± 4	...	...
28	17 58 41.560	−33 48 15.43	0.2	...	4.3 ± 1.2	...
29	17 58 53.396	−33 47 31.43	0.1	8 ± 2	4.3 ± 1.2	...
30	17 58 55.258	−33 46 38.68	0.3	...	3.7 ± 1.1	2MASS
31	17 58 24.932	−33 44 47.96	0.2	...	14 ± 3	...
32	17 58 51.943	−33 48 41.59	0.1	...	3.7 ± 1.1	...
33	17 58 35.714	−33 51 13.17	0.2	...	4.6 ± 1.3	...
34	17 58 55.982	−33 49 52.40	0.2	...	4.5 ± 1.2	...
35	17 58 59.228	−33 46 22.15	0.2	...	3.6 ± 1.2	...
36	17 58 36.358	−33 48 59.51	0.2	5.7 ± 1.9	4.0 ± 1.2	2MASS
37	17 57 53.117	−33 47 01.93	0.2	...	8 ± 7	...
38	17 58 58.107	−33 49 00.99	0.2	...	2.9 ± 1.0	...
39	17 58 25.308	−33 44 21.14	0.1	12 ± 4	20 ± 5	...
40	17 58 29.228	−33 44 02.49	0.2	8 ± 3	10 ± 2	...
41	17 58 43.075	−33 48 56.07	0.3	...	3.1 ± 1.0	...
42	17 58 51.382	−33 47 59.83	0.3	8 ± 2	...	...
43	17 58 45.690	−33 46 42.96	0.1	...	5.1 ± 1.2	...
44	17 58 43.694	−33 48 42.10	0.3	...	2.9 ± 1.0	...
45	17 58 40.548	−33 46 11.34	0.2	...	5.2 ± 1.4	...
46	17 58 20.885	−33 48 22.09	0.3	...	6.0 ± 1.6	...
47	17 58 25.897	−33 49 14.88	0.4	...	4.8 ± 1.5	...
48	17 58 38.894	−33 48 00.68	0.3	...	3.3 ± 1.0	...
49	17 58 49.783	−33 58 21.79	0.2	27 ± 7	...	...
50	17 58 51.420	−33 48 42.47	0.3	...	3.1 ± 1.0	2MASS
51	17 58 20.112	−33 49 04.92	0.3	19 ± 5	6 ± 2	...
52	17 58 49.906	−33 49 44.76	0.2	...	2.8 ± 0.9	...
53	17 58 45.112	−33 51 29.75	0.3	...	3.1 ± 1.0	...
54	17 58 42.143	−33 55 58.54	0.2	9 ± 3	...	...
55	17 58 39.876	−33 49 17.69	0.6	4.8 ± 1.8	...	...
56	17 58 11.545	−33 45 02.64	0.4	...	6 ± 3	...

Notes.—Units of right ascension are hours, minutes, and seconds, and units of declination are degrees, arcminutes, and arcseconds. Table 3 is also available in machine-readable form in the electronic edition of the *Astrophysical Journal*.

[a] Statistical error on the source position. Note that this does not include errors in the overall astrometry.

[b] Source flux on 2003 Sept 25 in the 0.3–10 keV band calculated assuming a power-law spectrum with photon index of 1.5 and corrected for the Galactic absorption column density of 3.1×10^{21} cm^{-2}.

[c] Source flux on 2004 June 25.

[d] Indicates counterparts in Angelini & White (2003) (AW2003), the 2MASS catalog (2MASS), or the *XMM-Newton* sources in Table 1 (XMM).

to the total size of the stationary radio lobes of 1E1740.7−2942 and GRS 1758−258 (Mirabel & Rodríguez 1999). The latter two sources are persistent X-ray emitters, similar in properties to 4U 1755−33 while it was X-ray bright. This may suggest that 4U 1755−33 represents the formation of a large-scale, nearly stationary jet.

The central source in 4U 1755−33 has turned off, and we now see the decay of the jet over a timescale of 10–40 years or perhaps longer for the northern part of the jet. While we can place only a lower bound of 23 years on the time over which the central source was active, and the jet was being energized, our detection of the decay of the jet suggests that the timescale for the energization of the jet is similar to or shorter than the decay time. We note that we detect flux decay only for the southern jet. The change in morphology is also stronger for the inner regions of the southern jet. This may suggest that the southern jet is the approaching and the northern jet is receding. Continued monitoring of 4U 1755−33 may reveal motion and decay of the northern jet.

A key question is the nature of the jet emission. We consider three possible emission mechanisms: thermal bremsstrahlung, inverse Compton, and synchrotron.

If the X-ray emission is thermal bremsstrahlung, then the total mass and energy of the jet can be estimated from its observed luminosity, temperature, and volume. For the volume, we assume that the jet occupies a roughly cylindrical volume with a diameter perpendicular to the direction of motion of $0\farcs2$ and a linear dimension of $6'$ multiplied by a filling factor of 0.2. The volume is then 2×10^{54} cm^3 for an assumed distance of 4 kpc. We took the flux from the X-ray spectral fits and set $kT = 5$ keV, which is the minimum temperature consistent with the fits. We find that the density of the jet material is 4 cm^{-3}, the total energy of the jet is 2×10^{47} ergs, and the total mass in the jet is 1×10^{31} g. The cooling time of the gas would then be 6×10^6 yr, which is much longer than the observed decay time. Also, if the jet were fed by the outflow from a mass accretion rate of 10^{19} g s^{-1}, corresponding the Eddington rate for a 10 $M_\odot$ compact object, at least 10^4 yr would be required to accumulate the needed mass. This is much longer than the observed decay timescale, and we conclude that the jet emission is unlikely to be thermal bremsstrahlung.

The best candidate source of seed photons for inverse Compton scattering is the interstellar radiation field (ISRF). The ISRF varies strongly with Galactocentric radius and height above the Galactic plane. On the sky, 4U 1755−33 is rather close to the Galactic center and it could be physically close to the Galactic center, although the low optical extinction suggests that the source is actually nearer than the Galactic bulge. We assume that 4U 1755−33 is at a distance of 8.5 kpc, close to the Galactic center, which maximizes the ISRF energy density. We adopt an energy density of 10 eV cm^{-3}, equal to the maximum found anywhere in the Milky Way (Strong et al. 2000) and assume, for simplicity, that all of the radiation is in the dominant component of ISRF near 1 μm (Mathis et al. 1983). To produce X-rays in the 0.3–10 keV, electrons with energies from $\sim$5 to $\sim$100 MeV are required. For an assumed X-ray spectral index $\alpha = -0.5$, defined as $S(\nu) \propto \nu^\alpha$, the total energy in relativistic electrons required is $\sim 10^{50}$ ergs. A 10 $M_\odot$ black hole producing energy at the Eddington rate with all of the energy going to perfectly efficient acceleration of electrons in the desired energy range would require $\sim$2000 yr to power the jet. This is much longer than the observed decay timescale. Therefore, it appears unlikely that the jet emits via inverse Compton radiation.

If X-ray emission is synchrotron, then synchrotron radio emission should be expected. To determine whether our upper limits on the radio flux are consistent with synchrotron emission, we consider the emission from the brightest X-ray spot along the jet. The X-ray spectrum was extracted from a circle with a radius of $28''$. This is slightly larger than the radio beam size at 2.4 GHz, so we can compare the X-ray flux density in the regions to the radio upper limit per beam, which we take as 3 times the rms noise level of 0.2 mJy. Comparing the X-ray and radio flux density, we derive a lower limit on the radio/X-ray spectral index $\alpha > -0.65$; i.e., the spectrum must be flatter than $\alpha = -0.65$. Therefore, our radio observations may simply be not sensitive enough to detect the radio synchrotron emission. The limit on the spectral index implies that the exponent, p, of the electron energy distribution, $N(E) \propto E^{-p}$, must be $p < 2.3$. This is within the range that can be produced by relativistic shocks. The spectral index is similar to that measured for the large-scale jets of the black hole candidate X-ray transient XTE J1550−564 of $\alpha = -0.660 \pm 0.005$ (Corbel et al. 2002) and consistent with the index of $\alpha = -0.45$ measured for the eastern lobe of SS 433 (Safi-Harb & Petre 1999).

To investigate the energetics of a jet radiating via synchrotron emission, we calculate the equipartition magnetic field. Using a spectral index $\alpha = -0.6$, which is consistent with the bound above, a lower frequency cutoff of 2.4 GHz, and the same assumption for distance and volume as for the thermal bremsstrahlung case, we find a magnetic field of 36 μG. The electrons producing the X-ray emission must have Lorentz factors up to 6×10^7, corresponding to energies of up to 60 TeV. The radiative lifetime of these electrons is of order 320 yr. The minimum total energy required is 2×10^{44} ergs, and the number of electrons needed to produce the observed radiation is 1.2×10^{46}. Assuming that the jet is composed of normal matter (i.e., roughly one proton per electron), then the required mass is 2×10^{22} g. These numbers are relatively insensitive to distance. For a distance of 9 kpc, the magnetic field decreases to 29 μG, the required energy increases to 1.5×10^{45} ergs, and the required mass increases to 1.3×10^{23} g. For the larger distance, the energy required corresponds to 2 weeks' accumulation at the Eddington rate for a 10 $M_\odot$ black hole and the mass could be accumulated in less than one day. Thus, the energy and material required for a synchrotron-emitting jet could easily have been accumulated over the 20 year active phase of the X-ray source. Using the decay rate calculated for the entire jet and the energy estimate from the synchrotron equipartition calculation, the energy loss rate is then $\sim 4 \times 10^{35}$ ergs s^{-1} for a 4 kpc distance. This is about 1% of the Eddington luminosity for a 10 $M_\odot$ black hole; therefore, the jet could have been energized by the conversion of a few percent of the energy into relativistic electrons.

The available data on the jet of 4U 1755−33 are consistent with the X-rays being synchrotron emission. Synchrotron emission also is the most favorable mechanism in terms of the required mass and energy. However, significantly deeper radio observations are required to test whether the predicted synchrotron radio emission is produced.

We thank an anonymous referee for useful comments and the *XMM-Newton* team for successfully executing the observation. P. K. acknowledges partial support from NASA grant NNG05GA08G and a faculty scholar award from the University of Iowa. J. A. T. acknowledges partial support from NASA grant NNG04GQ05G.

REFERENCES

Angelini, L., & White, N. E. 2003, ApJ, 586, L71
Butt, Y. M., Maccarone, T. J., & Prantzos, N. 2003, ApJ, 587, 748
Church, M. J., & Balucinska-Church, M. 1997, A&A, 317, L47
Corbel, S., Fender, R. P., Tzioumis, T., Tomsick, J. A., Orosz, J. A., Miller, J. M., Wijnands, R., & Kaaret, P. 2002, Science, 298, 196
Corbel, S., Kaaret, P., Fender, R. P., Tzioumis, A. K., Tomsick, J. A., & Orosz, J. A. 2005, ApJ, 632, 504
Corbel, S., Tomsick, J. A., & Kaaret, P. 2006, ApJ, 636, 971
Dickey, J. M., & Lockman, F. J. 1990, ARA&A, 28, 215
Heinz, S., & Sunyaev, R. 2002, A&A, 390, 751
Jones, C. 1977, ApJ, 214, 856
Kaaret, P. 2005, ApJ, 629, 233
Mason, K. O., Parmar, A. N., & White, N. E. 1985, MNRAS, 216, 1033
Mathis, J. S., Mezger, P. G., & Panagia, N. 1983, A&A, 128, 212
McClintock, J. E., Canizares, C. R., & Hiltner, W. A. 1978, IAU Circ. 3251
Migliari, S., Fender, R., Méndez, M. 2002, Science, 297, 1673
Mirabel, I. F., & Rodríguez, L. F. 1999, ARA&A, 37, 409
Pan, H. C., Skinner, G. K., Sunyaev, R. A., & Borozdin, K. N. 1995, MNRAS, 274, L15
Park, S. Q., Miller, J. M., McClintock, J. E., & Murray, S. S. 2005, ApJ, 618, L45
Roberts, M. S. E., Michelson, P. F., Cominsky, L. R., Marshall, F. E., Corbet, R. H. D., & Smith, E. A. 1996, IAU Circ. 6302
Safi-Harb, S., & Petre, R. 1999, ApJ, 512, 784
Sault, R. J., & Killeen, N. E. B. 1998, The Miriad User's Guide (Sydney: ATNF)
Strong, A. W., Moskalenko, I. V., & Reimer, O. 2000, ApJ, 537, 763
Wachter, S., & Smale, A. P. 1998, ApJ, 496, L21
Watson, M. G., Stewart, G. C., King, A. R., & Brinkmann, W. 1986, MNRAS, 222, 261
Watson, M. G., Willingdale, R., Grindlay, J. E., & Seward, F. D. 1983, ApJ, 273, 688
White, N. E., & Marshall, F. E. 1984, ApJ, 281, 354
White, N. E., Parmar, A. N., Sztajno, M., Zimmermann, H. U., Mason, K. O., & Kahn, S. M. 1984, ApJ, 283, L9
Wilms, J., Allen, A., & McCray, R. 2000, ApJ, 542, 914

Chapitre 5
Sources X ultra-lumineuses (ULX)

— Le monde tourne, c'est tout. On peut s'accrocher et tourner avec, ou se lever pour protester et se faire éjecter.

— Stephen King

5.1 Nature des sources X ultra-lumineuses

Suite à l'amélioration considérable de la sensibilité des télescopes X actuels – *XMM-Newton* et *Chandra* –, des progrès énormes ont été réalisés quant à la nature des sources X ultra-lumineuses (ULX). Il s'agit d'une population de sources X localisées dans des galaxies externes, mais dont la position est incompatible avec le coeur de la galaxie – il ne s'agit donc pas d'AGN. Contrairement aux systèmes binaires X extragalactiques, elles présentent la particularité d'avoir une luminosité apparente supérieure à la limite d'Eddington pour un trou noir classique de 10 $M_\odot$ (Fabbiano 1989; Colbert & Mushotzky 1999; Fabbiano 2006). Il pourrait s'agir de reste de supernova extrêmement lumineux, de trous noirs accrétant classiques – mais dont le rayonnement est très focalisé (King et al. 2001; Körding et al. 2002) – ou de trous noirs accrétant de "masse intermédiaire" de 100 à 10 000 $M_\odot$(Colbert & Mushotzky 1999).

La forte variabilité X, observée pour certaines de ces sources, favorise le scénario de source X accrétante (Makishima et al. 2000; Kaaret et al. 2001). Si l'émission X est isotrope, alors ces trous noirs devraient être beaucoup plus massifs que les trous noirs stellaires résultant de l'effondrement d'étoiles massives normales. Il devrait alors exister un nouveau mécanisme de formation de trous noirs de masse intermédiaire. On pourrait éventuellement imaginer qu'ils proviennent d'étoiles de population III ou de collisions à l'intérieur d'amas stellaires denses (voir Miller & Colbert 2004 pour une revue). Mais une question essentielle pour comprendre la nature de ces sources consiste à savoir si l'émission est focalisée ou non.

5.2 ULX = trous noirs de masse intermédiaires ?

5.2.1 Présence d'un disque d'accrétion "froid" ?

Sachant que les ULX ont été historiquement découvertes en X et vu leur distance lointaine, l'essentiel des informations acquises à ce jour provient du domaine des rayons X. Néanmoins, comme nous le verrons en section 5.3, la réponse pourrait de nouveau provenir des observations multi-longueurs d'onde. À ce jour, nous étions essentiellement limités à comprendre les mécanismes d'émission de ces sources à partir d'une étroite bande d'énergie de $\sim$ 0.5 à 10 keV.

Contrairement au passé, la résolution spatiale des satellites X actuels permet d'obtenir d'excellents spectres X sans contamination d'autres sources X éventuelles. Ceux ci sont habituellement décrits par un modèle comprenant un disque multi-couleur (MCD) et une loi de puissance – le tout corrigé de l'absorption interstellaire. Les paramètres de la composante thermique font l'objet d'un vif débat.

Nous avons été les premiers à mettre en évidence, de façon non ambiguë, que la température très basse du MCD pourrait impliquer la présence d'un trou noir de masse intermédiaire dans une ULX (Kaaret et al. 2003a). En effet, dans la source X–1 – de luminosité $> 10^{40}$ erg s^{-1} – de la galaxie irrégulière NGC 5408, nous mesurons une température du MCD de kT $= 0.11 \pm 0.03$ keV, c'est à dire au moins 10 fois plus faible que la température habituellement mesurée pour les trous noirs stellaires lorsqu'ils sont proches de la limite d'Eddington. Sachant que cette température est inversement proportionnelle à la racine quatrième de la masse du trou noir – $T \propto M^{-1/4}$, Frank et al. 2002 –, la comparaison avec les trous noirs stellaires impliquerait donc la présence d'un trou noir de plus de 80 $M_\odot$ au sein de NGC 5408 X–1 (Kaaret et al. 2003a).

Une telle composante froide – kT $\approx$ 0.1 – 0.2 keV – de disque d'accrétion a depuis été mise en évidence dans plusieurs ULX : NGC 1313 X–1, NGC 1313 X–2 (Miller et al. 2003), M81 X–9 ou Holmberg IX X–1 (Miller et al. 2004), Holmberg II X–1 (Dewangan et al. 2004) parmi d'autres. Cela entraînerait de nouveau la présence d'un trou noir avec une masse de l'ordre de quelques 10^{2-3} $M_\odot$ dans ces sources. Des études temporelles – analyse de spectres de puissance et recherche de QPO – en X pourraient aussi favoriser cette possibilité (Strohmayer et al. 2007).

Néanmoins, sachant que les ajustements de spectres X – "les fits" – ne sont pas uniques, nous n'avons pas spécialement favorisé cette interprétation dans Kaaret et al. (2003a). Au vu des propriétés radio (c.f. section 5.3) de NGC 5408 X–1 – première découverte de la contrepartie radio d'une ULX, Kaaret et al. 2003a –, nous avons au contraire étudié la possibilité d'une émission X focalisée. Il devenait possible que le rayonnement X de NGC 5408 X–1 soit du à un processus Compton inverse des photons du compagnon stellaire sur les électrons relativistes du jet – à l'origine de l'émission radio détectée.

En effet, le spectre X de NGC 5408 X–1 est parfaitement représenté par une loi de puissance "cassée" avec une coupure vers 0.65 keV (Kaaret et al. 2003a), en accord avec certaines prévisions théoriques (Georganopoulos et al. 2002). Ces caractéristiques impliqueraient que les émissions X et radio de NGC 5408 X–1 soient dues au rayonnement focalisé d'un jet relativiste pointant vers l'observateur – inclinaison inférieure à 10°– d'un trou noir normal de 10 $M_\odot$. NGC 5408 X–1 aurait pu être le premier exemple de microblazar, mais à ce jour nous considérons que cette conclusion n'est plus valable, compte tenu des nouvelles propriétés radio de NGC 5408 X–1 (c.f. section 5.3).

5.2.2 Réalité de l'excès en X mou ?

Quelques mots pour terminer sur la nature des spectres X des ULX. Les critiques se font de plus en plus nombreuses quant à l'interprétation de la composante thermique froide en un MCD classique. En effet, Gonçalves & Soria (2006) ont remarqué que dans certaines ULX brillantes, l'excès en X mou – correspondant au MCD – dépendait fortement de la modélisation de la composante en loi de puissance. Dans certains cas, l'excès pouvait même se transformer en déficit. De plus, selon King (2004), des éjections massives sont présentes dans tout objet accrétant proche de la limite d'Eddington. Elles pourraient ainsi constituer une enveloppe épaisse autour de la source, qui serait éventuellement à l'origine de la composante thermique (King 2004; Poutanen et al. 2006).

Il existe une analogie très intéressante dans notre Galaxie. En effet, SS 433 serait une source – trou noir ? – accrétant largement au dessus de la limite d'Eddington – d'un facteur 5000. Un vent très dense se formerait à partir des bords externes du disque d'accrétion entraînant une focalisation géométrique – ou mécanique, c'est à dire différente d'une focalisation due à l'amplification Doppler telle que proposée par Körding et al. 2002 – au sein de ce système (Begelman et al. 2006). Le système SS 433 étant vu par la tranche, l'émission du disque d'accrétion est invisible pour un observateur terrestre à cause du mur opaque constitué par le vent dense. Un rayonnement thermique de ce "mur" ou "cylindre" est par contre attendu vers l'ultraviolet (Begelman et al. 2006), mais l'absorption interstellaire dans la direction de SS 433 est trop forte pour espérer le détecter. Ce vent très dense serait ensuite à l'origine de la nébuleuse radio W50 au centre de laquelle est situé SS 433 (Dubner et al. 1998).

En considérant que les ULX soient similaires à SS 433 – donc des trous normaux super-Eddington –, mais vues de face cette fois-ci – la surface du disque d'accrétion quasi-tournée vers l'observateur –, il serait alors possible de voir la partie centrale du "cylindre", où l'épaisseur optique devient très faible. La composante thermique froide observée dans les ULX pourrait finalement provenir de cette zone de vent intense (Begelman et al. 2006; Poutanen et al. 2006).

Un nouvel argument pouvant aller dans ce sens : en modélisant les variations de température du MCD en fonction de la luminosité X de la source NGC 1313 X-2, Feng & Kaaret (2007) démontrent que l'évolution observée est incompatible avec un modèle standard de disque d'accrétion – $L \propto T^4$. Par contre elles reproduiraient bien les attentes du modèle "de type SS 433" (Poutanen et al. 2006). Donc, avant de vouloir déterminer la masse d'un trou noir au sein d'une ULX à partir d'approximation de spectres X, il est, avant tout, nécessaire de caractériser précisément la réalité de l'excès en X mou et surtout d'avoir une meilleure compréhension de la nature des mécanismes physiques impliqués, ce qui est loin d'être le cas à ce jour. Les trous noirs de masse intermédiaire demeurent donc actuellement une hypothèse de travail...

5.3 Une nébuleuse radio associée à NGC5408 X-1

En raison de la distance lointaine des ULX – au minimum quelques Mpc –, la recherche de contrepartie est rendue difficile à cause de leur flux très faible. Elle est rendue encore plus délicate à cause du manque de résolution spatiale et des problèmes de confusion avec la galaxie hôte. Néanmoins, nous avons pour la première fois détecté la contrepartie radio d'une ULX (voir la figure 5.1 de Kaaret et al. 2003a) : X–1 au sein de NGC 5408.

Dans la publication originelle (Kaaret et al. 2003a), nous détectons la contrepartie radio avec ATCA uniquement à 4.8 GHz. La limite supérieure à 8.6 GHz implique un spectre très pentu d'indice spectral > -1, indiquant que le rayonnement radio est caractéristique d'une émission synchrotron optiquement mince. La probabilité qu'il s'agisse d'une source radio en arrière plan est très faible. L'étude des rapports de flux ou des indices spectraux entre les bandes

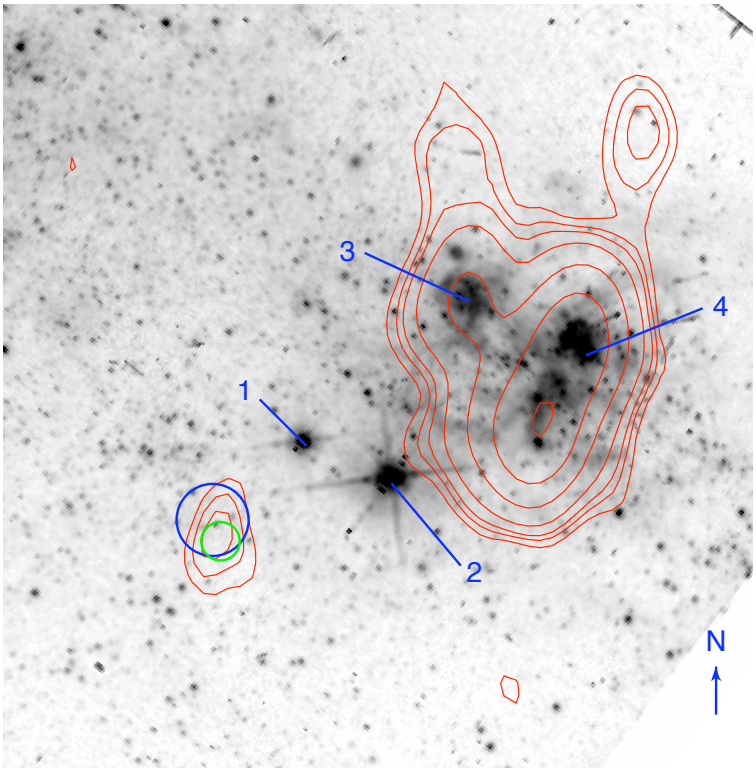

FIG. 5.1 – Image optique de NGC 5408. Les contours en rouge traduisent les différents niveaux d'émission radio détectée par ATCA. Les cercles en bleu (Chandra) et vert (ATCA) correspondent aux boites d'erreur X et radio. Figure extraite de Kaaret et al. (2003a).

radio, X et optique exclut qu'il puisse s'agir d'une étoile standard, d'une galaxie, d'un amas de galaxie, d'un reste de supernova, d'un AGN ou même de l'activité d'une binaire au sein de NGC 5408 (Kaaret et al. 2003a). À l'époque – sur la base de l'unique observation radio –, nous avions interprété cette détection comme étant le résultat de l'émission d'un jet relativiste – de type GRS 1915+105 – pointant vers l'observateur – inclinaison $< 10°$–, conclusion en accord avec la forme du spectre X (section 5.2). NGC 5408 X–1 aurait pu être le premier micro-blazar découvert... Mais la probabilité d'en détecter un était trop faible (Kaaret et al. 2003a) pour que cela soit confirmé !

En effet, nous avons poursuivi l'étude radio de NGC 5408 X–1 avec ATCA et le VLA jusqu'au début 2005 (Lang et al. 2007), tout comme Soria et al. (2006) avec ATCA. Premier constat : la contrepartie radio n'est pas variable (Soria et al. 2006; Lang et al. 2007) et semble être marginalement résolue selon Soria et al. (2006). Cela exclut irrémédiablement le scénario micro-blazar et une contribution due à l'émission standard d'un jet relativiste. Soria et al. (2006) expliquent le rayonnement radio comme celui d'une nébuleuse radio alimentée en énergie par un jet relativiste invisible. Grâce aux données VLA (voir la figure 5.2 Lang et al. 2007), nous confirmons que la source radio est étendue. La taille angulaire de la nébuleuse radio associée à X–1 est de 1.5″ à 2.0″, ce qui correspond à une taille physique de l'ordre de 35 à 56 pc. De plus, nous mesurons précisément, pour la première fois, la forme du spectre (voir la figure 5.2) et l'indice spectral est α = -0.82 $\pm$ 0.24 (Lang et al. 2007).

Ces observations radio apportent certaines contraintes quand à la nature de NGC 5408 X–1. La brillance de surface de la source radio est nettement plus grande que celle de toute supernova de taille équivalente. Il s'agit donc probablement d'une nébuleuse entourant la

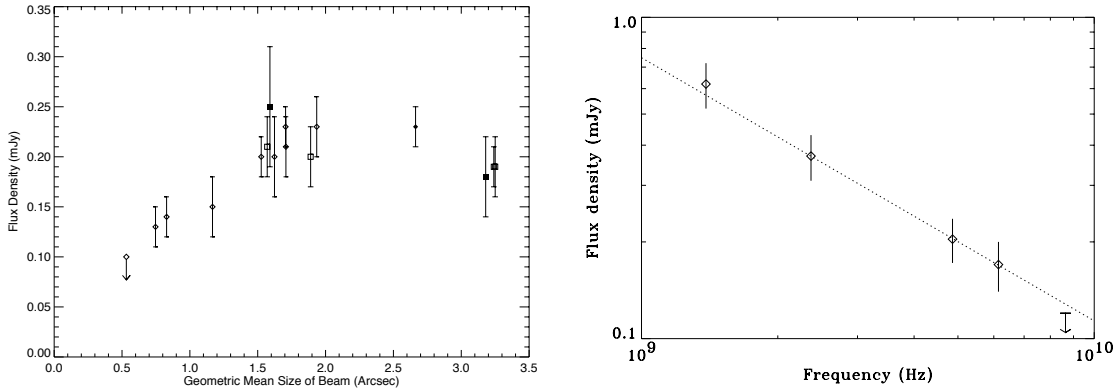

FIG. 5.2 – (Gauche) : Densité de flux radio à 4.8 GHz de NGC 5408 X–1 en fonction de la taille géométrique du faisceau principal du télescope (ATCA : carré, VLA : diamant). (Droite) : Spectre radio de NGC 5408 X–1. Figures extraites de Lang et al. (2007).

source X et elle est probablement alimentée par un jet relativiste. Les similarités sont très fortes avec la nébuleuse radio W50 de SS 433 (Dubner et al. 1998) qui a une taille physique d'environ 50 pc et dont l'indice spectral de l'émission radio varie de –0.5 à –0.8, en bon accord avec les mesures de NGC 5408 X–1.

Par contre, la brillance de surface de X–1 est cinq fois plus grande que celle de W50. En faisant le raisonnement classique de l'équipartition, on trouve que la luminosité totale de la nébuleuse radio est de 4×10^{34} erg s^{-1} et l'énergie minimale nécessaire pour illuminer cette nébuleuse est de 10^{49} erg. Le contenu énergétique des électrons relativistes de W50 est de l'ordre $(0.5 - 7) \times 10^{46}$ erg (Dubner et al. 1998), c'est à dire au moins deux ordres de grandeur plus faible que pour la nébuleuse de NGC 5408 X–1. Donc, si les deux nébuleuses sont similaires, alors le jet illuminant la nébuleuse entourant X–1 doit être plus puissant d'au moins deux ordres de grandeur que celui de SS 433 (Lang et al. 2007). Par suite, NGC 5408 X–1 est soit un trou noir standard accrétant bien au delà de la limite d'Eddington, soit un trou noir de masse intermédiaire – mais alors il reste toujours à expliquer la nature de l'émission X.

5.4 Nébulosités diverses et variées : vers la compréhension des ULX ?

Après la découverte de cette nébuleuse autour de NGC 5408 X–1, Miller et al. (2005) découvrirent aussi en radio une nébuleuse similaire autour de Holmberg II X–1 (Figure 5.3). Ses propriétés – bilan énergétique, dimension, spectre – sont identiques à celles de NGC 5408 X–1, avec un contenu énergétique d'un ordre de grandeur au delà de celui de W50.

À la même période, il est apparu que certaines ULX étaient entourées d'une nébuleuse ionisée. Par exemple, la nébuleuse optique (Pakull & Mirioni 2002; Kaaret et al. 2004) de Holmberg II X–1 (voir figure 5.3) est probablement photo-ionisée par la source X – et non pas par un jet relativiste. Les caractéristiques optiques impliquent de nouveau la présence d'un trou noir standard super-Eddington ou de nouveau un trou noir très massif et probablement bien au delà de 40 $M_\odot$ (Kaaret et al. 2004). Le nombre de détections (Pakull & Mirioni 2002, 2003) de telles nébuleuses optiques augmente rapidement : e.g. Holmberg IX X–1 (Grisé et al. 2006) ou NGC 1313 X–2 (voir Figure 5.4 extraite de Pakull et al. 2006) avec une dimension de plus de 300 pc pour Holmberg IX X–1, à comparer aux 50 pc de W50 (Grisé et al. 2006).

Il apparaît ainsi que la nature des ULX pourrait éventuellement être mieux comprise à

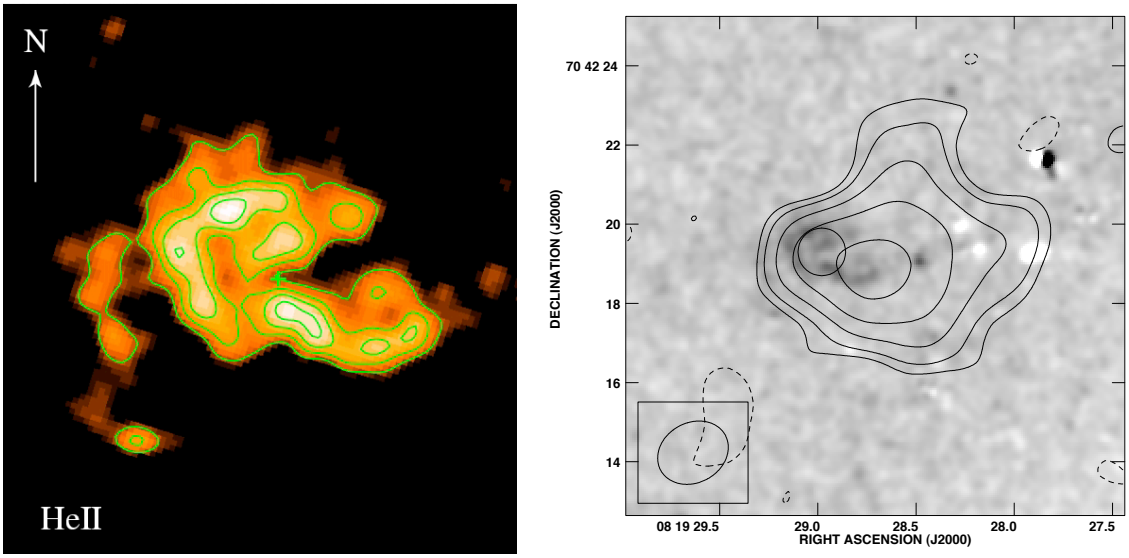

FIG. 5.3 – Holmberg II X–1. Gauche : Nébuleuse optique HeII. La flèche a une longueur de $1''$= 15 pc (Kaaret et al. 2004)), Droite : Contours de la carte VLA à 1.4 GHz superposés à l'image He II (Miller et al. 2005).

partir des propriétés de ces énormes nébuleuses détectées en radio et/ou optique. En effet, dans l'hypothèse où la nébuleuse optique est ionisée par le rayonnement X de la source compacte, elle peut servir de calorimètre permettant de mesurer la luminosité X réelle de l'ULX intégrée sur tous les angles de visée – sans faire d'hypothèse sur la focalisation ou non de l'émission X. De plus, si une nébuleuse synchrotron est découverte, il devient alors possible d'en étudier le contenu énergétique et éventuellement de relier le bilan énergétique du jet – non détecté – à la luminosité X déduite des observations. Ainsi, on pourrait éventuellement estimer la fraction de l'énergie issue de l'accrétion se retrouvant dans ces jets. Enfin, il serait intéressant de voir dans quelle mesure on pourrait relier la composante thermique froide (voir section 5.2) des spectres X de ces ULX aux propriétés de ces nébuleuses.

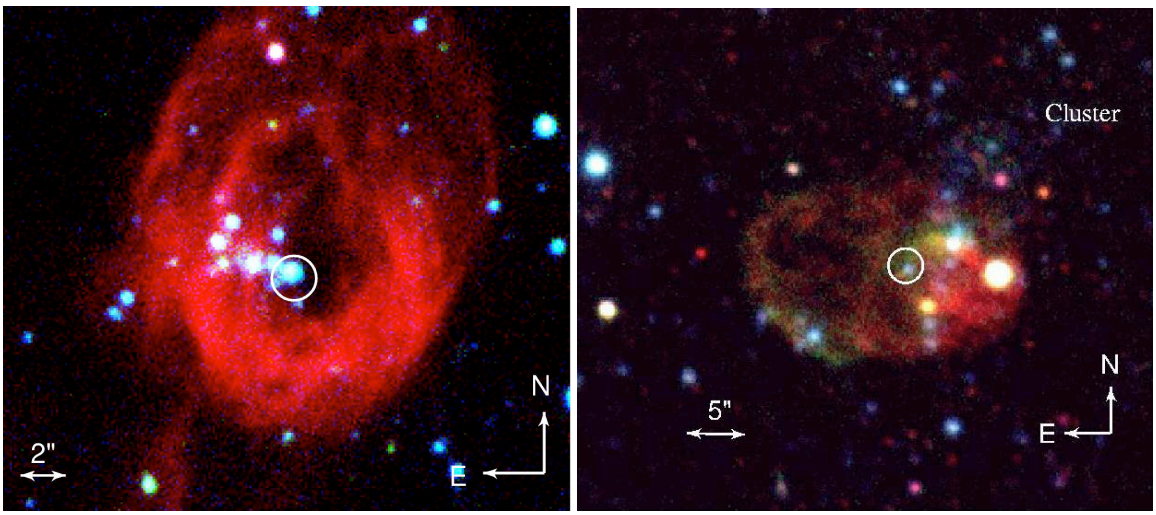

FIG. 5.4 – Présence de nébuleuse optique autour de Holmberg IX X–1 (Gauche, Grisé et al. 2006) et de NGC 1313 X–2 (Droite, Pakull et al. 2006).

5.5 Articles de recherche

5.5.1

Radio emission from an ultraluminous X-ray source.

Article publié dans :

Science, 2003, 299, 365-368

Kaaret, P., Corbel, S., Prestwich, A. H., Zezas, A.

REPORTS

Radio Emission from an Ultraluminous X-ray Source

Philip Kaaret,[1]* Stephane Corbel,[2] Andrea H. Prestwich,[1] Andreas Zezas[1]

The physical nature of ultraluminous x-ray sources is uncertain. Stellar-mass black holes with beamed radiation and intermediate black holes with isotropic radiation are two plausible explanations. We discovered radio emission from an ultraluminous x-ray source in the dwarf irregular galaxy NGC 5408. The x-ray, radio, and optical fluxes as well as the x-ray spectral shape are consistent with beamed relativistic jet emission from an accreting stellar black hole. If confirmed, this would suggest that the ultraluminous x-ray sources may be stellar-mass rather than intermediate-mass black holes. However, interpretation of the source as a jet-producing intermediate-mass black hole cannot be ruled out at this time.

One of the most enigmatic results to emerge from x-ray population studies of galaxies is the discovery of nonnuclear x-ray sources, which appear to have luminosity factors of tens to hundreds of times the Eddington luminosity for a neutron star—the so-called ultraluminous x-ray sources (*1*–*3*). The physical nature of these sources is controversial, and possible models include very luminous supernova remnants (*4*), gamma-ray burst remnants (*5*), accreting stellar-mass compact objects with radiation that is beamed mechanically (*6*) or relativistically (*7*), or accreting intermediate-mass black holes (*2*) with masses between 100 and several thousand solar masses ($M_\odot$). The detection of x-ray variability in several sources suggests that these sources are powered by accretion of material from a companion star or interstellar gas (*8, 9*) and are not supernova or gamma-ray burst remnants. If the radiation from these variable sources is isotropic, then a high inferred luminosity requires an intermediate-mass black hole. If the radiation is beamed, then a stellar-mass black hole could explain the observations.

Optical counterpart searches have shown that ultraluminous x-ray sources preferentially occur near star-forming regions (*10*) although they are also found in old globular clusters (*11, 12*). In star-forming systems, one unique massive star counterpart has been identified (*13*) and nebulae have been detected around several sources (*14*). In some cases, counterpart searches have shown that the sources are background objects (*15*). Further identification of optical and radio counterparts is needed to reveal the physical nature of the ultraluminous x-ray sources.

The dwarf irregular galaxy NGC 5408 contains a well-studied ultraluminous x-ray source, 2E 1400.2-4108 (*2, 16*–*18*). We observed the galaxy for a total exposure of 4683 s with the Chandra X-Ray Observatory on 7 May 2002 using the High-Resolution Mirror Assembly and the Advanced Camera Imaging Spectrometer spectroscopic array operated in an imaging mode suitable for a high count rate source (*19*). Images in the 0.3- to 8-keV band showed a point source (we place an upper limit on the source diameter of 0.9″) at a position of α(J2000) = $14^h03^m19^s.63$, δ(J2000) = −41°22′58″.7 with an error radius of 1″ at 90% confidence and a flux of 2.7×10^{-12} erg cm^{-2} s^{-1} in the 0.3- to 8-keV band corrected for Galactic absorption along the line of sight. If the x-ray emission is isotropic, then the source luminosity would be 1.1×10^{40} erg s^{-1} in the 0.3- to 8-keV band at the distance of 4.8 Mpc to NGC 5408 (*20*). The long-term x-ray light curve (Fig. 1) shows variability at a level of 40%.

A 4.8-GHz radio map of NGC 5408 from the Australia Telescope Compact Array (ATCA) showed a radio source at the location of the x-ray source. We reprocessed the 8-hour ATCA observation of NGC 5408 taken on 31 March 2000 (*21*) to produce a natural weighted map that provides optimum signal-to-noise ratio for point sources at the cost of angular resolution. We detected a 4.8-GHz radio source with a flux of 0.26 ± 0.04 mJy (1σ error) at a position of α(J2000) = $14^h03^m19^s.606$ and δ(J2000) = −41°22′59″.572 with an error radius of 0.1″ at 90% confidence (*22*), consistent with the Chandra position within the astrometric uncertainties. No source is present at the same location in 8.64-GHz data obtained simultaneously with the 4.8-GHz data and we place an upper limit (3σ) on the flux of 0.12 mJy based on the root-mean-square noise near that location. From the 4.8-GHz detection and the 8.64-GHz upper limit, we place a lower bound on the radio spectral index $\alpha_r > 1.0$, defined so $S_\nu \propto \nu_r^{-\alpha}$. From radio source counts (*23*) at 4.9 GHz, the probability of chance occurrence of a 0.18 mJy or brighter background radio source within the Chandra error circle is less than 1.0×10^{-5}. To estimate the probability of chance coincidence with a radio source internal to the galaxy, we compare NGC 5408 with NGC 1569, which is a dwarf irregular similar to NGC 5408 and has two sources that would have a 4.8-GHz flux of 0.18 mJy or larger if placed at the distance to NGC 5408 (*24*). The probability of chance coincidence within 1″ of the Chandra source given two radio sources within the optical extent of NGC 5408 is less than 0.002. Further, all of the radio sources in NGC 1569 have $\alpha_r < 0.6$, which is inconsistent with the steep spectrum of our radio source.

Several optical sources in a Hubble Space Telescope (HST) image of NGC 5408 (Fig. 2) lie within the ATCA/HST error circle; note that the relative error circle is dominated by the HST astrometric uncertainty. The brightest object in the radio or x-ray error circles

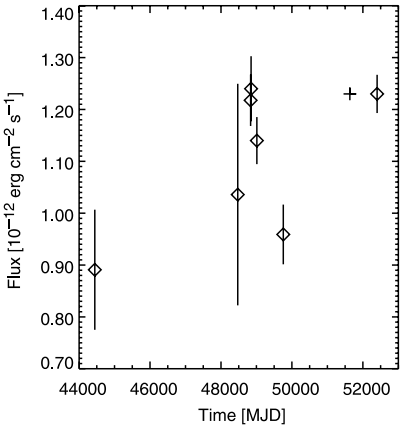

Fig. 1. Long-term x-ray light curve for the x-ray source in NGC 5408 (MJD, modified Julian date). Data shown as diamonds are, in chronological order, from the Einstein IPC (*40*), the ROSAT all-sky survey, the ROSAT HRI (*18*), two observations with the ROSAT PSPC (*16*), the ASCA SIS (*2*), and Chandra. The cross marks the time of the ATCA observation (the flux is arbitrary). The absorbed flux in the 0.5- to 2-keV band, calculated from each instrumental count rate using a spectral model derived from fitting the Chandra data, is plotted. The source appears variable with a ratio between the maximum and minimum fluxes of 1.4.

[1]Harvard-Smithsonian Center for Astrophysics, 60 Garden Street, Cambridge, MA 02138, USA. [2]Université Paris 7 and CEA Saclay (Federation APC), CE-Saclay, 91191 Gif-sur-Yvette Cedex, France.

*To whom correspondence should be addressed. E-mail: pkaaret@cfa.harvard.edu

REPORTS

has a visual magnitude of 22.1. The colors of the objects detected in both bands are similar to those of the overall stellar population of the galaxy (*20*). None of the objects show evidence of extended emission.

Given the radio counterpart and the brightest optical counterpart in the Chandra error circle (which we take as an upper limit to the optical flux), we find that the x-ray to optical flux ratio (*25*) is $f_x/f_v > 380$. We can also calculate two-point spectral indices (*26, 27*) between the radio, optical, and x-ray bands using the flux density at 4.8 GHz, the V band, and 1 keV. We find that the radio to x-ray index $\alpha_{rx} = 0.16$, the optical to x-ray index $\alpha_{ox} < 0.18$, and the radio-to-optical index $\alpha_{ro} > 0.15$. The ratio f_x/f_v of the object is much larger than the ratios found for stars, normal galaxies, clusters of galaxies, and active galactic nuclei (*25, 27*). We rule out the possibility that the object is a member of any of these classes of source. Identification as a blazar is ruled out because the f_x/f_v exceeds that of known blazars (*27, 28*); the radio spectrum is inconsistent with those of blazars, which have $\alpha_r < 0.8$ (*28*); and the x-ray to radio flux ratio is 9×10^{-9}, which is an order of magnitude larger than the most extreme known blazar (*28*).

Some young supernova remnants have high x-ray luminosities. However, supernova remnants produce copious optical line emission, which is not detected here. Taking the brightest source in the Chandra error circle, the upper limit on the Hα emission is 7×10^{-15} erg cm^{-2} s^{-1} if all of the flux in the HST F606W filter is Hα emission. A similarly obtained upper limit on the [O III] emission is 1.6×10^{-14} erg cm^{-2} s^{-1}. These upper limits are below the line fluxes measured for highly x-ray–luminous supernova remnants (*29, 30*). Optical line emission could be hidden by a high obscuring column (*31*), but such obscuration is inconsistent with the relatively low absorbing column density found from the x-ray spectrum (Fig. 3). Also, the observed x-ray variability would be unexpected for a supernova remnant. The line fluxes and the f_x/f_v ratio are also inconsistent with identification of the source as a young supernova.

X-ray binaries and rotation-powered neutron stars sometimes have high f_x/f_v ratios similar to what we find for the source in NGC 5408. The x-ray variability indicates the source is not a rotation-powered neutron star. If the source was located in the Milky Way, the luminosity would be of order 10^{33} to 10^{34} erg s^{-1}. Radio emissions when detected from Galactic x-ray binaries in such low luminosity states (*32, 33*) have flat or inverted spectra, which is inconsistent with the steep spectrum of the source and suggests that the source is not a low-luminosity x-ray binary in the Milky Way. The steep radio spectrum is consistent with optically thin synchrotron emission as produced by x-ray binaries in high luminosity states or during state transitions (*33–35*) and is consistent with the source being an x-ray binary in NGC 5408. The source x-ray variability may be less than seen from many x-ray binaries, but is consistent with that of Cyg X-1.

Radio emissions from x-ray binaries are associated with relativistic jets. The radio emission we detected from the ultraluminous x-ray source in NGC 5408 is probably from a

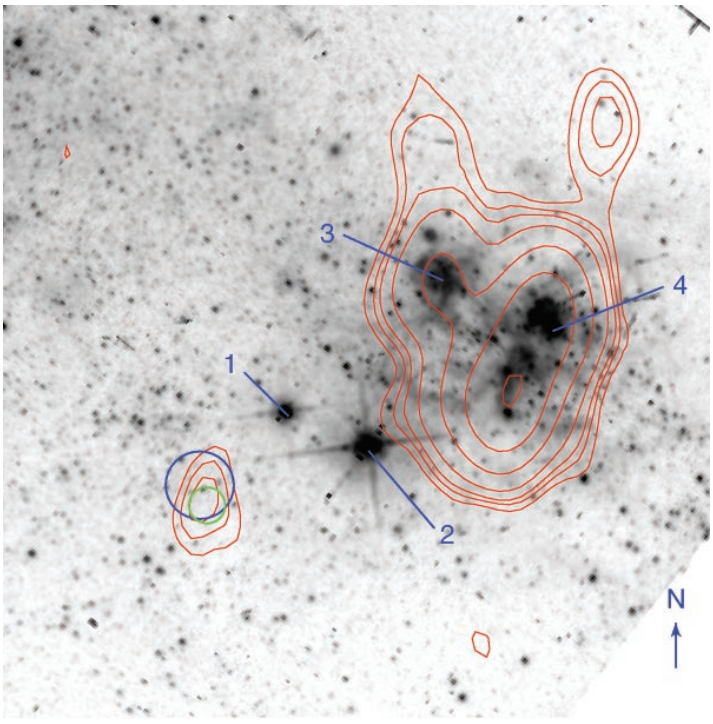

Fig. 2. An optical image of NGC 5408 showing the region containing the ultraluminous x-ray source with the ATCA 4.8-GHz radio contours (in red at flux densities of 0.12, 0.16, 0.2, 0.3, 0.6, 1.2, and 2.4 mJy/beam), error circles for the Chandra (blue) and ATCA (green) sources, and the main star formation regions [marked in blue as 3 and 4, note the associated radio emission (*21*); 1 and 2 are foreground stars (*18*)]. The arrow points north and has a length of 2″. To allow for the various astrometric uncertainties, we used a 1.5″ radius circle around the Chandra position and a 0.8″ radius circle around the ATCA position to identify possible optical counterparts. Two HST WPFC2 exposures (*20*), both 600 s and obtained on 4 July 2000, were analyzed using the HSTphot (*41*) stellar photometry package to obtain simultaneous photometry in the two filters (F814W and F606W) and corrected for reddening using an extinction E(B – V) = 0.068 based on dust maps (*42*) and an $R_V = 3.1$ extinction curve. The image shown is with the F606W filter, which includes the lines Hα and [O III]. We corrected the absolute astrometry of the HST images, using stars from the US Naval Observatory A2.0 catalog and the IMWCS tool from the Smithsonian Astrophysical Observatory Telescope Data Center. There are no US Naval Observatory A2.0 stars on the WF3 chips where the x-ray source is located, and we estimate a total astrometric error for positions on the WF3 chip of 0.5″.

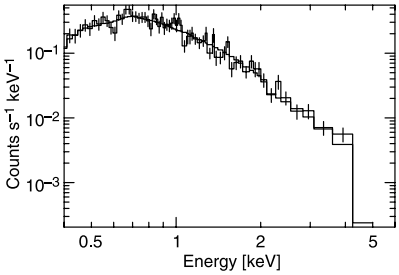

Fig. 3. X-ray spectrum for the ultraluminous x-ray source in NGC 5408 in the 0.4- to 8-keV band. The x-ray spectrum is inconsistent with simple single-component models. A broken power-law model with an absorbing column density equal to the Galactic line-of-sight value of 5.6×10^{20} cm^{-2} gave a good fit with $\chi^2/df = 62.5/61$, a low-energy power-law photon index between −0.8 and +1.7, a break energy of 0.65 ± 0.06 keV, and a high-energy power-law photon index of 3.1 ± 0.2. The spectrum is also adequately fitted ($\chi^2/df = 62.6/60$) with a model consisting of thermal emission from an accretion disk at a temperature $kT = 0.11 \pm 0.03$ keV with an added power-law component with photon index $\Gamma = 2.75 \pm 0.34$ and an absorption column density $N_H = (3.5 \pm 1.9) \times 10^{21}$ cm^{-2}, significantly above the Galactic column. Here and in the text, all errors quoted on spectral parameters are at the 90% confidence level for a single parameter. The spectral modeling was done with the ISIS software (http://space.mit.edu/ASC/ISIS) to correct for the moderate (14%) pileup due to the high counting rate.

relativistic jet. It could be from an accreting stellar-mass black hole producing relativistic jets (a microquasar) beamed toward us (*34*). The intensity of isotropic rest-frame emission from a continuous jet with a power law spectrum with radio spectral index α_r is amplified by a factor $\delta^{2+\alpha_r}$ where $\delta = \gamma^{-1}(1 - \beta \cos \theta)^{-1}$ is the Doppler factor (for the approaching jet) where β is the jet speed as a fraction of the speed of light and $\gamma = (1 - \beta^2)^{-0.5}$. The Galactic microquasar GRS 1915+105 has $\delta = 0.34$ and a distance near 11 kpc (*35*). GRS 1915+105 is highly variable. Radio fluxes of about 300 mJy at 4.8 GHz are observed in bright radio flares when superluminal jets are resolved, whereas the more typical radio fluxes are about 10 mJy while the source is x-ray active but not undergoing a bright radio flare. If the ATCA observation happened to catch the NGC 5408 source during such a bright flare, then a Doppler factor as low as $\delta = 2.1$ would suffice to produce the observed radio flux (with $\alpha_r = 1.0$). However, the probability of catching such an event with a single radio observation is low, unless the NGC 5408 source is an extremely active jet source. Scaling from the more typical radio flux of GRS 1915+105 of about 10 mJy, we find that a Doppler factor $\delta > 5.8$ would be needed to produce the observed flux. This is compatible with the constraints on the ejecta velocities for GRS 1915+105. If $\gamma = 5$ as inferred for GRS 1915+105, then tilts of the jet axis relative to the line of sight of up to 10° could produce $\delta > 5.8$. Roughly 1 of 70 of extragalactic microquasars should be aligned like this. A steeper radio spectral index or higher intrinsic luminosity would reduce the required δ.

The x-ray emission could also be relativistically beamed jet emission (*7*). The fact that $\alpha_r > \alpha_{rx}$ rules out the possibility that a single-component spectrum, like synchrotron emission, produces both the radio and x-ray emission. Inverse Comptonization of photons from a massive companion star by a jet may power the ultraluminous x-ray sources (*36*). The x-ray spectrum predicted by this process has the form of a broken power law with the break near 1 keV and a cutoff at energies above the x-ray band. The Chandra x-ray spectrum is consistent with this form (Fig. 3) with a break energy of 0.65 ± 0.06 keV and a spectral index at high energies of $\alpha_x = 2.1 \pm 0.2$. The beaming pattern for inverse-Compton emission with a photon source external to the jet—for example, from the companion star—varies as $\delta^{3+2\alpha_x}$ for a continuous jet, so very large amplifications are possible (e.g., 4×10^5 for $\delta = 6$). Hence, the jet x-ray luminosity may be as low as 10^{34} erg s^{-1}. The break energy we measure is similar to what has been modeled (*36*). However, our measured x-ray spectral parameters would imply an unusually steep power law index for the injected relativistic electrons of $p = 4.2 \pm 0.4$.

If the source is an accreting black hole and the x-ray emission is isotropic, then the luminosity implies a minimum mass of 80 $M_\odot$. The spectral index of the hard spectral component, if the spectrum is fitted with the sum of a power law plus thermal accretion disk emission, is $\alpha_x = 1.75 \pm 0.34$, which is similar to that found for black hole candidate x-ray binaries in their high flux states (*37*). The temperature of the soft thermal component is $kT = 0.11 \pm 0.03$ keV, which is lower than found for stellar-mass black holes in the Milky Way (*38*). Such a low temperature is also unlikely to arise from mechanically beamed radiation from a stellar-mass black hole (*6*). Some other ultraluminous sources have high temperatures, which is inconsistent with the presence of intermediate-mass black holes unless they are very rapidly rotating (*8*). The low temperature found for the NGC 5408 source is consistent with that expected for a nonrotating black hole with a mass above 100 $M_\odot$ (*2, 8*). The radio spectral index and the radio to x-ray flux ratio are similar to the (highly variable) ones measured for microquasars (*34, 35*) suggesting that the radio emission could arise from jets similar to those produced by microquasars. The source lies about 12″ from the star formation regions of NGC 5408 that contain super star clusters, giving a projected displacement of 280 pc. An x-ray binary with a speed of 10 km/s, from either interactions in a cluster or a supernova kick, could traverse this distance in 30 million years. Hence, an intermediate-mass black hole could have formed in one of the observed super star clusters (*39*) and moved to the present location within the lifetime of a massive companion star.

The ultraluminous x-ray sources have been interpreted as evidence for intermediate-mass black holes (*2*). The results presented here show that the radio, optical, and x-ray properties of the ultraluminous x-ray source in NGC 5408 are consistent with beamed emission of a relativistic jet from a stellar-mass black hole. This suggests that at least some of the ultraluminous x-ray sources may be beamed emission from stellar-mass black holes (*7*).

References and Notes

1. G. Fabbiano, *Annu. Rev. Astron. Astrophys.* **27**, 87 (1989).
2. E. J. M. Colbert, R. F. Mushotzky, *Astrophys. J.* **519**, 89 (1999).
3. T. P. Roberts, R. S. Warwick, *Mon. Not. R. Astron. Soc.* **315**, 98 (2000).
4. A. C. Fabian, R. Terlevich, *Mon. Not. R. Astron. Soc.* **280**, L5 (1996).
5. Q. D. Wang, S. Immler, W. Pietsch, *Astrophys. J.* **523**, 121 (1999).
6. A. R. King *et al.*, *Astrophys. J.* **552**, L109 (2001).
7. E. Körding, H. Falcke, S. Markoff, *Astron. Astrophys.* **382**, L13 (2002).
8. K. Makishmia *et al.*, *Astrophys. J.* **535**, 632 (2000).
9. P. Kaaret *et al.*, *Mon. Not. R. Astron. Soc.* **321**, L29 (2001).
10. T. P. Roberts *et al.*, *Mon. Not. R. Astron. Soc.* **325**, L7 (2001).
11. L. Angelini, M. Loewenstein, R. F. Mushotzky, *Astrophys. J.* **557**, L35 (2001).
12. H. Wu *et al.*, *Astrophys. J.* **576**, 738 (2002).
13. J.-F. Liu, J. N. Bregman, P. Seitzer, *Astrophys. J.* **580**, L31 (2002).
14. M. W. Pakull, L. Mirioni, in *New Visions of the X-ray Universe in the XMM-Newton and Chandra Era*, 26 to 30 November 2001, European Space Research and Technology Centre (ESTEC), Noordwijk, Netherlands; available at http://arxiv.org/abs/astro-ph/0202488 (2002).
15. L. Foschini *et al.*, *Astron. Astrophys.* **396**, 787 (2002); available at http://arxiv.org/abs/astro-ph/0209500.
16. G. C. Stewart *et al.*, *Mon. Not. R. Astron. Soc.* **200**, 61P (1982).
17. A. C. Fabian, M. J. Ward, *Mon. Not. R. Astron. Soc.* **263**, L51 (1993).
18. C. Motch, M. W. Pakull, W. Pietsch, in *Violent Star Formation from 30 Doradus to QSOs*, G. Tenorio-Tagle, Ed. (Cambridge Univ. Press, Cambridge, 1994), pp. 208–213.
19. M. C. Weisskopf *et al.*, *Proc. Astron. Soc. Pac.* **114**, 1 (2002).
20. I. D. Karachentsev *et al.*, *Astron. Astrophys.* **385**, 21 (2002).
21. I. R. Stevens, D. A. Forbes, R. P. Norris, *Mon. Not. R. Astron. Soc.* **335**, 1079 (2002).
22. J. E. Reynolds *et al.*, *Astron. Astrophys.* **304**, 116 (1995).
23. R. B. Partridge, K. C. Hilldrup, M. I. Ratner, *Astrophys. J.* **308**, 46 (1986).
24. A. Greve *et al.*, *Astron. Astrophys.* **381**, 825 (2002).
25. T. Maccacaro *et al.*, *Astrophys. J.* **253**, 504 (1982).
26. H. Tananbaum *et al.*, *Astrophys. J.* **234**, L9 (1979).
27. J. T. Stocke *et al.*, *Astrophys. J. Suppl. Ser.* **76**, 813 (1991).
28. H. Landt *et al.*, *Mon. Not. R. Astron. Soc.* **323**, 757 (2001).
29. Y.-H. Chu, C.-H. Chen, S.-P. Lai, in *Supernovae and Gamma-Ray Bursts*, M. Livio, N. Panagia, K. Sahu, Eds. (Cambridge Univ. Press, Cambridge, 2001), pp. 131–143.
30. W. P. Blair *et al.*, *Astrophys. J.* **272**, 84 (1983).
31. T. P. Roberts *et al.*, *Mon. Not. R. Astron. Soc.* **337**, 677 (2002); available at http://arxiv.org/abs/astro-ph/0208196.
32. R. P. Fender, *Mon. Not. R. Astron. Soc.* **322**, 31 (2001).
33. S. Corbel *et al.*, *Astrophys. J.* **554**, 43 (2001).
34. I. F. Mirabel, L. F. Rodríguez, *Annu. Rev. Astron. Astrophys.* **37**, 409 (1999).
35. R. P. Fender *et al.*, *Mon. Not. R. Astron. Soc.* **304**, 865 (1999).
36. M. Georganopoulos, F. A. Aharonian, J. G. Kirk, *Astron. Astrophys.* **388**, L25 (2002).
37. Y. Tanaka, N. Shibazaki, *Annu. Rev. Astron. Astrophys.* **34**, 607 (1996).
38. K. Ebisawa *et al.*, *Proc. Astron. Soc. Jpn.* **46**, 375 (1994).
39. T. Ebisuzaki *et al.*, *Astrophys. J.* **562**, L19 (2001).
40. D. E. Harris *et al.*, *The Einstein Observatory Catalog of IPC X-ray Sources* (Smithsonian Astrophysical Observatory, Cambridge, MA, 1993).
41. A. E. Dolphin, *Proc. Astron. Soc. Pac.* **112**, 1383 (2000).
42. D. Schlegel, D. Finkbeiner, M. Davis, *Astrophys. J.* **500**, 525 (1998).

43. We thank M. Georganopoulos for explaining the details of his model, the Chandra X-Ray Observatory team for carrying out the observations, M. Garcia and A. Kong for useful comments, J. Reynolds and T. Tzioumis for discussions of ATCA position uncertainties, and the Aspen Center for Physics where part of this work was carried out. Supported in part by a NASA Long-Term Space Astrophysics grant and a Chandra grant. We made use of NASA's High-Energy Astrophysics Science Archive Research Center. The Australia Telescope is funded by the Commonwealth of Australia for operation as a National Facility managed by the Commonwealth Scientific and Industrial Research Organisation.

21 October 2002; accepted 5 December 2002

5.5.2

A radio nebula surrounding the ultra-luminous X-ray source in NGC 5408

Article publié dans :

Astrophys. J., 2007, 666, 79

Lang, C., Kaaret, P., Corbel, S., Mercer, A.

THE ASTROPHYSICAL JOURNAL, 666:79–85, 2007 September 1

A RADIO NEBULA SURROUNDING THE ULTRALUMINOUS X-RAY SOURCE IN NGC 5408

CORNELIA C. LANG AND PHILIP KAARET
Department of Physics and Astronomy, University of Iowa, Van Allen Hall, Iowa City, IA 52242; cornelia-lang@uiowa.edu

STÉPHANE CORBEL
AIM-Unité Mixte de Recherche CEA-CNRS, Université Paris VII-UMR 7158, CEA Saclay, Service d'Astrophysique, F-491191 Gif sur Yvette, France

AND

ALLISON MERCER
Department of Physics and Astronomy, University of Iowa, Van Allen Hall, Iowa City, IA 52242
Received 2007 February 28; accepted 2007 May 4

ABSTRACT

New radio observations of the counterpart of the ultraluminous X-ray source in NGC 5408 show for the first time that the radio emission is resolved with an angular size of 1.5″–2.0″. This corresponds to a physical size of 35–46 pc, and rules out interpretation of the radio emission as beamed emission from a relativistic jet. In addition, the radio spectral index of the counterpart is well determined from three frequencies and found to be $\alpha = -0.8 \pm 0.2$. The radio emission is likely to be optically thin synchrotron emission from a nebula surrounding the X-ray source. The radio luminosity of the counterpart is 3.8×10^{34} erg s^{-1} and the minimum energy required to power the nebula is $\sim 1 \times 10^{49}$ erg. These values are 2 orders of magnitude larger than in any Galactic nebula powered by an accreting compact object.

Subject headings: black hole physics — galaxies: individual (NGC 5408) — galaxies: stellar content — X-rays: galaxies

1. INTRODUCTION

Ultraluminous X-ray sources (ULXs) are nonnuclear X-ray sources in external galaxies with apparent luminosities above the Eddington limit for a 20 $M_\odot$ black hole, the maximum mass of any dynamically measured black hole mass in the Galaxy (Remillard & McClintock 2006); for a review, see Fabbiano (2006). ULXs with strong variability are likely accreting objects and may either be "intermediate-mass" black holes (Colbert & Mushotzky 1999; Makishima et al. 2000; Kaaret et al. 2001) or normal (stellar-mass) black holes with beamed or super-Eddington radiation (King et al. 2001; Körding et al. 2002; Begelman 2002). The ULX in the dwarf irregular galaxy NGC 5408 (NGC 5408 X-1) is variable and is one of the few ULXs with a known radio counterpart (Kaaret et al. 2003). The radio emission could arise directly from a relativistic jet beamed toward our line of sight, in which case a stellar-mass black hole would suffice to produce the radio and X-ray emission, or from a nebula surrounding the compact object. Recent radio observations presented by Soria et al. (2006) suggest that the source has a steep spectrum ($\alpha < -1$), but show no indication of radio flux density variability.

In order to better understand the nature of the radio emission from NGC 5408 X-1, we obtained new joint observations in the radio using the Very Large Array (VLA) of the National Radio Astronomy Observatory[1] and in the X-ray using the *Chandra X-Ray Observatory*. In addition, because the target is a low-declination source ($\delta \sim -41°$), we present new and archival radio observations from the Australia Telescope Compact Array (ATCA). Finally, we also reanalyzed archival optical observations made using the *Hubble Space Telescope* (*HST*). We describe the observations and data reduction in § 2, present our results in § 3, and discuss the interpretation in § 4.

[1] The National Radio Astronomy Observatory is a facility of the National Science Foundation operated under cooperative agreement by Associated Universities, Inc.

2. OBSERVATIONS AND ANALYSIS

2.1. *VLA Observations*

VLA observations of the ULX source in NGC 5408 were made at 4.9 GHz (6 cm) with four different array configurations between 2003 December and 2005 January: A, BnA, B, and CnB (see Table 1). Each observation was approximately 3.5 hr long and corresponds to a joint *Chandra* X-ray observation. Standard procedures were carried out for flux and phase calibration using the Astronomical Imaging Processing System (AIPS) of the NRAO. We used the flux density calibrator, J1331+305, and the phase calibrator, J1353−441, a source which is located within 3° of the target. For all observations, fast switching between the target source and calibrator was used with a cycle time for the calibrator-source pair of 2.5–3 minutes (with 45 s on the calibrator and 90 to 120 s on the source).

The VLA image resolutions vary between 1.01″ × 0.28″ (A configuration) and 6.01″ × 3.30″ (CnB configuration). Because of the proximity of the bright starburst region in NGC 5408 and the weak radio emission associated with the ULX, obtaining an accurate flux density for this source is difficult. However, with the high resolution of the VLA A, BnA, and B configurations, it is possible to distinguish the radio emission associated with the ULX from the extended emission from the starburst region in most of our images.

In fact, in attempting to determine the accurate flux density and source structure, the extended emission from this starburst region turns out to be a key issue. One way to examine the contribution of the extended emission is to adjust the imaging weighting function. The Briggs' ROBUST parameter controls the data weights in the (u, v)-plane. Positive values of the ROBUST parameter (1–5) bring out the more extended structure by weighting the inner part of the (u, v)-plane more heavily ("natural weighting"). Such values will increase the signal to noise on extended features but lower the spatial resolution. Negative values of the

TABLE 1
Chandra AND VLA OBSERVATIONS OF NGC 5408

Date/Time	X-Ray Flux	VLA Configuration
2002 May 07 13:45:47	1.42	...
2003 Dec 20 13:06:33	1.49	B
2004 Feb 09 10:29:47	1.58	CnB
2004 Dec 20 13:14:36	1.47	A
2005 Jan 29 11:02:49	1.50	BnA

NOTE.—The *Chandra*/VLA observations of NGC 5408 including the date and UT time of the start of the *Chandra* observation (the VLA observations were roughly simultaneous), the ULX X-ray flux in the 0.3–8 keV band in units of 10^{-12} erg cm^{-2} s^{-1} during the observation, and the VLA array configuration.

ROBUST parameter (−1 to −5) give more equal weight to all points in the (u, v)-plane ("uniform weighting") which tends to maximize spatial resolution, but at the cost of signal to noise. A ROBUST = 0 is balanced between these extremes. As many four images were made from data for an individual configuration using varying ROBUST parameters.

In addition, a more quantitative way to remove extended flux is to limit the range of (u, v) baselines used for imaging. In cases where the emission from the ULX is contaminated by extended flux from the starburst, a (u, v) cutoff of 5 kλ was applied. This cutoff limits flux on angular size scales larger than $\sim 6''$. For the VLA B and VLA CnB configuration images, where extended flux is present, such cutoffs have been applied.

2.2. *ATCA Observations*

We also made continuum radio observations of NGC 5408 using the Australia Telescope Compact Array (ATCA) located in Narrabri, New South Wales, Australia. The ATCA consists of five 22 m antennas positioned along an east-west track with a short north-south spur and a sixth antenna at a fixed location. We obtained three new ATCA observations of 12 hr each on consecutive days with the 6 km configuration 6.0A (6A). This provides the best angular resolution possible with ATCA ($\sim 1''$ at 4.8 GHz). For the first two observations, we switched the feed horns at roughly one hour intervals observing in either the 6 cm band (4.8 GHz) or the 13 and 20 cm bands (1.4 and 2.4 GHz). The duty cycle of the switching was arranged so the integration at 6 cm was 4 times as long as those at 13 and 20 cm. On the last day, we observed with the 5 cm band (6.1 GHz) instead of the 6 cm band (4.8 GHz).

J1934−638 and J1349−439 were used for flux and phase calibration. Editing, calibration, imaging, and analysis were performed using standard routines in the MIRIAD software package (Sault & Killeen 1998). A radio counterpart to the ULX was detected at all frequencies. Because of the low declination of NGC 5408, the ATCA forms a more symmetric synthesized beam than the VLA. The extended emission associated with the starburst in NGC 5408 is present, but in the ATCA images, the radio counterpart to the ULX is clearly distinguished, especially in the 6A configuration data at 4.8 and 6.2 GHz. However, at the lower frequencies (1.4 and 2.3 GHz) there is still contamination from the starburst. During imaging, a variety of ROBUST parameters were also used to downweight the extended emission, similar to the procedure in the VLA imaging. In addition, we analyzed archival ATCA observations of NGC 5408 at a range of frequencies, observed during 2000–2004 (listed in Table 2). In the several of the ATCA data sets (e.g., the 6D array 4.9 GHz data [Kaaret et al. 2003], and the 2.3 and 1.4 GHz archival data sets) a (u, v) cutoff range of 3 kλ was used to remove flux on extended scales larger than $11''$.

2.3. *X-Ray Observations*

NGC 5408 was observed with the *Chandra X-Ray Observatory* (Weisskopf 1988) five times using the ACIS spectroscopic array (ACIS-S; Bautz et al. 1998) in imaging mode and the High-Resolution Mirror Assembly (HRMA; van Speybroeck et al. 1997). The observations began in 2002 and ended in 2005; see Table 1. Because a high X-ray count rate was expected, only the S3 chip was operated with a 1/4 subarray mode for the first observation and a 1/8 subarray for the other observations. This gave an exposure time of 0.8 s for the first observation and 0.4 s for the others. For each observation, we constructed an image using all valid events on the S3 chip and used the `wavdetect` tool, which is part of the CIAO data analysis package, to search for X-ray sources. Typically, only the ULX was detected in each observation. The position of the ULX was within $0.23''$ of R.A. = $14^{h}03^{m}19.63^{s} \pm 0.01^{s}$, decl. = $-41°22.5'8.65'' \pm 0.2''$ (J2000.0) in all observations.

We fit the X-ray spectrum of the ULX for each observation using the XSPEC (Arnaud 1996) spectral fitting tool which is part of the LHEASOFT X-ray data analysis package, and response matrices calculated using CIAO. As previously reported by Kaaret et al. (2003), we found that absorbed single power-law models did not provide an adequate fits (except for the last observation), while models consisting of either an absorbed broken power law or the absorbed sum of a multicolor disk blackbody plus a power law did provide adequate fits. There were no pronounced changes in spectra shape between the different observations. The fit parameters were similar to those quoted in Kaaret et al. (2003). The flux for each observation calculated using the fitted multicolor disk blackbody plus power-law model are given

TABLE 2
ATCA OBSERVATIONS OF NGC 5408

Date/Time	Array	Frequency (GHz)	Reference
2000 Apr 01 02:09	6D	4.8, 8.6	Kaaret et al. (2003)
2003 Mar 03 05:31	6A	4.8, 8.6	Archival 1
2003 May 20 22:05	1.5C	1.4	Archival 2
2003 Jul 27 17:45	6D	1.4	Archival 3
2003 Dec 07 10:05	6A	2.3, 4.8	This paper
2003 Dec 08 11:30	6A	2.3, 4.8	This paper
2003 Dec 09 11:02	6A	2.3, 6.1	This paper
2004 Dec 09 to Dec 11	6D	1.4, 2.3	Soria et al. (2006)
2004 Dec 09 to Dec 11	6D	4.8, 6.1	Soria et al. (2006)

NOTE.—The ATCA observations of NGC 5408 including the observation date, the frequency or frequencies of observation, and the measured flux density.

TABLE 3
4.9 GHz Flux Density of NGC 5408

Telescope Configuration	Robust Weight	Flux Density (mJy)	Geometric Beam Size	(u, v) cutoff
VLA A	−1	$<0.10 \pm 0.03$	0.53	...
VLA A	1	0.13 ± 0.02	0.75	...
VLA A	3	0.14 ± 0.02	0.83	...
VLA BnA	−1	0.15 ± 0.03	1.17	...
VLA BnA	1	0.20 ± 0.02	1.53	...
VLA BnA	3	0.23 ± 0.02	1.70	...
VLA B	−1	0.21 ± 0.03	1.71	...
VLA B	0	0.23 ± 0.03	1.93	...
VLA B	−5	0.20 ± 0.03	1.62	...
VLA B	5	0.23 ± 0.02	2.66	<5 kλ
ATCA 6A	−5	0.21 ± 0.03	1.57	...
ATCA 6A	0	0.20 ± 0.03	1.89	...
ATCA 6A	2	0.19 ± 0.02	3.25	...
ATCA 6A	5	0.19 ± 0.02	3.24	...
ATCA 6D	−5	0.25 ± 0.06	1.59	<3 kλ
ATCA 6D	5	0.18 ± 0.04	3.18	<3 kλ
VLA CnB	0	0.51 ± 0.03	4.45	...
VLA CnB	−5	0.46 ± 0.04	3.77	...
VLA CnB	−5	0.32 ± 0.04	3.71	<5 kλ
VLA CnB	−1	0.47 ± 0.03	4.08	...
ATCA 6D	5	0.43 ± 0.04	3.46	...

Note.—The 4.9 GHz flux densities for the radio counterpart of the ULX in NGC 5408. All fits are for an unresolved point source. It is not possible to distinguish between the source and background emission for the measurements in the last five rows.

in Table 1. We also did not observe any significant changes in the X-ray flux level between observations.

2.4. *HST Observations*

Two WFPC2 observations of NGC 5408 are present in the *Hubble Space Telescope* (*HST*) archive. The observations were obtained as part of a snapshot survey of nearby dwarf galaxy candidates (GO-8601; PI: P. Seitzer) and consist of 600 s WFPC2 exposures with the F606W and F814W filters obtained on 2000 July 4. After extracting the data from the *HST* archive, we used IRAF to mosaic and clean the images. We corrected the absolute astrometry of the *HST* image using stars from the 2MASS catalog (Skrutskie et al. 2006) using the Graphical Astronomy and Image Analysis Tool (GAIA). We used only 2MASS sources on the WF3 chips where the ULX is located in order to preclude issues regarding the relative positioning of the WFPC2 chips. We estimate that the astrometric uncertainty is 0.2″. We used the HSTphot stellar photometry package to obtain photometry (Dolphin 2000). We removed bad pixels, cosmic rays, and hot pixels and then obtained simultaneous photometry for the F606W and F814W images.

3. RESULTS

3.1. *Radio Counterpart*

The flux density of the radio emission associated with the ULX in the VLA and ATCA images was measured by fitting a two-dimensional (2D) Gaussian point source to the peak radio emission in each of the various images. In all cases, the source appears to be pointlike with slightly extended emission, but nothing which we can confidently resolve. The radio source position from our VLA B configuration image (resolution of $3.17'' \times 0.92''$) is R.A. $= 14^{h}03^{m}19.63^{s} \pm 0.01^{s}$, decl. $= -41°22'58.7'' \pm 0.2''$ (J2000.0), which is within 0.1″ of the ULX position calculated from the *Chandra* observations (Kaaret et al. 2003). This is well within the *Chandra* error circle. Using the ATCA 4.8 GHz and 6.1 GHz data, the position of the radio source is R.A. $= 14^{h}03^{m}19.61^{s} \pm 0.02$s, decl. $= 41°22.5'8.5'' \pm 0.2''$ (J2000.0).

3.1.1. *4.9 GHz Emission*

Table 3 lists the measured 4.9 GHz flux density and corresponding ROBUST weighting, array configuration, geometrical beam size $[(\theta_{maj}\theta_{min})^{1/2}]$, and an indication of any (u, v) cutoff used in the imaging. Radio emission was detected above 3 σ in 20 of the 21 images made at 4.9 GHz from the VLA and ATCA data. The source was not detected in the highest resolution 4.9 GHz

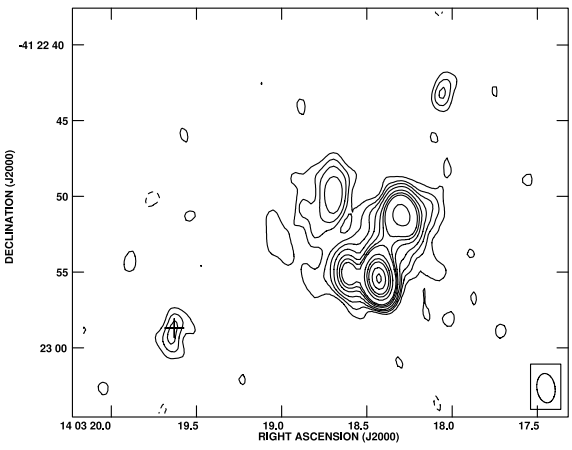

Fig. 1.—VLA 4.9 GHz BnA configuration image of the radio emission in NGC 5408. The compact radio source associated with the ULX is located in the lower left (SE) of the plot. The cross represents the position of the ULX. The spatial resolution of this image is $1.94'' \times 1.20''$, P.A. = 8°, and the image has been made with ROBUST = 1 weighting (slightly naturally weighted). The contour levels represent radio emission at −3, 3, 5, 7, 9, 10, 15, 20, 25, 50, 75, 100, 150, and 200 times the rms level of 20 μJy beam^{-1}.

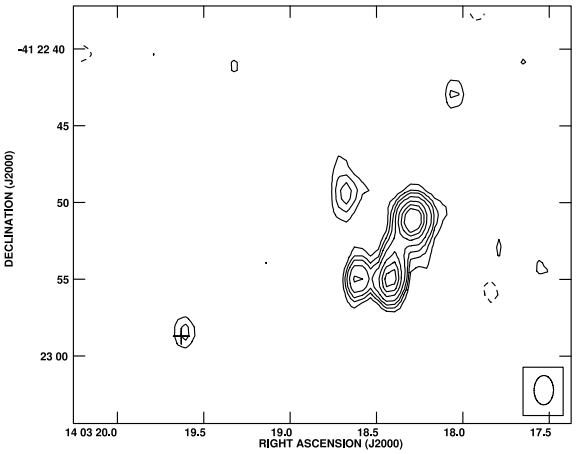

FIG. 2.—ATCA 4.8 GHz image of the radio emission in NGC 5408. The compact radio source associated with the ULX is located in the lower left (SE) of the plot. The crosses represents the position of the ULX. The spatial resolution of this image is $1.90'' \times 1.26''$, P.A. $= -55^{\circ}$, and contours represent radio emission at -3, 3, 4, 5, 7, 9, 11, 13, 18, 21, 25, 30, 52, 84, and 136 the rms level of 32 μJy beam^{-1}. The image was made with uniform weighting (ROBUST $= -5$).

VLA image ($1.01'' \times 0.28''$; A configuration, ROBUST $= -1$) with an upper limit of 0.1 mJy. The largest angular size detectable with the VLA in its A configuration is $10''$. The radio source is detected in the other two VLA A configuration images, but with modest detections ($\sim 7\ \sigma$ in both cases). Figure 1 shows the BnA configuration image of NGC 5408 (ROBUST $= 1$). The resolution of this image is $1.94'' \times 1.20''$, and the source is clearly detected at the 10 σ level.

Figure 2 shows the highest resolution 4.9 GHz ATCA image, which has a beam size very similar to the VLA BnA configuration image shown in Figure 1. In the majority of the VLA and ATCA images, the radio emission associated with NGC 5408 X-1 is obvious and clearly separated from the extended emission associated with the NGC 5408 starburst. However, in cases such as the VLA B configuration naturally weighted image, where the resolution is lower and favors the extended structures, a significant amount of extended emission is present (see Fig. 3, *left*). Removing the shortest (u, v) baselines (<5 kλ) for these lower resolution images produces an image, shown in Fig. 3 (*right*), where the radio emission associated with NGC 5408 X-1 is clearly separated from the extended emission associated with the starburst.

Figure 4 shows the flux density and associated errors versus the geometric beam size for measurements from 16 images of VLA (*diamonds*) and ATCA (*square*; new and archival) data taken from Table 3. The filled symbols indicate that a (u, v) cutoff was applied to the data in order to remove extended emission which may contaminate the flux density. However, not all measurements were included in Figure 4. Images made with the VLA CnB configuration at all robust weightings and with the ATCA 6D configuration have low enough resolution that it is difficult to separate the background emission from NGC 5408 from the radio emission at the position of the ULX. In fact, the flux densities for the VLA CnB configuration and ATCA 6D array measurements are in the range 0.32–0.51 mJy, up to twice as high as measurements made with more extended arrays, indicating that the background contributes significantly to the measurement. For this reason, only the measurements from images where we were confident we were separating out the radio emission associated with NGC 5408 X-1 were used to make Figure 4.

3.1.2. *Source Size and Structure*

Previously, Soria et al. (2006) had made some of the highest resolution observations of the ULX in NGC 5408 using the ATCA. They measured the flux density in images with beam sizes of $1.5''$–$3.5''$ and found an essentially flat distribution of flux density with beam size. However, their observations do not resolve the source and therefore are only consistent with emission from a point source (Soria et al. 2006). The VLA data presented here for the first time probe even higher angular resolutions ($0.5''$–$1.5''$). Figure 4 shows that the VLA data are crucial in studying the flux density versus geometric beam size for scales $<1.5''$. There is a clear trend of

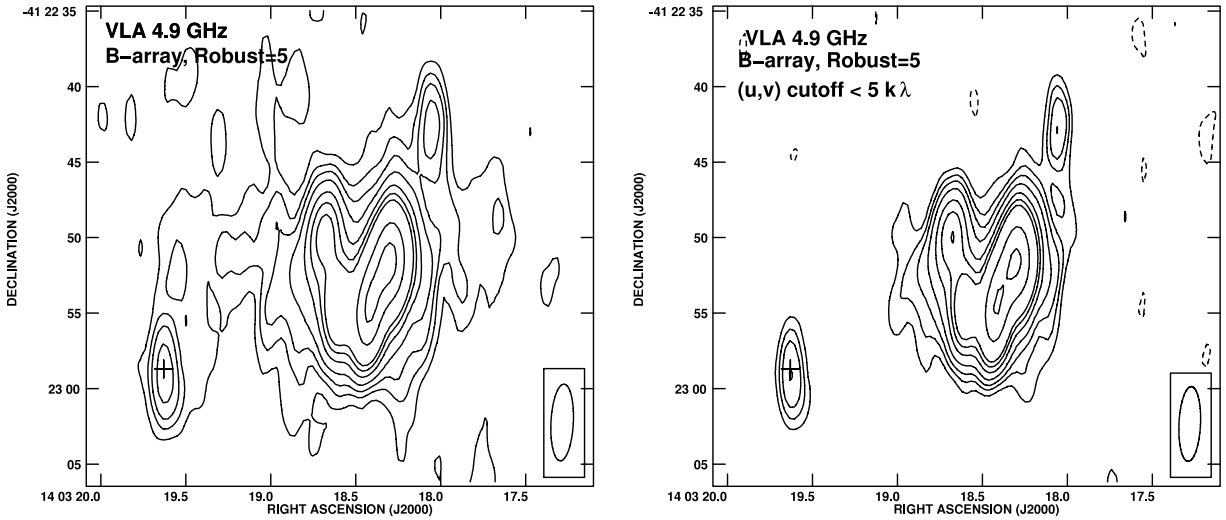

FIG. 3.—VLA 4.9 GHz B configuration images of the radio emission in NGC 5408 made with ROBUST $= 5$ (natural weighting). The left panel shows an image with a spatial resolution and the right panel shows an image made with data which have had a (u, v) cutoff <5 kλ applied to them. In both cases, the spatial resolution is $5.0'' \times 1.5''$, P.A. $= -3^{\circ}$, and contour levels reprsent -3, 3, 5, 7, 10, 15, 20, 25, 50, 75, 100, 125 and 150 times the rms level of 20 μJy beam^{-1}.

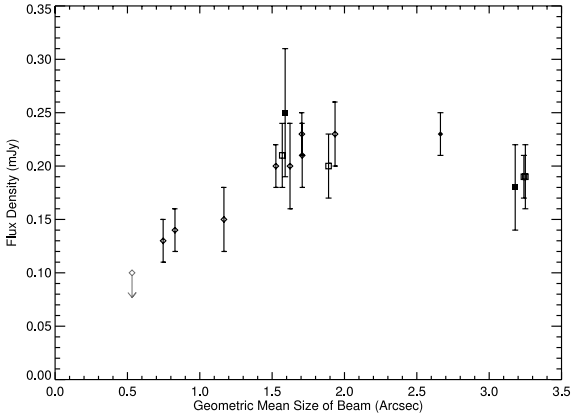

FIG. 4.—Flux density vs. geometric beam size for ATCA (*squares*) and VLA (*diamond*) radio observations at 4.9 GHz from this paper and from archival observations of Soria et al. (2006). Filled symbols represent measurements from images where the shortest (u, v) baselines have been removed to reduce contamination from the background galaxy. Error bars represent the error in fitting 2D Gaussians to the unresolved point source.

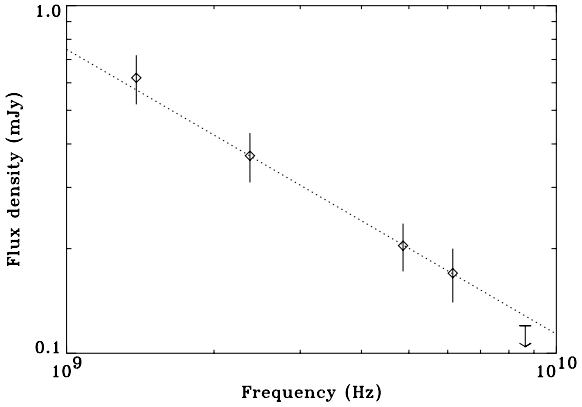

FIG. 5.—Flux density vs. frequency for the radio emission associated with NGC 5408 X-1. These measurements are from ATCA data, and the spectral index of $\alpha = -0.82 \pm 24$ is based on the 2.3, 4.9, and 6.1 GHz points. The 1.4 GHz flux density and 8.5 GHz upper limit are also included on this plot.

decreasing flux density at smaller beam sizes below a geometric beam size of 1.5″. The linear rise of flux density with beam size shown in Figure 4 indicates that there is extended emission associated with this source on beam size scales between ∼0.5″ and ∼1.5″. For beam sizes greater than ∼ 1.5″, the flux density measurements are relatively constant (within the errors), suggesting the source has an angular extent in the range 1.5″–2.0″.

3.1.3. *Variability*

Because the radio source associated with the ULX is likely to be somewhat extended, different configurations of the VLA radio telescope will be sensitive to emission on differing angular size scales. Therefore, it is not possible to look for flux variability in our high-resolution VLA observations (where the configuration ranges from A configuration to CnB configuration). However, ATCA observations over a number of epochs (e.g., Kaaret et al. 2003; Soria et al. 2006; this paper) have shown that the flux density at 4.9 GHz does not appear to vary significantly and has an average, overall value near 0.20 mJy.

3.1.4. *Multifrequency Data and Spectral Index*

Multifrequency observations at 1.4, 2.3, 4.9, and 6.1 GHz were made as part of the new ATCA data presented here. At each frequency, all existing ATCA data were combined (see Table 2), and a point source was fit to the radio emission associated with the ULX. We find flux densities of 0.62 ± 0.10 mJy at 1.4 GHz [geometric beam size of 6.7″; ROBUST = −5; (u, v) cutoff < 5 kλ], 0.37± 0.08 mJy at 2.4 GHz (geometric beam size of 3.3″; ROBUST = −5), 0.20 ± 0.03 mJy at 4.9 GHz (geometric beam size = 1.5″, ROBUST = −5), and 0.17 ± 0.03 at 6.1 GHz. At 1.4 GHz, the contribution from the extended background may be present even though we used uniform weighting and limited the shortest (u, v) data; the beam size is large. At 2.3 GHz, the image is made with uniform weighting and the contribution from the extended starburst region is not apparent. Therefore, we determine the spectral index based on the 2.4, 4.9, and 6.1 GHz measurements only and obtain $\alpha = -0.8 \pm 0.2$, where $S_\nu \propto \nu^\alpha$. Figure 5 shows the flux density versus frequency and includes the 1.4 GHz measurement as well as the 8.5 GHz ATCA upper limit from Kaaret et al. (2003). Although not included in the fit, the 1.4 and 8.5 GHz measurements are consistent with the fitted spectral index.

3.2. *Optical Counterpart*

Figure 6 shows the *HST* WFPC2 image in the F606W filter for the area near the ULX. The circle drawn on the figure is centered at the VLA source position quoted above and has a radius of 0.28″, which represents the relative position uncertainty including both the radio position uncertain and the optical astrometry uncertainty. Only one object lies within the error circle. It is located at a position of R.A. = $14^h03^m19.62^s$, decl. = 41°22.5′8.54″ (J2000.0) which is 0.17″ from the radio position and well inside the error circle. The next closest *HST* source is 0.43″ from the VLA position and is outside the error circle. We identify the *HST* source within the error circle as the likely optical counterpart of the ULX.

The optical counterpart has magnitudes, in the WFPC2 flight photometric system, of 22.387 ± 0.021 in the F606W filter and 22.396 ± 0.043 in the F814W filter (Dolphin 2000). The equivalent Johnson-Cousins magnitudes are $V = 22.4$ and

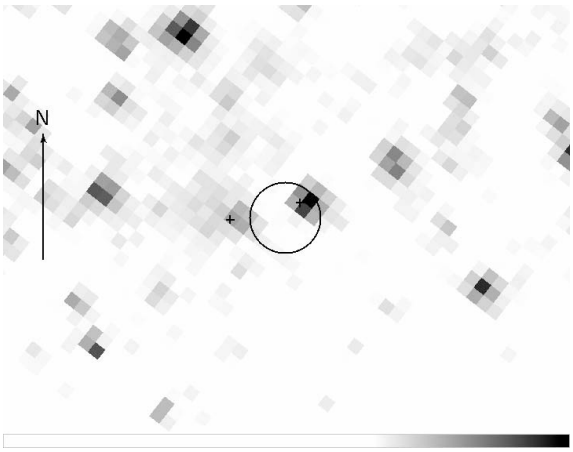

FIG. 6.—Image of the field near NGC 5408 X-1 in the F606W band. The circle is centered at the position of the VLA counterpart of the ULX and has a radius of 0.28″, which represents the relative position uncertainty including both the radio position uncertain and the optical astrometry uncertainty. Only one source lies within the error circle and we identify it as the likely optical counterpart of the ULX. The arrow has a length of 1″ and points north.

$I = 22.4$. We corrected for reddening using an extinction $E(B-V) = 0.068$ based on the dust maps of Schlegel et al. (1998) and using an $R_V = 3.1$ extinction curve. The dereddened magnitudes are $V_0 = 22.2$ and $I_0 = 22.3$ and the color is $V_0 - I_0 = -0.1 \pm 0.1$.

4. DISCUSSION

The radio counterpart size of 1.5″–2.0″ corresponds to a physical diameter of 35–46 pc at the distance of 4.8 Mpc to NGC 5408, as determined by from the tip of the red giant branch Karachentsev et al. (2002). Therefore, we can rule out the interpretation of the radio emission associated with the NGC 5408 ULX as a relativistically beamed jet (Kaaret et al. 2003).

The radio surface brightness of NGC 5408 at 4.9 GHz is $\sim 4 \times 10^{-20}$ W m^{-2} Hz^{-1} sr^{-1}, assuming a source size of 1.5″. Taking a spectral index of -0.8, we can calculate the surface brightness at 1.4 GHz in order to compare to values for known supernova remnants of similar sizes (Green 2004). The value of $\sim 1 \times 10^{-19}$ W m^{-2} Hz^{-1} sr^{-1} is significantly higher than that of known supernova remnants of similar size. It is therefore more likely that the radio emission associated with NGC 5408 X-1 arises instead from an extended radio lobe. The radio spectrum ($\alpha = -0.8$) of this source is consistent with optically thin synchrotron emission.

For comparison, the radio nebula W50 surrounds the relativistic jet source SS 433 (Margon 1984) and is thought to be powered by the relativistic outflow. SS 433 has been suggested as a possible Galactic analog to the ULXs (Fabrika & Mescheryakov 2001; Begelman et al. 2006). The radio nebula in W50 is interesting because the nebular radio emission is unlikely to be beamed. The physical size of W50 is roughly 50 pc and is similar to what we estimate for the radio nebula surrounding NGC 5408 X-1. The radio spectral indexes of the various components of W50 range from -0.5 to -0.8, also consistent with the spectral index of the radio emission in NGC 5408 X-1 ($\alpha \sim -0.8$). A comparison of the radio brightness can be made for the two sources. W50 has an integrated flux density at 1.4 GHz of ~ 70 Jy and a distance of ~ 5 kpc (Dubner et al. 1998). Assuming a spectral index of -0.5, that translates to a 4.9 GHz flux density of 40 Jy, and if it were at the distance of NGC 5408 (4.8 Mpc), its flux density would be ~ 40 μJy. The integrated flux density of NGC 5408 X-1 at 4.9 GHz is ~ 200 μJy, so its radio brightness is more than a factor of 5 greater than that of W50.

We investigate the energetics of the radio lobe assuming radiation via synchrotron emission, equipartition between particles and fields, and equal energy in electrons and baryons. We use a spectral index $\alpha = -0.8$ (see § 3.1.4), a lower frequency cutoff of 1.3 GHz, and an upper frequency cutoff of 6.2 GHz. The total radio luminosity of the source is 3.8×10^{34} erg s^{-1}. For a source diameter of 46 pc and a filling factor of unity, we find that the total energy required is 3.6×10^{49} erg, the magnetic field is 16 μG, and the synchrotron lifetime is ~ 20 Myr. For contrast, for a diameter of 35 pc and a filling factor of 0.1, the total energy required is 9×10^{48} erg, the magnetic field is 39 μG, and the lifetime is ~ 5 Myr. We note that the estimates of Soria et al. (2006) for the energy content of a synchrotron nebula surrounding NGC 5408 X-1 are about an order of magnitude larger. This is primarily because they assume an electron energy distribution that extends down to a Lorentz factor of 1, while we, conservatively, assume that the electron energy distribution extends only over the range needed to produce the observed radio emission (1.3–6.2 GHz).

The total energy content in relativistic electrons in W50 is in the range $(0.5–7) \times 10^{46}$ erg (Dubner et al. 1998). The total energy content in relativistic electrons in the radio nebula surrounding NGC 5408 X-1 is at least 2 orders of magnitude larger. Therefore, if two nebula are similar, then the jet powering the nebula surrounding NGC 5408 X-1 must be at least 2 orders of magnitude more powerful than that from SS 433 powering W50. The radio lobes powered by the persistent accreting stellar-mass black hole GRS 1758−258 have a radio luminosity of 3×10^{30} erg s^{-1}, require an energy content of 2×10^{45} erg (Rodríguez et al. 1992), and are even less powerful than W50. We note that the ULX Holmberg II X-1 has an associated radio nebula with a total energy similar to that of the NGC 5408 X-1 nebula (Miller et al. 2005).

At the distance to NGC 5408, the absolute magnitude of the optical counterpart would be $M_V = -6.2$. If the light arises only from the stellar companion, then the magnitude and color exclude main sequence and giant stars and require a supergiant star. The absolute magnitude and color are consistent with classification as a B or early A supergiant. The luminosity of such a star would be in the range of $1–5 \times 10^{38}$ erg s^{-1}. However, the stellar classification is suspect since light may arise from reprocessing of X-rays from the compact object and since the X-ray luminosity ($\sim 10^{40}$ erg s^{-1} if the emission is isotropic) exceeds the expected stellar luminosity by a factor of at least 20 and may strongly affect the physical state of the star.

The X-ray to optical flux ratio, defined following van Paradijs & McClintock (1995) as $\xi = B_0 + 2.5 \log F_X$, where F_X is the X-ray flux density at 2 keV in μJy, and we approximate $B_0 = V_0$ due to lack of a B-band image, is $\xi = 20.0$. If we use the flux density at 1 keV, this rises to $\xi = 21.1$. These values are higher than those of any high-mass X-ray binary (HMXB), other than LMC X-3, and are in the range typically found for low-mass X-ray binaries (LMXBs). Thus, it is possible that the companion star contributes little to the observed optical emission, e.g., it is not supergiant, and that most of the optical light arises from reprocessing of X-rays, as occurs in LMXBs (Kaaret 2005).

P. K. acknowledges partial support from *Chandra* grant CXC GO4-5035A and a Faculty Scholar Award from the University of Iowa. STSDAS and PyRAF are products of the Space Telescope Science Institute, which is operated by AURA for NASA. The authors also thank Michael Rupen for planning and carrying out the VLA observations.

REFERENCES

Arnaud, K. A. 1996, in ASP Conf. Ser. 101, Astronomical Data Analysis Software and Systems V, ed. G. H. Jacoby & J. Barnes (San Francisco: ASP), 17
Bautz, M. W., et al. 1998, Proc. SPIE, 3444, 210
Begelman, M. C. 2002, ApJ, 568, L97
Begelman, M. C., King, A. R., & Pringle, J. E. 2006, MNRAS, 370, 399
Colbert, E. J. M., & Mushotzky, R. F. 1999, ApJ, 519, 89
Dolphin, A. E. 2000, PASP, 112, 1383
Dubner, G. M., Holdaway, M., Goss, W. M., & Mirabel, I. F. 1998, AJ, 116, 1842
Fabbiano, G. 2006, ARA&A, 44, 323
Fabrika, S., & Mescheryakov, A. 2001, in IAU Symp. 205, Galaxies and Their Constituents at the Highest Angular Resolutions, ed. R. T. Schilizzi (San Francisco: ASP), 268
Green, D. A. 2004, Bull. Astron. Soc. India, 32, 335
Kaaret, P. 2005, ApJ, 629, 233
Kaaret, P., Corbel, S., Prestwich, A. H., & Zezas, A. 2003, Science, 299, 365
Kaaret, P., et al. 2001, MNRAS, 321, L29
Karachentsev, I. D., et al. 2002, A&A, 385, 21
King, A. R., et al. 2001, ApJ, 552, L109
Körding, E., Falcke, H., & Markoff, S. 2002, A&A, 382, L13

Makishima, K., et al. 2000, ApJ, 535, 632
Margon, B. 1984, ARA&A, 22, 507
Miller, N.A, Mushotzky, R. F., & Neff, S. G. 2005, ApJ, 623, L109
Remillard, R. A., & McClintock, J. E. 2006, ARA&A, 44, 49
Rodríguez, L. F., Mirabel, I. F., & Martí, J. 1992, ApJ, 401, L15
Sault, R. J., & Killeen, N. E. B. 1998, The Miriad User's Guide (Sydney: ATNF)
Schlegel, D., Finkbeiner, D., & Davis, M. 1998, ApJ, 500, 525
Skrutskie, R. M., et al. 2006, AJ, 131, 1163
Soria, R., Fender, R. P., Hannikainen, D. C., Read, A. M., & Stevens, I. R. 2006, MNRAS, 368, 1527
van Paradijs, J., & McClintock, J. E. 1995, in X-Ray Binaries, ed. W. H. G. Lewin, J. van Paradijs, & E. P. J. van den Heuvel (Cambridge: Cambridge Univ. Press), 58
van Speybroeck, L. P., Jerius, D., Edgar, R. J., Gaetz, T. J., Zhao, P., & Reid, P. B. 1997, Proc. SPIE, 3113, 89
Weisskopf, M. C. 1988, Space Sci. Rev., 47, 47

Chapitre 6
Le plan fondamental d'activité des trous noirs

—Le temps adoucit tout.
— Voltaire

6.1 Introduction

De nombreuses similarités existent entre les systèmes binaires X (XRB) et les noyaux actifs de galaxie (AGN). Tout d'abord, l'énergie colossale libérée par ces objets provient de l'accrétion sur un trou noir – voire parfois une étoile à neutrons pour les XRB. Des jets relativistes sont généralement observés de part et d'autre de ces systèmes. D'ailleurs, il faut signaler qu'il s'agit de la seule composante actuellement résolue spatialement dans ces sources. À cela, il faut ajouter le disque d'accrétion se manifestant sous la forme d'un disque α optiquement épais de type Shakura & Sunyaev (1973) que l'on détecte dans les X mous pour les binaires (McClintock & Remillard 2006) ou vers l'ultraviolet pour les AGN – le fameux "big blue bump", Sanders et al. 1989. La température de corps noir du disque d'accrétion traduit une loi d'échelle au niveau de la masse du trou noir impliqué (Frank et al. 2002).

Jets et disques semblent former des systèmes symbiotiques que l'on peut reproduire sur de grande échelle de masse du trou noir ou sur une large gamme de variation du taux d'accrétion (Falcke & Biermann 1995). L'inclinaison (Urry & Padovani 1995) de ces objets sur la ligne de visée – et par là-même l'amplification Doppler des jets pointant vers l'observateur – serait responsable d'un grand nombre de propriétés de ces AGN – on recherche toujours les microblazars galactiques ! ! !. La rotation du trou noir central entraîne probablement une modification de certaines caractéristiques observationnelles, mais à ce jour il n'existe pas de démonstration non ambiguë d'une telle rotation.

L'impact exact des variations du taux d'accrétion sur le rayonnement de ces objets reste actuellement le sujet d'un débat passionné. En effet, dans le cas des binaires, la variation du taux d'accrétion constitue le paramètre fondamental – unique ? – gouvernant les transitions entre états spectraux X (McClintock & Remillard 2006). À faible accrétion, la composante

X des binaires traduit dans le modèle standard l'influence d'un disque optiquement mince et radiativement inefficace – de type ADAF par exemple, voir Poutanen 1998. La découverte des jets compacts (chapitre 2) dans les binaires et sa possible contribution à haute énergie modifient notre perception du modèle standard. Il en est de même pour les AGN, étant donné qu'ils pourraient – de façon similaire aux XRB – présenter des états spectraux différents au vu de la détection – ou non – de la composante thermique du disque d'accrétion (Falcke et al. 2004).

Ainsi il serait possible de trouver des AGN analogues aux trous noirs Galactiques. D'où l'idée – récurrente – de comprendre les propriétés des AGN avec les systèmes binaires X. De là, émerge l'idée d'une unification des propriétés physiques de ces objets. La corrélation radio/X (c.f. chapitre 2) mise en évidence dans les binaires (Corbel et al. 2003; Gallo et al. 2003b) a suscité une extension aux AGN dont nous allons parler maintenant.

6.2 Le plan fondamental d'activité des trous noirs

6.2.1 Deux illustrations du plan fondamental

Peu après la publication de nos travaux (Corbel et al. 2003) sur les trous noirs Galactiques, deux groupes indépendants (Merloni et al. 2003; Falcke et al. 2004) ont mis en évidence une corrélation similaire au niveau des AGN. Plus intéressant encore, cette corrélation dans un hyperplan à trois dimensions – masse du trou noir, luminosités X et radio – suit la corrélation mesurée pour GX 339−4 (Corbel et al. 2003) et GS 2023+338 (Gallo et al. 2003b) si l'on tient compte d'un terme correctif lié à la masse du trou noir super-massif au centre des AGN considérés. Ce plan fondamental de l'activité des trous noirs est illustré sous ses deux formes sur les figures 6.1 et 6.2. La mise en évidence de cette corrélation traduit de nouveau une connexion disque–jet pour les trous noirs stellaires et aussi les super-massifs. Néanmoins, l'interprétation physique que ces deux groupes en font est fortement différente.

6.2.2 Le plan fondamental selon Merloni et al.

Merloni et al. (2003) ont compilé un échantillon d'environs 100 AGN possédant une estimation de la masse du trou noir, incluant des quasars (QSO), des AGN de faible luminosité (LLAGN), des galaxies de type Seyfert (type 1, 2 et NLSey1) et des radiogalaxies. Pour l'ensemble de ces sources, ils ont répertorié les mesures de luminosité X et radio. Ils n'incluent pas de BL Lac, connus pour être le siège d'effet d'amplication Doppler très important. En ce qui concerne les XRB, ils utilisent des mesures simultanées faites en X par RXTE/ASM et en radio par le GBI, ainsi que nos données de GX 339−4 (Corbel et al. 2003) et des sources comme LS 5039 – probablement une étoile à neutrons ? – ou XTE J1118+480. Aucun soin particulier n'est pris quant à la nature de l'état spectral X de la source.

Avec ces sources, le plan fondamental (figure 6.1) prend la forme suivante dans un espace à trois dimensions – log L_R, log L_X, log M – : $\log L_R = (0.60^{+0.11}_{-0.11}) \log L_X + (0.78^{+0.11}_{-0.09}) \log M + 7.33^{+4.05}_{-4.07}$, avec une dispersion importante de l'ordre de $\sigma_R = 0.88$. Ces résultats impliqueraient que les propriétés des jets des trous noirs seraient invariantes sous les variations de la masse du trou noir et du taux d'accrétion. De plus, l'émission X de la catégorie des trous noirs faiblement actifs – $<$ quelques % de L_{Edd} – ne serait pas compatible avec un disque d'accrétion de type α, elle serait marginalement compatible avec le rayonnement synchrotron optiquement mince du jet. Par contre, un modèle de flot d'accrétion radiativement inefficace – type ADAF – reproduirait parfaitement cette corrélation (pour plus de détails voir Merloni et al. 2003), l'émission radio, quant à elle, proviendrait toujours du jet.

6.2.3 Le plan fondamental selon Falcke et al.

En ce qui concerne l'illustration du plan fondamental par Falcke et al. (2004), des différences existent quant à la nature de l'échantillon. Leur objectif étant de sonder les propriétés des sources sub-Eddington, ils se sont donc attachés à sélectionner rigoureusement des sources

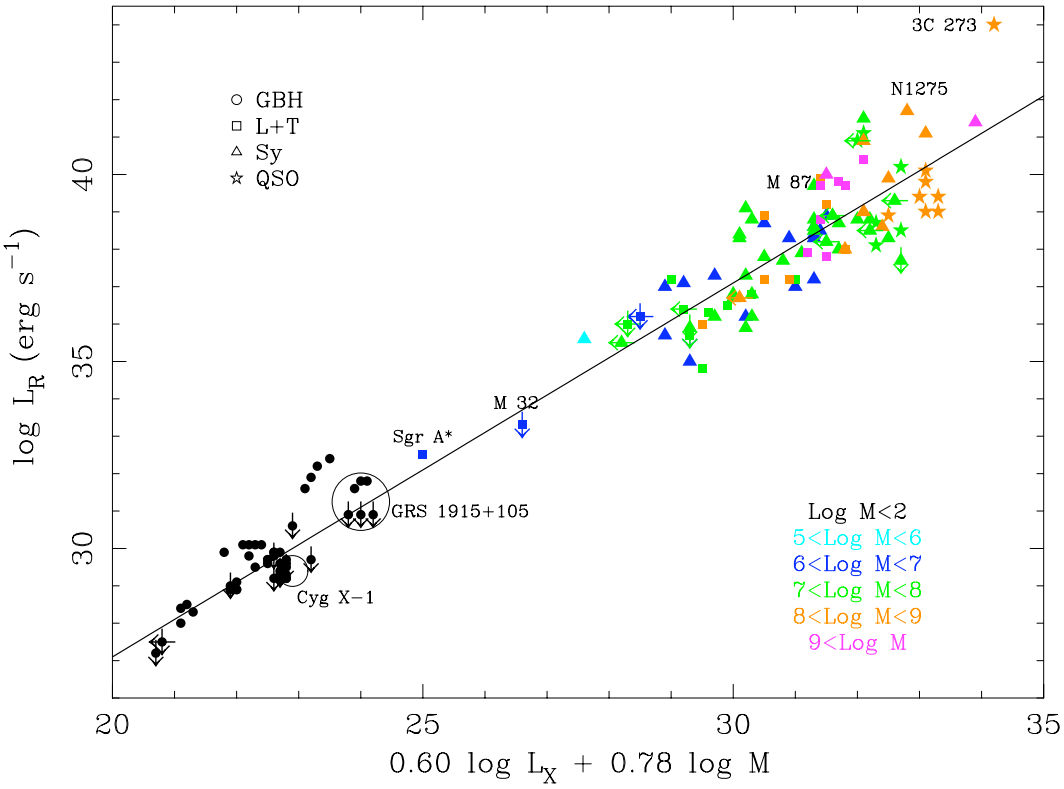

FIG. 6.1 – Illustration du plan fondamental d'activité des trous noirs selon Merloni et al. (2003). Représentation de la luminosité radio des sources de l'échantillon en fonction de leur luminosité X corrigée de la masse du trou noir super-massif.

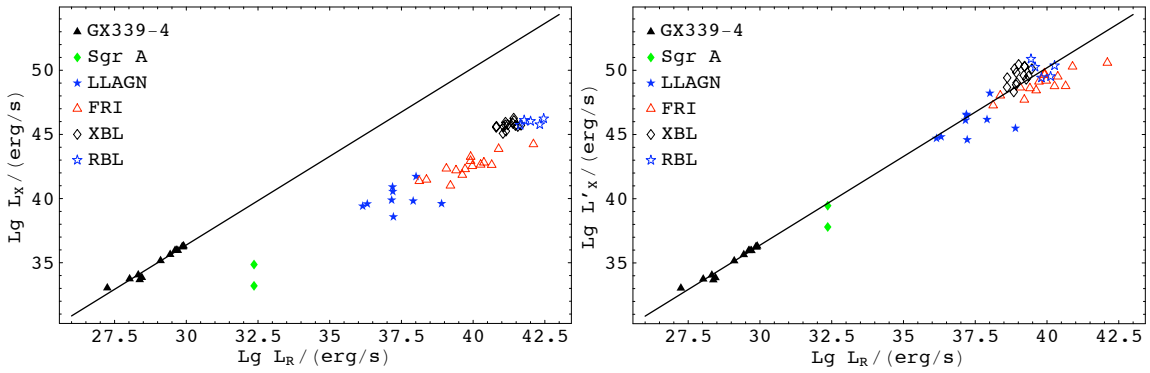

FIG. 6.2 – Illustration du plan fondamental d'activité des trous noirs selon Falcke et al. (2004). Représentation de la luminosité X des sources de l'échantillon en fonction de leur luminosité radio. Gauche : aucune correction n'a été apportée, Droite : la luminosité X a été corrigée par la masse du trou noir et est normalisée à un trou noir de 6 $M_\odot$. Les BL Lac ont été corrigés de l'amplification Doppler.

analogues à l'état dur des XRB, c'est à dire des AGN ne possédant pas de composante liée au disque d'accrétion standard – pas d'indication directe ou indirecte du "big blue bump". Les radiogalaxies de type FRI, les LLAGN, les LINER, les BL Lac et mêmes les sursauts quotidiens de Sgr A* seraient les analogues des XRB à faible accrétion. Pour les binaires, ils utilisent les données de la corrélation radio/X que nous avons obtenues sur GX 339−4 dans l'état dur (Corbel et al. 2003).

Il faut signaler qu'ils utilisent une procédure différente de Merloni et al. (2003) quant à l'estimation de la luminosité X. En effet pour les FRI et les BL Lac, ils extrapolent la luminosité optique en une luminosité X en utilisant une loi de puissance d'indice –0.6. Ils n'utilisent pas (comme Merloni et al. 2003) la luminosité X directement mesurée. Les données optiques du HST ont une meilleure résolution spatiale que les observatoires X. Il est aussi probable que pour certains de ces FRI le domaine X soit dominé par la coupure synchrotron, et donc l'émission X mesurée traduirait éventuellement le rayonnement synchrotron self-Compton (SSC). Nous rappelons que leur objectif est de sonder les propriétés du coeur compact de la galaxie et plus particulièrement de voir si l'émission de ces coeurs compacts serait compatible avec celle de jets relativites. Les mesures concernant les BL Lac sont corrigées d'un facteur Doppler moyen de 7.

Les résultats de Falcke et al. (2004) sont illustrés sur la figure 6.2. En tenant compte de la correction due à la masse du trou noir super-massif, tous ces AGN à faible taux d'accrétion sont situés sur l'extrapolation de la corrélation que nous avons obtenus pour GX 339−4. Les sursauts de Sgr A* se retrouvent eux aussi sur cette courbe, ce qui semble logique sachant que l'émission diffuse détectée représente celle d'un gaz diffus autour de ce trou noir.

Ces auteurs suggèrent donc que les trous noirs à faible accrétion – AGN et XRB – se retrouve dans un régime radiatif inefficace, dans lequel toute l'émission est contrôlée par les jets. Par simple loi d'échelle, les propriétés seraient identiques entre ces diverses populations de trous noirs et seraient conformes à celles attendues de la part de jets compacts. La distribution spectrale énergétique (SED) serait donc identique entre ces sources : un spectre plat de la radio jusqu'à une certaine fréquence de coupure (voir section 2.3) dû au rayonnement synchrotron auto-absorbé et une loi de puissance décroissante au delà traduisant le régime synchrotron optiquement mince. Ce régime dominé par les jets (JDAF) pourrait néanmoins coexister avec la couronne standard d'électrons chauds qui servirait de base aux jets, l'accélération ne commençant que vers quelques 100–1000 R_g.

6.3 De l'importance de l'échantillon statistique

Compte tenu des conclusions opposées, les auteurs du premier plan fondamental (Merloni et al. 2003) ont, d'une certaine façon, réagi aux travaux de Falcke et al. (2004). En effet, Heinz (2004) s'est attaché à démontrer que les jets compacts ne pouvaient pas être à l'origine de l'émission X des AGN, même à faible taux accrétion. Pour cela, Heinz (2004) dérive des relations d'échelle entre la luminosité radio, la luminosité synchrotron X, la masse et le taux d'accrétion du trou noir, la nouveauté étant qu'il inclut les pertes radiatives par effet synchrotron. Il en résulte que si on veut que la luminosité X synchrotron des jets reproduise les corrélations obtenus par Merloni et al. (2003), il serait nécessaire que la distribution énergétique des particules soit très pentue – avec $p \sim 3.3$ – et donc non standard, ou plus simplement pour lui, les jets ne peuvent pas reproduire les corrélations observées. Il ne resterait donc que les modèles liés aux phénomèmes d'accrétion faiblement radiatif, de type ADAF, qui l'expliqueraient.

6.3.1 Nature des échantillons

Ces deux groupes mettent donc en évidence pour les AGN une corrélation compatible avec une extrapolation des résultats obtenus pour les binaires X. Néanmoins, les interprétations de ce plan fondamental par les deux groupes divergent. Avec Elmar Körding – post-doc avec moi à l'époque – nous avons entrepris de comprendre la nature de ces résultats contradictoires (Körding et al. 2006a). Elle est en partie due à la composition de l'échantillon. En effet, Merloni et al. (2003) utilisent directement les luminosités radio et X d'AGN de tout type, en sélectionnant en proportion similaire des AGN brillants ou faibles. Il ne faut donc pas s'étonner que l'interprétation physique diffère de celle de Falcke et al. (2004), qui se sont intéressés uniquement aux sources à faible accrétion. Par la suite, l'échantillon modifié – c.f. ci dessous – de Merloni et al. (2003) sera noté MHDM, tandis que notre nouvel échantillon (basé sur Falcke et al. 2004) sera noté KFC.

Tout d'abord, l'échantillon des XRB est non représentatif dans le cas de Merloni et al. (2003). En effet, en plus de LS 5039 – probablement une étoile à neutrons, des sources comme GRS 1915+105 ou Cyg X−1 s'y trouvent alors qu'elles changent fréquemment d'état spectraux et ne sont donc pas représentatives des trous noirs sub-Eddington. Pour éviter les problèmes liés au traitement des limites supérieures – valable pour les AGN aussi – , nous les avons supprimés dans MHDM – tout comme GRS 1915+105, Cyg X−1 et LS 5039. À cela, nous y avons ajouté l'échantillon des XRB de Gallo et al. (2003b) qui est essentiellement dominé par GX 339−4 et GS 2023+338. Le quasar 3C273, exceptionnellement brillant, a été exclu du nouvel échantillon MHDM. Pour KFC, le nombre de LLAGN a été augmenté grâce à l'inclusion de nouveaux catalogues et à l'analyse de nouvelles données. L'influence des galaxies de type Seyfert y sera discutées séparément. Les XRB proviennent de Gallo et al. (2003b) à l'exclusion de GRS 1915+105 et de Cyg X−1. La logique de conserver des sources sub-Eddington est donc conservée.

Nous cherchons les paramètres du plan fondamental tel que :

$$\log L_{\mathsf{X}} = \xi_{\mathsf{R}} \log L_{\mathsf{R}} + \xi_{\mathsf{M}} \log M + b_{\mathsf{X}}, \tag{6.1}$$

où L_{X} est la luminosité dans la bande X et L_{R} traduit la luminosité radio à une certaine fréquence – νF_ν –, tandis que M est la masse du trou noir. Les ξ_{i} correspondent aux coefficients de la relation de corrélation, et b_{X} est une constante caractérisant la normalisation générale. Les prévisions pour un modèle où l'émission totale est dominée par le jet sont de $\xi_{\mathsf{R}} = 1.38$ et $\xi_{\mathsf{M}} = -0.81$, tandis que pour un modèle ADAF/jet – ADAF pour les X et jet pour la radio – elles sont de $\xi_{\mathsf{R}} = 1.64$ et $\xi_{\mathsf{M}} = -1.3$ (Merloni et al. 2003; Körding et al. 2006a). Nous avons apporté un soin particulier aux estimations des erreurs sur les paramètres de la corrélation.

6.3.2 Origine de l'émission X dans le modèle des jets

La figure 6.3 illustre les différents régimes d'émission attendus de la part d'un jet relativiste avec le spectre typique en forme de "bosses de chameau" dû aux contributions synchrotron et Compton inverse. Il est à noter la présence de plusieurs énergies de coupure particulières. En effet, en représentation de densité de flux d'un jet conique – ou compact –, le spectre est plat jusqu'à une énergie ϵ_t – régime synchrotron optiquement épais – où le milieu devient transparent – régime synchrotron optiquement mince – avec un spectre en loi de puissance décroissante avec un indice spectrale de l'ordre de –0.5. Les effets de refroidissement radiatif se font sentir à partir d'une énergie ϵ_{cool} entraînant un indice spectral plus fort de l'ordre de –1.

Finalement une coupure du spectre est attendue vers $\epsilon_{\rm cut}$ due au mécanisme accélérant les particules à l'origine du rayonnement synchrotron. Au delà de l'énergie $\epsilon_{\rm cut}$, la contribution

Compton inverse – externe ou SSC – peut devenir visible. La contribution relative de ces deux bosses dépend du facteur de Lorentz du jet et de l'inclinaison de la source.

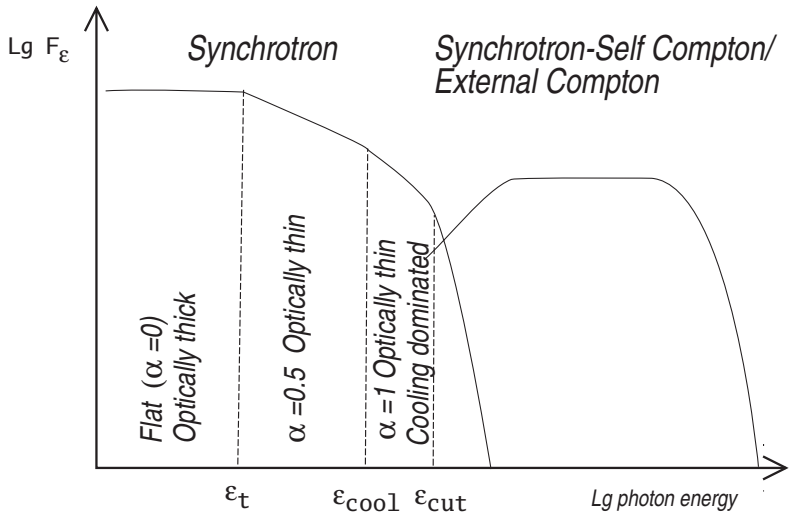

FIG. 6.3 – Schéma illustrant la distribution spectrale énergétique (SED) typique d'un jet dans le cas d'un BL Lac. À basse énergie, le spectre est dominé par l'émission synchrotron, tandis que la partie à haute énergie est habituellement expliquée par des processus de diffusion Compton inverse – SSC ou EC.

L'énergie de coupure $\epsilon_{\rm cut}$ semble dépendre de la puissance totale du système accrétant (Fossati et al. 1998; Ghisellini et al. 2002). Elle se situerait pour les sources de faible puissance vers la bande standard des X (0.5–10 keV), tandis que pour les objets fortement accrétants elle pourrait être aussi basse que 0.1 eV. On s'attend donc à ce que seuls les objets de faible puissance puissent être dominés par une éventuelle contribution synchrotron du jet. Selon Heinz (2004) (section 6.2), la prise en compte des pertes radiatives synchrotron entraînerait une impossibilité pour les jets compacts de contribuer à haute énergie. Il est exact que les pertes radiatives peuvent réduire la contribution éventuelle en X du jet, mais l'effet de l'énergie de coupure synchrotron $\epsilon_{\rm cut}$ est nettement plus dramatique. En effet, dans l'échantillon MHDM de Merloni et al. (2003), il faut remarquer que pour la plupart des AGN – à l'exception des LLAGN – la fréquence de coupure ϵ_{cut} sera en dessous de la bande X. Il n'y a donc aucune raison d'attendre une contribution synchrotron en X dans ces objets, la bande X sera dominée soit par les processus Compton inverse du jet, soit par l'émission du disque d'accrétion et de la couronne. Pour les LLAGN, cette énergie de coupure serait vers 40-400 keV (Fossati et al. 1998; Körding et al. 2006a). Nous rappelons que Merloni et al. (2003) utilisent directement le flux X mesuré pour les sources considérées, tandis que Falcke et al. (2004) extrapolent en X le flux synchrotron mesuré en optique pour les FRI et les BL Lacs. Il n'a donc aucune raison de s'attendre à ce que l'échantillon MHDM puisse tester le rôle des jets en X, car les flux X mesurés pour les AGN – sauf peut être pour les LLAGN – ne correspondent pas à la composante synchrotron du jet. Les conclusions de Merloni et al. (2003) ou Heinz (2004) n'ont donc aucun fondement quant à la contribution éventuelle des jets à haute énergie (Körding

et al. 2006a). Seul l'échantillon KFC pourra tester cette possibilité.

6.3.3 Résultats : raffinement du plan fondamental

En considérant l'intégralité de l'échantillon KFC, nous obtenons les paramètres suivants du plan fondamental :

$$\xi_{\mathsf{R}} = 1.41^{+0.14}_{-0.12} \quad \xi_{\mathsf{M}} = -0.87^{+0.15}_{-0.17} \quad b_{\mathsf{X}} = -5.01^{+3.4}_{-3.9}. \tag{6.2}$$

Les régions de confiance des deux principaux paramètres sont indiquées sur la figure 6.4 (haut). La dispersion intrinsèque autour du plan fondamental est alors de $\sigma_{int} = 0.38 \pm 0.06$. Dans la table 2 de Körding et al. (2006a) nous présentons les paramètres estimés du plan fondamental

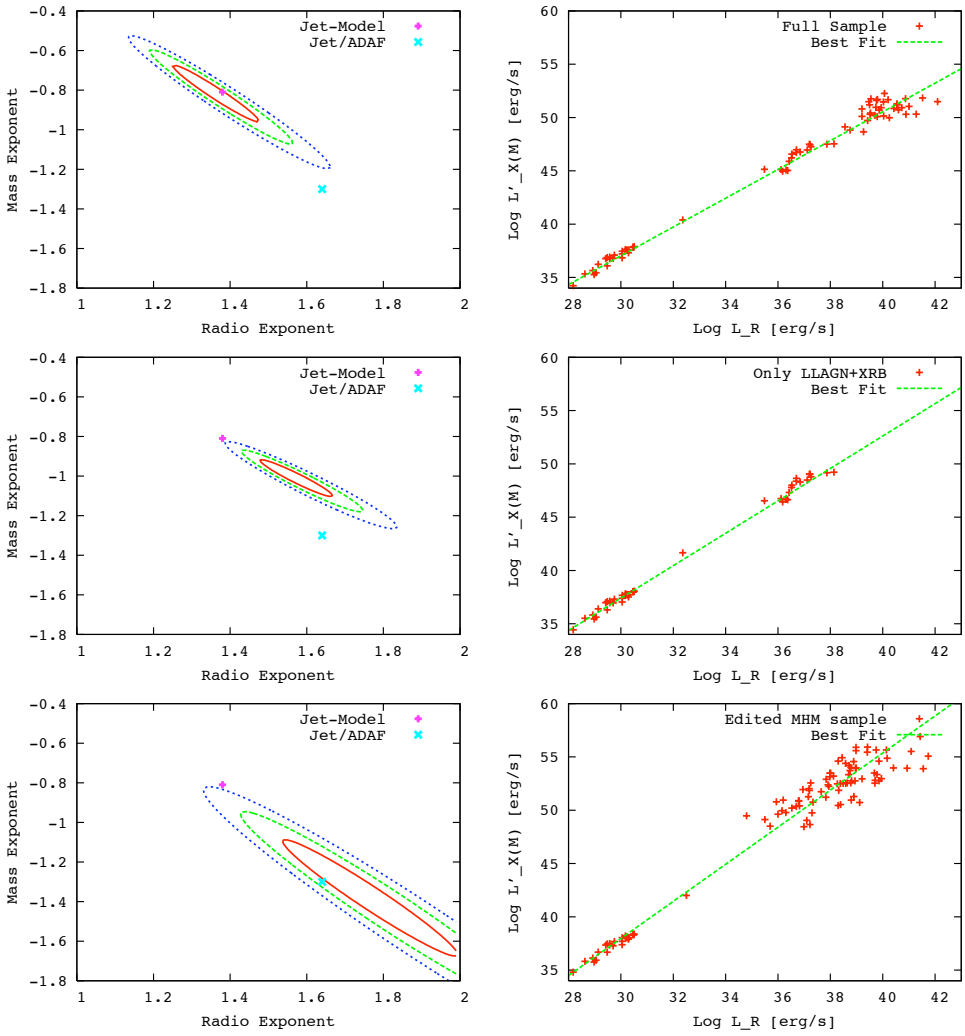

FIG. 6.4 – Sur la partie gauche, nous représentons les cartes de significativité des paramètres de la corrélation avec niveau de confiance à un (rouge), deux (vert) et trois (bleu) sigma. Les croix (à gauche) indiquent les prévisions théoriques du modèle de jet ou celles du modèle ADAF/jet. La partie droite représente la meilleure approximation du plan fondamental et indique l'échantillon considéré : KFC, KFC avec seulement les XRB et LLAGN, MHDM (de haut en bas).

en considérant différents sous-échantillons de KFC ou MHDM (voir aussi la figure 6.4) en jouant sur la présence ou non de certaines classes d'AGN.

Nous constatons que cela influence fortement les résultats et donc les conclusions pouvant en être extraites. Les coefficients de la corrélation ξ_R et ξ_M sont systématiquement plus grands dans l'échantillon MHDM que dans KFC. Le coefficient radio dans les échantillons de KFC est en bon accord avec la corrélation radio/X de GX 339−4, où nous avons mesuré $\xi_R \approx 1.4$ (Corbel et al. 2003). La dispersion intrinsèque est nettement plus grande dans MHDM que dans KFC (0.65 à la place de 0.39 ; erreur typique de 0.06). Tout cela peut être compris si différents processus physiques dominent dans chacun des sous-échantillons – jets pour les LLAGN et disques pour les quasars. Avec l'échantillon KFC, le plan fondamental est en bon accord avec les prévisions des modèles prédisant une contribution synchrotron des jets à haute énergie – contrairement aux affirmations de Heinz 2004.

Néanmoins, uniquement en prenant en compte les objets caractéristiques d'un état spectral dur, de type faible accrétion (XRB, LLAGN), on trouve un coefficient radio ($\xi_R = 1.59 \pm 0.21$) en bon accord avec la corrélation radio/X de GX 339−4, où nous avons mesuré $\xi_R \approx 1.4$ (Corbel et al. 2003). Dans ce cas, il est aussi très intéressant de noter qu'il s'agit du sous-échantillon où la dispersion intrinsèque ($\sigma_{int} = 0.11$ dex) est la plus faible de tous, favorisant l'idée que les processus physiques seraient similaires entre ces deux populations. Mais dans ce cas – voir graphe du milieu sur la figure 6.4 – le modèle de jet unique est à peine en accord avec les données (rejeté à 3 σ, celui d'ADAF/jet est rejeté encore plus sévèrement), suggérant qu'éventuellement le refroidissement radiatif ou l'énergie de coupure (ϵ_{cool} ou ϵ_{cut}) doit pris en compte (Körding et al. 2006a).

Pour résumer, les AGN de faible luminosité (LLAGN) ont le comportement se rapprochant le plus des binaires dans l'état dur – en accord avec Falcke et al. 2004. Cette très forte similarité renforce le lien physique entre ces populations de trous noirs de faible accrétion. Si on prend les échantillons dans leur ensemble, il est difficile d'en tirer des conclusions sur la nature des processus physiques en oeuvre, tant les paramètres issus de la corrélation sont dominés par la nature – et le nombre – des sources présentes dans l'échantillon considéré.

6.4 Au delà du plan fondamental

Comme tout résultat cherchant à unifier les propriétés d'objets "dissemblables", ces travaux ont entraîné un certains nombres de critiques, mais aussi de nouvelles extensions très intéressantes. Nous avons déjà discuté des problèmes éventuels pour les XRB dans la section 2.5, nous nous limiterons ici aux aspects liés au plan fondamental, c'est à dire à ceux incluant les AGN.

Tout d'abord, au delà de saisir l'interprétation physique du plan fondamental, Bregman (2005) a critiqué l'existence même de la corrélation. En effet, selon Bregman (2005) la corrélation ne serait qu'un artefact dû aux conversions des flux en luminosités dans un échantillon incomplet de sources ayant une large gamme de distance – même si des analyses statistiques semblaient déjà prouver sa réalité, Merloni et al. 2003. L'effet de la distance serait le suivant : à partir du moment où l'intervalle de distance devient grand devant l'intervalle des flux, les luminosités résultantes seront artificiellement corrélées à cause du facteur distance au carré. Des analyses supplémentaires de corrélation partielle ou de simulations Monte-Carlo (Körding et al. 2006a; Merloni et al. 2006) confirment de nouveau la significativité du plan fondamental. Son existence n'est pas due à des effets de sélection lié à la distance ou aux limites supérieure. La non linéarité de la corrélation traduit bien des caractéristiques intrinsèques des trous noirs accrétants (Merloni et al. 2006). On pourra aussi voir Wang et al. (2006) ou Panessa et al. (2007) pour l'étude du plan fondamental avec un nouvel échantillon d'AGN.

Au niveau des extensions intéressantes de ces corrélations, on peut citer les travaux de Körding et al. (2006b). Le rayonnement radio des jets compacts est utilisé comme traceur du taux d'accrétion du système considéré (XRB ou AGN) et cela indépendamment de la luminosité X. Ensuite, en comparant la luminosité bolométrique de ces sources avec cette "mesure" – estimation à partir du rayonnement radio du jet – du taux d'accrétion, il apparaît une variation quadratique pour les trous noirs dans l'état dur – à priori caractéristique d'une accrétion faible – et linéaire pour les étoiles à neutrons et les trous noirs des états de plus forte accrétion. Des conclusions quasi similaires sont extraites pour les AGN de l'échantillon KFC. La transition entre les régimes quadratique et linéaire se ferait à un niveau de 10 % $L_{\rm Edd}$. La comparaison des deux états d'accrétion renforcerait l'idée que pour les trous noirs à faible accrétion – état dur –, une partie de l'énergie d'accrétion serait advectée vers le trou noir, tandis que la puissance du jet pourrait excéder la luminosité X du système : il serait dans un état advectif dominé par les jets (JDAF).

Néanmoins, nous rappellerons les mises en garde dans la section 6.2 au sujet des variations possibles de la normalisation du plan fondamental. Une réévaluation de la corrélation pour les trous noirs stellaires est en cours en incluant un nombre de sources supplémentaires ainsi que différents sursauts de sources identiques. Le chemin vers l'unification des propriétés physiques des AGN et XRB est long, mais de nombreuses voies sont ouvertes comme celles de l'étude des diverses corrélations. On peut aussi citer l'unification des propriétés temporelles entre ces différentes populations (McHardy et al. 2006).

6.5 Articles de recherche

6.5.1

Refining the fundamental plane of accreting black holes.

Article publié dans :

Astron. & Astrophys., 2006, 456, 439-450

Körding, E., Falcke, H., Corbel, S.

A&A 456, 439–450 (2006)
DOI: 10.1051/0004-6361:20054144

Astronomy & Astrophysics

Refining the fundamental plane of accreting black holes

E. Körding[1,2], H. Falcke[3,4], and S. Corbel[1]

[1] AIM - Unité Mixte de Recherche CEA - CNRS - Université Paris VII - UMR 7158, CEA-Saclay, Service d'Astrophysique, 91191 Gif-sur-Yvette Cedex, France
[2] School of Physics and Astronomy, University of Southampton, Hampshire SO17 1BJ, UK
e-mail: elmar@phys.soton.ac.uk
[3] Radio Observatory, ASTRON, Dwingeloo, PO Box 2, 7990 AA Dwingeloo, The Netherlands
[4] Dept. of Astronomy, Radboud Universiteit Nijmegen, Postbus 9010, 6500 GL Nijmegen, The Netherlands

Received 2 September 2005 / Accepted 22 February 2006

ABSTRACT

Context. The idea of a unified description of supermassive and stellar black holes has been supported by the extension of the empirical radio/X-ray correlation from X-ray binaries to active galactic nuclei through the inclusion of a mass term. This has lead to the so-called fundamental plane of black hole activity in the black hole mass, radio and X-ray luminosity space. Two incarnations of this fundamental plane have so far been suggested using different underlying models and using two different samples of accreting black holes.
Aims. We improve the parameter estimates of the fundamental plane and estimate the scatter of the sources around the plane in both samples. This is used to look for possible constraints on the proposed theoretical models. Furthermore, we search for selection effects due to the inclusion of different classes of AGN or distance effects.
Methods. We present revised samples for both studies together with a refined statistical analysis using measured errors of the observables. This method is used to compare the two samples and infer parameters for the fundamental plane in a homogeneous way.
Results. We show that strongly sub-Eddington objects in a state equivalent to the low/hard state of X-ray binaries follow the fundamental plane very tightly; the scatter is comparable to the measurement errors. However, we find that the estimated parameters depend strongly on the assumptions made on the sources of scatter and the relative weight of the different AGN classes in the sample. Using only hard state objects, the fundamental plane is in agreement with the prediction of a simple uncooled synchrotron/jet model for the emitted radiation. Inclusion of high-state objects increases the scatter and moves the correlation closer to a disk/jet model. This is qualitatively consistent with a picture where low-state objects are largely dominated by jet emission while high-state objects have a strong contribution from an accretion disk.

Key words. X-rays: binaries – galaxies: active – radiation mechanisms: non-thermal – stars: winds, outflows – black hole physics – accretion, accretion disks

1. Introduction

Active galactic nuclei (AGN) and black hole X-ray binaries (XRBs) seem to have a similar central engine consisting of the central black hole, an accretion disk probably accompanied by a corona, and a relativistic jet (Shakura & Sunyaev 1973; Mirabel & Rodríguez 1999; Antonucci 1993). Jet and disk may form a symbiotic system (Falcke & Biermann 1995; Falcke et al. 1995) which can be scaled over several orders of magnitude in mass and accretion rate (Falcke & Biermann 1996, 1999) suggesting that a single central engine can be used to describe very different types of black holes.

While the general unification of stellar mass and supermassive black holes picture has now been established for some time, it has recently been tested on a detailed empirical level by correlations in the radio and X-ray band which have lead to the so-called fundamental plane of black hole activity (Merloni et al. 2003, hereafter MHDM; and Falcke et al. 2004, hereafter FKM). Similar unification efforts are also under way analysing and comparing the variability properties of AGN and XRBs (Uttley et al. 2002; Markowitz et al. 2003; Körding & Falcke 2004; Abramowicz et al. 2004).

To establish connections between stellar and supermassive black holes we have to consider that black hole XRBs can be found in distinct accretion states. In FKM we suggested that a number of AGN classes can be identified with corresponding XRB states and based on this proposed a power unification scheme for AGN and XRBs.

The two most prevalent XRB states are the low/hard state (LH state) and the high/soft state (HS state, see e.g., McClintock & Remillard 2006). In the LH state the radio spectrum is always consistent with coming from a steady jet (Fender 2001), which can sometimes be directly imaged (Stirling et al. 2001). Once the source enters the HS state, the radio emission seems to be quenched (Fender et al. 1999; Corbel et al. 2000). One possible scenario for the accretion flow of a LH state object is that its inner part is optically thin up to a transition radius, where the flow turns into a standard thin disk (Esin et al. 1997; Poutanen 1998). Usually, the X-ray emission of a LH state XRB is modeled using Comptonization (e.g. Sunyaev & Trümper 1979; Thorne & Price 1975), however, some models suggest that the compact jet may contribute to the X-ray emission or even dominate it (Markoff et al. 2001a; Markoff & Nowak 2004; Homan et al. 2005; Markoff et al. 2005). As the disk fades, the system may

become "jet-dominated" – meaning that the bulk of the energy output is in radiation and kinetic energy of the jet (Fender et al. 2003, FKM).

Indeed, Corbel et al. (2000, 2003) found a surprisingly tight correlation of the radio and X-ray fluxes of the black hole XRB GX 339−4 in its LH state which can be qualitatively and quantitatively well understood in the context of jet models (Markoff et al. 2003). Gallo et al. (2003) showed that this correlation does not only hold for one source but seems to be universal for all LH state XRBs. It has also been observed that, once an object enters the high state, the radio emission is quenched and it drops off the correlation (Fender et al. 1999; Tananbaum et al. 1972; Gallo et al. 2003). It has been suggested by Maccarone et al. (2003) that a similar effect can be found in AGN.

Radio/X-ray correlations have also been found for AGN, e.g., by Hardcastle & Worrall (1999) and Canosa et al. (1999). The final breakthrough came when it was shown possible to combine these correlations to a fundamental plane in the radio/X-ray/black hole mass space for XRBs and AGN (MHDM, FKM). This fundamental plane gives a tight relation between the radio and X-ray fluxes and the black hole mass, which is valid for AGN as well as XRBs. Thus, the correlation proves the similarity of the central engines of these accreting black holes.

However, there are at least two competing explanations for the fundamental plane. In the picture of FKM, the radio-through-X-ray emission for XRBs and the lowest luminosity AGN is attributed to synchrotron emission from a relativistic jet in the jet-dominated state (LH). As both components, the radio and the X-rays, originate from the same source – the jet – one can expect a tight correlation of both observables. We refer to this model as the "jet only" model. One would expect the correlation to break down once a source leaves the radiatively inefficient accretion flow state and is no longer jet-dominated. Hence, the picture should not apply for high-state objects.

On the other hand, MHDM suggested that the X-ray emission originates from the accretion flow, while the radio emission is still attributed to the relativistic jet. Both, the flow and the jet are presumed to be strongly coupled so that the radio and X-ray emission is correlated. Here we will mainly assume the accretion flow to be some variant of an advection-dominated accretion flow (ADAF, Narayan & Yi 1994; see also the convection dominated accretion flows e.g., Quataert & Gruzinov 2000) and refer to the model as "ADAF/jet" model. The ADAF solution is only one possible accretion flow model, e.g. one other possibility is presented in Haardt & Maraschi (1991). Here we will use the ADAF/jet model only as the example for possible "disk/jet" models.

In the recent past, the statistics and slopes of the radio/X-ray/mass correlations have been used to argue for and against the synchrotron/jet models (Heinz 2004, MHDM). Hence, further clarification is urgently needed. Additionally, Heinz & Merloni (2004) have used the correlation to search for constrains of the relativistic beaming. However, as we will show here, all these analyses depend strongly on the statistics of the samples, the construction of the samples, and the assumptions on the scatter of the measurements.

In this paper, we therefore investigate the problems of the parameter estimation of the fundamental plane of black hole activity. We will check the assumptions made by previous studies, and present an improved statistical analysis. We furthermore improve the samples presented by MHDM and FKM. With our refined parameter estimation method we analyze and compare both samples and investigate selection effects and the intrinsic scatter of the correlation. In this light, we discuss if the fundamental plane can be used to constrain the underlying emission mechanism as previously suggested. We will use the intrinsic scatter to test which classes of AGN belong to the analog of the LH state XRBs.

In Sect. 2 we discuss our method of parameter estimation, the improved samples, and discuss observing frequencies. In Sect. 3 we present our results and their implications and present our conclusions in Sect. 4.

2. Parameter estimation

We are searching for the parameters of the fundamental plane for accreting black holes:

$$\log L_{\rm X} = \xi_{\rm R} \log L_{\rm R} + \xi_{\rm M} \log M + b_{\rm X}, \quad (1)$$

where $L_{\rm X}$ is the X-ray luminosity in the observed band and $L_{\rm R}$ denotes radio luminosity at the observing frequency (νF_ν), M is the black hole mass, the $\xi_{\rm i}$ are the correlation coefficients, and $b_{\rm X}$ denotes the constant offset. To simplify the notation we omit the units in the logarithms. Throughout this paper all luminosities are measured in erg/s, distances in pc and masses in solar masses. In the notation we follow FKM. To derive the parameters as given in MHDM set $\xi_{\rm RX} = 1/\xi_{\rm X}$ and $\xi_{\rm RM} = \xi_{\rm M}/\xi_{\rm X}$.

The predicted values for the "jet only" model are $\xi_{\rm R} = 1.38$ and $\xi_{\rm M} = -0.81$ (FKM), while the values for the "ADAF/jet" model are $\xi_{\rm R} = 1.64$ and $\xi_{\rm M} = -1.3$ (MHDM).

2.1. The samples

Here we compare the published correlations by MHDM and FKM. While both samples are used to extend the radio/X-ray correlation found in LH state XRBs, they differ in the selection of sources and which observing frequencies are used for the X-ray luminosities.

MHDM sample

The MHDM sample is a real radio/X-ray sample, i.e., it directly uses the measured radio and X-ray fluxes. It contains XRBs and nearly all types of AGN except obviously beamed sources like BL Lac objects. The sources were extracted from the literature under the condition that good mass estimates exist. To obtain a representative sample the authors selected a similar number of bright active AGN and less active AGN. The sample contains low-luminosity AGN (LLAGN), LINERs (low ionization nuclear emission region), Seyferts (type 1 and 2), FR Radio Galaxies (Fanaroff & Riley 1974) and radio loud and quiet quasars (Kellermann et al. 1989) and the quiescence flux of Sgr A*. Thus, by using this sample one averages over nearly all types of AGN, whether they belong to the LH state or not.

To avoid dealing with upper limits in the data we exclude all those limits from the MHDM sample. The overall result of the fit does not seem to change due to this, as we can reproduce the best fit values of MHDM. This sample contains some XRBs that do not follow the correlation. Cyg X−1 changes its state frequently (Gallo et al. 2003) and seems to stay always near the transition luminosity, thus, it will not trace the correlation well. GRS 1915+105 is a rather unique system that seems to stay in the "canonical" very high state most of its time (Reig et al. 2003). We therefore exclude that source as well. It is still open whether LS 5039 is a black hole or a neutron star binary. Furthermore, its radio spectrum is peculiar for a LH state object (Ribó et al. 2005). Thus, besides the original sample we will also

consider the AGN subsample of MHDM and add a subsample of the Gallo et al. (2003) XRB sample (see below). The quasar sample contains two very radio loud objects (3C273, PG 1226+023), while most quasars are radio quiet. To demonstrate the selection effects we exclude these two sources from the quasar sample when we consider subsamples of the MHDM sample.

Our sample (KFC sample)

The sample of FKM tries to include only objects in the LH state. FKM suggest to classify LLAGN, LINER, FR I Radio Galaxies and BL Lac objects as the analog classes of the LH state in XRBs. As FKM use a jet model as the basis of their suggested unification scheme, they try to compare observations at frequencies that originate from synchrotron emission (see the discussion in Sect. 2.5). They therefore extrapolate optical observations for FR I Radio Galaxies and BL Lac objects to an equivalent X-ray flux (for details see FKM). The fluxes of the BL Lac sources have been deboosted with an average Doppler factor of 7 (FKM). In the current study we further increase the number of LLAGN sources by including all sources of the Nagar et al. (2005) sample with $L_R < 10^{38}$ erg/s for which we found X-ray fluxes in the literature. We will refer to this augmented sample as the "KFC sample"[1]. The FKM LLAGN sample is based on X-ray observations of the LLAGN sample studied by Terashima & Wilson (2003). Additionally we use fluxes from the following surveys in order of preference: The Chandra v3 pipeline (Ptak & Griffiths 2003, `www.xassist.org`), the XMM serendipitous X-ray survey (Barcons et al. 2002), and the ROSAT HRI pointed catalog (ROSAT Scientific Team 2000). Finally, NGC 4258 fluxes were taken from Young & Wilson (2004). In the KFC sample we only consider the non-Seyfert galaxies in the Nagar et al. (2005) sample; the Seyferts of this sample will be discussed separately as, even though they are of low luminosity, they still may belong to the supermassive analog of high state XRBs, because their black hole masses are so low. For Sgr A*, we include the hard X-ray flare by Baganoff et al. (2001), as the flare may be due to jet emission (see e.g., Markoff et al. 2001b). Besides the flare we also show the result for the quiescent Sgr A* flux.

XRB sample

The sample of LH state XRBs is based on the sample of Gallo et al. (2003). To avoid problems with state transitions we only include GX 334-9, V404 Cyg, 4U 1543-47, XTE 1118+480, XTE J1550-564. For all sources we only consider the data if the source is in the LH state. We excluded GRS 1915+105 and Cyg X−1 as discussed above. For GX 334−9 (Corbel et al. 2003) we used the updated X-ray fluxes from Nowak et al. (2005).

2.2. Problems of parameter estimation

The correlation between the radio and X-ray emission has been discussed for XRBs and AGN before and it has been shown by partial correlation analysis that the correlation is indeed real (MHDM, for AGN only see Hardcastle & Worrall 1999). For a discussion of the well constrained sources Sgr A*, NGC 4258, M81 and a XRB sample see Markoff (2005). Thus, we assume that the correlation exists and only check the parameter estimation process.

[1] Despite other associations the reader may have with this abbreviation, it is simply based on the present authorlist.

To estimate parameters for measured data with errors in all variables, one has to use the merit function (see e.g., Press 2002, MHDM). For measurements y_i and x_{ij}, which all have uncertainties, e.g., the y_i can denote the X-ray luminosities while x_{1i} denotes the radio luminosities and x_{2j} the black hole masses, the merit function is defined as:

$$\hat{\chi}^2 = \sum_i \frac{(y_i - b - \sum_j a_j x_{ij})^2}{\sigma_{y_i}^2 + \sum_j (a_j \sigma_{x_j})^2}, \tag{2}$$

where the σ are the corresponding uncertainties, and the a_j and b are the unknown parameters. The normal χ^2 fits, which do not consider scatter in all variables, will yield asymmetric results as for them only scatter in the "y"-axis is considered. The derivative of the merit function is non-linear in the a_j and has to be solved with a numerical optimization routine. For the parameter b one can still give an analytical solution:

$$b_{\min}(\boldsymbol{a}) = \frac{\sum \omega_i \left(y_i - b_j x_{ij}\right)}{\sum \omega_i} \tag{3}$$

with $\omega_i^{-1} = \sigma_{y_i}^2 + \sum_j \left(a_j \sigma_{x_{ij}}\right)^2$. Thus, we only have to solve a reasonably well behaved two dimensional function for which a standard numerical optimization routine can be used.

The resulting parameters depend strongly on the assumed uncertainties σ in the data. MHDM assume that these uncertainties σ are isotropic:

$$\sigma_{L_R} = \sigma_{L_X} = \sigma_M. \tag{4}$$

Thus, they do not use measured uncertainties but set them isotropically to a value such that the reduced χ^2 is unity. This is a strong assumption and its effect has to be checked. As a first test we explore the effect of an anisotropy of the uncertainties in the mass estimation and the scatter in the luminosities, while still assuming that the uncertainties in the $L_X - L_R$ plane are isotropic:

$$\sigma_{L_R} = \sigma_{L_X} = 2\alpha\sigma_0 \qquad \text{and} \quad \sigma_M = 2(1-\alpha)\sigma_0. \tag{5}$$

With these assumptions of the uncertainties, we use the merit function to derive the parameters of the original MHDM sample. The best fit values are strongly depending on the isotropy parameter α as shown in Fig. 1. An anisotropy parameter of 0.5 corresponds to an isotropic distribution of the uncertainties. For this isotropic case we can reproduce the values found by MHDM, which are also shown in the figure. $\alpha \approx 1$ corresponds to the case that the uncertainties in the luminosities dominate while for $\alpha \approx 0$ the uncertainties of the mass estimation are dominant. We observe that, for example, the parameter ξ_R can take any value between 1.4 and 3 for different α.

In case that the uncertainties only deviate slightly from the isotropic case the slope of the parameters tells us how strong these errors propagate to the final fit values. Unfortunately the slope of the parameters around $\alpha \approx 0.5$ is large. Thus, it is crucial to have a good estimate of the distribution of uncertainties. If we can improve the estimates of the uncertainties we can improve the validity of the parameter estimates. Any study based on a parameter estimate using isotropic uncertainties has to take the rather large additional uncertainties due to this assumption into account.

Besides the demonstrated effect of the anisotropy of the uncertainties of the mass estimates and the luminosity estimates, a similar effect can be found if $\sigma_{L_R} \neq \sigma_{L_X}$ We note that the best fit values do not depend on the absolute value of the combined σ but on the relative prominence of the different σ_i.

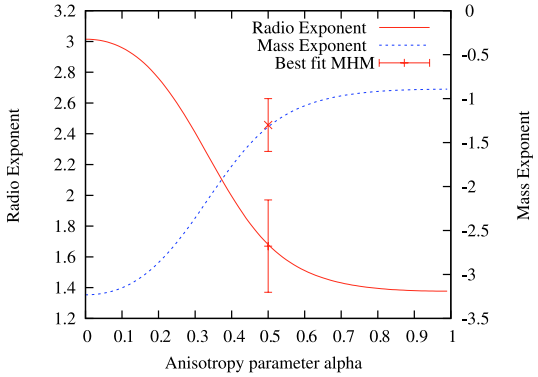

Fig. 1. The effect of anisotropic errors on the best fit parameters of the fundamental plane (Eq. (1)). The horizontal axis gives the anisotropy parameter α. A small value of α denotes that the uncertainties in the mass estimate dominate, while for large values the uncertainties of the luminosity are dominant. $\alpha = 0.5$ corresponds to isotropic errors as used by MHDM. Also shown are the best fit values of MHDM and their uncertainties. Depending on the choice of the uncertainties one can obtain values of the parameters ξ_R between 1.4 and 3 and ξ_M between –0.8 and –3.

One problem of this parameter estimation scheme is that we can not deal with coupled uncertainties. We include several measurements of the XRBs GX 339–4 and V404 Cyg so the uncertainties of the mass and distance measurements are not independent for these datapoint. We will neglect this effect for simplicity, but it may influence the estimated parameters especially for the small subsamples.

2.3. Error budget

Both luminosities depend on the measured flux and the distance, thus, the scatter in both quantities is coupled. To separate the equation into variables that have nearly independent errors, we separate the effect of the distance:

$$L_{R,X} = F_{R,X}\Xi_{R,X}D^2 \quad (6)$$

where $F_{R,X}$ denote the measured radio and X-ray fluxes and D denotes the distance. The $\Xi_{R,X}$ are conversion factors depending on the observed band. We therefore find:

$$\log F_X = \xi_R \log F_R + \xi_M \log M + (2\xi_R - 2)\log D + b_X + \log \Xi, \quad (7)$$

where the mathematical conversion factors are combined into Ξ. As they are just mathematical constants, they will not be discussed further.

We have seen in the previous section that the assumption of isotropic uncertainties (as used by MHDM) will effect the best fit parameters in an unknown way. To improve this situation, we estimate the errors attributed to each variable. The fluxes $F_{R,X}$ contain measurement errors and intrinsic scatter as discussed below. Besides this, the masses and distances are uncertain as well. However, as the correlation coefficient ξ_R will be around 1.4 the effect of errors in the distance estimation are less severe for the correlation than for the individual luminosities as it appears with a factor $(2\xi_R - 2)$. As the merit function requires Gaussian errors, we are always using symmetric errors in the log-log space, many of the errors below are indeed symmetric and the other parameters are only mildly asymmetric.

- Mass estimate: our XRBs LH state sample is dominated by GX 334–9 and V404 Cyg. For GX 339–4 Hynes et al. (2003) estimate a mass function of $5.8 \pm 0.5\ M_\odot$, which is therefore a lower limit for the mass of the black hole. We therefore assume a mass of $8 \pm 2.0\ M_\odot$. For V404 Cyg we use a mass of $12 \pm 2.5\ M_\odot$ (Orosz 2003 gives a range of 10–13.4 $M_\odot$). Note that there are several data points for each object. Thus, their uncertainties are coupled, which we can not take into account. The mass estimates of the other XRBs are also taken from Orosz (2003). For the AGN Merritt & Ferrarese (2001) give an absolute scatter of 0.34 dex for M–σ relation. The mass estimate using the M–σ relation is independent of the distance of the source (cf., Ferrarese & Ford 2005). This method is used for all galaxies except our BL Lac objects. For masses estimated with the M–σ relation we will use the scatter of the correlation as a measure of the uncertainty for the mass estimate: 0.34 dex. We use velocity dispersions from the Hypercat catalog (Prugniel et al. 1998). For the BL Lac objects we used indirectly derived velocity dispersions from Woo & Urry (2002). Thus, these indirect measurements will have a higher uncertainty. Bettoni et al. (2001) give an uncertainty of these indirectly measured velocity dispersions σ a value of $\delta\sigma = 18\ \mathrm{km\,s^{-1}}$, which yields an additional uncertainty of ≈0.3 dex for the mass estimate. Thus, we use an uncertainty of 0.46 dex for the mass estimate of the BL Lac objects. The indirect method to derive the velocity dispersion depends slightly on the distance. However, as we only use this method for BL Lac objects and the distances are accurate compared to 0.46 dex uncertainty, we will ignore this effect. For Sgr A*, M 81, and NGC 4258 we use direct mass measurements (see FKM), the mass uncertainties are as low as 10% (<0.05 dex).
- Distance measurement: The distance of GX 339–4 is still under debate. Shahbaz et al. (2001) and Jonker & Nelemans (2004) give a lower limit of 6 kpc, but the distance may be as high as 15 kpc (Hynes et al. 2004). We therefore adopt a distance of 8 ± 2 kpc. For V404 Cyg, we adopt the distance of 4 kpc (Jonker & Nelemans 2004). We use an uncertainty of 1 kpc, as we can not account for asymmetric uncertainties and have the issue of coupled errors. For nearby AGN we use updated distances from Maoz et al. (2005), Tonry et al. (2001). If these are not available, we use the distance estimates as given in the Tully (1988). The distance uncertainty is hard to access, as many different methods are used for which the uncertainty is sometimes not well known. We assume 40%, however, we checked that it does not change the result if one assumes less scatter. For AGN with distances derived from the Hubble law, we use an error estimate based on the peculiar velocities in the Hubble flow and the uncertainties of the Hubble constant (we assume $H_0 = 72\ \mathrm{km\,s^{-1}\,Mpc^{-1}}$ Spergel et al. 2003, 5% uncertainty, $\Omega_\Lambda = 0.7$ and $\Omega_M = 0.3$). Hawkins et al. (2003) give a peculiar velocity of $506\ \mathrm{km\,s^{-1}}$ which corresponds to 6.7 Mpc. Thus, for most sources the distance uncertainty is mainly due to the uncertainty in the Hubble flow. For the MHDM sample, we use the distances as provided by MHDM and assume a constant uncertainty of 40% in the distance estimation to avoid that we overestimate the intrinsic scatter, see below. Here, we also checked that this assumption is not critical. For most sources MHDM derive the distance from the Hubble law, so that the uncertainty is mainly due to the Hubble constant.
- Flux measurements: for all but the faintest objects are the fluxes very well constrained. Errors for radio and

optical/X-ray fluxes are usually less than 10%. Systematic errors, e.g., due to the extrapolation of the different observed energy bands to our used X-ray band (0.5–10 keV), will also be of a similar magnitude. Thus, as these errors are small compared with the scatter due to the mass measurements, we do not introduce significant changes by assuming that these errors are isotropic. Due to this assumption, it is possible to unify these flux errors with the intrinsic errors of the source.

- Intrinsic errors: besides the measurement errors above, there are several sources of intrinsic scatter of often unknown magnitude:
  - Non-simultaneous observations of the AGN: the radio and X-ray observations are non-simultaneous, there is often more than a year between the different observations. All accreting black holes (AGN and XRBs) are highly variable. Thus, already this effect can lead to a deviation by more than an order of magnitude. The orientation of this uncertainty is likely to be isotropic.
  - Beaming: in most models at least the radio emission is attributed to the relativistic jet and will thus be relativistically beamed. In case that the X-rays originate from the disk/corona they will not be beamed and the deviations from the correlation will be enormous. For jet models, the X-ray emission may be beamed like the radio emission or have a different beaming patters (e.g., a velocity structure in the jet Chiaberge et al. 2000; Trussoni et al. 2003). The asymmetry of this effect depends on the exact model, so we can only assume isotropy.
  - Source peculiarities: the surrounding environment of the black hole will play a role on the exact emission properties (e.g., there might be compact hotspots). There may also be an obscuring torus or other obstacles for the emission. This can result in strong X-ray absorption or the radio emission may also be absorbed. All models, however, only consider the nuclear emission.
  - Spectral energy distribution (SED): depending on the real emission model, it may be that we are not observing the same emission type in the X-rays for the different objects. For jet models the effect of radiative cooling and the synchrotron cut-off have to be mentioned (see Sect. 2.5). For disk models a similar effect may be due to the relative strength of the disk component, the jet component as observed in the resolved X-ray jets, and the Comptonization component. The X-rays in XRBs may not originate from the same process as those in AGN due to the mass scaling by whatever theory is used.

  The total intrinsic scatter will be derived from the scatter of the correlation. We will see below that the intrinsic scatter is surprisingly small considering this long list of possible errors.

For the two last sources of scatter, the flux measurements and the intrinsic errors, we do not have an exact knowledge of their magnitude and their asymmetry. We will therefore assume that they are isotropic in the $\log F_X - \log F_R$ plane and parameterize their combined magnitude as $\sigma_{\rm Int}$. This parameter $\sigma_{\rm Int}$ will be chosen, such that the reduced merit function is unity. With this choice we assume the error distribution just described; this will therefore affect the final fit values. If one distributes the excess variance in a different manner one will find slightly different best fit parameters. However, as we know several effects that introduce uncertainties in the radio and X-ray fluxes and the the excess variance in these variables is surprisingly low, it is sensible to include the excess variance only in the radio and X-ray fluxes.

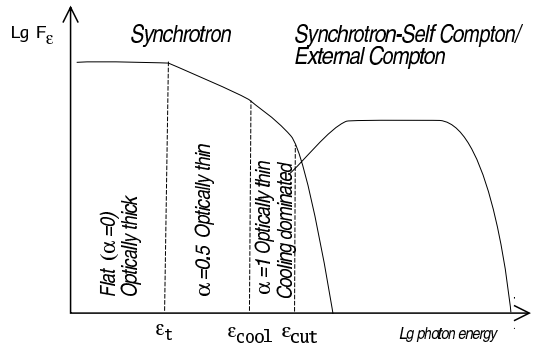

Fig. 2. Sketch of the SED of a relativistic jet as for example observed in BL Lac objects. At lower photon energies synchrotron emission is dominant while the high energy spectrum is usually explained by inverse Compton processes. See text for details.

2.4. The parameter $\sigma_{\rm Int}$

In Sect. 2.3 we present our assumptions on the uncertainties of the measured variables. In case that these assumptions are exact, e.g., the magnitude of the uncertainties and that they are Gaussian distributed, the fitted parameter $\sigma_{\rm Int}$ will describe the real intrinsic scatter of the sources. This value could then be used to constrain the different contributions like the effect of beaming. However, if we overestimate the uncertainties in the flux, distance, and mass estimation the derived $\sigma_{\rm Int}$ will be too small. Similarly, an underestimation will lead to an overestimation of the intrinsic scatter.

Our method can not treat coupled uncertainties correctly. For XRBs we include several data points for each source, but there is only one mass and distance estimates for that source. Thus, as we have to assume that our uncertainties are independent, we overestimate the measurement errors. Thus, the inferred $\sigma_{\rm Int}$ for XRBs alone is zero. This means that the deviations of the data points from the optimal correlation is within the measurement uncertainties. On the other hand, for the AGN samples the uncertainties are independent. Every source is included only once in the sample. Here, $\sigma_{\rm Int}$ should be a good measure for the intrinsic scatter.

2.5. Origin of X-ray emission in the jet model

The spectrum of a relativistic jet can be directly observed in BL Lac objects, as relativistic boosting increases the relative prominence of the jet component compared to the disk (Blandford & Rees 1978). An idealized spectrum of a jet, i.e., the "Camel's back", is shown in Fig. 2 in flux (F_ϵ) representation. Such a jet component exists at least in every AGN with a detectable jet, most likely in all AGN. The relative prominence of this component in respect to disk and corona emission will vary. Furthermore, the exact shape of the SED depends also on the inclination angle, the Lorentz factor of the jet and peculiarities of the source.

The spectrum of a conical jet is flat (in F_ν representation) due to optically thick synchrotron emission up to the turnover frequency ϵ_t. This is followed by the optically thin power law component with a typical energy index α ($F_\epsilon \sim \epsilon^{-\alpha}$) of around

$\alpha = 0.5$. This emission comes from the innermost region of the radiating jet. The power law continues up to the energy where radiative cooling plays a role ($\epsilon_{\rm cool}$); here the power law may steepen to $\alpha \approx 1$. Finally the synchrotron emission cuts off at ($\epsilon_{\rm cut}$), due to the acceleration mechanism creating the radiating particles. At photon energies above the synchrotron cut-off, synchrotron-self Compton emission and external Compton emission are visible. As the jet is relativistically boosted, the total observed power in these two humps depend on the jet Lorentz factor and the inclination of the source. The relative prominence of the synchrotron and the inverse-Compton emission depends on these two parameters as well.

The photon energy where the synchrotron emission cuts off, seems to depend on the total power of the accreting system, see e.g., the blazar sequence (Fossati et al. 1998; Ghisellini et al. 2002). For low power systems, like high-peaked BL Lac objects (see the previous references), the cut-off energy can be above or around the standard X-ray band of 0.5–10 keV, while for strongly accreting systems, e.g., flat spectrum radio quasars, this cut-off can be as low as 0.1 eV. Thus, we can expect that only the X-rays of low power systems actually originate from synchrotron emission.

Radiative cooling in the X-rays, as for example discussed by Heinz (2004), may play a role in some sources of low to intermediate accretion rates. Its main effect will be that the measured X-ray flux will be reduced to what one would expect from a simple uncooled jet. However, the X-ray reduction due to cooling is far less severe than the synchrotron cut-off. The effect of cooling will increase the observed intrinsic scatter as we are exploring only the simplest jet model: the uncooled jet. For most AGN besides the LLAGN in the MHDM sample this synchrotron cut-off will be below the X-ray band. The X-ray emission in these sources will not be due to synchrotron emission. It will either originate from inverse-Compton processes in the jet or from the disk/corona.

The cut-off energy ($\epsilon_{\rm cut}$) of LLAGN sources in the KFC sample will for most sources be above the ROSAT and Chandra bands. The radio luminosities of the LLAGN are in the range of 10^{36-38} erg/s. If one extrapolates Fig. 7 of Fossati et al. (1998) to these energies, one can expect a cut-off above 10^{19-20} Hz or 40–400 keV. For BL Lac objects and FR-I RGs, the KFC sample extrapolates optical fluxes to an equivalent X-ray flux. This treatment avoids the effect of the synchrotron cut-off also for these sources. The "jet only" model should therefore be applicable to the KFC sample.

2.6. Origin of the X-ray emission in the MHDM sample

The X-ray emission of many sources in the MHDM sample is very likely not due to synchrotron emission, due to the synchrotron cut-off. For example, for radio loud quasars, the synchrotron cut-off is far below the X-ray regime (see e.g., Tavecchio et al. 2002). Only the X-ray emission from the LLAGN may originate from synchrotron emission. Thus, the "jet-only" model is not applicable to the MHDM sample, and can therefore not be constrained using the MHDM sample.

The AGN sample of MHDM contains radio loud objects (e.g., Cyg A, 3C273, etc.). The X-ray spectral index of radio loud Quasars (RLQ) and those of radio quiet Quasars (RQQs) seems to be different: $\Gamma_{\rm RLQ} \approx 1.63 \pm 0.02$ compared to $\Gamma_{\rm RQQ} \approx 1.89 \pm 0.11$. Furthermore, RLQ show very weak or no reflection components and the strength of the soft excess seems to be anti-correlated with the radio-loudness. These effects are usually explained by a relativistic jet component in the RLQ case (see e.g., Reeves & Turner 2000; Piconcelli et al. 2005).

On the other hand, there are several detected "resolved" X-ray jets in AGN. For the source 3C 273, which is included in the MHDM sample, see Marshall et al. (2001). Marshall et al. (2005) and Sambruna et al. (2004) find in more than 50% of the observed radio loud sources resolved X-ray jets. The authors suggest that all bright radio jets may have X-ray counterparts. The X-ray emission from the AGN jets is usually explained by non-thermal processes (synchrotron, inverse-Compton, synchrotron-self-Compton), which process dominates seems to vary from source to source. For a discussion see Harris & Krawczynski (2002). As the jet is visible, it most likely contributes at least at some level to the core X-ray flux. Furthermore, many of the MHDM fluxes are derived from ASCA or GINGA data. In that case, the Chandra resolved X-ray jet will be observed as a point source. Note that the X-ray jets in AGN are often dominated by emission from knots, unlike what is expected for LH state XRBs as modeled by Markoff et al. (2001a). From the statistical studies and the direct observation of X-ray jets, we conclude that *at least some radio loud AGN in the MHDM sample have an X-ray component originating from the jet.*

Besides jet components, other features can contaminate the X-ray fluxes, especially for non-Chandra data. The flux may consist of several components originating from different physical processes, including the disk described by any model, the corona, the reflection component, warm gas and the jet (at least in radio loud objects).

2.7. Uncertainties of the estimated parameters

Given the data points and their estimated uncertainties we can derive the optimal fit parameters from Eq. (2). The merit function $\hat{\chi}^2$ can be used similarly to the usual χ^2 to estimate the confidence region of the parameters. The 1σ confidence region should be given by $\Delta\hat{\chi}^2 \approx 2.3$ as we have 2 degrees of freedom in our model besides the offset $b_{\rm X}$. As problems may arise due to the use of the nonlinear merit function or the unknown distribution function of the errors, we checked that this confidence region is in agreement with the confidence region derived by a Monte Carlo simulation and the Bootstrap method (see below).

In the Monte-Carlo simulation, the errors of the parameters are estimated by creating a large number (5000) of artificial datasets that have similar statistical properties compared to the measured dataset. For each of the artificial datasets, we estimate the best-fit parameters using the same method as for the original dataset. From these fitted parameters, we derive the confidence region and the $\Delta\hat{\chi}^2$ corresponding to the 1, 2 and 3σ confidence regions. To create the artificial data, we consider each population of sources of our measured dataset individually and measure their scatter and position in the $\log L_{\rm R}$–$\log L_{\rm X}$ plane. In the artificial dataset, we distribute the sources uniformly over their radio luminosities. The artificial dataset will therefore also contain simulated objects of all considered types. We assume that the scatter compared to the real correlation is Gaussian. As seen in Fig. 3 this seems to be roughly the case. We also introduce flux limits in the simulation to access the effects of the distance selection effect.

The bootstrap method functions as follows. From a set of N measured sources, we draw N at random with replacement, thus, creating an artificial dataset. This dataset contains some of the sources more than once, while others are omitted. The parameters of the fundamental plane will be estimated for this sample in the same way as for the original dataset. These simulated

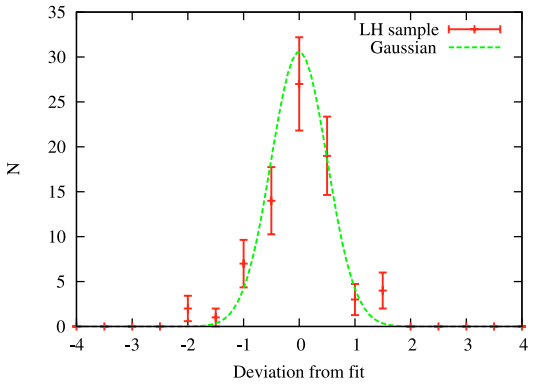

Fig. 3. Histogram of the scatter in the full KFC sample. The scatter can be well approximated by a Gaussian with the standard-deviation $\sigma = 0.50$.

parameters should be distributed around the original best fit values as the measured parameters are distributed around the real parameters (Press 2002). The benefit of this method is that it does not require prior knowledge of the distribution function from which the original dataset was drawn.

2.8. Different parameter estimators

Up to now we have only discussed the parameter estimation using the merit function (Eq. (2)). This method minimizes the average distance of the data-points from the plane weighted with the measured uncertainties. Other possible methods used in astronomy include the ordinary least squares estimation or Maximum Likelihood methods (see e.g., D'Agostini 2005). Even though Maximum Likelihood estimators find the most probable parameters of a model, the method is often biased towards lower fit parameters. To find the optimal fitting method for our problem, we compare the different fitting methods using a Monte Carlo simulation. We create several artificial samples with our Monte Carlo simulation and compare the results of the different estimators with the parameters used to create the sample. We set the intrinsic scatter of our artificial XRB and LLAGN sample to 0.2 and for BL Lac and FR-I RGs to 0.8, which is roughly double of what is found in our sample. The resulting intrinsic scatter of the simulated sample is $\sigma_{\rm int} = 0.65$. For each parameter estimator consider two cases: First, we only use the average intrinsic scatter (0.65) to estimate the parameters, and second, we use the exact probability distribution used to create each individual datapoint.

For each estimator we simulated 100 different datasets and give the average estimated parameters and the standard deviation in Table 1. While the merit function seems to be a fairly robust method, the maximum likelihood estimator is biased towards smaller fit values. Thus, we will estimate our parameters with the method using the merit function described in Sect. 2.

3. Results

Our fitting algorithm is only robust if our sources are normally distributed around the fundamental plane. As a first test we show a histogram of the scatter of the KFC sample around the best fit to the fundamental plane in Fig. 3. The deviations are roughly normally distributed with $\sigma \approx 0.5$. Thus, the developed analysis method can be utilized.

We fitted the KFC sample with the fundamental plane described in Eq. (7). The parameter estimation method is described in Sect. 2. We find as best fit values

$$\xi_{\rm R} = 1.41^{+0.14}_{-0.12} \quad \xi_{\rm M} = -0.87^{+0.15}_{-0.17} \quad b_{\rm X} = -5.01^{+3.35}_{-3.9}. \tag{8}$$

The confidence region of the two relevant parameters and the fit is shown in the top panel of Fig. 4. The given uncertainties are derived from the $\Delta\chi^2$ map. The intrinsic scatter in the fundamental plane is for this sample $\sigma_{\rm int} = 0.38 \pm 0.06$. The uncertainty of $\sigma_{\rm int}$ has been derived by bootstrapping the measured sample.

The results of the KFC sample and the MHDM sample and their subsamples is presented in Table 2. The errors given in this table are derived using the Bootstrap method. As the errorbars for the KFC sample are nearly identical for both methods, we present only the bootstrapped errorbars for the different subsamples. This error estimation is less dependent on the assumption of normal distributed scatter. As the uncertainties are not strongly anisotropic, we give a symmetric uncertainty to avoid problems with anisotropic errors. We note that the different fit values do not coincide within the errors for both samples due to the different source populations included in the sample.

The subsample of the KFC sample containing no FR-I radio galaxies has a larger radio coefficient ($\xi_{\rm R} = 1.64 \pm 0.13$) and a smaller mass coefficient ($\xi_{\rm M} = -1.08 \pm 0.14$) than the full sample. On the other hand, the subsample without BL Lac objects deviates in the other direction ($\xi_{\rm R} = 1.25 \pm 0.1$ and $\xi_{\rm M} = -0.74 \pm 0.12$). This difference arises, because FR-I radio galaxies are fainter in the optical and X-rays than the deboosted BL Lac objects (Chiaberge et al. 2000). The difference in the optical/X-ray luminosity can be explained by a velocity structure in the jet. As we include a similar number of BL Lac objects and FR-I radio galaxies in the full sample, these effects will partly average out. However, the final value for the parameters will depend on the total weight each AGN class has in the total sample.

The KFC subsample containing only XRBS, Sgr A* and LLAGN has similar best fit values as the subsample containing no FR-I RGs. Its correlation coefficient, $\xi_{\rm R} = 1.59 \pm 0.21$, is larger than the one found for the full sample. This is partly due to the fact that the intrinsic scatter of this subsample is extremely low: $\sigma_{\rm int} = 0.12$. Thus, the errors of the mass estimation dominate (0.34 dex) the overall error budget and one gets larger fit values as shown in Fig. 1. If one adds Seyferts and Transition objects, which may correspond to the high state, the correlation coefficient gets even larger. However, all KFC subsamples seem to be roughly in agreement with $\xi_{\rm R} \approx 1.4$ and $\xi_{\rm M} \approx -0.8$. This radio coefficient is in agreement with the radio/X-ray correlation for GX 339–4, which has $\xi_{\rm R} \approx 1.4$ (Corbel et al. 2003).

If one uses the quiescent flux of Sgr A* instead of the flare by Baganoff et al. (2001) in the KFC sample the best fit values for $\xi_{\rm R}$ increase. The subsample containing only XRBs, the quiescent Sgr A* and LLAGN yields $\xi_{\rm R} = 1.97$ and $\xi_{\rm M} \approx -1.41$. Interestingly, the latter subsample has an intrinsic scatter of zero, i.e., the scatter of the correlation is in agreement with the assumed measurement errors. However, the inferred fit for $\xi_{\rm R}$ is no longer in agreement with the value found for XRBs only ($\xi_{\rm R} = 1.4$). The quiescent X-ray emission from Sgr A* is an extended (Baganoff et al. 2003), while this is not the case for cores of the XRBs or AGN. Thus, it is not surprising that the fit values change.

For the previous fits we have used the same intrinsic scatter $\sigma_{\rm int}$ for all our objects. However, we have seen that XRBs and LLAGN can be fitted with significantly less excess scatter than the full sample. Thus, we can fix the intrinsic scatter of XRBs

Table 1. Performance of the different parameter estimators. The given uncertainties is the standard deviation of the fit parameters obtained from different artificial datasets.

Estimator	ξ_R	ξ_M	b_X
Assumed parameters	1.40	–0.85	–4.9
Merit function	1.42 ± 0.13	-0.87 ± 0.16	-5.4 ± 3.6
Merit function with exact knowledge of scatter	1.40 ± 0.08	-0.85 ± 0.09	-4.8 ± 2.3
Merit function with isotropic uncertainties	1.54 ± 0.16	-1.03 ± 0.19	-8.5 ± 4.4
Maximum likelihood	1.10 ± 0.08	-0.47 ± 0.09	3.5 ± 2.1
Maximum likelihood with exact knowledge of scatter	1.25 ± 0.06	-0.68 ± 0.07	-0.51 ± 1.68
Ordinary least squares	1.09 ± 0.08	-0.46 ± 0.09	4.0 ± 2.3

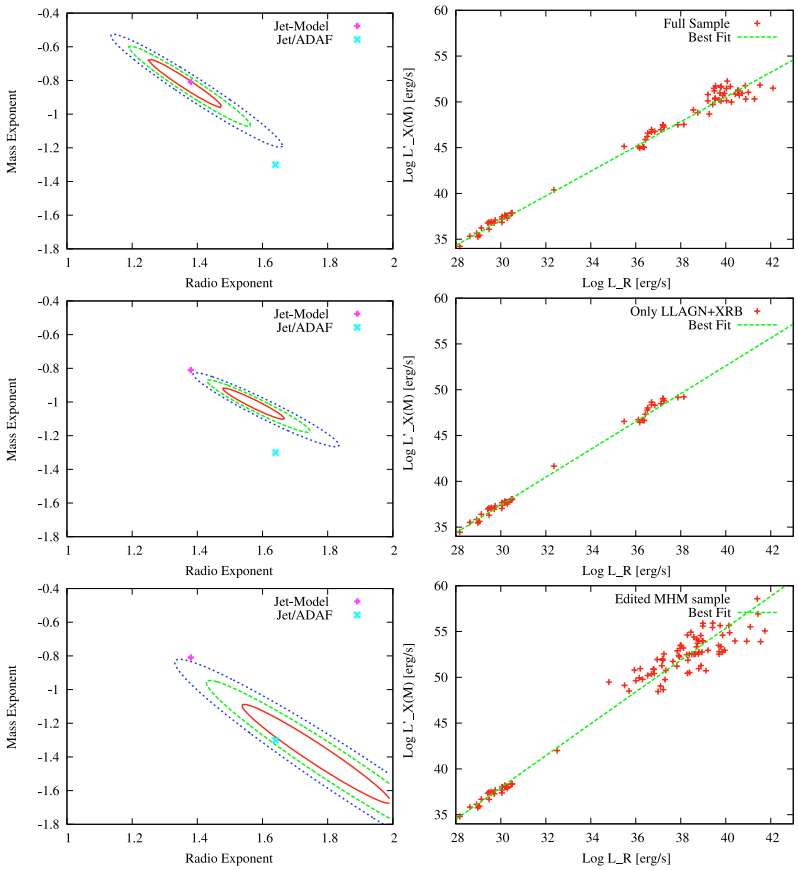

Fig. 4. On the left side we show the χ^2 map with one (solid line), two (dashed) and three sigma (dotted) levels together with the predictions of the "jet only" model and the ADAF/jet model. The right side shows the best fit and the AGN and XRB sample. The three rows show the different samples, *from Top to bottom*: KFC sample, Only XRBS and LLAGN of the KFC sample, and the edited MHDM sample.

and LLAGN to 0.1 dex and fit only the scatter in the BL Lac and FR-I RGs. Now, we find $\xi_R = 1.61 \pm 0.11$ and $\xi_M = -1.08$ which is similar to the result found for XRBs, Sgr A* and LLAGN only. The intrinsic scatter found for FR-I RGs and BL Lac objects is 0.55 dex. The statistical weight for these two classes is therefore significantly less than that of the LLAGN and XRBs. It is therefore not surprising that we find similar fit values: the fitting method puts only very a low weight on the additional sources. To observe selection effects it is therefore sensible to use a constant intrinsic scatter for all sources.

For the full edited MHDM sample, we find $\xi_R \approx 1.74^{+0.23}_{-0.19}$ and $\xi_M \approx -1.35^{+0.24}_{-0.30}$. As for the KFC sample, we also find a selection effect for the MHDM sample. The MHDM subsample containing no Seyfert objects yields as best fit parameters $\xi_R \approx 2.12$ and $\xi_M \approx -1.75$, while the one containing no Quasars gives $\xi_R \approx 1.55$ and $\xi_M \approx -1.15$. This effect can be explained by the fact that the quasars are more radio quiet than the other AGN in the sample. We note that the formal fits of ξ_R for most subsamples tend to be significantly higher than the value found by Corbel et al. (2003) of $\xi_R = 1.4$ for XRBs. Overall, we find the choice of the sample strongly influences the final fit value in both considered samples (MHDM and KFC). This is not necessarily worrisome, as one does expect somewhat different results for different black hole states.

Table 2. Best fit results for the KFC sample and the original and edited MHDM sample. Besides the full sample we also give the parameters for the subsamples containing only a limited set of AGN classes. Note that LINER sources classified by MHDM are not limited to LLAGN. The LH XRB sample is defined in Sect. 2.1. The column *N* denotes the number of sources in the sample.

	ξ_R	ξ_M	b_X	σ_{int}	$\xi_m \vert \xi r = 1.4$	$\sigma_{int} \vert \xi r = 1.4$	*N*
KFC sample							
Full sample (XRB, Sgr A*, LLAGN, FR-I, BL Lac)	1.41 ± 0.11	-0.87 ± 0.14	-5.01 ± 3.20	0.38	-0.86 ± 0.02	0.38	77
Full sample + Seyferts & Transition obj.	1.48 ± 0.13	-0.95 ± 0.16	-6.89 ± 3.83	0.44	-0.86 ± 0.02	0.44	100
XRB, Sgr A*, LLAGN, FR-I	1.25 ± 0.10	-0.74 ± 0.12	-0.46 ± 2.93	0.28	-0.91 ± 0.02	0.30	58
XRB, Sgr A*, LLAGN, BL Lac,	1.64 ± 0.13	-1.08 ± 0.14	-11.67 ± 3.59	0.18	-0.81 ± 0.02	0.23	62
XRB, Sgr A*, LLAGN	1.59 ± 0.21	-1.02 ± 0.21	-10.15 ± 6.17	0.12	-0.84 ± 0.02	0.15	43
XRB, Sgr A*, LLAGN, Seyfert & Transition	1.86 ± 0.35	-1.33 ± 0.36	-17.98 ± 9.92	0.35	-0.85 ± 0.02	0.39	66
Sgr A*, LLAGN, FR-I, BL Lac	1.70 ± 1.17	-2.17 ± 4.09	-5.21 ± 12.08	0.45	-1.15 ± 0.38	0.46	52
Full sample with quiescent Sgr A*	1.52 ± 0.14	-1.00 ± 0.18	-8.15 ± 4.11	0.39	-0.85 ± 0.02	0.40	77
XRB, quiescent Sgr A*, LLAGN	1.97 ± 0.11	-1.41 ± 0.10	-21.05 ± 3.05	0.00	-0.86 ± 0.02	0.23	43
Original MHDM sample	1.45 ± 0.17	-0.99 ± 0.22	-5.98 ± 5.02	0.72	-0.93 ± 0.03	0.73	116
MHDM sample with LH XRBs							
Full sample (XRB, Sgr A*, LINER, Quasar, Seyfert)	1.74 ± 0.20	-1.35 ± 0.27	-14.23 ± 5.75	0.65	-0.92 ± 0.03	0.68	103
XRB, Sgr A*, LINER, Seyfert	1.55 ± 0.19	-1.15 ± 0.24	-8.93 ± 5.37	0.64	-0.96 ± 0.03	0.64	92
XRB, Sgr A*, LINER, Quasar	2.12 ± 0.31	-1.75 ± 0.38	-25.20 ± 8.81	0.51	-0.90 ± 0.04	0.62	57
XRB, Sgr A*, Quasar, Seyfert	1.79 ± 0.28	-1.39 ± 0.37	-15.68 ± 7.87	0.63	-0.88 ± 0.03	0.65	82
XRB, Sgr A*, LINER	1.59 ± 0.35	-1.19 ± 0.40	-10.11 ± 10.13	0.50	-1.54 ± 0.21	0.71	46
XRB, Sgr A*, Quasar	2.03 ± 0.28	-1.55 ± 0.36	-22.76 ± 7.86	0.14	-0.74 ± 0.04	0.32	37
Sgr A*, LINER, Quasar, Seyfert	1.65 ± 0.26	-1.72 ± 0.50	-8.02 ± 8.06	0.74	-1.41 ± 0.22	0.76	78

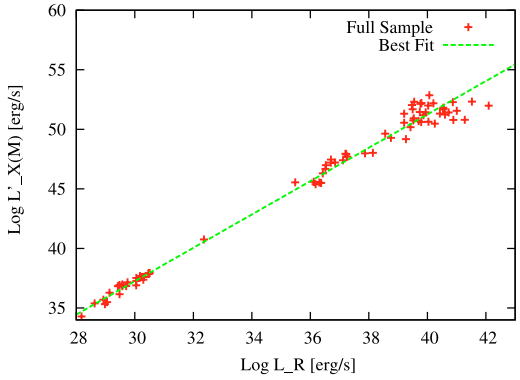

Fig. 5. Best fit for the full KFC sample if one fixes ξ_R to 1.4, which is the value found for XRBs. Only the mass scaling parameter is fitted. One finds: $\xi_M = -0.86 \pm 0.02$ and $b_X = -4.9$. The intrinsic scatter increases by less than 0.01 compared to the fit in both parameters ($\sigma_{int} = 0.38$).

The correlation index ξ_R for XRBs only is better constrained than in the case we are considering here, as one does not have to consider the mass scaling in that case. For XRBs only one finds $\xi_R \approx 1.4$ (Corbel et al. 2003; Gallo et al. 2003). If we use this prior knowledge to fix the correlation index ξ_R to 1.4 and only fit the mass scaling parameter ξ_M to our full KFC sample, we find $\xi_M = -0.86 \pm 0.02$ (see Table 2). This fit is shown in Fig. 5. The fit is not significantly worse than the original fit in both parameters, as the intrinsic scatter increases by less than 0.01 ($\sigma_{int} = 0.38$). Interestingly, the best fit value for the subsample of LLAGN, that had a higher correlation ($\xi_R = 1.59$) yields with the prior knowledge $\xi_M = -0.84 \pm 0.02$, in agreement with the value found for the full sample. For the MHDM sample, we find $\xi_M = -0.92 \pm 0.04$. As the correlation index ξ_R is well constrained for XRBs, fixing $\xi_R = 1.4$ will likely yield the best estimates for the parameters of the fundamental plane.

Besides checking the effect of anisotropic errors we also explore the effect that the uncertainties are not normally distributed but exponentially. In that case, one does not minimize the square of the deviations divided by the uncertainty but the absolute value. This "robust" estimation (Press 2002) yield $\xi_R = 1.39$ and $\xi_M = -0.84$. For the edited MHDM sample we find $\xi_R = 1.63$ and $\xi_M = -1.14$. Thus, the change of the distribution of the uncertainties does not significantly change the best fits.

In Table 2, we also show the intrinsic scatter measured for the different datasets. If we drop our assumption that the intrinsic scatter is the same for AGN and XRBs, e.g. if σ_{int} is smaller for XRBs than for AGN, then the correlation coefficient ξ_R will rise slightly.

3.1. The distance selection effect

Our sample of AGN and XRBs is a random sample of well studied objects and not a complete distance limited sample. Thus, one can fear that the fundamental plane is a spurious correlation created by distances selection effects. It has been shown with partial correlation analysis by MHDM that the fundamental plane is real and not spurious. This problem has been discussed in detail by Merloni et al. (2006), where the authors show further statistical and observational evidence that the fundamental plane

Table 3. Effect of the observing flux limits on correlated data: most radio fluxes in our sample are obtained with the VLA, which can detect 0.1 mJy within a 10 min snapshot. Chandra can go as deep as 10^{-14} erg/s/cm^2 in a 1000 s observation.

Radio limit [mJy]	X-ray limit [erg/s/cm^2]	ξ_R	ξ_M	b_X
no limit	no limit	1.40 ± 0.11	-0.86 ± 0.15	-4.84 ± 3.2
0.5	10^{-13}	1.37 ± 0.11	-0.80 ± 0.15	-4.21 ± 3.2
5	10^{-13}	1.34 ± 0.10	-0.77 ± 0.13	-3.67 ± 3.1
0.5	10^{-12}	1.36 ± 0.12	-0.76 ± 0.16	-3.94 ± 3.4
5	10^{-12}	1.27 ± 0.10	-0.64 ± 0.12	-1.75 ± 2.8

is indeed real. Here, we will just present some further tests for our sample.

The fundamental plane is an extension of radio/X-ray correlations in XRBs (Gallo et al. 2003). This correlation is highly significant and is not effected by distance effects as we can trace individual objects on the correlation. In AGN, Hardcastle & Worrall (1999) and Canosa et al. (1999) showed that a radio/X-ray correlation exists and is also not created as an artifact of plotting "distance against distance" in a flux limited sample. If one combines these two correlations with a mass term (which is needed, see Falcke & Biermann 1996), one arrives naturally at the fundamental plane.

One method to check if a correlation between two observables is only created by a third variable, is the partial correlation coefficient. In our case for radio and X-ray luminosity is the parameter that may create a spurious correlation the distance. The correlation coefficient is defined as:

$$r_{rx,d} = \frac{r_{rx} - r_{rd} r_{xd}}{\sqrt{(1. - r_{xd}^2)(1. - r_{rd}^2)}}, \quad (9)$$

where r_{ab} is the normal Pearson R for a and b. This correlation coefficient should remove the effect of the different distances.

If we fix the mass coefficient $\xi_M = -0.85$, we find $r_{rx,d} = 0.91$. We have written a small Monte Carlo simulation, to test if this coefficient is significant. We assume a uniform distribution for the distances and the fluxes in log-space, and assume that the fluxes are uncorrelated. We created 10^6 artificial datasets, and found that not a single dataset had a partial correlation coefficient as large as 0.8, even though the average normal correlation coefficient for the luminosities was 0.99. The standard deviation of the partial correlation coefficient is 0.11 and the mean, 0. Thus, the radio/X-ray correlation with a fixed mass coefficient is significant at the 8σ level. However, in our sample, we only include objects with measured radio and X-ray fluxes and do not include upper limits which could affect the significance.

On the other hand, if we fix $\xi_M = 1.4$ the fundamental plane suggests that $\frac{L_X}{L_R^{1.4}}$ and M are correlated. The Kendall τ for this correlation is $\tau = 0.6$, which is significant as for uncorrelated data τ is normally distributed around 0 with a standard deviation of 0.006. Again we can check whether this is due to the different distances in the sample: The partial correlation coefficient is $r_{L_X/L_R^{1.4},M,D} = 0.84$, which is again significant (7σ).

Even if the observational flux limits can not create a spurious fundamental plane, these limits might still bias the estimated parameters. This problem can be tested with our Monte Carlo simulation. We start with our fundamental plane and observe the parameter changes due to increasing flux limits. As the flux limits may reduce the observed scatter around the fundamental plane, we increase the intrinsic scatter by a factor of 2. The results are summarized in Table 3. As long as the flux limits stay in a reasonable range, the changes to the parameters are below 0.1, i.e., they are of the order of the uncertainties of the fits.

3.2. Comparison of the KFC sample and the MHDM sample

The correlation coefficient ξ_R in the MHDM sample and its subsamples seems larger than those usually found in the KFC sample and a similar effect can be found for ξ_M. The fits of the KFC sample and its subsamples are in agreement with the value found for LH state XRBs ($\xi_R = 1.4$), while the deviations are larger for the MHDM sample. This may be seen as a hint that the MHDM sample is not simply a continuation of the LH state correlation for XRBs, but it may contain other effects like a different source of emission.

The main statistical difference between the MHDM sample and the KFC sample is the smaller intrinsic scatter of the latter: $\sigma_{int} = 0.39$ compared to $\sigma_{int} = 0.65$. It is hard to assess the uncertainties of this value due to selection effects as the underlying distribution is unknown. Bootstrapping yields an error for both values around 0.06.

The discrepancy is partly due to the fact that the KFC sample has less AGN compared to XRBs than the MHDM sample. However, even if one adds the Seyferts and transition objects of Nagar et al. (2005) to create a sample of similar size than the MHDM sample, then the intrinsic scatter is still less ($\sigma_{int} = 0.46$) than for the MHDM case. The same is true for the subsamples of similar size.

The most homogeneous subsample is the sample containing only LLAGN, LH state XRBs and Sgr A*. Here we find $\sigma_{int} = 0.11$. This low value is not only due to the fact that we overestimated the errors of the XRBs, as the numerical value is below 0.1 for the LLAGN sample without XRBs as well. Thus, the correlation is extremely tight for the lowest luminosity objects. If we extend this sample to slightly higher accretion rates, i.e., include FR-I RGs and BL Lac objects the scatter increases due to peculiarities of these objects. The scatter further increases if we included objects FKM classify as high state objects. Thus, the reduced scatter supports the classification of AGN classes by FKM and suggests that there is a difference between LH state AGN and HS state objects.

3.3. Interpretation in the context of the proposed models

In Fig. 4, we show the χ^2 maps of the different samples and the predictions of the jet model and one disk/jet model. For the "jet only" model the predicted values are: $\xi_R = 1.38$ and $\xi_M = -0.81$ (FKM) while the values for the "ADAF/jet" model are $\xi_R = 1.64$ and $\xi_M = -1.3$ (MHDM). The exact value for a disk/jet model depends on the solution used for the accretion flow.

The full KFC sample contains some sources, for which we used optical fluxes to derive our equivalent X-ray luminosities. Thus, the "ADAF/jet" does not have to be valid. If we ignore this, the full KFC sample seems to favour the "jet only" model as, according to the confidence region, we can rule out the "ADAF/jet" possibility by more than 3σ. *However*, the exact fit values

depend on the choice of the sample and the used assumptions for the statistical model.

In contrast to the claims of Heinz (2004), the correlation *is* in agreement with a simple jet model in the regime where radiative cooling is not important. The choice of sources minimizes the effect of radiative cooling and the synchrotron cut-off as discussed in Sect. 2.5, but it can not be ruled out that cooling has some effect on this sample.

The correlation with the least scatter is found for the subsample of the KFC sample containing only LH state XRBs, Sgr A* and LLAGN. Its confidence region is shown in the middle row of the figure. As this subsample consists of "real" radio/X-ray data, both models claim to be valid. However, the fit is not in good agreement with both models. The "jet only" model is disfavoured with $\approx 3\sigma$ while the "ADAF/jet" model is even stronger rejected. The remarkable low scatter in this subsample $\sigma_{\rm Int} = 0.10$ supports the idea that LH state XRBs and LLAGN are indeed associated.

In the light of the jet model, it may be that the deviation of the fit from the predicted value is due to synchrotron cooling and the synchrotron cut-off. Even though we have designed this sample to minimize their effect, it may still play a role in some of the objects. To analyze this effect, one would have to compare the X-ray spectrum with the assumed hard power-law and take the spectral index into account. If one finds significant deviations in the spectral index one will have to resort to a more complicated study where the measured spectral index or a more complicated model of the SED is taken into account in the fitting. Another possible explanation for this deviation, is that we do not treat the coupled errors of the XRB data points correctly. As we treat all errors as independent we do not constrain the correlation index $\xi_{\rm R}$ from the XRBs as well as we could. If we set this index to $\xi_{\rm R} = 1.4$ and only fit $\xi_{\rm M}$ we find $\xi_{\rm M} = -0.85$ for the KFC subsample containing LLAGN and XRBs. See also Fig. 5. This is roughly in agreement with the value predicted by the jet/synchrotron model of $\xi_{\rm M} = -0.81$.

For a "disk/jet" model the discrepancy may be due to the disk model used. Besides the discussed ADAF solution, one can use any other accretion flow model to create the X-rays. This can change the prediction considerably, see e.g., MHDM. Thus, the discrepancy of the fit compared to the model predictions can not rule out any of the suggested models with certainty, but – in contrast to earlier claims – it does not support them either.

To compare the edited MHDM sample with the models, we now have to note that the "jet only" model claims to become invalid for the X-ray emission of high state objects like Quasars. Interestingly, the edited MHDM sample including high-state objects indeed disfavours the "jet only" model and is in agreement with the "ADAF/jet" model (1.2σ). However, also for this sample the selection effects are dominating the exact fit value as well.

3.4. The conspiracy

We have seen that the fundamental plane in the two described incarnations is only slightly different. For both samples we find only slightly different parameters, and the scatter seems to be less in the case of the KFC sample. The MHDM sample contains low luminosity objects as well as bright quasars. However, there do not seem to be obvious outliers.

The radio emission is usually attributed to the jet. For the higher observation frequencies there are objects in the two samples that are clearly jet dominated and others for which the accretion flow will be the dominant part at higher frequencies. The clearest examples for synchrotron emission are the BL Lac objects in the KFC sample but, also for FR-I RG this origin is well established (Chiaberge et al. 1999). On the other hand, the X-ray emission from radio quiet Quasars is very likely not synchrotron emission. Nevertheless, even though the inclusion of the Quasar subsample changes the correlation and increases the scatter, they do not drop off the correlation like HS state XRBs. Likewise, if the X-rays of LH state XRBs and LLAGN are created by the accretion flow, why do the BL Lac objects and FR-I RGs still follow the fundamental plane? There seem to be a "fundamental plane conspiracy": even though the emission processes are different the objects all lie near the fundamental plane.

Within the jet model one can explain part of the conspiracy by the different emission processes (see Fig. 2). If we observe a source at a frequency after the synchrotron cut-off, the Compton branch takes over. The inverse Compton emission can in many sources reach the values one would find if one extrapolates the synchrotron power-law to X-ray frequencies. It will mainly increase the scatter in the correlation.

4. Conclusions

In the previous sections we have reconfirmed the existence of the fundamental plane of accreting black hole in the black hole mass, radio and X-ray luminosity space. We find that the result of a statistical analysis of the radio/X-ray correlation depends strongly on the assumptions of the distribution and magnitude of the measurement errors and the intrinsic scatter. The measurement uncertainties have been taken from the literature. The unknown intrinsic scatter, e.g., the scatter due to relativistic beaming, non-simultaneous observations or source peculiarities, has been parameterized and estimated for the observed samples.

Using this refined method we compared the proposed radio/X-ray correlations of MHDM and the improved KFC sample based on FKM. Both samples differ in their source selection: while the KFC sample tries to include only sources belonging to the low/hard state, the MHDM sample includes all kinds of AGN. Also the observing frequencies differ for some sources, as the KFC sample uses extrapolated optical fluxes for FR-I RGs and BL Lac objects.

The best fit values of both samples depend on the relative number of sources in each class of objects, e.g., the relative number of quasars or FR-I RGs compared to LLAGN. This can be understood if different physical processes are dominant in the different classes, e.g., the emission from LLAGN may be due to the jet, while for quasars the disk emission dominates. The confidence regions do not reflect this problem and have to be viewed as a lower bound on the errors of the parameters.

The best fit values found for the KFC sample are $\xi_{\rm R} = 1.41 \pm 0.11$ and $\xi_{\rm M} = -0.87 \pm 0.14$ while we find for the MHDM sample $\xi_{\rm R} = 1.74 \pm 0.20$ and $\xi_{\rm M} = -1.35 \pm 0.27$. Thus, the KFC sample suggests a simple uncooled "jet only" model while the MHDM sample favours the "ADAF/jet" model. However, the selection effects are very hard to control.

The KFC sample seems to be a more homogeneous sample, as it has a lower intrinsic scatter. The fundamental plane for the subsample containing only LLAGNs and XRBs is surprisingly tight with a scatter of $\sigma_{\rm int} = 0.12$ dex, while the full sample has $\sigma_{\rm int} = 0.38$. Compared to this, the MHDM sample has a higher intrinsic scatter of $\sigma_{\rm int} \approx 0.6$ dex. This supports the AGN classification of FKM in low/hard and high/soft state objects.

In general, the fundamental plane of black hole activity is confirmed by our analysis. With a careful control of a homogeneous source selection (high-state versus low-state), the scatter can reach rather low values. This promises a wider application

of the "fundamental plane" in other contexts (see e.g., Merloni 2004; Maccarone 2005) and calls for improved radio and X-ray surveys in the future.

Acknowledgements. The authors thank Elena Gallo for the provision of the LH state XRB data points in electronic form. We thank Sera Markoff, Tom Maccarone, Sebastian Jester and Matthias Kadler for helpful discussions. We thank our referee for constructive comments.

References

Abramowicz, M. A., Kluźniak, W., McClintock, J. E., & Remillard, R. A. 2004, ApJ, 609, L63
Antonucci, R. 1993, ARA&A, 31, 473
Baganoff, F. K., Bautz, M. W., Brandt, W. N., et al. 2001, Nature, 413, 45
Baganoff, F. K., Maeda, Y., Morris, M., et al. 2003, ApJ, 591, 891
Barcons, X., Carrera, F. J., Watson, M. G., et al. 2002, A&A, 382, 522
Bettoni, D., Falomo, R., Fasano, G., et al. 2001, A&A, 380, 471
Blandford, R. D., & Rees, M. J. 1978, in Proc. of the Pittsburgh Conference on BL Lac Objects, 1978, 328
Canosa, C. M., Worrall, D. M., Hardcastle, M. J., & Birkinshaw, M. 1999, MNRAS, 310, 30
Chiaberge, M., Capetti, A., & Celotti, A. 1999, A&A, 349, 77
Chiaberge, M., Celotti, A., Capetti, A., & Ghisellini, G. 2000, A&A, 358, 104
Corbel, S., Fender, R. P., Tzioumis, A. K., et al. 2000, A&A, 359, 251
Corbel, S., Nowak, M. A., Fender, R. P., Tzioumis, A. K., & Markoff, S. 2003, A&A, 400, 1007
D'Agostini, G. 2005 [arXiv:physics/0511182]
Esin, A. A., McClintock, J. E., & Narayan, R. 1997, ApJ, 489, 865
Falcke, H., & Biermann, P. L. 1995, A&A, 293, 665
Falcke, H., & Biermann, P. L. 1996, A&A, 308, 321
Falcke, H., & Biermann, P. L. 1999, A&A, 342, 49
Falcke, H., Malkan, M. A., & Biermann, P. L. 1995, A&A, 298, 375
Falcke, H., Körding, E., & Markoff, S. 2004, A&A, 414, 895
Fanaroff, B. L., & Riley, J. M. 1974, MNRAS, 167, 31P
Fender, R., Corbel, S., Tzioumis, T., et al. 1999, ApJ, 519, L165
Fender, R. P. 2001, MNRAS, 322, 31
Fender, R. P., Gallo, E., & Jonker, P. G. 2003, MNRAS, 343, L99
Ferrarese, L., & Ford, H. 2005, Space Sci. Rev., 116, 523
Fossati, G., Maraschi, L., Celotti, A., Comastri, A., & Ghisellini, G. 1998, MNRAS, 299, 433
Gallo, E., Fender, R. P., & Pooley, G. G. 2003, MNRAS, 344, 60
Ghisellini, G., Celotti, A., & Costamante, L. 2002, A&A, 386, 833
Haardt, F., & Maraschi, L. 1991, ApJ, 380, L51
Hardcastle, M. J., & Worrall, D. M. 1999, MNRAS, 309, 969
Harris, D. E., & Krawczynski, H. 2002, ApJ, 565, 244
Hawkins, E., Maddox, S., Cole, S., et al. 2003, MNRAS, 346, 78
Heinz, S. 2004, MNRAS, 355, 835
Heinz, S., & Merloni, A. 2004, MNRAS, 355, L1
Homan, J., Buxton, M., Markoff, S., et al. 2005, ApJ, 624, 295
Hynes, R. I., Steeghs, D., Casares, J., Charles, P. A., & O'Brien, K. 2003, ApJ, 583, L95
Hynes, R. I., Steeghs, D., Casares, J., Charles, P. A., & O'Brien, K. 2004, ApJ, 609, 317
Jonker, P. G., & Nelemans, G. 2004, MNRAS, 354, 355
Kellermann, K. I., Sramek, R., Schmidt, M., Shaffer, D. B., & Green, R. 1989, AJ, 98, 1195
Körding, E., & Falcke, H. 2004, A&A, 414, 795
Maccarone, T. J. 2005, MNRAS, 360, L30
Maccarone, T. J., Gallo, E., & Fender, R. 2003, MNRAS, 345, L19
Maoz, D., Nagar, N. M., Falcke, H., & Wilson, A. S. 2005, ApJ, 625, 699
Markoff, S. 2005, ApJ, 618, L103
Markoff, S., Falcke, H., & Fender, R. 2001a, A&A, 372, L25
Markoff, S., Falcke, H., Yuan, F., & Biermann, P. L. 2001b, A&A, 379, L13
Markoff, S., Nowak, M., Corbel, S., Fender, R., & Falcke, H. 2003, A&A, 397, 645
Markoff, S., & Nowak, M. A. 2004, ApJ, 609, 972
Markoff, S., Nowak, M. A., & Wilms, J. 2005, ApJ, 635, 1203
Markowitz, A., Edelson, R., Vaughan, S., et al. 2003, ApJ, 593, 96
Marshall, H. L., Harris, D. E., Grimes, J. P., et al. 2001, ApJ, 549, L167
Marshall, H. L., Schwartz, D. A., Lovell, J. E. J., et al. 2005, ApJS, 156, 13
McClintock, J., & Remillard, R. 2006, in Compact Stellar X-ray Sources, ed. W. H. G. Lewin, & M. van der Klis (Cambridge University Press)
Merloni, A. 2004, MNRAS, 353, 1035
Merloni, A., Heinz, S., & Di Matteo, T. 2003, MNRAS, 345, 1057
Merloni, A., Koerding, E., Heinz, S., et al. 2006 [arXiv:astro-ph/0601286]
Merritt, D., & Ferrarese, L. 2001, ApJ, 547, 140
Mirabel, I. F., & Rodríguez, L. F. 1999, ARA&A, 37, 409
Nagar, N. M., Falcke, H., & Wilson, A. S. 2005, A&A, 435, 521
Narayan, R., & Yi, I. 1994, ApJ, 428, L13
Nowak, M. A., Wilms, J., Heinz, S., et al. 2005, ApJ, 626, 1006
Orosz, J. A. 2003, in IAU Symp., 365
Piconcelli, E., Jimenez-Bailón, E., Guainazzi, M., et al. 2005, A&A, 432, 15
Poutanen, J. 1998, in Theory of Black Hole Accretion Disks (Cambridge University Press), 100
Press, W. H. 2002, Numerical recipes in C++ : the art of scientific computing by William H. Press. xxviii, 1,002 p. : ill.
Prugniel, P., Zasov, A., Busarello, G., & Simien, F. 1998, A&AS, 127, 117
Ptak, A., & Griffiths, R. 2003, in Astronomical Data Analysis Software and Systems XII, ASP Conf. Ser., 295, 465
Quataert, E., & Gruzinov, A. 2000, ApJ, 539, 809
Reeves, J. N., & Turner, M. J. L. 2000, MNRAS, 316, 234
Reig, P., Belloni, T., & van der Klis, M. 2003, A&A, 412, 229
Ribó, M., Combi, J. A., & Mirabel, I. F. 2005, Ap&SS, 297, 143
ROSAT Scientific Team 2000, VizieR Online Data Catalog, 9028, 0
Sambruna, R. M., Gambill, J. K., Maraschi, L., et al. 2004, ApJ, 608, 698
Shahbaz, T., Fender, R., & Charles, P. A. 2001, A&A, 376, L17
Shakura, N. I., & Sunyaev, R. A. 1973, A&A, 24, 337
Spergel, D. N., Verde, L., Peiris, H. V., et al. 2003, ApJS, 148, 175
Stirling, A. M., Spencer, R. E., de la Force, C. J., et al. 2001, MNRAS, 327, 1273
Sunyaev, R. A., & Trümper, J. 1979, Nature, 279, 506
Tananbaum, H., Gursky, H., Kellogg, E., Giacconi, R., & Jones, C. 1972, ApJ, 177, L5
Tavecchio, F., Maraschi, L., Ghisellini, G., et al. 2002, ApJ, 575, 137
Terashima, Y., & Wilson, A. S. 2003, ApJ, 583, 145
Thorne, K. S., & Price, R. H. 1975, ApJ, 195, L101
Tonry, J. L., Dressler, A., Blakeslee, J. P., et al. 2001, ApJ, 546, 681
Trussoni, E., Capetti, A., Celotti, A., Chiaberge, M., & Feretti, L. 2003, A&A, 403, 889
Tully, R. B. 1988, Nearby galaxies catalog (Cambridge and New York: Cambridge University Press), 221
Uttley, P., McHardy, I. M., & Papadakis, I. E. 2002, MNRAS, 332, 231
Woo, J., & Urry, C. M. 2002, ApJ, 579, 530
Young, A. J., & Wilson, A. S. 2004, ApJ, 601, 133

Chapitre 7
SGR 1806−20 et son environnement

— Le monde est fait avec des astres et des hommes.
— Emile Verhaeren

7.1 Les répéteurs gamma mous : magnétars

7.1.1 Une brève histoire des magnétars

Magnetar, littéralement, étoile magnétique. Ce terme est apparu dans les années 1990 pour désigner une catégorie d'étoile à neutrons à fort champ magnétique (Kouveliotou et al. 1998, 1999). Il s'agissait initialement d'un modèle théorique pouvant expliquer les propriétés des répéteurs gamma mous – ou SGR pour Soft Gamma Repeater. La découverte des SGR est liée à l'histoire des sursauts gamma. À la fin des années 1960, le gouvernement des USA met en orbite la série de satellites "Vela" dans l'intention de contrôler l'interdiction des essais nucléaires atmosphériques. Des flashes de rayons gamma sont bien détectés, mais en provenance de l'espace ! Ces évènements constituèrent le début du mystère des sursauts gamma, qui se manifestaient donc par une intense bouffée de rayon gamma d'une durée de quelques secondes.

Par la suite, de multiples détecteurs de rayons gamma seront placés en orbite. L'année 1979 sera historique pour les SGR. En effet, elle marque la détection du premier répéteur gamma mou – SGR 1806−20– le 7 janvier 1979. Ensuite, le 5 mars 1979 (Mazets et al. 1979), un flash gamma – le plus intense jamais détecté à l'époque – est obervé dans la direction du grand nuage de Magellan – SGR 0525−66. Neuf jours plus tard, SGR 1900+14 se manifeste dans la constellation de l'Aigle. Ces trois mois de 1979 auront marqué la découverte des trois premiers SGR – sur 5, voire 6, connus à ce jour. Ce n'est qu'en 1987 que ces trois astres furent reconnus comme une nouvelle catégorie de sources X, distinctes des sursauts gamma (Atteia et al. 1987; Laros et al. 1987). Leurs propriétés principales étaient un caractère répétitif, une durée en générale inférieure à la seconde et un spectre haute énergie plus mou que les sursauts γ (Mazets & Golenetskii 1981).

7.1.2 Nature physique des magnétars

L'explication, retenue à ce jour, expliquant la nature des SGR découle des travaux théoriques de Duncan & Thompson (1992) et Thompson & Duncan (1995), qui visaient à expliquer l'origine du champ magnétique des pulsars radio. Ces chercheurs voulaient comprendre pourquoi le champ magnétique de ces pulsars était de l'ordre de quelques 10^{12} Gauss. Ils constatèrent dans leurs simulations que lors de la formation des étoiles à neutrons, un champ magnétique très élevé – jusqu'à 10^{16} Gauss en théorie – pouvait croître rapidement et se retrouver gelé à l'intérieur de l'astre s'il était né en rotation très rapide et s'il se refroidissait en un temps très court – quelques secondes. Les pulsars radio ne tournaient donc pas assez vite à leur naissance... Ainsi était née l'idée d'étoile magnétique ou magnétar.

D'un point de vue réaliste, des champs magnétiques dipolaires de l'ordre de 10^{14} – 10^{15} G étaient concevables, c'est à dire 100 à 1000 fois plus intense que pour les pulsars radio. Ils firent ensuite un certain nombre de prédictions qui furent par la suite confirmées pour certaines d'entre elles. Un champ magnétique si intense doit ralentir très rapidement de tels astres en rotation extrême avec une très forte dissipation de l'énergie magnétique en quelques milliers d'années. Les magnétars seraient donc des étoiles à neutrons jeunes – $\sim$ 10 000 ans – et en rotation lente – quelques secondes – à cause d'un taux de ralentissement très fort – en tout cas comparé aux pulsars classiques. Un tel champ magnétique chauffe considérablement l'intérieur de l'étoile et expliquerait ainsi l'émission résiduelle en X des SGR. Les phases de sursaut d'activité serait dues à des reconnections des lignes de champ magnétique suite à un stress intense – voire des déformations significatives – de la croûte de l'étoile à neutrons.

Lorsqu'il fut possible d'identifier des contreparties persistantes à ces sources, les observations ont confirmé les attentes théoriques de Duncan & Thompson (1992) et Thompson & Duncan (1995). De plus, les magnétars sont maintenant liés à une autre catégorie de pulsars X : les AXP – pour Anomalous X-ray Pulsars – tant au niveau théorique (Thompson & Duncan 1996) qu'observationnel (Woods & Thompson 2006). Il a été, aussi, observé pour les trois magnétars historiques des sursauts, dit géants, caractérisés par un bref – quelques 0.1 s – et intense pic initial, suivi d'une longue – quelques 100 s – décroissance, où l'émission X et γ est modulée par la période de rotation de l'étoile à neutrons.

L'énergie libérée lors de tels sursauts est considérable (Hurley et al. 2005; Palmer et al. 2005), car elle peut largement dépasser 10^{46} erg. Pour SGR 1806−20 en 2004, le pic initial fut de 2×10^{47} erg s^{-1} – pour une distance de 15 kpc, Corbel & Eikenberry 2004. C'est dire qu'il n'existe pas d'objet plus brillant dans notre Galaxie...Ces sursauts géants sont probablement liés à une reconfiguration complète du champ magnétique de l'étoile à neutrons. Pour une revue du sujet, on se rapportera à Woods & Thompson (2006).

Lors de ma thèse, je me suis impliqué dans les magnétars à partir de l'estimation de la distance de deux de ces sources. Au vu de l'importance et des conséquences d'un tel paramètre de base, je voudrais illustrer dans ce chapitre un cheminement personnel à travers l'évolution perpétuelle de travaux de recherches.

7.2 SGR 1806−20 et son environnement

7.2.1 Localisation de SGR 1806−20

Comme nous l'avions vu précédemment, SGR 1806−20 fait partie des trois sursauts historiques de 1979. Sa réactivation dans les années 90, suivie de la détection par *ASCA* d'un sursaut X et d'une contrepartie X, ont permis de raffiner sa localisation (Murakami et al. 1994; Sonobe et al. 1994). Elle était alors compatible avec le coeur d'une source radio étendue, G 10.0−0.3, interprétée comme un plérion (Kulkarni et al. 1994; Vasisht et al. 1995). À cette position

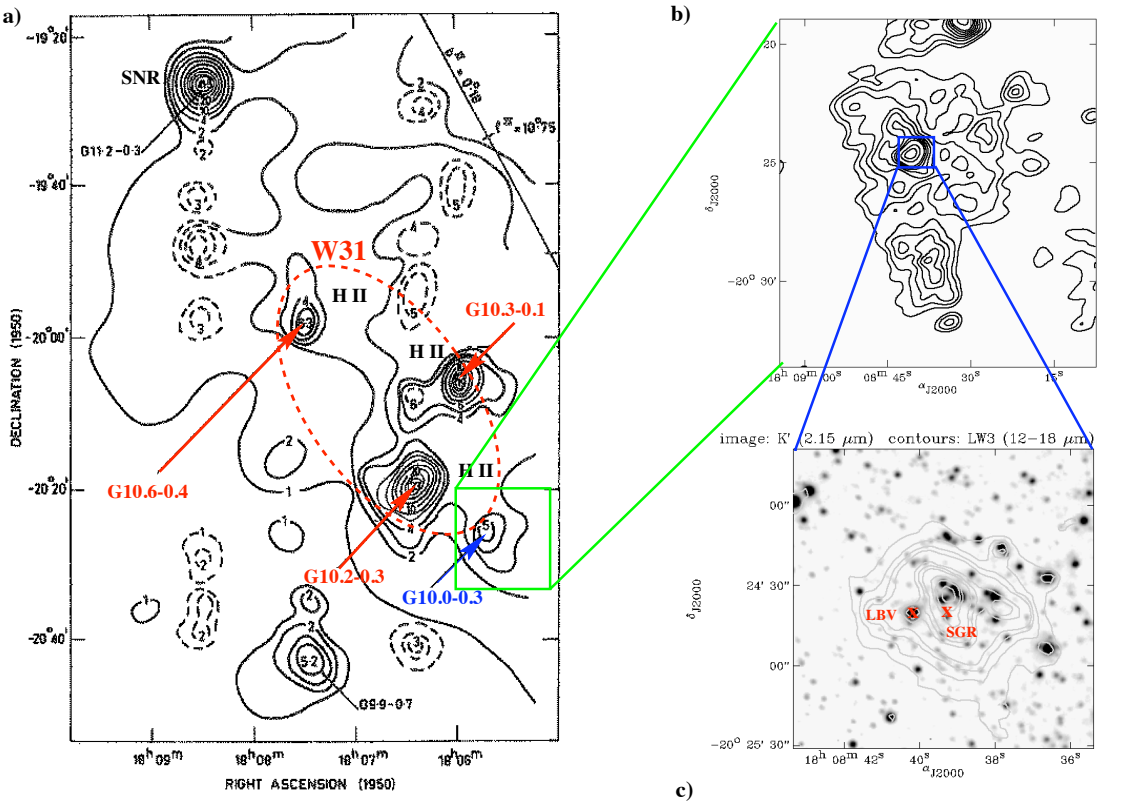

FIG. 7.1 – Localisation respective des sources introduites dans ce chapitre. a) Carte radio basse résolution de W31, b) Carte radio à 1.4 GHz de G 10.0−0.3, c) Image infrarouge K' (2.15 μm) du coeur de G 10.0−0.3 sur laquelle sont superposées les contours ISOCAM LW3 (12-18 μm). Les positions de SGR 1806−20 et de LBV 1806−20 sont indiquées. Figure extraite de Corbel & Eikenberry (2004).

fut aussi découverte (Kulkarni et al. 1995; van Kerkwijk et al. 1995) une étoile très brillante d'un type très rare : une étoile bleue variable et très intense – "Luminous Blue Variable" : LBV 1806−20.

Par la suite, il fut reconnu que 1) les positions de SGR 1806−20 et de LBV 1806−20 étaient incompatibles car il existait un écart entre ces deux sources de $\sim 12''$ (Hurley et al. 1999; Eikenberry et al. 2001; Kaplan et al. 2002), 2) G 10.0−0.3 n'est pas un plérion, mais une nébuleuse radio produite par le puissant vent de LBV 1806−20 (Gaensler et al. 2001), et 3) LBV 1806−20 se trouve au centre d'un amas d'étoiles très massives (Fuchs et al. 1999), auquel il serait possible que SGR 1806−20 appartienne.

La situation est encore plus complexe si on s'intéresse aux environs de G 10.0−0.3, qui comme les trois régions H II suivantes, G 10.2−0.3, G 10.3−0.1 et G 10.6−0.4, sont supposées faire partie d'un des plus grands complexes de régions H II de notre Galaxie : W31 (Shaver & Goss 1970; Ghosh et al. 1989). La figure 7.1 représente les divers objets mentionnés ci-dessus et leurs localisations respectives (Corbel & Eikenberry 2004).

7.2.2 Une distance contreversée ?

S'il est clair que la distance est un paramètre fondamental pour le bilan énergétique de tout objet astrophysique, il l'est encore plus si l'on veut avoir une vision plus globale des propriétés

des magnétars. Par exemple, la détection d'un sursaut géant de SGR 1806−20 en décembre 2004, a permis d'envisager qu'une fraction – 10 % ? – des sursauts gamma courts pourrait être des sursauts géants de magnétars, au vu de l'énergie considérable libérée et des implications sur les modèles théoriques.

Pendant ma thèse, je m'étais déjà penché sur le problème de la distance de SGR 1806−20 (Corbel et al. 1997), tout comme sur celle de SGR 1627−41 (Corbel et al. 1999). En étudiant les nuages moléculaires et le gaz HI situés sur la ligne de visée de SGR 1806−20, l'extinction optique de SGR 1806−20 et de LBV 1806−20, et les propriétés de W31, nous montrons (Corbel et al. 1997) que le complexe W31, associé à un nuage moléculaire de vitesse 13 km s^{-1} – noté MC13 –, se trouve à une distance de 14.5 $\pm$ 1.4 kpc.

Ce nuage moléculaire MC13 – et donc W31 – était préalablement associé au "bras en expansion à 3 kpc" – 3 kpc expanding arm – situé à une distance de $\sim$ 5 kpc de la Terre (Wilson 1974; Kalberla et al. 1982). Au vu de la très forte extinction optique – $A_v \sim 30$ mag. – de SGR 1806−20 et des propriétés de LBV 1806−20, nous fûmes conduits à associer SGR 1806−20, LBV 1806−20 et sa nébuleuse radio G 10.0−0.3 avec W31 et donc à une distance de 14.5 $\pm$ 1.4 kpc (Corbel et al. 1997).

Je pensais le problème de la distance de SGR 1806−20 clos, lorsque de nouvelles publications concernant W31 attirèrent mon attention. En effet, Blum et al. (2001) présentent des observations infrarouges d'étoiles de G 10.2−0.3 et en déduisent de façon non-ambiguë que G 10.2−0.3 – et par extension W31 – se trouve à une distance de 3.4 $\pm$ 0.6 kpc. Sachant que G 10.0−0.3 était supposé associé à W31, cette distance devint parfois la distance de SGR 1806−20.

Malgré tout, il faut remarquer que l'extinction optique de G 10.2−0.3 – $A_v \sim 15$ mag., Blum et al. 2001 – est incompatible avec celle de SGR 1806−20 – $A_v \sim 30$ mag., Corbel et al. (1997). De plus, des observations du continuum radio et de certaines transitions millimétriques (Kim & Koo 2002) montrèrent que G 10.0−0.3 est plutôt séparé des composantes de W31, G 10.0−0.3 ne serait donc pas forcément relié à W31. Au vu de l'importance de cette distance (c.f. section 7.3), nous avons donc décider de réestimer la distance des différentes objets de ce champ de vue (Corbel & Eikenberry 2004).

Tout d'abord, des observations millimétriques (Figure 7.2) à haute résolution spectrale (Corbel & Eikenberry 2004) indiquent que le nuage MC13 de Corbel et al. (1997) est actuellement résolue en deux composantes – noté MC13A et MC13B. Nous associons G 10.2−0.3 avec MC13B et G 10.3−0.1 avec MC13A d'après la valeur des vitesses des raies de recombinaison. L'analyse des raies d'absorption du continuum radio de G 10.0−0.3 permet d'avoir une limite inférieure de la distance de G 10.0−0.3 de 5.7 kpc (Corbel & Eikenberry 2004). Le spectre infrarouge de LBV 1806−20 confirme son absorption élevée – $A_v = 29 \pm 2$ magnitudes. De plus, à partir des raies d'émission de cette étoile, nous mesurons une vitesse radiale de LBV 1806−20 de $V_{LSR} = 10 \pm 20$ km s^{-1} (Corbel & Eikenberry 2004), compatible avec la vitesse du nuage MC13A.

Au vu des raies d'absorption devant G 10.0−0.3, nous montrons que LBV 1806−20 est associé avec MC13A à une distance de $15.1^{+1.8}_{-1.3}$ kpc. Nous montrons de plus que W31 est constitué de plusieurs composantes : G 10.2−0.3 situé sur le "bras spiral à −30 km s^{-1} " à 4.5 $\pm$ 0.6 kpc (compatible avec Blum et al. 2001) et G 10.3−0.1 associé avec le nuage moléculaire MC13A parent de LBV 1806−20 – et donc à 15.1 kpc aussi.

SGR 1806−20 et LBV 1806−20 ne sont séparés sur le plan du ciel que de 12″ et possèdent une extinction optique identique, ils appartiennent donc au même amas d'étoiles découvert par Fuchs et al. (1999). La distance de SGR 1806−20 est donc la même que celle de LBV 1806−20, c'est-à-dire $15.1^{+1.8}_{-1.3}$ kpc. Notre étude de LBV 1806−20 (section 7.3, Eikenberry et al. 2004), ainsi que des étoiles Wolf-Rayet de l'amas proche confirme notre estimation de distance. Un

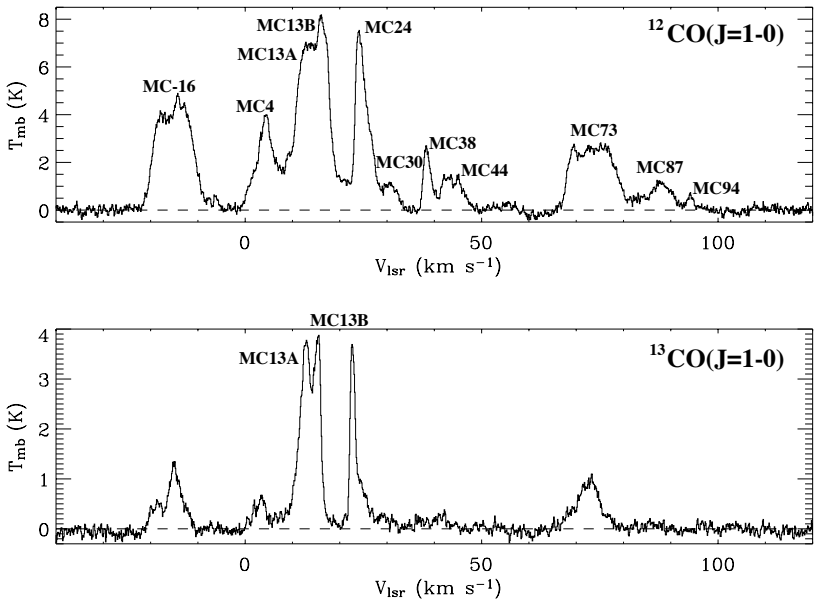

FIG. 7.2 – Spectres ^{12}CO(J=1−0) et ^{13}CO(J=1−0) vers LBV 1806−20 avec indication des différents nuages moléculaires le long de la ligne de visée. Figure extraite de Corbel & Eikenberry (2004).

schéma illustrant la position des diverses composantes d'émission est représenté sur la figure 7.3. Nous confirmons (après Grindlay 1994; Corbel et al. 1997) que tout comme SGR 1627−41 (Corbel et al. 1999) et SGR 0525−66 (Vancura et al. 1992; Banas et al. 1997), SGR 1806−20 est lui aussi localisé dans un nuage moléculaire massif. Cela indique une forte connexion entre magnétars et étoiles massives (voir section 7.3) par l'intermédiaire de nuages moléculaires géants.

7.2.3 Une distance robuste !

En avions nous fini avec cette distance ? Non, pas vraiment ! En effet, la luminosité extrême de LBV 1806−20 a suscité certaines polémiques. Figer et al. (2004) réalisent des observations spectroscopiques infrarouges de LBV 1806−20 à haute résolution spectrale. Leurs observations indiquent que LBV 1806−20 pourrait être un système binaire et ils en déduisent une vitesse radiale de $V_{LSR} = 35 \pm 6$ km s^{-1} pour LBV 1806−20. Bien qu'elle soit a priori en accord avec notre mesure – $V_{LSR} = 10 \pm 20$ km s^{-1} , Corbel & Eikenberry (2004) – , l'erreur très faible implique une distance de l'ordre de 11.8 kpc (Figer et al. 2004), incompatible avec notre valeur.

Mais la présentation de ces résultats est un peu biaisée, car leur intervalle de vitesse (29-41 km s^{-1}) entraîne un intervalle de distance de 11.4–13.4 kpc, quasi-compatible avec nos résultats ($15.1^{+1.8}_{-1.3}$ kpc). De plus, même si leur erreur de mesure (6 km s^{-1}) est faible, elle est obtenue en supposant des étoiles de masse identique dans l'hypothèse d'un système binaire. Lavigne et al. (en préparation) montre qu'il faut aussi rajouter une erreur systématique de 25 km s^{-1} due à l'incertitude sur le rapport de masses des éventuelles composantes du système binaire, mais aussi une erreur systématique de 10 km s^{-1} liée à la courbe de rotation de notre Galaxie. Les mesures de Figer et al. (2004) n'excluent donc pas notre distance...

De plus, indépendamment de mesures cinématiques, les propriétés des étoiles Wolf-Rayet

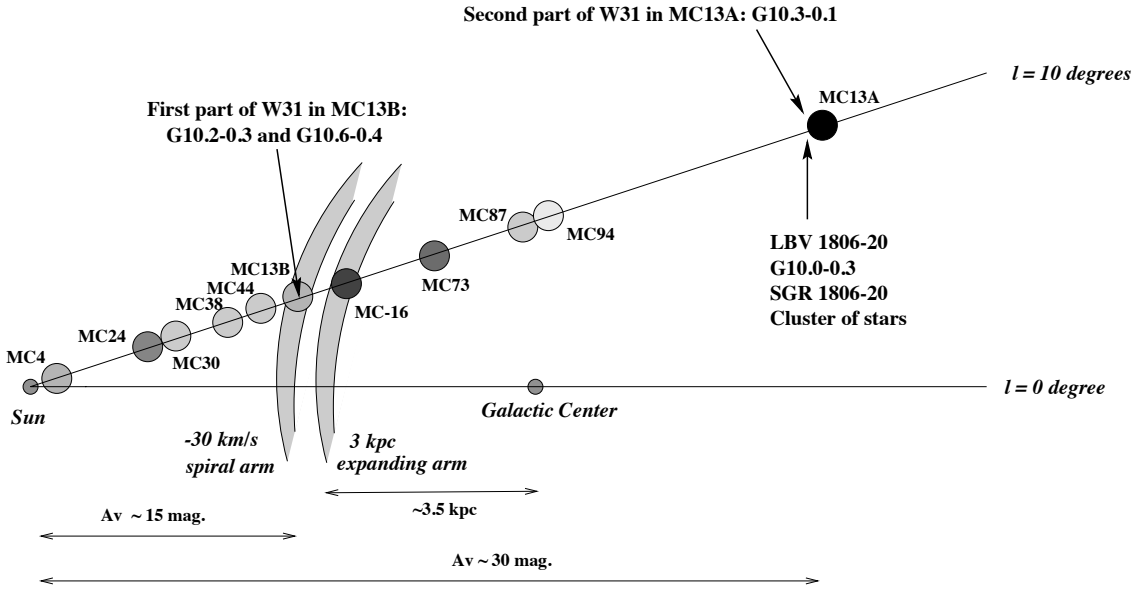

FIG. 7.3 – Diagramme schématique illustrant les différents nuages moléculaires (MC..) le long de la ligne de visée de SGR 1806−20, ainsi que la localisation de G 10.0−0.3, G 10.2−0.3, G 10.3−0.1, G 10.6−0.4, SGR 1806−20 et LBV 1806−20. Figure extraite de Corbel & Eikenberry (2004).

de l'amas d'étoiles où se trouve LBV 1806−20, impliquent une distance minimale de 14.7 kpc (Eikenberry et al. 2004, Lavigne et al., en préparation), parfaitement en accord avec notre estimation !

Suite au sursaut géant de SGR 1806−20 en décembre 2004, on pouvait s'attendre à avoir une nouvelle confirmation de cette distance. En effet, ce sursaut géant a été accompagné d'une énorme éruption radio – proche du Jy. Il fut donc possible de mesurer un spectre HI en absorption devant ce continuum intense, ainsi que devant une autre source radio – J1811−2055 – proche de SGR 1806−20 (Figure 7.4 extraite de Cameron et al. 2005). Malheureusement, l'interprétation de ces spectres fut erronée. La source extragalactique J1811−2055 présente une absorption vers ~ 120 km s^{-1} qui n'est pas observée pour SGR 1806−20, impliquant une distance maximale de SGR 1806−20 de l'ordre de 9.8 kpc (Cameron et al. 2005).

Néanmoins, McClure-Griffiths & Gaensler (2005) réagissent rapidement et montrent, que comme la séparation angulaire entre SGR 1806−20 et J1811−2055 est grande – > 1 °–, le contenu des lignes de visée n'est pas forcément identique. En effet, il n'existe quasiment pas de gaz HI vers ~ 120 km s^{-1} pour SGR 1806−20. La limite supérieure déduite par Cameron et al. (2005) est donc fausse. On ne peut juste en extraire qu'une limite inférieure de 6 kpc (McClure-Griffiths & Gaensler 2005).

Notre distance tient donc toujours ! S'il y avait une morale à tirer de ces travaux continus sur cette distance, c'est qu'il faut toujours rester attentif à tout développement, même mineur, pouvant parfois provenir de domaines très différents. Néanmoins, j'espère ne plus avoir à revenir sur cette source, au moins pour cette question... car les conséquences de cette distance ne sont pas négligeables.

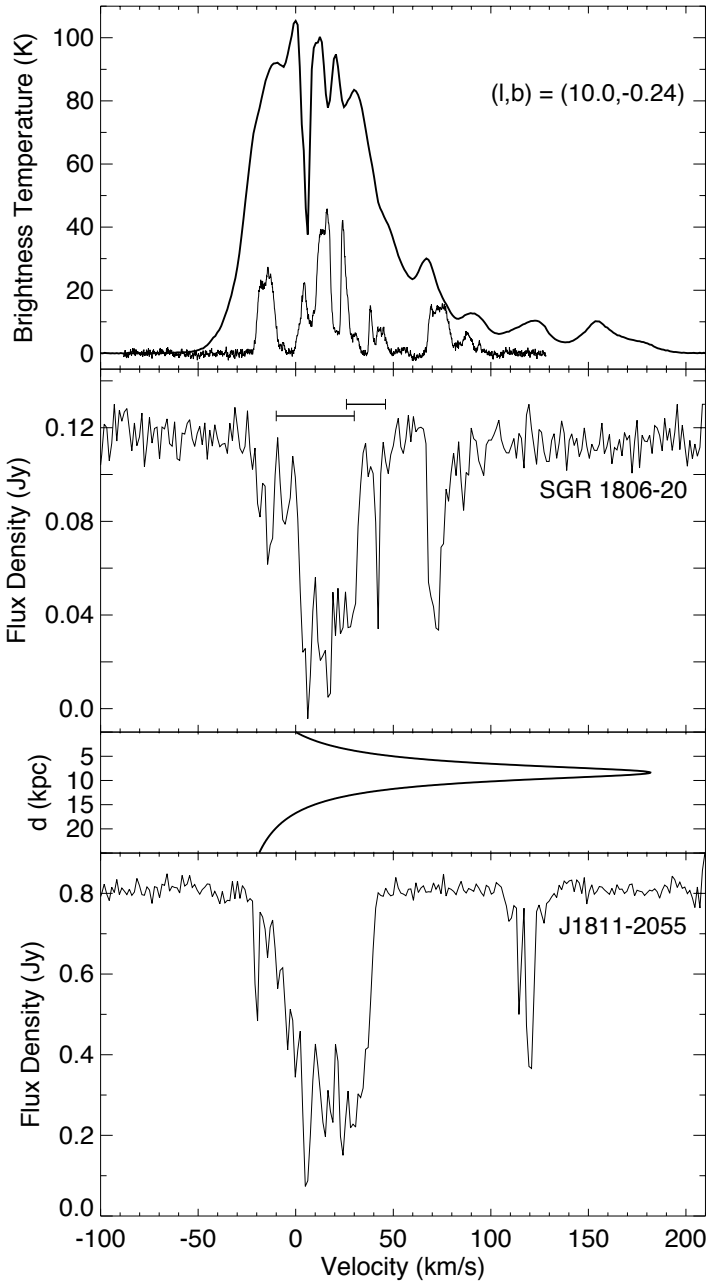

FIG. 7.4 – Spectre HI en émission (a) et en absorption (b) vers SGR 1806−20. Courbe de rotation de la Galaxie pour la ligne de visée de SGR 1806−20 (c). Spectre HI en absorption vers la source radio extragalactique J1811−2055 (d). Figure extraite de Cameron et al. (2005).

7.3 LBV 1806−20 : l'étoile la plus massive de la Galaxie ?

Comme nous l'avons signalé auparavant, proche de SGR 1806−20 se trouve l'étoile LBV 1806−20 localisée dans un amas stellaire massif. À l'aide de la distance – 15 kpc – que nous avons déterminée, LBV 1806−20 devenait une des étoiles les plus brillantes de notre Galaxie dont la luminosité est supérieure à 10^6 $L_\odot$ (van Kerkwijk et al. 1995; Corbel et al. 1997).

Pour contraindre la nature de cette étoile, de nouvelles observations spectroscopiques infrarouges ont été obtenues (Eikenberry et al. 2004). Ces observations confirment le statut de

LBV – "Luminous Blue Variable" – pour LBV 1806−20, d'un type spectral compris entre O9 et B2. Elles indiquent de plus :

1. que la température de LBV 1806−20 est de 20 000 à 26 000 K,
2. que l'extinction optique de LBV 1806−20 est de $A_v = 29 \pm 2$ mag. en accord avec nos mesures millimétriques pour une distance de 15 kpc, et
3. que la luminosité de LBV 1806−20 est $> 5 \times 10^6$ $L_\odot$ et pourrait atteindre $\sim 4 \times 10^7$ $L_\odot$.

Des observations complémentaires par imagerie speckle montrent que, jusqu'à une limite de résolution de 60 milliseconde d'arc, l'étoile LBV 1806−20 n'est pas résolue en infrarouge. Pour une distance de 15 kpc, cela correspond à une distance de 900 u.a. Il est ainsi probable que LBV 1806−20 n'est pas un amas d'étoiles non résolues. Toutefois, nous ne pouvons pas exclure qu'il s'agisse d'un système binaire et il serait possible que cette hypothèse soit privilégiée au vu des spectres infrarouges de Figer et al. (2004).

En supposant que LBV 1806−20 soit une étoile unique, nous en déduisons une limite inférieure de sa masse de 190 $M_\odot$. S'il s'agit d'une binaire serrée avec un demi-grand axe de 450 u.a., alors chacune des composantes du système doit avoir une masse de 90 $M_\odot$. Il est à noter qu'il n'est pas certain qu'un tel scénario soit réaliste. En effet, lors de leur formation initiale, la pression de rayonnement de l'étoile la plus massive va probablement inhiber la formation de la deuxième composante par photo-évaporation (Eikenberry et al. 2004). LBV 1806−20 pourrait donc être l'étoile la plus massive de notre Galaxie.

Est-il réaliste de former des étoiles si massive ? Les théories de formation stellaire prédisent

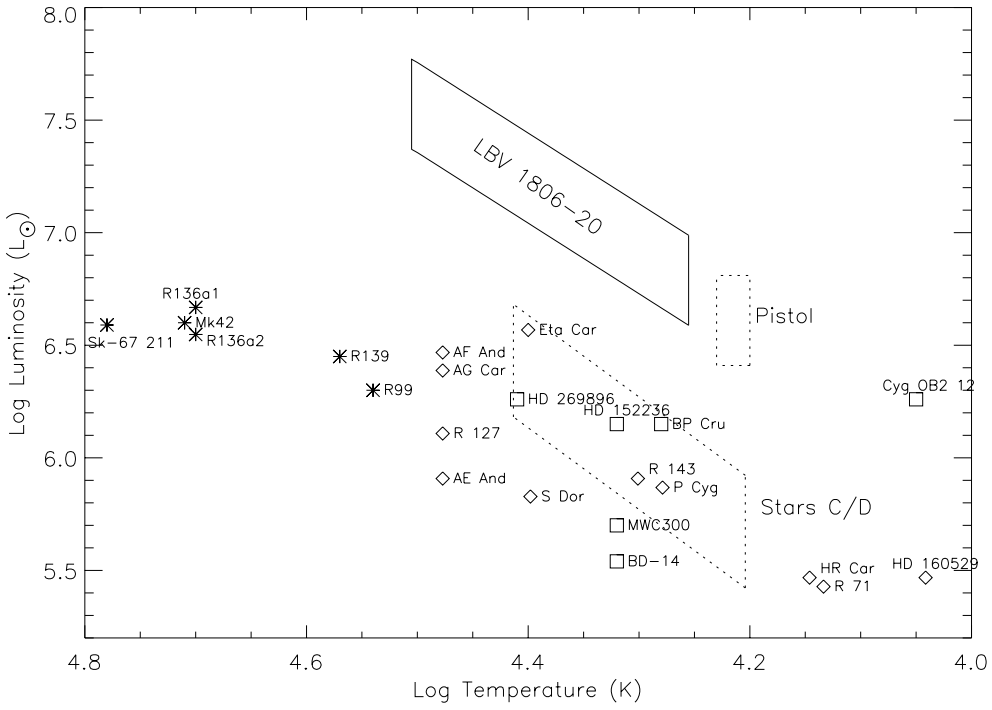

FIG. 7.5 – Diagramme Hertzsprung–Russell incluant LBV 1806−20 (diamant en trait continu), et autres étoiles lumineuses de notre Galaxie. L'étoile Pistol est indiqué par le carré. Figure extraite de Eikenberry et al. (2004).

que des étoiles de masse supérieure à $\sim 120\ M_\odot$ devraient être impossibles à former (Bond et al. 1984; Schaerer et al. 1993). L'existence de LBV 1806−20 – ou même de l'étoile Pistol (Figer et al. 1998) – pourrait imposer des modifications substantielles à ces modèles. La présence de supernovae pourrait permettre d'augmenter cette limite supérieure. Cette hypothèse est intéressante au vu de la présence d'étoiles évoluées – on même "mortes" comme SGR 1806−20– au sein de l'amas (Eikenberry et al. 2004). La formation d'étoiles induite par supernova pourrait éventuellement permettre d'augmenter cette limite supérieure de la masse des étoiles.

Ces informations permettent de comparer LBV 1806−20 avec les autres étoiles brillantes de notre Galaxie, dont l'étoile la plus comparable en terme de caractéristiques, e.g. "Pistol star" (Figer et al. 1998). La figure 7.5 illustre la localisation de LBV 1806−20 dans un diagramme luminosité–température. Il apparaît que LBV 1806−20 est très probablement l'étoile la plus brillante de notre Galaxie, nettement plus que d'autres LBV fameuses comme η de la Carène et même l'étoile Pistol. Au vu des similarités spectroscopiques avec l'étoile Pistol, il est probable que LBV 1806−20 se trouve dans la partie inférieure droite de la boite d'erreur associée de la figure 7.5. L'étoile Pistol est localisée près du centre galactique, tandis que LBV 1806−20 se trouve à une distance galactocentrique de ~ 7 kpc. La formation d'étoiles très massives semble donc un processus continu dans notre Galaxie et ne se limiterait pas à des environnements extrêmes comme celui du centre galactique (Eikenberry et al. 2004).

Que peut devenir une telle étoile massive ? Les scénarii d'évolution stellaire (e.g. Heger et al. 2003) indiquent que cette étoile va exploser en supernova de type Ib/c et va produire une étoile à neutrons – et non un trou noir à cause de l'énorme perte de masse par vent. On pourrait étendre ce résultat au pro-géniteur de SGR 1806−20 qui aurait explosé il y a quelques 10 000 ans – au vu des modèles de magnétar – et qui aurait donc pu être encore plus massif que LBV 1806−20. Il est intéressant de noter que SGR 1900+14 est localisé aussi au sein d'un amas d'étoiles massives (Vrba et al. 2000) et que SGR 1627−41 se trouve proche d'un nuage moléculaire massif (Corbel et al. 1999). Il en résulterait donc que non seulement le destin des étoiles très massives serait de former des étoiles à neutrons, mais surtout de former des étoiles à neutrons extrêmement magnétisées de type magnétar.

7.4 Articles de recherche

7.4.1

The Connection between W31, SGR 1806−20, & LBV 1806−20 : Distance, Extinction, and Structure.

Article publié dans :

Astron. & Astrophys., 2004, 419, 191-201

Corbel, S., Eikenberry, S. S.

A&A 419, 191–201 (2004)
DOI: 10.1051/0004-6361:20034054

Astronomy & Astrophysics

The connection between W31, SGR 1806–20, and LBV 1806–20: Distance, extinction, and structure

S. Corbel[1] and S. S. Eikenberry[2,⋆]

[1] Université Paris VII and Service d'Astrophysique, CEA Saclay, 91191 Gif-sur-Yvette Cedex, France
[2] Department of Astronomy, University of Florida, 211 Bryant Space Science Center, Gainesville, FL 32611, USA
e-mail: eiken@astro.ufl.edu

Received 4 July 2003 / Accepted 3 October 2003

Abstract. We present new millimeter and infrared spectroscopic observations towards the radio nebula G10.0−0.3, which is powered by the wind of the Luminous Blue Variable star LBV 1806–20 also closely associated with the soft gamma-ray repeater SGR 1806–20, and believed to be located in the giant Galactic H II complex W31. Based on observations of CO emission lines and NH_3 absorption features from molecular clouds along the line of sight to G10.0−0.3, as well as the radial velocity and optical extinction of the star powering the nebula, we determine its distance to be $15.1^{+1.8}_{-1.3}$ kpc in agreement with Corbel et al. (1997). In addition, this strengthens the association of SGR 1806–20 with a massive molecular cloud at the same distance. All soft gamma-ray repeaters with precise location are now found to be associated with a site of massive star formation or molecular cloud. We also show that W31 consists of at least two distinct components along the line of sight. We suggest that G10.2−0.3 and G10.6−0.4 are located on the −30 km s^{-1} spiral arm at a distance from the Sun of 4.5 ± 0.6 kpc and that G10.3−0.1 may be associated with a massive molecular cloud at the same distance as the LBV star, i.e. $15.1^{+1.8}_{-1.3}$ kpc, implying that W31 could be decomposed into two components along the line of sight.

Key words. stars: neutron – stars: individual: SGR 1806−20 – stars: individual: LBV 1806−20 – ISM: individual: W31 – Galaxy: structure – Galaxy: kinematics and dynamics

1. Introduction

W31 is one of the largest H II complexes in the Galaxy, with intense star-forming regions that have been observed from radio to near-infrared wavelengths (e.g. Ghosh et al. 1989; Blum et al. 2001; Kim & Koo 2002). At low spatial resolution, W31 appears as three main extended H II regions: G10.2−0.3, G10.3−0.1 and G10.6−0.4 (Shaver & Goss 1970) (Fig. 1). The radio nebula G10.0−0.3 lies within W31 on the plane of the sky (Fig. 1), and has drawn considerable attention in recent years due to the intriguing objects nearby. At one time, G10.0−0.3 was suggested to be a plerionic supernova remnant powered by a rare soft gamma-ray repeater, SGR 1806–20 (Kulkarni & Frail 1993; Kouveliotou et al. 1998). SGR 1806−20, in turn, was thought to be associated with an almost equally rare luminous blue variable (LBV) star (van Kerkwijk et al. 1995) which lies at the time-variable (in both flux and morphology) core of this nebula (Vasisht et al. 1995). However, the revised Inter-Planetary Network (IPN) localization of SGR 1806−20 provides a position inconsistent (see Fig. 1) with that of the LBV star and radio core of G10.0−0.3 (Hurley et al. 1999), though the LBV position is consistent with the radio core within the uncertainties (∼2″). Recent *Chandra* and infrared observations confirm that the SGR lies ∼12″ away from the LBV and radio core (Eikenberry et al. 2001; Kaplan et al. 2002). Furthermore, Gaensler et al. (2001) argue that G10.0−0.3 is not a supernova remnant at all, but is rather powered by the tremendous wind of the LBV star at its core. Infrared observations of the field of SGR 1806−20 reveal that the LBV star is not alone, but appears to be part of a cluster of embedded, hot, luminous stars (Fuchs et al. 1999), and the IPN position for SGR 1806−20 is consistent with membership in the star cluster (Eikenberry et al. 2001). Given this somewhat confusing history, we take a moment to summarize our current understanding of G10.0−0.3: 1. G10.0−0.3 is a radio nebula (NOT supernova remnant) with emission powered by the LBV star spatially coincident with its core. 2. The LBV star is part of a cluster of luminous stars embedded in a molecular cloud. 3. SGR 1806−20 is likely another member of this cluster of stars, and is spatially distinct from the LBV star. We plot in Fig. 1 the various objects (and their relative location on the plane of the sky) that we will discuss in this paper.

Send offprint requests to: S. Corbel,
e-mail: corbel@discovery.saclay.cea.fr

⋆ Visiting astronomer, Cerro Tololo Inter-American Observatory, National Optical Astronomy Observatories, which are operated by the Association of Universities for Research in Astronomy, under contract with the National Science Foundation.

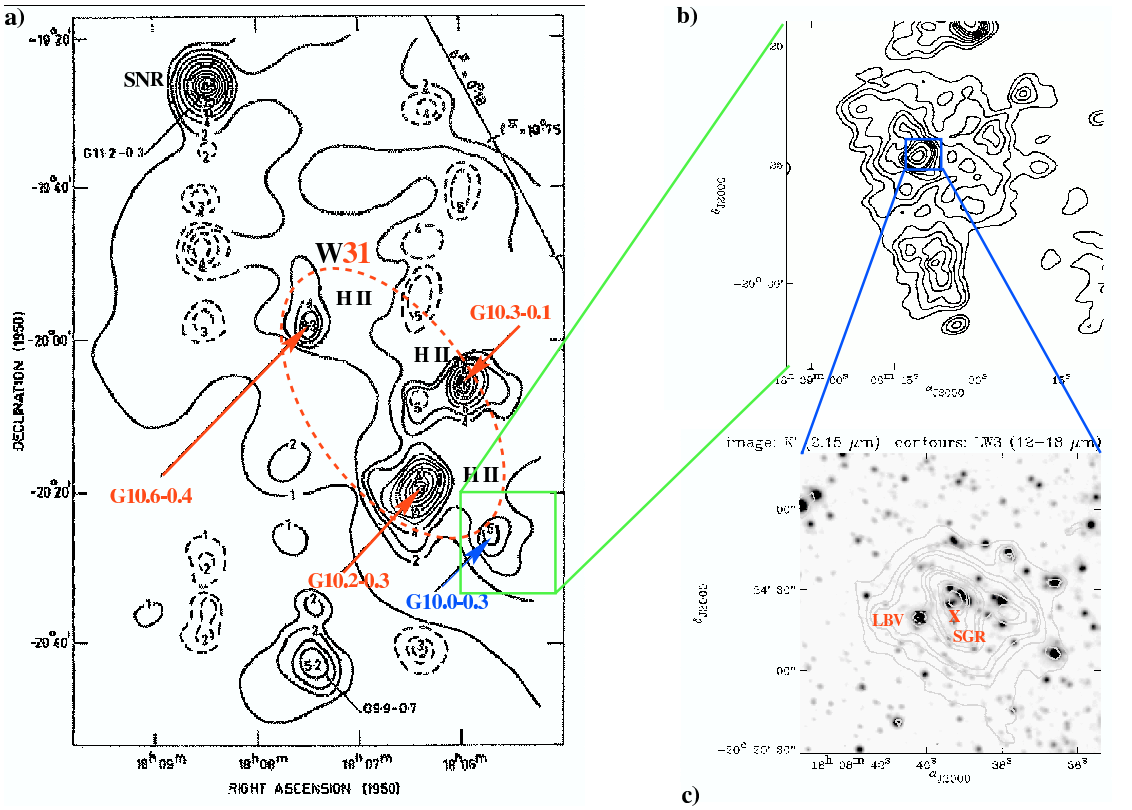

Fig. 1. Representation of the location of each object introduced in this paper and their relative positions on the plane of the sky. **a)** Large radio map at 408 MHz of the field of W31, adapted from Shaver & Goss (1970). The location of the main components of W31 are labeled, as well as the radio nebula G10.0−0.3 (produced by the wind of LBV 1806−20). **b)** Radio image of the radio nebula G10.0−0.3 at 1.4 GHz from Kulkarni et al. (1994). **c)** K' (2.15 μm) near-infrared image ($\sim 2' \times 2'$) of the core of G10.0−0.3. The location of LBV 1806−20 and SGR 1806−20 are indicated by a cross. The ISOCAM LW3 (12−18 μm) contours are superposed on this image in order to highlight the spatial extend of the cluster of massive stars around SGR 1806−20 (adapted from Fuchs et al. 1999).

Because of the proximity of these unusual objects, the distance to them can provide significant insight into their physical properties, giving this measurement particular importance. Corbel et al. (1997) proposed a distance estimate based on observations of molecular clouds along the line of sight. They used CO spectroscopy to estimate the hydrogen column density towards G10.0−0.3, and from that an absorption column density as a function of distance. Taking the measured X-ray absorption towards SGR 1806−20 and an estimate of the optical extinction to the LBV star, they concluded that G10.0−0.3, SGR 1806−20 and W31 lie 14.5 ± 1.4 kpc from the Sun.

However, this situation seemed complicated by newer infrared stellar spectroscopy by Blum et al. (2001) and radio/millimeter observations by Kim & Koo (2002). Blum et al. (2001) present infrared spectra of members of a star cluster in the H II region G10.2−0.3, also within W31 on the plane of the sky. Based on the spectra, they derive spectral/luminosity classes and extinctions for the stars, which, combined with infrared photometry, place them and G10.2−0.3 unambiguously at a distance of $d \simeq 3.4$ kpc. However, the extinction towards G10.2−0.3 is much smaller ($\Delta A_V \approx 15$ mag) than the extinction towards LBV 1806−20 and the star cluster close to SGR 1806−20 (Eikenberry et al. 2001) and the correlated X-ray absorption towards SGR 1806−20 (Mereghetti et al. 2000). Furthermore, 21-cm continuum and several molecular line maps of the region (Kim & Koo 2002) show that G10.0−0.3 is rather separated from the primary components of W31 (G10.2−0.3 and G10.3−0.1). Thus, as of this writing, there is no definitive physical linkage between G10.0−0.3 and the major components of W31. Together, these imply that G10.0−0.3 may lie at a different distance along the line of sight than G10.2−0.3. It is this new, more-complicated situation which motivates us to reconsider the distance to G10.0−0.3 (and by extension LBV 1806−20 and SGR 1806−20) in the light of previous work by Corbel et al. (1997) and Blum et al. (2001) as well as new observations.

In this paper, we present newer, higher velocity – resolution CO spectroscopy towards LBV 1806−20 and its associated radio nebula G10.0−0.3, and also towards 2 (out of 3) of

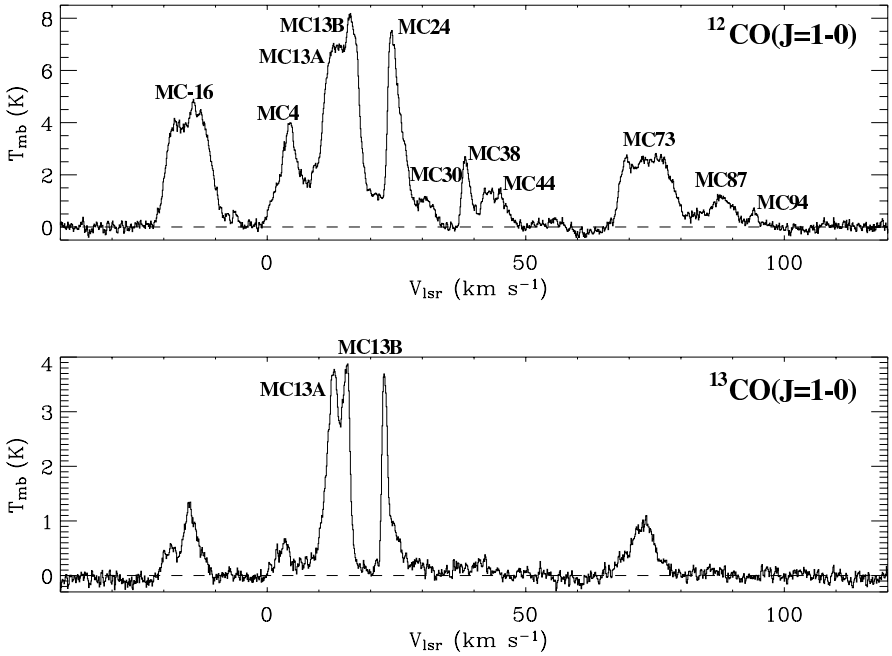

Fig. 2. ^{12}CO(J = 1–0) (*top*) and ^{13}CO(J = 1–0) (*bottom*) spectrum in the direction of LBV 1806–20 and SGR 1806–20. Antenna temperatures have been converted into main beam brightness temperatures. Each molecular cloud is labeled by its name.

the brightest H II regions of W31. We also present the NH_3 absorption spectrum originally mentioned in Corbel et al. (1997). We then add higher-resolution infrared spectroscopic observations of the LBV star at the center of G10.0–0.3. In Sect. 2, we present the observations and data reduction as well as the main results from our observations. In Sect. 3, we use these data to derive a robust distance estimate for LBV 1806–20 and G10.0–0.3. We then discuss in some detail the implications of this distance for SGR 1806–20 and LBV 1806–20, as well as the structure of W31 as a whole. Finally, in Sect. 4 we present our conclusions.

2. Observations

2.1. CO spectra

Following the work by Corbel et al. (1997), we obtained new millimeter observations with the 15 m Swedish-ESO Submillimeter Telescope (SEST) at La Silla, Chile, on 1998 August 27 and 1999 March 2. We took spectra at the position of LBV 1806–20 (same as in Corbel et al. 1997) at the transitions ^{12}CO(J = 1–0) and ^{13}CO(J = 1–0) for a total integration time of 5 min each (Fig. 2). As the full-width at half-maximum (*FWHM*) beamwidth of the SEST is 45″ at ∼115 GHz, the spectra toward LBV 1806–20 also include the region of SGR 1806–20. Additionally, at ^{12}CO(J = 1–0) we made spectral observations towards two H II regions of W31 (G10.2–0.3 and G10.3–0.1) with an integration time of 2 min each.

We acquired the spectra in position-switching mode which consists of switching (every one minute) between sources and an off-position free of emission. We then averaged the spectra after baseline removal. The back end was an acousto-optical spectrometer with 2000 channels and a frequency bandwidth of 86 MHz, giving a high velocity resolution of 0.11 km s^{-1} (to be compared with the velocity resolution of 2.3 km s^{-1} in Corbel et al. 1997). The receiver was calibrated with the standard chopper-wheel method. Systems temperature during the observations were typically in the range 200–350 K. We converted all CO spectra into main-beam brightness temperature ($\eta_{\rm eff}$ = 0.7), which is expressed in term of radial velocity in the Local Standard of Rest (LSR).

We note that there is a distance ambiguity for any molecular cloud within the solar circle at a given radial velocity (in the LSR). Indeed, at each radial velocity it is possible to locate the cloud on the near side (near distance) or on the far side (far distance) of the Galaxy. We assume an error of 10 km s^{-1} for the velocity-distance conversion using the rotation curve of the Galaxy of Fich et al. (1989) with the standard rotation constants of R_0 = 8.5 kpc and Θ_0 = 220 km s^{-1}. This is sufficiently large to cover any velocity deviation (∼4 km s^{-1}) with respect to the LSR frame of Galactic rotation (Combes 1991). This implies that the error bars associated to the distances are probably consistent with 2σ confidence levels.

The ^{12}CO spectra (Fig. 2) toward LBV 1806–20 reveal a complex line of sight, as already discussed in Corbel et al. (1997), with various molecular clouds detected (see Table 1

Table 1. Derived parameters for each of the molecular clouds along the line of sight of LBV 1806−20 and SGR 1806−20, using the ^{12}CO(J = 1−0) spectra.

Name	W(CO*)[a] (K km s^{-1})	V_{lsr}[b] (km s^{-1})	A_V (mag)	Near distance[b] (kpc)	Far distance[b] (kpc)	Distance[b] (kpc)
MC −16	28.4	−14.9	8.6 ± 1.7	n.a.	24.9	4.5
MC 4	12.7	4.3	3.9 ± 0.8	0.2	16.6	0.2
MC 13A	32.8	12.7	10.0 ± 2.0	1.7	15.1	15.1
MC 13B	9.8	16.7	3.0 ± 0.6	2.2	14.5	4.5
MC 24	18.3	23.6	5.6 ± 1.1	3.0	13.8	3.0
MC 30	2.6	30.0	0.8 ± 0.2	3.5	13.2	3.5
MC 38	3.6	38.4	1.1 ± 0.2	4.2	12.6	4.2
MC 44	5.0	43.5	1.6 ± 0.3	4.5	12.3	4.5
MC 73	19.8	73.4	6.0 ± 1.2	5.7	11.0	...[c]
MC 87	4.5	87.9	1.4 ± 0.3	6.1	10.6	...[c]
MC 94	1.7	94.2	0.5 ± 0.1	6.2	10.5	...[c]

[a] W(CO*) is the integrated line area of the cloud. The error on W(CO*) itself is negligeable compared to the 20% uncertainty we assume to take into account the uncertainties in the various conversion factors for A_V.
[b] In the text, we use a systematic error of ±10 km s^{-1} on the velocity of the cloud in order to derive a robust distance range (>2σ) for each of the molecular clouds.
[c] We did not attempt to resolve the distance ambiguity for MC 73, MC 87 and MC 94, since they are between MC −16 and MC 13A in either case.

for detailed informations). Due to the high velocity resolution, some of the molecular clouds mentioned in Corbel et al. (1997) are now split into two components; for simplicity the same notation is kept as in Corbel et al. (1997). MC 38 is decomposed into the component at ~38 km s^{-1} and a new cloud at ~44 km s^{-1} (now noted as MC 44). The resolution of the edge of the ^{12}CO line of MC 24 also reveals a new cloud at 30 km s^{-1} (MC 30). MC 87 is now split into MC 87 and MC 94. However, the most interesting feature in the new ^{12}CO(J = 1−0) spectrum toward LBV 1806−20 is the splitting of molecular cloud MC 13 into two components. This is confirmed by the ^{13}CO(J = 1−0) transition (an optically thin line, with narrower *FWHM*), which clearly reveals that MC 13 is resolved into two components (Fig. 2): one at 13.0 ± 0.1 km s^{-1} (hereafter MC 13A) and one at 15.5 ± 0.1 km s^{-1} (hereafter MC 13B). (These velocities are obtained if we naively fit the lines with Gaussian profiles.) This also implies that the shape of the ^{12}CO(J = 1−0) spectrum around 13 km s^{-1} is not due to opacity effects. Fitting the ^{12}CO(J = 1−0) spectra leads to velocities of 12.7 ± 0.1 km s^{-1} and 16.7 ± 0.1 km s^{-1} for MC 13A and MC 13B respectively.

According to Kim & Koo (2001), the velocity of the recombination line at the core of G10.2−0.3 is 16.4 ± 0.2 km s^{-1}, and it is therefore apparent that G10.2−0.3 is associated with the molecular cloud we labeled MC 13B. We remind the reader that in addition to the association in velocity, the map of the CO emission (Corbel et al. 1997) also points to an association of G10.2−0.3 with one of the clouds in this velocity range. We note that the velocity of the recombination line of the other major H II region studied by Kim & Koo, G10.3−0.1, is 7.7 ± 0.5 km s^{-1}, with a range from 7.7 to 11.9 km s^{-1} (Kim & Koo 2001), which is more consistent with the velocity of MC 13A.

2.2. NH_3 spectrum

In addition to the above CO observations, we also include an NH_3 absorption spectrum (Fig. 3) towards the radio nebula G10.0−0.3 (produced by the wind of LBV 1806−20) at the same position as the CO observations. This spectrum was originally mentioned, but not shown, in Corbel et al. (1997) as a "Note added in manuscript". As it is important for this work, we include it here. The NH_3 observations (total integration time of 30 min) were performed at the frequency of 23 694.49 MHz (velocity resolution of 0.5 km s^{-1}) with the NASA Deep Space Network Goldstone 34-m antenna located in California, USA, and giving a beamwidth of 1.6′. As the radio continuum against which the NH_3 absorption spectrum is measured is produced by the radio nebula G10.0−0.3, any absorption feature results from gas located in front of LBV 1806−20.

The most striking feature from this spectrum is the absorption line (detected at a significance level of 8.6σ) at a velocity of 70.9 ± 0.5 km s^{-1}, in full agreement with the CO velocity of the molecular cloud MC 73 that is detected along the line of sight to LBV 1806−20 (see Table 1). This detection thus demonstrates that the molecular cloud MC 73 is located in front of LBV 1806−20. The absorption line (4.2σ) at ~62 km s^{-1} may be related to an H I shell around MC 73 or to a different H I cloud (cf. Fig. 1 in Corbel et al. 1997) in front of G10.0−0.3. A possible weaker absorption feature (2.2σ)

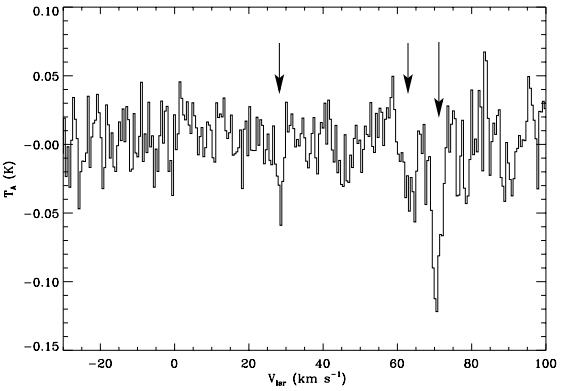

Fig. 3. NH_3 absorption spectrum measured against the radio nebula G10.0−0.3 produced by the wind of LBV 1806−20. Arrows indicate the main (∼9σ) absorption feature at 71 km s^{-1} as well as the possible features at 62 km s^{-1} (∼4σ) and 29 km s^{-1} (∼2σ).

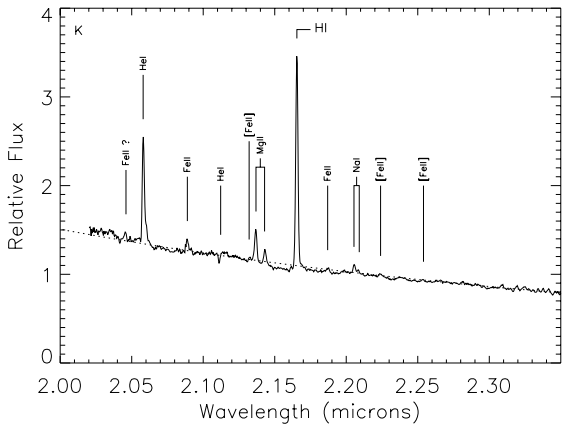

Fig. 4. Near-infrared spectrum of LBV 1806−20 in the K band, dereddened with A_V = 29 mag, following the reddening law of Rieke & Lebofsky (1985). The dotted line indicates the spectral shape of a blackbody with T > 12 000 K.

might also be present at 28.6 km s^{-1}, which would be in agreement with the velocity of the MC 30 cloud and would indicate that MC 30 may also lie front of LBV 1806−20.

2.3. IR spectra

We used the Ohio State InfraRed Imaging Spectrograph (OSIRIS) instrument (Depoy et al. 1993) and f/14 tip-tilt secondary on the Cerro-Tololo Inter-American Observatory (CTIO) 4-meter telescope on July 5, 2001 to obtain moderate resolution (R = 3000 for 2 pixels) spectra of LBV 1806−20 in the J, H, and K bands (1–2.4 μm). We present details of these observations and their reduction elsewhere (Eikenberry et al. 2003), and present a reduced K-band spectrum in Fig. 4.

The colors of LBV 1806−20 (van Kerkwijk et al. 1995) and its spectral continuum shape allow us to estimate the extinction towards LBV 1806−20. For such a hot star (as indicated by the He I 2.112 μm absorption feature – van Kerkwijk et al. 1995; Eikenberry et al. 2003), the intrinsic $J - K$ color is nearly neutral, and the observed red color of $J - K$ = 5.0 ± 0.15 mag corresponds to an extinction of A_V = 28 ± 2 mag (assuming the Rieke-Lebofsky reddening law, Rieke & Lebofsky 1985), matching the estimates based on CO observations (Corbel et al. 1997). (While a hypothetical near-infrared excess from LBV 1806−20 would alter these conclusions, Eikenberry et al. (2003) show that this is not present, based on the spectral continuum shape across JHK bands, and the close match in $J - K$ color between LBV 1806−20 and other cluster stars.) In addition, the H and K bands are in the Rayleigh-Jeans portion of the blackbody emission curve (the reason for the neutral colors noted above). Thus, we can estimate the extinction towards LBV 1806−20 by de-reddening the spectra until the continuum shape matches a Rayleigh-Jeans distribution. In this way, we obtain estimates of A_V = 31 ± 3 mag from the H-band continuum and A_V = 28 ± 3 mag from the K-band continuum, with uncertainties dominated by ∼10% uncertainty in the spectrograph response shape over a given waveband. Combining these with the extinction estimate from the $J - K$ color above, we adopt a final estimate for the extinction of A_V = 29 ± 2 mag towards LBV 1806−20.

From the emission lines, we can also measure a radial velocity for LBV 1806−20. We selected the Brγ line as a velocity fiducial, as it is the strongest line detection in the spectrum, and appears to be relatively free from contamination due to blending with other strong lines. We fit a Gaussian profile to this line, finding no significant residuals, and a centroid shifted from the atmospheric rest frame by −3 ± 20 km s^{-1}, where residuals in the spectral wavelength solution from atmospheric OH emission lines dominate the largely systematic uncertainty. After correcting for the Earth's barycentric motion and the Solar System barycenter motion relative to the local standard of rest, we determine a radial velocity for LBV 1806−20 of v_{lsr} = 10 ± 20 km s^{-1}. Cross-checks of this velocity determination with several other strong unblended lines in the spectra give consistent results for the velocity of LBV 1806−20. This velocity is important, as massive stars such as LBVs are a kinematically "cold" population, which do not generally deviate significantly in their velocities from their parent molecular clouds.

3. Results and discussion

3.1. The distance to LBV 1806−20 and its associated radio nebula G10.0−0.3

3.1.1. NH_3 absorption

A critical point for measuring the distance to LBV 1806−20 is the detection of the NH_3 absorption features (Fig. 3) against the radio continuum (G10.0−0.3) produced by the LBV star. A firm lower limit on the distance to G10.0−0.3 and LBV 1806−20 is the near distance associated with the absorption feature at 70.9 ± 0.5 km s^{-1}, i.e. 5.7 ± 0.4 kpc. We can then combine the full velocity range (−10 to 30 km s^{-1}) for LBV 1806−20

(Sect. 2.3 above) and the fact that LBV 1806−20 has to be located behind MC 73, together with the rotation curve of the Galaxy (Fich et al. 1989) to constrain the distance range for LBV 1806−20 without making any further assumptions regarding other molecular clouds along the line of sight. This straightforward calculation unambiguously places LBV 1806−20 in the distance range 13.2−21.5 kpc.

3.1.2. MC 13A, MC 13B, and G10.2−0.3

This determination of the distance to G10.0−0.3, while unambiguous, differs significantly from the distance determination for the nearby (on the sky) stellar cluster G10.2−0.3, which Blum et al. (2001) place at 3.4 ± 0.3 kpc. Given the similar radial velocities of LBV 1806−20 and G10.2−0.3 (∼10−16 km s^{-1}), this seems somewhat surprising. However, on the plane of the sky, they are separated by 10.7′. Furthermore, the measured optical extinction of LBV 1806−20 (29 ± 2 mag, Sect. 2.3) and G10.2−0.3 (15.5 ± 1.7 mag, Blum et al. 2001) are clearly not in agreement. This indicates that these two objects cannot be located at the same distance. G10.2−0.3, with a lower optical extinction, has to be located in the foreground relative to LBV 1806−20. Furthermore, Lavine et al. (2003) find that the stellar field surrounding LBV 1806−20 includes two distinct populations of stars – one with $A_V \sim 30$ mag (consistent with LBV 1806−20) and another with $A_V \sim 15$ mag (consistent with G10.2−0.3). Fuchs et al. (1999) also find the same bimodality in extinction, albeit with a much smaller sample. The fact that no stars are found with intermediate extinctions demonstrates that these are distinct populations, rather than a single population suffering from differential extinction across the field. Thus, we are forced to conclude that the stellar cluster of Blum et al. (2001) is a distinct cluster in the foreground to the cluster containing LBV 1806−20. Thus, discrepant distances for these two distinct clusters are not surprising, and in fact should be expected.

In order to understand the fact that these distinct populations have similar radial velocities, we need to take into account (as outlined in Sect. 2.1) that the molecular cloud labelled MC 13 in Corbel et al. (1997) is now known to consist of two distinct components that we have called MC 13A and MC 13B. Thus, the line of sight towards these objects is much more complex than previously thought, with two molecular clouds with similar velocities, one containing each stellar population. Based on the fact that MC 13B is associated with G10.2−0.3 (Sect. 2.1; Kim & Koo 2002), and that the upper limit for the distance to G10.2−0.3 (Blum et al. 2001) is much less than the 13.2 kpc lower limit for LBV 1806−20, we conclude that the molecular cloud MC 13B is located in the foreground relative to LBV 1806−20.

We can further constrain the parent molecular cloud of LBV 1806−20 by investigating the complex of molecular clouds along the line of sight. Absorption lines against the radio continuum of G10.2−0.3 (see Corbel et al. 1997, and references therein) showed that MC 4, MC 24, MC 30, MC 38, MC 44 are located at their near distances. Given the ammonia absorption towards LBV 1806−20 and its accompanying distance range of 13−21 kpc, the only remaining molecular clouds along the line of sight which could potentially be the site of LBV 1806−20 are MC 87, MC 94, and MC 13A. Of these, only MC 13A has a velocity consistent with LBV 1806−20 (Sect. 2.3), and we conclude that it is the parent molecular cloud for LBV 1806−20, SGR 1806−20, and G10.0−0.3. This association and the distance range for LBV 1806−20 now lift the near/far distance ambiguity for MC 13A, and we can use the velocity of MC 13A and the Galactic rotation curve to constrain the distance for both MC 13A and LBV 1806−20 to be $15.1^{+1.8}_{-1.3}$ kpc.

3.1.3. Extinction and distance

We can cross-check the above distance estimation, using the measured extinction towards LBV 1806−20. This extinction arises primarily within the molecular clouds along the line of sight, and we can determine its value for each cloud using the CO line area. In order to convert the molecular emission spectra into equivalent optical extinction along the line of sight, we follow the method outlined in Corbel et al. (1999) or Chapuis & Corbel (2003). We assume conservative errors of 20% (to take into account the uncertainties in the various conversion factors) for the contribution in terms of optical extinction of each molecular cloud. The discussion of Corbel et al. (1997) for the location of the various molecular clouds still holds with these new observations – we simply need to consider the revised distance of G10.2−0.3 and the splitting of MC 13. Separating the contribution of each of the two MC 13 clouds in terms of line area is not a simple task. But if we fit both ^{12}CO(J = 1−0) and ^{13}CO(J = 1−0) spectra with two Gaussian lines in the velocity range 8−20 km s^{-1}, we find that MC 13B and MC 13A contribute roughly 23% and 77% respectively in terms of line area. These should not be taken as firm numbers, but rather as indicative of the approximate relative contribution of each clouds. The resulting parameters (velocity, integrated area, optical extinction, distances) of the molecular clouds are presented in Table 1.

If we take the contribution from molecular hydrogen in all of the clouds up to MC 13A, we reach a total extinction of 32.5 ± 2.6 mag. Taking the contribution from atomic hydrogen (Corbel et al. 1997) implies that the total optical extinction up to MC 13A is 37.5±3.0 mag. While the uncertainties are not trivially small, this is at least consistent (at the ∼2σ level) with the extinction of 29 ± 2 mag for LBV 1806−20. Adding the contribution of MC 13A significantly increases this extinction to 47.5 ± 3.6 mag, implying that LBV 1806−20 is at or close to the near side of MC 13A. In Fig. 5a, we present a map of the integrated ^{13}CO(J = 1−0) emission (based on the data of Kim & Koo 2002). It shows that the position of LBV 1806−20, as well as SGR 1806−20 and the star cluster, is consistent with a location on the edge of the cloud MC 13A, as favoured by the measurement of the optical extinction. Thus, we find a straightforward explanation for the distance of G10.0−0.3 and LBV 1806−20, consistent with all reported data, is that the star is located in MC 13A at a distance of $15.1^{+1.8}_{-1.3}$ kpc.

3.2. The distance to G10.2−0.3 and the complex structure of W31

3.2.1. Distance and optical extinction of G10.2−0.3

With the distance of G10.0−0.3 and LBV 1806−20 clarified, we now turn to the more general issues of the structure of W31, which we now understand to have several discrete components at distinct distances. In their study, Blum et al. (2001) performed near-infrared spectroscopy and photometry of an embedded stellar cluster in G10.2−0.3 (the other major H II regions of W31 being G10.3−0.1 and G10.6−0.4). They derived a spectrophotometric distance for G10.2−0.3 (and by extension for W31) by assuming either zero-age main-sequence or dwarf luminosity class for the stars of the cluster, obtaining distances of 3.1 ± 0.3 kpc and 3.7 ± 0.3 kpc respectively. They derived an average optical extinction to G10.2−0.3 of $A_V = 15.5 \pm 1.7$ mag (Blum et al. 2001). Clearly, this distance range, as well as the optical extinction, are not in agreement with our previous estimate for W31 (Corbel et al. 1997), in which we associate W31 with the far kinematic distance of MC 13. However, as shown above, we now understand that MC 13 and W31 itself are composed of multiple discrete components distributed along the line of sight. Thus, as noted above, the distance to G10.2−0.3, MC 13B, and their portion of W31 is a separate issue from G10.0−0.3, LBV 1806−20, SGR 1806−20, MC 13A, and their portion of W31. Nevertheless, our investigation of the latter can provide important insights into the distance to the former.

First, as a cross-check on the relative placement of molecular clouds along the line of sight in Table 1, we can compare the extinction of the stars in G10.2−0.3 to that expected from the clouds along the line of sight (as done above for LBV 1806−20). If we use the ^{12}CO(J = 1–0) spectrum towards LBV 1806−20, the total visual extinction due to the molecular material located in front of MC 13B (MC 4, MC 24, MC 30, MC 38, MC 44, cf. Corbel et al. 1997) is 13.0 ± 1.5 mag. Adding the contribution from atomic hydrogen (as in Corbel et al. 1997) raises this number to 14.5 ± 1.8 mag, consistent with the above estimate of the optical extinction to G10.2−0.3 at the $\sim 1\sigma$ level. This re-confirms the relative placement of the clouds in Table 1.

3.2.2. G10.2−0.3: A location on the −30 km s^{-1} spiral arm

Given this, an important question remains if we want to fully understand the velocity field along this line of sight: what is the distance to the parental molecular cloud (MC 13B) of G10.2−0.3? A distance range of 2.8–4.0 kpc (Blum et al. 2001) would imply a velocity range of 22.0–38.0 km s^{-1}, which is at best marginally consistent with the observed velocity of G10.2−0.3 (16.4 ± 0.2 km s^{-1}, Kim & Koo 2001). Also, more importantly, absorption lines against the radio continuum of G10.2−0.3 are observed up to 43 km s^{-1} (e.g. Wilson 1974; Greisen & Lockman 1979; Kalberla et al. 1982), which is very difficult to reconcile with G10.2−0.3 at the near distance of $2.2^{+1.0}_{-1.6}$ kpc associated with the velocity of 16.4 km s^{-1}. Indeed, the cloud at the origin of the absorption at the velocity of 43 km s^{-1} is located at a distance greater than 4.5 kpc (see Table 1) if we assume circular motion. But we would like to note that absorption at velocities greater than ~50 km s^{-1} is not expected at these Galactic longitudes, because of a hole (Fig. 6) in the gas distribution (Dame et al. 1987; Corbel et al. 1997). The drop-off of absorption at ~43 km s^{-1} is just the sharp inner edge of the molecular ring (Dame et al. 2001). Thus, the lack of absorption should not be an argument for ruling out a possible location at a far distance (e.g. Fish et al. 2003 for G10.6−0.4).

To overcome these difficulties, Blum et al. (2001), as well as other authors (e.g. Wilson 1974; Kalberla et al. 1982), invoked the presence of non-circular motion that could affect the velocity of the cloud (in addition to the contribution of rotation around the Galactic Center, hereafter GC). Indeed, along the line of sight of W31 (and LBV 1806−20) is found the 3-kpc expanding arm. This arm can be described as a simple rotating ring at a galactocentric radius of 3.4 kpc (assuming a distance between the Sun and the GC of 8.5 kpc[1]) expanding out from the GC with a velocity of 53 km s^{-1} (e.g. Bania 1980).

As discussed in detailed in Corbel et al. (1997), the 3-kpc expanding arm is likely associated with the molecular cloud MC –16 and is very likely not associated with MC 13B and G10.2−0.3. This is confirmed if we look at the radial velocity profile of the 3-kpc expanding arm as a function of the Galactic longitude based on H I observations (see Fig. 4 of Menon & Ciotti 1970). This clearly show that a velocity of ~−15 km s^{-1} (as for MC –16) should be expected for this feature.

So, in order reconcile the fact that G10.2−0.3 is located on this side of the Galaxy (Blum et al. 2001) and the fact that absorption lines are observed up to a velocity of 43 km s^{-1}, we surmise that there might be another feature with non-circular motion on this side of the Galaxy. In fact, there is another arm, the −30 km s^{-1} spiral arm (unfortunately sometimes called the 4 kpc arm), that is also expanding from the GC at a galactocentric radius of 4 kpc (Menon & Ciotti 1970; Greaves & Williams 1994). Its expansion velocity measured at a Galactic longitude of 0° is −30 km s^{-1} (Menon & Ciotti 1970; Liszt et al. 1977; Linke et al. 1981; Greaves & Williams 1994; Sandqvist et al. 2003). This feature was originally detected in 1967 (Kerr & Vallak 1967), but we would like to point that no molecular counterpart has been associated with it. Indeed, unlike the 3 kpc expanding arm, the −30 km s^{-1} spiral arm can not be traced on the longitude−velocity CO map (Fig. 6), possibly due to its proximity with the molecular ring (Dame et al. 2001). The extrapolation of its radial velocity profile in Fig. 1 of Menon & Ciotti (1970) to a longitude of 10° is consistent with the velocity of MC 13B. We therefore conclude that G10.2−0.3 and MC 13B are located on the −30 km s^{-1} spiral arm. In that case, there is no problem with the fact that absorption lines against the radio continuum of G10.2−0.3 are detected up to 43 km s^{-1}, as they would originate in MC 44. We note that the −30 km s^{-1} spiral arm has to be closer to the Sun than the 3-kpc expanding arm with a separation of ~0.5 kpc

[1] Note that in old literature, this arm was sometimes called the "4-kpc expanding arm" due to a distance to the GC of 10.0 kpc.

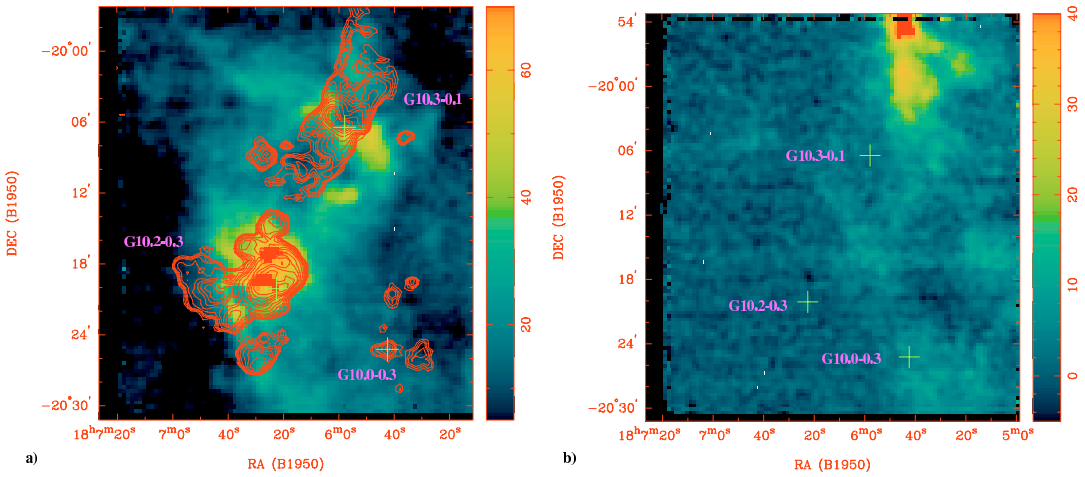

Fig. 5. a) Map of the ^{13}CO(J = 1–0) emission integrated between the velocities 8 to 20 km s^{-1}, using the data of Kim & Koo (2002). **b)** Map of the ^{13}CO(J = 1–0) emission integrated between the velocities 61 to 80 km s^{-1}. The location of G10.2–0.3, G10.3–0.1 and G10.0–0.3 are marked. The unit of the scale of the map is in K km s^{-1}. The contours represent the 21 cm radio continuum emission from this field of view (from Kim & Koo 2002).

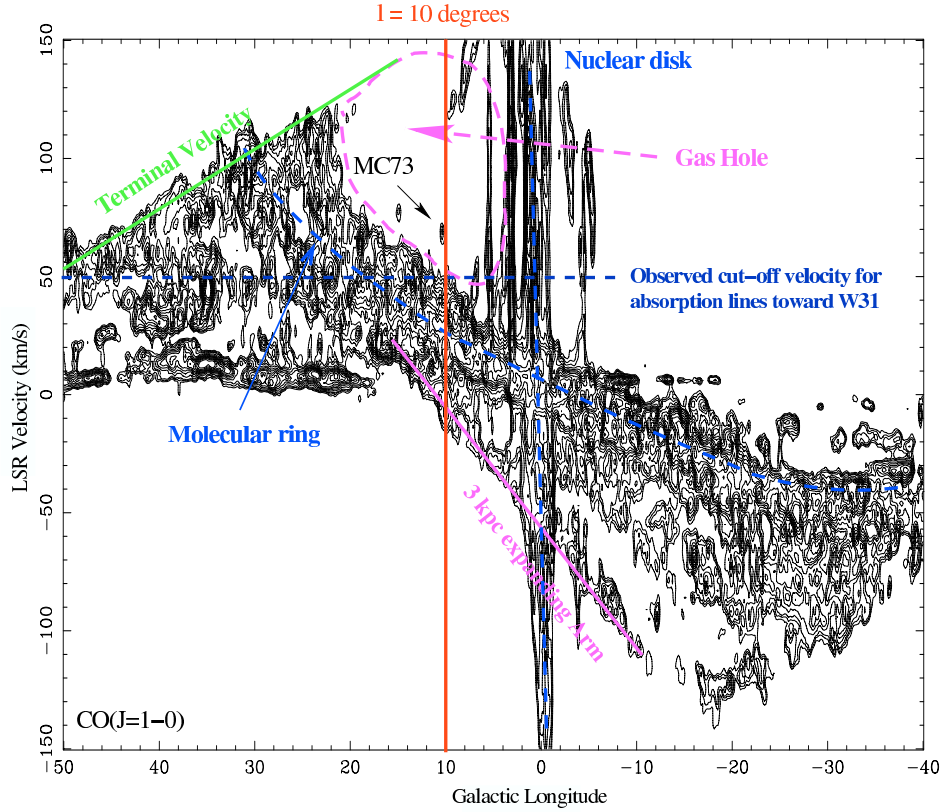

Fig. 6. Longitude – velocity map of Galactic CO emission, figure adapted from Dame et al. (2001). Between Galactic longitude of ~5° to 25°, a hole is apparent in the gas distribution at velocities greater than ~50 km s^{-1}. We note the location of MC 73 on the line of sight to G10.0–0.3. The locus point of the 3 kpc expanding arm can also be well traced.

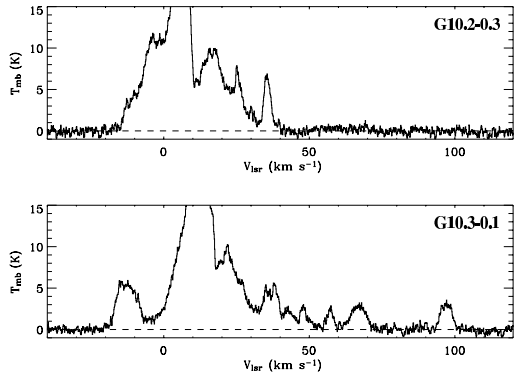

Fig. 7. ^{12}CO(J = 1–0) spectrum in the direction of the H II regions G10.2–0.3 (*top*) and G10.3–0.1 (*bottom*). Antenna temperature have been converted into main beam brightness temperature. The scale has been adjusted in order to highlight the emission above 40 km s^{-1}.

(Menon & Ciotti 1970). In any case, the distance to the −30 km s^{-1} spiral arm is set by the maximum velocity of the absorption lines, i.e. 4.5 ± 0.6 kpc, which is completely consistent with the spectrophotometric distance of 3.4 ± 0.6 kpc for G10.2–0.3 (Blum et al. 2001). We note that at a Galactic longitude of 0°, the 3 kpc expanding arm and the −30 km s^{-1} spiral arm have a velocity separation of ∼23 km s^{-1}, which is almost the difference in velocity between MC −16 and MC 13B. This therefore strengthens our association of the 3-kpc expanding arm with MC −16 and the −30 km s^{-1} spiral arm with MC 13B. We also note that these two arms could be related to the presence of a bar at the GC (e.g. Blitz & Spergel 1991).

3.2.3. The distance to G10.3–0.1 and G10.6–0.4

So if G10.2–0.3 is at a closer distance, are the other major components of W31 at the same distance? In their detailed study of W31, Kim & Koo (2002) performed a ^{13}CO(J = 1–0) map of G10.2–0.3 and G10.3–0.1 (see their Figs. 4, 5 and 9). Their peak CO maps over the velocity range 0–22 km s^{-1} shows two main components (one centered on each H II region) that could be interpreted as two separate molecular clouds (see also Fig. 5a with the integrated ^{13}CO(J = 1–0) map). But based on our new CO results, it might be possible that the southern part is associated with MC 13B as G10.2–0.3, and the northern part with MC 13A and G10.3–0.1 (Fig. 5a). If this is the case, it would imply that W31 could be decomposed into several components, with G10.3–0.1 located at the kinematic distance associated with MC 13A, i.e. $15.1^{+1.8}_{-1.3}$ kpc.

Figure 7 shows the ^{12}CO spectrum along the line of sight to these two H II regions. These profiles are very different, especially at velocities above ∼40 km s^{-1}, and the profile of G10.3–0.1 is very similar to the one of LBV 1806–20 (the additional CO emission above 40 km s^{-1} may also be related to the variation in galactic latitude of these sources). So it is not unlikely that this H II region, which has a recombination line at 7.7 ± 0.5 km s^{-1}, could be associated with MC 13A. As noted above (Sect. 2.1), the ^{13}CO(J = 1–0) map of this part of W31 by Kim & Koo (2002) could be interpreted as being due to the presence of two separate molecular clouds. In that case, one should wonder why no absorption line is detected, as in the case of LBV 1806–20, at ∼71 km s^{-1} for G10.3–0.1 (Kalberla et al. 1982)? In Fig. 5b, we used the ^{13}CO(J = 1–0) of Kim & Koo (2002) to illustrate the spatial extent of MC 73. We found almost no ^{13}CO(J = 1–0) emission in the velocity range 61 to 80 km s^{-1}, which is consistent with the non detection of absorption line above 50 km s^{-1} (Kalberla et al. 1982) toward G10.3–0.1, even if it were associated with MC 13A. However, our ^{12}CO(J = 1–0) spectrum towards G10.3–0.1 (Fig. 7) indicates a weak contribution of MC 73 along this line sight and suggest that the line of sight of G10.3–0.1 might be close to the edge of MC 73. More sensitive absorption measurement may be useful to further detect absorption line due to MC 73 in front of G10.3–0.1. We note that Kalberla et al. (1980) detected a weak absorption line at ∼−15 km s^{-1} in front of G10.3–0.1, that is consistent with the velocity of the 3-kpc expanding Arm (Corbel et al. 1997), i.e. the molecular cloud we called MC −16 and the fact that G10.3–0.1 could be associated with MC 13A. We note, however, that a similar but weaker feature, is also present in front of G10.2–0.3 (Kalberla et al. 1980).

In a recent study of absorption lines toward a large number of H II regions, Fish et al. (2003) deduced a scaling law in order to estimate the distance of an H II region. They state that when there is a "large difference between far and near kinematic distances" – as in our case for both MC 13A and MC 13B, see Table 1 – "high accuracy can be achieved by choosing the kinematic distance closer to 1.84 $|b|^{-1}$". In the case of G10.2–0.3, G10.3–0.1 and G10.6–0.4, this expression would be equal to 5.3, 12.3 and 4.7 kpc respectively with high accuracy[2]. This again will argue for an association of G10.2–0.3 and G10.6–0.4 with MC 13B in the −30 km s^{-1} spiral arm at a distance of 4.5 ± 0.6 kpc and a location of G10.3–0.1 in MC 13A at a distance of $15.1^{+1.8}_{-1.3}$ kpc. But again, as illustrated in Fig. 3 of Dame et al. (1987), between longitude 5° and 25°, we want to stress that the lack of absorption at velocities greater than ∼50 km s^{-1} is not an argument for the near distance due to the presence of the gas hole (Fig. 6) at low Galactic longitudes (Corbel et al. 1997).

Finally, to close the debate on the structure of W31 (as a location of G10.3–0.1 within the −30 km s^{-1} spiral arm can not be ruled out at this time), a spectrophotometric study (with optical extinction measurement), similar to what has been performed by Blum et al. (2001) for G10.2–0.3, should also be performed for G10.3–0.1 and G10.6–0.4 in light of our new results. A sketch of the line of sight with the new location of each object introduced in this paper is presented in Fig. 8.

3.3. The distance to SGR 1806–20

As we have seen before, G10.0–0.3 is associated with the wind of LBV 1806–20 and not SGR 1806–20 and is not the remnant of a supernova (Gaensler et al. 2001). SGR 1806–20 is

[2] Note that this argument cannot be applied to G10.0–0.3, simply because it is not an H II region.

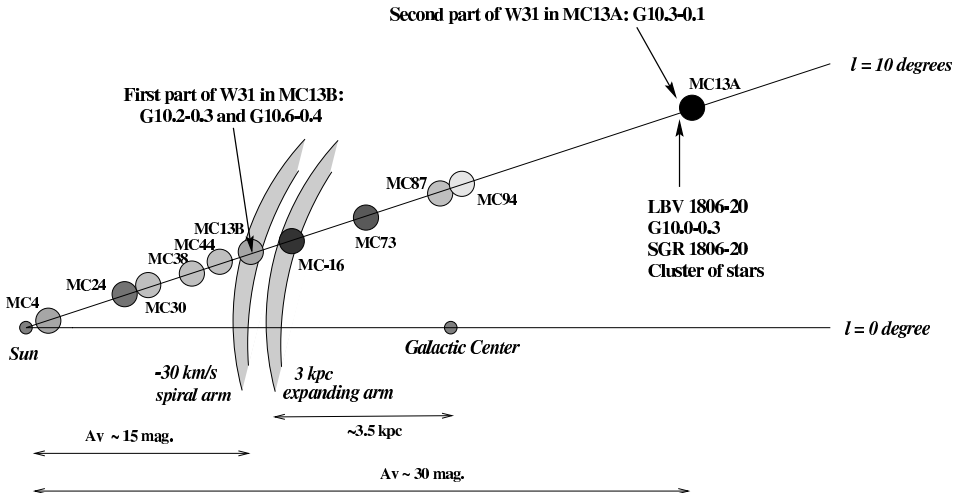

Fig. 8. Schematic diagram of the molecular clouds on the line of sight to W31, LBV 1806−20 and SGR 1806−20.

separated from LBV 1806−20 by an angular distance of 12″ (Hurley et al. 1999; Eikenberry et al. 2001; Kaplan et al. 2002). However, it still lies within the angular extent of the embedded cluster (see Fig. 1 and Fuchs et al. 1999), and its X-ray absorption matches the IR extinction towards the cluster members (Eikenberry et al. 2001), leading to the conclusion that SGR 1806−20 is a cluster member. This lead to the conclusion that all these objects, i.e. SGR 1806−20 and the cluster of stars, have to be located at the distance we have estimated for LBV 1806−20: $15.1^{+1.8}_{-1.3}$ kpc. An interesting consequence of this work is that all these massive stars are still located close to their parental molecular cloud (MC 13A), which is not surprising if we take into account their short lifetimes and the expectation that such massive stars are a kinematically "cold" population. We would like to point out that SGR 1900+14 is also associated with a cluster of massive stars (Vrba et al. 2000) and that SGR 1627−41 also appears to lie at the edge of a massive Giant Molecular Cloud (Corbel et al. 1999). The only known extragalactic soft gamma repeater (SGR 0526−66), which is associated with the SNR N49, also lies at the edge of a dense molecular cloud (Vancura et al. 1992; Banas et al. 1997). It now also means that all SGRs with precise location (4 out 6) are associated with GMC and/or massive star cluster. All of this probably points to a strong connection between massive stars and formation of SGRs by the way of Giant Molecular Clouds.

4. Conclusions

We have presented new millimeter and near-infrared observations of the field of view surroundings the radio nebula G10.0−0.3 (produced by the wind of LBV 1806−20) and the giant H II complex W31. Based on these observations combined with others in the literature, we reach the following conclusions:

- Based on NH_3 absorption from MC 73 and the velocity of LBV 1806−20, we unambiguously constrain the distance to G10.0−0.3 and LBV 1806−20 to be in the range of 13.2−21.5 kpc.
- Combining this constraint with CO observations of molecular clouds along the line of sight, we further refine the distance measurement to G10.0−0.3 and LBV 1806−20 to be $15.1^{+1.8}_{-1.3}$ kpc.
- This distance estimate is confirmed by the consistency between the measured extinction towards LBV 1806−20 and the extinction from the molecular clouds along the line of sight inferred from their CO spectra.
- Based on their distinct extinctions and the newly-resolved parental molecular clouds (MC 13A and MC 13B), we conclude that the stellar cluster in G10.2−0.3 lies in the foreground to the cluster containing LBV 1806−20. This shows that W31 consists of at least 2 discrete components along the line of sight.
- We suggest that G10.2−0.3 and G10.6−0.4 are located on the −30 km s^{-1} spiral arm at a distance from the Sun of 4.5 ± 0.6 kpc.
- We also suggest that G10.3−0.1 may be associated with a massive molecular cloud at the same distance as LBV 1806−20 ($15.1^{+1.8}_{-1.3}$ kpc).
- We confirm that SGR 1806−20 is located at a distance from the Sun of $15.1^{+1.8}_{-1.3}$ kpc and that it is associated with a very massive molecular cloud. All SGRs with precise location are associated with a site of massive star formation.

Acknowledgements. The authors would like to thank Tom Dame and Kee-Tae Kim for useful discussions and for critical review of this manuscript. We also wish to thank Claude Chapuis for conducting the 1998 SEST observations and stimulating discussion and Bill Mahoney for carrying out the DSN observations. We thank R. Blum and the CTIO staff for their help in acquiring the IR spectra. We gratefully acknowledge Kee-Tae Kim and Bon-Chul Koo for sharing their CO data of W31, as well as Yael Fuchs for her help with Fig. 1 and Tom Dame for his help with Fig. 6. We also thank Aage Sandqvist for providing information on the −30 km s^{-1} spiral arm. SSE is supported in part by an NSF CAREER award (AST-9983830).

References

Banas, K. R., Hughes, J. P., Bronfman, L., & Nyman, L.-A. 1997, ApJ, 480, 607
Bania, T. M. 1980, ApJ, 242, 95
Blitz, L., & Spergel, D. N. 1991, ApJ, 379, 631
Blum, R. D., Damineli, A., & Conti, P. S. 2001, ApJ, 121, 3149
Chapuis, C., & Corbel, S. 2004, A&A, 414, 659
Corbel, S., Wallyn, P., Dame, T. M., et al. 1997, ApJ, 478, 624
Corbel, S., Chapuis, C., Dame, T. M., & Durouchoux, P. 1999, ApJ, 526, L29
Combes, F. 1991, ARA&A, 29, 195
Dame, T. M., Ungerechts, H., Cohen, R. S., et al. 1987, ApJ, 322, 706
Dame, T. M., Hartmann, D., & Thaddeus, P. 2001, ApJ, 547, 792
Depoy, D., Atwood, B., Byard, P. L., Frogel, J., & O'Brien, T. P. 1993, SPIE, 1946, 667
Eikenberry, S. S., Garske, M. A., Hu, D., et al. 2001, ApJ, 563, L133
Eikenberry, S. S., Matthews, K., Garske, M. A., et al., ApJ, accepted
Fich, M., Blitz, L., & Stark, A. A. 1989, ApJ, 342, 272
Fish, V. L., Reid, M. J., Wilner, D. J., & Churchwell, E. 2003, ApJ, 587, 701
Fuchs, Y., Mirabel, F., Chaty, S., et al. 1999, A&A, 350, 891
Gaensler, B. M., Slane, P. O., Gotthelf, E. V., & Vasisht, G. 2001, ApJ, 559, 963
Ghosh, S. K., Iyengar, K. V. K., Rengarajan, T. N., et al. 1989, ApJ, 347, 338
Greaves, J. S., & Williams, P. G. 1994, A&A, 290, 259
Greisen, E. W., & Lockman, F. J. 1979, ApJ, 228, 740
Hurley, K., Kouveliotou, C., Cline, T., et al. 1999, ApJ, 523, L37
Kalberla, P. M. W., Goss, W. M., & Wilson, T. L. 1982, A&A, 106, 167
Kaplan, D. L., Fox, D. W., Kulkarni, S. R., et al. 2002, ApJ, 564, 935
Kerr, F. J., & Vallak, R. 1967, Austr. J. Phys., Astrophys. Suppl., 3, 3
Kim, K.-T., & Koo, B.-C. 2001, ApJ, 549, 979
Kim, K.-T., & Koo, B.-C. 2002, ApJ, 575, 327
Kouveliotou, C., Dieters, S., Strohmayer, T., et al. 1998, Nature, 393, 235
Kulkarni, S. R., & Frail, D. A. 1993, Nature, 365, 33
Kulkarni, S. R., Frail, D. A., Kassim, N. E., Murakami, T., & Vasisht, G. 1994, Nature, 368, 129
Linke, R. A., Stark, A. A., & Frerking, M. A. 1981, ApJ, 243, 147
Lavine, J., Eikenberry, S. S., & Smith, J. D., in preparation
Liszt, H. S., Burton, W. B., Sanders, R. H., & Scoville, N. Z. 1977, ApJ, 213, 38
Menon, T. K., & Ciotti, J. E. 1970, Nature, 227, 579
Mereghetti, S., Cremonesi, D., Feroci, M., & Tavani, M. 2000, A&A, 361, 240
Rieke, G. H., & Lebofsky, M. J. 1985, ApJ, 288, 618
Sandqvist, A., Bergman, P., Black, J. H., et al. 2003, A&A, 402, L63
Shaver, P. A., & Goss, W. M. 1970, Austr. J. Phys., Astrophys. Suppl., 14, 77
van Kerkwijk, M. H., Kulkarni, S. R., Matthews, K., & Neugebauer, G. 1995, ApJ, 444, L33
Vancura, O., Blair, W. P., Long, K. S., & Raymond, J. C. 1992, ApJ, 394, 158
Vasisht, G., Frail, D. A., & Kulkarni, S. R. 1995, ApJ, 440, L65
Vrba, F. J., Henden, A. A., Luginbuhl, C. B., et al. 2000, ApJ, 533, L17
Wilson, T. L. 1974, A&A, 31, 83

7.4.2

Infrared Observations of the Candidate LBV 1806-20 and Nearby Cluster Stars.

Article publié dans :

Astrophys. J., 2004, 616, 506-518

Eikenberry, S. S., Matthews, K., LaVine, J. L., Garske, M. A., Hu, D., Jackson, M. A., Patel, S. G., Barry, D. J., Colonno, M. R., Houck, J. R., Wilson, J. C., Corbel, S., Smith, J. D.

The Astrophysical Journal, 616:506–518, 2004 November 20

INFRARED OBSERVATIONS OF THE CANDIDATE LBV 1806-20 AND NEARBY CLUSTER STARS[1,2,3]

S. S. Eikenberry,[4,5,6] K. Matthews,[7] J. L. LaVine,[4] M. A. Garske,[5,8] D. Hu,[5] M. A. Jackson,[5] S. G. Patel,[4,5] D. J. Barry,[5] M. R. Colonno,[5] J. R. Houck,[5] J. C. Wilson,[5,9] S. Corbel,[10] and J. D. Smith[6,11]

Received 2003 September 19; accepted 2004 April 19

ABSTRACT

We report near-infrared photometry, spectroscopy, and speckle imaging of the hot, luminous star we identify as candidate LBV 1806-20. We also present photometry and spectroscopy of three nearby stars, which are members of the same star cluster containing LBV 1806-20 and SGR 1806-20. The spectroscopy and photometry show that LBV 1806-20 is similar in many respects to the luminous "Pistol star," albeit with some important differences. They also provide estimates of the effective temperature and reddening of LBV 1806-20 and confirm distance estimates, leading to a best estimate for the luminosity of this star of greater than $5 \times 10^6\ L_\odot$. The nearby cluster stars have spectral types and inferred absolute magnitudes that confirm the distance (and thus luminosity) estimate for LBV 1806-20. If we drop kinematic measurements of the distance ($15.1^{+1.8}_{-1.3}$ kpc), we have a lower limit on the distance of greater than 9.5 kpc and on the luminosity of greater than $2 \times 10^6\ L_\odot$, based on the cluster stars. If we drop both the kinematic and cluster star indicators for distance, an ammonia absorption feature sets yet another lower limit to the distance of greater than 5.7 kpc, with a corresponding luminosity estimate of greater than $7 \times 10^5\ L_\odot$ for the candidate LBV 1806-20. Furthermore, on the absis of very high angular resolution speckle images, we determine that LBV 1806-20 is not a cluster of stars but is rather a single star or binary system. Simple arguments based on the Eddington luminosity lead to an estimate of the total mass of LBV 1806-20 (single or binary) exceeding 190 $M_\odot$. We discuss the possible uncertainties in these results and their implications for the star formation history of this cluster.

Subject headings: infrared: stars — open clusters and associations: general — stars: early-type — stars: emission-line, Be — stars: Wolf-Rayet — supergiants

1. INTRODUCTION

Mounting evidence gathered in recent years indicates that stars may be formed with masses much greater than previously thought possible. The hot luminous "Pistol star" near our Galaxy's center, for instance, has an estimated mass of greater than 150 $M_\odot$ (Figer et al. 1998), and the stars R136a1 and R136a2 in the Large Magellanic Cloud each have masses of 140–155 $M_\odot$ (Massey & Hunter 1998). Since the luminosities of such massive stars exceed $10^6\ L_\odot$, relatively small populations of these stars can dominate the power output of their host galaxy during their lifetimes. Furthermore, their deaths may spread chemically enriched material into the galaxy and leave behind black holes as remnants. The death events may be responsible for gamma-ray bursts in the "collapsar" scenario (e.g., Price et al. 2003; Hjorth et al. 2003; Macfadyen et al. 2001), and the relatively large remnant black holes may also explain the so-called intermediate-mass black holes currently being discovered in nearby galaxies (e.g., Kaaret et al. 2001 and references therein). Thus, probing the upper limit for stellar mass has an important impact on our understanding of a wide range of astrophysical phenomena, including the chemical evolution of matter in our Galaxy and external galaxies, the history of galaxy and structure formation in the universe, the formation of black holes in their dying supernova events, and possibly the origin of gamma-ray bursts via collapsars.

We report here new observations of a luminous star we identify as LBV 1806-20.[12] This star was first identified as a potential counterpart to the soft gamma-ray repeater SGR 1806-20 (Kulkarni et al. 1995), with high near-infrared brightness ($K = 8.4$ mag) despite significant absorption from interstellar dust in the Galactic plane. Subsequent moderate-resolution ($R \sim 700$) infrared spectroscopy revealed it to be a candidate luminous blue variable (LBV) star and one of the most luminous stars in the Galaxy, with $L > 10^6\ L_\odot$ (van Kerkwijk et al. 1995; Corbel et al. 1997). This star is known

[1] Based on data obtained with the Cerro Tololo Inter-American Observatory 4 m telescope operated by the National Optical Astronomy Observatory, which is operated by the Association of Universities for Research in Astronomy, Inc., under cooperative agreement with the National Science Foundation.

[2] Based on data obtained at the Palomar Observatory 200 inch telescope, which is operated by the California Institute of Technology, the Jet Propulsion Laboratory, and Cornell University.

[3] This publication makes use of data products from the Two Micron All Sky Survey, which is a joint project of the University of Massachusetts and the Infrared Processing and Analysis Center/California Institute of Technology, funded by the National Aeronautics and Space Administration and the National Science Foundation.

[4] Department of Astronomy, University of Florida, Gainesville, FL 32611.

[5] Astronomy Department, Cornell University, Ithaca, NY 14853.

[6] Visiting Astronomer, Cerro Tololo Inter-American Observatory.

[7] Physics Department, California Institute of Technology, 1200 East California Boulevard, Pasadena, CA 91125.

[8] Physics Department, Northwest Nazarene University, Nampa, ID 83686.

[9] Department of Astronomy, P.O. Box 3818, University of Virginia, Charlottesville, VA 22903.

[10] Université Paris VII and Service d'Astrophysique, CEA Saclay, F-91191 Gif-sur-Yvette, France.

[11] Steward Observatory, University of Arizona, 933 North Cherry Avenue, Tucson, AZ 85721.

[12] We note that this star has not been observed to undergo a major LBV outburst yet, and thus some may not consider it to be an LBV (although it is undoubtedly luminous, blue, and variable and shares many spectral characteristics with bona fide LBV stars, as we show here). Hereafter, to avoid awkward phrasing, we refer to the candidate LBV as LBV 1806-20 as is done in the literature.

to lie at the brightness peak of the radio nebula G10.0-0.3 (Kulkarni & Frail 1993; Vasisht et al. 1995). However, the revised Interplanetary Network localization of SGR 1806-20 indicated that the SGR was significantly offset from the position of the candidate LBV star and the coincident core of G10.0-0.3 (Hurley et al. 1999). Recent *Chandra* and infrared observations confirm that the SGR lies $\sim 12''$ away from the candidate LBV (Kaplan et al. 2002; Eikenberry et al. 2001). In addition, Gaensler et al. (2001) show that G10.0-0.3 is not a supernova remnant at all but is a radio nebula powered by the tremendous wind of the candidate LBV star at its core. The apparent conundrum presented by this scenario—why we find two such rare objects so close to each other on the sky without any apparent physical connection—has been resolved by the observations of Fuchs et al. (1999), who showed that LBV 1806-20 is a member of a cluster of massive stars, and of Eikenberry et al. (2001), who showed that SGR 1806-20 appears to be a member of the same cluster. Thus, while these two rare objects are not identical, they are related through common cluster membership. Interestingly, Vrba et al. (2000) show that one of the other SGRs in the Milky Way may also be associated with a massive star cluster.

The distance to the candidate LBV, SGR, and their associated cluster has also been the subject of some discussion in the literature. Initial studies of CO emission from molecular clouds toward this line of sight and the detection of NH_3 absorption against the radio continuum indicated an extinction of $A_V = 35 \pm 5$ mag and a best estimate for the distance of 14.5 ± 1.4 kpc (Corbel et al. 1997), again confirming its status as one of the most luminous stars known. However, Blum et al. (2001) present infrared spectra of members of a cluster in the nearby H II region G10.2-0.3, which is also part of the (apparent) W31 giant molecular cloud complex containing G10.0-0.3, and find an apparently conflicting distance of $\sim 3.4 \pm 0.6$ kpc. This apparent conflict has also been recently resolved by Corbel & Eikenberry (2004), who present higher resolution millimeter and infrared observations of G10.0-0.3 and G10.2-0.3. They find that W31 is actually resolved into at least two components along the line of sight, with one component at $d \sim 4$ kpc and with extinction $A_V \sim 15$ mag (in excellent agreement with the Blum et al. 2001 observations of G10.2-0.3) and another component at a (refined) distance of $d = 15.1^{+1.8}_{-1.3}$ kpc and with $A_V = 37 \pm 3$ mag. The radial velocity of LBV 1806-20 matches both of these components, but the NH_3 absorption toward the core of G10.0-0.3 (and thus LBV 1806-20) due to a cloud at $d = 5.7$ kpc unambiguously places the star in the "far" component of W31. In addition, both the infrared extinction toward LBV 1806-20 (van Kerkwijk et al. 1995; see also below) and the X-ray absorption column toward SGR 1806-20 (Eikenberry et al. 2001; Mereghetti et al. 2000) match the expected extinction toward the "far" component of W31 and differ from that of the "near" component of Blum et al. (2001) by ~ 15 mag, thus confirming the association of the candidate LBV, SGR, and associated star cluster with the "far" component of W31.

In order to further investigate this intriguing object, we obtained near-infrared images and spectra of LBV 1806-20 and several nearby stars. In § 2, we describe these observations and their reduction. In § 3, we describe the analysis of the resulting data, including the spectral types of the candidate LBV and cluster stars, refined analyses of the reddening, confirmation of the distance estimate of Corbel & Eikenberry (2004), and the resulting luminosity estimate for LBV 1806-20. In § 4, we discuss the uncertainties in these measurements and their implications for our understanding of the formation and evolution of extremely massive stars and the birth environment of SGRs. Finally, in § 5 we present our conclusions.

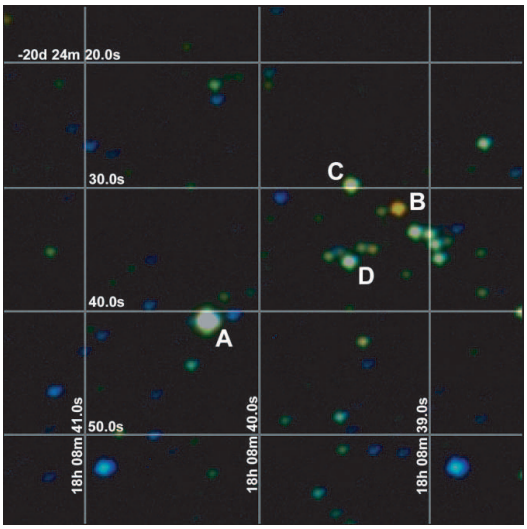

FIG. 1.—Three-color near-infrared image of the field of LBV 1806-20, coded with *J* band = blue, *H* band = green, and *K* band = red. Labels indicate LBV 1806-20 (A) and the three other stars (B, C, and D) for which we obtained near-infrared spectra. Blue colors indicate foreground objects, while colors similar to LBV 1806-20 indicate hot stars with similar reddening. Coordinates are J2000.0.

2. OBSERVATIONS AND DATA REDUCTION

2.1. *Cerro-Tololo Inter-American Observatory—2001 July*

We used the Ohio State Infrared Imaging Spectrograph (OSIRIS) instrument (Depoy et al. 1993) and f/14 tip-tilt secondary on the Cerro-Tololo Inter-American Observatory (CTIO) 4 m telescope on 2001 July 5–6 to observe LBV 1806-20 and nearby stars. In the OSIRIS imaging mode, we obtained *J*-, *H*-, and *K*-band images with a $0\farcs161$ pixel^{-1} plate scale. While conditions were nonphotometric because of high clouds, the seeing conditions were acceptable when the transparency allowed observations—using the tip-tilt secondary, typical images had FWHMs of $\sim 0\farcs6$–$0\farcs7$. In each band, we obtained a set of nine images in a 3×3 raster pattern with a $10''$ offset between images. We then subtracted dark frames from each image, divided the result by its own median, and then median-combined the resulting images into a normalized sky frame. We then subtracted the dark frame and a scaled version of the sky frame from each of the nine images and divided the result by a dome flat image. We shifted each of the nine frames to a common reference position and added them to give a final summed image in each band. Figure 1 shows a composite three-color image of the field of LBV 1806-20 in the following near-infrared bands: $J = 1.25$ μm (*blue*); $H = 1.65$ μm (*green*); $K = 2.2$ μm (*red*).

We also used the OSIRIS high-resolution spectroscopic mode to obtain moderate-resolution ($R = 1500$ for a 4 pixel slit) spectra of LBV 1806-20 and three nearby stars (B, C, and D in Fig. 1). This group of stars, approximately $12''$ west of LBV 1806-20, appears to be a cluster of young, hot, luminous

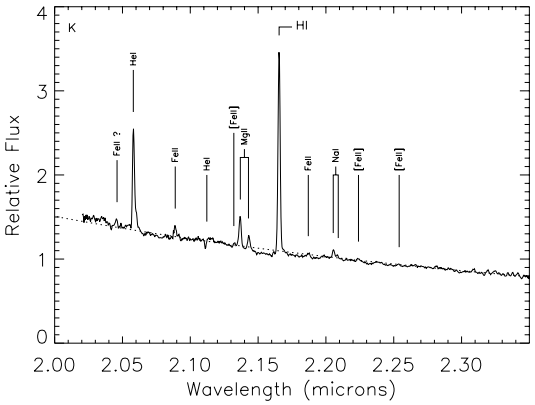

FIG. 2.—Near-infrared spectrum of LBV 1806-20 in the K band, dereddened with $A_V = 29$ mag, following the reddening law of Rieke & Lebofsky (1985). The dotted line indicates the spectral shape of a blackbody with $T > 12,000$ K. The spectrum closely resembles that of the Pistol star and AG Car and is typical for LBVs at this wavelength.

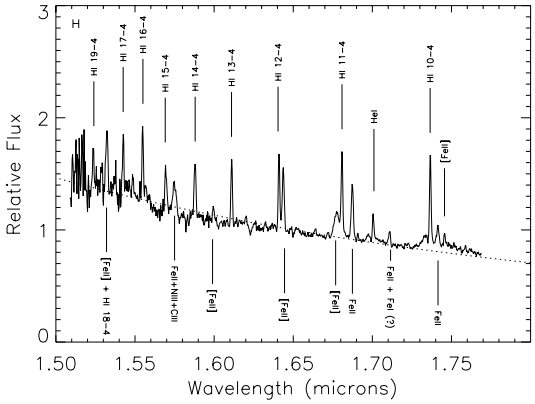

FIG. 3.—Same as Fig. 2, but for the H band. The emission lines are primarily due to the Brackett series and Fe II.

stars in the same molecular cloud as the candidate LBV star, and this cluster seems to include the candidate (Fuchs et al. 1999). At the estimated distance of 15.1 kpc (Corbel & Eikenberry 2004), this angular separation corresponds to a physical distance of only $\sim$1 pc between the candidate LBV star and the center of the cluster, implying a common origin. Thus, we chose the three brightest stars near the center of the association for spectroscopic observation. We oriented the OSIRIS slit to obtain spectra simultaneously of LBV 1806-20 and star B, and separately to obtain simultaneous spectra of stars C and D. We used the high-resolution slit of OSIRIS (4 pixels = 0.″67) and took 6×120 s exposures at positions offset along the slit. After each set of six exposures, we obtained a set of six spectra of the nearby G dwarf star HR 6998, with approximately the same positions along the slit. We repeated this approach for two different grating settings for each of the K and H bands and one grating setting for LBV 1806-20 in the J band. For both the science targets and the G star, we took each spectral frame, subtracted a dark frame from it, divided by its own median, and median-combined the six resulting images for a given grating tilt to create a normalized sky frame. We then subtracted a dark frame and a scaled sky frame from each image and divided by a spectral dome flat. We extracted spectra separately from each processed image with a Gaussian weighting in the spatial direction and tracking the curvature of the spectrum in the dispersion direction. We then divided each target spectrum by the G star spectrum with the nearest position on the slit to remove atmospheric absorption bands, after interpolating over the Brackett absorption features in the G star spectrum. We obtained a wavelength solution separately for each spectrum using the OH lines nearby on the sky (typical residuals $<$20 km s^{-1} in velocity space) and used this to correct each spectrum to a common wavelength scale before averaging the spectra to a single final spectrum. For the H and K bands, we averaged the two spectra from the different grating tilts where they overlapped. We multiplied the result by a 5600 K blackbody spectrum (corresponding to the temperature of HR 6998) and dereddened them for $A_V = 29$ mag (see below for further discussion on the reddening). We present these spectra in Figures 2–6.

2.2. *Hartung-Boothroyd Observatory—2001 July*

Because of the nonphotometric conditions during the CTIO observations, we were unable to photometrically zero-point–calibrate the images obtained at that time. Thus, we post-calibrated these images using observations of stars in the field of LBV 1806-20 and infrared standard stars on 2001 July 27 with the Hartung-Boothroyd Observatory 0.65 m telescope and its infrared array camera (J. R. Houck & M. R. Colonno 2004, in preparation), as well as with photometry from the Two Micron All Sky Survey (2MASS). We took seven images of the field of LBV 1806-20 in each band, with offsets of $\sim$15″ between images. We then processed the images in each band as described for the CTIO data above. We repeated this procedure on sets of seven images of the United Kingdom Infrared Telescope (UKIRT) standard FS26 in each band. We extracted the flux in ADU s^{-1} from each processed image of FS26 individually, using the average as the best estimate of the flux and the standard deviation divided by the square root of the number of exposures as the 1 σ uncertainty. We then used the known magnitudes of this star to calibrate similarly derived flux measurements and uncertainties for several bright stars in the field of

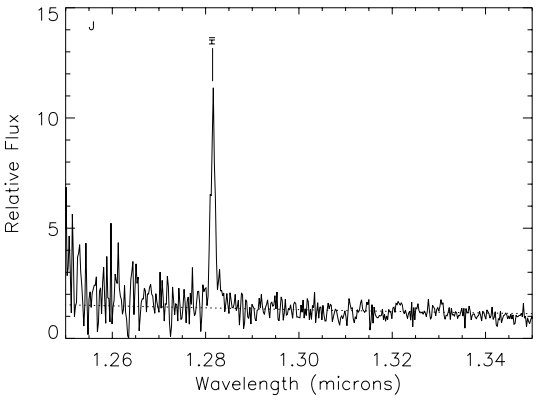

FIG. 4.—Same as Fig. 2, but for the J band. The single strong emission line is Paβ.

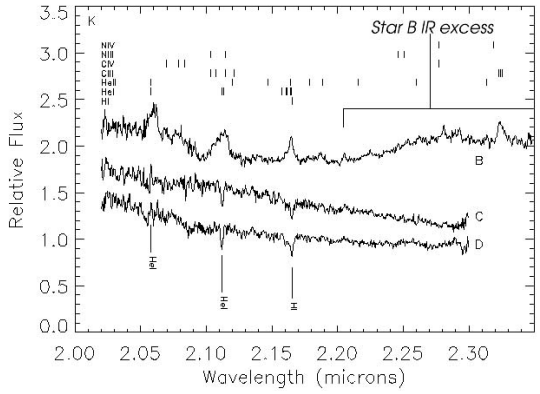

FIG. 5.—Near-infrared spectra of stars B, C, and D in the *K* band. All spectra have been dereddened with $A_V = 29$ mag, following the reddening law of Rieke & Lebofsky (1985), and the spectra of stars B and C are vertically shifted for clarity. Star B shows a bumpy continuum with a red excess along with broad blended helium, carbon, and nitrogen emission lines typical of dusty late WC-type Wolf-Rayet stars. Stars C and D both show blue continua with He I 2.112 μm and H I (Brγ) in absorption, typical of late O- or early B-type supergiants. Stars C and D also show some indications of He I 2.058 μm in emission/absorption, possibly a self-absorbed P Cygni profile.

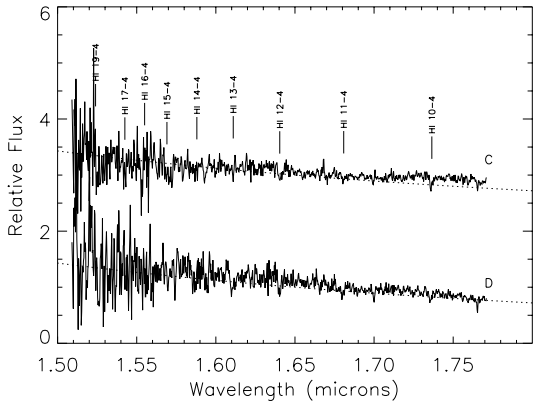

FIG. 6.—Near-infrared spectra of stars C and D in the *H* band, dereddened with $A_V = 29$ mag, following the reddening law of Rieke & Lebofsky (1985). The dotted lines indicate the spectral shape of a blackbody with $T > 12{,}000$ K. The relatively poor spectral quality is due to a combination of poor observing conditions and the reddening toward these stars.

LBV 1806-20. Differential photometry between these stars and the target stars provided the final photometric measurements. We used a photometric air mass solution derived from measurements of a star observed for another program over a range of air masses throughout the same night. We then verified this photometry with the 2MASS photometry for the *J* and *H* bands (omitting *K*, as 2MASS uses the K_s filter). We present the resulting photometry for the bright stars of Figure 1 in Table 1.

2.3. *Palomar—1999 July*

We obtained high angular resolution speckle imaging of LBV 1806-20 in 1999 June using the Palomar 5 m telescope. We used the facility near-infrared camera D78 with reimaging fore-optics providing a pixel scale of 0.″036 (±0.″001) pixel^{-1} to obtain *K*-band images of the star with 0.125 s exposures, effectively freezing the effects of image motion due to atmospheric turbulence. We observed LBV 1806-20 in six sets of 50 s on-target integrations, interleaved with observations of two nearby stars with similar near-infrared brightnesses taken in an identical manner. We used a "shift and add" technique to combine images of the individual stars: for each star (LBV 1806-20 and the two comparison stars) we shifted the images to align the brightest speckle in each frame with other frames and added the results. We used these nearby stars to create the model point-spread function (PSF), which was seen to have a FWHM of 0.″130—near the telescope's diffraction limit of 0.″110 at this wavelength. We then scaled the amplitude of this model PSF and subtracted it from the shifted and added image of LBV 1806-20. We also used Fourier filtering to remove a periodic diagonal pattern due to clocking noise in the camera electronics. Figure 7 shows an image of LBV 1806-20 and the resulting PSF-subtracted image. While the residuals in the subtracted image are statistically significant, they may be due to systematic effects, such as subpixel errors in image registration or secular small-scale variations in the speckle PSF, possibly due to low-level instability in the time-averaged properties of the speckle halo. For comparison, we also show simulated PSF-subtracted images of a theoretical extended source with a very small size (0.″06 FWHM). To simulate this source, we took the comparison star PSF and convolved it with a two-dimensional Gaussian profile with a width corresponding to the extended source intrinsic width. We then added noise corresponding to the photon noise in the LBV 1806-20 image to the resulting simulated image and then subtracted a scaled version of the single-star PSF as above. Note that the resulting simulations have residuals much greater than those for the actual PSF-subtracted image.

3. ANALYSIS

3.1. *Spectral Analysis*

3.1.1. *LBV 1806-20*

On the basis of the spectra in Figures 2–4, we present measured equivalent widths for emission and absorption lines from LBV 1806-20 in Table 2. The line features evident in the *K*-band spectrum of LBV 1806-20 (H I, He I, Fe II, Mg II, and Na I) are very similar to those observed in LBV stars such as AG Car (Morris et al. 1996), the Pistol star in the Quintuplet (Figer et al. 1998), and the LBV candidate star 362 also in the Quintuplet (Geballe et al. 2000; and at lower resolution from this same star in 1994; van Kerkwijk et al. 1995). The equivalent widths of the Fe II, Mg II, and Na I features are very close also, although the H I and He I lines are generally stronger in LBV 1806-20. P Cygni also displays a similar *K*-band spectrum (Smith 2001), although with an apparent absence of Na I emission. In the *H* band, LBV 1806-20 seems like a cross between P Cygni and the Pistol star, with 10 strong Brackett series lines and nine Fe II emission lines. While the Pistol star and AG Car exhibit similar iron features, their Brackett series lines are much weaker than seen in LBV 1806-20. P Cygni, on the other hand, shows strong Brackett series with weaker Fe II. Thus, while the spectrum of LBV 1806-20 does not uniquely match any particular LBV, its properties are well within the range exhibited by these stars. Thus, we conclude that on the basis of its spectrum LBV 1806-20 is in fact a LBV candidate, in confirmation of van Kerkwijk et al. (1995).

TABLE 1
PHOTOMETRY OF STARS

Star	*J* Band (1.25 μm) (mag)	*H* Band (1.65 μm) (mag)	*K* Band (2.2 μm) (mag)
LBV 1806-20	13.93 (8)	10.75 (5)	8.89 (6)
B	17.79 (28)	13.46 (5)	10.50 (6)
C	16.38 (8)	12.76 (5)	10.80 (6)
D	16.02 (8)	12.84 (8)	11.11 (9)

NOTE.—Values in parentheses indicate uncertainties in the final listed digit.

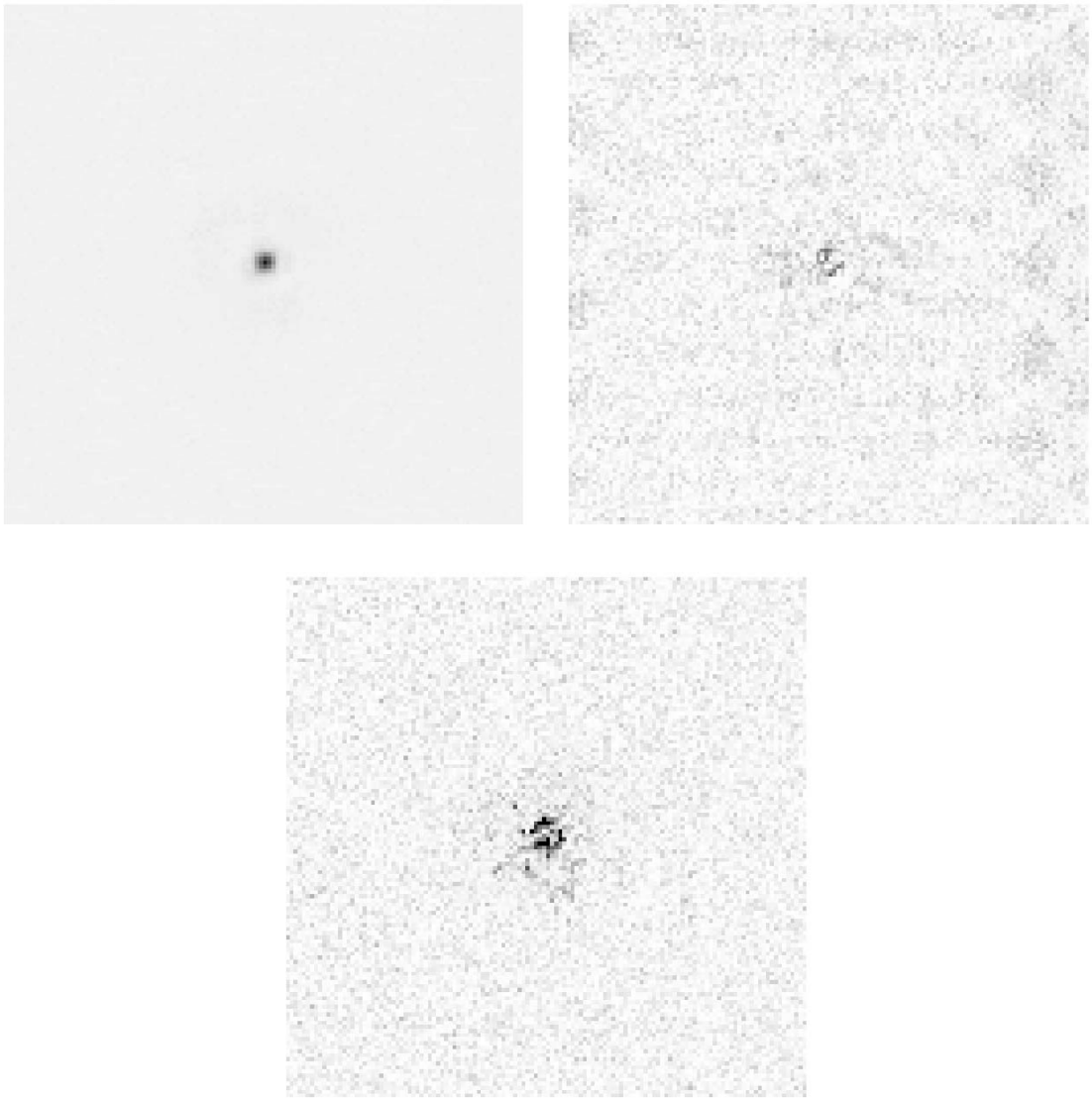

FIG. 7.—High-resolution speckle images of LBV 1806-20 in the *K* (2.2 μm) band taken at the Palomar 5 m telescope on 1999 June 30. *Top left:* LBV 1806-20 taken with a 0.″036 pixel^{-1} scale (4.″6 field of view) and a stretch from 0 (sky background) to the maximum of the image. This image has a FWHM of 0.″130, near the telescope diffraction limit of 0.″110. *Top right:* Difference between the image of LBV 1806-20 and two PSF reference stars, with a stretch from 0 (sky background) to 15 times the rms noise level (~0.005 times the peak in the top left image). *Bottom:* Residuals to a simulated cluster with a Gaussian profile of FWHM = 0.0039 pc, with the same stretch as the top right image. Note that residuals for such a cluster significantly exceed the actual observed residuals, indicating that LBV 1806-20 is not a cluster of stars.

TABLE 2
SPECTRAL LINES IN LBV 1806-20

Line Identification (1)	Wavelength (Å) (2)	Centroid (Å) (3)	W[a] (Å) (4)	ΔV[b] (km s^{-1}) (5)	Comment (6)
H I (Paβ)	12817	12816	−82 (5)	167	
H I (Br19-4)	15260	15241	−2.0 (9)	...	
Fe II and H I (Br18-4)	15330, 15341	15322	−4.6 (9)	197	Blend
H I (Br17-4)	15439	15425	−1.1 (6)	...	Broad P Cygni?
H I (Br16-4)	15557	15550	−6.9 (5)	...	
H I (Br15-4)	15701	15691	−6.4 (4)	189	
Fe II and N III and C III		15750	−7.2 (4)	...	Blend
H I (Br14-4)	15880	15880	−7.5 (5)	168	
Fe II		15993	−1.7 (3)	115	
H I (Br13-4)	16109	16110	−5.4 (3)	60	
H I (Br12-4)	16407	16404	−8.1 (3)	...	Blend
Fe II	1.6435	16444	−7.7 (3)	178	
Fe II	16768	16768	−6.7 (3)	...	Blend
H I (Br11-4)	16806	16816	−11.0 (3)	...	Blend
Fe II	16873	16874	−8.4 (4)	210	Structure?
He I	17003	17009	−3.5 (3)	0	P Cygni?
Fe I and Fe II (?)		17110	−1.60 (16)	122?	Blend?
H I (Br10-4)	17362	17365	−11.7 (2)	40?	P Cygni?
Fe II	17414	17415	−3.4 (2)	245?	Blend?
Fe II	17449	17456	−1.9 (2)	...	
Fe II (?)	20460	20460	−0.7 (3)		
He I	20581	20581	−17.4 (3)	100	Structure?
Fe II	20888	20888	−2.58 (19)	147	Blend?
He I	21121	21122	0.76 (17)	...	Blend
Fe II	21327	21321	−0.97 (12)	...	
Mg II	21368	21369	−7.20 (12)	174	
Mg II	21432	21429	−3.65 (12)	193	
H I (Brγ = Br7-4)	21655	21655	−44.2 (3)	159	
Fe II	21878	21870	−1.14 (11)	...	Blend
Na I	22056	22054	−2.38 (16)	...	
Na I	22083	22091	−0.95 (13)	...	
Fe II	22237	22240	−1.22 (10)	...	
Fe II	22534	22540	−0.41 (11)	...	

NOTE.—Col. (2): rest wavelength (in air); col. (3): observed line centroid wavelength (in air); col. (4): equivalent width; col. (5): line FWHM converted to Doppler velocity.

[a] Equivalent widths, with negative values indicating emission and positive values indicating absorption. Values in parentheses indicate uncertainties in the final listed digit.

[b] Line widths reported result from taking the measured line width and subtracting the instrumental response function in quadrature. The instrumental response was determined from OH sky lines expected to be free from blending.

The He I 2.112 μm absorption line provides important information on the temperature of LBV 1806-20. In 1994, the equivalent width of this line was 1.8 ± 0.4 Å (van Kerkwijk et al. 1995), consistent with spectral classes O9–B2 of supergiant stars (Hanson et al. 1996), indicating a surface temperature of 18,000–32,000 K.[13] The large range in temperature is due to the large scatter in this relationship (Hanson et al. 1996). By the time of the 2001 July observations, the equivalent width of the line had dropped to 0.76 ± 0.17 Å. Changes in the spectral type to hotter (O6.5–O8.5) surface temperature would produce such a reduction in the He I absorption line equivalent width (Hanson et al. 1996). Moreover, at the same time, we see a factor of ~4–6 increase in the equivalent width of emission lines such as Brγ and He I 2.058 μm, which could reflect an increase in the number of ionizing photons produced by the star as it moved to higher temperatures. However, such a temperature change might also imply a significant brightening in the K band (given a constant photospheric radius), contrary to the observations. In fact, our K-band photometry for LBV 1806-20 is marginally fainter than that of Kulkarni et al. (1995; $K = 8.4$ mag, with no quoted uncertainty). We can find an alternate solution that keeps the K-band brightness constant while decreasing the He I absorption and increasing the number of ionizing photons, by assuming that the photospheric radius decreases significantly as temperature increases. Simple calculations for a blackbody spectrum show that a change of temperature from 20,000 to 26,000 K (roughly B1.5–B0) accompanied by a ~25% decrease in photospheric radius could produce the observed behavior. Such anticorrelated variations in temperature and radius are characteristic of some LBV stars (Humphreys & Davidson 1994; Morris et al. 1996). Alternately, the stronger lines might indicate an increase in the stellar wind density absorbing more ultraviolet continuum photons and converting them into increased line

[13] We note that it is conceivable that the temperature–equvalent width relation for supergiants (which has rather large scatter) does not apply to candidate LBV stars. However, independent temperature measurements for the Pistol star (Figer et al. 1998) are consistent with the temperatures derived from its He I 2.112 μm absorption feature, indicating that this approximate relationship seems to continue to hold for candidate LBV stars.

emission. However, without detailed models of the atmosphere of LBV 1806-20, we can only conclude that it has a spectral type between O9 and B2.

3.1.2. *Star B*

From the color of star B in Figure 1, we can immediately see that it differs significantly from the other stars in the field because of its extreme redness ($J - K = 7.3$ mag vs. $J - K < 6.0$ mag for other stars). In addition, the emission-line spectrum (Fig. 5) differs significantly from LBV 1806-20, showing relatively weak Brγ and strong blended emission from He I, He II, C III, C IV, N III, and N IV. This *K*-band spectrum is typical for late-type Wolf-Rayet stars of the WC subclass, and comparison of the equivalent widths of these lines with other similar stars (Figer et al. 1997) gives a classification of WC9. The long wavelength excess in the continuum indicates the presence of warm dust with a thermal continuum extending into the near-infrared—another common feature in WCL (late-type WC) stars, which also explains the very red colors of this object. We should note that only 26 such WCLd (dust emission) stars are known at this time (van der Hucht 2001), making this a rather rare star.

3.1.3. *Stars C and D*

The next brightest stars in the cluster center, C and D, have similar colors to LBV 1806-20, with $J - K = 5.6$ mag and $J - K = 4.9$ mag, respectively. In their *K*-band spectra, both stars show Brγ and He I 2.112 μm absorption features. They also seem to show some sort of feature at the He I 2.058 μm line. This could be due either to a self-absorbed (nascent P Cygni) line or else to poor subtraction of a nearby strong OH sky line. On the basis of their strong He I 2.112 μm absorption lines, both of these stars would seem to have spectral classes in the range from B0 to B3 supergiants (Hanson et al. 1996). However, in both of these absorption lines, as well as the stronger of the Brackett series lines in the *H*-band spectra for these stars, we see some evidence for absorption wings (Fig. 6). Fits to these lines give velocity widths of greater than 200 km s^{-1} FWHM (after subtraction of the instrumental line widths), although some of these lines are potentially blended (particularly Brγ with nearby He lines). Such broad absorption wings are typical of the luminous blue hypergiants (luminosity class Ia+) and may indicate the presence of a mass-losing wind (de Jager 1998). Thus, we conclude (for the time being) that stars C and D are B0–B3 supergiant or hypergiant stars.

3.2. *The Reddening toward LBV 1806-20*

The colors of LBV 1806-20 and its spectral continuum shape allow us to estimate the extinction toward LBV 1806-20. For such a hot star (as indicated by the He I 2.112 μm absorption feature), the intrinsic $J - K$ color is nearly neutral, and the observed red color of $J - K = 5.0 \pm 0.15$ mag corresponds to an extinction of $A_V = 28 \pm 3$ mag (assuming the Rieke-Lebofsky reddening law; Rieke & Lebofsky 1985), matching the estimates based on CO observations (Corbel & Eikenberry 2004). (While a hypothetical infrared excess from LBV 1806-20 would alter these conclusions, as we discuss below there is good reason to believe that this is not present). Furthermore, the fact that stars C and D in the nearby cluster have very similar $J - K$ colors (as can also be seen for many other cluster stars' colors in Fig. 1) indicates that the stellar cluster is indeed at the same reddening and thus distance along the line of sight as LBV 1806-20, confirming the physical association between them (see also Eikenberry et al. 2001). In addition, the *H* and *K* bands are in the Rayleigh-Jeans portion of the blackbody emission curve for such a hot star (the reason for the neutral colors noted above). Thus, we can estimate the extinction toward LBV 1806-20 by dereddening the spectra until the continuum shape matches a Rayleigh-Jeans distribution. In this way, we obtain estimates of $A_V = 31 \pm 3$ mag from the *H*-band continuum and $A_V = 28 \pm 3$ mag from the *K*-band continuum, with uncertainties dominated by a $\sim$10% uncertainty in the spectrograph response shape over a given order.

For the $J - K$ measurement above, adoption of the Cardelli reddening law (Cardelli et al. 1989) gives a very small change in A_V ($<$0.4 mag), and the *K*-band spectral continuum shape is similarly unaffected (change of $<$0.1 mag). In the *H* band, the Cardelli law differs from Rieke-Lebofsky more significantly, causing a difference of $\sim$1.9 mag. Taking this into account, we increase our uncertainty in that measurement to $A_V = 28 \pm 4$ mag. Combining all three, we adopt a final estimate for the extinction of $A_V = 29 \pm 2$ mag toward LBV 1806-20.

3.3. *The Distance to LBV 1806-20*

The distance to LBV 1806-20 is a major subject of Corbel et al. (1997) and Corbel & Eikenberry (2004), and we refer the reader to those papers for detailed discussion. In summary, Corbel et al. (1997) and Corbel & Eikenberry (2004) use CO spectroscopy to identify molecular clouds along the line of sight toward LBV 1806-20 and use the cloud velocities to determine kinematic distances to them. The spectra of LBV 1806-20 presented here provide important insights into the distance of the star. From the emission lines, we can measure a radial velocity of LBV 1806-20. We selected the Brγ line as a velocity fiducial, as it is the strongest line detection in the spectrum and appears to be relatively free from contamination due to blending with other strong lines. We fitted a Gaussian profile to this line, finding no significant residuals, and a centroid shifted from the atmospheric rest frame by -3 ± 20 km s^{-1}, where residuals in the spectral wavelength solution from atmospheric OH emission lines dominate the largely systematic uncertainty. After correcting for the Earth's barycentric motion and the solar system barycenter motion relative to the local standard of rest, we determine a radial velocity for LBV 1806-20 of $v_{\rm LSR} = 10 \pm 20$ km s^{-1}. Cross-checks of this velocity determination with several other strong unblended lines give consistent results for the velocity of LBV 1806-20. This velocity is important, as massive stars such as LBVs are a kinematically "cold" population and do not generally deviate significantly in velocity from their parent molecular clouds. Combined with the CO velocity maps of Corbel et al. (1997) and Corbel & Eikenberry (2004), this velocity then confirms the association of LBV 1806-20 with molecular clouds in W31 at kinematic distances of either $\sim$4 or $\sim$15 kpc, based on the Galactic rotation curve (Fich et al. 1989) and with the ambiguity being due to the near/far degeneracy of kinematic distances.

Corbel & Eikenberry (2004) also present an NH_3 absorption spectrum that uses the radio emission from LBV 1806-20 as the background source, revealing strong absorption from a molecular cloud whose velocity (in both NH_3 absorption and CO emission) places it at a near distance of 5.7 kpc, setting this as the lower limit to the distance of LBV 1806-20. This observation eliminates the "near" distance as a possibility for LBV 1806-20, leaving only the "far" distance of $d = 15.1^{+1.8}_{-1.3}$ kpc.

As a "sanity check," Corbel & Eikenberry (2004) go on to show that the observed reddening toward LBV 1806-20 combined with CO observations of clouds along the line of sight is consistent with the "far" distance and is inconsistent with the "near" distance.

On the basis of these results, we adopt the distance determination of Corbel & Eikenberry (2004) of $d = 15.1^{+1.8}_{-1.3}$ kpc. We note that an independent distance estimate for star B (below) matches this estimate and is also strongly inconsistent with the "near" distance noted above. We discuss this issue further in § 4.1.3.

3.4. *The Luminosity of LBV 1806-20*

Combining the above measurements, we then arrive at luminosity estimates for LBV 1806-20. Taking its brightness of $K = 8.89 \pm 0.06$ mag and applying an extinction correction of $A_K = 3.2 \pm 0.2$ mag (corresponding to $A_V = 29 \pm 2$ mag and $A_K = 0.112A_V$; Rieke & Lebofsky 1985) and a distance modulus of 15.9 ± 0.2 mag (from $d = 15.1^{+1.8}_{-1.3}$ kpc), we arrive at an absolute K magnitude of $M_K = -10.2 \pm 0.3$ mag. The absolute visual magnitude and bolometric luminosity of LBV 1806-20 from this number are functions of the star's spectral class and also may be affected by free-free contributions to the K-band emission of LBV 1806-20. As discussed below, we do not believe that this contribution is large for LBV 1806-20 (it is <0.1 mag for the Pistol star as well), and we include it as an additional 0.1 mag uncertainty in the lower bound for the absolute K-band magnitude, for which we now adopt $M_K = -10.2^{+0.4}_{-0.3}$ mag. For a spectral class of O9, the upper end of the range, we have $V - K = -0.8$ mag to give an absolute visual magnitude of $M_V = -11.0^{+0.4}_{-0.3}$ mag. The bolometric correction is BC $= -3.2 \pm 0.2$ mag, giving a bolometric magnitude of $M_{\rm bol} = -14.2^{+0.5}_{-0.4}$ mag, or a luminosity of $\sim 4 \times 10^7\ L_\odot$. At the low end of the temperature range (B2 spectral type), the corresponding values are $M_V = -10.6^{+0.4}_{-0.3}$ mag, $M_{\rm bol} = -12.0^{+0.5}_{-0.4}$ mag, or a luminosity of $\sim 5 \times 10^6\ L_\odot$. We have plotted these temperature/luminosity values in Figure 8, along with the corresponding locations of other known extremely luminous stars. Note that even for the lower end of the possible temperature range for LBV 1806-20, it has a luminosity equal to or greater than that of the famous LBV η Car (Hillier et al. 2001) and the Pistol star (Figer et al. 1998). Thus, it seems that LBV 1806-20 may (marginally) be the most luminous star currently known.

3.5. *The Absolute Magnitude and Distance of Star B*

Given the photometry, distance estimate, and reddening above, we can also arrive at an absolute magnitude for star B. If we assume that the reddening toward star B is identical to that for LBV 1806-20 and a distance of 15.1 kpc, the absolute K-band magnitude for this star is $M_K = -8.6 \pm 0.3$ mag. Note that this is in excellent agreement with the range of absolute magnitudes for WC9 stars in the Galactic center ($M_K = -8$ to -11 mag; Blum et al. 2003). Furthermore, the observed $H - K$ colors of star B are consistent with the assumed reddening if the intrinsic colors are $H - K \sim 1.1$ mag, also in excellent agreement with the observed range of intrinsic colors of other WC9 stars ($H - K = 0.9$ to 1.6 mag; Blum et al. 1996).[14]

[14] We note that there is not always a one-to-one mapping between infrared and optical spectral classifications of W-R stars, which might suggest some uncertainty here. However, we are using an infrared spectral classification of star B to compare its infrared properties with other infrared-classified WC9 stars here. Therefore, we conclude that this comparison should be relatively free from any confusion due to differing optical/infrared classifications.

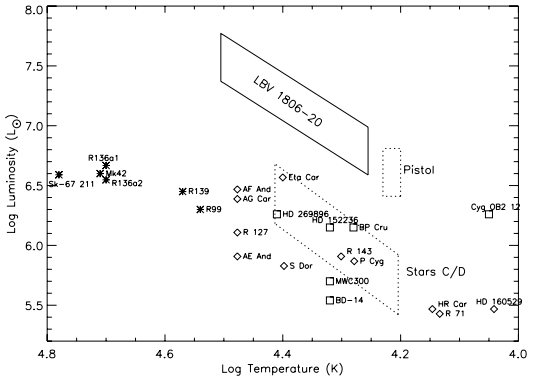

FIG. 8.—Hertzsprung-Russell diagram including LBV 1806-20 and other hot luminous stars. Diamonds indicate candidate LBV stars, squares indicate Ia+ hypergiants, asterisks indicate O-type supergiants, and regions indicate the locations of LBV 1806-20, stars C and D, and the Pistol star. Uncertainties in the temperatures of LBV 1806-20 and stars C and D dominate the uncertainty in their luminosities. Note that even at the lowest temperature, the luminosity of LBV 1806-20 exceeds that of the famous LBV η Car and overlaps the upper end of the Pistol star's luminosity range. The allowed luminosity/temperature range of stars C and D includes several known blue hypergiants, further reinforcing their identification as such stars based on luminosity and spectral features.

Thus, the spectral classification and photometry of star B confirm the distance and reddening estimates used for the luminosity of LBV 1806-20 above.

Taking a slightly different approach, we can use the observed range of intrinsic colors and absolute magnitudes for WC9 stars to constrain the distance to star B and provide a completely independent cross-check on the distance to the cluster of stars including LBV 1806-20. The intrinsic color range of Blum et al. (1996) combined with the observed $H - K = 2.96 \pm 0.08$ mag and the Rieke-Lebofsky reddening law gives a range of 3.6 mag $> A_K >$ 2.8 mag. Combining this with the observed range of M_K (Blum et al. 2003) for Galactic center WC9 stars and the observed $m_K = 10.50 \pm 0.06$ mag gives a range for the distance modulus to star B of $m_d = 14.9$ mag (low luminosity, intrinsically blue, high reddening) to 18.7 mag (high luminosity, intrinsically red, low reddening). Thus, a lower limit on the distance of star B is $d > 9.5$ kpc, assuming it is no fainter than the intrinsically faintest known WC9 star in the Galactic center (an assumption confirmed by the recent discovery of another, even fainter WC9 star in this same cluster (J. L. LaVine, S. S. Eikenberry, & J. D. Smith 2004, in preparation). Note that at an alternate assumed distance of $\sim$4 kpc (consistent with the G10.2-0.3 cluster of Blum et al. 2001), star B would be 6 times less luminous than any other known WC9 star, which seems very unlikely (especially given the even fainter WC9 of J. L. LaVine et al. 2004, in preparation). Thus, this provides yet another independent confirmation that these stars lie in the "far" component of W31 at $d = 15.1^{+1.8}_{-1.3}$ kpc, as opposed to the "near" component observed by Blum et al. (2001).

3.6. *The Luminosities of Stars C and D*

The same analyses applied to LBV 1806-20 can also provide luminosity estimates for stars C and D. On the basis of their strong He I 2.112 μm absorption lines, both of these stars have spectral classes in the range from B0 to B3 (Hanson et al.

1996). Following the analyses for LBV 1806-20 (above), at the distance of 15.1 kpc, for a B1 spectral class, they would have bolometric luminosities of $\sim 1.6 \times 10^6$ and 1.4×10^6 $L_\odot$, respectively. These luminosities are too high for "normal" supergiant stars of this spectral type. However, these luminosities are similar to those observed in early B hypergiants (luminosity class Ia+; de Jager 1998) (see Fig. 8). Furthermore, hypergiants are distinguished from "normal" supergiants by the presence of broad absorption lines indicative of mass loss through a wind, much as we see in the greater than 200 km s^{-1} line widths of the Brackett and He I absorption features in stars C and D (although, as noted above, line blending may have a nonnegligible effect for these lines at this resolution). Therefore, the luminosity and spectral features of stars C and D appear to support their identification as class Ia+ blue supergiants at the same distance and reddening as LBV 1806-20.

Furthermore, if we take the same reddening and distance used for LBV 1806-20, we derive absolute magnitudes of $M_K = -8.3 \pm 0.3$ mag and $M_K = -8.0 \pm 0.3$ mag, respectively, for stars C and D, without reference to (potentially uncertain) bolometric correction. We note that there are several luminous stars in the Galactic center with similar effective temperatures (i.e., stars IRS 16SW and IRS 16NE; Najarro et al. 1997) and absolute magnitudes of $M_K = -7.5$ to -8.0 mag, in excellent agreement with stars C and D. While the IRS 16 stars are emission-line objects and stars C and D are absorption-line objects, we can at least see that the absolute magnitudes of the brightest B-type stars in this cluster are consistent with the brightest B-type stars in the Galactic center. This supports at least the *consistency* of the distance and reddening estimates used for LBV 1806-20. Finally, we note that in a cluster such as this, it seems quite likely that some of the brightest stars are in fact binaries, given the large fraction of binarity in high-mass stars. Thus, by selecting the brightest stars in this cluster for spectroscopy, we may be biasing ourselves toward binary stars with apparent luminosity excess (see below for a more detailed discussion of multiplicity in LBV 1806-20).

4. DISCUSSION

4.1. *Caveats to the Luminosity Estimate for LBV 1806-20*

4.1.1. *Near-Infrared Excess*

One issue for the above luminosity estimate is that LBV 1806-20 might exhibit a near-infrared excess of continuum emission due to warm circumstellar dust (as star B does), free-free emission in the LBV wind, or other processes. Such an IR excess would interfere with our luminosity estimate in several ways. First, it would artificially enhance the *K*-band brightness of the star and thus directly cause us to overestimate the luminosity of LBV 1806-20. Second, it would artificially decrease the apparent equivalent width of the He I 2.112 μm absorption feature, causing us to misestimate the star's temperature and thus its bolometric correction. Finally, it would redden the colors and spectral continuum shape of candidate LBV 1806-20, causing us to overestimate the reddening correction for the star. Thus, we see that the hypothetical presence of such an excess could significantly alter our luminosity estimate.

However, careful inspection of the observational results gives no evidence for such an excess and provides several indications against its existence. First of all, as we noted above and as can be seen in Figure 1, there are several stars near LBV 1806-20 with very similar *JHK* colors. If LBV 1806-20 has a significant near-IR excess, then we must also postulate that the majority of the bright stars in/near the cluster also have significant (and virtually identical!) excesses. This is extremely unlikely if not positively unphysical. Second, the spectral continuum shape in *both* the *H* and *K* bands is consistent with a reddened Rayleigh-Jeans distribution for LBV 1806-20 (as well as stars C and D). On the other hand, the spectral continuum shape in star B clearly reveals its near-IR excess (likely due to warm dust). Therefore, for an excess to be present in LBV 1806-20, it must extend smoothly over at least the entire *H* and *K* bands, thereby significantly altering the observed colors of the star. This conflicts with the observed color match with other cluster stars noted above.

We also note that the LBV stars that most closely resemble LBV 1806-20 in their emission-line spectra, AG Car and the Pistol star, do not show large free-free emission contributions in this wavelength range. The free-free contribution of the Pistol star in the *K* band is negligible for models of the spectral energy distribution (Figer et al. 1998) and estimated to be less than 0.1 mag (D. Figer 2002, private communication), while in AG Car the inferred *K*-band contribution is $\sim$0.2 mag (McGregor et al. 1988). While AG Car *does* exhibit mid-IR excess emission, it does not contribute significantly at wavelengths $\lesssim$10 μm.

Finally, we note that the supposed dilution of the He I absorption feature by a large (e.g., >50%) near-IR excess would imply an intrinsic equivalent width greater than 4 Å (for an IR excess equal to the blackbody continuum in the *K* band). However, the temperature range we infer for LBV 1806-20 is near the maximum strength of this line. In fact, *none* of the stars in the census of Hanson et al. (1996) have equivalent widths greater than 3 Å. Thus, the presence of significant dilution of this line by an IR excess would make its spectrum inconsistent with any known type of star.

For all of these reasons, we conclude that LBV 1806-20 does not exhibit any *significant* near-IR excess emission over that expected for a reddened blackbody. By "not significant," we mean here that the contribution of any IR excess is not large compared to the other uncertainties in our measurement of the star's luminosity ($\sim$0.4 mag). However, as noted in § 3.4, we have added an additional 0.1 mag of uncertainty to the lower bound for LBV 1806-20, based on a possible expectation of this level of free-free emission as observed in the similar Pistol star.

4.1.2. *Temperature*

The issue of the precise temperature for LBV 1806-20 is a difficult one. At a crude level, the spectral continuum shape in the *H* and *K* bands gives us a firm lower limit of $\sim$12,000 K, below which we would see spectral curvature away from a Rayleigh-Jeans law, contrary to the observations. However, our primary indicator for the temperature of the star is its He I 2.112 μm absorption feature. The simple presence of this line also indicates an effective temperature greater than 12,000 K (Hanson et al. 1996). Assuming the relation found between temperature and equivalent width for supergiant stars gives the temperature range from 18,000 to 32,000 K, as noted above. The case of the Pistol star seems to confirm that this relationship extends to some candidate LBV stars also (Figer et al. 1998).

The variability of this line in LBV 1806-20 unfortunately complicates the matter. As noted above, a change in the stellar temperature to either greater or smaller values could produce

the observed reduction in equivalent width. It has been argued (Humphreys & Davidson 1994) that LBVs have essentially constant bolometric luminosities and that their apparent brightness variations are due to anticorrelated radius/temperature variations induced by their near-Eddington radiative instability. Thus, a star can experience an increase in temperature with a simultaneous decrease in radius, keeping the bolometric luminosity constant but significantly altering its apparent brightness at wavelengths near the peak of the blackbody spectrum. The observed decrease in the He I line from LBV 1806-20 could represent such a temperature/radius change. The timescale of this change—several years—is in keeping with the observed timescales for similar changes in other candidate LBV stars. Assuming constant bolometric luminosity with an increase in temperature, observations in the Rayleigh-Jeans tail of the emission spectrum should follow a dependence $F_\nu \propto T^{-3}$. Thus, the possible drop by $\sim$0.5 mag between the observations of Kulkarni et al. (1995) and our observations here could indicate a temperature increase in LBV 1806-20 by $\sim$10%, with a corresponding decrease in He I equivalent width. Also note that if the He I decrement were due to a temperature *decrease* to 12,000–14,000 K (and corresponding radius *increase*), we would expect an apparent *K*-band *brightening* in LBV 1806-20 by $\sim$1.0 mag, which is ruled out by the observations.

In any case, we note that our temperature estimate is based on the higher equivalent width of He I (lower temperature) and thus provides us with a lower estimate on the bolometric luminosity. Furthermore, the temperature changes hinted at by the He I variability and possible associated photometric variability described above are well within the range of our stated uncertainties in temperature. Finally, we note that a more precise determination of the temperature (and thus luminosity) of LBV 1806-20 may be possible in the future, using detailed models for the stellar spectrum as developed by Figer et al. (1998) for the Pistol star.

4.1.3. *Distance*

As noted above, the distance to this cluster is the primary subject of Corbel et al. (1997) and Corbel & Eikenberry (2004), and those papers provide detailed discussion. However, two new points are worth emphasizing here. First of all, the radial velocity of LBV 1806-20 confirms its association with the molecular clouds at $\sim$4 or $15.1^{+1.8}_{-1.3}$ kpc. It is important to note that intermediate distances are essentially ruled out, as they would require peculiar velocities of LBV 1806-20 of at least 100 km s^{-1}, which is much larger than the typical velocity dispersions for such massive stars. Secondly, the spectral types for stars B, C, and D are all consistent with their absolute *K*-band magnitudes if they (and thus LBV 1806-20) are all located at the distance of $15.1^{+1.8}_{-1.3}$ kpc given by Corbel & Eikenberry (2004). Furthermore, the observed magnitude of star B combined with the known range of absolute magnitudes for WC9 stars strongly rules out the "near" distance for this cluster of stars and independently sets a minimum distance of at least 9.5 kpc. Thus, these stars provide independent confirmation of the original distance arguments of Corbel et al. (1997) and Corbel & Eikenberry (2004), resulting in a total of three independent lines of evidence (kinematic distance plus NH_3 absorption, absolute magnitude range of star B, and IR extinction) that show that LBV 1806-20 lies at the "far" distance of $15.1^{+1.8}_{-1.3}$.

For the sake of completeness, we also consider the luminosity of star A using distance estimates that exclude the kinematic distance measurement discussed above and in Corbel & Eikenberry (2004). That leaves two major distance indicators: the ammonia absorption feature, which places LBV 1806-20 at a distance of at least 5.5 kpc, and the absolute *K*-band magnitude of star B, which places the cluster at $d >$ 9.5 kpc. Note that these two indicators are consistent with each other, as they are lower limits, and both confirm that LBV 1806-20 does not lie at the "near" kinematic distance of $\sim$4 kpc. Taking $d = 9.5$ kpc as a lower limit on the distance to the cluster, we can place lower limits on the luminosity of LBV 1806-20. For a temperature at the minimum of our range above, we have for the lower limit $L_{\rm bol} > 2 \times 10^6\ L_\odot$. At the upper end of our temperature range above, the lower limit becomes $L_{\rm bol} > 1.6 \times 10^7\ L_\odot$. We note again that these estimates ignore the kinematic information on LBV 1806-20, which places it at $\sim$15 kpc. If LBV 1806-20 were in fact to lie at $\sim$10 kpc, it would have a velocity deviation of several tens of kilometers per second from the Galactic rotation curve. We also note that J. L. LaVine et al. (2004, in preparation) have identified another WC9 star in this cluster that is $\sim$1 mag fainter than star B, which would increase the "nonkinematic" distance lower limit to $\sim$12.5 kpc, which is close to the lower end of the confidence interval for the kinematic distance estimate of Corbel & Eikenberry (2004).

We also note here that there is strong reason to believe that all of these stars (the candidate LBV, stars B, C, and D, and the soft gamma repeater SGR 1806-20) are in fact members of the same cluster. The great rarity of LBV candidates and SGRs in the Galaxy makes a chance association of two so close together very small ($<10^{-5}$ probability; Kulkarni et al. 1995). This probability is decreased even further by the fact that the measured IR extinction toward the LBV candidate matches the X-ray absorption toward the SGR (Eikenberry et al. 2001). The additional discovery of a very rare WC9d star (star B) and two OB stars (C and D), all with identical reddening, seems to further show strong evidence for the existence of a physical association of these massive stars and their remnants. Additional support comes from the mid-infrared observations of Fuchs et al. (1999), which show that all of these stars lie within an extended envelope of mid-IR emission, presumably due to hot dust in their natal molecular cloud. The work of J. L. LaVine et al. (2004, in preparation) reveals an additional two Wolf-Rayet stars (one WC9 and one WN5), as well as multiple other OB stars in this region, increasing the overdensity of massive stars here, which would seem to cement the conclusion that this is in fact a physical association of massive stars at the same distance. In fact, the surface density of very massive stars here is within a factor of a few of the most dense concentrations seen in our Galaxy, such as the Arches cluster (Figer et al. 2002).

Finally, if we exclude both the kinematic arguments above *and* the absolute magnitude of star B, the ammonia absorption feature places another lower limit on the distance to the candidate LBV 1806-20 of greater than 5.7 kpc (Corbel & Eikenberry 2004). This results in a luminosity lower limit of greater than $7 \times 10^5\ L_\odot$. Note again that this distance is problematic when one considers the measured velocity of the molecular cloud and the candidate LBV, requiring them to have peculiar velocities of $\sim$100 km s^{-1} compared to the expected Galactic rotation curve at this location—an extreme deviation considering that such massive stars are generally a "cold" population in kinematic terms. Furthermore, at this distance, star B would be approximately 4 times less luminous than any WC9 star seen in the Galactic center (and the WC9 of

J. L. LaVine et al. 2004, in preparation, would be ~12 times less luminous than any of the Galactic center WC9 stars). Thus, this distance seems incompatible with several observational facts. Nevertheless, we include this distance estimate here for completeness.

4.1.4. *Is It a Cluster or Multiple System?*

Perhaps the strongest caveat to (at least the lower limit for) the luminosity of LBV 1806-20 is the issue of the star's possible multiplicity. A proposed explanation for the observed luminosities of objects such as the Pistol star and LBV 1806-20 is that they are in fact unresolved *clusters* of luminous stars. However, our speckle observations contradict this conclusion in the case of LBV 1806-20. For a distance of 15.1 kpc, the upper limit of 60 mas on any extension corresponds to 0.0044 pc, or ~900 AU FWHM. This is more than an order of magnitude smaller than any known cluster. Thus, it is very unlikely that LBV 1806-20 is an unresolved cluster of stars.

On the other hand, OB stars in open clusters are often (>50% fraction) in binaries, implying that LBV 1806-20 may also be a binary system. Our current observations do not strictly rule out a close binary (or even triple system) as an explanation for LBV 1806-20. For a circular orbit with a ~450 AU semimajor axis and a total binary mass of ~200 $M_{\odot}$ (see below), even seen edge-on, we derive differential orbital velocities for similar-mass components of ~5–10 km s^{-1}—well below the observed line widths. Thus, it seems quite possible that LBV 1806-20 is a binary/multiple system. However, we note that even at our lower luminosity range, for equal components, each star would be approximately as luminous as η Car. For mass ratios different from 1, the more massive component would increase in luminosity from this level. Thus, even if LBV 1806-20 is in fact a binary/multiple system, we are still left with extremely luminous (and massive) stars composing the system.

Finally, the observed emission-line variability and depth of the He I 2.112 μm feature also present some possible evidence against multiplicity in LBV 1806-20. The emission lines vary by factors of several, as shown above, implying that one object is probably the dominant source of radiation in the system. On the other hand, in an ultraluminous binary (such as LBV 1806-20 would have to be), wind-wind collisions may be a significant source of line emission and thus explain the large-amplitude variability in this context. The observed depth of the He I absorption line is less easy to explain away. The depth of this line is such that either one component has a weaker feature and the other star has the deepest such absorption feature known (to compensate) or both stars have nearly equally deep absorption features. While this latter seems somewhat unlikely, it is still possible. Therefore, we conclude that the issue of multiplicity in LBV 1806-20 remains an open question.

4.2. *The Mass of LBV 1806-20*

If we assume that LBV 1806-20 is in fact a single star, its luminosity provides a current mass estimate, assuming that the star radiates at its Eddington luminosity where radiation pressure at the surface matches the star's gravity. At the lower end of the luminosity range for the best distance estimate ($d = 15.1^{+1.8}_{-1.3}$ kpc), we derive a minimum present-day mass of $M > 133\ M_{\odot}$, assuming $N(\mathrm{H})/N(\mathrm{He}) = 10$ (Hillier et al. 2001). Furthermore, the Eddington limit is a lower limit to the mass—realistic models of massive stars typically have $L \sim 0.6$–$0.7 L_{\mathrm{Edd}}$ (i.e., Hillier et al. 2001; Figer et al. 1998). Thus, a realistic lower limit on the mass of LBV 1806-20 in the same context as similar estimates for other massive stars is $M > 190\ M_{\odot}$. (For completeness, at the alternative distance lower limits, this mass limit becomes $M > 76\ M_{\odot}$ [$d > 9.5$ kpc, ignoring kinematic measurements] and $M > 27\ M_{\odot}$ [$d > 5.5$ kpc, ignoring the absolute magnitudes of the WC9 stars]). The following discussion assumes the mass to be greater than 190 $M_{\odot}$.

On the other hand, LBV 1806-20 may be a relatively tight binary, with a projected semimajor axis less than 450 AU (based on our speckle imaging above). If so, then the most even distribution of luminosity (which deviates most from the single-star arguments above) has each star at greater than $2.5 \times 10^6\ L_{\odot}$. Following the same arguments above based on Eddington luminosities, then each binary component has a present-day mass greater than 90 $M_{\odot}$. It is not currently clear whether this scenario is physically plausible. For instance, if during formation one of the stars ignited slightly before the other, the radiation pressure from such a luminous object so nearby might photoevaporate the second binary component. (However, as argued below, shock-induced star formation may invalidate this argument to some extent). In any case, our reliance on the Eddington luminosity for mass estimation indicates that for $L > 5 \times 10^6\ L_{\odot}$, the total system mass should be greater than 190 $M_{\odot}$.

4.3. *Comparison with the Pistol Star*

The star that most closely resembles LBV 1806-20 in spectral characteristics (see discussion above) and luminosity is the Pistol star (Figer et al. 1998). This is particularly important in that segments of the astronomical community have been slow to accept the luminosity estimates for the Pistol star, and various appeals to exceptional circumstances in the Pistol star's unique properties and location (very close to the Galactic center) are often made. However, the close match in spectral characteristics and luminosity between these two stars demonstrates that the Pistol star is not unique in its properties. Furthermore, LBV 1806-20 is located at a Galactocentric radius of ~7 kpc—nearly out to the solar circle and certainly very far removed from the Galactic center itself. This shows conclusively that the formation of very massive stars is an ongoing process in our Galaxy in the current epoch and furthermore that this process is not limited to the extreme environment of the Galactic center.

We also note that the similarity between the spectra of LBV 1806-20 and the Pistol star may indicate that LBV 1806-20 lies at the lower end of the allowed luminosity range in Figure 8. However, verification of this possibility requires higher resolution spectra and detailed modeling of the stellar atmosphere, which should be carried out as future work.

4.4. *The Ultimate Fate of LBV 1806-20*

As a result in large part of the apparent connection between supernovae and gamma-ray bursts (i.e., Price et al. 2003; Hjorth et al. 2003), there has been considerable progress in recent years concerning the end-state evolution of very massive stars. Heger et al. (2003) present final evolutionary scenarios for a wide range of stellar masses and metallicity. If we assume that LBV 1806-20 had an initial mass of ~200 $M_{\odot}$ and has near-solar metallicity, Heger et al. (2003) show that the star will end its days as an SNIb/c explosion producing a neutron star. This result is contrary to the previous "standard" assumption that all very massive stars produce black holes (or disintegrate in pair-instability supernovae) and depends on heavy mass loss

due to tremendous stellar winds to strip the stellar core bare and diminish the final core mass. Note that Gaensler et al. (2001) infer the presence of just such a strong wind from LBV 1806-20 from the radio emission of G10.0-0.3.

This result could also extend to the progenitor of SGR 1806-20—if it was only slightly more massive than LBV 1806-20, it could in fact evolve more rapidly, explode, and yet leave behind a neutron star remnant. The fact that SGR 1806-20 is not an ordinary neutron star but also an SGR and magnetar (Kouveliotou et al. 1998) and that other SGRs seem to be associated with massive star clusters (Vrba et al. 2000) may indicate that the final evolution of some very massive stars not only produces neutron stars but in fact tends to produce *highly magnetized* neutron stars.

4.5. *The Origin of LBV 1806-20 and the Cluster*

Previously, theorists have argued that stars (and implicitly tight binaries) greater than $\sim 100\ M_{\odot}$ should be impossible to form under normal circumstances at solar metallicity, because of radiation pressure on dust grains in the star-forming material, radiative heating of the accreting gas, and formation of H II regions before the complete accretion of the envelope (Bond et al. 1984). These calculations assume spherical symmetry, and the likely deviations from this symmetry (e.g., an accretion disk) will raise the upper limit on stellar masses. However, most currently published models of stellar evolution stop at ~ 100–$120\ M_{\odot}$ (i.e., Leitherer et al. 1999; Schaerer et al. 1993), at least implicitly accepting this as an upper limit to stellar masses. Thus, it would seem that the existence of LBV 1806-20 and of other massive stars (the Pistol star, R136a1, R136a2) may require some revision in our understanding of very massive star formation, particularly if they are near solar metallicity. Alternately, pressure-induced star formation due to expanding H II regions or supernova shocks presents another possible exception to the upper limit above.

This possibility is particularly intriguing given the environment of LBV 1806-20: the cluster contains both a late-type Wolf-Rayet star (star B), as well as at least one neutron star (SGR 1806-20; see Eikenberry et al. 2001). Since both of these objects are thought to be more evolved than the candidate LBV (Massey 2003; Conti 1976) and stellar evolution progresses more rapidly for more massive stars, we are left to conclude either that their progenitors were even more massive than LBV 1806-20 (which seems unlikely though not necessarily impossible; see below) or that star formation in this location did not occur at a single epoch but has been spread over time. SGR 1806-20 alone implies that at least one supernova event must have occurred previously in this region (although it is not at all certain that this particular event occurred *before* the formation of the candidate LBV star). As a consequence, it seems quite possible that the formation of LBV 1806-20 was triggered by the expanding H II regions or supernova events from prior epochs of star formation at this location, resulting in its unusually high mass. We also note the simultaneous presence of candidate LBV and W-R stars in the Quintuplet cluster (Figer et al. 1998), as well, confirming that this situation is not unique and revealing yet another similarity between LBV 1806-20 and the Pistol star.

5. CONCLUSIONS

We have presented near-infrared imaging and spectroscopy of the luminous star LBV 1806-20 and three other nearby luminous stars. On the basis of the results, we conclude that LBV 1806-20 has spectral characteristics very similar to those of AG Car, the Pistol star, and P Cyg—all luminous blue variables—and is thus likely to be an LBV itself. The nearby luminous stars B, C, and D are Wolf-Rayet WC9d and possible blue hypergiant stars forming part of a cluster that includes LBV 1806-20. Their absolute magnitudes and bolometric luminosities are consistent with other known stars with similar spectral types, confirming the distance and reddening estimates for LBV 1806-20 ($15.1^{+1.8}_{-1.3}$ kpc and $A_V = 29 \pm 2$ mag). With a surface temperature in the range 18,000–32,000 K, LBV 1806-20 has a bolometric luminosity greater than $5 \times 10^6\ L_{\odot}$. If we drop kinematic measurements of the distance ($15.1^{+1.8}_{-1.3}$ kpc), we have a lower limit on the distance of greater than 9.5 kpc and on the luminosity of greater than $2 \times 10^6\ L_{\odot}$, based on the cluster stars. If we drop both the kinematic and cluster star indicators for distance, an ammonia absorption feature sets yet another lower limit to the distance of greater than 5.7 kpc, with a corresponding luminosity estimate of greater than $7 \times 10^5\ L_{\odot}$ for the candidate LBV 1806-20. Our speckle imaging shows conclusively that LBV 1806-20 is *not* an unresolved cluster of stars, although it may be a binary/multiple system. If LBV 1806-20 is a single or multiple star, its total mass exceeds 190 $M_{\odot}$ (at the $\sim$15 kpc distance). Finally, the presence of LBV 1806-20 with more evolved stars in the same cluster (i.e., the W-R WCL star and SGR 1806-20) implies that star formation may have occurred over multiple epochs in this region of space.

The authors thank R. Blum and A. Alvarez for help in obtaining the observations at CTIO, K. Dunscombe, J. Mueller, and K. Rykoski for assistance at Palomar, and T. Herter for helpful discussions of these results. S. S. E. is supported in part at Cornell by an NSF CAREER award (NSF-9983830), and S. G. P. and D. H. were partially supported by this grant. M. A. J. was supported at Cornell by a NASA Space grant summer research fellowship, and M. A. G. was supported by a NSF REU fellowship.

REFERENCES

Blum, R. D., Damineli, A., & Conti, P. S. 2001, AJ, 121, 3149
Blum, R. D., Ramirez, S. V., Sellgren, K., & Olsen, K. 2003, ApJ, 597, 323
Blum, R. D., Sellgren, K., & DePoy, D. L. 1996, ApJ, 470, 864
Bond, J. R., Arnett, W. D., & Carr, B. J. 1984, ApJ, 280, 825
Cardelli, J. A., Clayton, G. C., & Mathis, J. S. 1989, ApJ, 345, 245
Conti, P. 1976, Mem. Soc. R. Sci. Liège, 9, 193
Corbel, S., & Eikenberry, S. S. 2004, A&A, 419, 191
Corbel, S., Wallyn, P., Dame, T. M., Durouchoux, P., Mahoney, W. A., Vilhu, O., & Grindlay, J. E. 1997, ApJ, 478, 624
de Jager, C. 1998, A&A Rev., 8, 145
Depoy, D., Atwood, B., Byard, P. L., Frogel, J., & O'Brien, T. P. 1993, Proc. SPIE, 1946, 667
Eikenberry, S. S., Garske, M. A., Hu, D., Jackson, M. A., Patel, S. G., Barry, D. J., Colonno, M., & Houck, J. R. 2001, ApJ, 563, L133
Fich, M., Blitz, L., & Stark, A. 1989, ApJ, 342, 272
Figer, D. F., McLean, I. S., & Najarro, F. 1997, ApJ, 486, 420
Figer, D. F., Najarro, F., Morris, M., McLean, I. S., Geballe, T. R., Ghez, A. M., & Langer, N. 1998, ApJ, 506, 384
Figer, D. F., et al. 2002, ApJ, 581, 258
Fuchs, Y., Mirabel, F., Chaty, S., Claret, A., Cesarsky, C. J., & Cesarsky, D. A. 1999, A&A, 350, 891
Gaensler, B. M., Slane, P. O., Gotthelf, E. V., & Vasisht, G. 2001, ApJ, 559, 963
Geballe, T. R., Najarro, F., & Figer, D. F. 2000, ApJ, 530, L97

Hanson, M. M., Conti, P. S., & Rieke, M. J. 1996, ApJS, 107, 281
Heger, A., Fryer, C. L., Woosley, S. E., Langer, N., & Hartmann, D. H. 2003, ApJ, 591, 288
Hillier, J. D., Davidson, K., Ishibashi, K., & Gull, T. R. 2001, ApJ, 553, 837
Hjorth, J., et al. 2003, Nature, 423, 847
Humphreys, R. M., & Davidson, K. 1994, PASP, 106, 1025
Hurley, K., Kouveliotou, C., Cline, T., Mazets, E., Golenetskii, S., Frederiks, D. D., & van Paradijs, J. 1999, ApJ, 523, L37
Kaaret, P., Prestwich, A. H., Zezas, A., Murray, S. S., Kim, D.-W., Kilgard, R. E., Schlegel, E. M., & Ward, M. J. 2001, MNRAS, 321, L29
Kaplan, D. L., Fox, D. W., Kulkarni, S. R., Gotthelf, E. V., Vasisht, G., & Frail, D. A. 2002, ApJ, 564, 935
Kouveliotou, C., et al. 1998, Nature, 393, 235
Kulkarni, S. R., & Frail, D. A. 1993, Nature, 365, 33
Kulkarni, S. R., Matthews, K., Neugebauer, G., Reid, I. N., van Kerkwijk, M. H., & Vasisht, G. 1995, ApJ, 440, L61
Leitherer, C., et al. 1999, ApJS, 123, 3
Macfadyen, A., Woosley, S., & Heger, A. 2001, ApJ, 550, 410
Massey, P. 2003, preprint (astro-ph/0307531)
Massey, P., & Hunter, D. A. 1998, ApJ, 493, 180
McGregor, P. J., Hyland, A. R., & Hillier, D. J. 1988, ApJ, 324, 1071
Mereghetti, S., Cremonesi, D., Feroci, M., & Tavani, M. 2000, A&A, 361, 240
Morris, P. W., Eenens, P. R. J., Hanson, M. M., Conti, P. S., & Blum, R. D. 1996, ApJ, 470, 597
Najarro, F., Krabbe, A., Genzel, R., Lutz, D., Kudritzki, R. P., & Hillier, D. J. 1997, A&A, 325, 700
Price, P. A., et al. 2003, Nature, 423, 844
Rieke, G. H., & Lebofsky, M. J. 1985, ApJ, 288, 618
Schaerer, D., Meynet, G., Maeder, A., & Schaller, G. 1993, A&AS, 98, 523
Smith, N. 2001, in ASP Conf. Ser. 233, P Cygni 2000: 400 Years of Progress, ed. M. de Groot & C. Sterken (San Francisco: ASP), 125
van der Hucht, K. A. 2001, NewA Rev., 45, 135
van Kerkwijk, M. H., Kulkarni, S. R., Matthews, K., & Neugebauer, G. 1995, ApJ, 444, L33
Vasisht, G., Frail, D. A., & Kulkarni, S. R. 1995, ApJ, 440, L65
Vrba, F. J., Henden, A. A., Luginbuhl, C. B., Guetter, H. H., Hartmann, D. H., & Klose, S. 2000, ApJ, 533 L17

Troisième partie

Conclusions et perspectives scientifiques

Conclusions et perspectives scientifiques

À quoi bon soulever des montagnes quand —
il est si simple de passer par dessus
—Boris Vian

Conclusions

Diverses questions ont été posées dans l'introduction de ce manuscrit. Il est approprié de mettre maintenant en exergue les résultats essentiels de mes travaux de recherches. L'originalité de ceux-ci résulte de l'étude simultanée de phénomènes transitoires au sein des systèmes binaires X dans toutes les longueurs d'onde.

Différents régimes d'accrétion se manifestent au sein de ces objets. Dans un état de faible accrétion – état spectral dit "dur" –, correspondant à une luminosité X inférieure à $\sim$ 10% $L_{\rm Edd}$, nous mettons en évidence l'ubiquité des jets compacts (section 2.2). Malgré leur faible luminosité radio, nous montrons que le rayonnement de ces jets est continu de la radio jusqu'à l'infrarouge proche (section 2.3). Il en résulte une forte luminosité des jets compacts, équivalente à au moins 10 % de la puissance d'accrétion (section 2.4).

Nous illustrons le couplage très fort entre les phénomènes d'accrétion et d'éjection par la mise en évidence, pour la première fois, d'une très forte corrélation entre les rayonnements radio et X (section 2.5). Nous démontrons ainsi que deux domaines de fréquences, et leurs composantes associées – jet et couronne –, pouvaient être reliés de façon très intime. Auparavant, ces composantes étaient étudiées séparément, avec parfois une occultation totale des phénomènes d'éjection. Aujourd'hui, la plupart des modèles actuels essaye d'inclure – parfois de façon ad'hoc, une composante d'émission liée à une éjection de plasma par le système.

Cette corrélation soulève, de plus, la possibilité que les jets compacts puissent contribuer à haute énergie (X/γ), contrairement au modèle standard communément accepté de la couronne d'électrons chauds. Nous avons testé le scénario d'une contribution des jets à haute énergie en appliquant un modèle de jet compact aux distributions spectrales énergétiques de GX 339−4 collectées lors de diverses campagnes d'observations. Compte tenu du caractère préliminaire du modèle de l'époque, il était satisfaisant de voir qu'il arrivait à reproduire les données spectrales de manière cohérente. Les évolutions récentes apportées à ce modèle – composante en réflexion, contribution synchrotron self-compton, ... – montrent qu'il peut maintenant répondre aux principales critiques qui lui étaient faites. De plus, il s'agit du seul modèle incluant un jet compact à se confronter aux données d'un point de vue statistique (section 2.6).

La corrélation des flux radio/X observée dans l'état dur est étendue à l'état de repos des trous noirs, où l'accrétion sur le trou noir est très réduite. Il serait envisageable que les jets compacts puissent y avoir un rôle important afin d'extraire la puissance d'accrétion du système. De plus, le ramollissement des spectres X, que nous observons lors des phases de repos, pourrait éventuellement être du à une inefficacité des processus accélérant les particules énergétiques des jets compacts (section 3.1).

Nous avons aussi établi un schéma d'unification des propriétés des jets le long des différents états spectraux X (section 3.4). En effet, si on suit l'évolution classique de l'activité d'un trou noir lors d'un sursaut, nous montrons que les jets compacts existent de la phase de repos à

l'état dur et jusqu'à l'intermédiaire dur. Lors de la transition vers l'état intermédiaire mou – habituellement associée à une accrétion proche de la limite d'Eddington –, des éjections relativistes majeures prennent naissance et peuvent apparaître superluminiques pour un observateur terrestre. Ces éjections pourraient être liées à la destruction du jet compact, qui n'est, ensuite, plus observé pendant l'état thermique (section 3.2). Il faut attendre le retour à l'état dur – lors de la décroissance du sursaut – pour observer une réapparition du jet compact jusqu'au repos. On notera que les observations historiques de Cyg X−1, présentées en introduction de ce mémoire (Figure 1.1), s'expliquent naturellement par la formation d'un jet compact lors d'une transition d'un état thermique vers un état dur.

Nous avons aussi caractérisé certaines propriétés de ces systèmes lors de la phase terminale – décroissance – du sursaut. Le retour à l'état dur est identifié par certaines propriétés très précises au niveau de l'émission X (section 3.3). La séparation réelle des différentes composantes d'émission – disque, jet et/ou couronne – est toutefois délicate.

Au delà de ces phases actives des binaires X, j'ai pu montrer que le plasma éjecté, lors des éjections discrètes, continue de voyager incognito dans le milieu interstellaire. Lors d'une collision avec une phase plus dense de ce milieu, nous observons, pour la première fois, – et cela parfois à large distance de l'objet compact – un rallumage de ces jets. La formation de tels lobes d'interaction est associée à la production de particules très énergétiques, d'énergies supérieures au TeV. D'après les résultats du chapitre 4, ce phénomène pourrait être fréquent parmi les microquasars.

J'ai récemment considéré l'extension de ces travaux à l'étude de sources extragalactiques. Tout d'abord, nous avons détecté, pour la première fois, la contrepartie radio d'une source X ultralumineuse (chapitre 5). La nébuleuse radio associée à NGC5408 X−1 est probablement formée par de puissants jets relativistes, mais demeurant invisibles à l'observateur. Nous avons, ensuite, raffiné le plan fondamental d'activité des trous noirs, qui vise à unifier les propriétés des trous noirs stellaires et super-massifs (chapitre 6). En tenant compte de la masse des trous noirs super-massifs, nous montrons qu'ils suivent la même corrélation entre les luminosités radio et X que pour les trous noirs stellaires. L'interprétation physique du plan fondamental n'est pas unique compte tenu de la diversité des sources dans les échantillons considérés. Néanmoins, il semblerait exister de très fortes similitudes entre les trous noirs stellaires à faible accrétion et les noyaux actifs de galaxie de faible luminosité (LLAGN).

Pour terminer, en prenant l'exemple de mes travaux sur SGR 1806−20 et LBV 1806−20, j'ai voulu montrer mon cheminement intellectuel de chercheur (chapitre 7). Il en résulte qu'il est nécessaire de rester à l'affût de tout nouveau résultat, même s'il concerne des domaines éloignés de mes thématiques de prédilection. J'espère toutefois que les nouveaux développements, concernant SGR 1806−20 et ses environs, ont permis d'établir avec solidité sa distance.

D'une certaine façon, je dirais que l'ensemble de mes travaux de recherche a contribué significativement à faire prendre conscience à la communauté internationale astrophysique des hautes énergies, de l'importance des diverses "saveurs" de jets – jets compacts, éjections discrètes, lobes d'interaction – dans la modélisation des binaires. La question de la contribution X/γ des jets compacts est toujours ouverte. Malgré tout, mes travaux ont permis d'illustrer, pour la première fois, la production de particules extrêmement énergétiques par des jets relativistes lors de l'interaction avec le milieu interstellaire, et la production associée de larges lobes en X. Je soulignerais, toutefois, que les jets relativistes constituent la seule composante actuellement résolue spatialement dans les trous noirs stellaires et super-massifs. Il est donc particulièrement difficile d'en faire abstraction... Il pourrait donc s'agir d'une solution naturelle à beaucoup des problèmes rencontrés.

Perspectives

Pour tester le scénario d'une éventuelle contribution des jets compacts à haute énergie, différentes possibilités s'offrent à nous. Il n'est évidemment pas envisageable de les résoudre spatialement, y compris avec les projets futurs de télescopes X. On pourrait éventuellement imaginer l'utilisation de polarimètre X – inexistant à ce jour – pour détecter un rayonnement synchrotron du jet compact, qui est par nature polarisée.

Néanmoins, l'usage de méthodes indirectes me semble actuellement la voie la plus prometteuse pour sonder les processus d'émission à haute énergie. En effet, la contribution éventuelle des jets compacts à haute énergie résulte de la mise en évidence de la corrélation des luminosités radio et X pour GX 339−4 et GS 2023+338 – ainsi que d'autres sources compatibles avec la "corrélation universelle" observée dans l'état dur. Il faudrait donc développer les travaux suivants, pour lesquels les archives actuelles sont sûrement déjà fortement intéressantes :

- Étude de corrélation des luminosités radio et X pour un large éventail de sources transitoires. Il serait important de comparer l'évolution de cette corrélation entre différents sursauts d'activité d'une même source, voire de rechercher des différences – hystérésis, changement de couplage, ... – entre les états durs initial et final. Il serait nécessaire de réaliser ces études dans différentes bandes d'énergie en X et à différentes fréquences en radio. Les quelques sources ne semblant pas obéir à cette "corrélation universelle" pourrait aussi apporter un éclairage nouveau sur les processus physiques impliqués.
- Étude de corrélation des luminosités infrarouge et X. En effet, des suivis réguliers existent actuellement en optique et en infrarouge. Une binaire X en sursaut est toujours observé quasi-quotidiennement par *RXTE*, il est donc possible de sonder la contribution du jet compact en infrarouge (indice spectral, fréquence de coupure, hystérésis, ...), tout en testant les propriétés X.
- Étude de ces corrélations pour des sources autres que les trous noirs stellaires. On pourrait citer les étoiles à neutrons pour lesquelles des travaux préliminaires semblent montrer un couplage différent – des trous noirs – entre les rayonnements X et radio. La conséquence immédiate est qu'il est peu probable que les jets compacts contribuent à haute énergie pour les étoiles à neutrons. Il est évident que l'unification avec les diverses classes de noyaux actifs de galaxie doit se poursuivre.

Une autre méthode permettant de sonder le rôle des jets consisterait à modéliser la distribution spectrale énergétique avec le modèle de jet compact mentionné au chapitre 2. À ce jour, on peut dire que ce modèle en est encore à ses balbutiements puisque l'espace des paramètres n'a été exploré que pour quelques sources à peine. Il faut donc le tester – avec les méthodes standards en astrophysique des hautes énergies – sur diverses sources et à différents niveaux de luminosités. Ce modèle – statique aujourd'hui – devra évoluer pour essayer de reproduire les évolutions observées lors des transitions spectrales. Il sera de plus primordial d'inclure les signatures temporelles très fortes – et variables – qui sont aussi une source de contraintes additionnelles.

Le modèle unifié des diverses "saveurs" de jets devra être testé plus en détail pour comprendre la nature, l'origine et les raisons des éjections discrètes, dites superluminiques. La mise en évidence de l'interaction des jets avec le milieu interstellaire apporte une nouvelle ressemblance avec les noyaux actifs de galaxie, où de tels lobes sont fréquents. Au delà des ressemblances observationnelles, il va falloir aller y chercher des contraintes additionnelles au niveau des mécanismes physiques impliqués. De plus, l'accélération de particules au TeV lors de ces collisions implique des chocs trans-relativistes qui présentent certaines similarités avec le choc en retour des sursauts gamma ou celui associé au sursaut géant de SGR 1806−20. Il y a là tout un volet observationnel qui s'ouvre, pouvant apporter d'éventuelles informations sur les mécanismes d'accélération de particules.

Ces nouvelles avancées ne pourront se faire sans de nouvelles contraintes observationnelles. Un pas décisif sera certainement franchi avec *GLAST*. En effet, par rapport à son prédécesseur – *EGRET* –, *GLAST* permettra un bond prodigieux en terme de sensibilité et de résolution spatiale. En un jour, il produira une carte du ciel γ avec une sensibilité équivalente à celle d'*EGRET* durant toute sa durée de vie – 9 ans. *GLAST* observera quotidiennement l'intégralité du ciel et sera l'instrument idéal pour repérer tout phénomène transitoire dans les γ. Il s'agira d'une phase exploratoire compte tenu de notre ignorance totale de l'émission des trous noirs stellaires à ces énergies. À plus long terme, la mission Simbol-X sera une avancée de premier plan en apportant la sensibilité et la résolution spatiale du domaine X mou dans les X durs. Il sera ainsi possible de séparer plus précisément les composantes d'émission thermique et non-thermique, ce qui sera fondamental pour différencier les différents modèles actuels. Il pourra de plus explorer sans souci le domaine peu étudié des trous noirs au repos.

Au niveau radio, cela faisait longtemps qu'il n'y avait pas de révolution observationnelle. Néanmoins, la situation évolue actuellement avec l'ouverture de la fenêtre basse fréquence. En effet, le projet *LOFAR* va explorer ce domaine avec un facteur 100 en termes de gain de sensibilité et de résolution spatiale. *LOFAR* et *GLAST* seront opérationnels simultanément. Cette excellente synergie devrait permettre d'étudier les phénomènes non thermiques de l'univers, qui se manifestent de la radio jusqu'aux gamma.

Les futurs progrès attendus dans les domaines sub-millimétrique et infrarouge moyen seront intéressants pour l'étude des jets compacts. À très long terme, des projets ambitieux comme *XEUS* ou *SKA* seront indispensables pour permettre des avancées significatives par rapport aux travaux actuels. Dans cette optique, l'exploration des environs immédiats d'un trou noir sera un objectif de tout premier chox, qui pourrait être rempli grâce à l'image directe de son ombre, ou par la mesure de sa vitesse de rotation.

Bibliographie

Angelini, L. & White, N. E. 2003, *Astrophys. J.*, 586, L71

Atteia, J.-L., Boer, M., Hurley, K., et al. 1987, *Astrophys. J.*, 320, L105

Ball, G. H., Narayan, R., & Quataert, E. 2001, *Astrophys. J.*, 552, 221

Banas, K. R., Hughes, J. P., Bronfman, L., & Nyman, L.-A. 1997, *Astrophys. J.*, 480, 607

Begelman, M. C., Blandford, R. D., & Rees, M. J. 1984, Reviews of Modern Physics, 56, 255

Begelman, M. C., King, A. R., & Pringle, J. E. 2006, *Mon. Not. R. Astron. Soc.*, 370, 399

Belloni, T. 2005, in AIP Conf. Proc. 797 : Interacting Binaries : Accretion, Evolution, and Outcomes, ed. L. Burderi, L. A. Antonelli, F. D'Antona, T. di Salvo, G. L. Israel, L. Piersanti, A. Tornambè, & O. Straniero, 197–204

Belloni, T., Homan, J., Casella, P., et al. 2005, *Astron. & Astrophys.*, 440, 207

Blandford, R. D. & Begelman, M. C. 1999, *Mon. Not. R. Astron. Soc.*, 303, L1

Blandford, R. D. & Konigl, A. 1979, *Astrophys. J.*, 232, 34

Bloom, S. D., Marscher, A. P., Gear, W. K., et al. 1994, *Astron. J.*, 108, 398

Blum, R. D., Damineli, A., & Conti, P. S. 2001, *Astron. J.*, 121, 3149

Bond, J. R., Arnett, W. D., & Carr, B. J. 1984, *Astrophys. J.*, 280, 825

Bregman, J. N. 2005, ArXiv Astrophysics e-prints

Buxton, M. M. & Bailyn, C. D. 2004, *Astrophys. J.*, 615, 880

Cameron, P. B., Chandra, P., Ray, A., et al. 2005, *Nature*, 434, 1112

Casse, F. & Ferreira, J. 2000, *Astron. & Astrophys.*, 353, 1115

Chaty, S., Haswell, C. A., Malzac, J., et al. 2003, *Mon. Not. R. Astron. Soc.*, 346, 689

Chaty, S., Rodríguez, L. F., Mirabel, I. F., et al. 2001, *Astron. & Astrophys.*, 366, 1035

Church, M. J. & Balucinska-Church, M. 1997, *Astron. & Astrophys.*, 317, L47

Colbert, E. J. M. & Mushotzky, R. F. 1999, *Astrophys. J.*, 519, 89

Corbel, S., Chapuis, C., Dame, T. M., & Durouchoux, P. 1999, *Astrophys. J.*, 526, L29

Corbel, S. & Eikenberry, S. S. 2004, *Astron. & Astrophys.*, 419, 191

Corbel, S., Fender, R., & Tzioumis, A. 2002a, *IAU Circ.*, No. , 7795, 2

Corbel, S. & Fender, R. P. 2002, *Astrophys. J.*, 573, L35

Corbel, S., Fender, R. P., Tomsick, J. A., Tzioumis, A. K., & Tingay, S. 2004, *Astrophys. J.*, 617, 1272

Corbel, S., Fender, R. P., Tzioumis, A. K., et al. 2000, *Astron. & Astrophys.*, 359, 251

Corbel, S., Fender, R. P., Tzioumis, A. K., et al. 2002b, Science, 298, 196

Corbel, S., Kaaret, P., Fender, R. P., et al. 2005, *Astrophys. J.*, 632, 504

Corbel, S., Kaaret, P., Jain, R. K., et al. 2001a, in AIP Conf. Proc. 587 : Gamma 2001 : Gamma-Ray Astrophysics, ed. S. Ritz, N. Gehrels, & C. R. Shrader, 126–+

Corbel, S., Kaaret, P., Jain, R. K., et al. 2001b, *Astrophys. J.*, 554, 43

Corbel, S., Nowak, M. A., Fender, R. P., Tzioumis, A. K., & Markoff, S. 2003, *Astron. & Astrophys.*, 400, 1007

Corbel, S., Tomsick, J. A., & Kaaret, P. 2006, *Astrophys. J.*, 636, 971

Corbel, S., Wallyn, P., Dame, T. M., et al. 1997, *Astrophys. J.*, 478, 624

Dewangan, G. C., Miyaji, T., Griffiths, R. E., & Lehmann, I. 2004, *Astrophys. J.*, 608, L57

Dhawan, V., Mirabel, I. F., & Rodríguez, L. F. 2000, *Astrophys. J.*, 543, 373

Dove, J. B., Wilms, J., Maisack, M., & Begelman, M. C. 1997, *Astrophys. J.*, 487, 759

Dubner, G. M., Holdaway, M., Goss, W. M., & Mirabel, I. F. 1998, *Astron. J.*, 116, 1842

Duncan, R. C. & Thompson, C. 1992, *Astrophys. J.*, 392, L9

Eikenberry, S. S., Garske, M. A., Hu, D., et al. 2001, *Astrophys. J.*, 563, L133

Eikenberry, S. S., Matthews, K., LaVine, J. L., et al. 2004, *Astrophys. J.*, 616, 506

Esin, A. A., McClintock, J. E., & Narayan, R. 1997, *Astrophys. J.*, 489, 865

Fabbiano, G. 1989, *Annu. Rev. Astron. Astrophys.*, 27, 87

Fabbiano, G. 2006, *Annu. Rev. Astron. Astrophys.*, 44, 323

Falcke, H. 1996, *Astrophys. J.*, 464, L67+

Falcke, H. & Biermann, P. L. 1995, *Astron. & Astrophys.*, 293, 665

Falcke, H. & Biermann, P. L. 1996, *Astron. & Astrophys.*, 308, 321

Falcke, H., Körding, E., & Markoff, S. 2004, *Astron. & Astrophys.*, 414, 895

Fender, R., Corbel, S., Tzioumis, T., et al. 1999a, *Astrophys. J.*, 519, L165

Fender, R., Wu, K., Johnston, H., et al. 2004a, *Nature*, 427, 222

Fender, R. P. 2001, *Mon. Not. R. Astron. Soc.*, 322, 31

Fender, R. P., Belloni, T. M., & Gallo, E. 2004b, *Mon. Not. R. Astron. Soc.*, 355, 1105

Fender, R. P., Garrington, S. T., McKay, D. J., et al. 1999b, *Mon. Not. R. Astron. Soc.*, 304, 865

Fender, R. P., Hjellming, R. M., Tilanus, R. P. J., et al. 2001, *Mon. Not. R. Astron. Soc.*, 322, L23

Fender, R. P. & Pooley, G. G. 2000, *Mon. Not. R. Astron. Soc.*, 318, L1

Fender, R. P., Pooley, G. G., Durouchoux, P., Tilanus, R. P. J., & Brocksopp, C. 2000, *Mon. Not. R. Astron. Soc.*, 312, 853

Feng, H. & Kaaret, P. 2007, ArXiv Astrophysics e-prints

Ferrarese, L. & Merritt, D. 2000, *Astrophys. J.*, 539, L9

Ferreira, J. 1997, *Astron. & Astrophys.*, 319, 340

Ferreira, J., Petrucci, P.-O., Henri, G., Saugé, L., & Pelletier, G. 2006, *Astron. & Astrophys.*, 447, 813

Figer, D. F., Najarro, F., & Kudritzki, R. P. 2004, *Astrophys. J.*, 610, L109

Figer, D. F., Najarro, F., Morris, M., et al. 1998, *Astrophys. J.*, 506, 384

Fomalont, E. B., Geldzahler, B. J., & Bradshaw, C. F. 2001a, *Astrophys. J.*, 553, L27

Fomalont, E. B., Geldzahler, B. J., & Bradshaw, C. F. 2001b, *Astrophys. J.*, 558, 283

Fossati, G., Maraschi, L., Celotti, A., Comastri, A., & Ghisellini, G. 1998, *Mon. Not. R. Astron. Soc.*, 299, 433

Frank, J., King, A., & Raine, D. J. 2002, Accretion Power in Astrophysics : Third Edition (Accretion Power in Astrophysics, by Juhan Frank and Andrew King and Derek Raine, pp. 398. ISBN 0521620538. Cambridge, UK : Cambridge University Press, February 2002.)

Fuchs, Y., Mirabel, F., Chaty, S., et al. 1999, *Astron. & Astrophys.*, 350, 891

Fuchs, Y., Rodriguez, J., Mirabel, I. F., et al. 2003, *Astron. & Astrophys.*, 409, L35

Gaensler, B. M., Slane, P. O., Gotthelf, E. V., & Vasisht, G. 2001, *Astrophys. J.*, 559, 963

Galeev, A. A., Rosner, R., & Vaiana, G. S. 1979, *Astrophys. J.*, 229, 318

Gallo, E., Corbel, S., Fender, R. P., Maccarone, T. J., & Tzioumis, A. K. 2004, *Mon. Not. R. Astron. Soc.*, 347, L52

Gallo, E., Fender, R., & Corbel, S. 2003a, *The Astronomer's Telegram* , 196, 1

Gallo, E., Fender, R., Kaiser, C., et al. 2005a, *Nature*, 436, 819

Gallo, E., Fender, R. P., & Hynes, R. I. 2005b, *Mon. Not. R. Astron. Soc.*, 356, 1017

Gallo, E., Fender, R. P., Miller-Jones, J. C. A., et al. 2006, *Mon. Not. R. Astron. Soc.*, 370, 1351

Gallo, E., Fender, R. P., & Pooley, G. G. 2003b, *Mon. Not. R. Astron. Soc.*, 344, 60

Georganopoulos, M., Aharonian, F. A., & Kirk, J. G. 2002, *Astron. & Astrophys.*, 388, L25

Ghisellini, G., Celotti, A., & Costamante, L. 2002, *Astron. & Astrophys.*, 386, 833

Ghosh, S. K., Iyengar, K. V. K., Rengarajan, T. N., et al. 1989, *Astrophys. J.*, 347, 338

Giacconi, R., Gursky, H., Paolini, F. R., & Rossi, B. B. 1962, Physical Review Letters, 9, 439

Gonçalves, A. C. & Soria, R. 2006, *Mon. Not. R. Astron. Soc.*, 371, 673

Grindlay, J. E. 1994, *Astrophys. J. Suppl. Ser.*, 92, 465

Grisé, F., Pakull, M. W., & Motch, C. 2006, in IAU Symposium, ed. E. J. A. Meurs & G. Fabbiano, 302–303

Han, X. & Hjellming, R. M. 1992, *Astrophys. J.*, 400, 304

Hannikainen, D., Campbell-Wilson, D., Hunstead, R., et al. 2001, Astrophysics and Space Science Supplement, 276, 45

Hannikainen, D. C., Hunstead, R. W., Campbell-Wilson, D., & Sood, R. K. 1998, *Astron. & Astrophys.*, 337, 460

Hardee, P. E. 2000, *Astrophys. J.*, 533, 176

Harris, D. E. & Krawczynski, H. 2006, *Annu. Rev. Astron. Astrophys.*, 44, 463

Heger, A., Fryer, C. L., Woosley, S. E., Langer, N., & Hartmann, D. H. 2003, *Astrophys. J.*, 591, 288

Heinz, S. 2002, *Astron. & Astrophys.*, 388, L40

Heinz, S. 2004, *Mon. Not. R. Astron. Soc.*, 355, 835

Hjellming, R. M., Gibson, D. M., & Owen, F. N. 1975, *Nature*, 256, 111

Hjellming, R. M. & Johnston, K. J. 1988, *Astrophys. J.*, 328, 600

Hjellming, R. M. & Rupen, M. P. 1995, *Nature*, 375, 464

Hjellming, R. M., Rupen, M. P., Mioduszewski, A. J., et al. 1999, *Astrophys. J.*, 514, 383

Homan, J. & Belloni, T. 2005, *Astro. & Space Sc.*, 300, 107

Homan, J., Buxton, M., Markoff, S., et al. 2005, *Astrophys. J.*, 624, 295

Homan, J., Wijnands, R., van der Klis, M., et al. 2001, *Astrophys. J. Suppl. Ser.*, 132, 377

Hurley, K., Boggs, S. E., Smith, D. M., et al. 2005, *Nature*, 434, 1098

Hurley, K., Kouveliotou, C., Cline, T., et al. 1999, *Astrophys. J.*, 523, L37

Hynes, R. I., Haswell, C. A., Cui, W., et al. 2003, *Mon. Not. R. Astron. Soc.*, 345, 292

Igumenshchev, I. V. & Abramowicz, M. A. 1999, *Mon. Not. R. Astron. Soc.*, 303, 309

Jain, R. K., Bailyn, C. D., Orosz, J. A., McClintock, J. E., & Remillard, R. A. 2001, *Astrophys. J.*, 554, L181

Jones, C. 1977, *Astrophys. J.*, 214, 856

Kaaret, P., Corbel, S., Prestwich, A. H., & Zezas, A. 2003a, Science, 299, 365

Kaaret, P., Corbel, S., Tomsick, J. A., et al. 2003b, *Astrophys. J.*, 582, 945

Kaaret, P., Corbel, S., Tomsick, J. A., et al. 2006, *Astrophys. J.*, 641, 410

Kaaret, P., Prestwich, A. H., Zezas, A., et al. 2001, *Mon. Not. R. Astron. Soc.*, 321, L29

Kaaret, P., Ward, M. J., & Zezas, A. 2004, *Mon. Not. R. Astron. Soc.*, 351, L83

Kaiser, C. R., Gunn, K. F., Brocksopp, C., & Sokoloski, J. L. 2004, *Astrophys. J.*, 612, 332

Kaiser, C. R., Sokoloski, J. L., Gunn, K. F., & Brocksopp, C. 2005, *Astro. & Space Sc.*, 300, 283

Kaiser, C. R., Sunyaev, R., & Spruit, H. C. 2000, *Astron. & Astrophys.*, 356, 975

Kalberla, P. M. W., Goss, W. M., & Wilson, T. L. 1982, *Astron. & Astrophys.*, 106, 167

Kalemci, E. 2002, PhD thesis, AA(UNIVERSITY OF CALIFORNIA, SAN DIEGO)

Kalemci, E., Tomsick, J. A., Buxton, M. M., et al. 2005, *Astrophys. J.*, 622, 508

Kalemci, E., Tomsick, J. A., Rothschild, R. E., et al. 2006a, *Astrophys. J.*, 639, 340

Kalemci, E., Tomsick, J. A., Rothschild, R. E., et al. 2003, *Astrophys. J.*, 586, 419

Kalemci, E., Tomsick, J. A., Rothschild, R. E., Pottschmidt, K., & Kaaret, P. 2004, *Astrophys. J.*, 603, 231

Kalemci, E., Tomsick, J. A., Rothschild, R. E., et al. 2006b, in VI Microquasar Workshop : Microquasars and Beyond

Kaplan, D. L., Fox, D. W., Kulkarni, S. R., et al. 2002, *Astrophys. J.*, 564, 935

Kim, K.-T. & Koo, B.-C. 2002, *Astrophys. J.*, 575, 327

King, A. R. 2004, Nuclear Physics B Proceedings Supplements, 132, 376

King, A. R., Davies, M. B., Ward, M. J., Fabbiano, G., & Elvis, M. 2001, *Astrophys. J.*, 552, L109

Klein-Wolt, M., Fender, R. P., Pooley, G. G., et al. 2002, *Mon. Not. R. Astron. Soc.*, 331, 745

Kong, A. K. H., Kuulkers, E., Charles, P. A., & Homer, L. 2000, *Mon. Not. R. Astron. Soc.*, 312, L49

Kong, A. K. H., McClintock, J. E., Garcia, M. R., Murray, S. S., & Barret, D. 2002, *Astrophys. J.*, 570, 277

Körding, E., Falcke, H., & Corbel, S. 2006a, *Astron. & Astrophys.*, 456, 439

Körding, E., Falcke, H., & Markoff, S. 2002, *Astron. & Astrophys.*, 382, L13

Körding, E. G., Fender, R. P., & Migliari, S. 2006b, *Mon. Not. R. Astron. Soc.*, 369, 1451

Körding, E. G., Jester, S., & Fender, R. 2006c, *Mon. Not. R. Astron. Soc.*, 372, 1366

Kotani, T., Kawai, N., Nagase, F., et al. 2000, *Astrophys. J.*, 543, L133

Kouveliotou, C., Dieters, S., Strohmayer, T., et al. 1998, *Nature*, 393, 235

Kouveliotou, C., Strohmayer, T., Hurley, K., et al. 1999, *Astrophys. J.*, 510, L115

Kulkarni, S. R., Frail, D. A., Kassim, N. E., Murakami, T., & Vasisht, G. 1994, *Nature*, 368, 129

Kulkarni, S. R., Matthews, K., Neugebauer, G., et al. 1995, *Astrophys. J.*, 440, L61

Lang, C. C., Kaaret, P., Corbel, S., & Mercer, A. 2007, ArXiv e-prints, 705

Laros, J. G., Fenimore, E. E., Klebesadel, R. W., et al. 1987, *Astrophys. J.*, 320, L111

Makishima, K., Kubota, A., Mizuno, T., et al. 2000, *Astrophys. J.*, 535, 632

Malzac, J., Merloni, A., & Fabian, A. C. 2004, *Mon. Not. R. Astron. Soc.*, 351, 253

Markoff, S., Falcke, H., & Fender, R. 2001, *Astron. & Astrophys.*, 372, L25

Markoff, S., Nowak, M., Corbel, S., Fender, R., & Falcke, H. 2003, *Astron. & Astrophys.*, 397, 645

Markoff, S. & Nowak, M. A. 2004, *Astrophys. J.*, 609, 972

Markoff, S., Nowak, M. A., & Wilms, J. 2005, *Astrophys. J.*, 635, 1203

Martí, J., Mirabel, I. F., Rodríguez, L. F., & Smith, I. A. 2002, *Astron. & Astrophys.*, 386, 571

Mazets, E. P. & Golenetskii, S. V. 1981, *Astro. & Space Sc.*, 75, 47

Mazets, E. P., Golentskii, S. V., Ilinskii, V. N., Aptekar, R. L., & Guryan, I. A. 1979, *Nature*, 282, 587

McClintock, J. E., Narayan, R., Garcia, M. R., et al. 2003, *Astrophys. J.*, 593, 435

McClintock, J. E. & Remillard, R. A. 2006, Black hole binaries (Compact stellar X-ray sources), 157–213

McClure-Griffiths, N. M. & Gaensler, B. M. 2005, *Astrophys. J.*, 630, L161

McHardy, I. M., Koerding, E., Knigge, C., Uttley, P., & Fender, R. P. 2006, *Nature*, 444, 730

Meier, D. L. 2001, *Astrophys. J.*, 548, L9

Meier, D. L., Koide, S., & Uchida, Y. 2001, Science, 291, 84

Merloni, A. & Fabian, A. C. 2002, *Mon. Not. R. Astron. Soc.*, 332, 165

Merloni, A., Heinz, S., & di Matteo, T. 2003, *Mon. Not. R. Astron. Soc.*, 345, 1057

Merloni, A., Körding, E., Heinz, S., et al. 2006, New Astronomy, 11, 567

Migliari, S., Fender, R., & Méndez, M. 2002, Science, 297, 1673

Migliari, S. & Fender, R. P. 2006, *Mon. Not. R. Astron. Soc.*, 366, 79

Migliari, S., Fender, R. P., Blundell, K. M., Méndez, M., & van der Klis, M. 2005, *Mon. Not. R. Astron. Soc.*, 358, 860

Migliari, S., Tomsick, J. A., Maccarone, T. J., et al. 2006, *Astrophys. J.*, 643, L41

Miller, J. M., Fabbiano, G., Miller, M. C., & Fabian, A. C. 2003, *Astrophys. J.*, 585, L37

Miller, J. M., Fabian, A. C., & Miller, M. C. 2004, *Astrophys. J.*, 614, L117

Miller, J. M., Fabian, A. C., Wijnands, R., et al. 2002, *Astrophys. J.*, 570, L69

Miller, J. M., Homan, J., & Miniutti, G. 2006a, *Astrophys. J.*, 652, L113

Miller, J. M., Homan, J., Steeghs, D., et al. 2006b, *Astrophys. J.*, 653, 525

Miller, M. C. & Colbert, E. J. M. 2004, International Journal of Modern Physics D, 13, 1

Miller, N. A., Mushotzky, R. F., & Neff, S. G. 2005, *Astrophys. J.*, 623, L109

Mirabel, I. F. & Rodriguez, L. F. 1994, *Nature*, 371, 46

Mirabel, I. F. & Rodríguez, L. F. 1999, *Annu. Rev. Astron. Astrophys.*, 37, 409

Mirabel, I. F., Rodriguez, L. F., Cordier, B., Paul, J., & Lebrun, F. 1992, *Nature*, 358, 215

Miyamoto, S., Kimura, K., Kitamoto, S., Dotani, T., & Ebisawa, K. 1991, *Astrophys. J.*, 383, 784

Murakami, T., Tanaka, Y., Kulkarni, S. R., et al. 1994, *Nature*, 368, 127

Nowak, M. A. 2003, in New Views on MICROQUASARS, the Fourth Microquasars Workshop, Institut d'Etudes Scientifiques de Cargèse, Corsica, France, May 27 - June 1, 2002. Edited by Ph. Durouchoux, Y. Fuchs, and J. Rodriguez. Published by the Center for Space Physics : Kolkata (India), p. 3., ed. P. Durouchoux, Y. Fuchs, & J. Rodriguez, 3–+

Orosz, J. A., Groot, P. J., van der Klis, M., et al. 2002, *Astrophys. J.*, 568, 845

Pakull, M. W., Grisé, F., & Motch, C. 2006, in IAU Symposium, ed. E. J. A. Meurs & G. Fabbiano, 293–297

Pakull, M. W. & Mirioni, L. 2002, ArXiv Astrophysics e-prints

Pakull, M. W. & Mirioni, L. 2003, in Revista Mexicana de Astronomia y Astrofisica Conference Series, ed. J. Arthur & W. J. Henney, 197–199

Palmer, D. M., Barthelmy, S., Gehrels, N., et al. 2005, *Nature*, 434, 1107

Panessa, F., Barcons, X., Bassani, L., et al. 2007, ArXiv Astrophysics e-prints

Park, S. Q., Miller, J. M., McClintock, J. E., & Murray, S. S. 2005, *Astrophys. J.*, 618, L45

Portegies Zwart, S. F., Makino, J., McMillan, S. L. W., & Hut, P. 1999, *Astron. & Astrophys.*, 348, 117

Poutanen, J. 1998, in Theory of Black Hole Accretion Disks, ed. M. A. Abramowicz, G. Bjornsson, & J. E. Pringle, 100–+

Poutanen, J., Lipunova, G., Fabrika, S., Butkevich, A. G., & Abolmasov, P. 2006, ArXiv Astrophysics e-prints

Poutanen, J. & Zdziarski, A. A. 2003, in New Views on MICROQUASARS, the Fourth Microquasars Workshop, Institut d'Etudes Scientifiques de Cargèse, Corsica, France, May 27 - June 1, 2002. Edited by Ph. Durouchoux, Y. Fuchs, and J. Rodriguez. Published by the Center for Space Physics : Kolkata (India), p. 87, ed. P. Durouchoux, Y. Fuchs, & J. Rodriguez, 87–+

Quataert, E. & Gruzinov, A. 2000, *Astrophys. J.*, 539, 809

Quataert, E. & Narayan, R. 1999, *Astrophys. J.*, 520, 298

Rees, M. J. & Meszaros, P. 1994, *Astrophys. J.*, 430, L93

Remillard, R. A. & McClintock, J. E. 2006, *Annu. Rev. Astron. Astrophys.*, 44, 49

Remillard, R. A., Sobczak, G. J., Muno, M. P., & McClintock, J. E. 2002, *Astrophys. J.*, 564, 962

Revnivtsev, M., Chernyakova, M., Capitanio, F., et al. 2003, The Astronomer's Telegram, 132, 1

Reynolds, C. S. & Nowak, M. A. 2003, Physics Reports, 377, 389

Roberts, M. S. E., Michelson, P. F., Cominsky, L. R., et al. 1996, *IAU Circ.*, No. , 6302, 2

Rodriguez, J., Corbel, S., Kalemci, E., Tomsick, J. A., & Tagger, M. 2004, *Astrophys. J.*, 612, 1018

Rodriguez, J., Corbel, S., & Tomsick, J. A. 2003, *Astrophys. J.*, 595, 1032

Rodriguez, L. F. & Mirabel, I. F. 1998, *Astron. & Astrophys.*, 340, L47

Rodríguez, L. F. & Mirabel, I. F. 1999, *Astrophys. J.*, 511, 398

Rupen, M. P., Mioduszewski, A. J., & Dhawan, V. 2003, The Astronomer's Telegram, 142, 1

Russell, D. M., Fender, R. P., Gallo, E., & Kaiser, C. R. 2007, *Mon. Not. R. Astron. Soc.*, 376, 1341

Safi-Harb, S. & Petre, R. 1999, *Astrophys. J.*, 512, 784

Salpeter, E. E. 1964, *Astrophys. J.*, 140, 796

Sams, B. J., Eckart, A., & Sunyaev, R. 1996, *Nature*, 382, 47

Sanders, D. B., Phinney, E. S., Neugebauer, G., Soifer, B. T., & Matthews, K. 1989, *Astrophys. J.*, 347, 29

Schaerer, D., Meynet, G., Maeder, A., & Schaller, G. 1993, *Astron. & Astrophys. Suppl. Ser.*, 98, 523

Seward, F., Grindlay, J., Seaquist, E., & Gilmore, W. 1980, *Nature*, 287, 806

Shakura, N. I. & Sunyaev, R. A. 1973, *Astron. & Astrophys.*, 24, 337

Shapiro, S. L., Lightman, A. P., & Eardley, D. M. 1976, *Astrophys. J.*, 204, 187

Shaver, P. A. & Goss, W. M. 1970, Australian Journal of Physics Astrophysical Supplement, 14, 77

Smith, D. A. 1998, *IAU Circ.*, No. , 7008, 1

Sobczak, G. J., McClintock, J. E., Remillard, R. A., et al. 2000, *Astrophys. J.*, 544, 993

Sonobe, T., Murakami, T., Kulkarni, S. R., Aoki, T., & Yoshida, A. 1994, *Astrophys. J.*, 436, L23

Soria, R., Fender, R. P., Hannikainen, D. C., Read, A. M., & Stevens, I. R. 2006, *Mon. Not. R. Astron. Soc.*, 368, 1527

Stewart, R. T., Caswell, J. L., Haynes, R. F., & Nelson, G. J. 1993, *Mon. Not. R. Astron. Soc.*, 261, 593

Stirling, A. M., Spencer, R. E., de la Force, C. J., et al. 2001, *Mon. Not. R. Astron. Soc.*, 327, 1273

Strohmayer, T. E., Mushotzky, R. F., Winter, L., et al. 2007, *Astrophys. J.*, 660, 580

Sunyaev, R. A. & Titarchuk, L. G. 1980, *Astron. & Astrophys.*, 86, 121

Tananbaum, H., Gursky, H., Kellogg, E., Giacconi, R., & Jones, C. 1972, *Astrophys. J.*, 177, L5+

Thompson, C. & Duncan, R. C. 1995, *Mon. Not. R. Astron. Soc.*, 275, 255

Thompson, C. & Duncan, R. C. 1996, *Astrophys. J.*, 473, 322

Tigelaar, S. P., Fender, R. P., Tilanus, R. P. J., Gallo, E., & Pooley, G. G. 2004, *Mon. Not. R. Astron. Soc.*, 352, 1015

Tomsick, J. A. 2006, Advances in Space Research, 38, 2805

Tomsick, J. A., Corbel, S., Fender, R., et al. 2003a, *Astrophys. J.*, 597, L133

Tomsick, J. A., Corbel, S., Fender, R., et al. 2003b, *Astrophys. J.*, 582, 933

Tomsick, J. A., Corbel, S., Goldwurm, A., & Kaaret, P. 2005, *Astrophys. J.*, 630, 413

Tomsick, J. A., Corbel, S., & Kaaret, P. 2001, *Astrophys. J.*, 563, 229

Tomsick, J. A., Kalemci, E., & Kaaret, P. 2004, *Astrophys. J.*, 601, 439

Tremaine, S., Gebhardt, K., Bender, R., et al. 2002, *Astrophys. J.*, 574, 740

Urry, C. M. & Padovani, P. 1995, *Pub. Astron. Soc. Pacific*, 107, 803

van Kerkwijk, M. H., Kulkarni, S. R., Matthews, K., & Neugebauer, G. 1995, *Astrophys. J.*, 444, L33

Vancura, O., Blair, W. P., Long, K. S., & Raymond, J. C. 1992, *Astrophys. J.*, 394, 158

Vasisht, G., Frail, D. A., & Kulkarni, S. R. 1995, *Astrophys. J.*, 440, L65

Vrba, F. J., Henden, A. A., Luginbuhl, C. B., et al. 2000, *Astrophys. J.*, 533, L17

Wang, R., Wu, X.-B., & Kong, M.-Z. 2006, *Astrophys. J.*, 645, 890

Wang, X. Y., Dai, Z. G., & Lu, T. 2003, *Astrophys. J.*, 592, 347

Wilson, T. L. 1974, *Astron. & Astrophys.*, 31, 83

Woods, P. M. & Thompson, C. 2006, Soft gamma repeaters and anomalous X-ray pulsars : magnetar candidates (Compact stellar X-ray sources), 547–586

Yuan, F. & Cui, W. 2005, *Astrophys. J.*, 629, 408

Yuan, F., Cui, W., & Narayan, R. 2005, *Astrophys. J.*, 620, 905

Zdziarski, A. A., Lubiński, P., Gilfanov, M., & Revnivtsev, M. 2003, *Mon. Not. R. Astron. Soc.*, 342, 355

Zhang, S. N., Mirabel, I. F., Harmon, B. A., et al. 1997, in AIP Conf. Proc. 410 : Proceedings of the Fourth Compton Symposium, ed. C. D. Dermer, M. S. Strickman, & J. D. Kurfess, 141–+

Quatrième partie

Informations administratives

Chapitre 8
Informations administratives

8.1 Curriculum Vitae

État civil

Stéphane CORBEL (37 ans)
Marié, trois enfants
Né le 8 février 1970 à Landerneau (Finistère).
Nationalité française

Fonctions et établissement actuel

Maître de conférences, UFR de Physique, Université Paris 7 Diderot, Section 34

Distinction :

Prix Jeune Chercheur 2006 de la Société Française d'Astronomie et d'Astrophysique (SF2A).

Coordonnées professionnelles :

AIM – Astrophysique Interactions Multi-échelles (UMR n° 7158)
Service d'Astrophysique, CEA Saclay, Bât. 709
Orme des Merisiers, 91191 Gif sur Yvette Cedex
Tel : 01 69 08 45 62
Fax : 01 69 08 65 77
Courriel : stephane.corbel@cea.fr

Domaine de recherche :

Astrophysique des hautes énergies – Objets compacts : trous noirs et étoiles à neutrons – Jets relativistes – Accélération de particules – Couplage accrétion - éjection – Relations trous noirs galactiques / noyaux actifs de galaxie – Sources X ultralumineuses (ULX) – Répéteurs gamma mous (SGR magnétars) – Observations multi-longueur d'onde (radio, infrarouge, optique, X et gamma) – Milieu interstellaire.

Études et parcours professionnel

- Depuis septembre 2000 : Maître de conférences, Université Paris 7 Diderot
- 2000 : Post-doctorat, Harvard-Smithsonian Center for Astrophysics, Cambridge, USA
- 1996-99 : Doctorat de l'université Pierre et Marie Curie. Spécialité : Méthodes instrumentales en astrophysique et applications spatiales. Mention très honorable avec les félicitations du jury.

Titre : "*Multiples facettes des étoiles compactes : distance, extinction optique et comportement multi-longueur d'onde*".
Thèse soutenue le 12 octobre 1999. Jury : Pierre Encrenaz (président), Jean-Marie Hameury et Gilbert Vedrenne (rapporteurs), Philippe Durouchoux (directeur de thèse), Thomas Dame, Isabelle Grenier, Felix Mirabel et Martine Mouchet (examinateurs)

- 1995/96 : Étudiant (graduate) au California Institute of Technology, Pasadena, USA. Étalonnage, réduction et analyse de données du télescope gamma à masque codé GRIP-2. Directeur : Thomas Prince
- 1994 : DEA Astronomie et Techniques Spatiales, Université Pierre et Marie Curie, Paris
- 1993 : Maîtrise de physique fondamentale, Université de Bretagne Occidentale, Brest

8.2 Activités en matière d'enseignement

Service statutaire d'un maître de conférences, soit 192 h/an.

- 2007-2008 :
  - Cours + colles ME1 : Mécanique / hydrostatique / hydrodynamique, Niveau L1. Responsabilité d'une équipe enseignante d'une douzaine de personnes. Amphi de 150 étudiants.
  - Cours Exobiologie (semestre 1 et 2). Niveau L1 à L3. Nouvel enseignement que j'ai créé.
  - TD Thermodynamique. Niveau L2.
  - TP M2 recherche : Techniques instrumentales en astrophysique des hautes énergies.
- 2006-2007 :
  - Cours + colles ME1 : Mécanique / hydrostatique / hydrodynamique, Niveau L1. Responsabilité d'une équipe enseignante d'une douzaine de personnes. Amphi de 150 étudiants.
  - Cours Exobiologie (semestre 1 et 2). Niveau L1 à L3. Nouvel enseignement que j'ai créé.
  - TP M2 recherche : Techniques instrumentales en astrophysique des hautes énergies.
- 2005-2006 :
  - Cours + TD + colles ME1 : Mécanique/hydrostatique/hydrodynamique, Niveau L1. Responsabilité de l'équipe enseignante. Amphi de 150 étudiants.
  - Cours Exobiologie (semestre 1 et 2). Niveau L1 à L3. Nouvel enseignement que j'ai créé.
  - TP M2 recherche : Techniques instrumentales en astrophysique des hautes énergies.
- 2004-2005 : TD PH101 Mécanique/hydrostatique, Niveau L1 + TD Astrophysique Niveau L2 STU + TP Projets Physique Niveau L1
- 2003-2004 : TD PH101 Mécanique/hydrostatique, Niveau L1 + TP Physique Niveau L1
- 2002-2003 : TD PH101 Mécanique/hydrostatique, Niveau L1 + TP Physique Niveau L1
- 2001-2002 : TD Physique, PCEM Lariboisière + TP Physique L1
- 2000-2001 : TD Physique, PCEM Lariboisière

8.3 Activités d'encadrement

- 2007 : Thèse Mickael Coriat. "Jets relativistes des trous noirs accrétants".
- 2007 : Stage M2 Recherche Astrophysique. Mickael Coriat. "Couplage accrétion/éjection : GX 339−4".
- 2005 : Encadrement du séjour post-doctoral d'Elmar Koerding.
- 2005 : Stage M2 Recherche Astrophysique. Supakrit Maharakkhaka, "Étude des varia-

tions spectrales de 4U 1636-53 avec RXTE". Poursuite en thèse à l'IAS Orsay.
- 2002 : Stage M2 Recherche Astrophysique. Philippe Merck, " Étude du trou noir XTE J1118+480" . Poursuite en thèse à l'observatoire de Paris.
- Encadrement de stagiaires de niveau L1 à L2. Initiation et découverte du travail de recherche.

8.4 Responsabilités administratives et collectives

Université

- 2007-présent : Membre élu du Conseil National des Universités (CNU), section 34.
- 2003-présent : Membre de la Commission de spécialistes section 34 de l'Université Paris 7. Membre du bureau (2003-06)
- 2006-présent : Membre du jury de licence (L1 à L3) Sciences de la Terre et de l'Univers

Communauté

- 2005-2007 : Membre du comité de l'Agence Spatiale Européenne (ESA) "Integral User Group".
- 2006 : Membre du Time Allocation Comittee (TAC) du satellite Chandra de la NASA

Organisation de congrès/écoles scientifiques

- Organisation de la conférence "7th Microquasar workshop : Microquasars and beyond", du 1 septembre au 5 septembre 2008, Izmir, Turquie. Membre du SOC.
- Organisation de la conférence "The 7th INTEGRAL workshop : an INTEGRAL view of compact objects", du 8 septembre au 11 septembre 2008, Copenhague, Danemark. Membre du SOC.
- Organisation de la conférence "Bursts, Pulses and Flickering", du 12 au 17 juin 2007, Kerastari, Grèce. Membre du SOC et du LOC
- Organisation de l'école internationale de printemps "Observing the X and Gamma-ray sky", du 3 au 14 avril 2006, Cargèse, France. Membre du SOC et du LOC
- Membre du comité local d'organisation de l'école internationale "Black holes in the Universe", Cargèse, Mai 2003
- Organisation des premières journées APC, Dieppe, Novembre 2002

Activités de vulgarisation scientifique

- Deux conférences de presse + 7 communiqués de presse (voir section 8.5)
- Diffusion des connaissances : interventions dans des écoles maternelles et primaires en régions Ile de France, Centre et Bretagne.
- Séminaires grand public sur les trous noirs.
- Rencontres avec journalistes de la presse scientifique et généraliste.
- Invité dans l'émission "Mondes et Merveilles" (France 5).

Divers

- Rapporteur pour le Fond Québécois pour la Recherche Scientifique (Canada)
- Rapporteur régulier pour les revues internationales : Astrophysical Journal, Astronomy and Astrophysics et Monthly Notices of Royal Astronomy Society.
- Évaluation de livres scientifiques et universitaires pour Pearson Education.

8.5 Activité de recherche

Nombre total de publications scientifiques : 111

53 articles publiés dans des revues à comité de lecture
41 articles publiés dans des actes de colloque
17 Circulaires IAU ou télégrammes astronomiques

Nombre total d'exposés de revue sur invitation dans des conférences internationales : 11

Le site ADS (http ://adsabs.harvard.edu/abstract_service.html) fait apparaître (au 1^{er} janvier 2008) 149 publications à mon nom, dont 12 comme premier auteur dans des journaux à comité de lecture.

Il fait aussi ressortir un total de 1577 citations, avec 12 articles ayant plus de 40 citations (dont 3 avec plus de 100 citations). Sur ces 12 publications, je suis premier auteur sur 7 d'entres elles.

- Scientifique associé au satellite GLAST de la NASA. Membre des groupes "multi-longueur d'onde", "catalogues" et "sources non identifiées"
- Membre du consortium FLOW, associé au nouveau radio télescope européen LOFAR

8.5.1 Liste des exposés de revue sur invitation dans des conférences internationales

1. "The radio/X-ray correlation and unicity of physics in accreting black holes", in "Micro-quasars/AGN workshop", Agios Nikolaos, Grèce, Juin 2007
2. "Jets from X-ray binaries", in "Astrophysics in the Lofar era", Emmen, Pays Bas, Avril 2007
3. "Relativistic Jets", in "International spring school : Observing the X and Gamma - ray sky", cours 3 h , Cargese, France, Avril 2006
4. "Relativistic Jets", in "Triggering Relativistic Jets", Cozumel, Mexique, Avril 2005
5. "Relativistic Jets from X-ray Binaries : Link to AGNs ?" in "Cospar Colloquium on : Spectra & Timing of Accreting X-ray Binaries", Mumbai, Inde, Janvier 2005
6. "Similarities and scaling laws for AGN and X-ray binaries" in "Multiband Approach to AGN", Bonn, Allemagne, Septembre 2004
7. "Relativistic jets" in "COSPAR symposium : High-Energy Radiation from Black Holes : from Supermassive Black holes to Galactic Solar Mass Black holes", Paris, Juillet 2004
8. "Large scale jets in microquasars" in "From X-ray Binaries to Quasars : Black Hole accretion on all mass Scales", Amsterdam, Pays Bas, Juillet 2004

9. "SIMBOL-X and relativistic jets" in "First SIMBOL-X workshop", Paris, Mars 2004
10. "Relativistic jets in the RXTE era" in "X-ray Timing 2003 : Rossi and beyond", Boston, USA, Novembre 2003
11. "X-ray jets in microquasars" in "AAS/High Energy Astrophysics Division", Mont Tremblant, Canada, Mars 2003

8.5.2 Liste des publications dans des revues à comité de lecture

⊙ Année 2008 :

1. Rodriguez, J., Hannikainen, D.C., Shaw, S.E., Pooley, G., **Corbel, S**, Tagger, M., Mirabel, I.F., Belloni, T., Cabanac, C., Cadolle Bel, M., Chenevez, J., Kretschmar, P., Lehto, H.J., Paizis, A., Varnière, P., Vilhu, O., 2008, *Astron. & Astrophys.*, sous presse : "Two years of INTEGRAL monitoring of GRS 1915+105 Part 1 : multiwavelength coverage with INTEGRAL, RXTE and the Ryle radio telescope.
2. Rodriguez, J., Shaw, S.E., Hannikainen, D.C., Belloni, T., **Corbel, S**, Cadolle Bel, M., Chenevez, J., Prat, L., Kretschmar, P., Lehto, H.J., Mirabel, I.F., Paizis, A., Pooley, G., Tagger, M., Varnière, P., Cabanac, C., Vilhu, O., 2008, *Astron. & Astrophys.*, sous presse : "Two years of INTEGRAL monitoring of GRS 1915+105 Part 2 : X-ray spectro-temporal analysis.

⊙ Année 2007 :

3. Migliari, S., Tomsick, J.A., Markoff, S., Kalemci, E., Bailyn, C., Buxton, M., **Corbel, S.**, Fender, R.P., Kaaret, P., 2007, *Astrophys. J.*, 670, 610 : "Tracing the jet contribution to the mid-IR over the 2005 outburst of GRO 1655−40 via broadband spectral modeling".
4. Lang, C.C., Kaaret P., **Corbel, S.**, Mercer, A., 2007, *Astrophys. J.*, 666, 79 : "A radio nebula surrounding the ultraluminous X-ray source in NGC 5408".
5. Fender, R.P., Dahlem, M., Homan, J., **Corbel, S.**, Sault, R., Belloni, T.M., 2007, *Mon. Not. R. Astron. Soc.*, 380, 25, "The variable radio counterpart and possible large-scale jet of the new Z source XTE J1701−462".
6. Cadolle Bel, M., Ribo, M., Rodriguez, J., Chaty, S., **Corbel, S.**, Goldwurm, A., Frontera, F., Farinelli, R., D'Avanzo, P., Tarana, A., Ubertini, P., Laurent, P., Goldoni, P., Mirabel, I.F. 2007, *Astrophys. J.*, 659, 549 : "Simultaneous multiwavelength observations of the Low/Hard State of the X-ray transient source SWIFT J1753.5−0127".
7. Rodriguez, J., Cadolle Bel, M., Tomsick, J.A., **Corbel, S.**, Brocksopp, C., Paizis, A., Shaw, S., Bodaghee, A., 2007, *Astrophys. J.*, 655, L97 : "The discovery outburst of the X-ray transient IGR J17497−2821 observed with RXTE and ATCA"
8. Joinet, A., Jourdain, E., Malzac, J., Roques, J. P., **Corbel, S.**, Rodriguez, J., Kalemci, E., 2007, *Astrophys. J.*, 657, 400 : "Hard X-ray emission of the microquasar GX 339-4 in the low/hard state"

⊙ Année 2006 :

9. Koerding, E., Falcke, H, **Corbel, S.** 2006, *Astron. & Astrophys.*, 456, 439 : "Refining the fundamental plane of accreting black holes" (**17 citations**)
10. **Corbel, S.**, Tomsick, J.A., Kaaret, P. 2006, *Astrophys. J.*, 636, 971 : "On the origin of black hole X-ray emission in quiescence : Chandra observations of the black holes XTE J1550-564 and 1H 1743-322"

11. Kaaret, P., **Corbel, S.**, Tomsick, J.A., Lazendic, J., Tzioumis, A.K., Butt, Y., Wijnands, R. 2006, *Astrophys. J.*, 641, 410 : "Evolution of the X-Ray Jets from 4U 1755−33"
12. Rodriguez, J., Shaw, S.E., **Corbel, S.**, 2006, *Astron. & Astrophys.*, 451, 1045 : "The faint 2005 hard state outburst of Aquila X-1 seen by INTEGRAL and RXTE"
13. Rodriguez, J., Bodaghee, A., Kaaret, P., Tomsick, J.A., Kuulkers, E., Malaguti, G., Petrucci, P.-O., Cabanac, C., Chernyakova, M., **Corbel, S.**, Deluit, S., Di Cocco, G., Ebisawa, K., Goldwurm, A., Henri, G., Lebrun, F., Paizis, A., Walter, R., Foschini, L. 2006, *Mon. Not. R. Astron. Soc.*, 366, 274 : "INTEGRAL and XMM-Newton observations of the X-ray pulsar IGR J16320−4751/AX J1631.9−4752"
14. Kalemci, E., Tomsick, J.A., Rothschild, R.E., Pottschmidt, K., **Corbel, S.**, Kaaret, P. 2006, *Astrophys. J.*, 639, 340 : "The Galactic black hole transient H 1743−322 during outburst decay : connections between timing noise, state transitions and radio emission"

⊙ Année 2005 :

15. **Corbel, S.**, Kaaret, P., Fender, R.P., Tzioumis, T., Tomsick, J.A., Orosz, J.A. 2005, *Astrophys. J.*, 632, 504 : "Discovery of X-ray jets in the microquasar H 1743-322" (**17 citations**)
16. Tomsick, J.A., **Corbel, S.**, Goldwurm, A., Kaaret, P. 2005, *Astrophys. J.*, 630, 413 : " X-ray observations of the black hole transient 4U 1630-47 during two years of X-ray activities" (**13 citations**)
17. Foschini, L., Chiaberge, M., Grandi,P., Grenier, I.A., Guainazzi, M., Hermsen, W., Palumbo, G.G.C., Rodriguez, J., Chaty, S., **Corbel, S.**, Di Cocco, G., Kuiper, L., Malaguti, G. 2005, *Astron. & Astrophys.*, 433, 515 : "Investigating the EGRET-radio galaxies link with INTEGRAL : the case of 3EG J1621+8203 and NGC 6251"
18. Kalemci, E., Tomsick, J.A. Buxton, M.M., Rothschild, R.E., Pottschmidt, K., **Corbel, S.**, Brocksopp, C., Kaaret, P. 2005, *Astrophys. J.*, 622, 508 : "Multi-wavelength observations of the Galactic black hole transient 4U 1543-47 during outburst decay : state transitions and jet contribution" (**20 citations**)
19. Brocksopp, C., **Corbel, S.**, Fender, R. P., Rupen, M., Sault, R., Tingay, S. J., Hannikainen, D., O'Brien, K. 2005, *Mon. Not. R. Astron. Soc.*, 356, 125 : "The 2003 radio outburst of a new X-ray transient : XTE J1720-318"
20. Nowak, M. A., Wilms, J., Heinz, S., Pooley, G., Pottschmidt, K. **Corbel, S.**, 2005, *Astrophys. J.*, 626, 1006 :"Is the "IR Coincidence" Just That?" (**19 citations**)

⊙ Année 2004 :

21. **Corbel, S.**, Fender, R. P., Tomsick, J. A., Tzioumis, A. K., Tingay, S. 2004, *Astrophys. J.*, 617, 1272 : "On the Origin of Radio Emission in the X-Ray States of XTE J1650-500 during the 2001-2002 Outburst" (**35 citations**)
22. Orosz, J. A., McClintock, J. E., Remillard, R. A., **Corbel, S.**, 2004, *Astrophys. J.*, 616, 3760 : "Orbital Parameters for the Black Hole Binary XTE J1650-500" (**17 citations**)
23. Rodriguez, J., **Corbel, S.**, Hannikainen, D. C., Belloni, T., Paizis, A., Vilhu, O. 2004, *Astrophys. J.*, 615, 416 : "Spectral Properties of Low-Frequency Quasi-periodic Oscillations in GRS 1915+105" (**18 citations**)
24. Cadolle Bel, M., Rodriguez, J., Sizun, P., Farinelli, R., Del Santo, M., Goldwurm, A., Goldoni, P., **Corbel, S.**, Parmar, A. N., Kuulkers, E., Ubertini, P., Capitanio, F., Roques, J.-P., Frontera, F., Amati, L., Westergaard, N. J. 2004, *Astron. & Astrophys.*, 426, 659 : "High-energy observations of the state transition of the X-ray nova and black hole candidate XTE J1720-318" (**13 citations**)

25. Rodriguez, J., **Corbel, S.**, Kalemci, E., Tomsick, J. A., Tagger, M. 2004, *Astrophys. J.*, 612, 1018 : "An X-Ray Timing Study of XTE J1550-564 : Evolution of the Low-Frequency Quasi-periodic Oscillations for the Complete 2000 Outburst"
26. **Corbel, S.**, *Science*, 2004, 303, 1480 : "Watching black holes spin"
27. Eikenberry, S., Matthews, K., Lavine, J. L., Garske, M., Hu, D., Jackson, M. A., Patel, S. G., Barry, D. J., Colonno, M. R., Houck, J. R., Wilson, J. C., **Corbel, S.**, Smith, J. D., 2004, *Astrophys. J.*, 616, 506 : "Infrared Observations of LBV 1806-20 and Nearby Cluster Stars" (**23 citations**)
28. **Corbel, S.** and Eikenberry, S.E., 2004, *Astron. & Astrophys.*, 419, 191 : "The Connection between W31, SGR 1806-20, & LBV 1806-20 : Distance, Extinction, and Structure" (**44 citations**)
29. Chapuis, C, and **Corbel, S.**, 2004, *Astron. & Astrophys.*, 414, 659 : "On the optical extinction and distance of GRS 1915+105" (**20 citations**)
30. Gallo, E., **Corbel, S.**, Fender, R.P., Maccarone, T. and Tzioumis, T., 2004, *Mon. Not. R. Astron. Soc.*, 347, L52 : "A transient large-scale relativistic radio jet from GX 339-4" (**28 citations**)

⊙ Année 2003 :

31. Tomsick, J.A., **Corbel, S.**, Fender, R.P., Miller, J.M., Orosz, J.A., Rupen, M., Tzioumis, T., Wijnands, R., and Kaaret, P., 2003, *Astrophys. J.*, 597, L133 : "Chandra Detections of Two Quiescent Black Hole X-Ray Transients" (**18 citations**)
32. Walter, R., Rodriguez, J., Foschini, L., de Plaa, J., **Corbel, S.**, Courvoisier, T. J.-L., den Hartog, P. R., Lebrun, F., Parmar, A. N., Tomsick, J. A. and Ubertini, P, 2003, *Astron. & Astrophys.*, 411, L427 : "INTEGRAL discovery of a bright highly obscured galactic X-ray binary source IGR J16318−4848" (**42 citations**)
33. Rodriguez, J., **Corbel, S.** and Tomsick, J. A., 2003, *Astrophys. J.*, 595, 1032 : "Spectral Evolution of the Microquasar XTE J1550−564 over Its Entire 2000 Outburst" (**34 citations**)
34. Tomsick, J.A., Kalemci, E., **Corbel, S.** and Kaaret, P., 2003, *Astrophys. J.*, 592, 1100 : "X-Ray Flares and Oscillations from the Black Hole Candidate X-Ray Transient XTE J1650−500 at Low Luminosity" (**19 citations**)
35. Rodriguez, J., Tomsick, J. A., Foschini, L., Walter, R., Goldwurm, A., **Corbel, S.** and Kaaret, P., 2003, *Astron. & Astrophys.*, 407, L41 :"An XMM-Newton observation of IGR J16320-4751 = AX J1631.9-4752" (**31 citations**)
36. Porquet, D., Rodriguez, J., **Corbel, S.**, Goldoni, P., Warwick, R. S., Goldwurm, A., Decourchelle, A., 2003, *Astron. & Astrophys.*, 406, 299 : "XMM-Newton study of the persistent X-ray source 1E 1743.1−2843 located in the Galactic Center direction" (**12 citations**)
37. Kalemci, E., Tomsick, J. A., Rothschild, R. E., Pottschmidt, K., **Corbel, S.**, Wijnands, R., Miller, J. M., Kaaret , P., 2003, *Astrophys. J.*, 586, 419 : "X-Ray Temporal Properties of XTE J1650-500 during Outburst Decay"(**19 citations**)
38. **Corbel, S.**, Nowak, M. A., Fender, R. P., Tzioumis, A. K., Markoff, S., 2003, *Astron. & Astrophys.*, 400, 1007 : "Radio/X-ray correlation in the low/hard state of GX 339-4" (**103 citations**)
39. Kaaret, P., **Corbel, S.**, Prestwich, A.H. and Zezas, A., 2003, *Science*, 299, 365 : "Radio Emission from an Ultraluminous X-ray Source" (**70 citations**)

40. Kaaret, P., **Corbel, S.**, Tomsick, J. A., Fender, R., Miller, J. M., Orosz, J. A., Tzioumis, A. K., Wijnands, R., 2003, *Astrophys. J.*, 582, 945 : "X-Ray Emission from the Jets of XTE J1550-564" (**27 citations**)
41. Tomsick, J.A., **Corbel, S.**, Fender, R., Miller, J.M., Orosz, J.A., Tzioumis, T., Wijnands, R. and Kaaret, P., 2003, *Astrophys. J.*, 582, 933 : "X-Ray Jet Emission from the Black Hole X-Ray Binary XTE J1550-564 with Chandra in 2000" (**19 citations**)
42. Markoff, S., Nowak, M., **Corbel, S.**, Fender, R., Falcke, H., 2003, *Astron. & Astrophys.*, 397, 645 : "Exploring the role of jets in the radio/X-ray correlations of GX 339-4" (**93 citations**)

⊙ Année 2002 :

43. **Corbel, S.**, Fender, R. P., Tzioumis, A. K., Tomsick, J. A., Orosz, J. A., Miller, J. M., Wijnands, R., Kaaret, P., 2002, *Science*, 298, 196 : "Large-Scale, Decelerating, Relativistic X-ray Jets from the Microquasar XTE J1550-564" (**78 citations**)
44. **Corbel, S.**, Fender, R. P., 2002, *Astrophys. J.*, 573, L35 : "Near-Infrared Synchrotron Emission from the Compact Jet of GX 339-4" (**46 citations**)
45. Wachter, S., Hoard, D.W., Bailyn, Charles D., **Corbel, S.**, Kaaret, P., 2002, *Astrophys. J.*, 568, 901 : "A Closer Look at the Soft X-Ray Transient X1608-52 : Long-Term Optical and X-Ray Observations" (**12 citations**)

⊙ Année 2001 :

46. Miller, J. M., Wijnands, R., Homan, J., Belloni, T., Pooley, D., **Corbel, S.**, Kouveliotou, C., van der Klis, M., Lewin, W. H. G., 2001, *Astrophys. J.*, 563, 928 : "High-Frequency Quasi-Periodic Oscillations in the 2000 Outburst of the Galactic Microquasar XTE J1550-564" (**51 citations**)
47. Tomsick, J.A., **Corbel, S.**, Kaaret, P., 2001, *Astrophys. J.*, 563, 229 : "X-Ray Observations of XTE J1550-564 during the Decay of the 2000 Outburst. I. Chandra and RXTE Energy Spectra" (**33 citations**)
48. **Corbel, S.**, Kaaret, P., Jain, R. K., Bailyn, C. D., Fender, R. P., Tomsick, J. A., Kalemci, E., McIntyre, V., Campbell-Wilson, D., Miller, J. M., McCollough, M. L., 2001, *Astrophys. J.*, 554, 43 : "X-Ray States and Radio Emission in the Black Hole Candidate XTE J1550-564" (**66 citations**)

⊙ Année 2000 :

49. **Corbel, S.**, Fender, R.P., Tzioumis, A.K., Nowak, M., McIntyre, V., Durouchoux, P. and Sood, R., 2000, *Astron. & Astrophys.*, 359, 251 : "Coupling of the X-ray and radio emission in the black hole candidate and compact jet source GX 339–4" (**112 citations**)

⊙ Année 1999 :

50. **Corbel, S.**, Chapuis, C., Dame, T.M. and Durouchoux, P., 1999, *Astrophys. J.*, 526, L29 : "The distance of the soft gamma repeater SGR 1627–41" (**24 citations**)
51. Fender, R.P., **Corbel, S.**, Tzioumis, A.K., McIntyre, V., Campbell-Wilson, D.C., Nowak, M., Sood, R.K., Hunstead, R., Harmon, A., Durouchoux, P. and Heindl, W.A., 1999, *Astrophys. J.*, 519, L165 : "Quenching of the radio jet during the X-ray high state of GX 339–4" (**124 citations**)
52. Smith, I.A., Liang, E.P., Lin, D., Moss, M., Crider, A., Fender, R.P., Durouchoux, P., **Corbel, S.** and Sood, R.K. , 1999, *Astrophys. J.*, 519, 762 : "Multiwavelength Observations of GX 339-4 in 1996. I. Daily Light Curves and X-ray and Gamma-Ray Spectroscopy"

⊙ Année 1998 :

53. Durouchoux, P., Vilhu, O., **Corbel, S.**, Wallyn, P., Dwarakanath, K.S., Huovelin, J., Anantharamaiah, K.R., Grindlay, J.E., Chapuis, C., Park, Y.S., Bally, J. and Mahoney, W.A., 1998, *Astrophys. J.*, 507, 781 : "Multiwavelength observations of a new black hole candidate : EXS 1737.9-2952"

⊙ Année 1997 :

54. **Corbel, S.**, Wallyn, P., Dame, T.M., Durouchoux, P., Mahoney, W.A. and Vilhu, O. 1997, *Astrophys. J.*, 478, 624 : "The distance of the soft gamma repeater SGR 1806-20" **(45 citations)**
55. Schindler, S.M., Cook, W.R., Hammond, J.A., Harrison, F.A., Prince, T.A., Wang, S., **Corbel, S.** and Heindl, W.A. 1997, *Nuclear Inst. & Meth. –A*, 384, 425 : " GRIP-2 : A sensitive balloon-borne imaging gamma-ray telescope"

8.5.3 Circulaires IAU et télégrammes astronomiques

1. Kalemci, E., Tomsick, J., Migliari, S, Pottschmidt, K., **Corbel, S.**, Buxton, M., Bailyn, C., Kaaret, P., Belloni, T. 2007, ATel, 1074 : Recurrent black hole transient GX 339−4 in transition to the hard state.
2. **Corbel, S.**, Tzioumis, T., Brocksopp, C., Fender, R. 2007, ATel, 1007 : ATCA radio observations of GX 339−4
3. Brocksopp, C., **Corbel, S.**, Rupen, M., Sault, B., Tzioumis, T., Dhawan, V., Mioduszewski, A., Cimo, G., Fender, R. 2005, ATel, 612 : Renewed Radio Emission from GRO J1655−40
4. Tomsick, J. A., Lingenfelter, R., **Corbel, S.**, Goldwurm, A., Kaaret, P., 2004, ATel, 224 : Two New INTEGRAL Sources : IGR J15479-4529 and IGR J16418-4532
5. **Corbel, S.**, Fender, R.P., Tzioumis, T. and Brocksopp, C., 2003, ATel 208 : Radio observations of XTE J1748-361 (=A1744-36 ?)
6. Gallo, E., Fender, R., Corbel, S., 2003, ATel 196 : GX 339-4 in a very low luminosity state
7. Tomsick, J. A., Lingenfelter, R., Walter, R., Rodriguez, J., Goldwurm, A., **Corbel, S.**, Kaaret, P., 2003, IAUC 8076 : IGR J16320-4751
8. Rupen, M. P., Brocksopp, C., Mioduszewski, A. J., Dhawan, V., Sault, R., Fender, R., **Corbel, S.**, 2003, IAUC 8054 : XTE J1720-318
9. Fender, R., **Corbel, S.**, Tzioumis, T., Tingay, S., Brocksopp, C., Gallo, E., 2002, ATel 107 : The recent evolution of radio emission from GX 339-4
10. Tomsick, J.A., Rupen, M.P., **Corbel, S.**, Dhawan, V., Fender, R., Kaaret, P., Kuulkers, E., Miller, J.M., Mioduszewski, A.J., Orosz, J.A., Tzioumis, T., Wijnands, R., 2002, ATel 105 : Low Quiescent X-Ray and Radio Flux Levels from the Black Hole Transient V4641 Sgr
11. Kalemci, E., Tomsick, J., Rothschild, R., **Corbel, S.**, Kaaret, P., McClintock, J., 2002, ATel 103 : State Transition of the Black Hole Candidate 4U 1543-47
12. Smith, D. M., Belloni, T., Heindl, W. A., Kalemci, E., Remillard, R., Nowak, M., Swank, J. H., **Corbel, S.**, 2002, IAUC 7912 : GX 339-4
13. Smith, D. M., Belloni, T., Heindl, W. A., Kalemci, E., Remillard, R., Nowak, M., Swank, J. H., **Corbel, S.**, 2002, ATel 95 : State Changes in GX 339-4
14. Tomsick, J. A., Kalemci, E., **Corbel, S.**, Kaaret, P., 2002, IAUC 7837 : XTE J1650-500

15. **Corbel, S.**, Fender, R., Tzioumis, A., 2002, IAUC 7795 : XTE J1550-564
16. **Corbel S.**, Hannikainen,D., Gonzalez, J.F. and Hainaut O.R., 1998, IAUC 6824 : QX Normae
17. Durouchoux P., **Corbel S.**, Wallyn P. and Grindlay, J., 1994, IAUC 6000 : GRS 1915+105

8.5.4 Articles dans des actes de colloque

1. **Corbel, S.**, 2007, Revista Mexicana de Astronomia y Astrofisica, 27, 122, "Flavors of relativistic jets from black hole binaries"
2. Rodriguez, J., Pooley, G., Hannikainen, D., Lehto, H. J., Belloni, T., Cadolle-Bel, M., & **Corbel, S.** 2006, Proceedings of the VI Microquasar Workshop : Microquasars and Beyond, 24, "An INTEGRAL monitoring of GRS 1915+105 using simultaneous space and ground based instruments"
3. Kalemci, E., Tomsick, J. A., Rothschild, R. E., Pottschmidt, K., Migliari, S., **Corbel, S.**, & Kaaret, P. 2006, Proceedings of the VI Microquasar Workshop : Microquasars and Beyond, 12, "State transitions and jet formation in black hole binaries"
4. Cadolle Bel, M., Ribó, M., Rodriguez, J., Chaty, S., **Corbel, S.**, Goldwurm, A., & Malzac, J. 2006, Proceedings of the VI Microquasar Workshop : Microquasars and Beyond, 3, "Broad-band spectral changes of the microquasars Cygnus X-1 and SWIFT J1753.5-0127"
5. **Corbel, S.** 2006, Advances in Space Research, 38, 2867, "Relativistic jets from black hole binaries"
6. **Corbel, S.**, 2005, Astrophysics and Space Science, 300, 1-3, 275, "Large Scale Jets in Microquasars"
7. **Corbel, S.**, 2005, Memorie della Societa Astronomica Italiana, 76, 73, "Large Scale Jets in Microquasars"
8. Cadolle Bel, M., Rodriguez, J., Sizun, P., Farinelli, R., Del Santo, M., Goldwurm, A., Goldoni, P., **Corbel, S.**, Parmar, A. N., Kuulkers, E., Roques, J.-P., Westergaard, N. J. , 2004, SF2A, EdP-Sciences, Conference Series, 331, "High-energy observations of the state transition of the X-ray nova and black hole candidate XTE J1720-318"
9. Tomsick, J. A., Lingenfelter, R., **Corbel, S.**, Goldwurm, A. ; Kaaret, P. 2004, Proceedings of the Fifth INTEGRAL Workshop, ESA SP-552, 413, "An INTEGRAL Observation of the Black Hole Transient 4U 1630-47 and the Norma Region of the Galaxy"
10. Foschini, L., Tomsick, J. A., Rodriguez, J., Walter, R., Goldwurm, A., **Corbel, S.**, Kaaret, P. 2004, Proceedings of the Fifth INTEGRAL Workshop, ESA SP-552, 247, "High-energy emission from IGR J16320-4751"
11. Rodriguez, J., Fuchs, Y., Hannikainen, D., Vilhu, O., Shaw, S., Belloni, T., & x**Corbel, S.**, 2004, ESA SP-552 : Proceedings of the Fifth INTEGRAL Workshop, ESA SP-552, 377, "Strong QPOs and High Energy Tail in Simultaneous RXTE/INTEGRAL Observations of GRS 1915+105"
12. **Corbel, S.**, 2004, AIP Conference Proceedings, Vol. 714, 127, "Relativistic Jets in the RXTE Era"
13. Kaaret, P., **Corbel, S.**, Tomsick, J. A., Butt, Y., Fender, R. P., Lazendic, J., Miller, J. M., Orosz, J. A., Tzioumis , A. K., Wijnands, R. 2004, Nuclear Physics B Proceedings Supplements, 132, 354, "Large-scale X-ray jets from Galactic black holes"

14. Markoff, S., Nowak, M., **Corbel, S.**, Fender, R., Falcke, H. 2003, New Astronomy Reviews, 47, 6-7, 491, "Modeling the X-ray contribution of XRB jets"
15. **Corbel, S.**, Fender, R. P., Tzioumis, A. K., Tomsick, J. A., Orosz, J. A., Miller, J. M., Wijnands, R., Kaaret, P. 2003, New Astronomy Reviews, 47, 6-7, 477, "Moving relativistic large-scale X-ray jets in the microquasar XTE J1550-564"
16. Tomsick, J. A., **Corbel, S.**, Fender, R. P., Miller, J. M., Orosz, J. A., Tzioumis, T., Wijnands, R., Kaaret, P 2002, New Views on MICROQUASARS, the Fourth Microquasars Workshop, 221, "X-ray jet emission from the black hole X-ray binary XTE J1550-564 with CHANDRA in 2000"
17. Corbel, S.; Fender, R. P., Tzioumis, A. K., Tomsick, J. A., Orosz, J. A., Miller, J. M., Wijnands, R., Kaaret, P. 2002, New Views on MICROQUASARS, the Fourth Microquasars Workshop, 197, "Moving relativistic large-scale X-ray jets in the microquasar XTE J1550-564"
18. Markoff, S., Nowak, M. A., **Corbel, S.**, Fender, R., Falcke, H. 2002, New Views on MICROQUASARS, the Fourth Microquasars Workshop, 140, "Assessing the X-ray contribution from jets in X-ray binaries"
19. Kalemci, E., Tomsick, J. A., Rotschild, R. E., Pottschmidt, K., **Corbel, S.**, Wijnands, R., Miller, J. M., Kaaret, P., 2002, New Views on MICROQUASARS, the Fourth Microquasars Workshop, 81, "State transition of the new black hole transient XTE J1650-500"
20. Rodriguez, J., **Corbel, S.**, Kalemci, E., Tomsick, J. A., Tagger, M. 2002, New Views on MICROQUASARS, the Fourth Microquasars Workshop, 64, "Evolution of a low frequency QPO during the 2000 outburst of XTE J1550-564"
21. **Corbel, S.**, 2001, SF2A, EdP-Sciences, Conference Series, 353, "Black holes candidates in the Low-Hard state"
22. **Corbel, S.**, Kaaret, P., Jain, R. K., Bailyn, C. D., Fender, R. P., Tomsick, J. A., Kalemci, E., McIntyre, V., Campbell-Wilson, D., Miller, J. M., McCollough, M. L. 2001, AIP Conference Proceedings, 587, 126, "The Compact Jet of the Black Hole Candidate XTE J1550-564 during the 2000 X-ray Outburst"
23. Durouchoux, Ph., Sood, R., Oka, T., Segers, M., Safi-Harb, S., Vilhu, O., Huovelin, J., Thresher, D., **Corbel, S.**, O'Neill, P. 2000, Advances in Space Research, 25, 3-4, 703, "Jet Interaction of SS 433 With the Ambient Medium"
24. Durouchoux, Ph., Sood, R., Smith, I., **Corbel, S.**, Hannikainen, D., Loyer, R. 2000, Advances in Space Research, 25, 3-4, 765, "Millimeter Observations of the Candidate Soft Gamma-Ray Repeater SGR 1814-13"
25. **Corbel, S.** and Chapuis, C., 2000, Nuclear Physics B Proceedings Supplements, Vol. 80, 15/06, "The 1998 X-ray outburst of 4U 1608-52"
26. Chapuis, C., **Corbel, S.**, Durouchoux, P., Mahoney, W.A. and Gautier, T.N., 1999, ASP Conference Series, 159, 97 : "Near-infrared photometry of blazars"
27. Chapuis, C., **Corbel, S.**, Durouchoux, P., Mahoney, W.A. and Gautier, T.N., 1999, Astrophysical Letters and Communications : 3rd INTEGRAL Workshop Proceedings, 39, 73 : "Photometry of blazars in the near-infrared range"
28. Smith, I.A., Liang, E.P., Lin, D., Bottcher, M., Crider, A., Fillipenko, D.C., Leonard, R.C., Fender, R.P., Durouchoux, P., **Corbel, S.** and Sood, R.K., 1999, Astrophysical Letters and Communications : 3rd INTEGRAL Workshop Proceedings, 38, 265, "Observations of GX 339–4 in 1996"

29. Smith, I.A., Hurley, K., van Paradijs J., Waters, L.B.F.M., Schultz, A.S.B., Durouchoux, P., Joyce, R., Vrba, F.J., Hartmann, D., Kouveliotou, C., Wallyn, P. and **Corbel, S.**, 1998, Adv. Space Res., Vol. 22, No. 7, 1133 : "Infrared, submillimeter, and millimeter Observations of the Soft Gamma-Ray Repeaters

30. Mahoney, W.A., **Corbel, S.**, Durouchoux, P., Higdon, J.C., Gautier, T.N., Ressler, M.E. and Wallyn, P., 1998, AIP Conference Proceedings 428, 931 : "Mid-Infrared spectra of SGR 1806-20 and SGR 1900+14"

31. Smith, I.A., Hurley, K., Chermin L.M., Schultz, A.S.B., Waters, L.B.F.M., van Paradijs J., Kouveliotou, C., Vrba, F. J., Hartmann, D., Durouchoux, P., Wallyn, P. and **Corbel, S**, 1998, AIP Conference Proceedings 428 :"Infrared, submillimeter, and millimeter Observations of the Soft Gamma-Ray Repeaters"

32. Sood, R.K., Campbell - Wilson, D., Durouchoux, P., **Corbel, S.**, Fender, R.F., Spencer, R., Nowak, M.A. and Tzioumis, A., 1998, ASP Conference Series, 144, 349 : "Radio properties of the X-ray binary GX 339-4"

33. **Corbel, S.**, Cook, W.R., Harrison, F.A., Prince, T.A., Schindler S.M. and Wang, S., 1997, Proceedings 2nd INTEGRAL Workshop "The Transparent Universe", ESA SP-382, 217 : "Hard X-ray imaging survey of the Galactic plane with the Caltech Gamma Ray Imaging Payload GRIP-2"

34. Hannikainen, D., Durouchoux, P., Vilhu, O., Huovelin, J., **Corbel, S.** and Wallyn, P., 1997, Proceedings 2nd INTEGRAL Workshop "The Transparent Universe", ESA SP-382, 331 : "HCO^+ ionization from SGR 1806-20"

35. Wallyn P., Ling J.C., Mahoney, W.A., Wheaton, W.A., Durouchoux, P., **Corbel, S.**, Astier-Perret, L. and Poirot L.,1997, Proceedings 2nd INTEGRAL Workshop "The Transparent Universe", ESA SP-382, 109 "Measuring the 511 keV emission in the direction of 1E 1740.7-2942 with BATSE"

36. Durouchoux, P., Mahoney, W.A., Clenet, Y., Ling, J., Wallyn, P, Wheaton, W., **Corbel, S** and Chapuis, C., 1997, Proceedings 2nd INTEGRAL Workshop "The Transparent Universe", ESA SP-382, 137 : "Hard X-ray spectra of neutrons stars and black hole candidates"

37. Smith, I.A., Joyce, R., Schultz, A.S.B., Hurley, K., Vrba, F.J., Hartmann, D., Kouveliotou, C., van Paradijs J., Waters, L.B.F.M., Chermin L.M., Durouchoux, P., **Corbel, S.** and Wallyn, P., 1997, Proceedings 2nd INTEGRAL Workshop "The Transparent Universe", ESA SP-382, 191 "Infrared, submillimeter and millimeter observations of the Soft Gamma-Ray Repeaters"

38. **Corbel, S.**, Fender, R.F., Durouchoux, P., Sood, R.K., Tzioumis, A., Spencer, R. and Campbell - Wilson, D., 1997, AIP Conference Proceedings 410, 937 "Radio Observations of the Black Hole Candidate GX 339–4"

39. Smith, I.A., Liang E.P., Moss, M., Dobrinskaya, J., Fender, R.P., Durouchoux, P., **Corbel, S.**, Sood, R.K., Filippenko, A.V. and Leonard, D.C., 1997, AIP Conference Proceedings 410, 932 "Multiwavelength Observations of GX 339–4"

40. Mahoney, W.A., **Corbel, S.**, Durouchoux, W.A., Gautier, T.N., Higdon, J.C. and Wallyn, P., 1997, AIP Conference Proceedings 410, 912 "Near Infrared Observations of GRS 1915+105"

41. Wallyn, P., Mahoney, W.A., **Corbel, S.**, Cao, Y., Durouchoux, P., Vilhu, O., 1995, *Astr. & Space Sc.*, 231, 89 : "Millimeter and infrared observations of SGR 1806-20"

8.5.5 Séminaires et présentations orales dans des colloques :

1. "De l'importance des jets relativististes dans les microquasars", Institut d'Astrophysique de Paris, Février 2007.
2. "Relativistic Jets from black holes", Prix de la SF2A 2006, Paris, Juin 2006.
3. "High Energy emission from relativistic jets", Atelier PCHE (invité), Paris , Juin 2006.
4. "Relativistic jets and cosmic rays production", Workshop "SNR et superbulles (invité)", Paris, Juin 2005
5. "Jets relativistes et processus énergétiques autour des trous noirs", Observatoire de Grenoble, 25 novembre 2004
6. "Microquasars", Forum SAp, CEA Saclay, Juin 2004
7. "The relativistic jets of XTE J1550-564", GDR PCHE, Rencontre de la SF2A, Bordeaux, Juin 2003
8. "Jets relativistes et microquasars", SAp, CEA Saclay, 5 juin 2003
9. "Relativistic Jets from X-ray Binaries (Microquasars)", Harvard CfA Colloquium, Cambridge, USA , 3 avril 2003
10. "Discovery of relativistic X-ray jets in the microquasar XTE J1550-564", Journée APC "Trou noir accrétant", Novembre 2002
11. "Black hole candidates in the low-hard state", GDR PCHE, Rencontre de la SF2A, Lyon, Juin 2001
12. "" In the neighbourhood of Soft Gamma Repeaters", Joint CfA/MIT Seminar on Neutron Stars and Supernova Remnants, Cambridge, USA, 21 juin 2000
13. "Etude multi-longueur d'onde du candidat trou noir GX 339-4 : couplage accrétion-éjection.", Observatoire de Strasbourg, 28 Avril 2000
14. "Accretion – ejection in the black hole candidate GX 339–4", Conférence Rossi 2000, Greenbelt, USA, 24 mars 2000
15. "Étude multi-longueur d'onde du candidat trou noir GX 339–4", Université de Toulouse III, CESR, 18 novembre 1999
16. "Étude multi-longueur d'onde du candidat trou noir GX 339–4", Observatoire de Meudon, DAEC, 9 novembre 1999
17. "Multiples facettes des étoiles compactes : distance, extinction optique et comportement multi-longueur d'onde", Soutenance de thèse, CEA-Saclay, 12 octobre 1999
18. " A multi-wavelength study of the galactic black hole candidate GX 339–4", Amsterdam Astrophysics Colloquia, Astronomical Institute "Anton Pannekoek", 17 septembre 1999
19. "GX 339–4, une source à micro-jet", Forum SAp, CEA-Saclay, 12 février 1999
20. "Multiwavelength Observertions of the Black Hole Candidate GX 339–4", Second Workshop on Relativistic Jet Sources in the Galaxy, Paris, 12 décembre 1998
21. "The Soft Gamma Repeater SGR 1806–20", Marschall Space Flight Center, Huntsville, USA, 19 novembre 1997
22. "Le mystère des sursauts gamma", Fête de la science, CEA - Saclay, 12 octobre 1997
23. "La distance du Soft Gamma Repeater SGR 1806–20", DEMIRM, Ecole Normale Supérieure, Paris, 5 janvier 1996
24. "La distance du Soft Gamma Repeater SGR 1806–20", CEA - Saclay, 12 décembre 1995
25. "The Distance to the Soft Gamma Repeater SGR 1806-20", California Institute of Technology, Pasadena, USA, 5 décembre 1995

8.6 Activités de vulgarisation scientifique

8.6.1 Conférences de presse et impact médiatique

1. Première image en rayons X des jets de matière autour d'un trou noir de notre Galaxie (c.f. publication numéro 41 sur la liste).

   A cette occasion, deux conférences de presse ont été organisées : une (télévisée) au siège de la NASA à Washington (USA) et une au siège du CEA à Paris.
   • Dossier et communiqués de presse sur :
   - CEA et Université Paris 7 : http ://www-dapnia.cea.fr/Phys/Sap/Actualites/CORBEL/indexcorbel_fr.sht
   - NASA (USA) : http ://chandra.harvard.edu/press/02_releases/press_100302.html
   - ATNF (Australie) : http ://www.csiro.au/index.asp ?type=mediaRelease&id=Prblackhole
   • Articles de presse :
   - Le Monde : 18 octobre 2002
   - Ciel et Espace : décembre 2002
   - Science News : novembre 2002 (http ://www.sciencenews.org/20021109/bob9.asp)
   - New Scientist : 3 octobre 2002 (http ://www.newscientist.com/news/news.jsp ?id=ns99992880)
   - CNN : http ://www.cnn.com/2002/TECH/space/10/03/black.holes/index.html
   • Impact divers (sélection) :
   - http ://chandra.harvard.edu/chronicle/0303/top_ten/index.html (découverte classée parmi les dix plus importantes de Chandra pour l'année 2002-2003,
   voir aussi : http ://www.space.com/scienceastronomy/chandra_top_10_030902-5.html).
   - Space.com : http ://www.space.com/scienceastronomy/black_hole_011003.html
   - Astronomy.com : http ://www.astronomy.com/Content/Dynamic/Articles/000/000/001/049ouxmh.asp
   - Chandra : http ://chandra.harvard.edu/photo/2002/xtej1550/index.html
   - Imagine the Universe : http ://imagine.gsfc.nasa.gov/docs/features/news/13nov02.html
   - SpaceFlight.com : http ://spaceflightnow.com/news/n0210/03chandra/

2. LBV 1806-20 : l'étoile la plus massive de notre Galaxie ? (c.f. publication numéro 25 et 26)

   • Dossier et communiqué de presse sur :
   - American Astronomical Society (le 5/1/2004) : (communiqué non disponible en ligne)
   - University of Florida : http ://www.napa.ufl.edu/2004news/bigbrightstar.htm
   • Articles de presse (sélection) :
   - International Herald Tribune (6/01/2004) : http ://www.iht.com/articles/123850.html
   - BBC News (13/01/2004) : http ://news.bbc.co.uk/1/hi/sci/tech/3393161.stm
   - The Atlanta Journal Constitution (6/01/2004) :
   http ://www.ajc.com/news/content/news/science/0104/06star.html
   - The Times of India : http ://timesofindia.indiatimes.com/articleshow/408307.cms
   • Impact divers :
   - Space.com : http ://www.space.com/scienceastronomy/brightest_star_040106-1.html
   - Astronomy.com : http ://www.astronomy.com/Content/Dynamic/Articles/000/000/001/630qknci.asp

3. Découverte de sources X obscurcies. (c.f. publication numéro 30)

   • Dossier et communiqué de presse sur :
   - CEA : http ://www-dapnia.cea.fr/Phys/Sap/Actualites/INTEGRAL/indexintegral0212_fr.shtml

- Agence Spatiale Européenne (ESA) : http ://www.esa.int/sci_mediacentre/release2003.html ?release=47

• Articles de presse :
- Le Figaro : samedi 1 novembre 2003

• Impact divers :
- Courier du Cern : http ://www.cerncourier.com/main/article/43/10/17
- SpaceRef.com : http ://www.spaceref.com/news/viewpr.html ?pid=12806
- Spaceflight.com : http ://spaceflightnow.com/news/n0310/18blackholes/

4. Une source-X ultra-lumineuse identifiée : le premier microquasar extra-galactique ? (c.f. publication numéro 37)
   Dossier sur : http ://www-dapnia.cea.fr/Phys/Sap/Actualites/Breves/corbel030122/corbel030122_fr.shtm

5. Divers :
   Commentaires sur les résultats WMAP sur le fond diffus cosmologique : Le monde : 15 février 2003
   Commentaires sur les sources X ultralumineuses : Le Figaro : 19 mai 2007